

博士論文

**Experimental and Numerical Analyses of Soil
Arching and Stability Mechanism under Trapdoor
and Underground Cavity Conditions**

(地盤内の空洞生成や落とし戸模型実験におけるアーチ
効果に関する実験及び解析的検討)

Syed Umair Ali Naqvi

サイエド ウマイル アリ ナクイ

A dissertation submitted in partial fulfillment of the requirements for the degree
of

Doctor of Philosophy

2020年03月

Department of Civil Engineering

The University of Tokyo

Japan

ABSTRACT

Soil arching is one of the widely found natural phenomena in granular materials. Arching action initiates in the soil in the case when a certain part of soil mass yields relative to the surrounding static mass. As a preventive measure to collapse, soil particles rearrange to form an arch to transmit the forces above yielding mass to the rigid mass on the sides. Soil arching can be well observed in two major phenomena: namely trapdoor and underground cavities. Trapdoor condition is constituted for a small yielding of soil mass, whereas the underground cavity condition is followed when a large soil yielding is encountered.

Past researchers have tried to explain the arching phenomenon and corresponding stress increment/decrements, focusing on the settling portion of the soil mass. The aim of the current work is to quantify the stress increment under different configurations of the trapdoor. Furthermore, the effects of basic parameters, e.g. density, particle size, and particle shape need to be explored in detail. Also, there is a need to assess the presence and absence of soil arching for practical purposes. Experimental results can show the macro behavior and force distributions. However, how the particles interact once the soil yielding initiates, can only be observed through numerical simulations. Subsequently, a detailed full-scale numerical analysis can validate not only the experimental results but also show insight into the arching mechanism.

In the case of arching under cavity conditions, there is a lack of research on a suitable numerical model to performed microanalyses. The aim is to develop a basic model that can result in the particulate level study of the cavity formation. Experimental tests for cavity formation and loading are performed on various glass beads; as the glass beads, material properties and shapes can be easily considered in numerical simulations as well.

The stress increment due to soil arching largely depends upon the sample density, shape and soil height. The stress concentration factor (α), that quantifies the increase in stress due to trapdoor condition, was found to be independent of the particle size effect for the peak values, depending on the particle shape and density. However, the residual value of α was observed to be independent of shape parameters and size for the given range. Shear stress distribution was observed to be a key factor, that can assess the absence or presence of the arching in the soil mass. Similarly, the trapdoor configuration showed a striking effect on the arching mechanism and α values, in case the length of lowering region is increased. However, increasing the central fixed portion does not affect the arching behavior significantly. An empirical relation was developed to quantify the stress concentration for various trapdoor configurations.

A capillary force-based contact model was developed and incorporated in the DEM simulations and the cavity simulations were performed with different particle sizes, shape, and cavity dimensions. The results were compared with the model cavity stability tests using several glass beads types and the comparison was observed to have a matching trend. For the surface loading tests above the cavity, the loading rate dependency was observed for the unsaturated or saturated samples, both in experiments and simulations. Similarly, both approaches showed that the loading plate width does not impart a significant difference in overall load-settlement plots. Both experiments and numerical simulations showed a convergent behavior with varying loading rates with dry samples. The effects of rupture distance on the load-settlement relation were also noted numerically, and a more brittle behavior was observed with a smaller rupture distance. A decreasing loading rate showed a reducing gap between the peak stresses for different rupture distances. Overall, in the case of the cavity model tests and numerical simulations, the cavity stability chart under different cavity sizes was found to follow the field in-practice stability chart.

The arching observed in the case of the cavity tests was found to be similar to that of trapdoor tests. Once a stable sample is formed in cavity or trapdoor tests, particles rotated and rearranged to form strong contact force chains around the yielding mass. In the case of the trapdoor, the arch shape was observed to form half ellipse shape; whereas the cavity tests showed arch shape extending from the half ellipse and approaching to a full ellipse shape, as the yielding mass in case of the cavity tests is much larger compared to the trapdoor tests. The arching mechanism was explored and found that during the arch propagation, particles rotate and form new contact chains, that results in a contact fabric variation to match the arch propagation. Particle rotation plots and 2nd order contact fabric plots validated this phenomenon. The width of the arching region was found to be dependent upon particle shape. Spherical particles showed a wider strip of the arching region compared to non-spherical particles. Overall, the essence of the arching in both cases was observed to be similar in nature, stabilizing the yielding soil by transferring the loads to the surroundings. Soil arching thus can be termed as the ‘self-defense mechanism’ of soil against yielding to stabilize itself.

DEDICATION

Dedicated to

My Late Father

Who would have been the happiest person to see me achieving this goal

My Mother

Who prays for me in every moment of my life

And

My Wife

her continuous support and encouragement, along with managing the house and the kids,
empowered me to accomplish my objectives

and lastly, my kids

*Rushda, Nabeeha &
Zainab*

Their innocent smiles always made me smile as well

ACKNOWLEDGMENT

All prayers to my Lord, for enabling me to accomplish this goal with great honor and for creating in me a sense of responsibility and determination.

I would like to express my deep gratitude and respect for my supervisor, Professor Reiko Kuwano. Her continuous support gave me the inspiration to do my best. It was not possible to achieve this target without her precious counseling and comments. She was there to help me anytime I asked and never minded even if I made some mistake or asked basic questions.

I am also grateful to my committee members, Prof. Junichi Koseki, Prof. Kenji Watanabe, Prof. Takashi Kiyota from the University of Tokyo, and Prof. Mamoru Kikumoto from Yokohama National University. Their kind support and pieces of advice were a source of guidance throughout the academic period.

I am particularly thankful for the continuous support and guidance of Dr. Masahide Otsubo during my degree. He indeed stood by me throughout the period and was there for the help any time I required so. I learned a great lot of things from him during my stay.

Mr. Takeshi Sato is another person whom I want to thank due to his technical support about equipment and apparatus for my lab testing. His ever-willing attitude to support the students is matchless. Besides him, the kind moral support from Ms. Ryoko Sera was always there with me. The support of Lab secretary, Ms. Satoko Kichibayashi made my life much easier in both, university and for my stay in Japan. Also, the kind attitude of lab technician Mr. Makoto Kuno is admiring.

I was lucky to have such a great gathering of supportive lab members. They were the source of inspiration and joy in the hectic study life. Especially Dr. Troyee and my tutor Mr. Itsuki, along with Dr. Dayani. All other members, Mr. Ohara, Mr. Kominami, Ms. Hotta, Mr. Nakata, Mr. Tingshen, Mr. Kawaguchi, Mr. Zhou, Mr. Arian, Mr. Hirano, Mr. Taguchi, Mr. Karasaki, Mr. Junming, Ms. Hiroshima, Ms. Beatrice, Mr. Sanjei, and Mr. Yang; all helped me in different occasions during my stay here.

Last but not least, I would extend my heartiest gratitude to the Japan Ministry of Education, Culture, Sports, Science, and Technology (MEXT) scholarship program, which enabled me to attain my desire for a terminal degree from a world reputed organization.

Table of Contents

ABSTRACT	II
DEDICATION	IV
ACKNOWLEDGMENT	V
LIST OF FIGURES	XIII
LIST OF TABLES.....	XXIX
LIST OF ABBREVIATIONS.....	XXXI
CHAPTER 1: INTRODUCTION	1
1.1 GENERAL	1
1.2 WHAT IS SOIL ARCHING?.....	2
1.2.1 Active arching:.....	2
1.2.2 Passive Arching:	2
1.3 BACKGROUND OF THE ARCHING PHENOMENON.....	3
1.4 SOIL ARCHING IN MAJOR GEOTECHNICAL PHENOMENA	4
1.4.1 Trapdoor condition:	4
1.4.2 Underground cavity condition	4
1.5 SOIL ARCHING: BENEFICIAL OR DETRIMENTAL	7
1.6 DISCRETE ELEMENT METHOD.....	8
1.6.1 Advantages of Using DEM.....	8
1.7 PROBLEM STATEMENT AND THE OBJECTIVE OF THE RESEARCH	9
1.8 THESIS ORGANIZATION	11
CHAPTER 2: LITERATURE REVIEW	14
2.1 TRAPDOOR PROBLEM	14
2.1.1 Active and passive trapdoor cases	14
2.1.2 Physical experiments under trapdoor conditions	14
2.1.3 Effect of soil cover.....	16
2.1.4 Trapdoor configuration effect.....	16
2.1.5 Effect of material density.....	17
2.1.6 The shape of the arch	18
2.1.7 The magnitude of the trapdoor movement.....	18
2.2 UNDERGROUND CAVITIES PHENOMENON	19
2.2.1 Model tests for cavities caused by buried pipelines.....	20

2.2.2	Model tests for the stability of developing cavities	20
2.2.3	Effect of soil density on cavity stability	21
2.2.4	Effect of crack width on cavity development	21
2.3	CAPILLARY FORCES AND CAVITY	22
2.4	NUMERICAL SIMULATIONS FOR THE UNDERGROUND CAVITIES	22
2.5	NUMERICAL MODELS FOR CAPILLARY FORCES	23
2.6	DISCRETE ELEMENT METHOD (DEM)	24
2.6.1	Calculation sequence in DEM	24
2.6.2	Governing Equation of DEM.....	26
2.6.3	Dynamic Equilibrium Equation:	26
2.6.3.1	Implicit Approach:.....	26
2.6.3.2	Explicit Approach:.....	27
2.6.4	Contact models in DEM.....	27
2.6.4.1	Normal Contact	27
2.6.4.2	Tangential Contact.....	28
2.7	IMPORTANT PARAMETERS IN DEM	29
2.7.1	Inter-particle friction coefficient.....	29
2.7.2	Particle shape	29
2.7.3	Coordination number	30
2.7.4	Damping.....	31
2.7.5	Timestep in DEM simulations	32
CHAPTER 3: EXPERIMENTAL & NUMERICAL SETUP FOR TRAPDOOR		34
3.1	EXPERIMENTAL SETUP FOR TRAPDOOR TESTS	34
3.1.1	Trapdoor movement mechanism.....	37
3.1.2	Calibration Factors for load cells	38
3.1.3	Calibration for motor speed	46
3.1.4	Material description	47
3.1.5	Trapdoor testing program	50
3.1.6	Sample ground preparation	51
3.2	NUMERICAL SIMULATION PLAN USING DEM	52
3.2.1	Hardware used for numerical simulations	52
3.2.2	Software for numerical simulations	54
3.2.3	Contact model	54

3.2.4	Particle shapes and particle size distribution	54
3.2.5	Model space for DEM simulations and boundary conditions.....	55
3.2.6	Pluviation of sample	57
3.2.7	Lowering of base plates and input parameters.....	57
3.2.8	Simulation plan	58
CHAPTER 4: STRESS DISTRIBUTION IN TRAPDOOR TESTS: EXPERIMENTAL & NUMERICAL ANALYSES		60
4.1	INITIAL NORMAL AND SHEAR STRESS DISTRIBUTION	60
4.2	PEAK NORMAL STRESS DISTRIBUTION FOR TOYOURA SAND	61
4.2.1	Dense Toyoura sand.....	61
4.2.2	Loose Toyoura sand.....	63
4.3	NORMAL STRESS DISTRIBUTION FOR KASHIMA RIVER SAND	63
4.4	NORMAL STRESS DISTRIBUTION FOR SPHERICAL GLASS BEADS.....	64
4.5	NORMALIZED NORMAL STRESSES UNDER DEM NUMERICAL SIMULATIONS	65
4.5.1	Validation of using periodic boundary in DEM simulations.....	65
4.5.2	Validation of using half-width samples	69
4.5.3	Normalized normal stress distribution in DEM simulations.....	72
4.6	GENERAL MECHANISM OF NORMALIZED STRESS DISTRIBUTION TREND	75
4.7	STRESS CONCENTRATION ON THE CENTRAL BASE PLATE ‘A’	76
4.8	SHEAR STRESS DISTRIBUTION DURING TRAPDOOR CONDITION	82
4.9	ARCH VALIDATION USING SHEAR STRESS DISTRIBUTION PATTERN	86
CHAPTER 5: PARTICLE SCALE ANALYSES OF SOIL ARCHING IN TRAPDOOR TESTS.....		91
5.1	SOIL ARCHING AND DIFFERENTIAL SURFACE SETTLEMENT.....	91
5.1.1	Experimental analyses	91
5.1.2	Numerical analyses	98
5.2	VERTICAL DISPLACEMENT OF PARTICLES	100
5.3	STRONG FORCE NETWORK FOR ARCH ANALYSES	104
5.3.1	Comparison between spherical and non-spherical particle results	107
5.4	CONTACT FABRIC ANALYSES	110
5.4.1	Selection of sample and size of analysis subsets	110
5.4.2	Contact Fabric for larger H/B	113

5.4.3	Contact fabric for smaller H/B	121
5.5	PARTICLE ROTATION DURING THE ARCH FORMATION	124
5.5.1	Sample preparation and calculation sequence	125
5.5.2	Particle rotation using subsets.....	127
5.5.3	The rotation at the particulate level	133
5.5.4	Rotation analysis for spherical particles	135
CHAPTER 6: TRAPDOOR CONFIGURATION EFFECT		141
6.1	TRAPDOOR CONFIGURATION: MODEL TESTS AND DEM SIMULATIONS.....	141
6.1.1	Model test configuration variation.....	143
6.1.2	Configuration variation in DEM simulations:	143
6.1.3	Sample Pluviation	146
6.2	THEORETICAL MAXIMUM STRESS CONCENTRATION FACTOR ON THE CENTRAL FIXED PLATE.....	149
6.3	TRAPDOOR SIMULATIONS.....	150
6.3.1	Trapdoor configuration with three base plates.....	150
6.3.2	Trapdoor configuration with five base plates	157
6.3.3	Trapdoor configuration with seven base plates	162
6.3.4	Trapdoor configuration with nine base plates.....	167
6.4	COMPARISON OF DIFFERENT TRAPDOOR CONFIGURATIONS	171
6.5	CONVERGED RESPONSE OF TRAPDOOR CONDITION UNDER ANY SYMMETRIC CONFIGURATION	176
6.5.1	An empirical assessment of stress concentration.....	176
6.5.1.1	The shape of the arch.....	176
6.5.1.2	The equation for the arch shape.....	177
6.5.1.3	Load distribution calculations using Ellipse shape.....	180
6.6	EFFECT OF VARYING STATIC PLATE WIDTH	192
6.6.1	Stress response	193
6.6.2	Stress concentration factor ' α '	195
6.6.3	Particle vertical displacement plots	197
6.7	SUMMARY.....	201
CHAPTER 7: SOIL ARCHING AROUND CAVITIES & NECESSITY OF CAPILARRY FORCES.....		202
7.1	UNDERGROUND CAVITIES AND SOIL ARCHING.....	202

7.1.1	Formation of underground cavities in dry conditions.....	203
7.1.2	DEM cavity simulations in dry conditions	206
7.1.3	Necessity of water (capillary) forces	207
7.2	DEM MODEL MODIFICATION.....	208
7.2.1	Constituents of capillary forces	208
7.2.1.1	Surface tension:	209
7.2.1.2	Matric suction.....	210
7.2.2	Conditions of inter-particle capillary forces	212
7.2.3	DEM model with inter-particle suction as an input parameter	214
7.2.3.1	When $D \leq 0$:	217
7.2.3.2	When $0 \leq D \leq D_r$	219
7.2.3.3	When $D \geq D_{rup}$	219
7.2.4	DEM model with a degree of saturation as an input parameter.....	219
7.2.4.1	Initial debugging:.....	225
7.3	CAPILLARY FORCE MODEL VALIDATION.....	226
7.4	SUMMARY.....	231
CHAPTER 8: EXPERIMENTAL AND NUMERICAL SETUP FOR CAVITY TEST		
CONDITIONS		232
8.1	EXPERIMENTAL SETUP FOR MODEL CAVITY TESTS	232
8.1.1	Basic construction.....	232
8.1.2	Working mechanism	234
8.2	MATERIALS.....	235
8.2.1	Spherical glass beads	235
8.2.2	Rough and smooth surface particles	237
8.2.3	Deformed and clumped glass beads.....	239
8.3	EXPERIMENTAL TESTING PLAN.....	240
8.3.1	Cavity stability tests.....	240
8.3.2	Cavity surface loading tests	244
8.3.2.1	Types of the loading plate	250
8.4	NUMERICAL SIMULATION PLAN FOR CAVITY STABILITY ANALYSES	255
8.4.1	Simulation plan using Suction as input.....	257
8.4.2	Simulation plan using the degree of saturation as input	257
8.4.3	Simulation plan using a variable degree of saturation	263
8.4.4	Increase in the self-weight of particles due to saturation:.....	264

8.5	SIMULATION PLAN FOR CAVITY SURFACE LOADING	264
8.5.1	Loading rate comparison.....	265
8.6	SUMMARY.....	267
CHAPTER 9: CAVITY STABILITY ANALYSES.....		268
9.1	MODEL TESTS ON CAVITY STABILITY	268
9.1.1	Material description	268
9.1.2	Effect of particle size	269
9.1.3	Effect of surface roughness.....	274
9.1.4	Effect of initial water level	275
9.1.5	Effect of sample density.....	277
9.1.6	Effect of particle shape	278
9.2	EXPERIMENTAL COMPARISON WITH CAVITY STABILITY CHART.....	280
9.3	NUMERICAL ANALYSES OF THE CAVITY STABILITY USING SUCTION-TENSION MODEL	282
9.3.1	Numerical simulations with inter-particle suction as an input parameter.....	282
9.3.1.1	Particle size effect.....	283
9.3.2	Numerical simulations with a degree of saturation as an input parameter	286
9.3.2.1	Small-sized sample.....	287
	Sample saturation effect.....	287
	Particle size effect with non-spherical particles.....	288
	Contact fabric distribution around arching	289
9.3.3	Cavity stability simulations using a large sample size – 1.0mm particle size ...	293
9.3.3.1	Effect of cavity size on stability	295
9.3.4	Cavity stability simulations with 0.5mm mean particle size	304
9.3.4.1	Cavity dimension effect on stress variation.....	304
9.3.4.2	Cavity stability and kinetic energy variation.....	309
9.3.4.3	Force distribution under extreme shapes of cavities.....	313
9.3.5	Cavity stability simulations using variable saturation and weight of the water	317
9.3.5.1	Using R2 particles with 0.5mm mean size	317
9.3.5.2	Using R3 particles with 1.0mm diameter	320
9.4	SUMMARY.....	324
CHAPTER 10: EXPERIMENTAL AND NUMERICAL ANALYSES OF CAVITY SURFACE LOADING		325
10.1	EXPERIMENTAL ANALYSES OF CAVITY SURFACE LOADING.....	325

10.1.1	Effect of surface roughness.....	325
10.1.2	Effect of surface loading rate on cavity stability using spherical particles....	327
10.1.3	Effect of surface loading rate on cavity stability using deformed particles...	330
10.1.4	Effect of surface loading rate on cavity stability using clumped particles	333
10.1.5	Effect of plate width for the surface loading	337
10.2	MODEL SURFACE LOADING TESTS WITHOUT CAVITY	340
10.2.1	Combination of fully saturated and partially saturated sample	340
10.2.2	Surface loading on dry conditions	342
10.2.3	Surface loading tests for fully saturated samples.....	343
10.2.4	Surface loading tests with unsaturated condition.....	345
10.3	NUMERICAL ANALYSES OF CAVITY SURFACE LOADING	347
10.3.1	Effect of loading plate width.....	347
10.3.2	Effect of loading rate in numerical simulations	349
10.3.2.1	Simulations with a base cavity & uniform saturation level.....	349
10.3.2.2	Surface loading without base cavity for uniformly saturated conditions	355
10.3.2.3	Surface loading without the capillary forces	356
10.3.3	Effect of rupture distance between particles	357
10.4	SUMMARY.....	359
CHAPTER 11: CONCLUSIONS AND RECOMMENDATIONS		360
11.1	OVERALL SUMMARY.....	360
11.2	MAIN FINDINGS.....	362
11.2.1	Normal stress distribution under trapdoor conditions.....	362
11.2.2	Shear stress distribution under trapdoor conditions.....	364
11.2.3	Trapdoor configuration effect	364
11.2.4	Particulate level analyses of soil arching	365
11.2.5	Use of periodic boundaries	365
11.2.6	Model cavity stability tests	366
11.2.7	Numerical simulations on cavity stability.....	366
11.2.8	Cavity surface loading	367
11.2.9	Capillary force model	368
11.2.10	Soil arching under cavity conditions.....	369
11.3	RECOMMENDATIONS.....	369
REFERENCES		357

LIST OF FIGURES

<i>Figure 1. 1: Earth pressure distribution on a buried structure when (a) both soil and structure have same stiffness, (b) when a buried structure is stiffer and (c) when soil is stiffer</i>	3
<i>Figure 1.2 Trapdoor configuration used by Terzaghi (1936)</i>	6
<i>Figure 1.3 Arch around underground cavity and cavity expansion process to result in a cave-in</i>	6
<i>Figure 2. 1 Schematic diagram for calculation sequence in DEM</i>	25
<i>Figure 3. 1 Trapdoor model test apparatus</i>	35
<i>Figure 3.2 Schematic figure of soil chamber in model trapdoor test</i>	36
<i>Figure 3.3 Schematic diagram of base loading system of trapdoor apparatus</i>	37
<i>Figure 3.4 Resultant position of base plates for the trapdoor tests</i>	38
<i>Figure 3.5 Front view of load cell numbering in trapdoor model tests</i>	38
<i>Figure 3.6 Calibration curves for Load cells 1 to 4</i>	40
<i>Figure 3.7 Calibration curves for Load cells 5 to 8</i>	41
<i>Figure 3.8 Calibration curves for Load cells 9 to 12</i>	42
<i>Figure 3.9 Calibration curves for Load cells 13 to 16</i>	43
<i>Figure 3.10 Calibration curves for Load cells 17 to 20</i>	44
<i>Figure 3.11 Calibration curves for Load cells 21 to 24</i>	45
<i>Figure 3.12 Calibration curves for Load cell 25</i>	46
<i>Figure 3.13 Calibration curve for motor speed</i>	47
<i>Figure 3.14 SEM images of (a) Toyoura sand, (b) Kashima river sand and (c) spherical glass beads</i>	49
<i>Figure 3.15 Camera images of the (a) Toyoura sand, (b) Kashima river sand and (c) spherical glass beads</i>	50
<i>Figure 3.16 Oakforest-PACS supercomputer</i>	53

<i>Figure 3.17 shape of (a) non-spherical and (b) spherical particles modeled in numerical simulations</i>	<i>54</i>
<i>Figure 3.18 Particle size distribution for Spherical and non-spherical particles.....</i>	<i>55</i>
<i>Figure 3.19 Approximate arching region in trapdoor model test configuration.....</i>	<i>56</i>
<i>Figure 3.20 Model space in DEM simulations</i>	<i>57</i>
<i>Figure 4.1 Normal stress distribution in trapdoor at (a) initial and (b) final condition.....</i>	<i>61</i>
<i>Figure 4.2 Normalized normal stress for dense Toyoura sand samples under different soil heights.....</i>	<i>62</i>
<i>Figure 4.3 Normalized normal stress for loose Toyoura sand samples under different soil heights.....</i>	<i>63</i>
<i>Figure 4.4 Normalized normal stress for Kashima river sand samples under different soil heights.....</i>	<i>64</i>
<i>Figure 4.5 Normalized normal stress for spherical glass beads samples under different soil heights.....</i>	<i>65</i>
<i>Figure 4.6 Model trapdoor test configuration and DEM model space used in simulations ...</i>	<i>66</i>
<i>Figure 4.7 DEM simulation space for (a) configuration similar to model trapdoor tests and (b) configuration with central three base plates with periodic boundaries.....</i>	<i>67</i>
<i>Figure 4.8 Vertical displacement of particles for (a) sample with lateral rigid boundary and (b) sample with periodic boundary.....</i>	<i>68</i>
<i>Figure 4.9 Comparison of normalized vertical stress ratio for samples with a rigid wall (fixed) and periodic lateral boundaries ($H/B = 4.0$).</i>	<i>69</i>
<i>Figure 4.10 Comparison of Model trapdoor test base plate width with full scale and half scale DEM simulations</i>	<i>70</i>
<i>Figure 4.11 Comparison of Normalized normal stress distribution for (a) full width and (b) half width DEM simulations</i>	<i>71</i>
<i>Figure 4.12 Comparison of full scale and half scale DEM simulations with varying H/B values against peak alpha value, using spherical particles.....</i>	<i>72</i>

<i>Figure 4.13 Normalized normal stress distribution for DEM simulations (a) spherical particles (b) non-spherical particles at trapdoor displacement, $\delta = 0.25\text{mm}$.....</i>	<i>73</i>
<i>Figure 4.14 Approximate regions contributing to normal stress distribution at the base of the sample in the presence of the arching.....</i>	<i>75</i>
<i>Figure 4. 15 ‘α’ variation with trapdoor settlement ‘δ’ for (a) dense Toyoura sand, (b) Kashima river sand and (c) spherical glass beads</i>	<i>77</i>
<i>Figure 4.16 α variation on the central fixed plate for DEM simulations using spherical and non-spherical particles</i>	<i>78</i>
<i>Figure 4.17 Post peak softening in α as observed in (a) model trapdoor test at H/B: 1.0 and (b) DEM simulation with H/B: 0.87 for spherical particles</i>	<i>79</i>
<i>Figure 4.18 Experimental data for variation in α with trapdoor movement δ for Toyoura sand (dense and loose), Kashima river sand and glass beads with $H = 400\text{ mm}$ ($H/B = 4.0$) and $H = 100\text{ mm}$ ($H/B = 1.0$)</i>	<i>80</i>
<i>Figure 4.19 (a) Peak value of stress concentration (α_{peak}) against H/B for all cases and (b) the residual value of stress concentration (α_{residual}) for model tests.</i>	<i>81</i>
<i>Figure 4.20 Peak shear stress distribution for model trapdoor tests on Toyoura sand with (a) dense and (b) loose samples</i>	<i>83</i>
<i>Figure 4.21 Peak shear stress distribution for Kashima river sand for different sample heights.....</i>	<i>84</i>
<i>Figure 4.22 Peak shear stress distribution for Spherical glass beads under different sample heights.....</i>	<i>85</i>
<i>Figure 4.23 Combined peak shear stress distribution for Toyoura sand dense, Kashima river sand and spherical glass beads under H/B of 1.0 and 4.0.....</i>	<i>85</i>
<i>Figure 4.24 Portion of shear stress distribution considered for analyses.....</i>	<i>86</i>
<i>Figure 4.25 Peak shear stresses for all tested materials on the right-half portion of samples under varying H/B values</i>	<i>87</i>
<i>Figure 4.26 Direction nomenclature of shear force under trapdoor condition</i>	<i>88</i>
<i>Figure 4.27 Particle movement vector for (a) H/B: 4.35 and (b) H/B: 0.87 using DEM simulations on spherical particles</i>	<i>89</i>

<i>Figure 5.1 Trapdoor test on Kashima river sand for $H/B = 1.0$ at (a) initial condition and (b) final condition.....</i>	<i>91</i>
<i>Figure 5.2 Trapdoor test on Kashima river sand for $H/B = 2.0$ at (a) initial condition and (b) final condition.....</i>	<i>92</i>
<i>Figure 5.3 Trapdoor test on Kashima river sand for $H/B = 3.0$ at (a) initial condition and (b) final condition.....</i>	<i>92</i>
<i>Figure 5.4 Trapdoor test on Kashima river sand for $H/B = 4.0$ at (a) initial condition and (b) final condition.....</i>	<i>92</i>
<i>Figure 5.5 Trapdoor test on spherical glass beads for $H/B = 1.0$ at (a) initial condition and (b) final condition</i>	<i>93</i>
<i>Figure 5.6 Trapdoor test on spherical glass beads for $H/B = 2.0$ at (a) initial condition and (b) final condition</i>	<i>93</i>
<i>Figure 5.7 Trapdoor test on spherical glass beads for $H/B = 3.0$ at (a) initial condition and (b) final condition</i>	<i>94</i>
<i>Figure 5.8 Trapdoor test on spherical glass beads for $H/B = 4.0$ at (a) initial condition and (b) final condition</i>	<i>94</i>
<i>Figure 5.9 Differential surface settlement and the arching pattern for all tested materials under H/B of 2.0 and 4.0 in model trapdoor tests</i>	<i>95</i>
<i>Figure 5.10 Location of laser displacement sensors installed in model trapdoor tests</i>	<i>96</i>
<i>Figure 5.11 Normalized surface settlement data with varying H/B values for Kashima river sand and spherical glass beads.....</i>	<i>97</i>
<i>Figure 5.12 Location of the regions at the ground surface for surface settlement analyses...</i>	<i>98</i>
<i>Figure 5.13 Normalized surface settlement data with varying H/B values for DEM simulations using spherical and non-spherical particles</i>	<i>99</i>
<i>Figure 5.14 Vertical movement of particles in DEM simulations using spherical particles.</i>	<i>101</i>
<i>Figure 5.15 Vertical movement of particles in DEM simulations using non-spherical particles</i>	<i>103</i>

<i>Figure 5.16 Strong force distribution for DEM simulations using spherical particles at the initial and final stages for different H/B values.....</i>	<i>107</i>
<i>Figure 5.17 Strong force distribution network for non-spherical particles in DEM simulations under different H/B values.....</i>	<i>108</i>
<i>Figure 5.18 Strong contact force diagrams in DEM simulations (a) spherical particles for H/B = 0.87 (b) non-spherical particles for H/B = 0.87 (c) spherical particles for H/B = 4.35 and (d) non-spherical particles for H/B = 4.40 at $\delta = 0.25\text{mm}$</i>	<i>109</i>
<i>Figure 5.19 Subset size variation to select the minimum size possible</i>	<i>112</i>
<i>Figure 5.20 2nd order contact fabric and number of atoms in each size, plotted against the sample dimension.....</i>	<i>113</i>
<i>Figure 5.21 Configuration of subsets for the evaluation of 2nd order contact fabric, for an H/B = 4.35 using spherical particles.....</i>	<i>114</i>
<i>Figure 5.22 2nd order contact fabric distribution in a sample with H/B = 4.35 having spherical particles with (a) being the bottom most layer and the (g) being the top most layer</i>	<i>118</i>
<i>Figure 5.23: 2nd order contact fabric distribution for different layers in a sample, represented along with a vertical displacement diagram of DEM sample with H/B = 4.35.</i>	<i>120</i>
<i>Figure 5.24 2nd order contact fabric values for with H/B = 0.87 having spherical particles at (a) bottom layer and (b) at top of the sample</i>	<i>122</i>
<i>Figure 5.25 2nd order contact fabric distribution for H/B = 0.87 along with similar DEM simulation showing vertical displacement and strong contact forces plot.....</i>	<i>123</i>
<i>Figure 5.26 Configuration of subset distribution for particle rotation calculation for H/B = 4.35 in DEM simulation space.....</i>	<i>125</i>
<i>Figure 5.27 Particle rotation calculation sequence in DEM simulations using non-spherical particles.....</i>	<i>126</i>
<i>Figure 5.28 (a) Approximate configuration of a subset with a group of particles within, under trapdoor lowering and (b) enlarged subset at the initial and final stage of the simulation..</i>	<i>128</i>
<i>Figure 5.29 Particle rotation magnitude in each subset of DEM simulation with H/B = 4.35 having non-spherical particles</i>	<i>129</i>

<i>Figure 5.30 Particle rotation magnitude in each subset of DEM simulation with $H/B = 0.87$ having non-spherical particles</i>	<i>130</i>
<i>Figure 5.31 Rose plot for particle orientation with (a) location of subset numbers, (b) orientation after simulation and (c) before simulation.....</i>	<i>132</i>
<i>Figure 5.32 Particle rotation diagram for DEM simulation with non-spherical particles having $H/B = 4.35$</i>	<i>133</i>
<i>Figure 5.33 Gearing action between neighboring particles to cause opposite rotation</i>	<i>134</i>
<i>Figure 5.34 change in orientation of (a) non-spherical particle and (b) spherical particles in case of absence of translation motion.....</i>	<i>135</i>
<i>Figure 5.35 Plot for (a) angular velocity and (b) particle rotation with non-spherical particles having $H/B = 4.35$.....</i>	<i>137</i>
<i>Figure 5.36 Angular velocity plot for DEM simulation with spherical particles under $H/B = 4.35$.....</i>	<i>138</i>
<i>Figure 5.37 Angular velocity plot for spherical (on left) and non-spherical (on right) particles for $H/B = 4.35$.....</i>	<i>139</i>
 <i>Figure 6.1 Trapdoor configurations used in (a) model trapdoor equipment and (b) DEM simulation.....</i>	 <i>141</i>
<i>Figure 6.2 (a) Arching as obtained in model trapdoor tests and (b) half arch produced in DEM simulations with lateral periodic boundaries.....</i>	<i>142</i>
<i>Figure 6.3 Trapdoor configurations in DEM simulations using spherical particles with (a) $L/B = 3.0$, (b) $L/B = 5.0$, (c) $L/B = 7.0$, and (d) $L/B = 9.0$.....</i>	<i>144</i>
<i>Figure 6.4 Dimension nomenclature in trapdoor configuration effect simulations</i>	<i>148</i>
<i>Figure 6.5 Vertical displacement plots for trapdoor configuration with three base plates, for varying sample heights</i>	<i>151</i>
<i>Figure 6.6 Strong force (normalized) plots for trapdoor configuration with three base plates, for varying sample heights.....</i>	<i>152</i>
<i>Figure 6.7 Normal stress distribution of trapdoor cases with varying sample height with an $L/B = 3.0$</i>	<i>154</i>

<i>Figure 6.8 Normalized normal stress distribution of trapdoor cases with varying sample height with an $L/B = 3.0$</i>	<i>154</i>
<i>Figure 6.9 α variation under trapdoor cases with varying sample height with an $L/B = 3.0$</i>	<i>155</i>
<i>Figure 6.10 Shear stress distribution for $L/B = 3.0$ under varying ground heights.....</i>	<i>155</i>
<i>Figure 6.11 Vertical displacement plots for trapdoor configuration with five base plates, for varying sample heights</i>	<i>158</i>
<i>Figure 6.12 Strong force (normalized) plots for trapdoor configuration with five base plates, for varying sample heights.....</i>	<i>159</i>
<i>Figure 6.13 Normalized normal stress distribution of trapdoor cases with varying sample height with an $L/B = 5.0$</i>	<i>160</i>
<i>Figure 6.14 α variation under trapdoor cases with varying sample height with an $L/B = 5.0$</i>	<i>160</i>
<i>Figure 6.15 Shear stress distribution for $L/B = 5.0$ under varying ground heights.....</i>	<i>161</i>
<i>Figure 6.16 Vertical displacement plots for trapdoor configuration with seven base plates, for varying sample heights.....</i>	<i>163</i>
<i>Figure 6.17 Strong force (normalized) plots for trapdoor configuration with seven base plates, for varying sample heights</i>	<i>164</i>
<i>Figure 6.18 Normalized normal stress distribution of trapdoor cases with varying sample height with an $L/B = 7.0$</i>	<i>165</i>
<i>Figure 6.19 'α' variation under trapdoor cases with varying sample height with an $L/B = 7.0$</i>	<i>166</i>
<i>Figure 6.20 Vertical displacement plots for trapdoor configuration with nine (09) base plates, for varying sample heights</i>	<i>168</i>
<i>Figure 6.21 Strong force (normalized) plots for trapdoor configuration with nine base plates, for varying sample heights.....</i>	<i>169</i>
<i>Figure 6.22 Normalized normal stress distribution of trapdoor cases with varying sample height with an $L/B = 9.0$</i>	<i>170</i>

Figure 6.23 ‘ α ’ variation under trapdoor cases with varying sample height with an $L/B = 9.0$	170
Figure 6.24 Vertical displacement plots for samples with (a) $L/B = 3.0$, (b) $L/B = 5.0$, (c) $L/B = 7.0$ and (d) $L/B = 9.0$, having an $H/B = 10.2$ for all cases	172
Figure 6.25 Vertical displacement plots for samples with (a) $L/B = 3.0$, (b) $L/B = 5.0$, (c) $L/B = 7.0$ and (d) $L/B = 9.0$, having an $H/B = 6.95$ for all cases	173
Figure 6.26 Peak values of ‘ α ’ for different sample height with varying configuration values	174
Figure 6.27 ‘ α_{peak} ’ vs H/B for each configuration of trapdoor	175
Figure 6.28 Freely hanging chain at two ends, representing a catenary shape	177
Figure 6.29 Approximate shapes of the arching during model trapdoor tests on Kashima river sand for (a) $H/B = 4.0$ and (b) $H/B = 2.0$	178
Figure 6.30 Approximate shape of an arch under DEM simulations with a sample having stable arching	179
Figure 6.31 Comparison of basic equations for the catenary and the Ellipse shapes	179
Figure 6.32 Ellipse with its constituting dimensions	181
Figure 6.33 Representation of a DEM sample having two ellipsoid portions constituting arch	182
Figure 6.34 Arching surface for shallower ground sample heights	185
Figure 6.35 α_{peak} values obtained through empirical relation, for varying H/B with $L/B = 3.0$	187
Figure 6.36 α_{peak} values obtained through empirical relation, for different trapdoor configurations with $k = 1.0$	188
Figure 6.37 α_{peak} values obtained through empirical relation, for different trapdoor configurations with $k = 1.5$	189
Figure 6.38 α_{peak} values obtained through empirical relation, for different trapdoor configurations with $k = 2.0$	190
Figure 6.39 α_{peak} values obtained through empirical relation, for different trapdoor configurations with $k = 0.75$	190

<i>Figure 6.40</i> <i>peak values obtained through empirical relation, for different trapdoor configurations with $k = 0.50$.....</i>	<i>191</i>
<i>Figure 6.41</i> <i>Normalized normal stress distribution with different central static plate widths</i>	<i>193</i>
<i>Figure 6.42</i> <i>Shear stress distribution for varying central static plate widths</i>	<i>195</i>
<i>Figure 6.43</i> <i>'α' variation with trapdoor movement for different central base plate widths..</i>	<i>196</i>
<i>Figure 6.44</i> <i>'α' variation on the side trapdoors for central plate width of (a) 50mm, (b) 75mm, (c) 100mm and (d) 150mm</i>	<i>197</i>
<i>Figure 6.45</i> <i>Vertical displacement plot at the particulate level for different central static base plate widths</i>	<i>198</i>
<i>Figure 6.46</i> <i>Vertical displacement plot for (a) five base-plates with 50mm width and (b) three base plates with central 150mm width plate.....</i>	<i>200</i>
 <i>Figure 7.1</i> <i>Underground cavity and the arch formation around it.....</i>	 <i>203</i>
<i>Figure 7.2</i> <i>Model cavity test apparatus</i>	<i>204</i>
<i>Figure 7.3</i> <i>Model cavity tests on dry samples with different sizes of glass beads at various stages of test.....</i>	<i>205</i>
<i>Figure 7.4</i> <i>Model trapdoor tests with different sizes of silica sand at (a) start and (b) end of the test</i>	<i>206</i>
<i>Figure 7.5</i> <i>DEM based numerical cavity tests using (a) spherical and (b) non-spherical particles at start of simulations and end of the simulation.....</i>	<i>207</i>
<i>Figure 7.6</i> <i>Surface tension at interface of liquid and air</i>	<i>209</i>
<i>Figure 7.7</i> <i>A lump of soil with numerous particles in a partially saturated condition, resulting in matric suction</i>	<i>211</i>
<i>Figure 7.8</i> <i>Two spherical particles connected through a thin water film</i>	<i>212</i>
<i>Figure 7.9</i> <i>Force-overlap plot between two spherical particles having water film between them.....</i>	<i>214</i>
<i>Figure 7.10</i> <i>Relation between capillary force and inter-particle distance under different suction pressures (Ref. Gras et al., 2013).....</i>	<i>215</i>

<i>Figure 7.11 Relation between capillary force and inter-particle distance under different suction pressures (Ref. Wang et al., 2017)</i>	<i>216</i>
<i>Figure 7.12 Decrease in capillary force with increasing inter-particle distance through a quadratic reduction factor</i>	<i>217</i>
<i>Figure 7.13 Approximate linear variation of water bridge surface between two spherical contacting particles.....</i>	<i>218</i>
<i>Figure 7.14 Representation of Young-Laplace equation parameters in water bridge between two spherical particles.....</i>	<i>221</i>
<i>Figure 7.15 Fully saturated condition for spherical particles in rectangular assembly.....</i>	<i>222</i>
<i>Figure 7.16 Water meniscus angles with the centroid of particle</i>	<i>223</i>
<i>Figure 7.17 Difference between apparent and real 'b' value</i>	<i>224</i>
<i>Figure 7.18 Comparison of contact force calculation through model response and an empirical relation.....</i>	<i>226</i>
<i>Figure 7.19 Capillary force model response against the degree of saturation</i>	<i>227</i>
<i>Figure 7.20 Model response for the degree of saturation vs suction force</i>	<i>228</i>
<i>Figure 7.21 Capillary force through modified model against particle size</i>	<i>229</i>
<i>Figure 7.22 Comparison of Sun (2018) model to the current model for inter-particle suction pressure with varying diameters of particles.....</i>	<i>230</i>
<i>Figure 7.23 Comparison of Sun (2018) model to the current model for inter-particle suction forces with varying particle diameters</i>	<i>230</i>
 <i>Figure 8.1 (a) Cavity model test apparatus and (b) schematic diagram.....</i>	 <i>233</i>
<i>Figure 8.2 Milling machine for the particle roughness.....</i>	<i>237</i>
<i>Figure 8.3 Comparison of surface texture for the (a) smooth and (b) rough glass beads using SEM analyses, having a mean diameter of 1.7mm</i>	<i>238</i>
<i>Figure 8.4 Deformed glass beads in (a) Digital image and (b) SEM image having a smooth surface.....</i>	<i>241</i>
<i>Figure 8.5 Deformed glass beads in (a) Digital image and (b) SEM image having a rough surface.....</i>	<i>242</i>

<i>Figure 8.6 Comparison of clumped glass beads images at (a) smooth and (b) rough condition using digital imaging and (c) rough condition using SEM.....</i>	<i>243</i>
<i>Figure 8.7 Cavity surface loading test under triaxial machine loading system</i>	<i>246</i>
<i>Figure 8.8 Calibration curve for load cell 1.....</i>	<i>247</i>
<i>Figure 8.9 Calibration curve for load cell 2.....</i>	<i>247</i>
<i>Figure 8.10 Calibration curve for external displacement meter 1</i>	<i>248</i>
<i>Figure 8.11 Calibration curve for external displacement meter 2</i>	<i>248</i>
<i>Figure 8.12 Calibration curve for motor speed 1.....</i>	<i>249</i>
<i>Figure 8.13 Calibration curve for motor speed 2.....</i>	<i>249</i>
<i>Figure 8.14 Calibration curve for motor speed 3.....</i>	<i>250</i>
<i>Figure 8.15 Different sizes of the plates used in cavity surface loading tests</i>	<i>251</i>
<i>Figure 8.16 Rigid particle R3, with three constituent spherical particles.....</i>	<i>256</i>
<i>Figure 8.17 Shape of the sample used in cavity stability simulations with saturation as an input parameter.....</i>	<i>260</i>
 <i>Figure 9.1 Model cavity tests for glass beads with $D_{50} = 1.7\text{mm}$ for a fully saturated condition at (a) initial stage, and (b) after bottom slit opening.....</i>	 <i>270</i>
<i>Figure 9.2 Model cavity tests for spherical glass beads with $D_{50} = 1.7\text{mm}$ for a partially saturated condition at (a) initial stage, and (b) after bottom slit opening</i>	<i>270</i>
<i>Figure 9.3 Model cavity stability tests for various sizes of spherical glass beads at (a) initial condition and (b) at end of the test</i>	<i>271</i>
<i>Figure 9.4 Model cavity stability test for spherical glass beads with a mean diameter of 0.2mm at various stages of the test.....</i>	<i>272</i>
<i>Figure 9.5 Model cavity stability tests for mixed grading of spherical glass beads at (a) initial condition and (b) at the end of the test</i>	<i>274</i>
<i>Figure 9.6 Comparison of the cavity stability using spherical glass beads having a mean diameter of 0.5mm with (a) smooth and (b) rough surface</i>	<i>275</i>
<i>Figure 9.7 Effect of initial water level on cavity stability for spherical glass beads with $D_{50} = 0.725\text{mm}$ at (a) initial state and (b) final state of the test.....</i>	<i>276</i>

<i>Figure 9.8 Effect of sample density on the stability of the cavity for spherical glass beads having $D_{50} = 0.725\text{mm}$ at (a) initial state and the (b) final state of the test</i>	<i>277</i>
<i>Figure 9.9 Cavity stability test using rough deformed glass beads with a mean particle size of 1.0mm at (a) initial and (b) final state</i>	<i>278</i>
<i>Figure 9.10 Cavity stability test using smooth clumped glass beads with a mean particle size of 0.6mm at (a) initial and (b) final state</i>	<i>279</i>
<i>Figure 9.11 Cavity stability chart being followed generally in the construction industry of Japan</i>	<i>280</i>
<i>Figure 9.12 Experimental results of critical cavity size just before collapse, plotted on cavity stability chart</i>	<i>281</i>
<i>Figure 9.13 Particle speed plot using spherical particles with a mean diameter of 1.7mm, at various inter-particle suction values</i>	<i>284</i>
<i>Figure 9.14 Particle speed plot using spherical particles with a mean diameter of 0.6mm, with 500 Pa inter-particle suction value</i>	<i>285</i>
<i>Figure 9.15 Strong force distribution for 0.6mm spherical particles at (a) initial stage before making cavity and (b) end of simulation with 500 Pa suction</i>	<i>286</i>
<i>Figure 9.16 Particle velocity for spherical 1.7mm diameter case (a) initial state, (b) final state for 5% S_r, (c) 50% S_r and (d) 90% S_r</i>	<i>288</i>
<i>Figure 9.17 Particle velocity plot for non-spherical particles (a) initial state 1.7mm (b) final state 1.7mm and (c) initial state 1.0mm (d) final state 1.0mm</i>	<i>289</i>
<i>Figure 9.18 Division of model space into 136 number of overlapping subsets</i>	<i>290</i>
<i>Figure 9.19 2nd order contact fabric for simulation with non-spherical particles having a mean size of 1.0mm at (a) initial state and (b) final state of the simulation</i>	<i>292</i>
<i>Figure 9.20 Simulation plan for non-spherical particles with a mean particle size of 1.0mm</i>	<i>294</i>
<i>Figure 9.21 Division of numerical sample into four regions for analyses</i>	<i>295</i>
<i>Figure 9.22 ‘α’ variation for varying degree of saturation of the sample</i>	<i>296</i>
<i>Figure 9.23 Strong force variation with time in the sample with a 50mm wide cavity with 50mm height</i>	<i>297</i>

<i>Figure 9.24 Normalized normal stress distribution for different cavity widths having (a) height of 60mm and (b)70mm</i>	<i>297</i>
<i>Figure 9.25 Strong force distribution for 30mm cavity width with different heights at initial and final states of the simulation</i>	<i>298</i>
<i>Figure 9.26 ‘α’ variation for varying cavity height under a cavity width of (a) 30mm, (b) 40mm, and (c) 50mm.....</i>	<i>299</i>
<i>Figure 9.27 Kinetic energy plot for all cavity stability simulations grouped into (a) 30mm width (b) 40mm width and (c) 50mm width of the cavity.....</i>	<i>300</i>
<i>Figure 9.28 Kinetic energy plot for matching cavity heights with varying widths.....</i>	<i>302</i>
<i>Figure 9.29 Comparison of Kinetic Energy variation with similar cavity dimensions for (a) $S_r = 5\%$ and (b) $S_r = 90\%$.....</i>	<i>303</i>
<i>Figure 9.30 Simulation plan for cavity stability with a mean particle size of 0.5mm (non-spherical)</i>	<i>305</i>
<i>Figure 9.31 Normalized normal stress distribution under varying cavity widths for a cavity height of 20mm.....</i>	<i>306</i>
<i>Figure 9.32 Normalized normal stress distribution under varying cavity widths for a cavity height of 40mm.....</i>	<i>306</i>
<i>Figure 9.33 Normalized normal stress distribution under varying cavity heights for a cavity width of 30mm.....</i>	<i>307</i>
<i>Figure 9.34 ‘α’ variation with increasing cavity height for a cavity width of 10mm.....</i>	<i>308</i>
<i>Figure 9.35 ‘α’ variation with increasing cavity width for a cavity height of 40mm.....</i>	<i>308</i>
<i>Figure 9.36 Kinetic energy variation with changing cavity height for a given cavity width, using non-spherical particle mean size of 0.5mm.....</i>	<i>310</i>
<i>Figure 9.37 Kinetic energy variation with changing cavity width for a given cavity height, using non-spherical particle mean size of 0.5mm.....</i>	<i>311</i>
<i>Figure 9.38 Cavity stability chart plotted for the numerical simulation results of cavity tests using non-spherical particles with a mean size of 0.5mm</i>	<i>312</i>
<i>Figure 9.39 Modified cavity stability chart plotted for the numerical simulation results of cavity tests using non-spherical particles with a mean size of 0.5mm.....</i>	<i>313</i>

<i>Figure 9.40 Strong force distribution for the extreme cases of cavity formations using non-spherical particles having a mean size of 0.5mm</i>	<i>314</i>
<i>Figure 9.41 Strong force comparison before and after the simulation with larger sample dimensions having cavity width of 80mm</i>	<i>315</i>
<i>Figure 9.42 Vector diagram of particle movement overlaid on dz color plot</i>	<i>316</i>
<i>Figure 9.43 Particle movement plots with a cavity size of 30mm x 30mm on R2 particles under three different conditions at (a) start of the simulation, (b) mid of simulations and (c) at the end of the simulation.....</i>	<i>318</i>
<i>Figure 9.44 Kinetic energy variation for the R2 particle sample with a cavity size of 30mm x 30mm, under different conditions</i>	<i>319</i>
<i>Figure 9.45 Particle movement plot for R3 particle sample having a cavity of 40mm x 40mm at the (a) start, (b) mid and the (c) end of the simulation.....</i>	<i>321</i>
<i>Figure 9.46 Strong force and particle movement plot for R3 particle sample with a cavity size of 30mm x 30mm under variable saturation condition at (a) the start, (b) mid and (c) end of the simulation.....</i>	<i>322</i>
<i>Figure 9.47 Kinetic energy plot for the R3 particles having different cavity sizes, under varying degree of saturation.....</i>	<i>323</i>
 <i>Figure 10.1 Load-settlement plot for smooth and rough surface texture with spherical glass beads having a mean diameter of 0.5mm, without any cavity</i>	 <i>326</i>
<i>Figure 10.2 Final state of samples after surface loading using 5cm wide plate for (a) smooth and (b) rough glass beads having a mean diameter of 0.5mm.....</i>	<i>326</i>
<i>Figure 10.3 Load-settlement plot for smooth and rough surface texture with spherical glass beads having a mean diameter of 0.5mm, with a base cavity.....</i>	<i>327</i>
<i>Figure 10.4 Model tests for cavity formation and surface loading at with different loading rates.....</i>	<i>329</i>
<i>Figure 10.5 Load-settlement curves for spherical glass beads with a mean diameter of 0.5mm, for various surface plate loading rates</i>	<i>330</i>

<i>Figure 10.6 Cavity surface loading tests for different loading rates, shown at (a) initial condition, (b) after cavity formation and (c) after surface loading, for rough deformed glass beads with mean size of 1.0mm and 85% relative density.....</i>	<i>331</i>
<i>Figure 10.7 Cavity surface loading test results on rough deformed particle samples with different surface loading rate.....</i>	<i>332</i>
<i>Figure 10.8 Cavity surface loading tests for different loading rates, shown at (a) initial condition, (b) after cavity formation and (c) after surface loading, for clumped glass beads with mean size of 0.6mm and 90% relative density</i>	<i>334</i>
<i>Figure 10.9 Cavity surface loading test results on clumped particle samples with varying surface loading rate</i>	<i>335</i>
<i>Figure 10.10 comparison of resistance to surface loading above cavity using spherical and clumped type particles</i>	<i>336</i>
<i>Figure 10.11 Cavity loading rate comparison with a plate with of 10cm on clumped particle sample</i>	<i>338</i>
<i>Figure 10.12 Cavity loading rate comparison with a plate with of 2cm on clumped particle sample</i>	<i>338</i>
<i>Figure 10.13 Comparison of plate width effect on cavity strength on clumped particle sample using 5cm and 2cm wide plates at the highest loading rate</i>	<i>339</i>
<i>Figure 10. 14 Comparison of plate width effect on cavity strength on clumped particle sample at the lowest loading rate.....</i>	<i>339</i>
<i>Figure 10.15 Loading rate effect for clumped particle sample under saturated and unsaturated combined condition, without the presence of the cavity</i>	<i>341</i>
<i>Figure 10.16 Loading rate effect for clumped particle sample under dry condition, without the presence of a cavity.....</i>	<i>342</i>
<i>Figure 10.17 Loading rate effect for clumped particle sample under fully saturated condition, without the presence of a cavity.....</i>	<i>343</i>
<i>Figure 10.18 Comparison of surface loading tests with the fully saturated condition and the combination of saturated and unsaturated condition, using clumped particles.....</i>	<i>344</i>
<i>Figure 10.19 Combined plot of all cases for surface loading tests using clumped glass beads without any presence of the cavity.....</i>	<i>346</i>

<i>Figure 10.20 Cavity loading test results on clumped glass beads without a cavity for a dry case with maximum loading rate and all other cases with least loading rate</i>	<i>346</i>
<i>Figure 10.21 Load-settlement plots for DEM simulations using non-spherical clumped particles for different widths of loading plate on a sample with a 30mm wide cavity</i>	<i>348</i>
<i>Figure 10.22 Load-settlement response of numerical simulations for varying loading rates with the presence of a base cavity.....</i>	<i>350</i>
<i>Figure 10.23 Particle velocity plot for various loading rates</i>	<i>352</i>
<i>Figure 10.24 Strong force chains for various loading rates</i>	<i>353</i>
<i>Figure 10.25 Particle vector movement plot overlaid on a color plot of dz for 0.1m/s loading rate</i>	<i>354</i>
<i>Figure 10.26 Failure plane as observed in DEM simulation for a larger settlement of surface plate loading</i>	<i>354</i>
<i>Figure 10.27 Load-settlement response of numerical simulations for varying loading rates without a base cavity under unsaturated conditions.....</i>	<i>355</i>
<i>Figure 10.28 Load-settlement response of numerical simulations for varying loading rates without a base cavity without capillary forces</i>	<i>356</i>
<i>Figure 10.29 Effect of rupture distance on sample shear strength for (a) 0.1m/s, (b) 0.05m/s and (c) 0.025m/s loading rate.....</i>	<i>358</i>

LIST OF TABLES

<i>Table 3.1 Factors for load cell calibration.....</i>	<i>39</i>
<i>Table 3.2 Calibration factors for the motor speed</i>	<i>46</i>
<i>Table 3.3 Material properties of used material in trapdoor tests.....</i>	<i>48</i>
<i>Table 3.4 Trapdoor model testing plan</i>	<i>50</i>
<i>Table 3.5 Specifications of the Oakforest-PACS supercomputer</i>	<i>53</i>
<i>Table 3.6 Input parameters used in DEM trapdoor simulations.....</i>	<i>58</i>
<i>Table 3.7 DEM simulation plan.....</i>	<i>59</i>
<i>Table 6.1 Simulation plan for trapdoor configuration of 15cm length.....</i>	<i>145</i>
<i>Table 6.2 Simulation plan for trapdoor configuration of 25cm length.....</i>	<i>145</i>
<i>Table 6.3 Simulation plan for trapdoor configuration of 35cm length.....</i>	<i>146</i>
<i>Table 6.4 Simulation plan for trapdoor configuration of 45cm length.....</i>	<i>146</i>
<i>Table 6.5 Number of particles in each simulation case with full width and half-width, for varying configurations</i>	<i>147</i>
<i>Table 6.6 Simulation plan with variable central static base plate widths</i>	<i>192</i>
<i>Table 6.7 Maximum possible stress increase on the central static plate under different width combinations</i>	<i>194</i>
<i>Table 7.1 Model cavity tests with different materials in dry conditions.....</i>	<i>203</i>
<i>Table 7.2 Surface tension of water against temperature</i>	<i>210</i>
<i>Table 8.1 Material properties for spherical glass beads.....</i>	<i>236</i>
<i>Table 8.2 Material properties for spherical glass beads.....</i>	<i>236</i>
<i>Table 8.3 Test cases and properties for non-spherical glass beads</i>	<i>240</i>
<i>Table 8.4 Cavity model test plan for stability analyses</i>	<i>245</i>
<i>Table 8.5 Cavity surface load test on spherical particles with 0.5mm mean diameter</i>	<i>252</i>

<i>Table 8.6 surface load test on spherical particles with 0.5mm mean diameter without the presence of the cavity.....</i>	<i>252</i>
<i>Table 8.7 Cavity surface loading test plan for clumped particles</i>	<i>254</i>
<i>Table 8.8 Cavity surface loading test plan for deformed particles.....</i>	<i>254</i>
<i>Table 8.9 Simulation plan with Input Suction using small samples</i>	<i>258</i>
<i>Table 8.10 Simulation plan on a small sample with saturation as an input parameter</i>	<i>259</i>
<i>Table 8.11 Simulation plan with the larger sample having saturation as input with 1.0mm particle dia.....</i>	<i>261</i>
<i>Table 8.12 Simulation plan with the larger sample having saturation as input with 0.5mm particle dia.....</i>	<i>262</i>
<i>Table 8. 13 Simulation plan having variable saturation with three constituent rigid particles (R3)</i>	<i>263</i>
<i>Table 8 14 Numerical simulation plan for plate loading rate using non-spherical particles of 0.5mm mean diameter.....</i>	<i>266</i>
<i>Table 8.15 Surface loading simulation plan with different plate sizes with a mean particle diameter (non-spherical, R2) of 0.5mm</i>	<i>267</i>
<i>Table 9.1 Degree of residual saturation for different materials.....</i>	<i>273</i>

LIST OF ABBREVIATIONS

a	Radius of circular contact area
α	Stress concentration factor
α_{peak}	Peak stress concentration factor
$\alpha_{residual}$	Residual stress concentration factor
$\alpha_{max}^{theoretical}$	Theoretical maximum value of stress concentration factor
B	Width of the buried structure/central fixed plate
c	Cohesion
C	Damping matrix
CN	Mean coordination number
C_u	Coefficient of uniformity
D	Particle diameter
D_{50}	Median particle diameter
D_{50}	Diameter of particles with 85% passing
D_r	Relative density
e	Void ratio
e_{min}	Minimum void ratio
e_{max}	Maximum void ratio
e_o	Initial void ratio
E	Young's modulus
Ep^*	Equivalent Young's modulus of contacting particles

F	Force
F'	Load taken by the arch
ΔF	Incremental force vector
g	Gravitational acceleration
G	Shear modulus
Gp^*	Equivalent shear modulus of contacting particles
G_s	Specific gravity
H	Height of the sample
h	Height of the particle
h_{arch}	Height of the arch
h_w	Height of water surface
i	Particle i
I	Moment of inertia
K	Global stiffness matrix
k	Empirical constant
KN	Secant normal contact stiffness
kN	Normal contact stiffness
m	Particle mass
M	Mass matrix
N	Number of the base plates
Np	Number of particles

N_c	Number of contacts
P_x	Shear stress
$P_{x,peak}$	Peak shear stress
P_{z_0}	Initial normal stress
$P_{z,center}$	Normal stress at the central fixed plate
$P_{z,p}$	Peak normal stress
q	Surcharge load
r_1	Minor radius of the ellipse
r_2	Major radius of the ellipse
R	Particle radius
R^*	Equivalent radius of contacting particles
RPM	Revolutions per minute
SEM	Scanning electron microscope
t	Time
T	Tangential contact force
u	Overlap between particles
u_x^a	Incremental translational displacement of particle ‘a’ in x-direction
u_y^a	Incremental translational displacement of particle ‘a’ in y-direction
u_z^a	Incremental translational displacement of particle ‘a’ in z-direction
\ddot{x}	Particle acceleration
δ	Settlement of the trapdoors/plate

γ	Unit weight of the material
τ	Torque acting on the particles
ν	Poisson's ratio
θ	Angle of water meniscus with the particle center
$\ddot{\theta}$	Angular acceleration
ϕ	The angle of shear resistance
ϕ_{XX}	2 nd order contact fabric in X-direction
ϕ_{YY}	2 nd order contact fabric in Y-direction
ϕ_{ZZ}	2 nd order contact fabric in Z-direction
μ	Coefficient of inter-particle friction
ϕ	Eigenvectors
ω	Angular frequency

CHAPTER 1: INTRODUCTION

1.1 General

The arching phenomenon is one of the most abundantly visible phenomena at both above and below the surface of the earth. The arching phenomenon below the earth's surface can be well observed in deep cavities and around almost all types of buried structures. Arching action is not just limited in the granular soils. Soils with interparticle cohesion or the rock mass also contribute towards arching. Man has widely used the nature-learned arching phenomenon for the construction activities since prehistoric times. The earliest possible construction of an arch-based structure can be regarded as the *caves* used by the stone-age man. Unknowingly at that time, the stability of the caves was much dependent upon the strong arch action above the cave surface, resulting in the transfer of load to the sides.

The inclusion/construction of any buried structure mostly follows the initiation of the arching action. Use of underground space for human needs dates thousands of years back, where the growing needs of the people in a locality forced them to utilize the underground space, e.g. supply of water, collection of wastes through surface or sub-surface drain or using underground space for the storage of their valuables and food. (Ramkumar et al., 2018) showed the evidence for use of buried structures at Kaveri–Kollidam interfluvium around 2000 years ago up to a depth of 3.5m below the surface.

The human needs are growing more and more with each passing day. People tend more to live in a place where life necessities can easily be approached, resulting in a rapid increase in urbanization. A shortage of space for the growing needs of people has led to utilizing the underground space. Construction of buried structures like transportation network tunnels, box girders, utility lines, etc. have become more common to facilitate the people. Buried structures thus not only carry the weight of above soil but also the burden of the surface structures. However, normally the forces on the buried structures are not equal to the forces caused by the above structures or the overburden soil. Hence a detailed evaluation of forces is required for the stability of both buried and the surface structures.

1.2 What is soil arching?

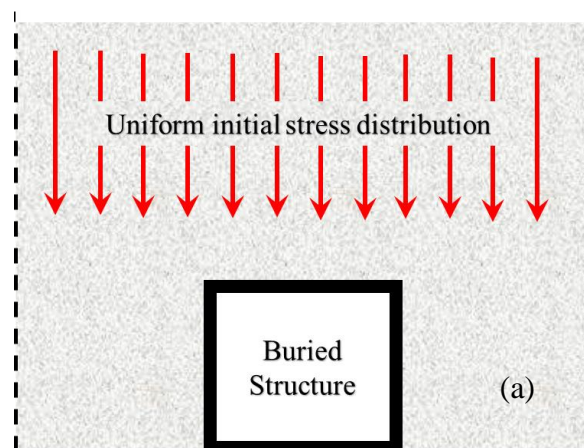
Arching is the preventive measure by nature against the probable collapse of the soil mass. According to Terzaghi (1943), soil arching is the phenomenon where, in case a certain portion of a rigid soil mass yields, the movement of that part is resisted by the shear stresses in the static mass. This process decreases the stresses on the yielding part and lowering the stresses in the yielding part. Arching can widely be divided into two main categories; namely active and passive arching. A better understanding between both types can be made by Figure 1.1, where the cases for the absence of the arching, passive and active cases are presented.

1.2.1 Active arching:

A case when the buried structure is lesser rigid than the surrounding soil. In that case, the buried structure will settle more than the surrounding soil. This situation will result in a situation where the load on the buried structure is lesser than the surrounding yielding mass.

1.2.2 Passive Arching:

In case that the buried structure is rigid enough and the soil around it is relatively softer, the shear stresses will tend to add additional load on the rigid buried structure and lower stress on the surrounding yielding mass.



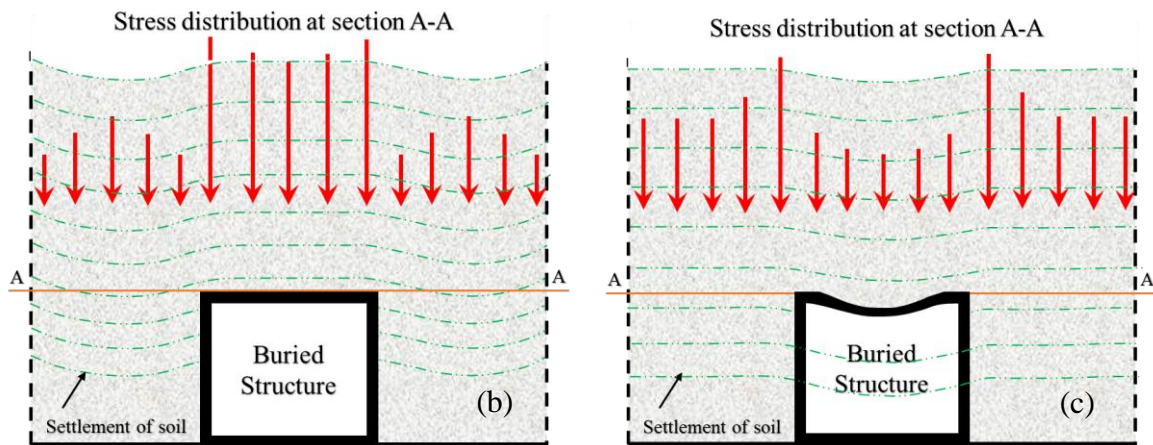


Figure 1.1: Earth pressure distribution on a buried structure when (a) both soil and structure have the same stiffness, (b) when a buried structure is stiffer and (c) when soil is stiffer

As shown in Figure 1.1(a), a uniform stress distribution can occur in case the structure and the soil mass have similar load-displacement characteristics. However, it is almost impossible to have such similarity due to the peculiar nature of structural materials like concrete, steel or wood. Also, the stress distribution is shown in Figure 1.1(b & c) is for uniformly behaving materials, that is normally not the case. The structure can show much complex behavior and the stresses can vary in a more complex manner than shown above.

1.3 Background of the arching phenomenon

The arching phenomenon was first documented around 200 years back. Arching is well recognized in most of the geotechnical engineering related aspects. However, the first encounter with the arching phenomenon dates back to the early 1800s for a non-geotechnical phenomenon when French military engineers observed it during the design of magazine silos (Feld, 1948). It was observed that the central portion of silos showed a part of the load due to the above weight in silos, whereas the sidewall carried more load than anticipated. Further investigation leads them to believe that an arching action was developed due to the layout conditions of the structure.

In the later 1800s, this information was further used in the design of silos for other materials. In the early 20th century deformation of drainage pipes was observed in central Europe after the backfilling of soil (Spangler & Handy, 1982). Investigations showed the variation in earth pressure with change in backfill thickness, stiffness of pipes, installation procedure. The load

variation on the pipes was then related to the arch development in the soil under given conditions.

Arching action was also observed in tunnel design in the same era, encouraging designers to utilize the natural arching phenomenon for more economical design due to reduced loads above the tunnel. This appeal resulted in several empirical expressions for the tunnel support loads and inspired more researchers for experimental investigation of the arching phenomenon (Evans, 1984). Researchers like Terzaghi, Proctor & White did extensive experimental and theoretical investigations to have a deep insight into arching. The use of large culverts and box girders gained more popularity in the mid of the 20th century for expanding infrastructure and enabling researchers to acquire techniques for better load redistribution around the buried structures. In the 1960s, the focus of the arching related studies diverted towards soil-structure interaction for the design of underground defense facilities (Charles 1984). With the commercial introduction of high-performance computers, more and more numerical work has been done to explain the process of the arching under different situations using different numerical techniques like finite element method (FEM) and discrete element method (DEM).

1.4 Soil arching in major geotechnical phenomena

Soil arching is observed in many geotechnical engineering phenomena; like the trapdoor condition, cavity formation, tunneling, silos, buried structures, and even between the closely planted trees. However, arching in the trapdoor and underground cavity is considered to be most abundant and crucial.

1.4.1 Trapdoor condition:

Trapdoor condition was first described by Terzaghi (1936), which consisted of a soil chamber with a base block capable of moving downwards (Figure 1.2). Terzaghi obtained the design information from the tunneling projects of that era and formulated the design values for tunnel load supports. This configuration was named as the '*Trapdoor Condition*'. The stresses on the lowering trapdoor are reduced significantly compared to the other static portion.

1.4.2 Underground cavity condition

Underground cavities are one of the most commonly occurring natural geotechnical engineering phenomena in the world. The collapse of underground cavities initiates the

cave-in incidents and thousands of cases are reported every year damaging the infrastructures and causing casualties as well. Cavities are broadly divided into two categories: deep and shallow. Deep cavities are initiated due to soil piping and suffusion in the deep layers and are normally stable enough to have construction activities above them. However, some of the deep cavities are prone to expansion due to the unsuitable underground environment for a stable soil structure. Such cavities lead to a cave-in or collapse of the upper surface. Deep cavities once collapsed, can cause huge surface damage due to the growing size since their inception. There are numerous cave-in phenomena throughout the world. For instance, a sinkhole with a diameter of 20m and a depth of 100m appeared on the surface in Guatemala in February 2007. Similarly, a sinkhole in Hokkaido Japan in 2009 and a series of sinkholes in Pokhara, Nepal in 2013 are some of the famous examples of deep underground cavity collapse.

Whereas the shallow cavities are the critical ones that can cause acute damage to the surface infrastructure. Mostly the root cause of the cavity initiation at shallow depths is the defect in the buried structures like box girders, sewer pipes or main water supply lines. A small defect due to construction imperfection or the aging structure can cause the surrounding soil to washout by internal erosion. However, the presence of water is a pre-requisite for the initiation process. Once a small cavity is formed, strong arching develops around its periphery in a regular shape, stabilizing the yielding mass to prevent it from further expanding. Arching along with the capillary forces amongst the soil particles mutually act to make the soil mass stable. In case if the water level fluctuates around a cavity, the capillary forces can reduce significantly. Resultantly, the arching action becomes weaker and the soil mass yields further to expand the cavity. Due to the shallow depth of buried structures, cavities formed above them can be detrimental to cause a collapse. A typical case of shallow cavity formation due to damaged buried structure is shown in Figure 1.3(a) below, along with the cavity expansion process owing to the rise in the groundwater table.

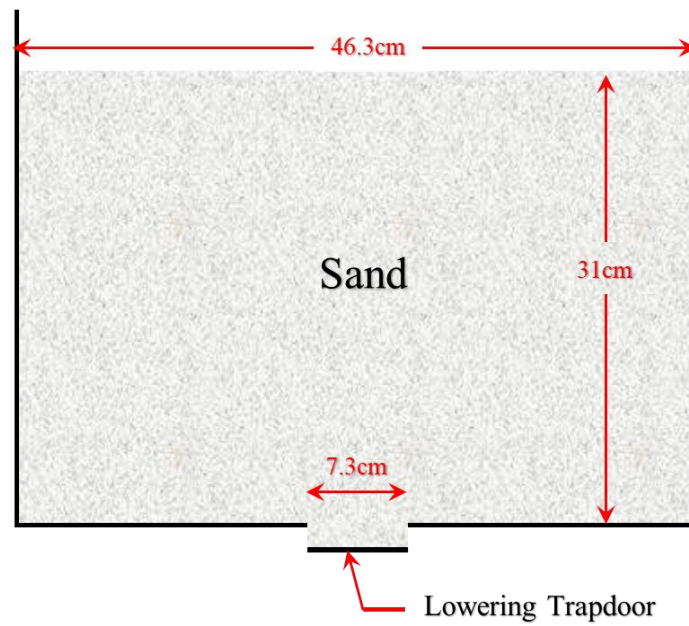


Figure 1.2 Trapdoor configuration used by Terzaghi (1936)

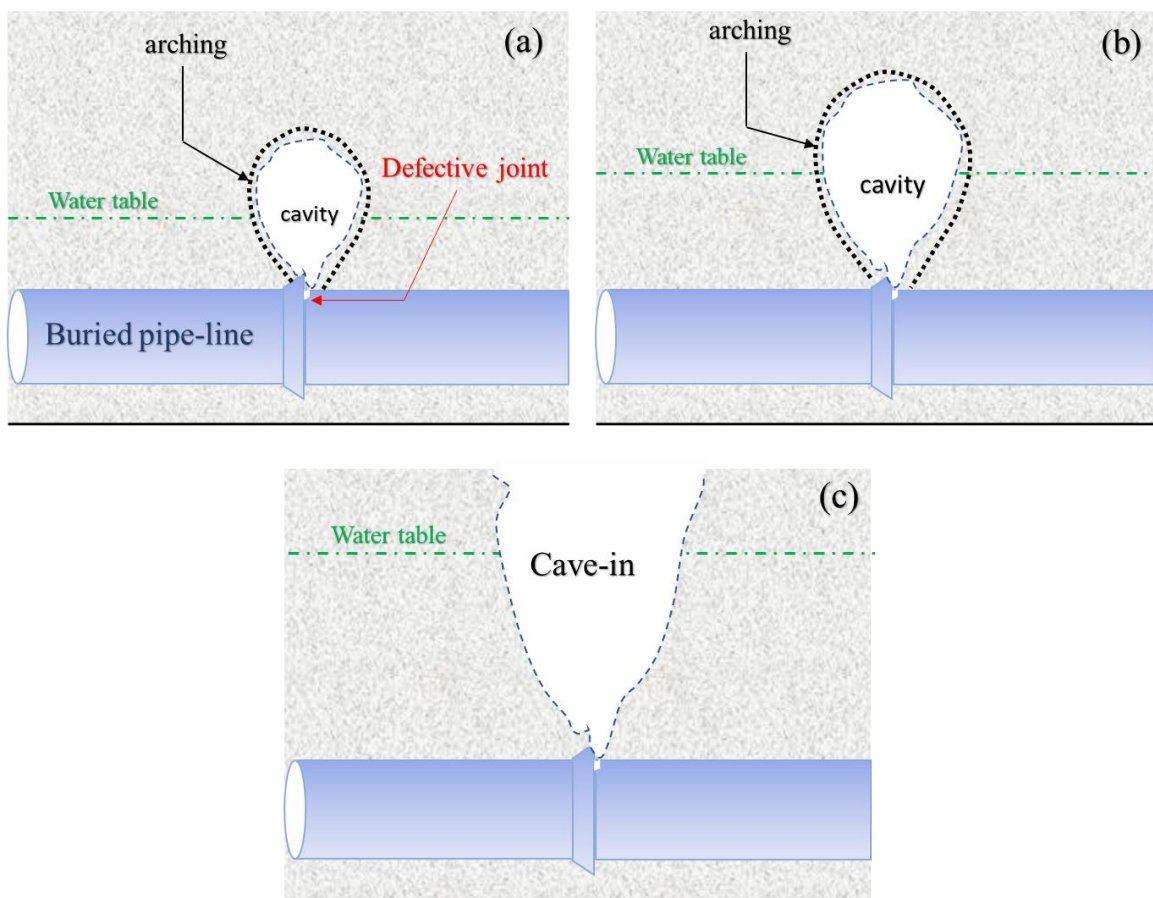


Figure 1.3 Arch around underground cavity and cavity expansion process to result in a cave-in

1.5 Soil arching: beneficial or detrimental

As already discussed, buried structures are mainly responsible for the initiation of soil arching phenomenon either due to relative settlement between structure and the soil or due to the soil erosion in the vicinity of defects found above the buried structures. Hence, to judge the soil arch being beneficial or detrimental, we must consider the safety of both the soil strata and the buried structure by itself as well. Usually, two kinds of responses can be observed from the underground soil arch formation, first being the elimination of differential surface settlement probability and the other being stress increase on the buried structure caused by the arching action.

Soil arch tries to separate the yielding soil mass from the adjacent static soil mass and to transfer the soil load above the yielding portion to either side. This action ensures that no differential surface settlement occurs even at a large yielding strain. Prevention of differential surface settlements can end up saving not only money but also the probability of human injuries. Failure of soil to sustain stable arching action could result in catastrophic incidents at sometimes. There are numerous incidents for the cave-in and cavity collapse around the world. Even in Japan, hundreds of cave-in accidents are reported every year (MLIT-2019). Normally the arch development is hidden from the human eye and remains unnoticeable up to its sudden collapse. Hence the presence of strong and stable arching action is considered to be a blessing for the safety and the cost-saving.

However, another aspect that needs attention is the load increment on the buried structure due to strong arching action. A buried structure is normally stiffer than the adjacent soil due to the use of construction materials like steel, aggregates, etc. Stiffer structure causes the settlement of adjacent soil, that produces the arching action transferring more load towards the structure. According to the Japan Road Association design guidelines (1999), the load increase can reach up to a factor of 1.6. However, the load increment is thought to be even more, which can put the structural integrity of the buried structure to danger. Normally a factor of safety is used for the structural design. However, playing between both the economy and the strength, the factor of safety cannot be taken to multitudes of design load. In case the stresses produced by the arching action exceed the structural strength of the buried structure, the structure would fail, leading towards the collapse of soil strata and causing not only the damage to infrastructure but a large financial loss as well due to the failure of the buried structure.

Keeping in view the above facts, after the construction of a buried structure, both the structural integrity of the structure and the absence of any surface differential settlement is pre-requisite for the successful commissioning of the project. Hence, it is a pre-requisite to have a proper understanding of both soil behavior and soil-structure interaction. Both the structural and geotechnical design is correlated to each other to result in a well-designed and well-implemented project.

1.6 Discrete Element Method

Discrete Element Modelling (DEM) is a numerical modeling or computer simulation approach helpful in simulating the soils and other granular material. The benefit of this technique is that individual particles are considered explicitly in granular material along with their interactions. It can be considered as a substitute for the older technique where the soil was considered as a continuum mechanic framework for simulating the mechanical behavior. In continuum mechanics, the soil is considered as a continuous material with constant properties and relative movement and rotations of particles are not incorporated.

DEM is a method where finite rotations and displacements are considered. During the simulations, particles can come close and far to each other, can lose contacts and generate the newer ones on its own. DEM can be applied in a wide variety of fields, from the soil, powder technology, agriculture, and mining engineering, though soil (granular materials) remains the foremost vital as it was considered in the development of DEM theory by Cundall & Strack (1979).

In the current study, a modified version of Granular LAMMPS (Plimpton, 1995), well compatible with parallel computing/high-performance computing, is used. The explanation of the DEM related parameters is somewhat also documented in the user-manual of software PFC-3D (Itasca, 2007)

1.6.1 Advantages of Using DEM

There are numerous benefits of using DEM for simulating granular material behavior. Most profound are the following reasons:

- i- A virtual sample can be prepared with any size and particles can be given numerous shapes. Deformations and loads can be applied to that virtual sample

conforming to our requirements or laboratory tests. Due to its particle to particle interaction, a very detailed material response can be monitored. From the number of contacts to energy dissipation, fabric tensors, contact orientations, particle rotations and movements, particle velocities, all can be comfortably monitored through our virtual sample. Consequently, we can obtain not only macro, rather micro response of the material as well. Such a detailed amount of information is almost impossible to be obtained through laboratory testing. Since most of the knowledge in the soil mechanics field is derived from empirical relations and observations gathered from laboratory response of the material. DEM provides a platform for the researchers to develop a deep understanding of material response and behavior and to develop the old empirical methods on a scientific basis with the help of insight information provided by DEM.

- ii- Another very interesting use of DEM is in the analysis of large displacement problems. DEM can easily analyze the mechanism of systems that involves large strains and displacement, that may not be correctly obtained through continuum mechanics theory or Finite Element Modelling. There are cases where large displacements created through Cone Penetration Tests are successfully simulated with the help of DEM. This benefit allows us to well understand the failure mechanism including scouring and erosion.

1.7 Problem statement and the objective of the research

It is well understood that the presence of a buried structure initiates the arching action. Furthermore, arching could be both beneficial and detrimental, based upon the quantification of the load increments due to arch formation. However, there are several factors that require attention for a better understanding of the arching action. Some of those factors include the following aspects for the trapdoor conditions:

- 1- How does the depth of the buried structure affect arch formation?
- 2- What is the role of backfill soil density on the arching phenomenon?
- 3- Does the type of backfill material/soil affect arch behavior?
- 4- Is the JRA design guidelines safe enough for load increment?
- 5- How does the configuration of trapdoor conditions affect the load increase on the buried structure?

- 6- Does the particle size play some role in the arching phenomenon?
- 7- Can numerical simulations validate and explain the inter-particle behavior of granular material under trapdoor conditions?

Similarly, in case of a buried shallow cavity, there are certain un-answered aspects:

- 1- Can the numerical method be used to imitate the cavity phenomenon?
- 2- Can a dry soil show cavity formation?
- 3- What is the effect of particle size and shape in cavity stability?
- 4- Why does the cavity expand?
- 5- How stable is the surface above a stable shallow cavity?

To answer the above queries, the 3D model test apparatus for the study of the arching in both trapdoor and cavity phenomena were devised under plane strain conditions. Numerous tests with different materials under varying conditions were performed. Besides the model experiments, equivalent numerical simulations were also performed using the discrete element method to have a particle scale insight to the material response. The main objectives of this study will be focused on the following points:

- Effect of particle shape, density, and size on the stress increase on the buried structure in trapdoor case.
- Investigation of maximum stress increment factor on the buried structure for different trapdoor configurations.
- Prediction of the arch development or absence for any given soil cover
- Verification of soil arching at the particulate level through Discrete Element Simulations in the trapdoor and underground cavity conditions.
- Modifying the DEM code to account for capillary forces as observed in the cavity phenomenon.
- Checking the stability of surface above the cavity under surface loading in model lab tests and validation through equivalent DEM simulations
- Investigation of the cavity/trapdoor width and the soil cover
- Comparison of soil arching under trapdoor/cavity conditions.

1.8 Thesis organization

The thesis consists of eleven (11) chapters and the short description of each chapter is presented below:

CHAPTER 1: INTRODUCTION

This chapter presents the research background and definitions. Along with the basic information, this chapter contains the current challenges in the given research topic and the objectives of the research. Outline of the thesis is also presented in the same chapter

CHAPTER 2: LITERATURE REVIEW

This chapter presents a summary of the findings relating to the current research that have already been done. The literature review includes the arching mechanism in soils, the effect of shape parameters of soil on arching trapdoor conditions. Relating to the arching in the underground cavity, the effect of sample size, soil cover and degree of sample saturation is discussed. Furthermore, basic parameters that are used in DEM simulations are also discussed in this chapter.

CHAPTER 3: EXPERIMENTAL AND NUMERICAL SETUP FOR THE TRAPDOOR TESTS

This chapter includes the description of the model test apparatus along with its mechanism. Materials that are tested are also presented with their basic parameters. For equivalent DEM simulations, the simulation plan along with the input parameters for the simulations are described in detail as well.

CHAPTER 4: STRESS DISTRIBUTION IN TRAPDOOR TESTS – EXPERIMENTAL AND NUMERICAL ANALYSES

The normalized normal stress distribution is discussed in this chapter. Use of shear stress distribution for the prediction of the arching phenomenon explained and the results are then compared with the numerical results. The stress increase in the central static plate is also presented in the same chapter.

CHAPTER 5: PARTICLE SCALE ANALYSIS OF SOIL ARCHING IN TRAPDOOR TESTS

Numerical simulation results using DEM are presented in this chapter. Different techniques that can confirm the presence or absence of the arching phenomenon are discussed in this part.

CHAPTER 6: TRAPDOOR CONFIGURATION EFFECT

The effect of changing the configuration of base plates and the movement directions are presented in this chapter. The effect of configuration change on the arching behavior is also presented.

CHAPTER 7: SOIL ARCHING AROUND CAVITY AND NECESSITY OF CAPILLARY FORCES

To incorporate the capillary forces in DEM code, a new suction-tension model is introduced in this chapter that is then utilized for further numerical simulations for cavity stability and loading conditions.

CHAPTER 8: EXPERIMENTAL & NUMERICAL SETUP FOR CAVITY TEST CONDITIONS

The model test apparatus used in this study to investigate the cavity development and expansion is explained in this section. Material properties along with the testing program are also described. Furthermore, the DEM simulation method, input parameters and test cases are presented in this chapter.

CHAPTER 9: CAVITY STABILITY ANALYSIS

This chapter presents the results of model tests and numerical simulations for various cavity conditions. Effects of particle shape, size and density on the stability of the given cavity are discussed along with the saturation level. Furthermore, the strong force distribution for different cases is also compared in this chapter.

CHAPTER 10: EXPERIMENTAL AND NUMERICAL ANALYSES OF CAVITY SURFACE LOADING

Stress-strain response of material against the surface loading above a stable cavity is explained in this chapter. Numerical results are compared with the experimental finding and the variation of the arching pattern with surface loading in DEM simulations is discussed in this chapter.

CHAPTER 11: CONCLUSIONS AND RECOMMENDATIONS

Major findings of the current research are presented in this chapter along with the future recommendation.

REFERENCES:

Lastly, all the sources for the literature consultation are given in this section.

CHAPTER 2: LITERATURE REVIEW

2.1 Trapdoor problem

Trapdoor problem has long been discussed in the field of geotechnical engineering. Normally trapdoor phenomenon is divided into two main categories, active and passive, that are defined below:

2.1.1 Active and passive trapdoor cases

Active and passive trapdoor problem was first discussed by Terzaghi (1936). An active trapdoor condition exists when the load on the yielding soil increases compared to 'at rest' condition. In other words, the active condition corresponds to the upward movement of the trapdoor. Contrary to that, the passive condition exists when the trapdoor moves downwards and causes a reduction in earth pressure on the lowering trapdoors. In that case, the adjoining static portion will experience an increase in earth pressure.

It is also experienced that active trapdoor conditions can cause an increase in the earth-pressure above the trapdoors to many folds, whereas the passive condition can cause a reduction in earth pressure above moving trapdoor up to 95% (Evans, 1984).

Trapdoor phenomenon due to the formation of soil arching exists in both granular and cohesive materials. However, in cohesive materials, a sustained trapdoor condition can cause a reduction in the increased stress due to the prolonged creep effect. Even in some cases, the earth-pressure can return to the initial state (Peck, 1969). In granular materials, external vibration can also cause a reduction in increased earth pressure. However, the magnitude of the decrease is not as high compared to the cohesive materials (Proctor & White, 1977; Spangler & Handy, 1982).

2.1.2 Physical experiments under trapdoor conditions

Model tests or the physical experiments have been the most favorite medium of an investigation into the soil arching under trapdoor conditions. The researcher extensively used physical experiments to discuss the stress variation above the yielding mass of soil.

The first of them can be well regarded as Terzaghi (1936), who formulated testing equipment consisting of a soil chamber with a movable base plate with a length of 7.3cm. The height of equipment was 31cm and the length was measured as 46.3cm. The trapdoor was lowered slowly and the load along with settlement was measured above the lowering trapdoor. The variation in stresses in the soil mass above the trapdoor was measured indirectly using the friction tape method.

Terzaghi (1943) used plane strain behavior of the soil to have a theoretical analysis of the arching phenomenon in trapdoor conditions. It was further emphasized that the soil at a height of $2B$ (B = width of trapdoor) acts as a surcharge only. Hence the shear resistance is only mobilized in a soil height less than twice the width of the trapdoor and the above soil is unaffected by the amount of trapdoor movement. The final equation obtained is as under:

$$F = \frac{B^2(\gamma - \frac{2c}{B})}{2K \tan \phi} \times \left(1 - e^{-2K \tan \phi \left(\frac{h}{B}\right)}\right) + Bq e^{-2K \tan \phi \left(\frac{h}{B}\right)} \quad (2.1)$$

where F is the force per unit length, q is any applied surcharge weight, c is the cohesion, K is an empirical constant. B and h are the width of the trapdoor and the sample height respectively.

Many researchers after Terzaghi tried to investigate on a similar line of action, e.g. McNulty (1965), Ladanyi & Hoyaux (1969) and Vardoulakis et al. (1981). Recently, Tanaka & Sakai (1993), Dewoolkar et al. (2007), Costa et al. (2009), Chevalier (2008), Kuwano & Ebizuka (2010) and some others have used the physical experiments using soil chamber and moving trapdoor to investigate the arching phenomenon and the earth pressure variation above trapdoor. However, the majority of the researchers except for Kuwano & Ebizuka (2010) used a single moving trapdoor and discussed only the stress variation above moving trapdoor. Stress distribution as a result of trapdoor movement above the surrounding static portions or in other words, above the buried structure, is totally overlooked.

Some of the researchers also utilized centrifugal testing for the arching mechanism, where the centrifugal tests allow to implement higher gravitational forces by rotating the test equipment at a certain rate. The advantage of the centrifugal testing is that the stresses in the actual ground at any given depth can be examined by adjusting the rotation speed.

The idea of centrifugal tests was first initialized by Phillips (1869) and was modernized by Schofield (1980) in the field of geotechnical engineering. Centrifugal testing was also used to investigate arching in trapdoor condition e.g. Adachi (1997), Ellis & Aslam (2009a & 2009b), Dewoolkar et al. (2007), Costa et al. (2009). Baudouin et al. (2010) performed the 3D model centrifugal tests for arching behavior in a group of piles. Iglesia et al. (2014) performed the trapdoor tests with the similar setup as implemented by Terzaghi (1936) using different sizes of glass beads, and the coarse sand and related the relative reduction in earth pressure on the lowering trapdoor with grain size, density, soil cover and amount of trapdoor movement.

2.1.3 Effect of soil cover

The effect of soil height over the lowering trapdoor is often discussed in the literature. Amongst the earliest can be regarded as Terzaghi (1936, 1943) and McNulty (1965) who discussed the effect of varying soil height on the stress redistribution over the trapdoor. Not only the stress distribution but also the surface settlement is thought to be dependent upon the soil cover above trapdoors. Pardo & Sáez (2014) used the soil height above trapdoor to define the region of soil displacement. Thongrapha et al. (2015) showed that soil cover is a major factor for the ground subsidence above the lowering trapdoors. Khatami et al. (2019) used the ratio of trapdoor width B and the soil height H to discuss the stress variation and soil displacement zones using the image correlation technique.

2.1.4 Trapdoor configuration effect

The initial work on the trapdoor problem used a single moving trapdoor placed in the central portion of the soil box. However, it was later observed that variation in the size of the moving trapdoor and the relative position of trapdoors and the static portions can have a drastic effect on the load-displacement characteristics. Lai et al. (2016) found that the smaller spacing between the piles i.e. smaller L/B ratio produces a greater degree of the arching. Also, Wang et al. (2017) varied B and found that increasing H/B increases the degree of stress concentration on the pile heads.

Rui et al. (2016) used varying trapdoor widths for his 2D DEM simulations and showed that the trapdoor width has a unique relationship with the evolution pattern of

the arch. He divided the arching pattern into three different categories based upon the ratio of sample height to trapdoor width. Furthermore, the effect of particle size on the smaller trapdoor width was discussed. Effect of particle size and the trapdoor width on the post-peak stress behavior was also discussed by Garnier et al. (2007) and Iglesia et al. (2014). In short, the trapdoor configuration effect is briefly discussed in the literature, and the discussion in the literature is discussed mostly for a group of piles. However, the trapdoor effect on the stress distribution behavior under the presence of a buried structure is not well explained in the past literature.

2.1.5 Effect of material density

Material density plays a significant role in the development of the arching under trapdoor conditions. A denser material has higher inter-particle contacts with better load transfer abilities, which is hence thought to develop the more clear arching region.

The magnitude of dilation was correlated with the level of density and it was found that the higher densities result in a higher magnitude of dilatancy above lowering trapdoors (Mitchell & Soga, 1976; Rowe, 1962). The effect of density on the dilatancy is also discussed by Khosravi et al. (2011) where they noticed a similar pattern as discussed earlier. Dewoolkar et al. (2007) found that increasing relative density had insignificant effects on the force-characteristics of the arching. Whereas, Costa et al. (2009) showed that loose samples showed three times more differential settlement compared to dense sample for the same material under trapdoor conditions. Kuwano & Ebizuka (2010) performed the model trapdoor tests on dense and loose Toyoura sand and highlighted the differences in stress distribution under varying sample height for both sample types. It was noted that the thickness of overburden soil plays a vital role in arching characteristics. Some researchers in the past indicated an insignificant effect of soil density on the arching phenomenon under trapdoor conditions (Evans, 1984). However, to develop a unique consensus about the effect of density and to study the effects of density combined with the presence of buried structure is yet to be explored in detail.

2.1.6 The shape of the arch

The shape of the arch was also a point of interest for the researchers in the recent past. Handy (1985) proposed the arching shape to be similar to catenary and described a coefficient for the load transfer at the arch edge to the surrounding soil. Similarly, Wang et al. (2013) found that the arching action in soil between cantilever piles forms a catenary shape. A catenary shape is defined as an analog to a freely hanging chain that is tied to both ends. Hence, the arching action in the soil is regarded as similar to the inverted catenary shape.

Eskişar et al. (2012) performed small 3D model tests on piled embankments using different combinations of materials and found that each material possessed a unique shape of the arching. Yun-min et al. (2008) proposed a semi-cylindrical arch shape in his experimental evidence. However, three distinct arching shapes were observed by Iglesia et al. (2013) during his centrifugal trapdoor tests. Similarly, Chevalier et al. (2009) observed different evolution patterns of the arching under trapdoor conditions.

Though there are different opinions on the shape of the arch under trapdoor conditions, this aspect still requires more insightful observation.

2.1.7 The magnitude of the trapdoor movement

Researchers in the past have plotted the variation of vertical stress or earth pressure above the lowering trapdoor and the displacement of the trapdoor. Normally the stress distribution varies with a varying displacement of the trapdoor.

Adachi et al. (1997), Paikowsky & Tien (2002) and Kikumoto et al. (2011) reported the extreme values of earth pressure at a very minute trapdoor settlement in their model tests. Shahin (2004) showed in his trapdoor model tests that the stress distribution reached peak value at around 1cm displacement of the trapdoor. Dewoolkar et al. (2007) studied the increased load on the buried structure through model experiments under normal gravity and centrifuge tests on circular piles and concluded that the maximum arching was achieved when the trapdoor settlement reached 1.5% of trapdoor diameter. Chevalier et al. (2008) showed that load transfer becomes maximum for a very small trapdoor movement but did not quantify the increase in the load. Similarly, Chevalier & Otani (2011) observed different parameters of the arching by comparing experimental

and numerical results using DEM simulations and showed that the arching phenomenon initiated as soon as the trapdoor movement started.

Pardo & Sáez (2014) performed experiments under trapdoor conditions similar to Terzaghi (1936) using clean sand and found that with a minor trapdoor settlement, load on the static parts around the trapdoor obtained a peak and with further increase in the settlement the peak value did not show much variation.

In all the above-presented researches, earth pressure distribution on the lowering trapdoor was the main focus. Pressure distributions on the surrounding parts of the trapdoor are not discussed in detail. Post peak softening behavior of earth pressure with the moving trapdoor also lacks information.

Soil arching has well been discussed in the previous literature. However, there are still some aspects that demand more clarity. One of them is the effect of particle shape on the arching behavior of the soil. Furthermore, the combined effect of a particle with density would be of much interest to the researchers. Besides the shape and density effect, the stress increase on the buried structures due to the arching phenomenon has not been discussed in earlier literature and is one of the main points of interest in the presented work.

2.2 Underground cavities phenomenon

Cave-in incidents, caused by the collapse of cavities, cause huge financial loss to the government exchequer (Galve et al. 2012). Cavities are mainly developed due to the internal erosion of the soil. Cavities can be broadly divided into two main categories; namely deep and shallow cavities. Deep cavities are more stable compared to the shallow ones, that are more exposed to expansion and leading towards a surface collapse or cave-in to form a sinkhole.

Incidents of road subsidence to the collapse of sub-surface shallow cavities are quite common, especially in a country like Japan where the number of such incidents has significantly increased in the last few decades (NILIM 2006; M. C. Wang & Hsieh, 1987). Cavities induced losses are being experienced all over the world with an increasing rate (Elhoud, 2012).

2.2.1 Model tests for cavities caused by buried pipelines

Buried structures like buried pipelines etc. are one of the main sources for sub-surface cavity development (R. Kuwano, Hori, & Kohashi, 2006). Specifically, in Japan, the majority of the existing sub-surface utility pipelines network is decades old, with a probability of being out of serviceability limits (Tohda & Hachiya, 2005; Tohda & Yoshimura, 2004; NILIM 2006). Similarly, in Germany, more than half of the buried pipeline network has an average age of above 50 years (Burn et al., 1999).

The existence of defective sub-surface structure to cause cavity development is long been recognized in the literature (Sekiguchi et al. 2003; Skempton & Brogan, 1994). Recently, PWRI (2006) have performed model tests in plain strain condition for the seepage effect around buried structures. Kuwano et al. (2006) performed the model tests with a defective buried pipeline and showed that the leakage of water from the pipe caused the disturbance in soil fabric in the surrounding and initiated the flow of surrounding soil into the pipeline to cause a cavity. Mukunoki et al. (2009) performed the model tests with buried pipelines to visualize the change in density due to pipe leakage by using an x-ray CT scan. The effect of particle size was discussed by Indiketiya, et al. (2017) and it was found that 0.3mm particles are highly susceptible to be washed away through a 5mm wide bottom slit.

All the above experimentation dealt with the problem of buried structure to cause cavity development and the loosening of the surrounding area. However, the effects of soil density, soil cover above the cavity, saturation of sample and the type of material used in the testing still require detailed discussion.

2.2.2 Model tests for the stability of developing cavities

In the case of the cavity development around a buried structure, the surrounding soil can be washed away and consequently causes the loss of support for the buried structure. Such a situation can lead to structural failure of the structure as well, along with the surface collapse danger (Abraham & Wirahadikusumah, 1999; Balkaya, Moore, & Sağlam, 2012; Moore, 2008). A collapse of buried structure can then trigger the surface collapse and hence a proper investigation is required for the stability of the buried structure as well. Soil arching produced around a cavity can also increase the stresses on the structure to produce a similar result of structural failure and surface collapse.

Indiketiya et al. (2017) performed the model tests apparatus with a bottom slit that can be opened to allow soil flow and representing the defect in the buried structure. Using particle image velocimetry techniques, it was observed that the particles right above the slit opening showed vertical movement trend, that was associated with the development of the arching action around the cavity.

The internal stability of the soil is discussed by several researchers in the past (Burenkova, 1993; Chang & Zhang, 2013; Kenney & Lau, 1985). To summarize, the stability of the soil strata above a buried structure or above an existing cavity depends upon several factors. These factors include the Particle size distribution and the stiffness of the soil (density effect). The effect of stability was correlated with direct and indirect parameters both. It was observed that flow direction, flow rate, moisture contents, soil compaction, and the capillary forces amongst particles, all play a part to evaluate the stability of soil mass.

2.2.3 Effect of soil density on cavity stability

Soil density plays a vital role in the stability of surface against cavity development (Renuka, 2012; M. Sato & Kuwano, 2010; Mari Sato & Kuwano, 2015). It is also observed that a denser material can hold a surface stable even for shallow cavities (Ohara, Kuwano, & Sera, 2019). However, for cohesive soils, it was observed that the density of the soil does not have a significant effect on the stability of soil strata (Benahmed & Bonelli, 2012), rather a smaller degree of saturation with higher clay contents can increase resistance against soil erosion.

2.2.4 Effect of crack width on cavity development

The effect of crack width has a significant effect on the particle migration to form a cavity. For quantifying the effect of crack width (or defect size in buried structure), the researcher used a parameter of D_{85} .

Rogers & Britain (1986) used a parameter of B/D_{85} , where B is the width of the crack. He studied the unidirectional flow of water for fine sands and gravels using a model test apparatus and gradually increasing the width of the bottom opening to study the slit width effect on the particle flow. It was found that a defect size ranging from 2.5

to $4.5D_{85}$ can constantly keep the particles to flow out. However, as per Mukunoki et al. (2009), the critical width of the crack is 5.9 times the size of the largest particle. For their tests, a number of crack sizes and orientations were used, and the effect of crack orientation was found to have insignificant effects on soil migration. However, the crack width and the area of crack exposed to the soil was the key factor influencing the soil flow.

Researchers like Guo et al. (2013); Renuka (2012); M. Sato & Kuwano (2013) etc. used a single shape of bottom opening to study the effect of size on the erosion of the particles and flow.

2.3 Capillary forces and cavity

The presence of water or moisture is a pre-requisite for the development of an underground cavity and its sustainability. Water induces the capillary effect in the soil structures, developing a pseudo cohesion amongst the particles and adding towards the stability of structure around the cavity.

Capillary forces in water can be divided into two categories namely the suction and the surface tension. Fisher (1928) and Haines (1927) were amongst the pioneers to discuss the capillary forces in the soil materials. Toll (1988) found the dependence of total stress contribution towards the saturation of the sample. Besides that, many researchers in the past used the soil water characteristics curve to represent the relationship of suction-saturation and showed that there exists no or negligible suction when the sample is fully saturated (Marinho & Chandler, 1994; Fredlund, Sheng, & Zhao, 2011; Gallage & Uchimura, 2010; Lu, Godt, & Wu, 2010; Vanapalli, Sillers, & Fredlund, 1998; Lu, Kaya, & Godt, 2014). Once the air entry point has been crossed, a small variation in the degree of saturation (S_r) can affect the soil suction largely. Similarly, from a dry point, adding a small amount of water can largely increase the strength of soil mass (Hornbaker et al., 1997; Scheel et al., 2008).

2.4 Numerical simulations for the underground cavities

Despite the extensive experimental work on the cause of the cavity formation, expansion and internal erosion of soil, very limited or almost negligible studies are found on the numerical simulation of the cavity related problems. One of the reasons for lesser research in this field is

the non-availability of a model in numerical simulations that can deal with the corresponding soil response. Soil erosion and cavity development process mainly deal with the granular soils and the cohesive soils are normally thought to resist the particle migration (Benahmed & Bonelli, 2012). In such a context, FEM analysis is less applicable to this phenomenon, compared to DEM or other granular methodologies. DEM models normally lack the capillary interaction between particles, which is a pre-requisite for the cavity phenomenon.

Otsubo, Ali, & Kuwano (2018) performed cavity simulations using DEM to investigate the particle shape effect. Dong et al. (2018) performed 3D DEM simulations on spherical particles to investigate the scale effect on cylindrical cavity expansion. Li et al. (2015) performed numerical simulations on cylindrical cavity evolution using coupled DEM-LBM (Lattice Boltzmann Method) technique using circular disks to investigate the cavity stability and its evolution.

2.5 Numerical models for capillary forces

To accurately simulate the particle behavior in the cavity phenomenon, the incorporation of capillary forces in numerical modeling is essential. Traditional DEM model being unable to do so, researchers tried to modify the discrete element code. Willett et al. (2000) explained a new method for the evaluation of capillary forces on pendular liquid bridges using spherical particles with similar and unequal radii. Farouk et al. (2004) proposed a model to be used in DEM numerical simulations for estimation of matric suction-based upon given water contents. Lu et al., (2010) proposed a suction-stress characteristic curve and introduced a closed-form equation for calculating effective stress in the soil mass. Ji-Peng et al. (2017) introduced the water bridge effect in the pendular state for contacting spherical particles and formulated the calculation of suction and surface tension. Monnet et al. (2017) explained a theoretical retention model for the calculation of capillary forces between two spherical particles having a similar size. Zhou et al. (2018) introduced a new constitutive model for partially saturated granular materials using the degree of capillary saturation and effective inter-particle stress. Sun & Sakai (2018) introduced a water bridge model using spherical particles for a particle to particle and particle to wall interactions and compared it with the experimental results and other similar notable models.

The majority of the researchers presented a model for the capillary forces in unsaturated conditions for a given water volume, using spherical particles for simplification. Also, the

models presented are used in powder technology, pharmaceuticals or multiphase flow, instead of geotechnical aspects. It is rare to find literature that utilized the models in cavity simulations using DEM and to explain the arch development and the force chains around the cavitated space. Furthermore, existing models also lack the effects of capillary forces on the degree of saturation and particle size effect on the rupture distance of the water bridge.

2.6 Discrete Element Method (DEM)

The discrete element method (DEM) is a powerful tool, capable of analyzing the granular assemblies and based upon the basic theory of Cundall & Strack (1979). Since then, DEM is being used in a wide variety of applications, e.g. powder technology, pharmaceuticals, fluid dynamic, concrete engineering and a bit recently in geotechnical engineering as well.

2.6.1 Calculation sequence in DEM

A schematic diagram for the calculation steps in DEM is presented in Figure 2. 1. The first step for the DEM simulations is the inputting geometry of the granular sample, which is achieved by giving boundary conditions and coordinates of individual particles. The second step is the input parameters, including stiffness both in normal and shear direction, time step, shear rates, mass density, friction coefficients. The nature of simulation (either dynamic, transient or quasi-static) is decided for the simulation.

Simulation is run for a specific time or specific stress/deformation magnitude, that involves the calculations in numerous time steps. For each time step, the magnitude of interparticle forces is calculated that is used to determine the resultant forces and torque including the moments. These resultant forces and moments are then further used to determine the translational movement and rotational motion of particles respectively. The following basic equations are utilized for this.

$$F = m(\ddot{x} - g) \quad (2.1)$$

$$\tau = I\ddot{\theta} \quad (2.2)$$

where F is particle force, m is the mass of the particle, \ddot{x} is the particle acceleration, g is the acceleration due to gravity ($= 9.81 \text{ N/m}^2$), τ is the torque acting on the particle, I is the moment of inertia of particle, and the $\ddot{\theta}$ is the angular acceleration of the particle.

Once we are familiar with the translational and rotational movements, particle inertia is used for determining the acceleration for both translational and rotational movements. Through these accelerations, a central difference type integration scheme is implied to get the velocities and consequently the displacements and rotations of each particle. These incremental displacements and rotations are used to update the particle positions for the next time step. The same step is repeated for the next time step until we reach our desired value of the parameter. It can be said that Discrete Element Analysis is a dynamic analysis even though it may respond in a quasi-static manner.

To incorporate the basic steps for a DEM based algorithm, calculate the forces between particles and update the position of particles, Newton's 2nd law of motion is the incepting equation.

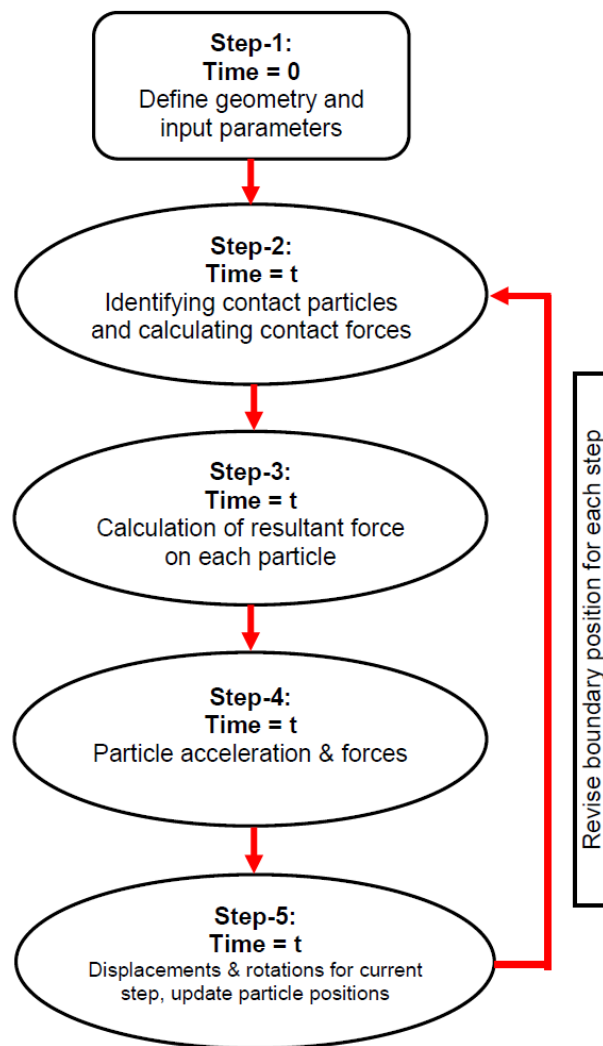


Figure 2. 1 Schematic diagram for calculation sequence in DEM

2.6.2 Governing Equation of DEM

Basic principles of DEM are normally introduced by directly considering the dynamic equilibrium of individual particles. It is useful to consider DEM from matrix structural analysis where particles are analog to the degree of freedom. Using this analogy, the overall governing equation of the system is expressed as:

$$M\ddot{\mathbf{u}} + C\dot{\mathbf{u}} + K\mathbf{u} = \Delta\mathbf{F} \quad (2.3)$$

Where M is the Mass matrix (both translational and rotational inertia), C is damping matrix and K is the Global Stiffness matrix, $\ddot{\mathbf{u}}$ is acceleration, $\dot{\mathbf{u}}$ is velocity and \mathbf{u} is the incremental displacement. $\Delta\mathbf{F}$ is an incremental force vector (including moments). The objective of the analysis is to solve for the incremental displacement, that is used to locate the particles for the next time step and the same procedure is continued.

2.6.3 Dynamic Equilibrium Equation:

Dynamic Equilibrium Equation (eq. 2.3) can be solved by two methods:

- 1- Implicit approach
- 2- Explicit approach

2.6.3.1 Implicit Approach:

In an implicit approach, the solution for incremental displacement is solved in such a manner that a single vector \mathbf{u} can be created to account for the cumulative incremental displacements of all particle centroids (O'Sullivan, 2011).

$$\mathbf{U} = \begin{pmatrix} u^1_x \\ u^1_y \\ u^1_z \\ u^a_x \\ u^a_y \\ u^a_z \\ u^{Np}_x \\ u^{Np}_y \\ u^{Np}_z \end{pmatrix} \quad (2.4)$$

In eq. 2.4, u^a_x , u^a_y , u^a_z are the incremental translational displacements of particle a in three axes respectively. There is a total N_p number of particles in the

system. Incremental force vector (ΔF) is created in a similar way, Mass matrix (M), Damping Matric (C), and Global Stiffness matrix (K) are combined in a similar manner as that of FEM.

Primarily, the implicit approaches proposed by Kishino (1989) and (Holtzman et al. (2008)). For solving the dynamic equilibrium equations produced through this approach, a large number of simultaneous equations are generated that results in the inversion of a very large stiffness matrix. Resultantly, it'll take a lot of machine time and power to solve the equations.

2.6.3.2 Explicit Approach:

To overcome the problem of time and machine power, the explicit approach is used where instead of forming a single global system of equation, we use the equilibrium in individual particles. This approach results in lesser memory requirements. Zhu et al. (2007) gave the most general dynamic equilibrium equation for a particle P with mass m_p .

$$m_p \ddot{u}_p = \sum_{c=1}^{N_{c,p}} F_{pc}^{con} + \sum_{j=1}^{N_{nc,p}} F_{pj}^{non-con} + F_p^f + F_p^g + F_p^{app} \quad (2.5)$$

where, \ddot{u}_p is acceleration vector of particle P , F_{pc}^{con} are contact forces due to contact c when there are $N_{c,p}$ contacts between particle p and other particles or boundary. $F_{pj}^{non-con}$ are non-contact forces between particle P and other particles.

2.6.4 Contact models in DEM

The basic model used in the LAMMPS utilizes the simplified Hertz-Mindlin model in both normal and tangential direction, and well explained in Johnson (1985).

2.6.4.1 Normal Contact

The Hertzian contact model (Hertz, 1882) for normal contact between particles is frequently used in DEM based software. Although the Hertz model is

for smooth surfaces, the resultant force-deformation relation is non-linear elastic and the normal force is described as (Johnson, 1985):

$$N = \frac{4}{3} E_p^* R^{*0.5} u^{1.5} \quad (2.6)$$

where u is the overlap between two contacting particles; E_p^* is the equivalent Young's modulus, and R^* is the equivalent radius of two contacting particles (particle 1 and particle 2) given as:

$$E_p^* = \left(\frac{1-\nu_1^2}{E_{p1}} + \frac{1-\nu_2^2}{E_{p2}} \right)^{-1} \quad (2.7)$$

The equivalent radius, R is described by Derjaguin (1934) as:

$$R^* = \left(\frac{1}{R_1} + \frac{1}{R_2} \right)^{-1} \quad (2.8)$$

In the above expression (2.7), ν is the Poisson's ratio of two contacting particles.

2.6.4.2 Tangential Contact

The work done by Hertz (1882) was later extended by Mindlin (1949) to add the tangential component in the model. The incremental contact stiffnesses in the normal direction (K_N) and the tangential direction (K_T) are given as:

$$K_N = \frac{dN}{d\delta} = 2E_p^* a \quad (2.9)$$

$$K_T = 8G_p^* a \theta \quad (2.10)$$

where θ is the degree of partial slip, G_p^* is the equivalent shear modulus of two contacting particles, and a is the radius of circular contact area between two particles in contacts, described by the following relations:

$$G_p^* = \left(\frac{2-\nu_1}{G_{p1}} + \frac{2-\nu_2}{G_{p2}} \right)^{-1} \quad (2.11)$$

$$a = \sqrt{R^* \delta} \quad (2.12)$$

Degree of partial slip (θ) was described by Mindlin (1949) for the initial loading case as follows:

$$\theta_{loading} = \left(1 - \frac{T}{\mu N} \right)^{1/3} \quad (2.13)$$

where T is tangential contact force and μ is the coefficient of inter-particle friction. Later, the relationship for $\theta_{unloading}$ and $\theta_{re-loading}$ was demonstrated by Mindlin & Deresiewicz (1953).

2.7 Important parameters in DEM

A pre-requisite for an accurate DEM simulation is to provide precise and accurate parameters. A number of input parameters are required by any DEM based computer program for the smooth simulation process, e.g. interparticle friction value, damping coefficient, time step, particle density, etc. Besides that, several micromechanical parameters are also used commonly in DEM. In the following sections, some of the basic DEM parameters are discussed.

2.7.1 Inter-particle friction coefficient

Interparticle friction can be regarded as an important factor affecting the behavior of granular material. Konishi et al. (1983) did a laboratory experiment on oval-shaped rods with different aspect ratios and showed that by increasing the interparticle friction, peak friction angle also increased.

Härtl & Ooi (2011) performed direct shear tests on spheres and paired spheres with different aspect ratios and inter-particle friction using DEM. He found that limiting bulk friction was found to increase in a nonlinear manner with the increase of particle friction. Thornton (2000) also showed that the friction angle increases with the increase of interparticle friction value. Still, there is less information available for the effect of interparticle for cyclic loading. A maximum value of 0.5 was suggested by Huang et al. (2014) for the accuracy of simulations. It was found that there exists more rolling of particles than the frictional slip when the friction coefficient, μ value is larger than the given limit.

2.7.2 Particle shape

Experimentally, extensive work has been done to investigate the particle shape effect for geomechanics. Recently, DEM based studies have started incorporating different shapes of a particle in their numerical simulations. The exponential rise in the

computational power of current computers has highly aided to explore the shape effect of particles using DEM.

DEM has eased the incorporation of different particle shapes. In the past, different researchers have used different shapes of particles to incorporate them in their simulations, based upon their purpose or the ease of contact model for certain shapes. Out of all, majority of researchers used ellipse or ellipsoidal shapes (Bagherzadeh-Khalkhali & Mirghasemi, 2009; Lin & Ng, 1997; Ng, 1994; Rothenburg & Bathurst, 1992; Ting, Khwaja, Meachum, & Rowell, 1993. etc) or polygonal shapes (Bagherzadeh-Khalkhali, Mirghasemi, & Mohammadi, 2008; Barbosa & Ghaboussi, 1992; Matuttis, Luding, & Herrmann, 2000; Mirghasemi, Rothenburg, & Matyas, 1997, 2002. etc.).

Rothenburg & Bathurst (1992) performed biaxial shearing numerical simulations using ellipsoid particles and found that increasing eccentricities affected the coordination number and the peak internal friction angle of the sample. Similar sort of results were also obtained by Ting et al. (1993) in their biaxial shear and isotropic compression stages using two-dimensional elliptical particles. Angularity effect on shear strength of the sample was investigated by Mirghasemi et al. (2002) and using polygonal particles in simulations, it was concluded that shear strength and angularity have direct relation. Yan (2009) incorporated clumps of particles with different aspect ratios for direct shear test and determined that longer particles showed higher shear strength and more dilation. Similarly, Abedi & Mirghasemi (2011) showed that for particles with different shapes in the biaxial compression test, higher angularity showed higher dilation and residual shear strength. Hence, the majority of results show that there is a significant effect of particle shape on the mechanical characteristics of granular material.

Jensen et al. (1999) used the combination of circular disks that touch each other, without any overlap. However, few recent researchers used the overlapping of spherical particles to result in a realistic or close to realistic grain shape (Matsushima, Saomoto, Matsumoto, Toda, & Yamada, 2003; Soltanbeigi et al., 2018).

2.7.3 Coordination number

Kuhn (2006) defined the coordination number as the ratio of twice the number of contacts to the total number of particles:

$$\text{Coordination number} = \frac{2 \times N_c}{N_p} \quad (2.14)$$

Where N_c is the number of contacts and N_p is the total number of particles in the specimen. For stability of simulation, a minimum of coordination number was defined by Rothenburg & Krut (2004). According to him, for the stability of a 2D assembly, the coordination number must be greater than 3. The coordination number is useful in describing the evolution of the contact signature.

Several researchers in the past (Graton & Fraser, 1935; Smith, Foote, & Busang, 1929; Cui & O'Sullivan, 2006; Magnanimo et al., 2008) correlated the coordination number with the void ratio of the sample. A correlation of coordination number with the void ratio of the sample can be used for better assessment of small strain stiffness of the granular packing.

2.7.4 Damping

In DEM simulations, damping is applied in two different ways. One is the local damping or the contact damping, and the other is the global damping or the viscous damping. The former being implemented only for the contacting particles, whereas the latter is applicable for all particles with respect to time each time step. The basic purpose of introducing damping in simulations is to dissipate the energy in the system.

Munjiza (2004) stated that the DEM code lacks '*material damping*'. Such lack of damping in DEM simulations results in constant vibration of particles like elastic springs due to the absence of yield after frictional sliding (O'Sullivan, 2011).

The concept of global damping was originated by Cundall & Strack (1979) and each particle acted as a dashpot and experienced damping proportional to its mass. Local damping was proposed by Cundall (1987) and explained in Itasca (2007) as:

$$F_d = -\alpha^* |F^p| \text{sign} V_p \quad (2.15)$$

where F_d is the force of damping on particle p , F^p is the resultant force on particle p , V_p is velocity vector and α^* is the damping constant.

Very few researchers have taken the effect of damping as an input parameter to their DEM simulations. Ng (2006) performed conventional triaxial drained and undrained tests on an assembly of ellipsoid particles in DEM simulations with varying

damping factor values and found that the shear strength and the volumetric strains are directly proportional to the damping factor. Ng et al. (2015) performed DEM simulations for granular media with different values of damping and found that the higher damping values result in lower sample density due to the excess dissipation of energy and the slower settling speed of particles. It was also concluded that by controlling the damping coefficient during the pluviation stage, samples with different densities can be obtained.

2.7.5 Timestep in DEM simulations

DEM algorithm is an explicit central difference time-integrated method (Cundall & Strack, 1979). However, inherently it has a limitation of being conditionally stable that results in an impact of time-step on the overall results of numerical simulation. However, using an implicit time integration scheme can overcome the dependency of time step but it would be computationally costly as well. A discussion on merits and demerits for both implicit and explicit scheme is presented by Belytschko, Liu, & Moran (2000) and O’Sullivan & Bray (2001).

The critical time step (Δt_c), that defines the boundary of balanced or unbalanced numerical simulation, as defined by Cundall & Strack (1979) as follows:

$$\Delta t_c = 2 \sqrt{\frac{m}{k}} \quad (2.16)$$

where the above equation is valid for a single degree of freedom with particle mass m connected to ground with a spring having a stiffness of k .

Above presented critical time step was further elaborated by Hart et al. (1988) with minimum particle mass (m_{min}) and largest contact stiffness (k_{max}) and a multiple contact parameter (α), in the following manner:

$$\Delta t_c = \alpha \sqrt{\frac{m_{min}}{k_{max}}} \quad (2.17)$$

The above relations are more appropriate for the DEM codes that utilize the linear contact models. However, the currently available DEM programs and commercial software mostly use the non-linear contact models, that require the changing stiffness

values. Consequently, researchers have modified the Cundall & Strack (1979) equation to incorporate non-linear behavior, e.g. Johnson (1985) and Jensen et al. (2014).

Otsubo et al. (2017) performed three-dimensional triaxial compression tests using face-centered cubic packing using uniform spheres for the monodisperse system and found that the critical time step is directly proportional to the diameter of the particles.

CHAPTER 3: EXPERIMENTAL & NUMERICAL SETUP FOR TRAPDOOR

Trapdoor condition is one of the main phenomena for the soil arching. A trapdoor condition exists when a part of soil yields compared to the surrounding static mass. Such a condition allows the particles above the yielding portion to rearrange and form a shape of the arch to transfer a load of above static soil mass towards the stable surroundings of yielding mass. Soil arching under trapdoor conditions ensures the stability of soil strata by redistributing the earth-pressure to the base soil. However, at the same instance, the stresses on the static base magnify to manifolds, endangering the structures present directly under that portion.

The current chapter discusses the experimental setup for the Model Trapdoor Tests along with the numerical simulation setup and plan.

3.1 Experimental setup for trapdoor tests

To study the arching under trapdoor conditions and the stress variation as a result of the arch formation, a model test equipment was used (Figure 3. 1). Shown trapdoor model test apparatus was developed in the Institute of Industrial Science, the University of Tokyo. More details of apparatus development can be obtained through Kuwano & Ebizuka (2010).

The apparatus consists of two main parts: the upper part with the soil chamber and the lower part with a loading system. The soil chamber has a length of 700mm with a 294mm width and 555mm height. The base of the soil chamber consists of seven plates with dimensions of 99.8mm (X), 293.6mm (Y) and 105mm (Z). Out of seven base plates, the inner five plates are capable of moving upwards and downwards in any combination as required. Whereas the side plates are fixed and cannot be moved. The Schematic figure of trapdoor equipment is shown in Figure 3.2 for clarity.

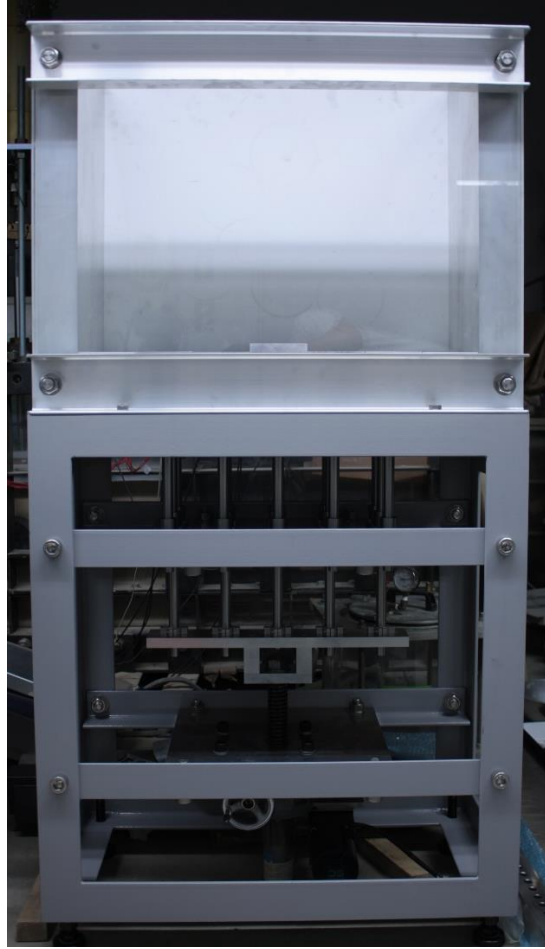


Figure 3. 1 Trapdoor model test apparatus

Each movable base plate is further divided into five sub-plates with a width of approximately 20mm each. However, the sub-plates cannot move separately, and their motion is a combined effect of all five sub-plates in the group. Each sub-plate is fitted with a load cell, capable of measuring both vertical and horizontal loads acting on them. In total, 25 numbers of load cells are attached to the base plates (five per base plate).

Keeping in view the fact that shearing stresses are much smaller compared to the normal stresses, the measurement of shearing stresses is challenging. To overcome this difficulty and to investigate the exact behavior of shearing forces, the top surface of movable base plates was attached with 120 Grit sandpaper, that amplified the shearing response.

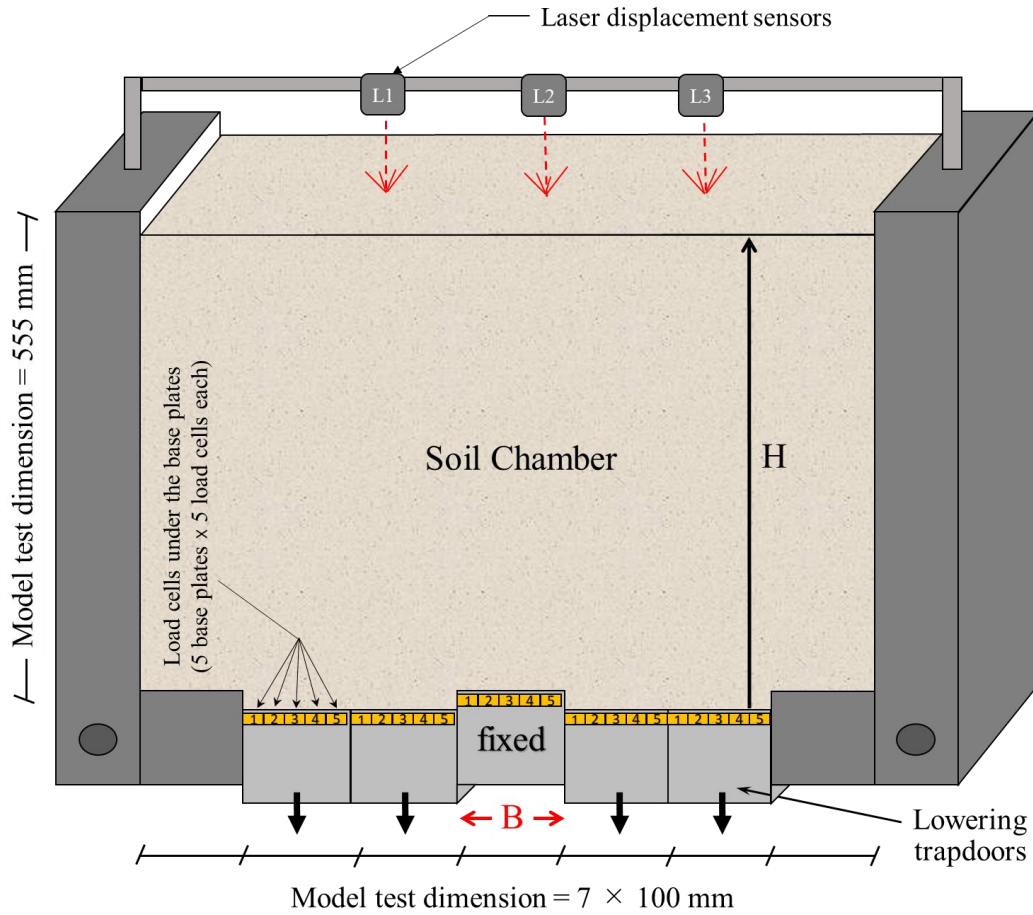


Figure 3.2 Schematic figure of soil chamber in model trapdoor test

The front face of the soil chamber is fitted with a thick acrylic transparent plate. The acrylic plate serves two purposes: to help in visualizing the on-going particle movement during the test and to reduce the friction between particles and plate with a relatively smooth surface having a smaller coefficient of friction (Bowden, Tabor, & Palmer, 1951).

Base plates of the soil chamber are moved in either upward or downward direction with the help of the bottom loading system, that consists of a motor being regularized with a control unit. The movement of the motor is translated into linear motion of a vertical shaft with the help of a gearing mechanism (Figure 3.3). In the given trapdoor series, a passive condition was tested, representing a buried structure at the center and surrounding settling soil. Such conditions resulted in a central fixed plate and the lowering side plates. To attain such a motion, a downward movement of the bottom main shaft is applied with the help of a connected motor and control unit (Figure 3.3).

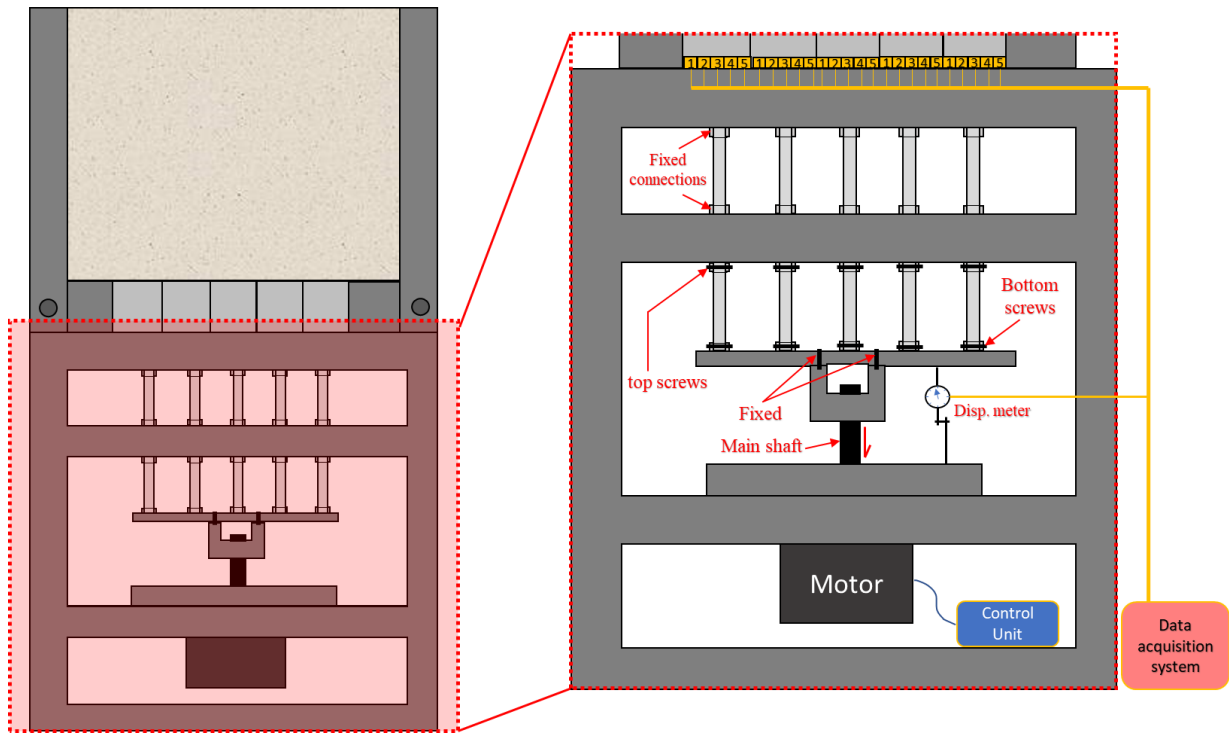


Figure 3.3 Schematic diagram of base loading system of trapdoor apparatus

3.1.1 Trapdoor movement mechanism

Top screws connect the base plates with the rigid frame in the lower part to keep their position firm. However, the bottom screws connect the base plates with the moving lower main shaft, connected with the motor assembly. To ensure the central base plate of the soil chamber to be static, the bottom screws for the central plate loading system are kept loose, whereas the top screws for the same are kept tight. This setup enables the central plate to maintain its position, without being affected with the lowering main shaft. Contrary to the central plate, the bottom screws for the side plates are kept tight and the upper screws are allowed loose enough to facilitate shaft movement. Such assembly provides the setup for the passive analysis of trapdoor conditions (as described in Chapter 1) and the resultant movement of the base plates is shown in Figure 3.4 below.

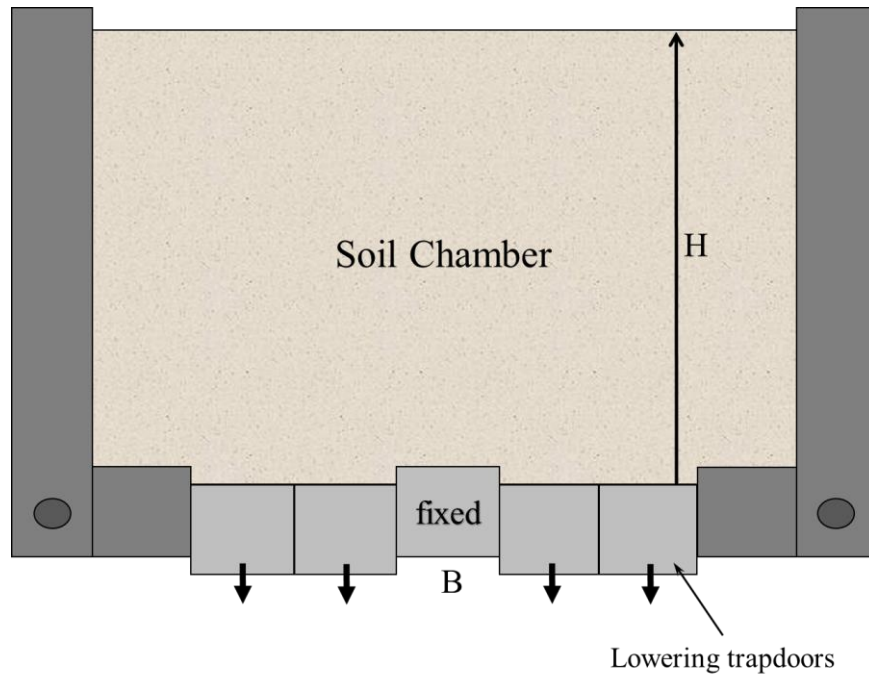


Figure 3.4 Resultant position of base plates for the trapdoor tests

As shown in Figure 3.2, three laser displacement meters were installed above the soil chamber. The position of laser displacement meters was adjusted in such a way that one of them faced the center of the central static plate, whereas the other two were installed in the middle of lowering plates on each side. To monitor the displacement of base plates, a displacement meter was also installed in the lower part of the apparatus, which was also connected with the data acquisition system.

3.1.2 Calibration Factors for load cells

Calibration was performed for all load cells in the base plates. A total of 25 load cells were calibrated for the normal load case. However, for calibration factors in the horizontal direction, factors provided by Ebizuka (2011) were utilized. Figure 3.5 below shows the numbering of the load cells used in the model trapdoor tests.

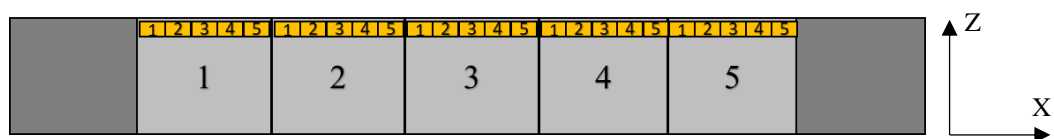


Figure 3.5 Front view of load cell numbering in trapdoor model tests

Table 3.1 below illustrates the calibration factors in both horizontal and vertical direction in volts/g of the applied load.

Table 3.1 Factors for load cell calibration

Base Plate Number	Load Cell Number	Load factors (Volts/gram)	
		Shear	Normal
1	1	5.8608	6.2200
	2	6.2886	6.2185
	3	6.1986	6.1976
	4	6.3602	6.1767
	5	6.2731	6.360
2	1	5.3046	6.1314
	2	5.8701	5.8901
	3	6.7305	6.3877
	4	6.5482	5.8659
	5	5.8617	6.0565
3	1	-5.9145	5.9875
	2	6.1962	6.6576
	3	6.1312	6.0736
	4	5.3809	5.6693
	5	5.9341	6.3427
4	1	5.2652	6.7169
	2	4.9378	6.2502
	3	6.1197	6.1156
	4	5.2128	5.8653
	5	6.1503	6.2471
5	1	4.8382	6.4818
	2	6.2044	5.8842
	3	6.1953	6.5652
	4	6.1495	6.1818
	5	6.0150	6.0709

Calibration graphs for all 25 load cells are given below in Figure 3.6 to Figure 3.12 below:

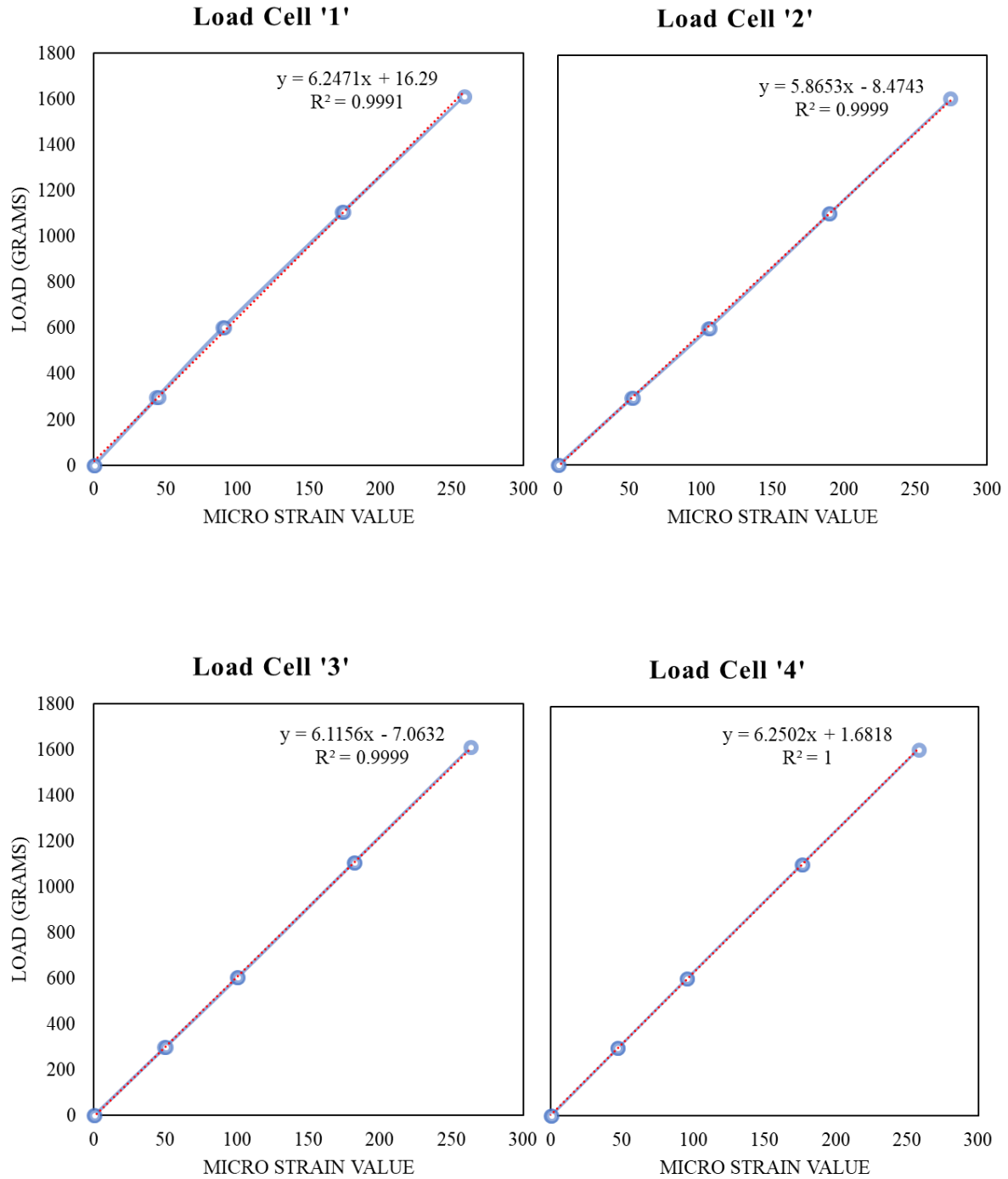


Figure 3.6 Calibration curves for Load cells 1 to 4

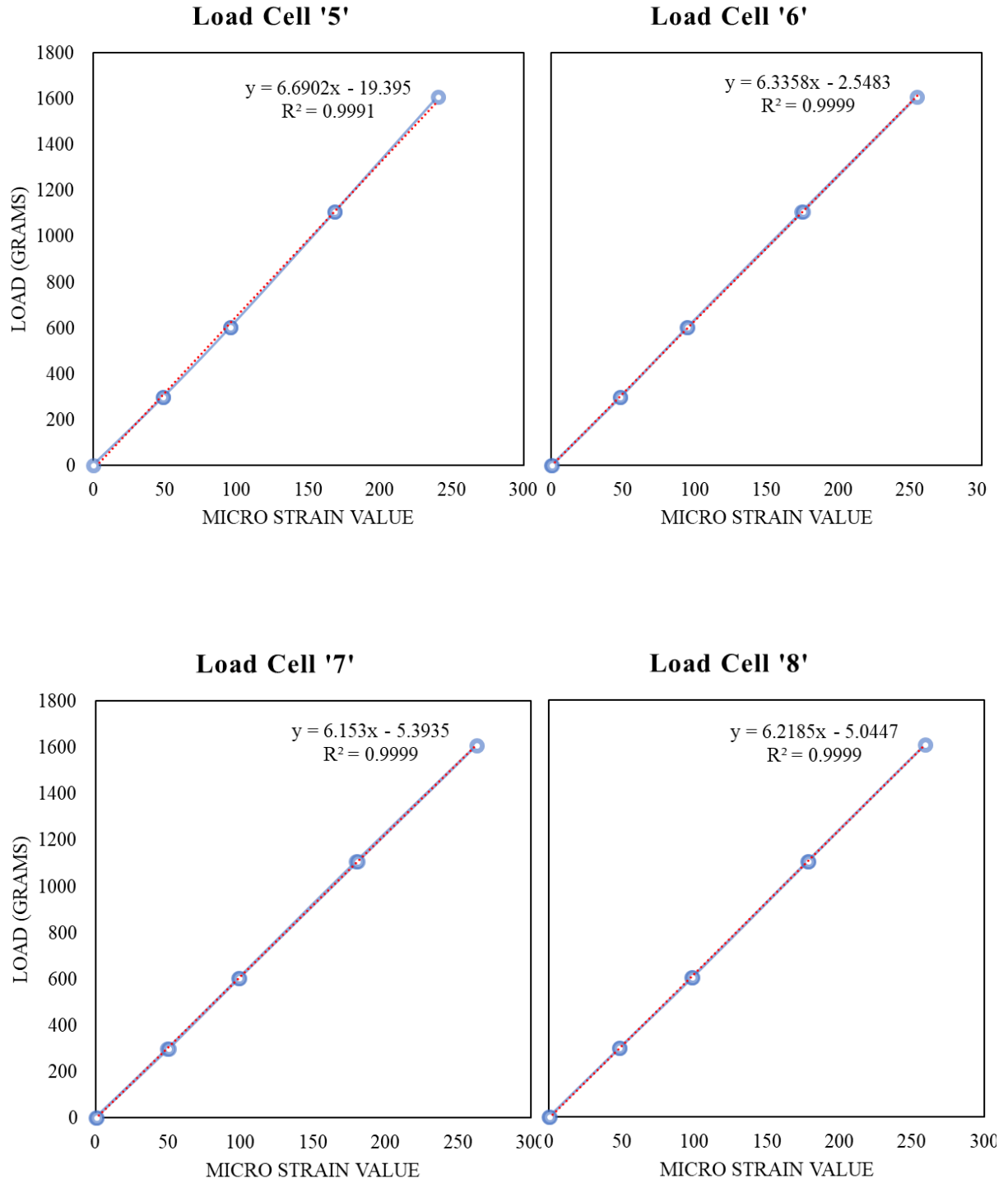


Figure 3.7 Calibration curves for Load cells 5 to 8

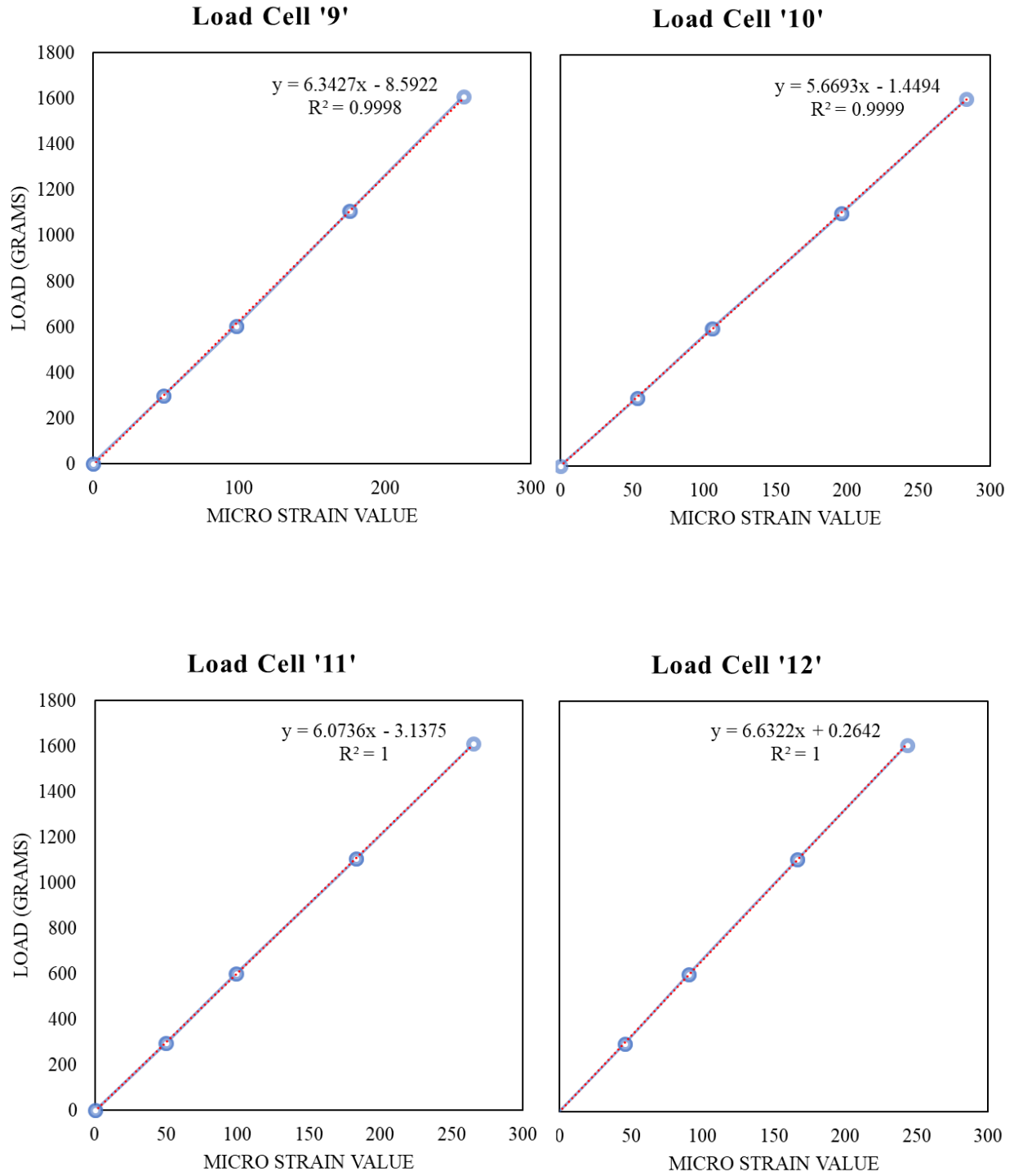


Figure 3.8 Calibration curves for Load cells 9 to 12

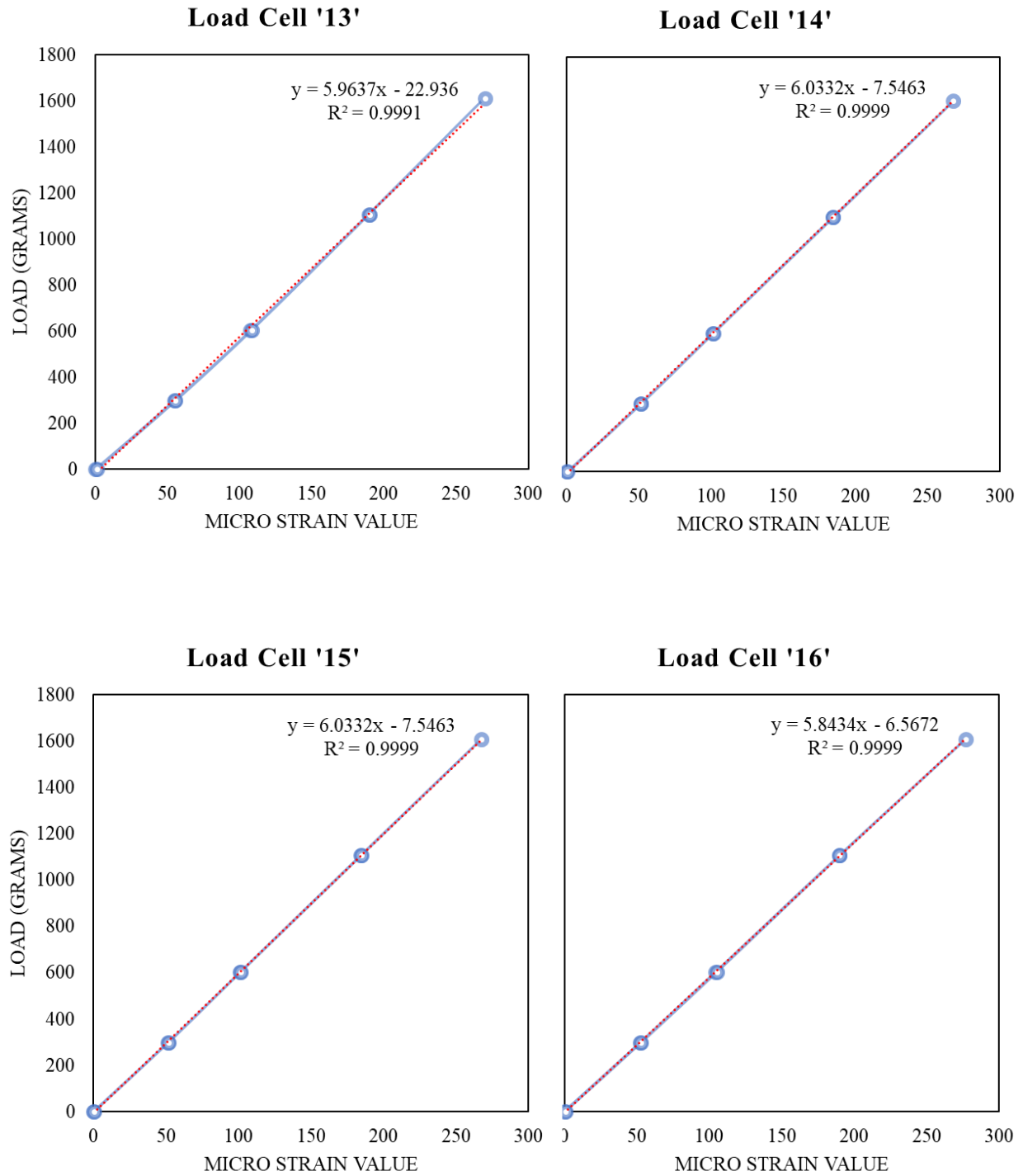


Figure 3.9 Calibration curves for Load cells 13 to 16

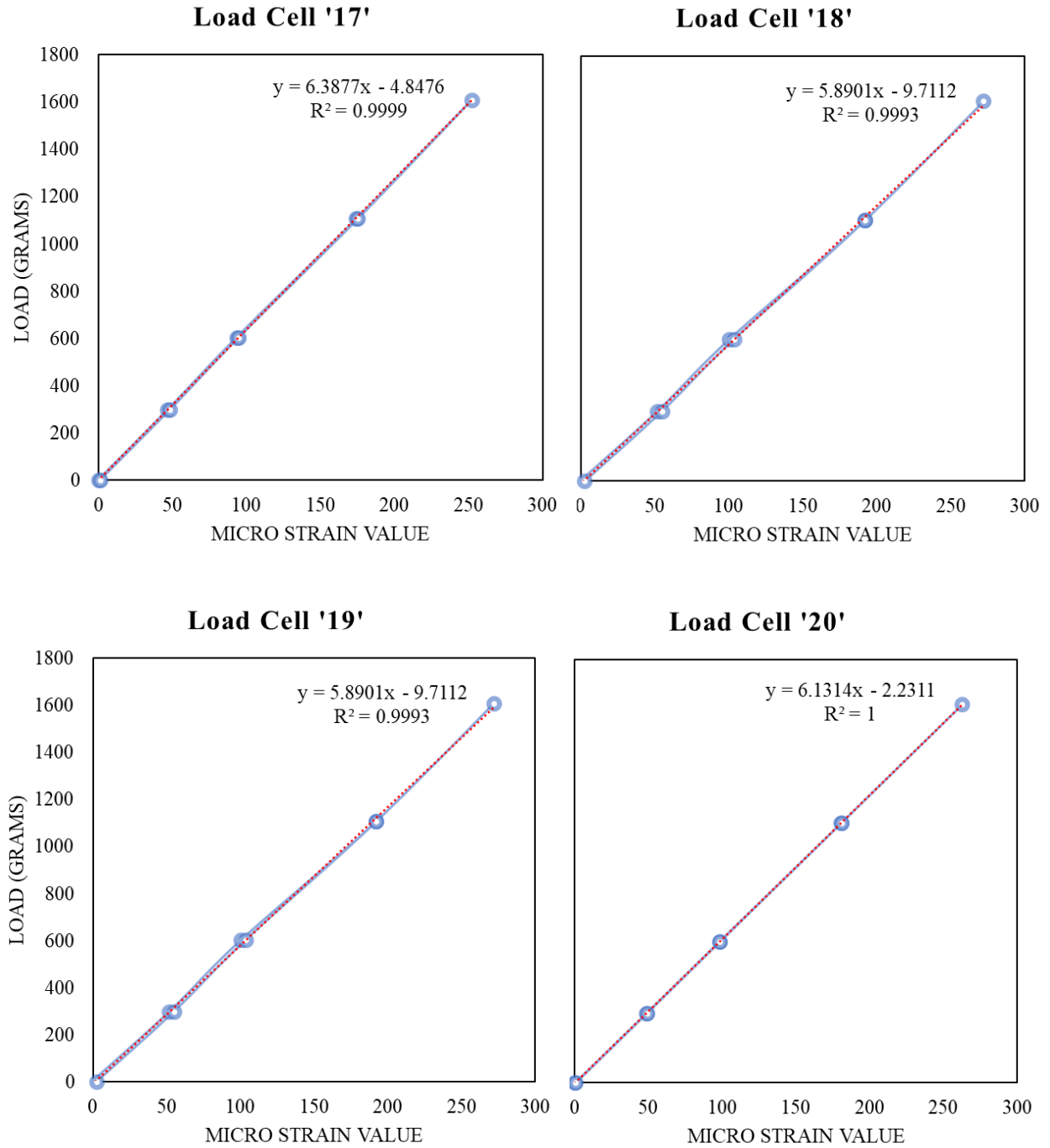


Figure 3.10 Calibration curves for Load cells 17 to 20

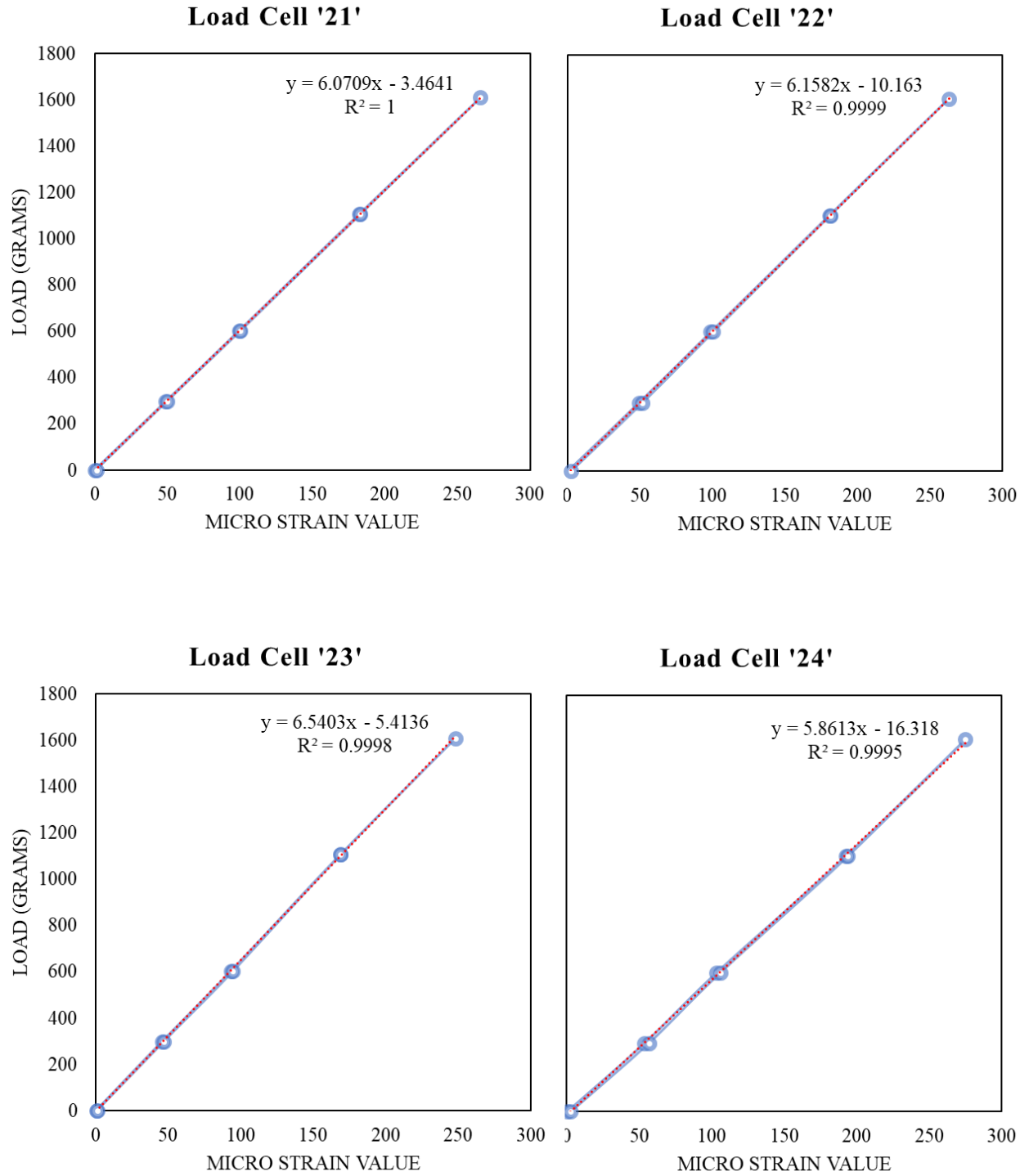


Figure 3.11 Calibration curves for Load cells 21 to 24

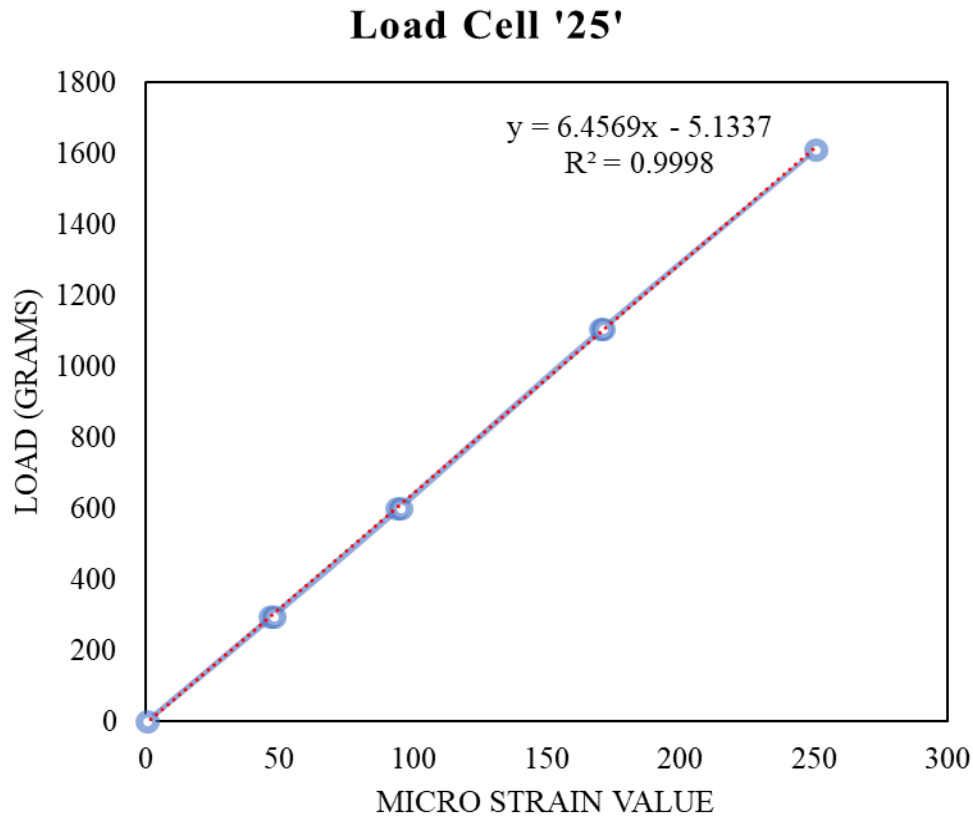


Figure 3.12 Calibration curves for Load cell 25

3.1.3 Calibration for motor speed

The motor was controlled through a control unit with options either to push the base plates upwards or the downwards with varying speeds, ranging from 100 to 2000 rev/min. Each revolution speed was then correlated with the displacement of the plate, measured through an external displacement meter. The calibration factor for the displacement meter was measured to be 0.01 mm/ $\mu\epsilon$. Table 3.2 below summarizes the calibration factors.

Table 3.2 Calibration factors for the motor speed

Motor Speed (rpm)	0	100	200	300	400	500	1000	2000
Average ($\mu\epsilon/s$)	0	0.112	0.1178	0.252	0.463	0.559	1.08	1.98
mm/sec	0	0.0011	0.0012	0.0025	0.005	0.0056	0.011	0.02
mm/min	0	0.068	0.0718	0.153	0.281	0.3387	0.653	1.199

Figure 3.13 below shows the calibration curve for corresponding the motor RPM to rate of plate lowering in mm/min.

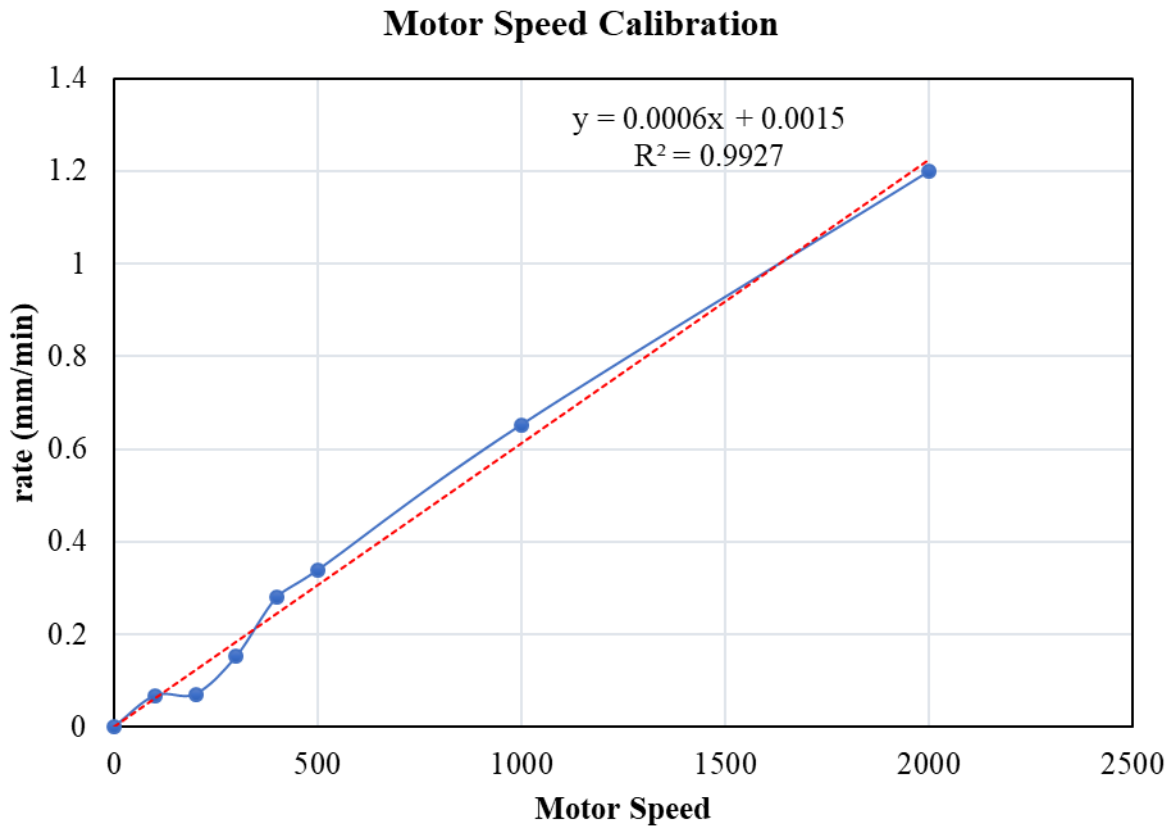


Figure 3.13 Calibration curve for motor speed

3.1.4 Material description

For the trapdoor model tests, a total of three types of materials were compared, namely:

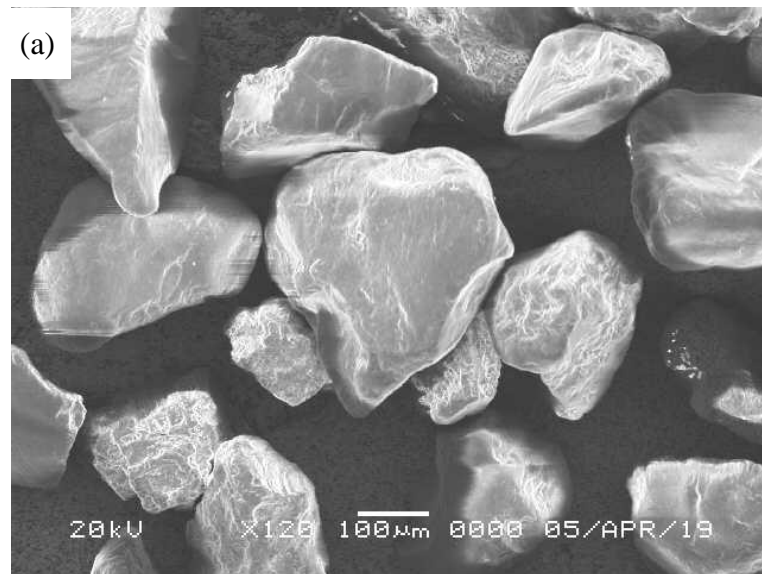
- i- Spherical glass beads
- ii- Kashima river sand
- iii- Toyoura sand

Out of these materials, the first two were physically tested in the current study. Whereas, the results of Toyoura sand (Ebizuka, 2010) were compared in this study. The median particle size (D_{50}) of Toyoura sand was about nine times smaller than Kashima river sand or glass beads (Table 3.3). Representative scanning electron microscope

(SEM) images of the tested materials were taken using a Jeol JSM-5600LV Scanning Electron Microscope and the difference in their shapes is shown in Figure 3.14. For a better comparison, Table 3.3 provides the coefficient of uniformity ($C_u = D_{60}/D_{10}$), the specific gravity (G_s), the minimum and maximum void ratios (e_{\min} and e_{\max}) and shape parameters; where sphericity is the ratio of surface area of equal volume sphere to the surface area of given particle (Hakon, 1935) and convexity is the ratio of the projected particle area to the gross area (Altuhafi, Matthew, & Vasiliki, 2016). The shape factors (convexity and sphericity) listed in Table 3.3 are the median values corresponding to 50% cumulative distribution. These values were quantified using QicPic equipment, where the measurements were conducted for dropping particles with random directions (Fatin Altuhafi et al. 2013; Witt, Köhler, & List, 2004).

Table 3.3 Material properties of used material in trapdoor tests

material	D_{50} (mm)	C_u	G_s	e_{\min}	e_{\max}	sphericity	convexity
Toyoura sand	0.203	1.61	2.64	0.637	0.946	0.892	0.933
Kashima river sand	1.72	1.25	2.62	0.552	0.798	0.888	0.986
Glass beads	1.80	1.20	2.50	0.571	0.671	0.943	0.988



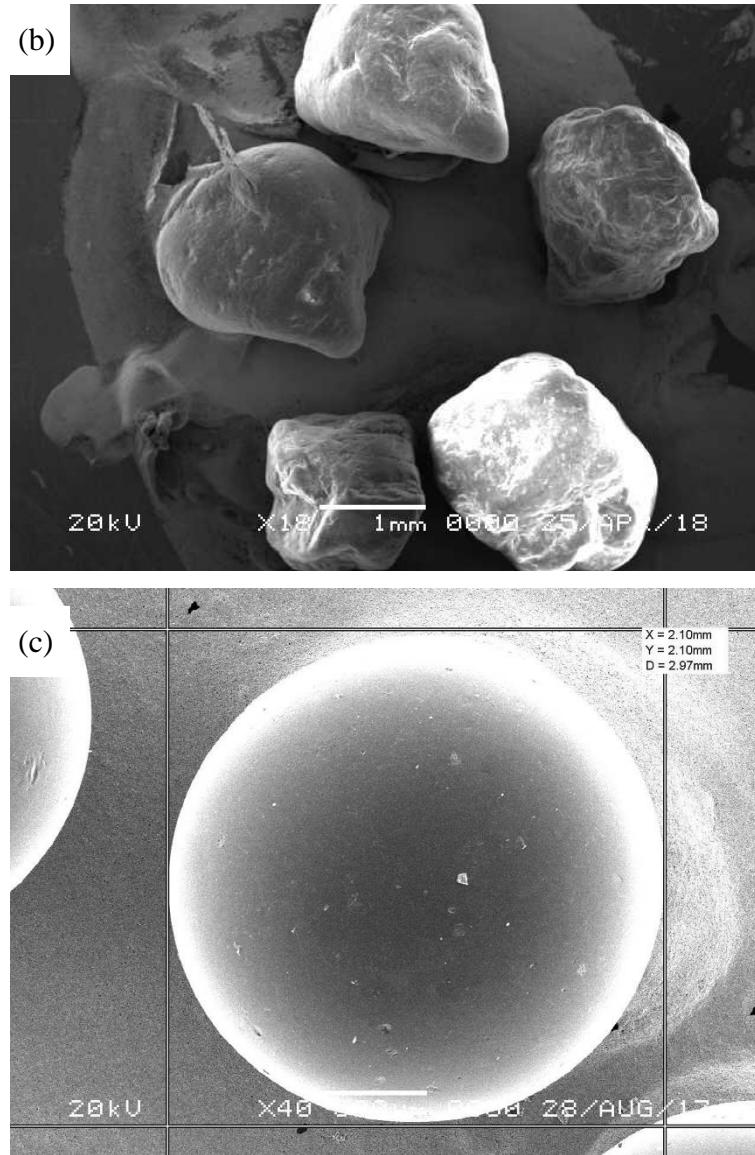


Figure 3.14 SEM images of (a) Toyoura sand, (b) Kashima river sand and (c) spherical glass beads

All materials that are presented here differ not only in their mean particle size, but also differ in the particle shape as well. Toyoura sand being more angular possesses a higher range of void ratio, whilst the spherical glass beads being almost perfectly spherical offer the least range of void ratio. The surface roughness of glass beads also varies compared to other materials. However; surface roughness is not quantified in this study.

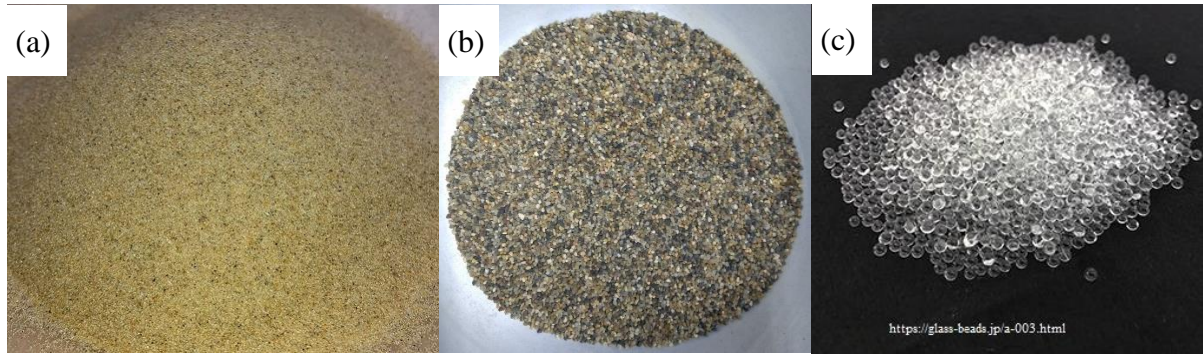


Figure 3.15 Camera images of the (a) Toyoura sand, (b) Kashima river sand and (c) spherical glass beads

3.1.5 Trapdoor testing program

Trapdoor model tests were performed in the model test apparatus as discussed earlier in this chapter using Kashima river sand and spherical glass beads. However, the test results of Toyoura sand, performed by Ebizuka (2010) using the same apparatus, were also compared with the current data.

Toyouura sand tests comprised of two density conditions: dense and loose. The dense case possessed a relative density (D_r) of 95% whereas the loose case had a relative density of 40%. Further to that, tests were performed with five different soil height. Similarly, the Kashima river sand was also tested with D_r values of 90% and 55% with varying soil heights. However, the spherical glass beads were tested using D_r value of 65% only. The detailed testing plan is presented below in Table 3.4.

Table 3.4 Trapdoor model testing plan

test case	material	H (mm)	B (mm)	H/B	D_r (%)	e
T1	Toyouura sand (dense)	100	100	1	95	0.621
T2		200		2		0.637
T3		300		3		0.647
T4		400		4		0.647
T5		450		4.5		0.667
T6	Toyouura sand (loose)	100	100	1	40	0.760
T7		200		2		0.798
T8		300		3		0.818
T9		400		4		0.807
T10		450		4.5		0.822

K1		100		1		0.580
K2	Kashima river	200	100	2	≈ 90	0.573
K3	sand - Dense	300		3		0.574
K4		400		4		0.570
K5		100		1		0.657
K6	Kashima river	200	100	2	≈ 55	0.660
K7	sand - loose	300		3		0.680
K8		400		4		0.665
G1		100		1		0.605
G2	Glass beads	200	100	2	≈ 65	0.608
G3		300		3		0.604
G4		400		4		0.592

3.1.6 Sample ground preparation

The test samples with a loose condition for all kinds of materials were prepared using dry pluviation techniques, in that the sample was dropped from a fixed height of 55.5cm, resulting in a peculiar density. However, this method resulted in a slight variation of soil density with increased sample height due to the gravitational effects (Gibson type ground) that can be considered as a limitation of this technique. Consequently, the mean value of D_r was used as a representative value.

Dense Toyoura sand was prepared by Ebizuka (2010) by controlling the opening size of sieves used for a multi-layered pluviator, keeping in view the fact that the mean particle size of Toyoura sand is small enough to control the density with pluviator opening size. However, for the dense Kashima river sand cases, a certain mass of material was used to obtain the desired density and surface compaction was performed to control the desired sample height.

In all cases, a colored sample was used close to the front acrylic wall at an interval of 50mm in height to better visualize the ground movement. The sample heights (H) were 100, 200, 300, 400 mm and an additional height of 450 mm for Toyoura sand, giving H/B of 1, 2, 3, 4 and 4.5 respectively. In all cases, the elevation of the central platen was fixed, representing a stiff buried structure, whilst the remaining four trapdoors were moved downwards, representing relatively larger settlement in the softer subsoil and presenting a periodic situation around the central fixed plate. The trapdoors were lowered with a

constant rate of 0.0012 mm/sec for Toyoura sand, and 0.001 mm/sec for other cases, up to a trapdoor displacement (δ) of 10 mm. A check was made to confirm that a further lower rate did not alter the overall test results. An external displacement transducer was attached to the lower shaft assembly to record the lowering displacement of trapdoors. Sandpapers with a standard size of 120 Grit were glued to the top surface of the base platens to enhance shear stress measurement. The lateral boundaries consisted of smooth acrylic plates, resulting in reduced friction between particles and the wall.

3.2 Numerical simulation plan using DEM

For validation and for further elaboration of soil arching and load transfer mechanism, an equivalent discrete element method (DEM) was used to performed numerical simulations. Full-scale numerical simulations were performed to have a better comparison, rather than having a scaled model space. The numerical setup and simulations plan along with the particle types are elaborated in the following paragraphs.

3.2.1 Hardware used for numerical simulations

Since the scope of presented work involves the full-scale numerical simulations, requiring millions of particles in some instances, a normal person does not have enough capacity to perform the simulation within a limited time. Hence, to overcome the time-domain limitation, a High-Performance Computing system (HPC) was utilized.

The simulations presented in this contribution were performed using the Fujitsu PRIMERGY CX600M1/CX1640M1 (Oakforest-PACS) in the Information Technology Center, The University of Tokyo (Table 3.4).

Oakforest was ranked as number one in the first IO-500 list of supercomputers in 2017. It is also considered in the top-ranked fastest supercomputer of the world. Oakforest-PACS is the '*largest massively parallel cluster supercomputer*' in Japan and consists of 8208 primary CX1640 M1 nodes. Each node contains 64 cores. The main specifications of the system are provided in Table 3.5 below:



Figure 3.16 Oakforest-PACS supercomputer

Table 3.5 Specifications of the Oakforest-PACS supercomputer

Item		Specifications
Total theoretical calculating performance		25.004 PFlops
Total number of nodes		8208
Total main storage capacity		897 TByte
Network topology		Full-bisection Fat Tree
Parallel file system	System name	Lustre file system
	Server (OSS)	DDN SFA14KE
	Number of servers (OSS)	10
	Storage capacity	26 PB
	Storage data transmission speed	500 GB/sec
Fast file cache systems	Server	DDN IME14K
	Number of servers	25
	Capacity	940 TB
	Storage data transmission speed	1,560 GB/sec

Ref. <https://www.cc.u-tokyo.ac.jp/en/supercomputer/ofp/system.php>

3.2.2 Software for numerical simulations

To cope with the HPC system stated above, a program namely LAMMPS was utilized. LAMMPS is a '*classical molecular dynamic code*', stands for 'Large-scale Atomic/Molecular Massively Parallel Simulator'. LAMMPS is developed by Sandia National Laboratories, which is owned by the US Department of Energy. A modified version of Granular LAMMPS was used in the current numerical simulation program. LAMMPS is an open-source program under a general public license (GPL).

3.2.3 Contact model

Granular LAMMPS utilizes the simplified Hertz-Mindlin contact model. The description of the Hertz-Mindlin model is already described in Chapter-2.

3.2.4 Particle shapes and particle size distribution

Since the experimental trapdoor tests consisted of both spherical glass beads and angular soil material, numerical simulations were performed using both spherical and non-spherical particles. Particle size distribution was also matched with the spherical glass beads, where the diameter ranged from 1.2mm-2.2mm. Non-spherical particles consist of two adjoining spherical particles with a rigid connection, acting as a single unit. The shape of both particles is described in Figure 3.17 below.

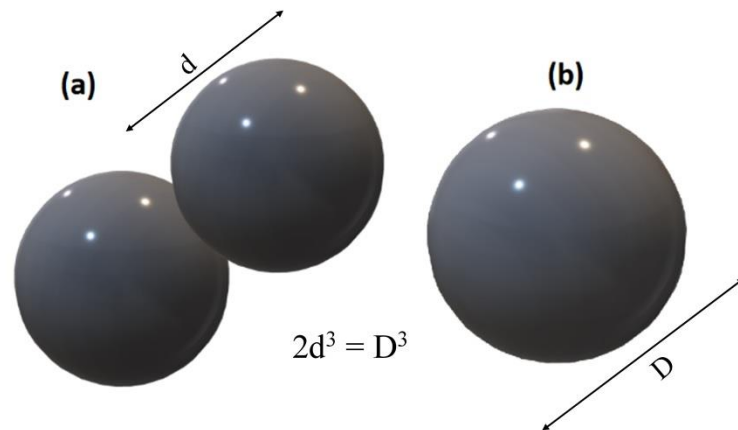


Figure 3.17 shape of (a) non-spherical and (b) spherical particles modeled in numerical simulations

Non-spherical particles were selected in such a way that the volume of the non-spherical particle equaled the volume of a spherical particle. Particle size distribution for both spherical and non-spherical particles is given below in Figure 3.18.

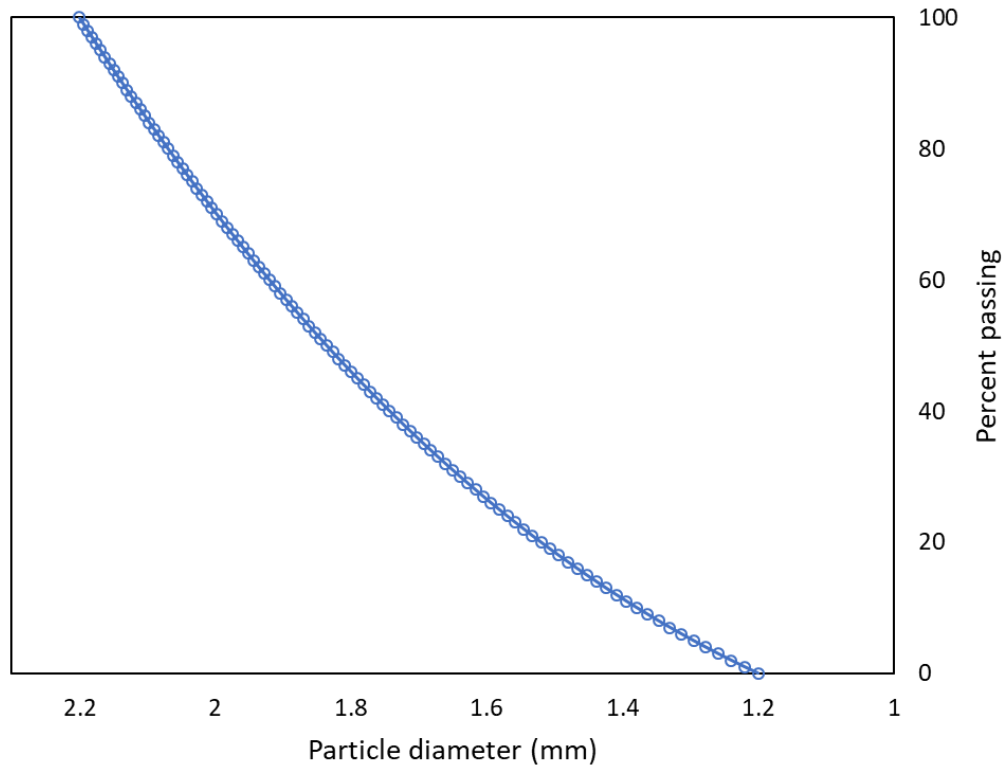


Figure 3.18 Particle size distribution for Spherical and non-spherical particles

3.2.5 Model space for DEM simulations and boundary conditions

As explained in the earlier section of this chapter, the model trapdoor test configuration consists of seven base plates wherein central and the extreme plate remain static and the inner plates move downwards. Such configuration produces an arching action above the moving plates (trapdoors). The approximate arching shape is shown in Figure 3.19 below.

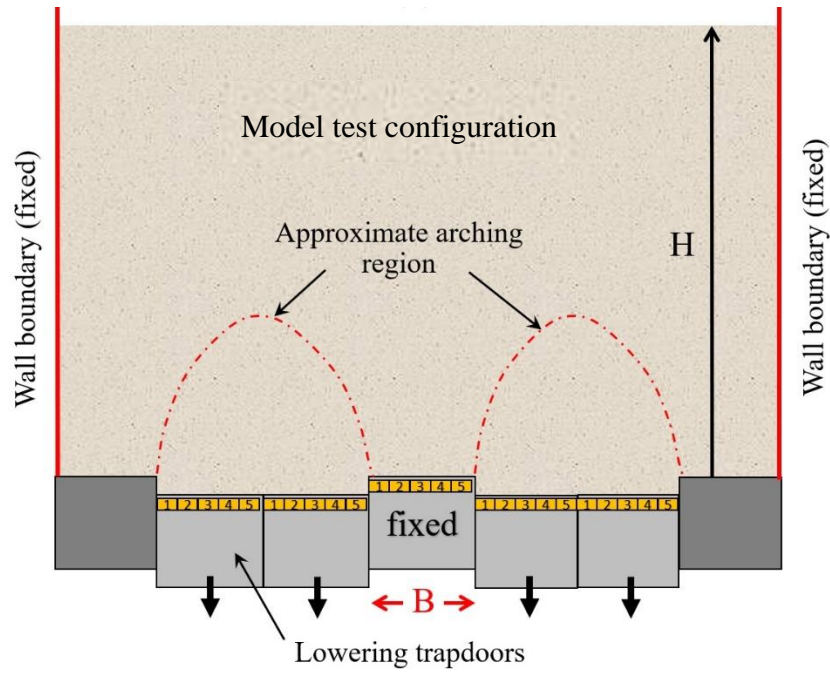


Figure 3.19 Approximate arching region in trapdoor model test configuration

However, it is visible from the above figure that the arch shape is symmetrical along the Z-axis. The significant computational cost can be saved if we only model the inner half shape of the symmetrical arch in our DEM simulations. However, such a condition could impart significant boundary effects on the simulation results, which was avoided by using lateral periodic boundary in the DEM simulation model space (Figure 3.20).

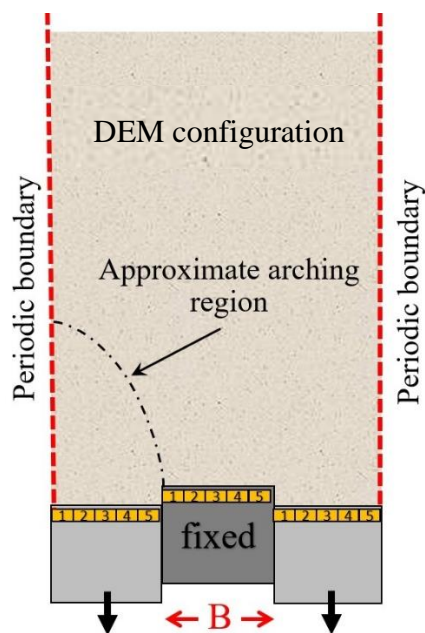


Figure 3.20 Model space in DEM simulations

Validation for using a periodic boundary with a smaller width in DEM simulations was also performed and will be discussed in Chapter 4 of this thesis.

3.2.6 Pluviation of sample

Once the particle size, shape and boundary conditions are decided, particles are generated in a certain domain, based upon the particle size distribution. An initial high value of the void ratio is given to the sample to assure that no particles are touching each other. Once the particles are generated, they are allowed to be settled under the action of gravity. However, no damping force is applied during this process. Once the void ratio attains a stable value, the damping force is applied to remove the excess energy.

To distinguish between the dense and the loose samples, the initial value of the friction coefficient is vital. A smaller friction coefficient during the pluviation stage ensures the denser packing, whereas the higher friction coefficient produces a loose packing of particles. Further to that, spherical particles can attain a specified density under a slightly higher friction coefficient compared to the non-spherical particle. Such a condition exists due to the fact that the non-spherical particle has a higher aspect ratio and relatively lower sphericity and convexity (indirectly, higher angularity). Hence smoother surface is required for the non-spherical particles to attain a void ratio comparable to spherical particles.

3.2.7 Lowering of base plates and input parameters

After the pluviation of the sample, base plates are lowered at a constant rate, smaller enough to ensure quasi-static conditions. The friction coefficient is increased before the start of the base plate lowering to correspond particle roughness. However, during trapdoor lowering, both spherical and non-spherical simulation cases were given a similar friction coefficient. Hence, the friction coefficient played a double role in the simulations. During the pluviation, the friction coefficient was used to control the density of the sample, whereas during trapdoor lowering it is used as a material property to investigate the effect of particle shape.

Similarly, the time step for the simulations is kept well below the critical time step to ensure a stable simulation process. Forces and strains are calculated using the input file and obtained as an output. Simulations are run for a certain number of steps, that are decided based upon our requirement of stresses or strains. The basic input parameters used in the trapdoor simulations are presented in the table below.

Table 3.6 Input parameters used in DEM trapdoor simulations

Input parameter		Value used
Specific gravity, G_s		2.5
Modulus of Elasticity, E		71.6 GPa
Modulus of rigidity, G_p		29.1 GPa
Poisson's ratio, ν		0.23
Coefficient of friction in pluviation, μ_{pluv}	Spherical	0.05
	Non-spherical	0.01
Coefficient of friction in trapdoor condition, μ_{shear}	Spherical	0.35
	Non-spherical	0.35
Timestep, t		$1.0e^{-7}$ sec

3.2.8 Simulation plan

Model trapdoor tests consisted of certain H/B values (B is the width of the base plate and H being the soil height). However, in DEM simulations, an initial sample height is selected before pluviation and then particles are allowed to set to form a stable sample. This process yields a stable sample height that might be different from the model test values. Hence, obtaining a whole number value for H/B was not possible in the current simulation plan.

Simulations for both spherical and non-spherical particle cases were performed with varying sample height, resulting in a range of H/B values. Table 3.7 below compares the simulation plan for both cases.

Table 3.7 DEM simulation plan

Test case	Material type	Number of particles	H mm	B mm	H/B	e
D1	Spherical particles	50,000	44	50	0.88	0.624
D2		100,000	88		1.76	0.616
D3		150,000	130		2.60	0.614
D4		200,000	174		3.48	0.613
D5		250,000	218		4.36	0.610
D6	Non-spherical particles	50,000*	45	50	0.90	0.664
D7		120,000*	107		2.14	0.652
D8		180,000*	172		3.45	0.652
D9		250,000*	220		4.40	0.631

*The number of non-spherical (clumped) particles

CHAPTER 4: STRESS DISTRIBUTION IN TRAPDOOR TESTS: EXPERIMENTAL & NUMERICAL ANALYSES

Once the sample is fully prepared after pluviation, the next step is to allow specified base plates to move downwards with a certain velocity low enough to suppress dynamic behavior and to act as quasi-static. As soon as the trapdoors start lowering, the stress distribution changes significantly due to the initiation of the arching phenomenon. This section describes the stress variation analyses under the trapdoor conditions for both experimental trapdoor tests and numerical simulations. Further to that, an increase of earth pressure on the buried structures due to the trapdoor action, as described by Japan Road Association code 1999, is discussed and compared with the experimental and numerical results.

4.1 Initial normal and shear stress distribution

The trapdoor condition being analyzed in current research corresponds to a buried structure in the center with a static central base plate. The lowering side plates represent the settling of backfill soil, that initiates the arching action.

The initial condition in the field can correspond to the state right after the backfilling above the buried structure. Figure 4.1(a) represents the initial configuration of the trapdoor test and corresponding normal stress distribution at the plane that touches the top surface of the buried structure (top of base plates in model test) in the XY plane. As visible, the initial stress distribution in the normal direction is almost uniform, showing that the overburden soil is acting uniformly at all points in the vertical direction. However, the shear stress distribution would be approaching zero as the only dominant force is the gravitational force, without any significant lateral movement of the particles.

As soon as the trapdoor start moving, the stress distribution in both normal and shear direction varies significantly and the stresses on the central static base plate are supposed to be increased. However, the shear stress distribution whilst the trapdoors are being lowered, largely depends upon the sample condition, including the sample height, density and particle shape. Figure 4.1(b) describes the approximate shapes of stress distribution after the initiation of trapdoor lowering.

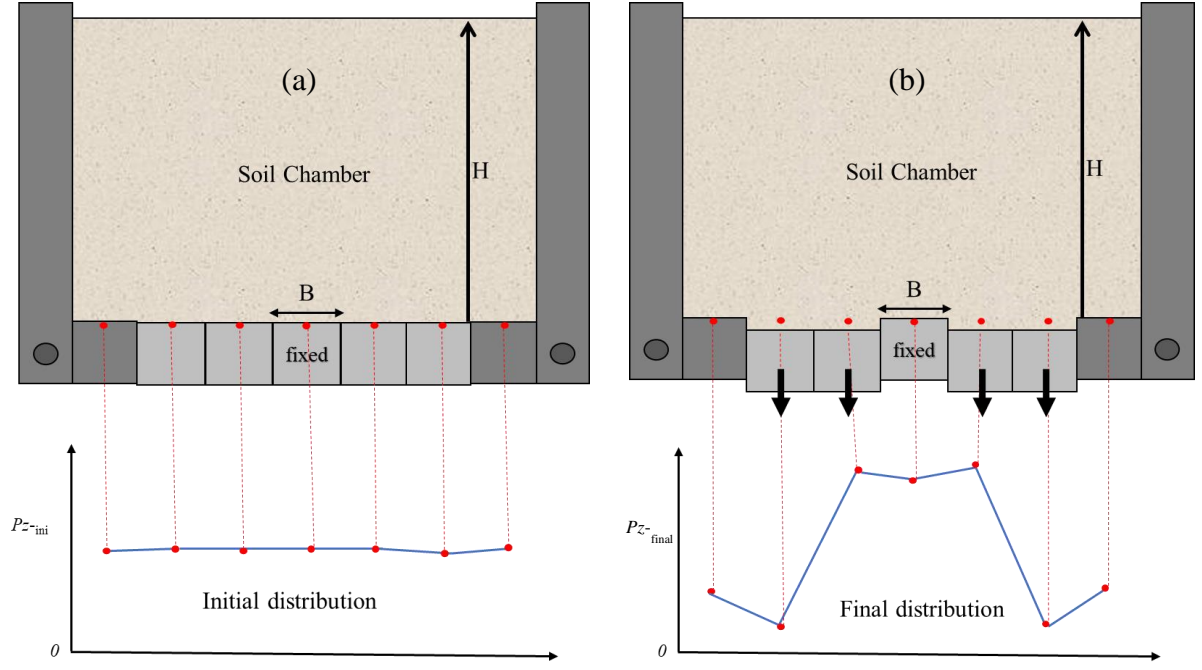


Figure 4.1 Normal stress distribution in trapdoor at (a) initial and (b) final condition

4.2 Peak normal stress distribution for Toyoura sand

Trapdoor model tests on Toyoura sand were performed by Ebizuka (2010) and are reproduced here for comparison purposes only.

4.2.1 Dense Toyoura sand

With a D_r value of 95%, model trapdoor tests were performed using five different H/B values, ranging from $H/B = 1.0 - 4.5$. Initial stress before the lowering of the trapdoors is termed as the P_{z0} and the peak normal stress at the central fixed base plate after the trapdoors have started moving is termed as P_{zp} . The ratio of initial normal stress to the final normal pressure is termed as *Normalized Normal Stress* and is plotted for different soil height in Figure 4.2. Mathematically it is represented as below:

$$\text{Normalized normal stress} = \frac{P_{z,0}}{P_{zp}} \quad (4.1)$$

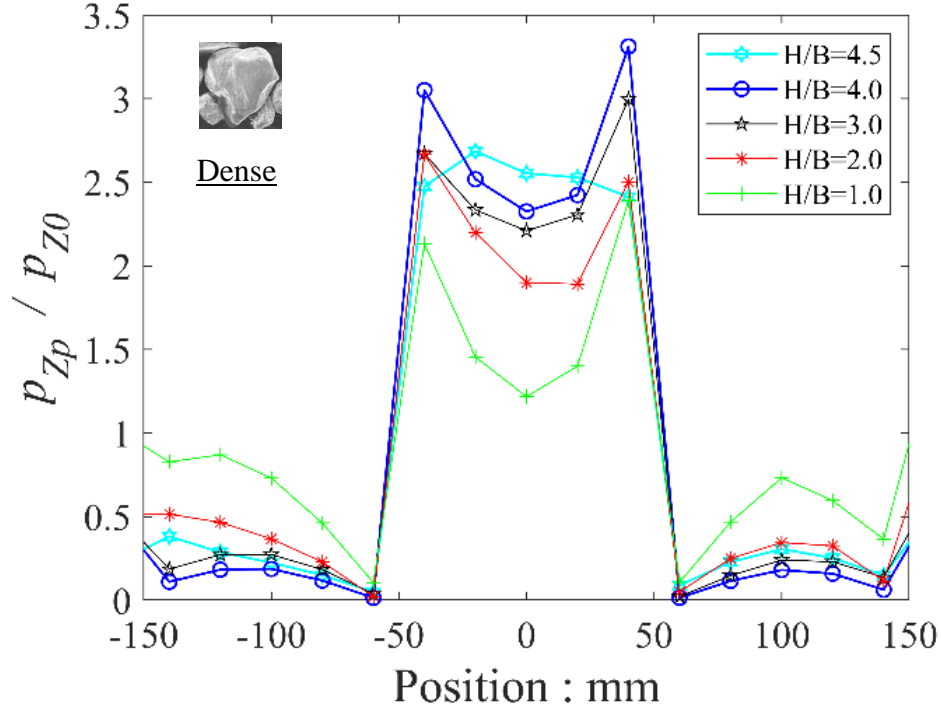


Figure 4.2 Normalized normal stress for dense Toyoura sand samples under different soil heights

Figure 4.2 is plotted against the normalized normal stress and the sample width. The sample width consists of five base plates that are embedded with load cells. Each base plate had a 100mm width. Extreme two base plates did not include any load cell. However, in the above figure, the central three base plate width is shown. The reason for this will be discussed later in the chapter in the simulation results.

Even for the smallest H/B value, the stress distribution in the central base plate (position = -50 to +50mm) increased compared to the initial stress, whereas the stress distribution on the sides reduced significantly compared to the initial state. This redistribution of stresses portrays that there is some rearrangement of particles to form an arch shape above the lowering trapdoors, causing reduced stress above them.

However, a further increase in the soil height (or H/B), the trend is further enlarged. A further H/B increase from 3.0 did not significantly increase the normalized normal stress that signifies that the arch has fully been developed. It is also evident that the peak stress distribution is found just on the outer sides of the edges of the central fixed base plate. Such trend exists due to the rigidity of static base plate and this phenomenon is well discussed by Kuwano & Ebizuka (2010) that describes that the relative stiffness of

settling soil and buried structure, as well as the density of the soil, is responsible for the shape of the peak normalized normal stress distribution.

4.2.2 Loose Toyoura sand

Normalized stress distribution for the loose Toyoura sand is shown in Figure 4.3. The general trend of the stress distribution is similar to that of dense Toyoura sand with lesser peak stress values. However, the peak value of normalized normal stress is visible at the center of the central fixed base plate, contrary to the dense case where the peak value was exhibited just at the edges of the central plate.

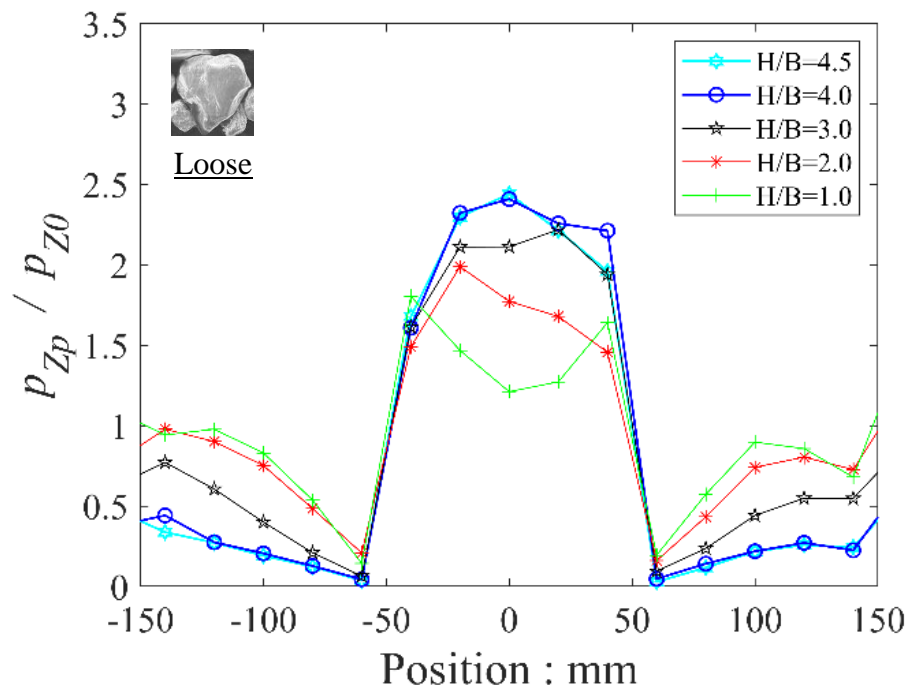


Figure 4.3 Normalized normal stress for loose Toyoura sand samples under different soil heights

4.3 Normal stress distribution for Kashima river sand

Kashima river sand, having a mean diameter significantly larger than Toyoura sand, was tested for four different soil height with an H/B values of 1.0 - 4.0. Increasing the height of the sample resulted in increased normalized stress at the central fixed base plate. However, the magnitude was found to be smaller than that of the dense Toyoura sand case. The reason being the lesser relative density of Kashima river sand samples compared to the Toyoura sand.

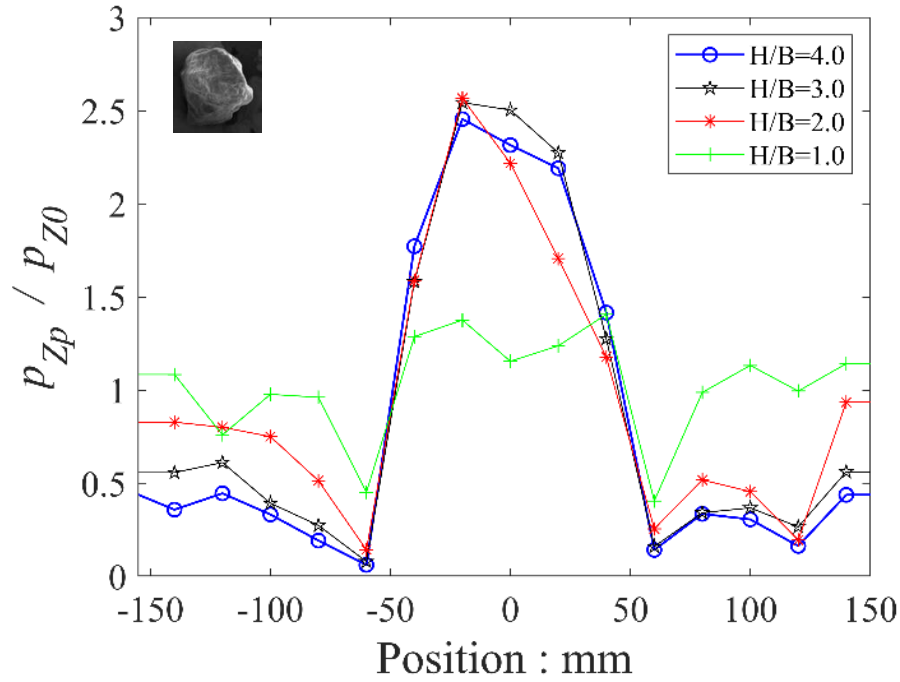


Figure 4.4 Normalized normal stress for Kashima river sand samples under different soil heights

4.4 Normal stress distribution for Spherical glass beads

Similar to Kashima river sand, spherical glass beads were also tested for four different sample heights. The mean diameter of the spherical glass bead was 1.7mm, which was more comparable with the Kashima river sand size.

Normalized normal stress plot (Figure 4.5) showed a very similar trend compared to the previous cases except that the peak normalized stress value was the least amongst all samples. The reason for that can be associated with the higher sphericity with smaller aspect ratio and smaller angularity of spherical glass beads. Since the relative density of spherical glass beads and the Kashima river sand did not vary much, the difference in their normalized normal stress value can be regarded due to the particle shape difference.

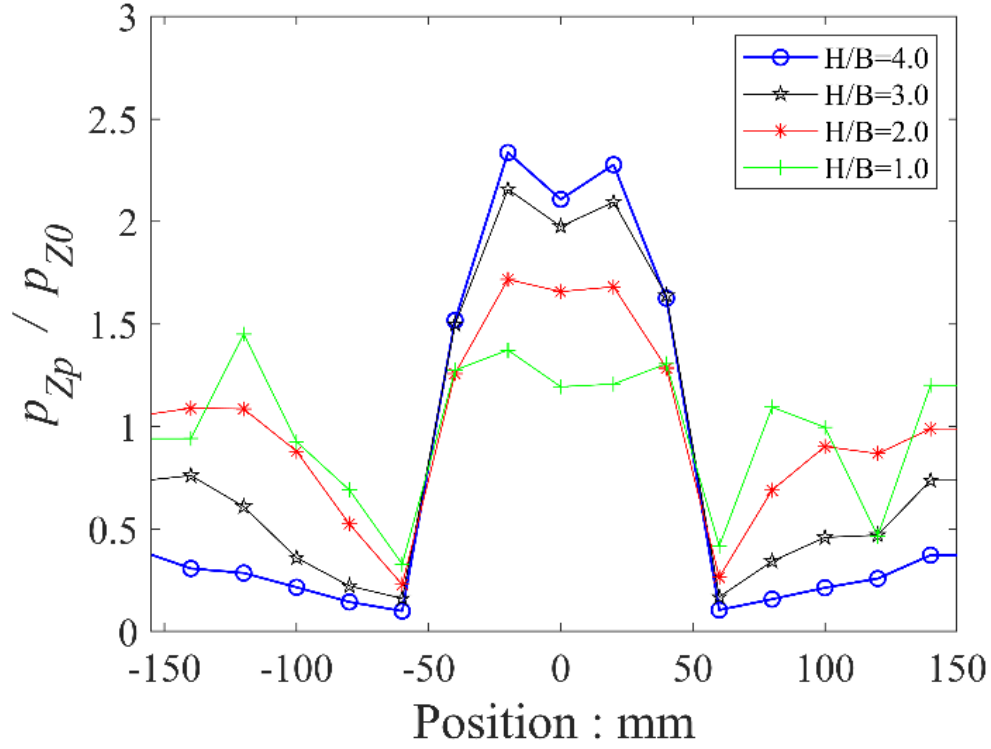


Figure 4.5 Normalized normal stress for spherical glass beads samples under different soil heights

4.5 Normalized normal stresses under DEM numerical simulations

Equivalent DEM simulations using a modified version of granular LAMMPS were performed using two types of particle shapes: spherical and non-spherical particles. However, before discussing the stress variation in numerical simulation, initially, the justification of using a periodic boundary is provided below.

4.5.1 Validation of using periodic boundary in DEM simulations

As already explained in Chapter 3, the DEM simulations were performed with a smaller lateral extent compared to the model trapdoor tests for the purpose of saving computational energy. To avoid the boundary effects for the reduced width samples in DEM simulations, lateral periodic boundaries were applied to the samples. For more clarity, Figure 4.6 shows the trapdoor model test configuration and the offset represents the DEM simulation model space.

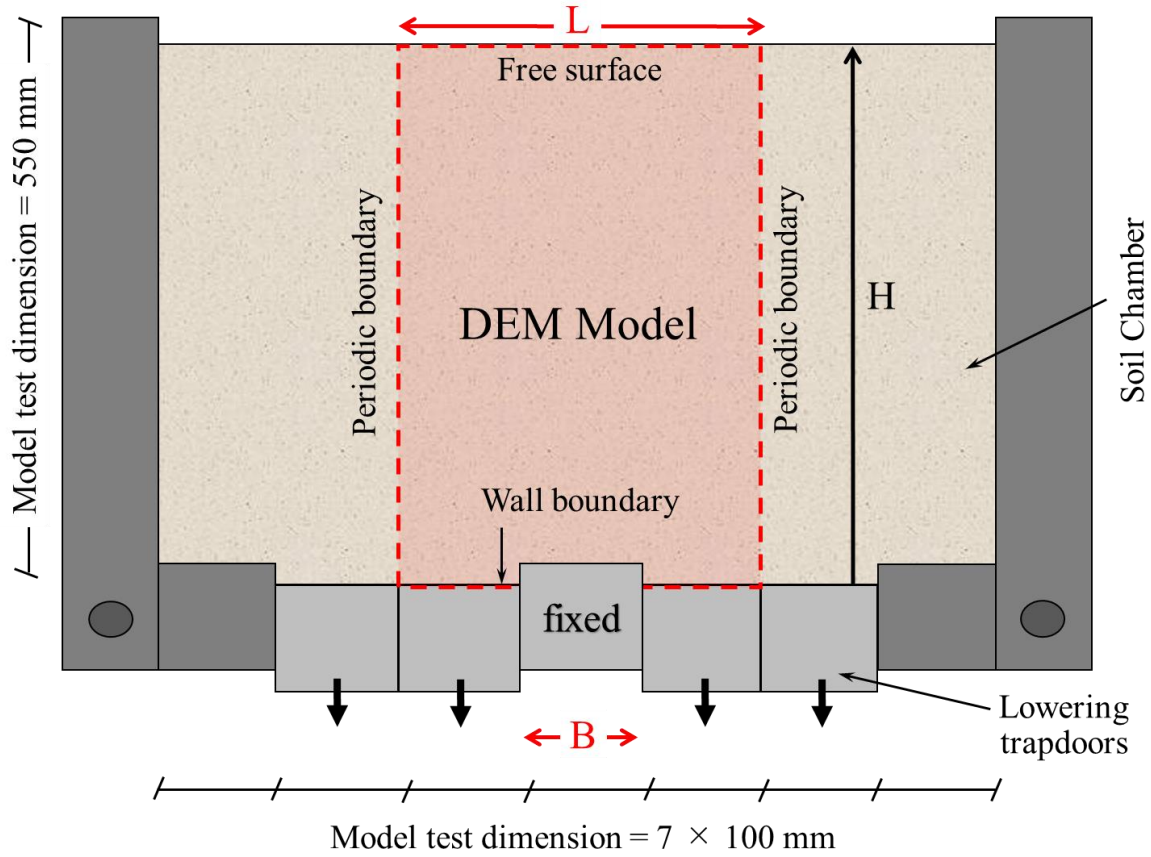


Figure 4.6 Model trapdoor test configuration and DEM model space used in simulations

As a matter of fact, the DEM simulations should have been performed using a model configuration with a width equivalent to the trapdoor model tests, i.e. seven base plates with central and the side plates being static. However, the DEM simulations only constituted the central three plates. To verify the use of central three plates with periodic boundary, a simulation was performed with seven base plates, having lateral wall boundary (similar to model trapdoor tests), and the results were compared with a simulation condition that contained three central base plates with lateral periodic boundaries, as shown in Figure 4.7. Since the higher ground heights are thought to impact more on the accuracy of the results while using periodic boundaries, the test simulations were performed with the maximum H/B value of 4.0, as performed in model trapdoor tests. The base plates were also moved in a similar manner compared to model trapdoor tests.

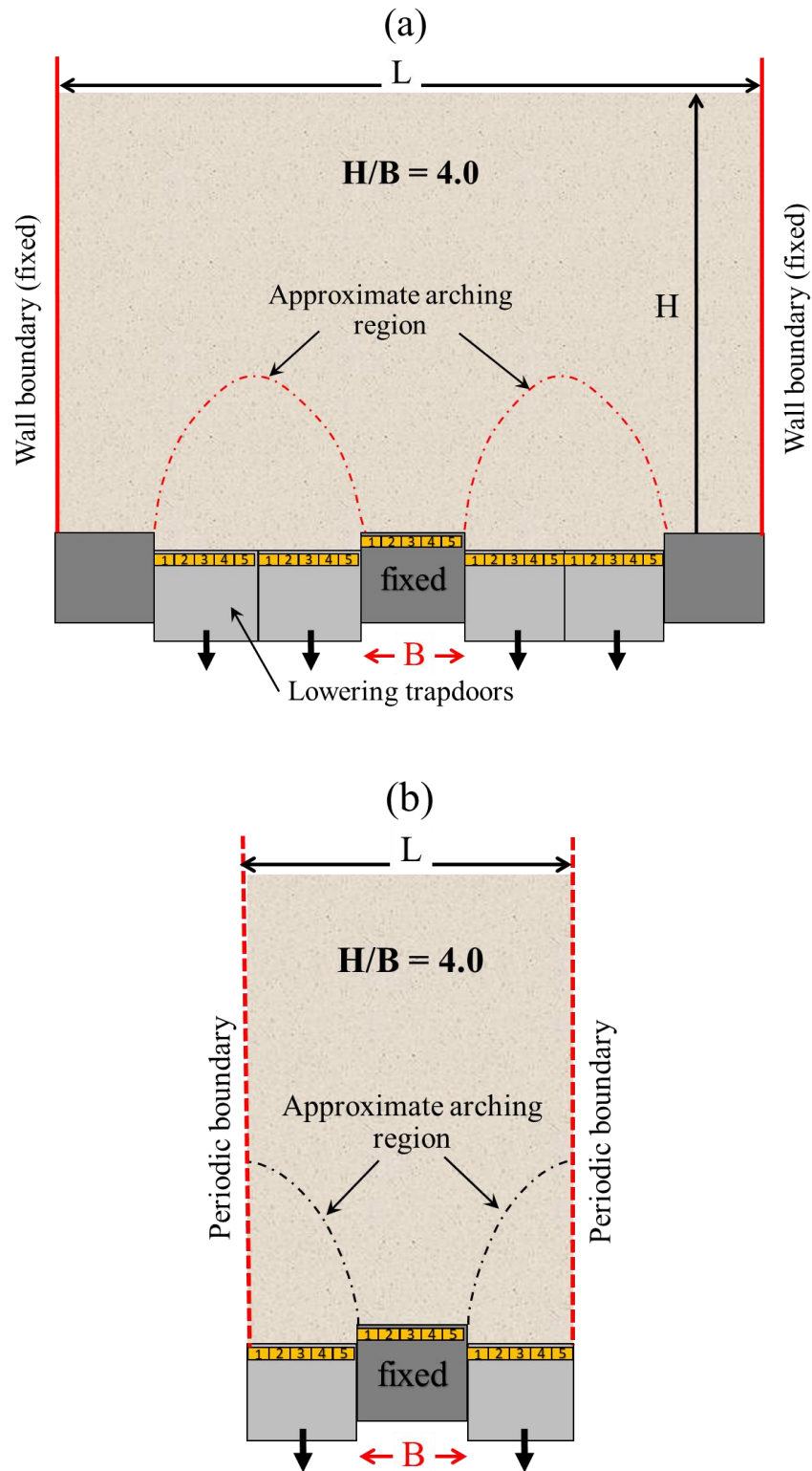


Figure 4.7 DEM simulation space for (a) configuration similar to model trapdoor tests and (b) configuration with central three base plates with periodic boundaries

It was observed that the particle movement data are similar between the wider sample with rigid walls and the simulation with periodic boundaries when the middle part of the model is considered. Figure 4.8 below compares the vertical displacement trend for the samples with rigid walls and the periodic lateral boundaries. The area near the lateral extents is visibly affected by the presence of rigid walls (Figure 4.8 left). However, the effect is almost diminished in the middle part that is equivalent to the DEM case with lateral periodic boundaries. The arching pattern in both samples is also very similar, which is represented by the blue colors in the figures below.

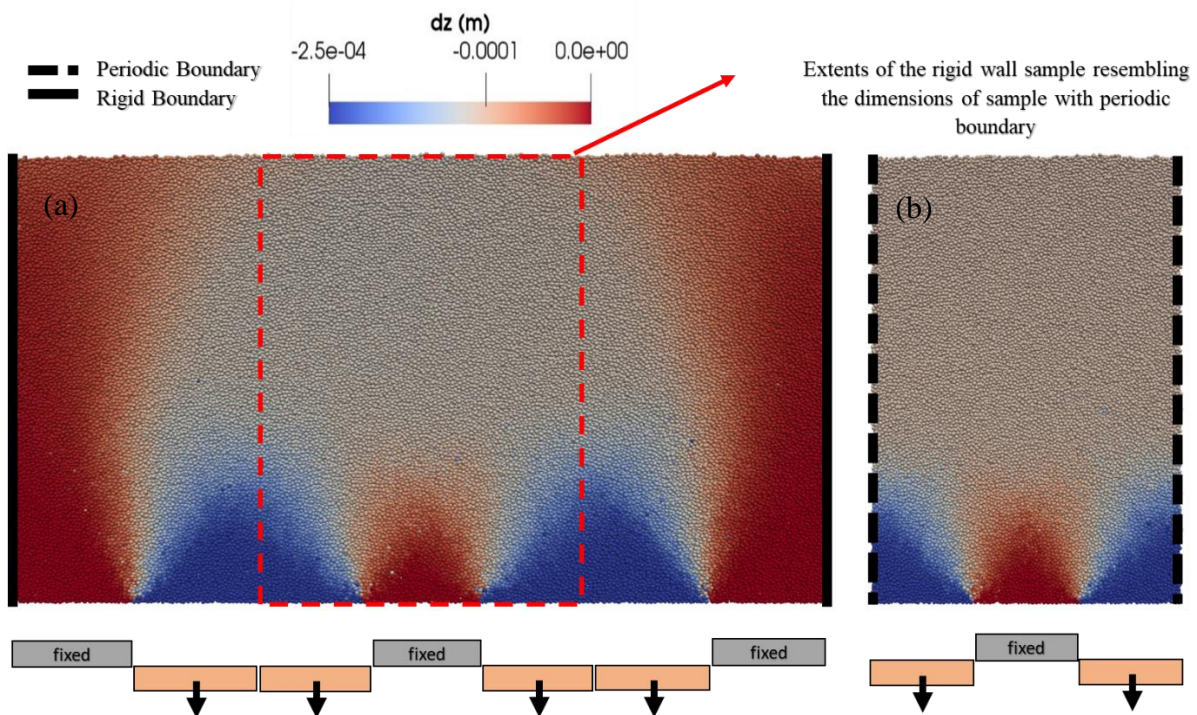


Figure 4.8 Vertical displacement of particles for (a) sample with lateral rigid boundary and (b) sample with periodic boundary

Besides, Figure 4.9 shows that the normalized normal stress plot (p_{zp}/p_{z0}) for both cases produce similar results, reinforcing the statement that samples with periodic boundaries produce results equivalent to the trapdoor model tests. The peak normalized normal stresses in the central fixed base plate, as well as the reduced normalized stresses above the lowering plates around the central plate, showed a very similar trend and values.

Note that Huang et al. (2014) and Kuhn & Bagi (2009) suggested that using periodic boundaries yields results that are closer to the actual material behavior. Thus,

the present research adopted the periodic boundary, which also reduces the computational cost significantly without compromising the accuracy of the simulation results.

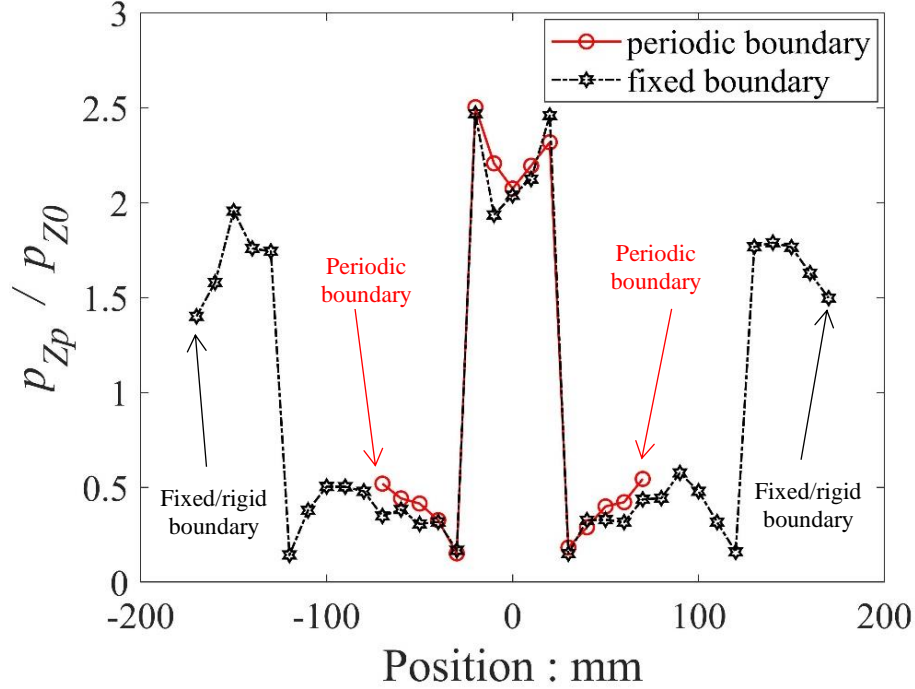


Figure 4.9 Comparison of normalized vertical stress ratio for samples with a rigid wall (fixed) and periodic lateral boundaries ($H/B = 4.0$).

4.5.2 Validation of using half-width samples

Once the use of periodic boundaries with the modified configuration of trapdoor tests, there still existed a need to minimize the computational energy as the simulations involved several hundred thousand or sometimes millions of particles in simulations. However, the accuracy of simulation results could not be compromised as well. Hence resultantly, the width of each base plate was reduced, keeping the number of plates to the same number as discussed in the previous section.

In the model trapdoor tests, the width of each base plate was measured to be approximately 100mm. To save the computational power and to reduce the simulation time consequently, the width of the trapdoor was reduced to half of the width in trapdoor model tests (50mm for each base plate). Figure 4.10 better compares the base plate width difference between all approaches. Initially, a series of simulations was performed only to check the effect of width reduction. Otsubo, Kuwano, Ali, & Ebizuka (2018)

performed the full-scale DEM simulations with a base plate width of 100mm using spherical particles to check the stress redistribution response. Their results are compared with simulation results having a base plate width of 50mm, having similar particle size, boundary conditions, and input parameters.

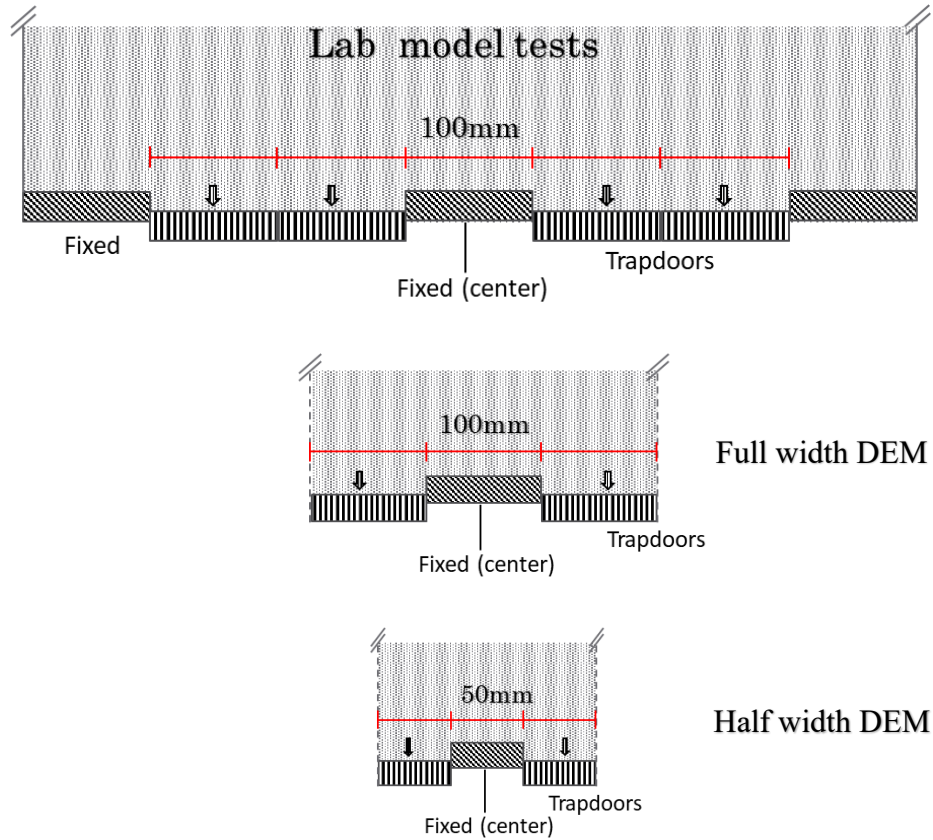


Figure 4.10 Comparison of Model trapdoor test base plate width with full scale and half scale DEM simulations

Normalized normal stress distributions for the full scale and the half-scale DEM simulations are presented in Figure 4.12. It is clear that the full scale (width) and the half-scale simulations resulted in similar trends, both quantitatively and qualitatively. The general trend of increasing normalized stress with increasing H/B was well captured by both approaches.

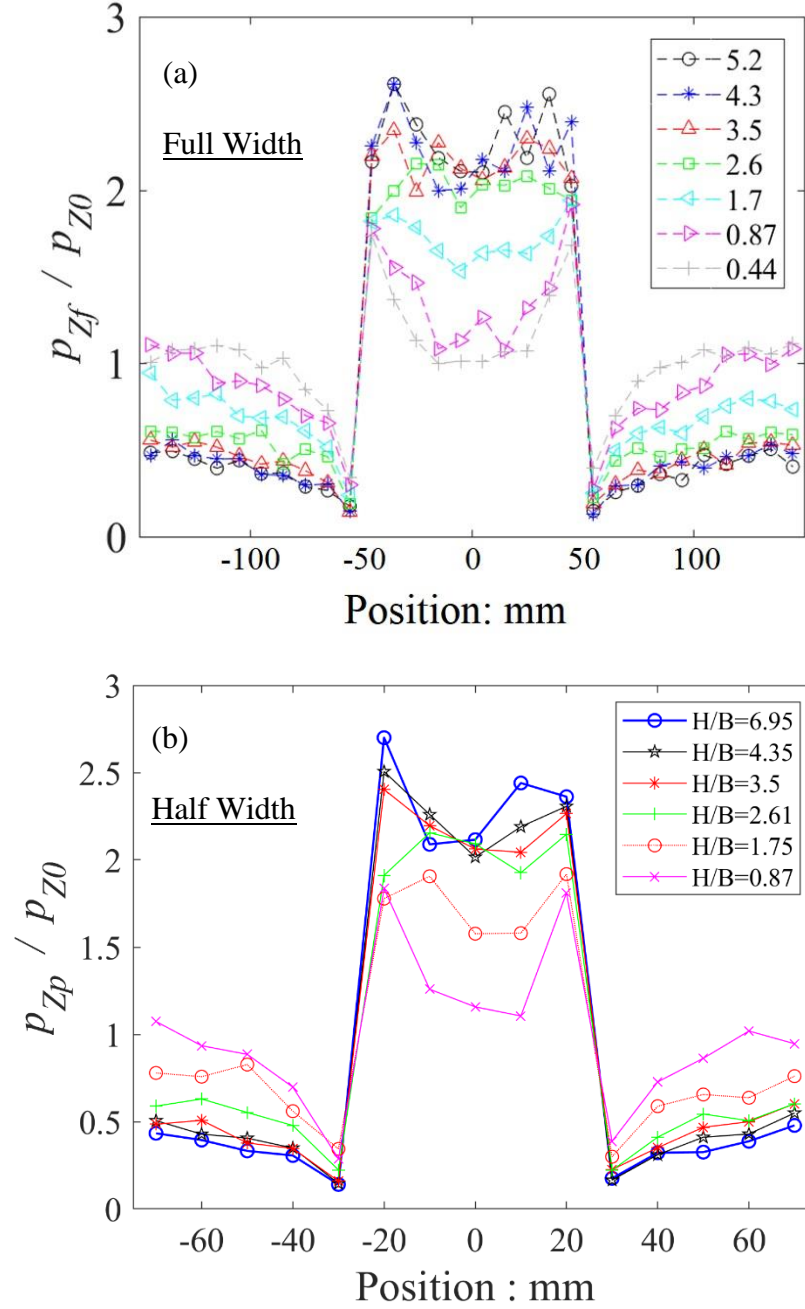


Figure 4.11 Comparison of Normalized normal stress distribution for (a) full width and (b) half width DEM simulations

For a better understanding of the half-scale simulation comparison, a plot against the alpha ' α ' (increased stress on the central base plate) and the H/B is presented in Figure 4.12 below for the spherical particles. The detailed explanation of ' α ' will follow in the next section. Clear convergence between both approaches is visible for all presented H/B range, which reinforced that the half-scale simulations can be adopted in the current study without jeopardizing the accuracy of results for comparison with model trapdoor tests.

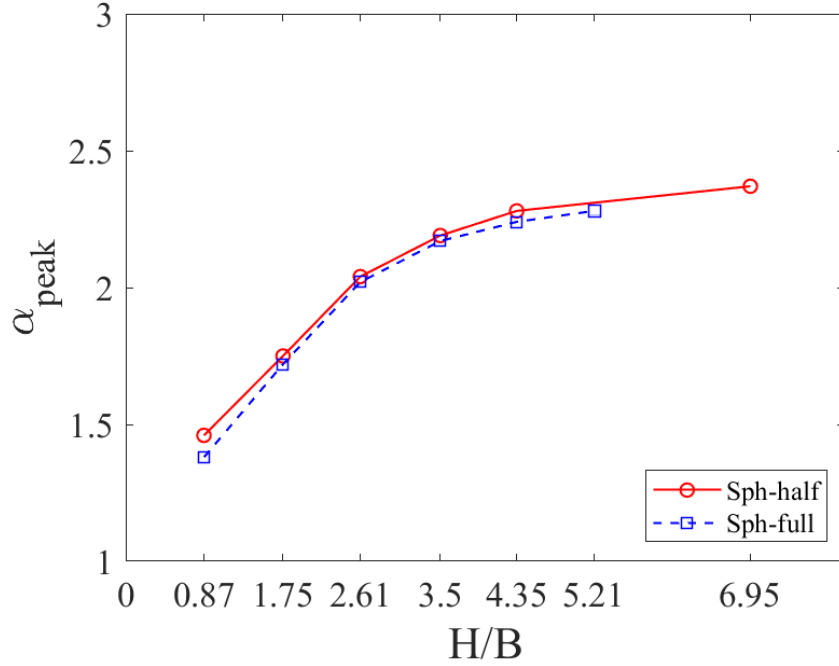


Figure 4.12 Comparison of full scale and half scale DEM simulations with varying H/B values against peak alpha value, using spherical particles

Head (1994) suggested that the sample thickness should be larger than ten times the largest particle size in shear tests. Kuhn & Bagi (2009) performed DEM simulations on a varying number of particles using different boundary conditions to show the convergence in stress-strain response after a certain increase in the number of particles. Both sample size and number of particles used in this study satisfies the above-referred conditions for the accuracy of the DEM simulations.

4.5.3 Normalized normal stress distribution in DEM simulations

After validating the use of periodic boundaries and half-width of the base plate, DEM simulations were performed with two kinds of particle shapes: spherical and non-spherical. Particle shape discussion has already been done in chapter 3 previously. The input parameters for both spherical and non-spherical particle simulations were kept similar, except the friction coefficient μ , that was kept smaller for non-spherical cases during the pluviation stage to attain a matching void ratio with spherical particle sample.

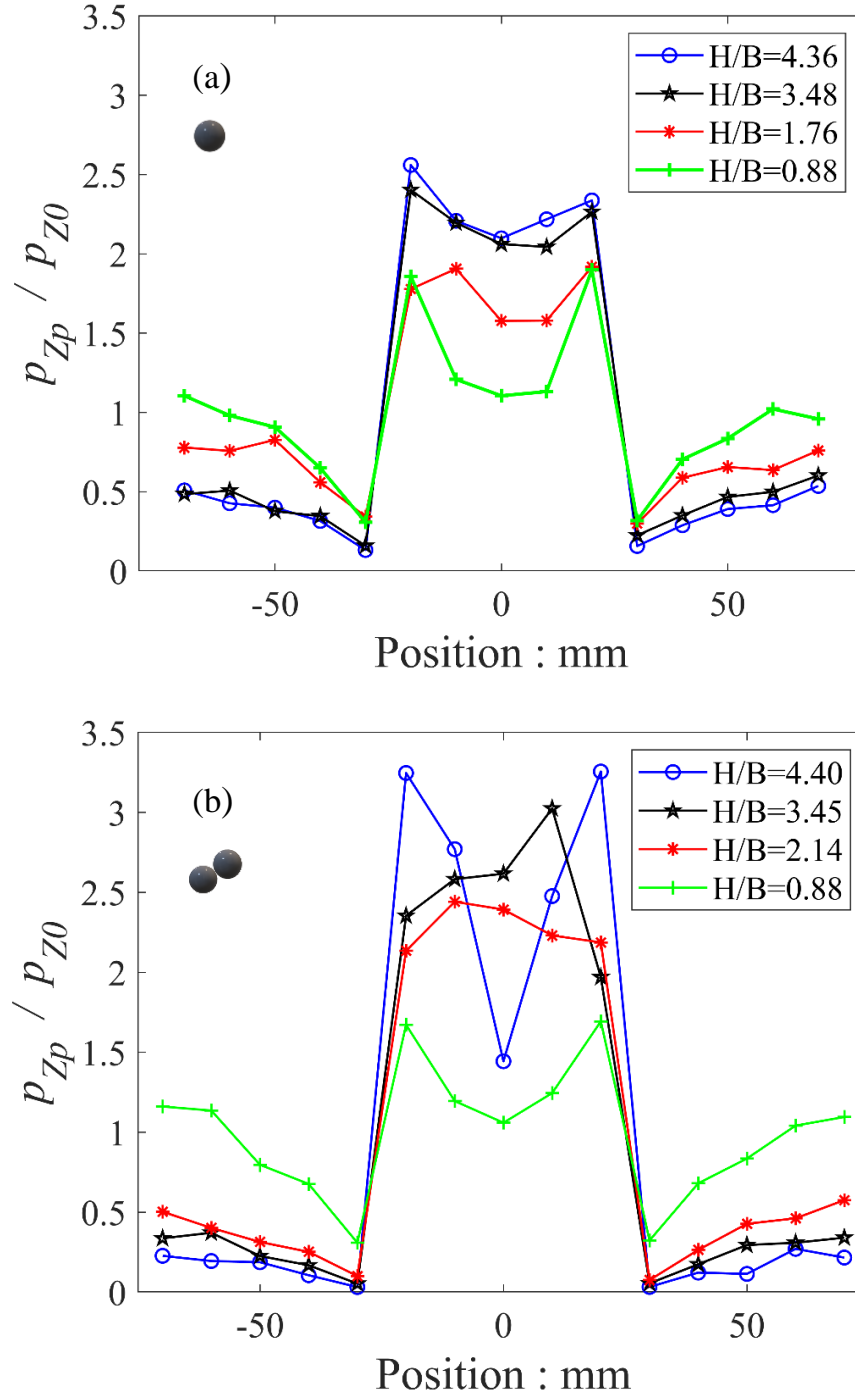


Figure 4.13 Normalized normal stress distribution for DEM simulations (a) spherical particles (b) non-spherical particles at trapdoor displacement, $\delta = 0.25\text{mm}$

The general trend of stress increased with increasing ground height is visible in both cases of spherical and non-spherical particle simulations, as visible in Figure 4.13. There is a clear difference in the peak value of normalized stress between the spherical case and non-spherical case, at the central region of the specimen that signifies the portion above the central static base plate. Although the conditions other than the particle

shape are common between both cases, the difference in the stress value signifies the particle shape effect.

Another interesting fact is the resemblance of stress distribution for the DEM spherical case with the model trapdoor test for the spherical glass beads, as presented in Figure 4.5. both, values and the trends are close enough to each other as both cases utilized similar shapes with a similar gradation of material. Also, the material properties of alkaline glass beads (the material used in model trapdoor tests) were applied to the particle properties in DEM simulations. Resultantly, the output for both cases showed a striking similarity.

In the case of non-spherical particles in DEM simulations (Figure 4.13b), the normalized stress distribution can be well compared with the stress distribution of dense Toyoura sand results (Figure 4.2). Relative densities for the DEM simulation and the model tests with dense Toyoura sand were comparable as well. The peak normalized stress values for dense Toyoura sand were insignificantly higher than the values with non-spherical DEM simulation case, that can be related to the higher angularity of Toyoura sand. However, many other factors contribute to this phenomenon including the slight difference in void ratios of both types, particle size difference etc.

The similarities between the DEM simulation results and the model test results not only mutually validate each other but also the correspondence of spherical DEM simulations with spherical glass beads and non-spherical DEM simulations with non-spherical model test results verifies that there exists a strong particle shape influence on the stress distribution under trapdoor condition. Consequently, it can also be said that the arching pattern within the soil mass varies with the variation of particle shape.

Another interesting point is the effect of particle size on the stress distribution, in both numerical and model tests. Non-spherical particles used in DEM simulations, being approximately nine times larger than the mean size of Toyoura sand, did not show any significant difference in the stress distribution behavior. This aspect will be discussed in the following section in detail.

4.6 General mechanism of normalized stress distribution trend

As repeatedly observed in the above figures, the stress distribution on the lowering trapdoor just next to the central fixed plate shows the lowest values, whereas it shows the maximum value just to the inward of the central fixed plate. Figure 4.14 illustrates an arch formed above the lowering trapdoors where the base of the arch touches the edge of the central fixed plate.

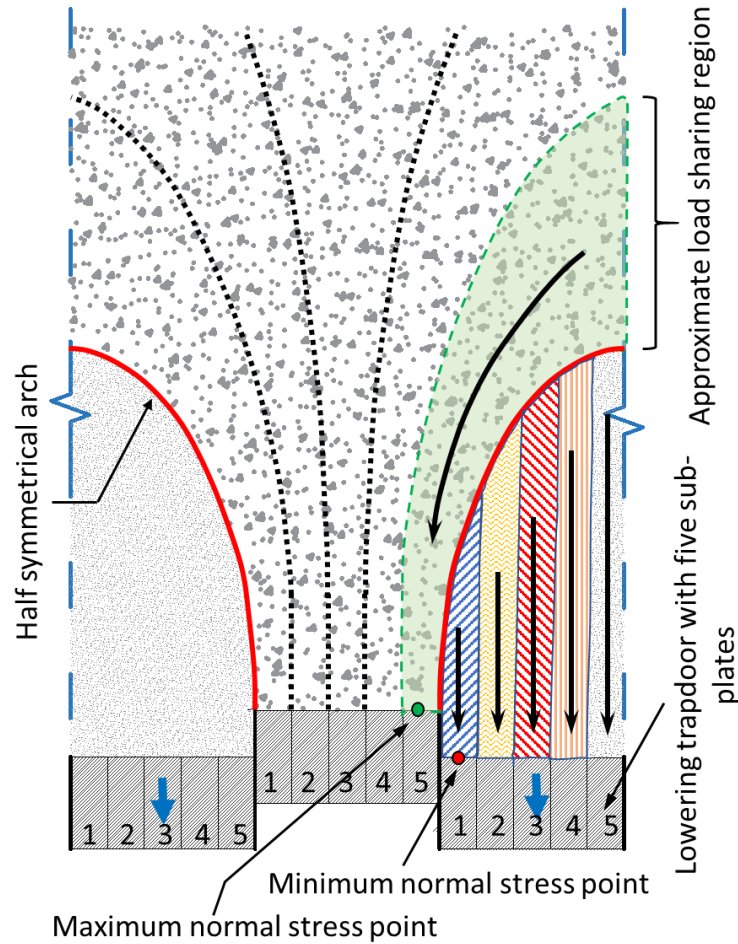


Figure 4.14 Approximate regions contributing to normal stress distribution at the base of the sample in the presence of the arching

This explains briefly why such a sudden change occurs at the boundary between the central fixed plate and the side lowering trapdoors. The load above the arch is carried by the arch itself towards the inner edge of the central fixed plate. Thus, Figure 4.13 represents the highest stress values on sides of the central plate for the denser samples, which can be well explained by the fact that denser Toyoura sand yield higher values of mobilized friction along the arch. However, the lowering trapdoors below the arch only carry the portion of the load caused by the sample encompassed under the arch. Since the arch shape is normally catenary

(Z. Q. Wang et al., 2013), a negligible amount of sample is present right under the starting point of the arch (besides the central fixed plate, Figure 4.14). Hence, the normalized normal stress is minimum near to the central fixed plate. In all cases, as the normalized stress ratio increases above the central portion of the specimen, it decreases simultaneously at the edges due to the fact that the summation of stresses caused by a gravitational force above all the base plates would remain the same at each instance.

4.7 Stress concentration on the central base plate ‘ α ’

In the current test scenario, the central fixed base plate represents the buried structure in the field. As several researchers and organizations have tried to study the stress increase on the buried structure, e.g. Japan Road Association code (1999), there is a need to quantify the load increment on the buried structure (base central plate) in our study. As a means to quantify the degree of stress increase on the buried structure due to the settlement of the surrounding soil, the following expression can be used.

$$\alpha = \frac{p_{z,center}}{p_{z0}} \quad (4.2)$$

where $p_{z,center}$ is the mean normal stress on the central fixed plate at a given trapdoor settlement (δ).

Figure 4. 15 shows the normalized stress increase ‘ α ’ on the central fixed base plate (buried structure) against the trapdoor movement δ for all three materials analyzed in trapdoor model tests. The value of stress increment increases with increasing H/B values for all presented cases. However, the increment of stress reduces with increasing H/B and at a certain value of H/B , the ‘ α ’ value is almost converged, signifying the development of the arching action within the soil mass.

The peak value of ‘ α ’ can be observed at a very early stage of trapdoor lowering. A similar trend was also observed by Chevalier & Otani (2011) in his trapdoor model tests and numerical simulations. Both Toyoura sand and Kashima river sand exhibited a post-peak softening behavior as well. This post-peak behavior correlates to the rearrangement of soil arching boundary with a large soil displacement.

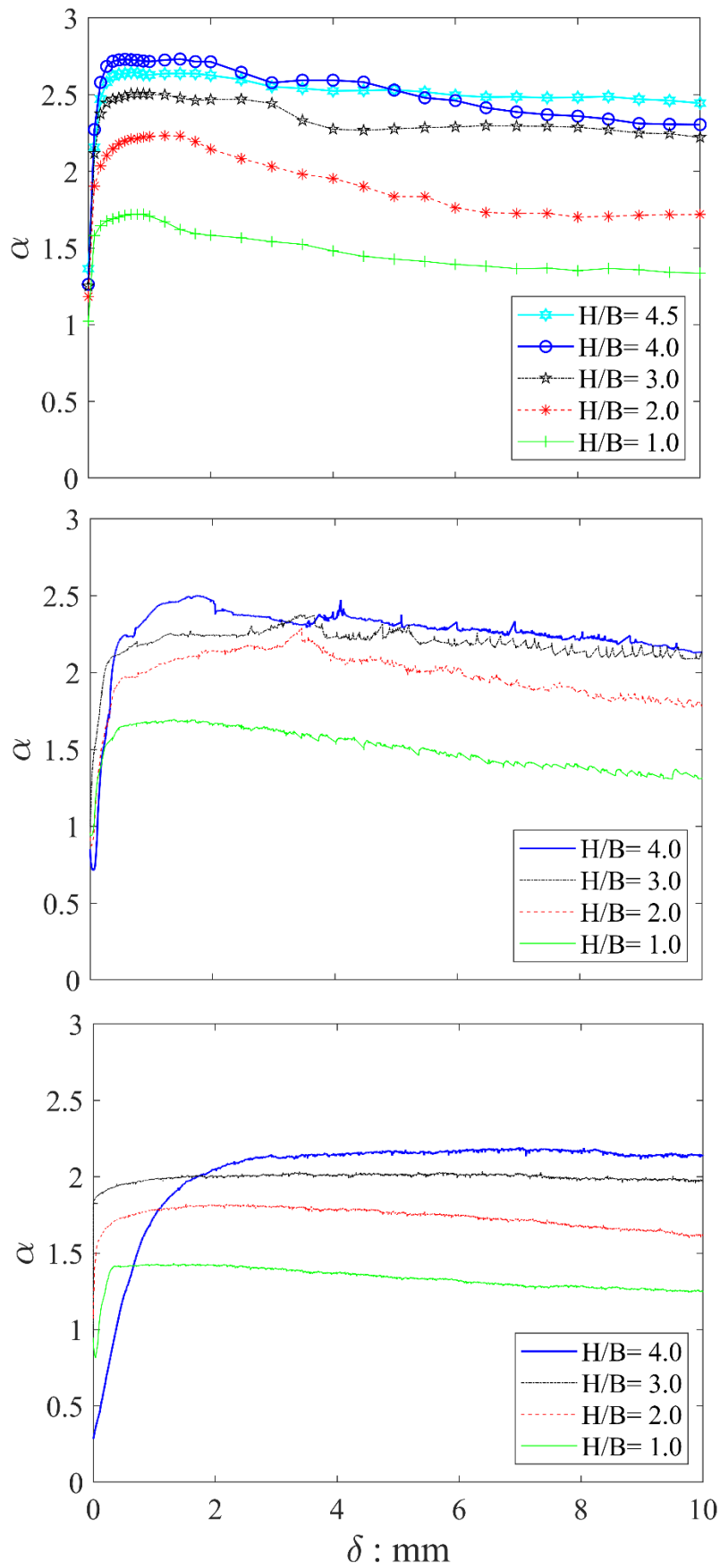


Figure 4. 15 ' α ' variation with trapdoor settlement ' δ ' for (a) dense Toyoura sand, (b) Kashima river sand and (c) spherical glass beads

Stress concentration of the buried structure (α) for the DEM simulations is presented below (Figure 4.16) for both spherical and non-spherical particle cases. For better clarity, the highest and the lowest values of H/B are presented in the figure below for each particle shape. A clear difference in the α is observed between the samples with higher ground heights and the lower ground height. Furthermore, for similar ground heights, non-spherical particles showed higher α value compared to the spherical case, although all other input parameters were kept similar for both types of simulations. The difference in stress concentration due to particle shape difference, as observed in model trapdoor tests, is also validated using DEM simulations.

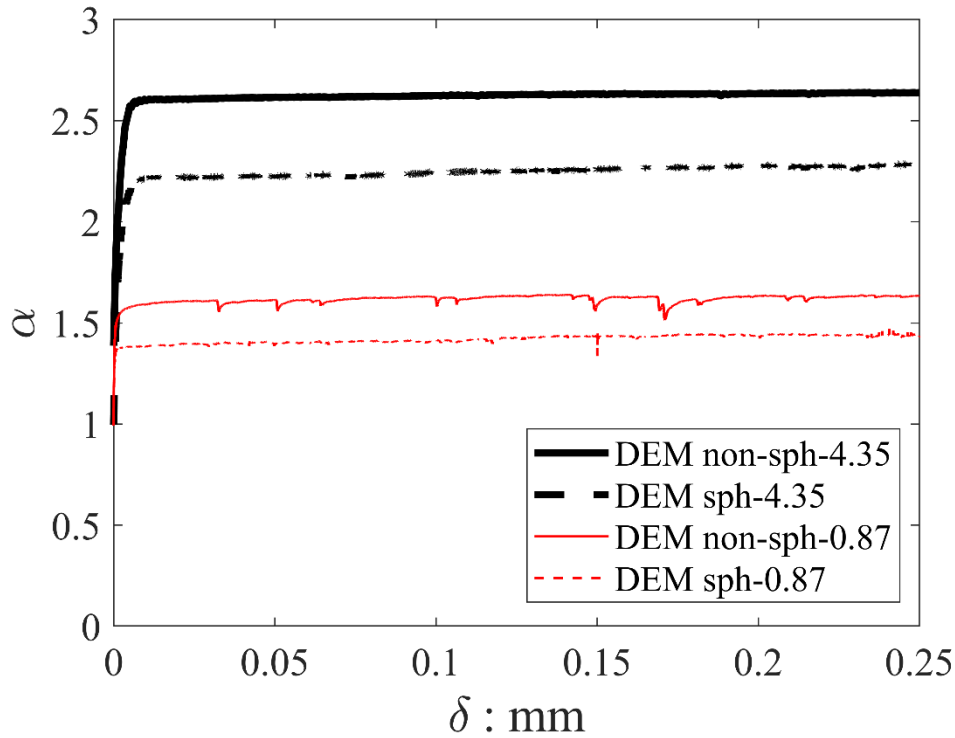


Figure 4.16 α variation on the central fixed plate for DEM simulations using spherical and non-spherical particles

A major difference between the α plots of DEM simulations and the model trapdoor tests is the absence of post-peak softening behavior in the DEM results. The reason can be associated with the very small trapdoor displacement in the case of DEM simulations. The base plates were lowered to a smaller value ($= 0.25\text{mm}$) in order to minimize the simulation time. Another reason being the appearance of peak value at a settlement much earlier than the given range of 0.25mm . However, in order to verify whether DEM can capture the post-peak softening behavior of stress concentration value at the central fixed base plate, a simulation with $H/B = 0.87$ having spherical particles, was prolonged to attain 10mm trapdoor settlement.

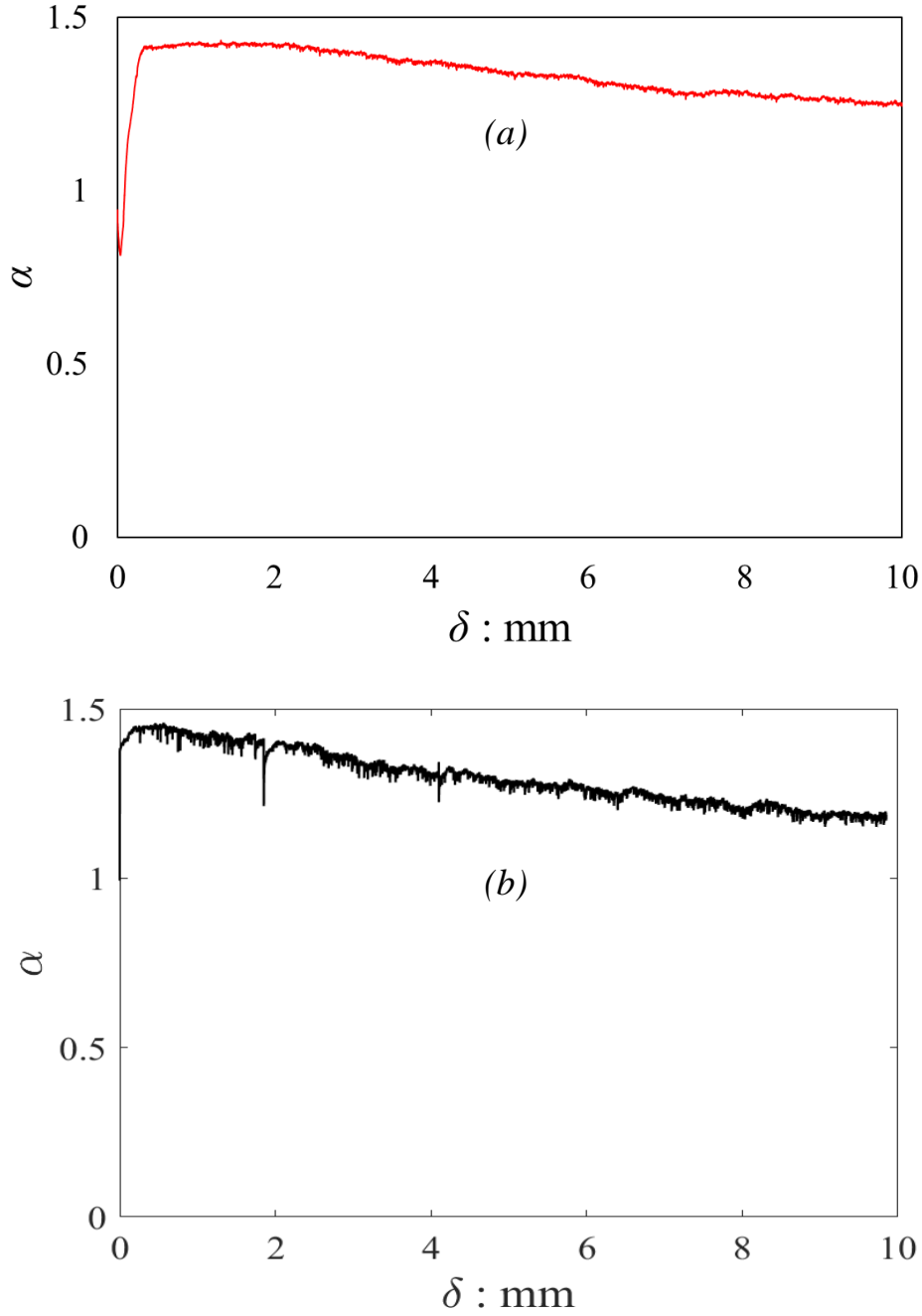


Figure 4.17 Post peak softening in α as observed in (a) model trapdoor test at H/B : 1.0 and (b) DEM simulation with H/B : 0.87 for spherical particles

The post-peak softening phenomenon was well captured by the DEM simulation as well, as represented by Figure 4.17(b) above. The stress concentration factor α for different H/B values and varying ground heights is shown in Figure 4.18 for all experimental cases.

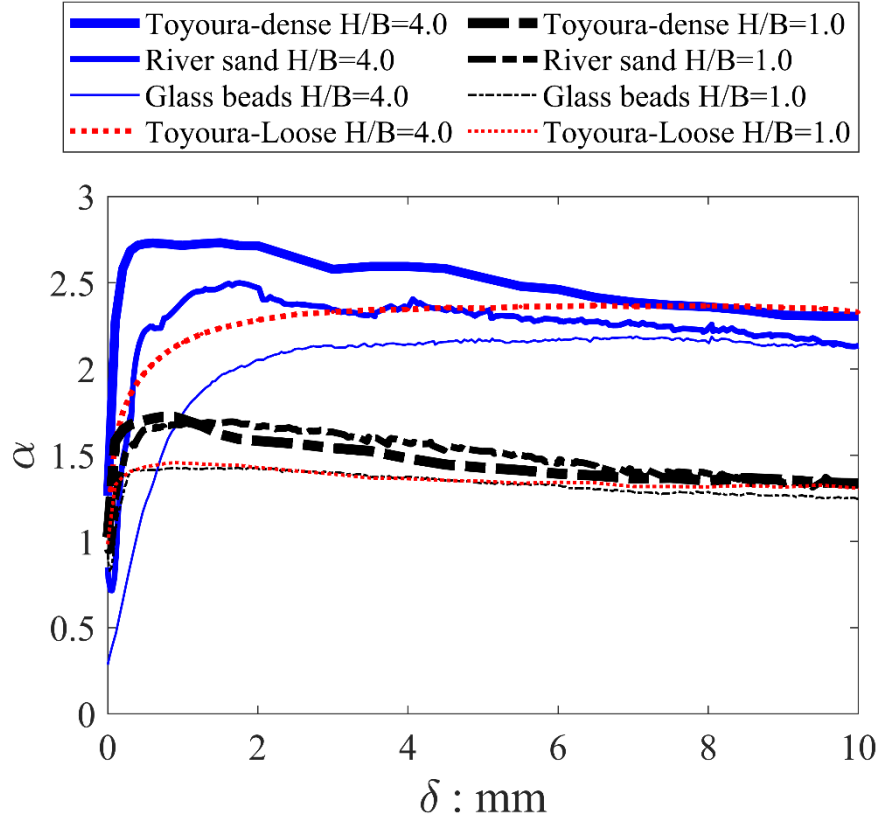


Figure 4.18 Experimental data for variation in α with trapdoor movement δ for Toyoura sand (dense and loose), Kashima river sand and glass beads with $H = 400$ mm ($H/B = 4.0$) and $H = 100$ mm ($H/B = 1.0$)

The combined plot clearly demonstrates the effect of particle shape and ground height on the stress concentration at the buried structure (central fixed plate). The smaller H/B for the same material resulted in smaller stress increment. However, for the same H/B , the sample having higher angularity depicted sharper peak development and higher α value, reinstating the importance of material shape parameters.

It is to be noted that the residual value of α , as visible in Figure 4.18 above the trapdoor settlement of 10mm, resulted in a converged value, rather than showing the effect of sample density or shape parameters. Hence, it can be concluded that the peak value of stress concentration factor α_{peak} depends upon the sample density and particle angularity, however, the $\alpha_{residual}$ is independent of particle size, shape, and density for the given range of materials at a certain H/B value.

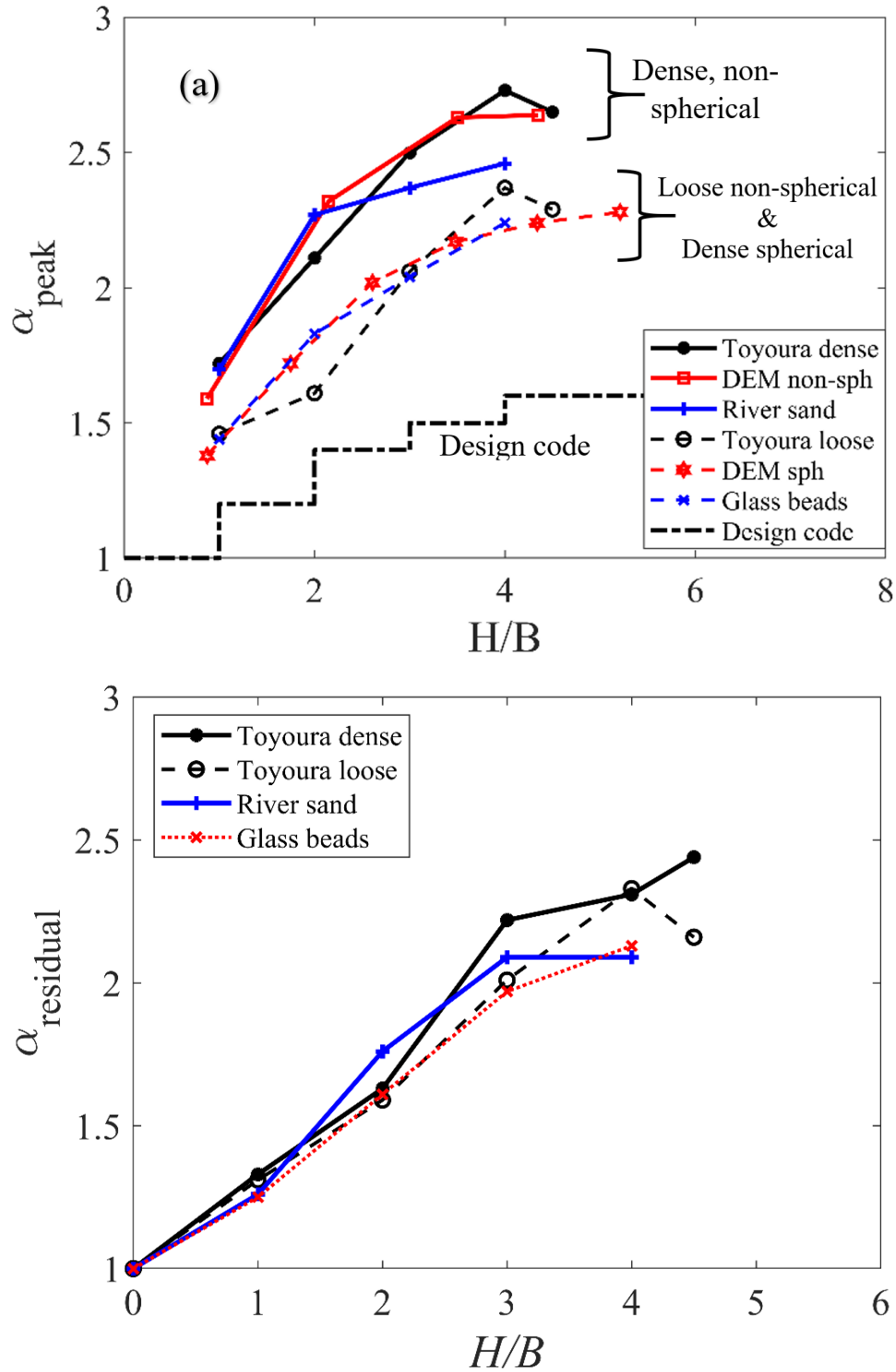


Figure 4.19 (a) Peak value of stress concentration (α_{peak}) against H/B for all cases and (b) the residual value of stress concentration ($\alpha_{residual}$) for model tests.

Figure 4.19(a) combines α_{peak} values for all tested cases along with the values presented by Japan Road Association design code (1999); the results can be divided into two clear groups irrespective of the particle sizes: (i) medium dense or dense sample with non-spherical particles

and (ii) loose with non-spherical or dense with spherical particles. Each group represents similar trends of α_{peak} with varying H/B where a close match between DEM data and laboratory data is evident. This indicates that both particle shape and sample density impart larger effects on the stress increase on buried structures compared with the particle size. Dutta (2019) conducted triaxial compression tests under dried conditions and reported that the peak friction angles (ϕ_{peak}) for the spherical glass beads and Kahima river sand are 29.1° and 42.5° , respectively, at a similar void ratio tested in the present model tests. This indicates a close link between stress concentration (equivalent to α_{peak}) and ϕ_{peak} , as also described by Stone & Muir-Wood (1992). The variation of α_{peak} for dense-spherical or loose non-spherical particles is similar to that of $\alpha_{residual}$, resulted from a similar stress response between the peak and residual states (Figure 4.18).

In all cases, as presented in Figure 4.19(a) above, the α value presented by the JRA (1999) design code showed the least conservative results. However, it is to be considered that the JRA (1999) design values are based upon the limited data of field measurement, without taking into account the particle shape or the soil cover effect.

4.8 Shear stress distribution during trapdoor condition

The shear stresses redistribution is also observed during the trapdoor tests. Unlike the normal stresses, the initial shear stresses on the base plate (or on the top of the buried structure) approach to zero due to the absence of lateral movement of particles. However, as soon as the trapdoor lowering is started, the particles move in a particular pattern in order to respond to the trapdoor movement.

The relative magnitude of the shear stresses is much smaller compared to the normal stresses. However, the distribution pattern of shear stresses can be of vital importance in determining the soil behavior under trapdoor conditions.

As explained in Chapter 3, sandpapers were used on the surface of the base plates in order to enhance the shearing response of the material. The results of the shear stress distribution are presented below in Figure 4.20 for Toyoura sand (dense and loose) under varying ground height conditions. The shear stress distribution is plotted against the sample width, and the distribution can be observed as a symmetrical mirror image about the centerline.

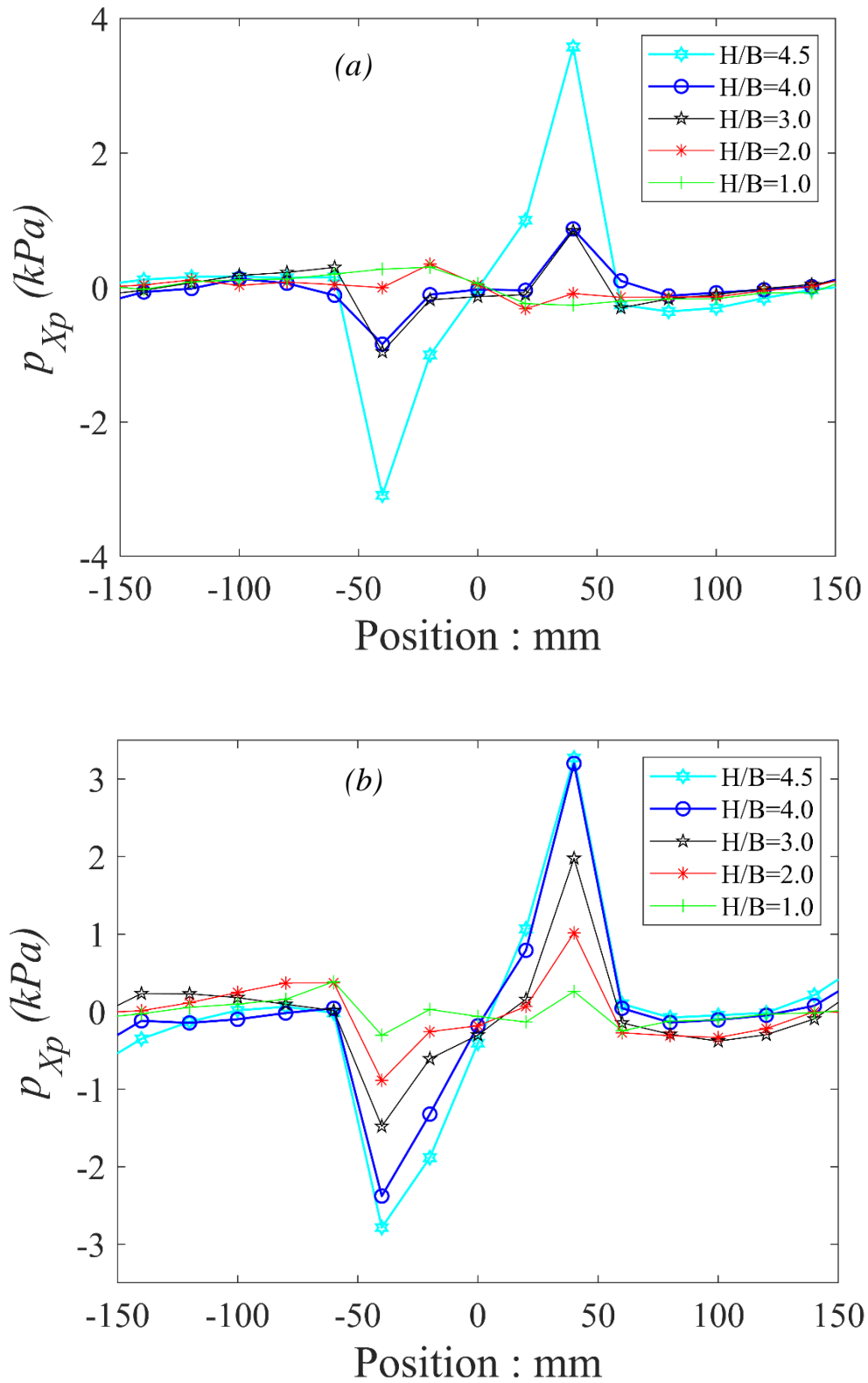


Figure 4.20 Peak shear stress distribution for model trapdoor tests on Toyoura sand with (a) dense and (b) loose samples

The shear stresses show increased value with increasing sample height. However, above a certain H/B , the trend is reversed in direction. Loose and dense Toyoura sand samples did not differ much in terms of result trends. The only difference is the relatively higher value of shear stresses in dense samples.

In a similar manner, the shear stress distribution for the Kashima river sand and the spherical glass beads is provided in Figure 4.21 and Figure 4.22 below, respectively. Both materials showed the trends as observed in the case of Toyoura sand samples, with relatively smaller shearing stresses. Spherical glass beads, having a smooth surface with the highest sphericity value, showed the least values of shearing stresses. The phenomenon of reversal of stress direction at a particle H/B is also observed in the case of Kashima river sand and the spherical glass beads. This reversal of shear stress distribution will be discussed later in this chapter.

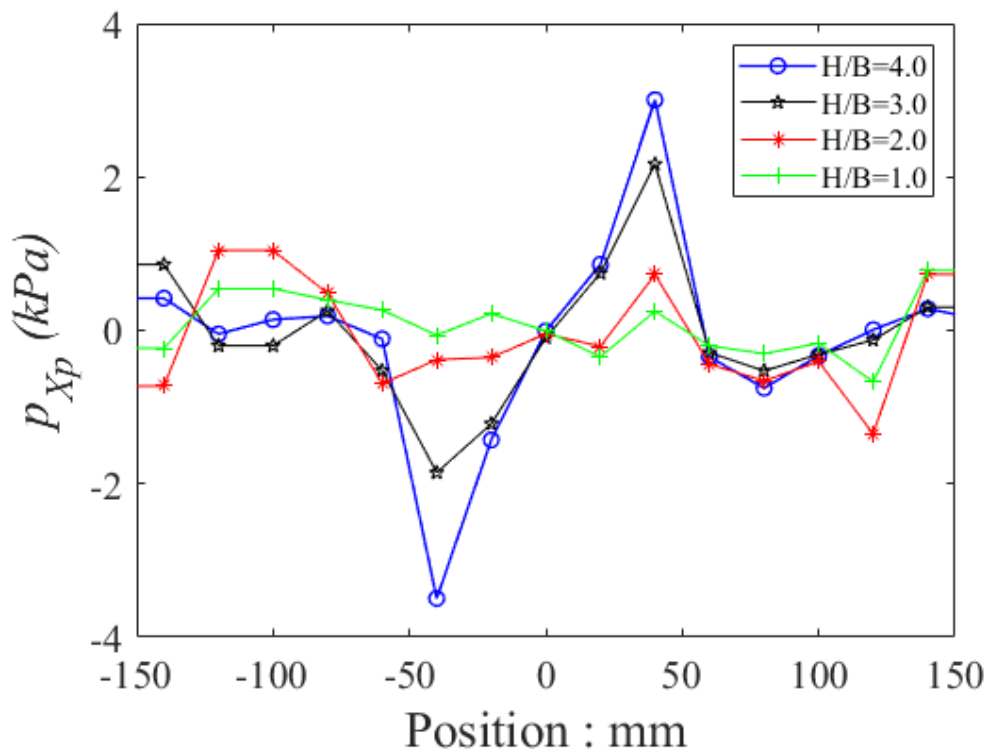


Figure 4.21 Peak shear stress distribution for Kashima river sand for different sample heights

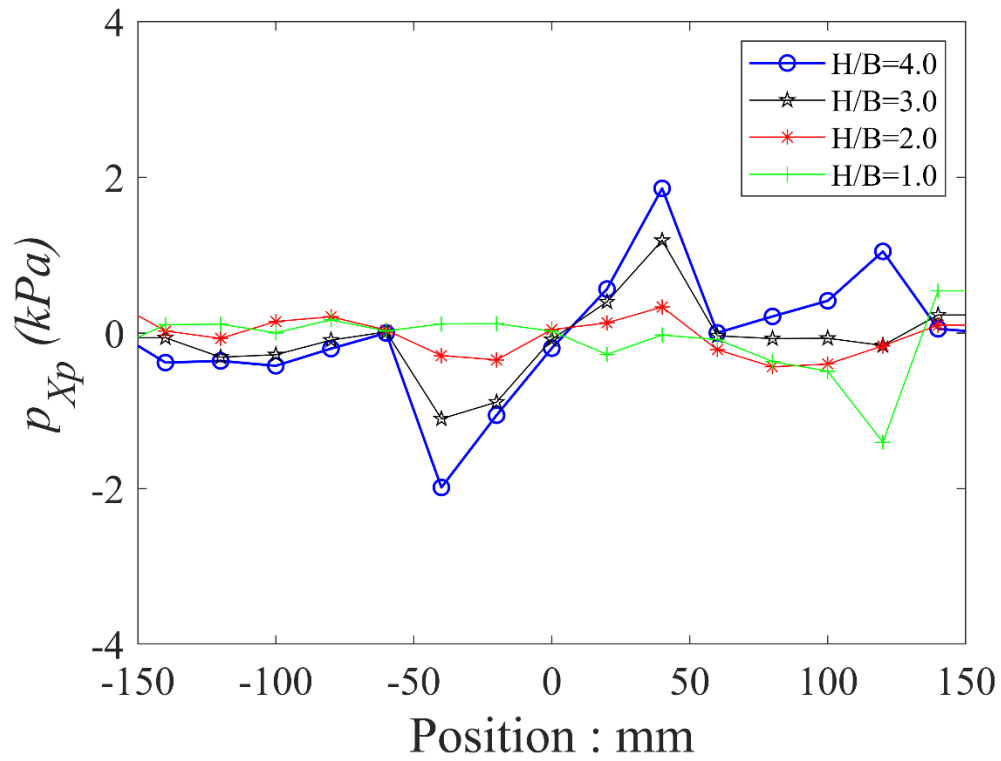


Figure 4.22 Peak shear stress distribution for Spherical glass beads under different sample heights

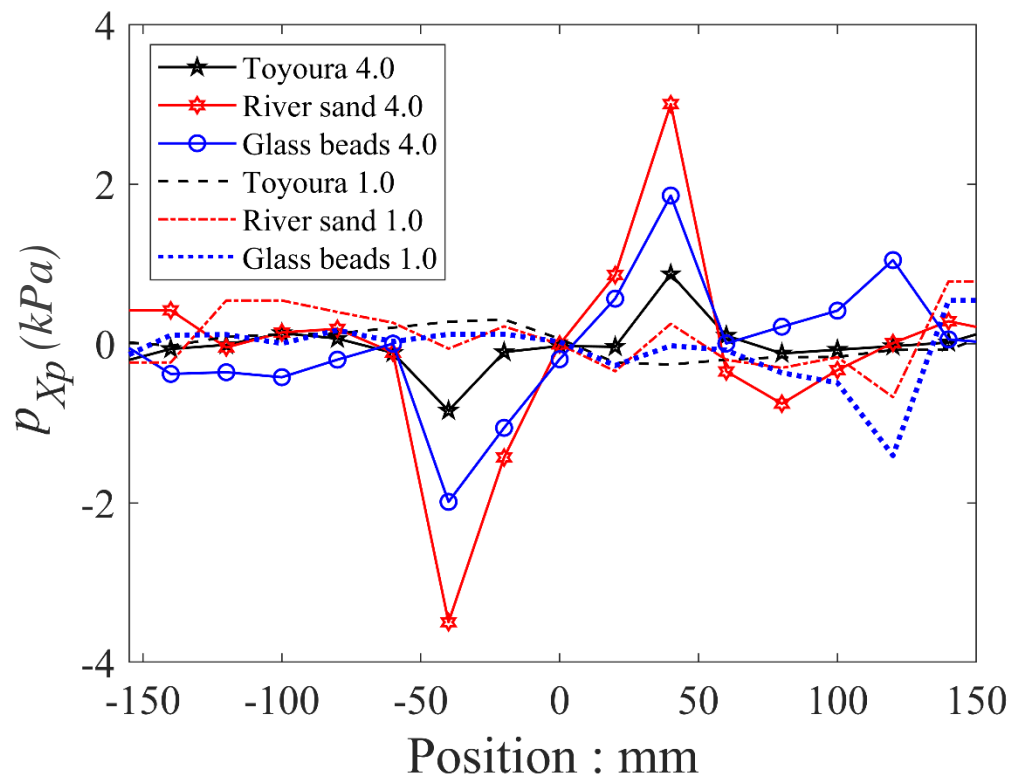


Figure 4.23 Combined peak shear stress distribution for Toyoura sand dense, Kashima river sand and spherical glass beads under H/B of 1.0 and 4.0

In Figure 4.23, the combined shear stress distribution is plotted for all three tested materials (dense Toyoura sand, Kashima river sand, and the spherical glass beads) under two sets of H/B values: 1.0 and 4.0. The absolute values of shear stresses for all three materials have insignificant differences. Furthermore, the general trend for both H/B values is very similar in all cases. Keeping in view the generality, there could be a possible relation between the arching under different sample heights and the shear stress distribution pattern, that reverses at a certain H/B value.

4.9 Arch validation using shear stress distribution pattern

As discussed above, the presence of a particular shear stress pattern for varying sample height can be used in order to predict the absence or presence of the arching. Since the shear stress distribution possesses a rotational symmetry along the central line, analysis of either half portion of the shear stress curve would suffice the discussion.

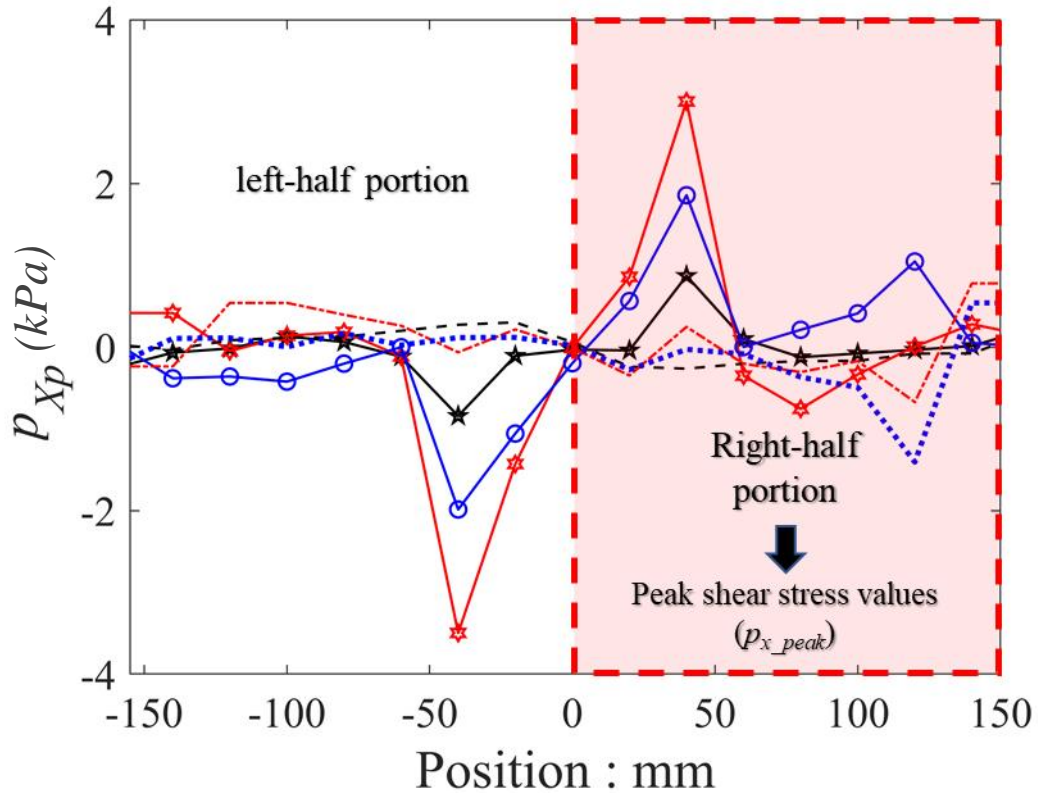


Figure 4.24 Portion of shear stress distribution considered for analyses

For simplicity, the *right-half* portion, as shown in Figure 4.24, was selected for analysis for all tested materials. The analysis was performed for all H/B values and the peak shear stresses were monitored in all cases, either positive or negative in magnitude.

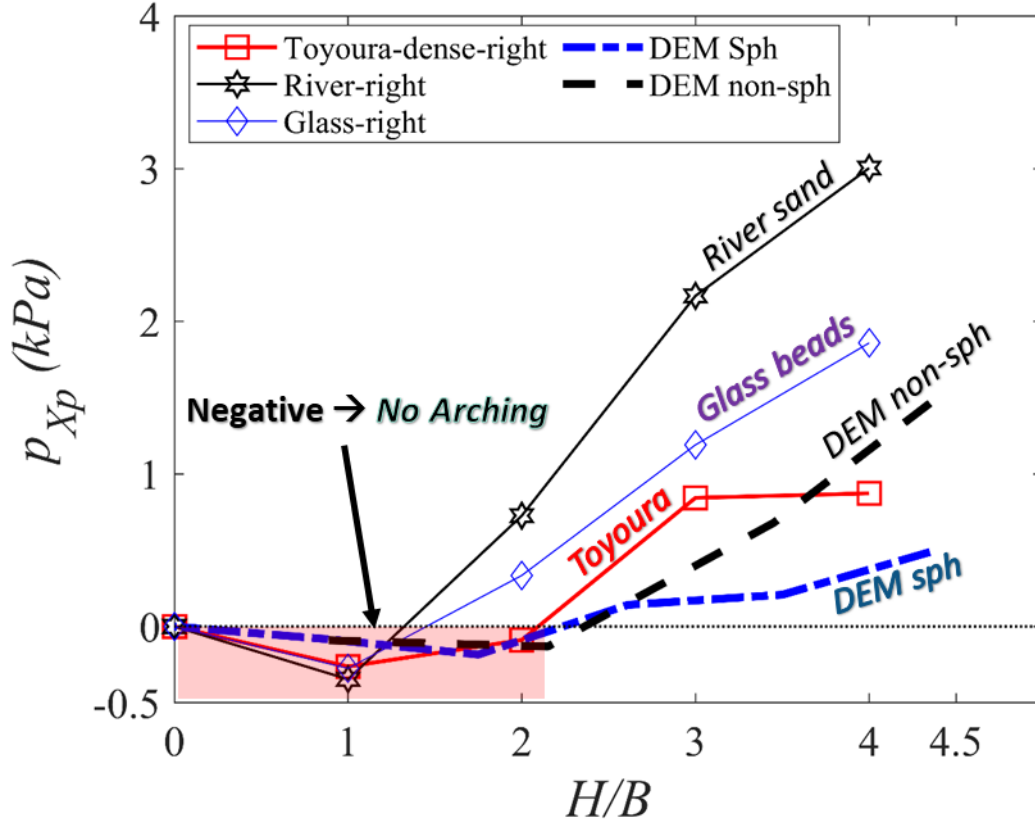


Figure 4.25 Peak shear stresses for all tested materials on the right-half portion of samples under varying H/B values

In Figure 4.25, it is clear that the negative peak shear stress (P_{x-peak}) was obtained for a range of $H/B < 2.0$. for most of the cases. For H/B beyond 2.0, the P_{x-peak} yielded positive values. It is worth noticing that the nomenclature for the shear force direction is such that it produces positive values if the particles are moving towards the right side (positive x-axis) and vice versa for the leftwards movement of particles (negative x-axis). The direction of shear stresses is further clarified through Figure 4.26.

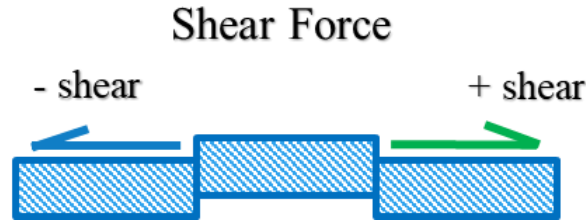


Figure 4.26 Direction nomenclature of shear force under trapdoor condition

Keeping in view the above-presented direction of shear force, the particles change the movement direction once the sample height exceeds a limit value, keeping a specific configuration of the test apparatus. It is thus believed that the reversal of shear stress direction is due to the arching action being formed inside the tested material. Once, the ground being tested attains a minimum required depth for the transmission of the arching forces, the particle movement is reversed at the top surface of base plates, resulting in a reversal of shearing stresses. However, the cases with smaller H/B values, arching forces do not get enough space to interconnect with neighboring particles to result in a defined shape.

The above-presented mechanism takes place at the particulate level and its quantification during model tests is not possible. However, DEM simulations can well capture the presented theory. To do so, two extreme cases were selected with H/B of 0.87 and 4.35 using spherical particles. Using post-processing, the particle movement vectors were generated and plotted for both cases of H/B . Spherical particles were selected in this analysis as they are the extreme case and least expected to generate the arching pattern. A probable verification of soil arching using spherical particles could hence easily be applied to all other particle shapes.

Figure 4.27(a) represents the particle movement vector diagram for $H/B = 4.35$, which is the highest ground case. The surface settlement data showed the absence of differential surface settlement for the same case, which will be discussed in the following chapter in detail. The absence of differential surface settlement signified the presence of a strong arching action in the material being tested. Particle movement analysis around the central base plate reveals that the particles are trying to move outwards from the edges of the central plate. Or in other words, particles are moving towards the arch. In such configuration, the right half of the sample is moving towards the right side, implying positive shear stress on the right half. The left half behaves vice versa, and the stress distribution is negative in that region. Consequently, a shear stress distribution for higher H/B values, as shown in Figure 4.23 and others, is produced. This

trend that is obtained for the higher H/B values is believed to exist due to the presence of the arching above the lowering trapdoors.

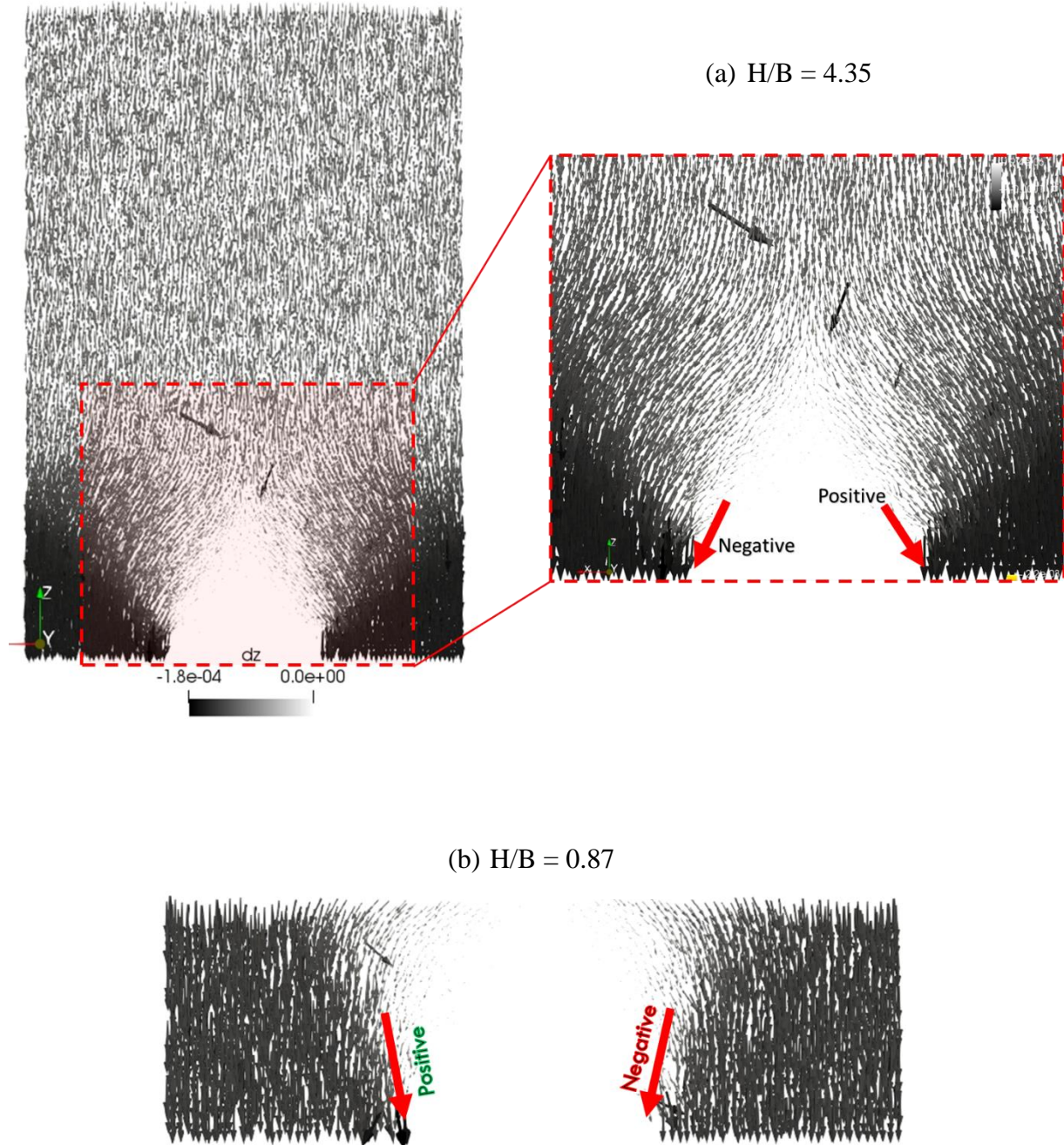


Figure 4.27 Particle movement vector for (a) H/B : 4.35 and (b) H/B : 0.87 using DEM simulations on spherical particles

However, in the case of smaller sample heights, as presented in Figure 4.27(b) with $H/B = 0.87$, the right-half portion of the sample portrays a particle movement direction towards the

left side of the specimen. Whereas, the left-half portion represents particle movement towards the right side of the specimen. Such distribution of movement vectors produces a shear stress distribution curve being represented in Figure 4.22, Figure 4.21 or Figure 4.20 for smaller H/B value samples. Since the particles are moving inwards/towards the central static base plate, no arching phenomenon exists in such a case; that is also represented by the differential surface settlement of the specimen that will be presented in the following chapter.

In short, the shear stress distribution can be well used to determine whether a soil mass under trapdoor condition is accompanied by arching forces, or there is no such arching mechanism. Consequently, the shear stress distribution can be used to determine the adequacy of soil cover for any given buried structure. A higher soil cover would ensure the presence of strong arching forces, causing a stress concentration on the buried structure to multitudes of initial stresses and ensuring the stability of the surface above the buried structure. However, higher ground cover above buried structures also increases the normal stresses and earth pressure, which might cause a structural failure of the buried structure. Hence an engineering approach, considering all involved parameters, should be used for a safe and economical design of buried structures.

CHAPTER 5: PARTICLE SCALE ANALYSES OF SOIL ARCHING IN TRAPDOOR TESTS

Stress redistribution under trapdoor conditions and the increased stresses on the buried structure are discussed in detail in the previous chapter. Also, as discussed earlier, shear stresses also show a peculiar behavior under trapdoor conditions, that could be utilized in determining arch evolution in the ground. However, all these normal and shear stress patterns are solely dependent upon the rearrangement of particles in the soil mass under the arching effect. Soil arching phenomenon and its verification, both experimentally and numerically, are discussed in the current chapter.

5.1 Soil arching and differential surface settlement

5.1.1 Experimental analyses

The trapdoor model tests were performed on Toyoura sand (Ebizuka, 2010), Kashima river sand and spherical glass beads. For each material, four different ground heights were considered, except the Toyoura sand that included an additional case of ground height with H/B of 4.5. During each test, photographs were captured at a regular interval to observe the temporal variation in the ground surface. The initial and the final stages of Kashima river sand and spherical glass beads for the least and the highest H/B values are presented below in Figure 5.1 to Figure 5.4.

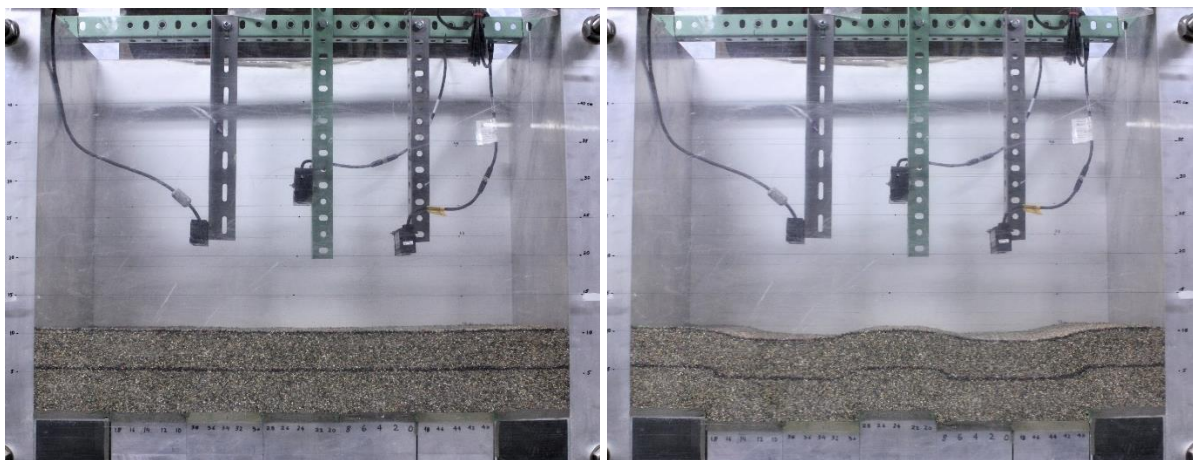


Figure 5.1 Trapdoor test on Kashima river sand for $H/B = 1.0$ at (a) initial condition and (b) final condition

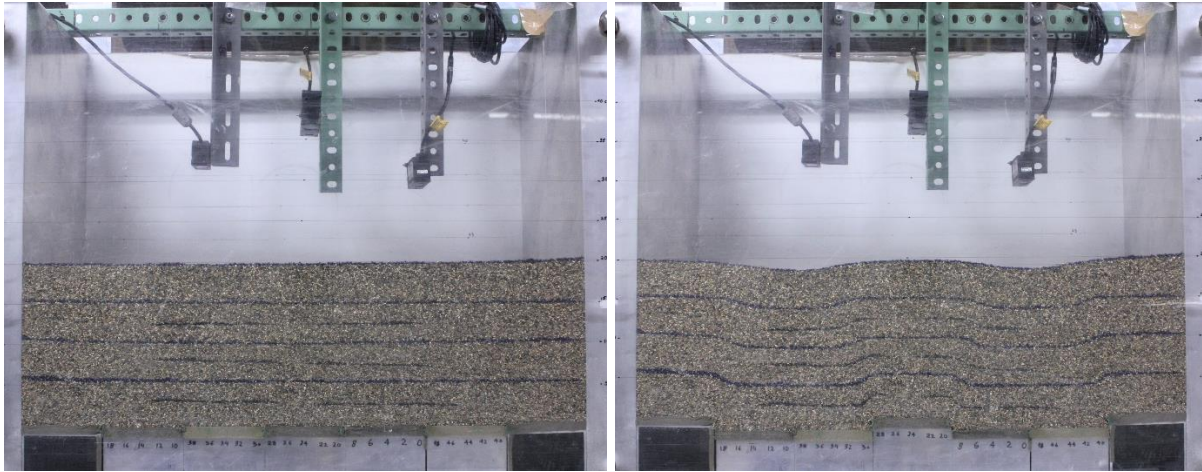


Figure 5.2 Trapdoor test on Kashima river sand for $H/B = 2.0$ at (a) initial condition and (b) final condition

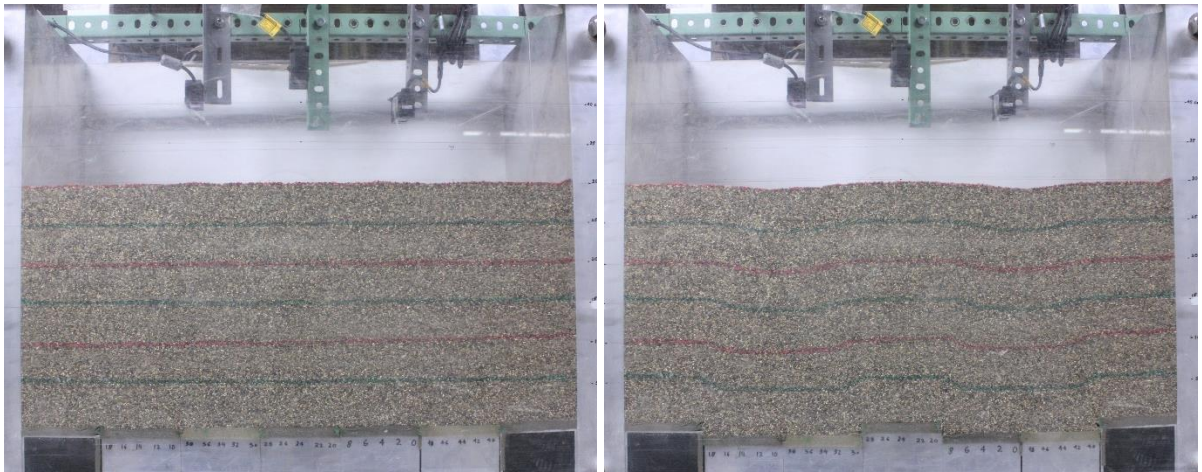


Figure 5.3 Trapdoor test on Kashima river sand for $H/B = 3.0$ at (a) initial condition and (b) final condition

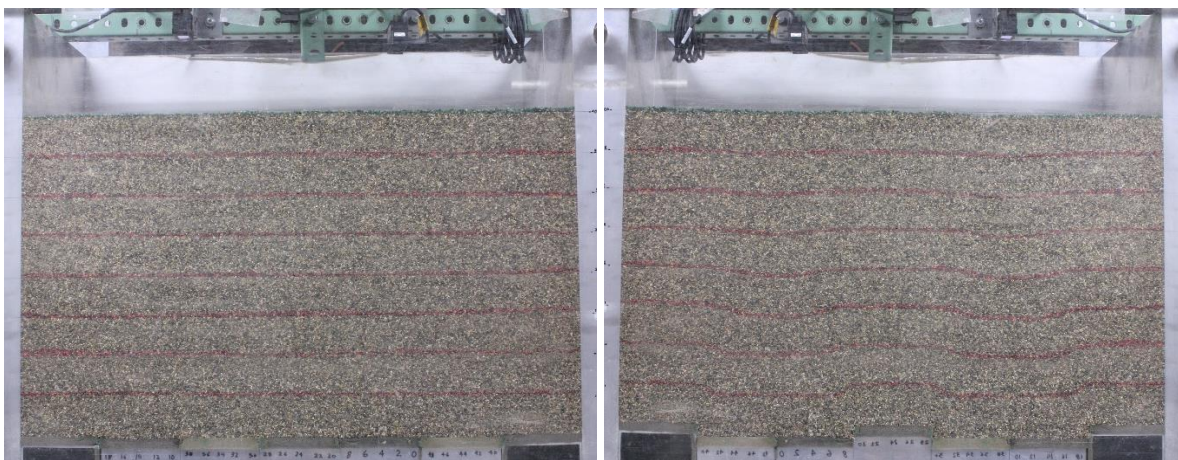


Figure 5.4 Trapdoor test on Kashima river sand for $H/B = 4.0$ at (a) initial condition and (b) final condition

Thin layers of colored particles were provided near the front acrylic plate at a distance of 50mm in height. Also, laser displacement meters were installed on the top of samples to measure surface settlement at three different locations on the ground surface. Similar to river sand, initial and the final test pictures for the spherical glass beads with the least and highest H/B are provided below in Figure 5.5 to Figure 5.8.

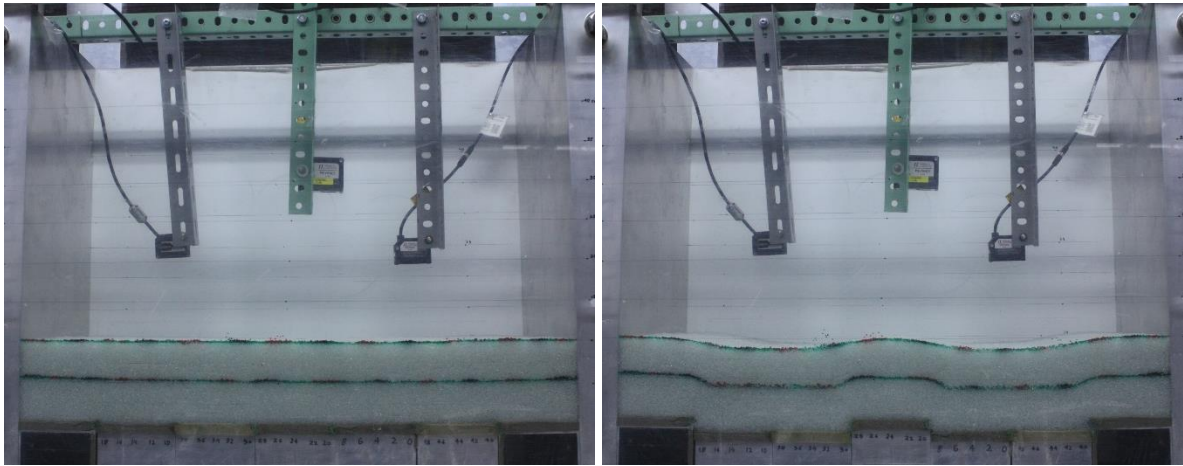


Figure 5.5 Trapdoor test on spherical glass beads for $H/B = 1.0$ at (a) initial condition and (b) final condition

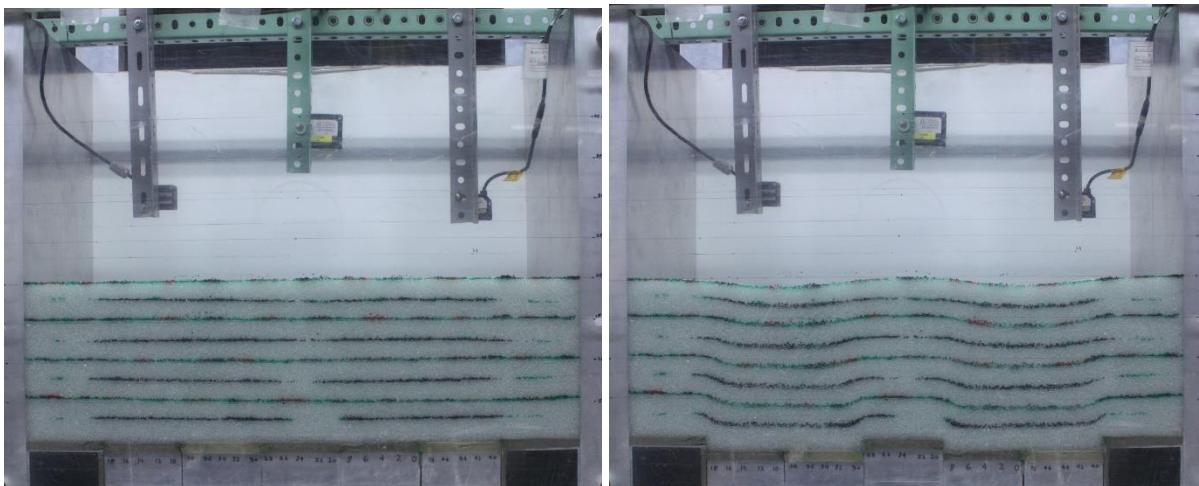


Figure 5.6 Trapdoor test on spherical glass beads for $H/B = 2.0$ at (a) initial condition and (b) final condition

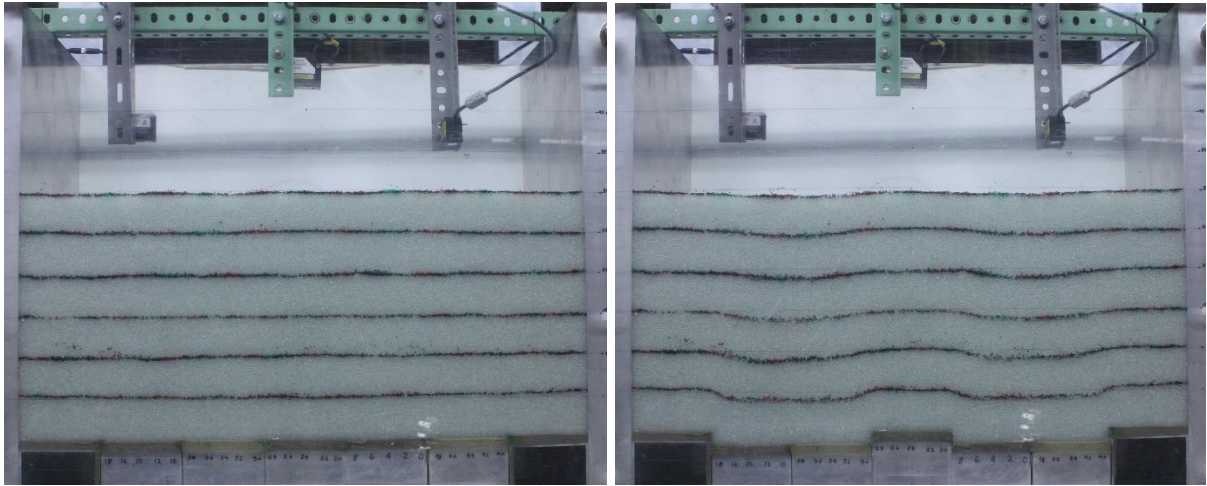


Figure 5.7 Trapdoor test on spherical glass beads for $H/B = 3.0$ at (a) initial condition and (b) final condition



Figure 5.8 Trapdoor test on spherical glass beads for $H/B = 4.0$ at (a) initial condition and (b) final condition

In all models test cases, samples with $H/B = 1.0$ resulted in a large surface settlement above the lowering trapdoors, whilst the ground above the static central base plate did not show any significant settlement. Such a situation resulted in a larger differential surface settlement above the base plates (or the buried structures). With increasing H/B values, the trend of differential surface settlement reduced and at the maximum value of $H/B = 4.0$, all tested materials exhibited a minute uniform surface settlement, instead of a large differential settlement. To have a better understanding of differential surface settlement and uniform surface settlement, *Figure 5.9* shows the combined pictures for all three tested materials for two different H/B values. In addition, observed arching patterns are also overlaid in *Figure 5.9*,

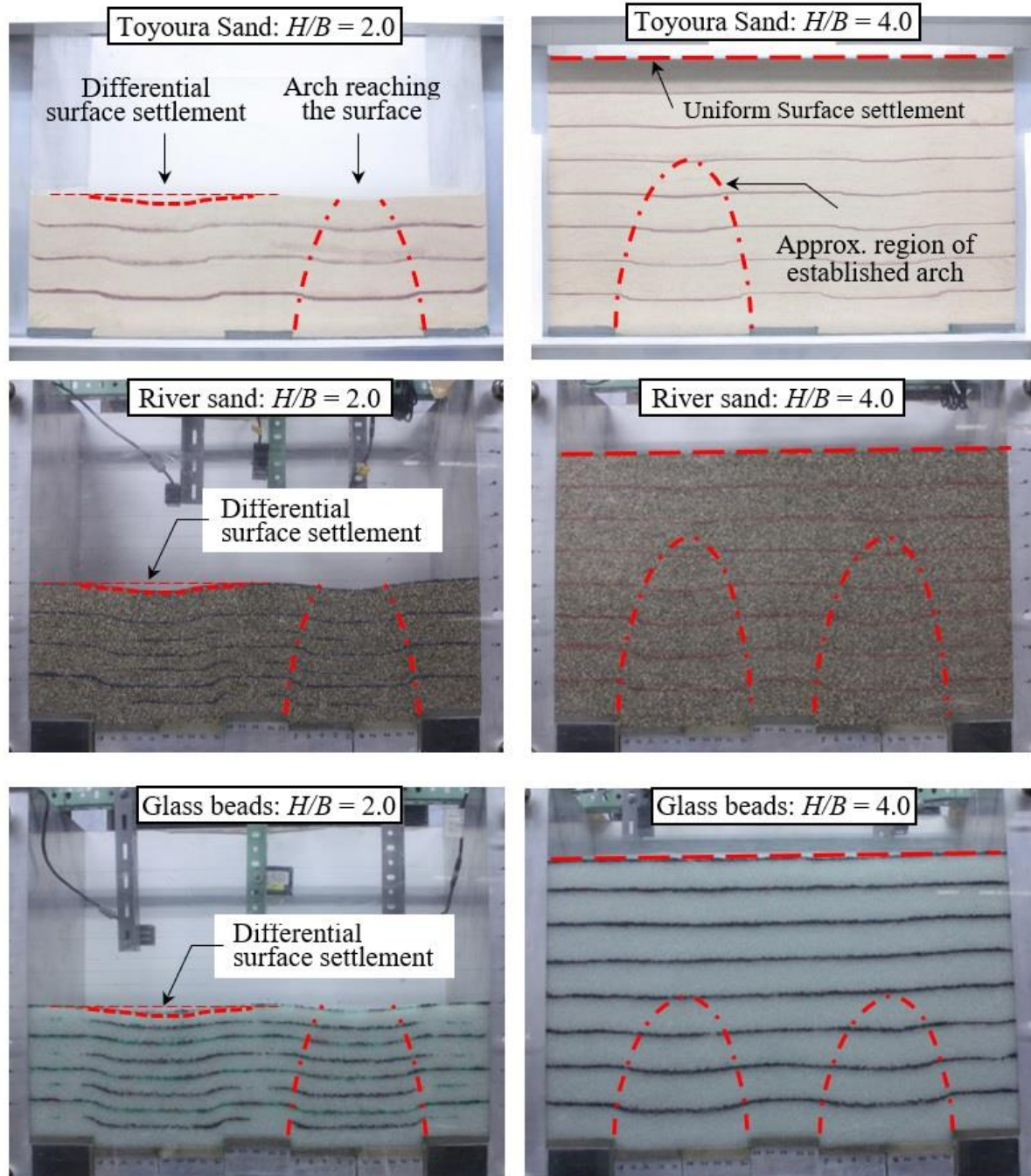


Figure 5.9 Differential surface settlement and the arching pattern for all tested materials under H/B of 2.0 and 4.0 in model trapdoor tests

In the above figure, it is clear that the arching action is initiated in all cases irrespective of their H/B value. However, the samples with smaller ground heights showed clear differential surface settlement as the developed arch did not find enough sample height to complete its loops and consequently reached the ground surface level.

This shape led to behavior with discontinued arching, resulting in a larger differential surface settlement.

Contrary to the former case, the arch was fully developed above the lowering trapdoors for the cases with higher ground surfaces. The arching action helped in diverting the stresses of stabilized soil mass above lowering trapdoors to be diverted towards either side. Such diversion of stresses due to arching action causes the stress redistribution, that is discussed in detail in the previous chapter. The result of the arching action is that there exists no differential surface settlement. Rather a very small uniform surface settlement is observed in all material types, as shown in Figure 5.9 above.

Three numbers of laser displacement sensors were also installed on top of the model test apparatus at locations represented by Figure 5.10 below. Surface settlement data was collected for Kashima river sand and the spherical glass beads cases. Results for the surface settlement are plotted in Figure 5.11.

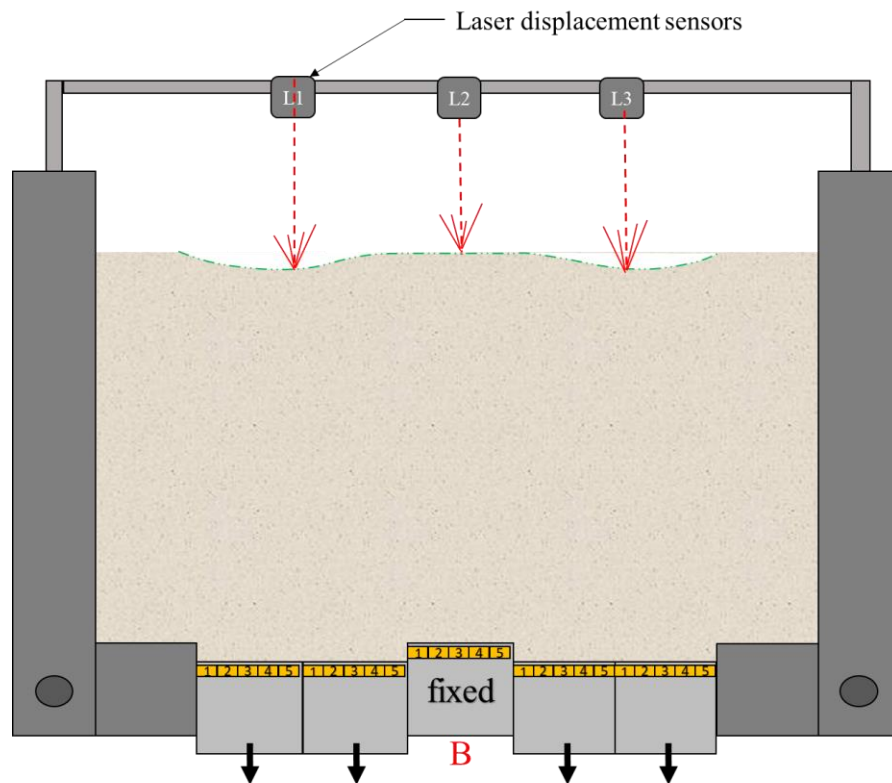


Figure 5.10 Location of laser displacement sensors installed in model trapdoor tests

Figure 5.11 is plotted between H/B values for Kashima river sand and spherical glass beads, against the normalized surface settlement. The normalized surface settlement is obtained by dividing the surface settlement value obtained in the test results (δ) with the maximum value of trapdoor settlement (δ_o). the results of the surface settlement obtained from the laser sensors installed on the left and right sides were averaged for simplicity and clarification and plotted with the settlement value obtained through the central laser displacement sensor. For both materials, it is observed that for smaller H/B values, there exists a large gap between the normalized settlement values. Side sensors produced a large surface settlement, whereas the central sensor did not show significant surface settlement values. With an increase in the ground height, this difference reduced and for the maximum value of H/B , there was a negligible amount of differential surface settlement. Such absence of differential surface settlement is an indirect means to assess the presence of strong arching forces within the soil mass.

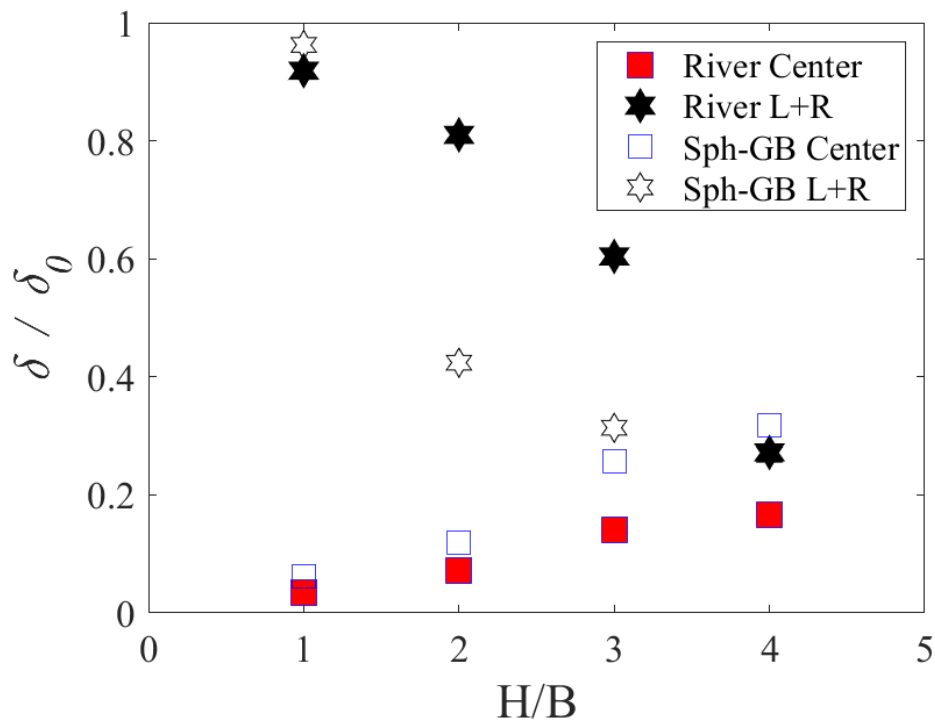


Figure 5.11 Normalized surface settlement data with varying H/B values for Kashima river sand and spherical glass beads

5.1.2 Numerical analyses

Numerical simulations were performed with a varying ground height to result in a wide range of H/B values. However, in order to save the computational energy and to reduce the simulation time, all simulations were performed for a trapdoor displacement (δ) of 0.25mm. Quantification and comparison of this small displacement were cumbersome and consequently, normalized displacement as adopted in experimental results was used in the numerical simulations as well.

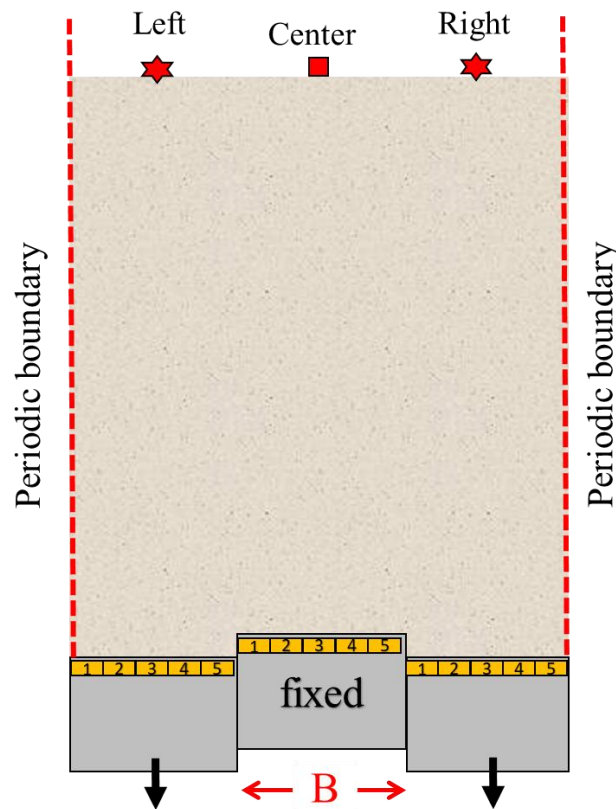


Figure 5.12 Location of the regions at the ground surface for surface settlement analyses

For each DEM simulation for both spherical and non-spherical particles, several particles located above the left lowering trapdoor, central fixed plate and the right lowering trapdoor were selected (Figure 5.12) to compare the surface settlement ($\delta_{surface}$) normalized by the trapdoor settlement (δ) in Figure 5.13. For smaller H/B , particles above the central plate show negligible settlement, whereas particles above the lowering trapdoor showed settlement nearly equal to the displacement of the trapdoors (δ). In the case of spherical particles, particles above the central fixed plate showed a little higher movement for smaller H/B due to the fact that spherical particles have lesser interlocking

and might slip due to the neighboring moving particles above the trapdoors (Figure 5.13). However, for larger H/B , the uniform surface settlement is observed due to soil arching, for both spherical and non-spherical particles.

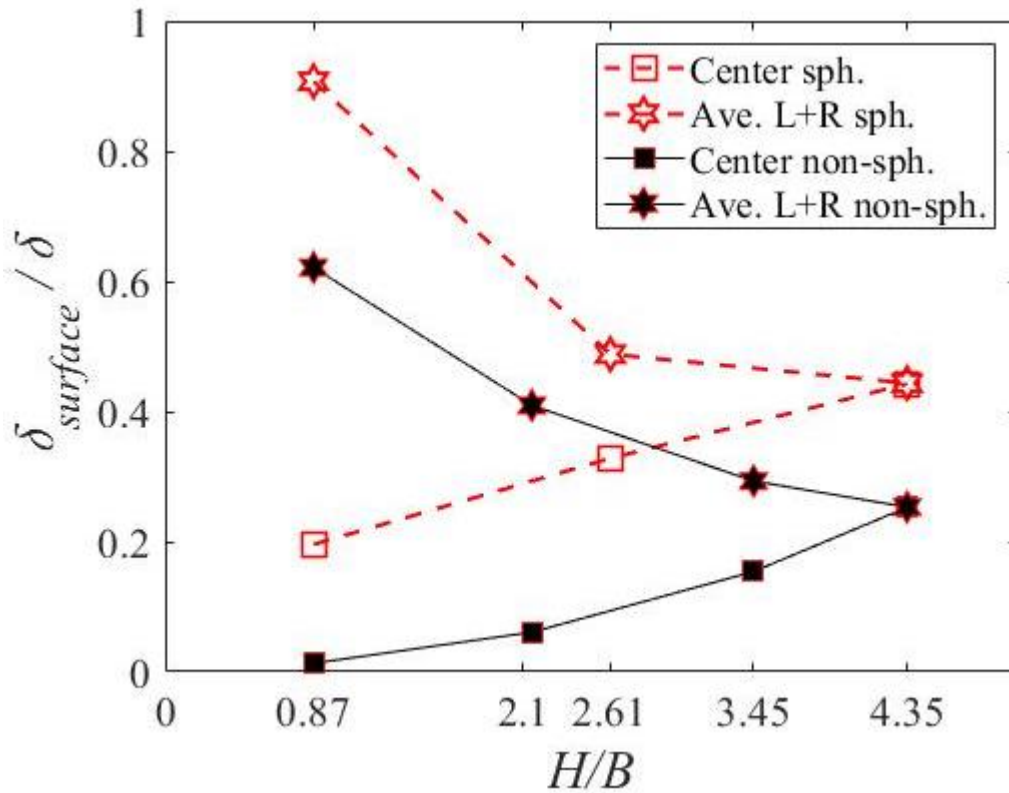
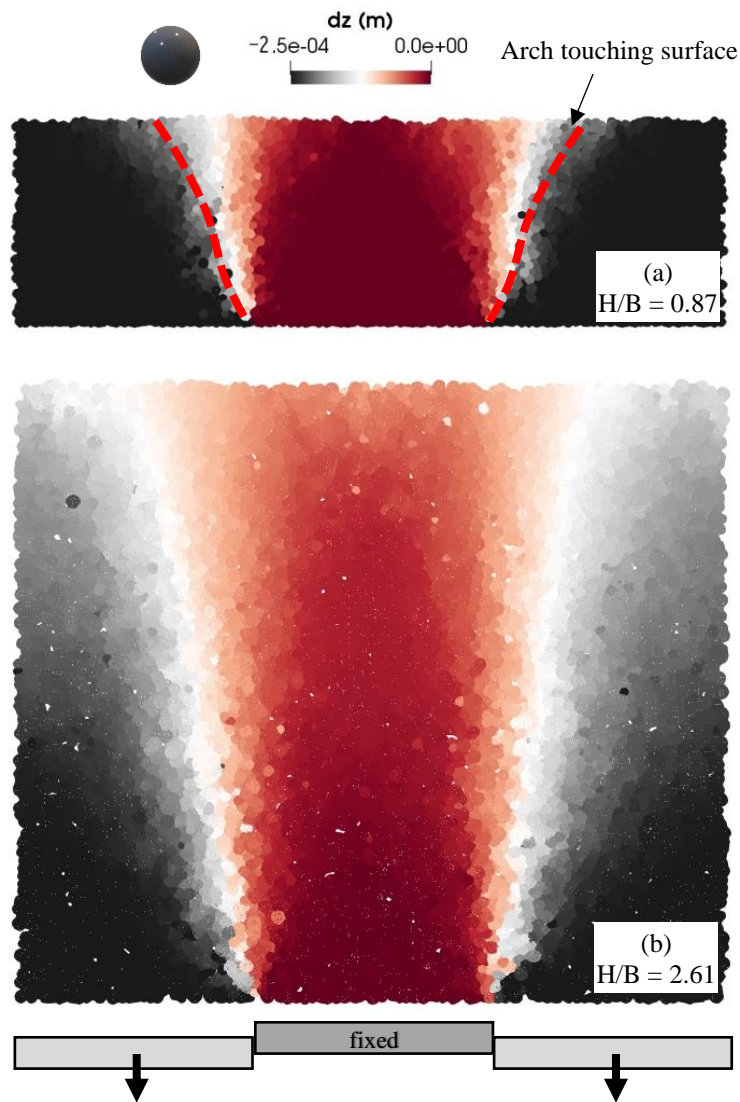


Figure 5.13 Normalized surface settlement data with varying H/B values for DEM simulations using spherical and non-spherical particles

The results from DEM numerical simulations presented above are well in line with the experimental finding presented earlier. Combining all results for surface settlement analyses, it can be concluded that the differential surface settlement occurs when the ground height above the lowering trapdoors is small enough to restrict arch evolution. However, for the cases with sufficient ground height above lowering trapdoors, there is enough space available for force transmission through an arching effect to form a closed shape. Consequently, there exists only a small amount of uniform surface settlement instead of a large differential surface settlement.

5.2 Vertical displacement of particles

Another means to verify the arching phenomenon under trapdoor conditions is to quantify the vertical displacement of the specimen at the particulate level. Hence DEM data was used to analyze the particle movement during trapdoor tests. The base plates were moved with a displacement velocity of $1\text{e-}4$ m/s, which was found to be small enough to result in a quasi-static approach. Particle displacement data was then plotted using the Paraview program and the results for the simulations with spherical particles are presented below in Figure 5.14.



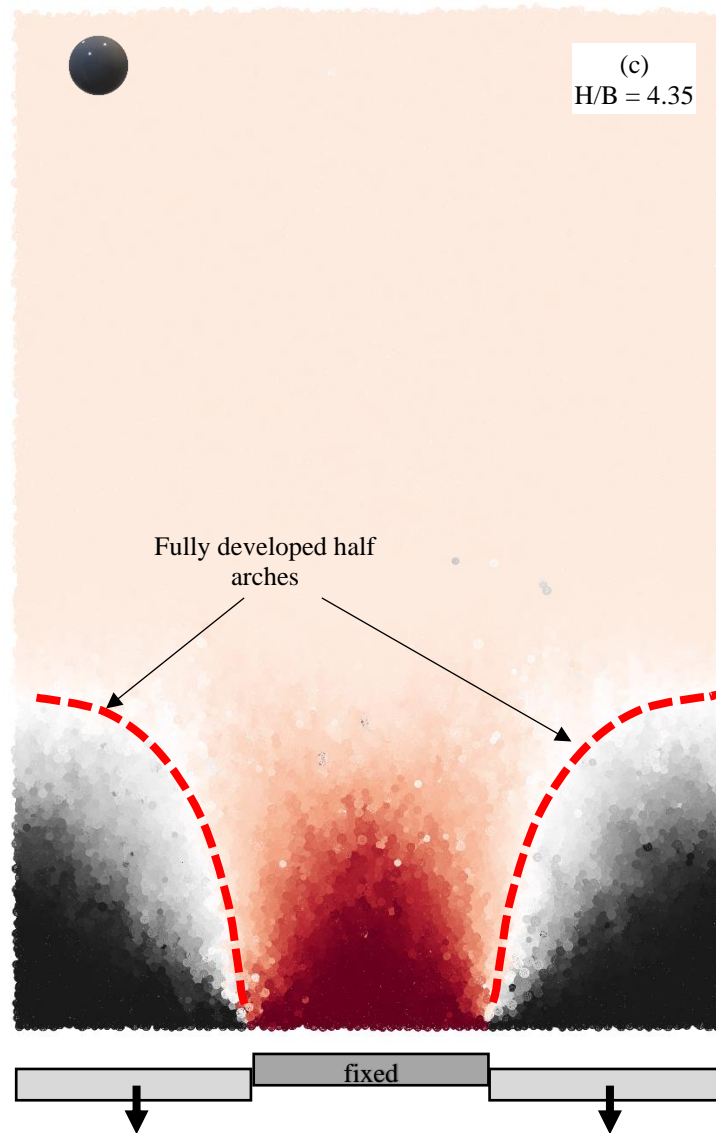


Figure 5.14 Vertical movement of particles in DEM simulations using spherical particles

The formation of an arch occurs from the boundary between the central fixed plate and the lowering trapdoors, and it propagates outwards diagonally to form a closed arch. However, for smaller H/B values, the sample height is insufficient to fully form an arch. Figure 5.14 also shows the half portion of the fully developed arch on both sides of the central fixed plate for the case of $H/B = 4.35$. Shahin et al. (2004) reported that the soil cover above the tunnel surface influences the surface settlement in their 3D trapdoor model tests. Chevalier & Otani (2011) observed the vertical movement of particles induced by trapdoor movement using CT scanning; their DEM simulation reproduced a similar pattern of movement. Wang (2013) found that the soil arching developed between cantilever piles forms a catenary shape. When a catenary-

shaped arch is created under a trapdoor condition, the minor axis can be the width of lowering trapdoors, and the longer axis can be the height of the arch.

In Figure 5.14(c), half a portion of fully formed arches can be seen on either side of the specimen. Only half portion is visible due to the usage of periodic boundaries in the lateral direction to reduce the computational effort and simulation time. Since the arching action has fully been developed in that case, the ground surface of the sample does not portray any differential surface settlement, visible by the presence of a constant color of the top layer. Thus, the simulation results reiterated the experimental results for surface settlement analyses with different ground heights.

Similar plots were also obtained using non-spherical particle shapes and presented below in Figure 5.15 for different ground heights. Non-spherical particles plot showed a very similar trend as showed by spherical particle simulation results. However, the arching regions are clearer with a clear distinction between the moving and static portions of the soil mass. Similar to the spherical particles, samples with smaller H/B values demonstrated clear differential surface settlement, as observed in experimental cases as well. The arching region also intersected with the ground surface in the case of smaller H/B . A clear distinction of a static portion (showed with red color in the figures) can be made from the settling portions (shown as black to a grayish color). For the case with $H/B = 3.45$, as shown in Figure 5.15(c), arching action can be seen by the similar colored region around the central fixed base plate. However, the top surface, in that case, shows a very small amount of differential surface settlement. Such condition demonstrates that the arching action has not attained its fully stabilized condition. Further increase in the ground surface level to a small amount would result in a fully developed arching mechanism, that is then verified by Figure 5.15(d) with $H/B = 4.35$, having distinct arching regions.

Consequently, it can be concluded that the vertical particle movement analyses can be well utilized for investigating the arch development withing the sample using discrete element simulations. Spherical particles, that possess a very minute amount of interlocking between particle due to their particular shape, also demonstrated the arching behavior under the given condition, that matched well with the experimental results of trapdoor tests using spherical glass beads. The phenomenon of differential surface settlement, that was observed in the model trapdoor tests with different ground height condition, was well understood with the help of vertical displacement analyses using discrete element simulations.

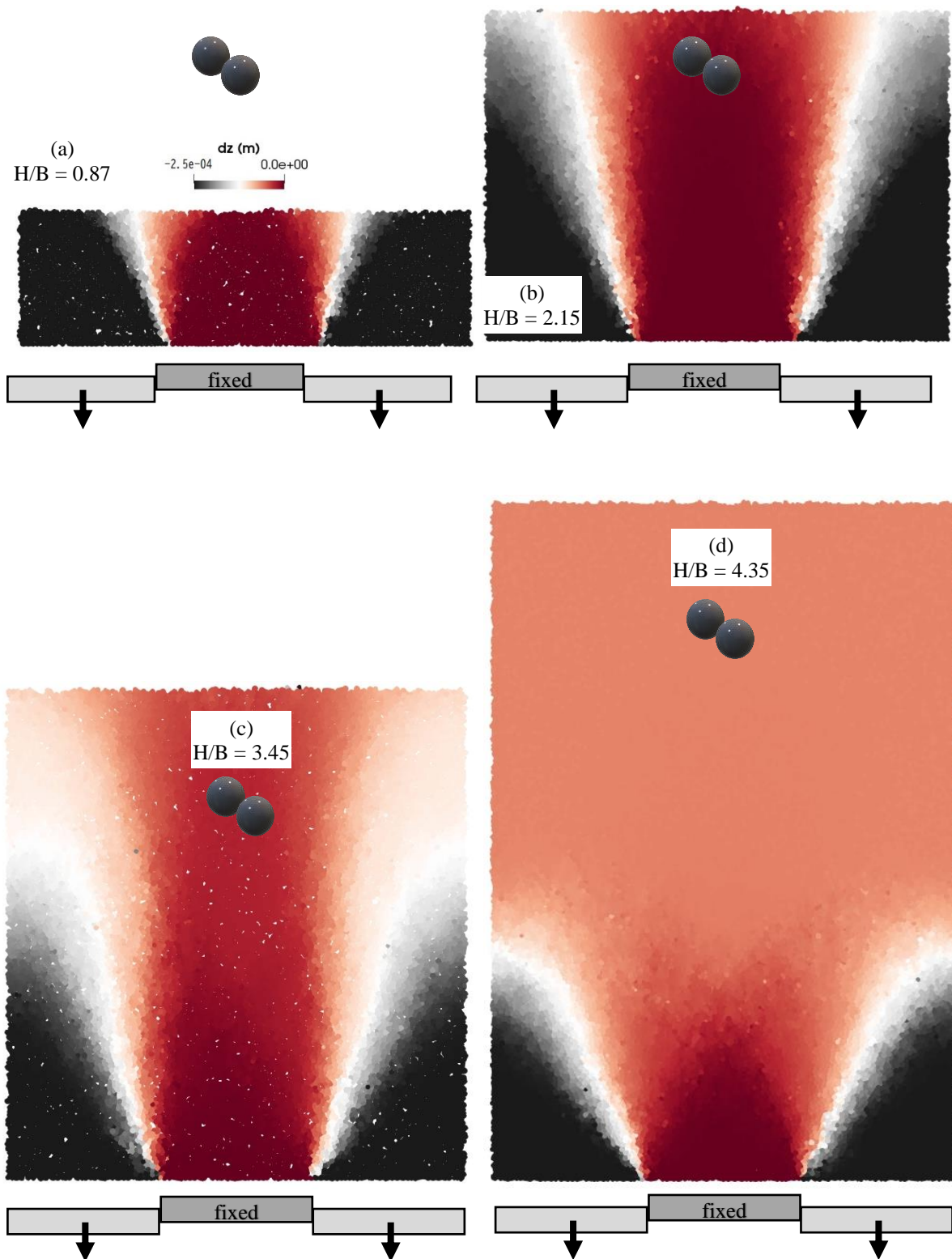


Figure 5.15 Vertical movement of particles in DEM simulations using non-spherical particles

5.3 Strong force network for arch analyses

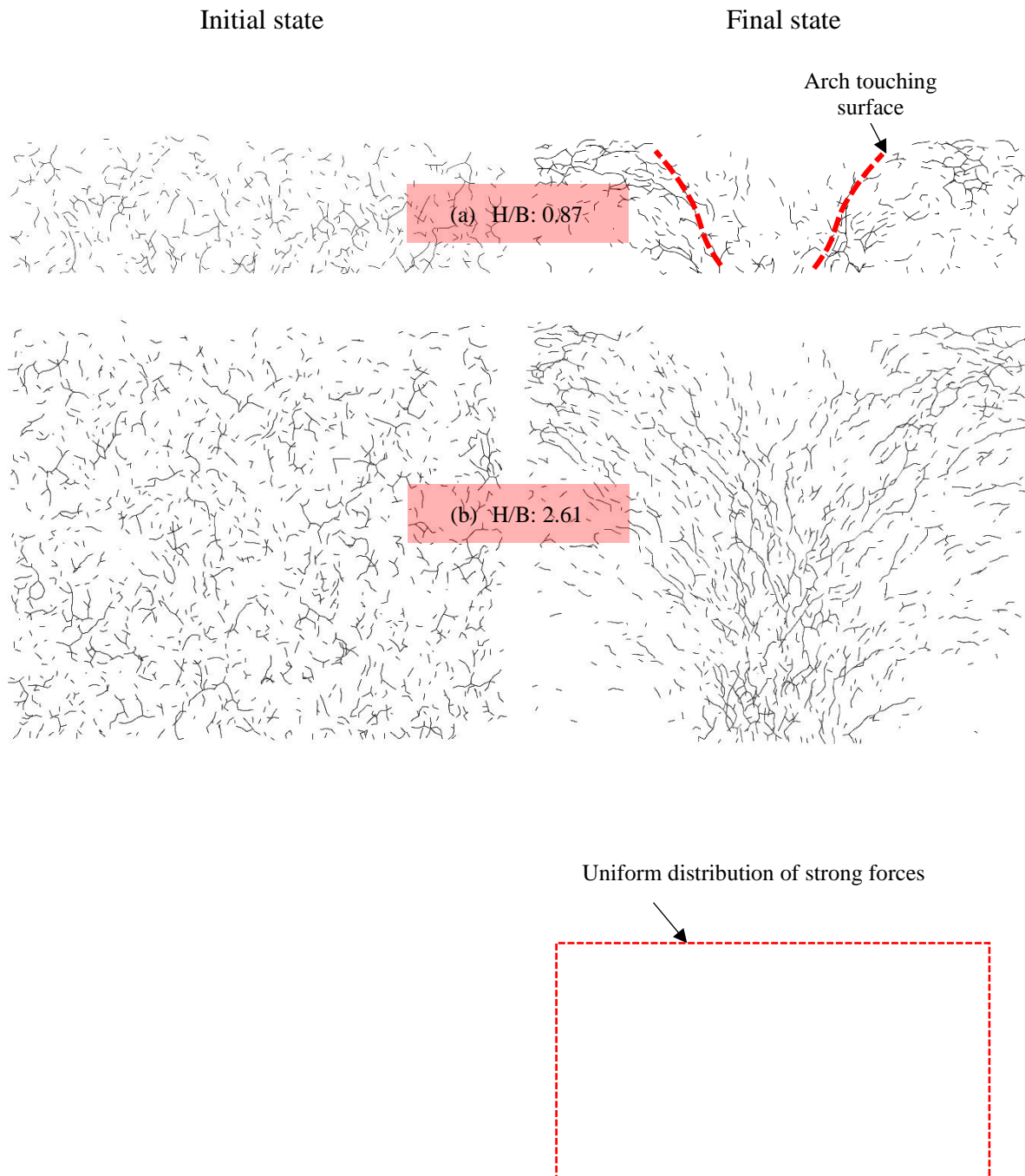
Under the trapdoor conditions, stresses are redistribution amongst the soil mass, resulting in a situation with higher stresses in particular parts. Portions of the soil mass having higher stresses possess interparticle forces higher than the surrounding portion. Thus, the assessment of such particles having greater contact forces can lead to assess the arching phenomenon.

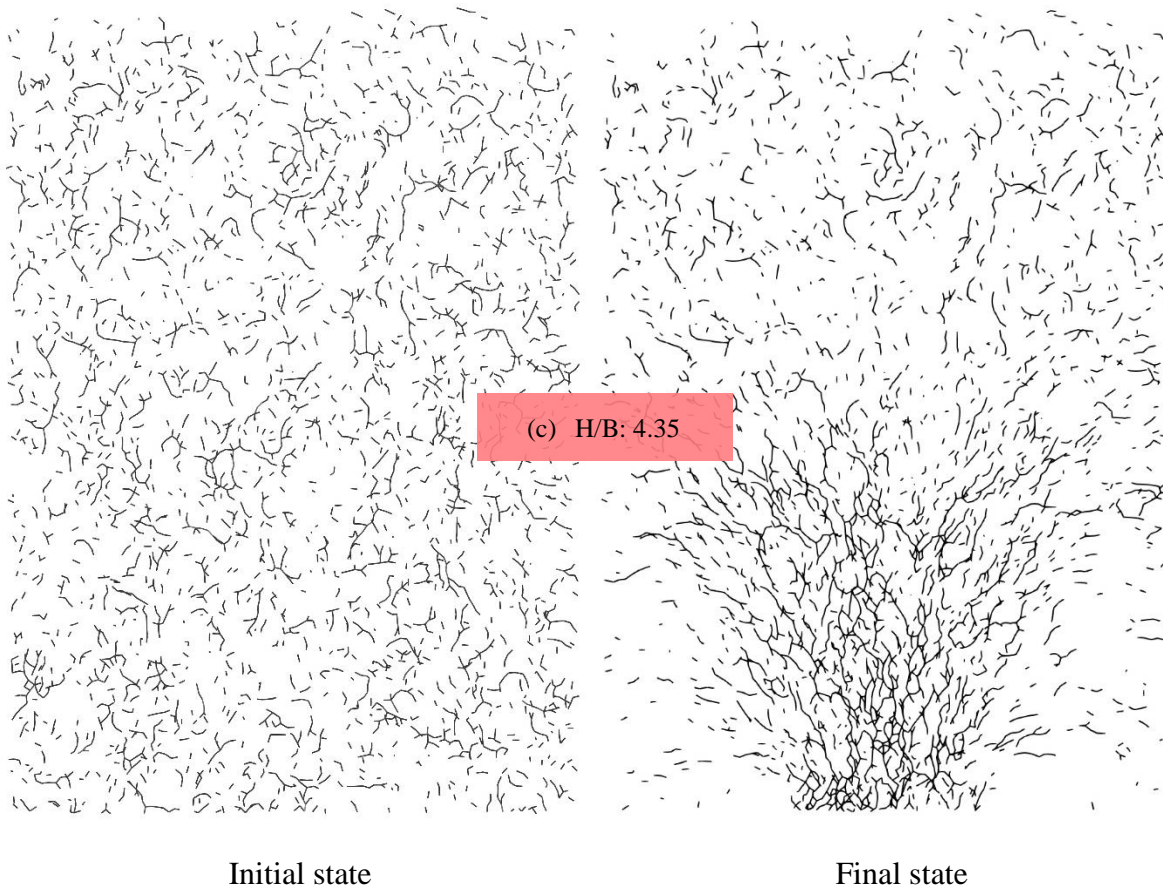
Behringer et al. (2008) described a strong force chain as a “filamentary” structure that carries a substantial share of forces compared to the rest of the system. The regions that carry negligible contact force were expressed as “dormant” by Kuhn (1999). The lines connecting the centroids of contacting particles that transmit strong forces in the middle portion of the sample are illustrated in this section; where strong forces are defined as the contact forces that carry greater than 90% of the maximum contact force in the sample. To eliminate the effect of overburden pressure, contact forces are normalized by the depth of each contact location, measured from the sample surface.

The initial state for the DEM simulations with spherical particles is presented in Figure 5.16 below, along with the final state of strong contact forces, for a range of H/B values. Uniformly distributed strong contact forces are observed in the initial state prior to commencement of trapdoor lowering, under all ground heights of samples. Once the trapdoors are initiated to move downwards with a specific velocity, the contact forces rearrange to initiate soil arching. The formation of an arch seems to initiate irrespective of the sample height; however, for smaller H/B , the propagating arch touches the sample surface, resulting in the differential surface settlement (Figure 5.16 a&b final state) as discussed in the earlier section of this chapter. The differential surface settlement can be deduced by the visual inspection of the top region of samples with smaller H/B cases, where the central portion of the samples does not contain any strong forces, compared to the sides with a strong force network. Such differing force networks near the surface of the sample could result in large differential surface settlement.

For samples with higher H/B values (Figure 5.16 c&d final state), a strong force network is visible at a particular region above the lowering trapdoors, forming a clear arching shape. However, the strong force distribution above the arching zone is very uniformly distributed. Such uniform distribution of strong forces above the arching zones is the primary cause of the small amount of uniform surface settlement instead of differential surface settlement for the

cases with higher H/B values. Such observation was also noted using the experimental results and the vertical displacement analyses of particles using DEM simulations.





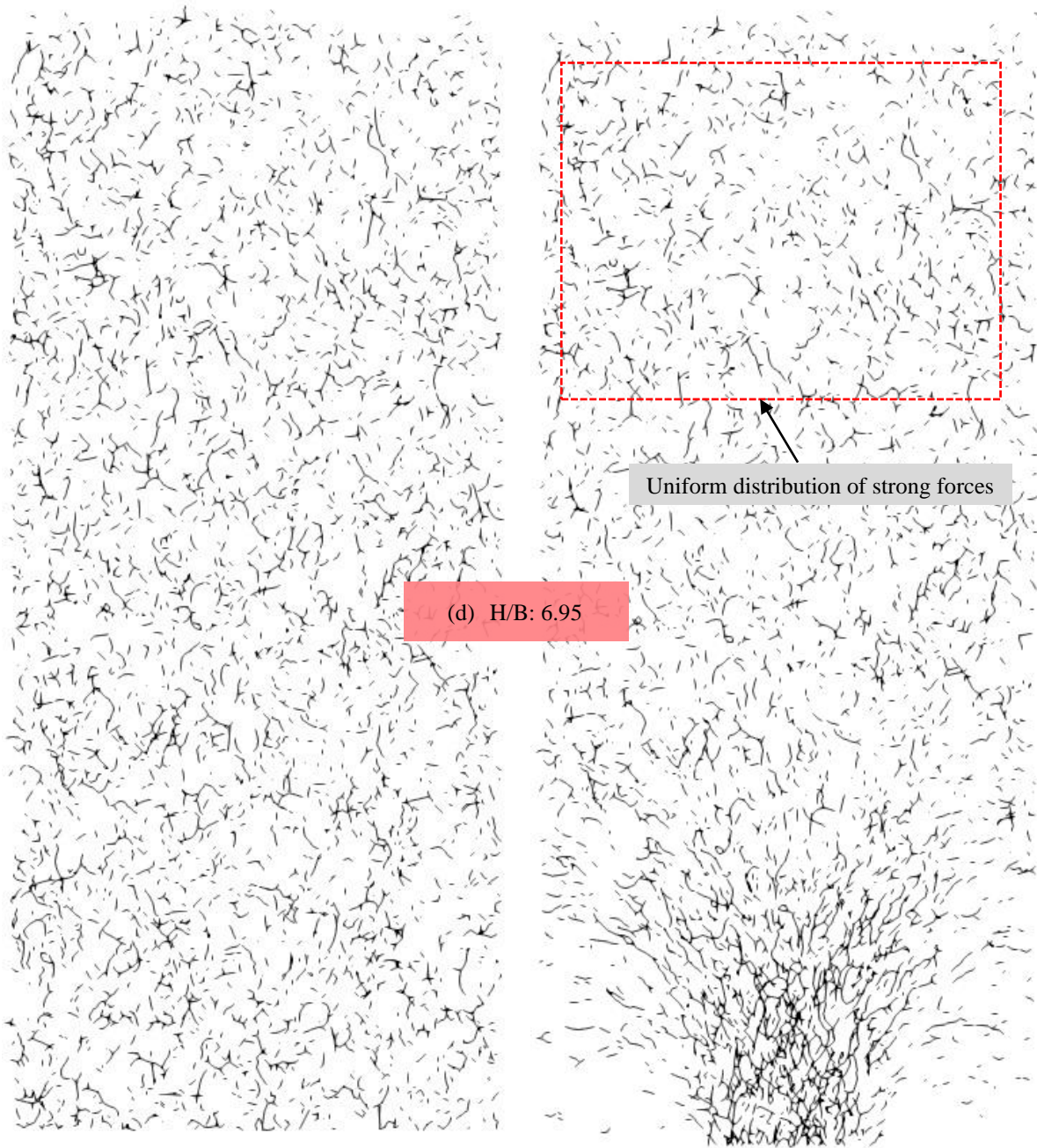


Figure 5.16 Strong force distribution for DEM simulations using spherical particles at the initial and final stages for different H/B values

5.3.1 Comparison between spherical and non-spherical particle results

Strong force distribution during DEM simulations was also observed for the non-spherical particle shapes under four different types of ground height. The initial strong force distribution for the non-spherical particles was also observed to be uniform throughout the sample space, as observed in spherical particle cases. The final state of the strong force distribution network is shown below in Figure 5.17

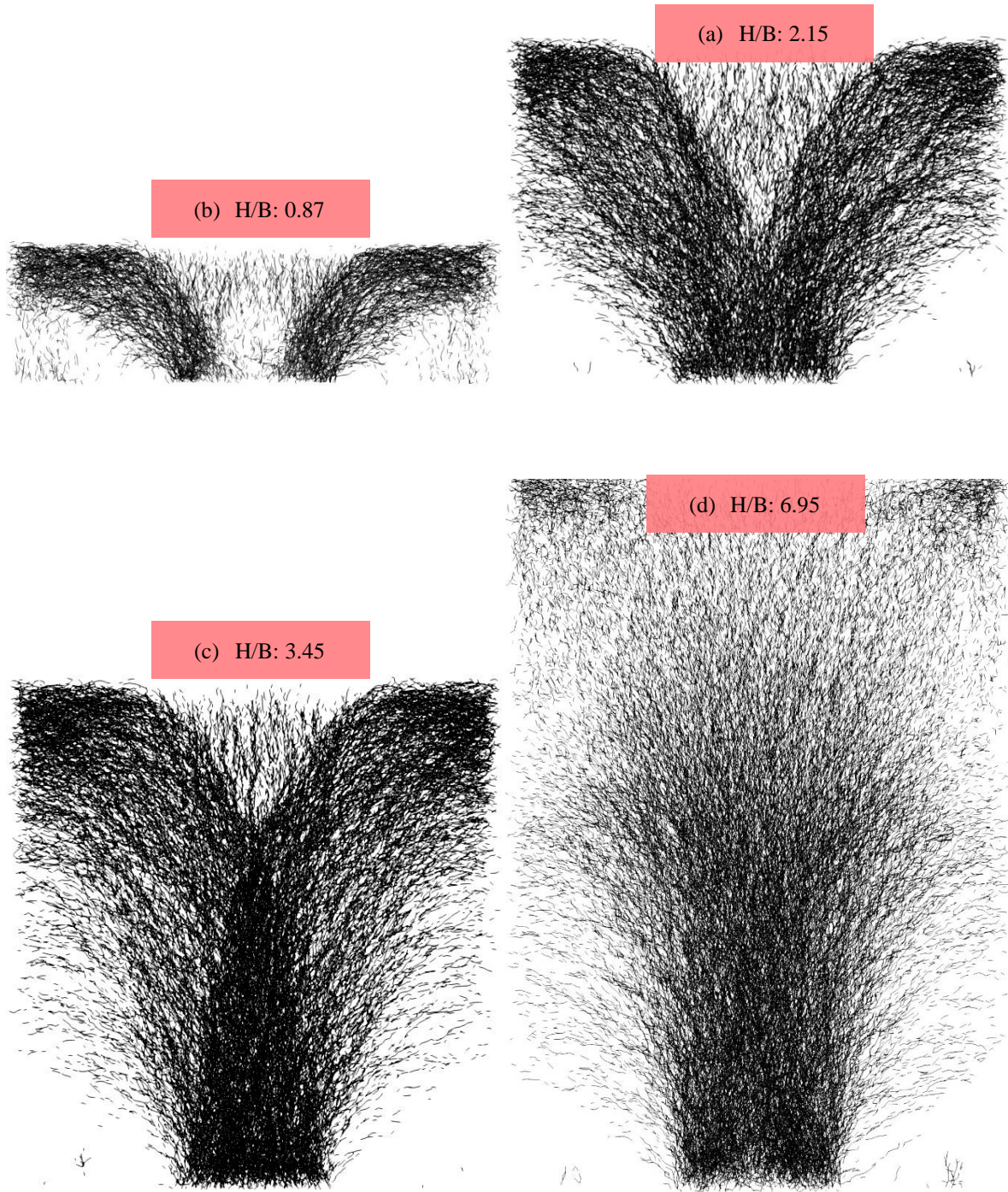


Figure 5.17 Strong force distribution network for non-spherical particles in DEM simulations under different H/B values

Non-spherical particles represented a similar trend compared to spherical particles. However, the strong forces are more intense compared to the earlier case, which could be associated with the fact that non-spherical particles contain better particle interlocking, resulting in a larger number of contacts and hence large inter-particle forces. Furthermore,

since the non-spherical particles in this study are constituted by attaching two spherical particles side-by-side, making a rigid connection, each rigid non-spherical particle can have contacts due to each constituting member particle.

Further to that, the case with H/B 3.45 could be regarded as a critical condition, or a condition between a fully arched and partially arched situation. A similar observation was also made for the same H/B with non-spherical particles under vertical movement analyses of particles. For a better comparison with spherical particle cases, two H/B conditions are plotted side-by-side for both types of particles in Figure 5.18.

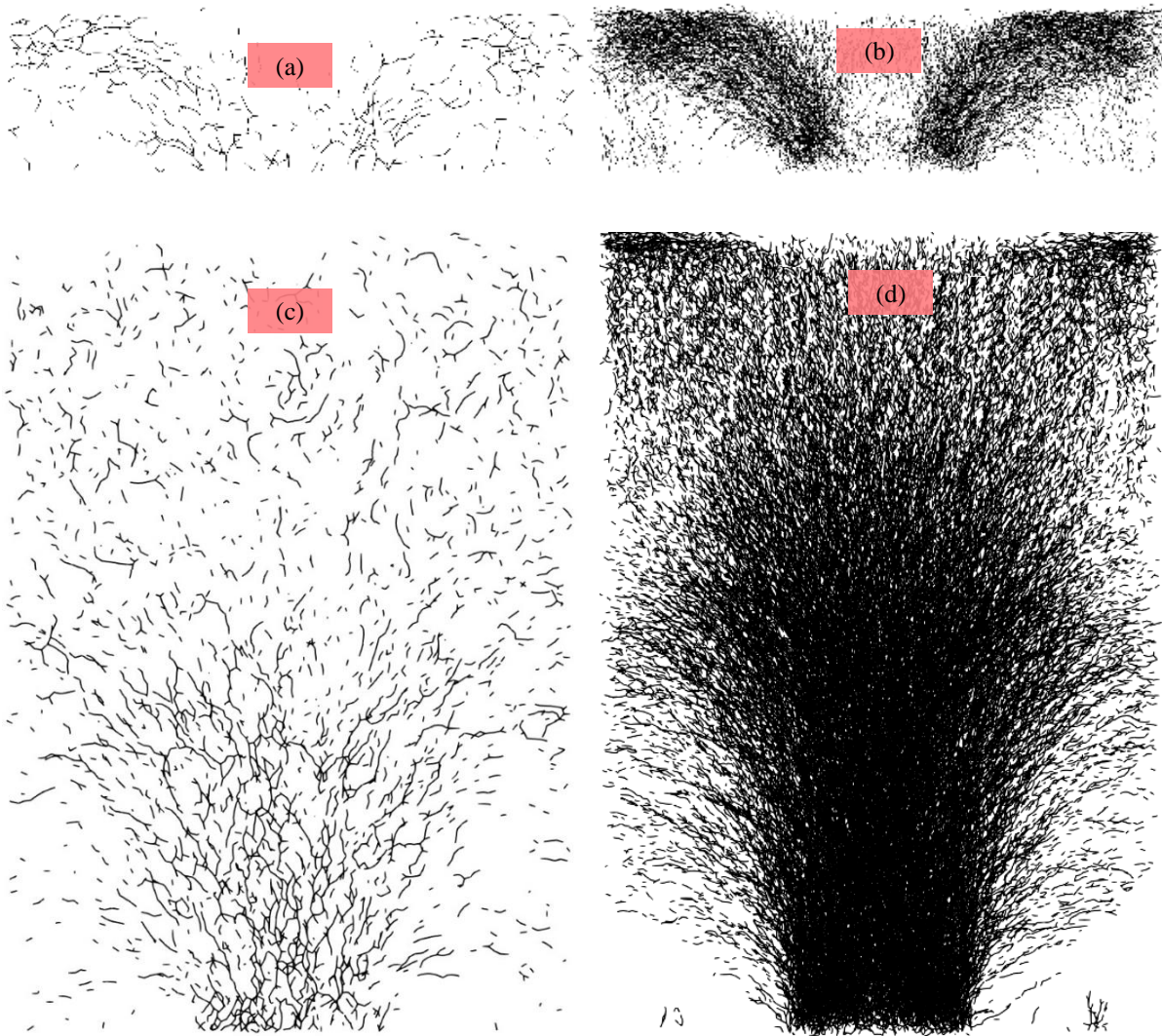


Figure 5.18 Strong contact force diagrams in DEM simulations (a) spherical particles for $H/B = 0.87$ (b) non-spherical particles for $H/B = 0.87$ (c) spherical particles for $H/B = 4.35$ and (d) non-spherical particles for $H/B = 4.40$ at $\delta = 0.25\text{mm}$

Chapter 4 discussed the stress distributions under trapdoor conditions, and it was observed that the non-spherical particles yielded a higher stress concentration factor (α) compared to the spherical particles. This difference was associated with the particle shape effect. Figure 5.18 can be used to explain the process of higher ' α ' values for non-spherical cases. The strong force concentration above the central fixed base plate for non-spherical particles is much larger compared to the spherical particles (Figure 5.18). A larger concentration of strong forces represents that more stresses from the overburden material above lowering trapdoors are being diverted towards the central base plate. Furthermore, it is observed that non-spherical particle cases required higher ground elevations for developing a fully stabilized arching action. Strong forces, as well as the vertical displacement diagrams for non-spherical particles having an $H/B = 3.45$, showed a partially developed arch. However, with similar ground height, the spherical particles showed a fully developed arch. The reason can be associated with the fact that non-spherical particles being more angular and having a higher aspect ratio, connect a wider range of particles through a higher number of contacts, hence comparably higher ground surface is required for the arching action to fully develop and to have a closed shape (Figure 5.17c). However, once the arching pattern has fully been developed, the region containing arch forces tends to become thinner than the initial condition, as visible in Figure 5.18(d).

5.4 Contact Fabric analyses

Up till now, the trapdoor stress redistribution is compared with the differential surface settlement and arch evolution using strong force distribution. However, the development of strong forces can be associated with the redistribution of contacts within the soil mass under trapdoor conditions. Hence, it is believed that the evaluation of contact fabric can also be used to assess the arching in the trapdoor condition using DEM simulations.

5.4.1 Selection of sample and size of analysis subsets

Due to the adopted air-pluviation process, the longer axis of a soil grain tends to lie in the horizontal plane, that would create more contacts in the vertical (Z-) direction, whilst a uniform distribution of contacts can be found in the horizontal (XY-) plane. When

the orientation of contacts is of concern, the second-order fabric tensor can be assessed, defined as (O'Sullivan, 2011):

$$\varphi_{ij} = \frac{\sum_{k=1}^{N_c} n_i^k n_j^k}{N_c} \quad (5.1)$$

where N_c is the total number of contacts and n_i, n_j are components of unit vectors in i and j directions for k^{th} particle pair, describing the contact normal orientation. For three-dimensional case, second-order contact fabric is given by the following equation:

$$\begin{bmatrix} \varphi_{xx} & \varphi_{xy} & \varphi_{xz} \\ \varphi_{yx} & \varphi_{yy} & \varphi_{yz} \\ \varphi_{zx} & \varphi_{zy} & \varphi_{zz} \end{bmatrix} = \frac{1}{N_c} \begin{bmatrix} \sum_{k=1}^{N_c} n_x^k n_x^k & \sum_{k=1}^{N_c} n_x^k n_y^k & \sum_{k=1}^{N_c} n_x^k n_z^k \\ \sum_{k=1}^{N_c} n_y^k n_x^k & \sum_{k=1}^{N_c} n_y^k n_y^k & \sum_{k=1}^{N_c} n_y^k n_z^k \\ \sum_{k=1}^{N_c} n_z^k n_x^k & \sum_{k=1}^{N_c} n_z^k n_y^k & \sum_{k=1}^{N_c} n_z^k n_z^k \end{bmatrix} \quad (5.2)$$

where N_c is the total number of contacts and n_x, n_y and n_z are unit vectors in x, y and z directions for k^{th} particle pair, describing the contact normal orientation. The second-order fabric tensor was represented by the diagonal elements of the above equation (i.e. $\varphi_{xx}, \varphi_{yy}$, and φ_{zz}).

As soon as the bottom trapdoors start lowering, particles re-arrange to transmit forces. As discussed above, soil arching is evident for the cases with higher H/B ; hence, the contact fabric of a DEM sample with $H/B = 4.35$ using spherical particles were analyzed. Spherical particles were selected in order to verify as the weakest case to have arching forces. Verification with the spherical particles would assure the presence of particle arching with an effect on fabric redistribution.

Once the H/B and the particle types are selected, the next step is to select the size of the subset sample for fabric analyses. As per Head (1994), under a laboratory test, the minimum width of the sample should be more than 10 times the size of the largest particle to have a representative sample response. Keeping in view this fact, the size of the search window or the subset was varied until a suitable dimension. Selecting a large size of subset could result in an accurate representation of contact fabric condition. However, such a condition would result in a few numbers of subsets to develop a clear relationship. Hence the aim was to select a minimum size of the subset that would still be able to

represent the localized behavior. To do so, initially, a larger size of subset was selected, which was then slowly reduced to note its effects in contact fabric value up to a point where the critical condition was reached. Figure 5.19 explains the sample variation process using a given H/B value. The subset size, as shown in the figure below, was reduced to select the minimum possible subset size that could result in accurate contact fabric calculation. Initially selected large subset is represented as '1' in Figure 5.19 below, whereas the finally selected subset size is titled as '*final size*'.

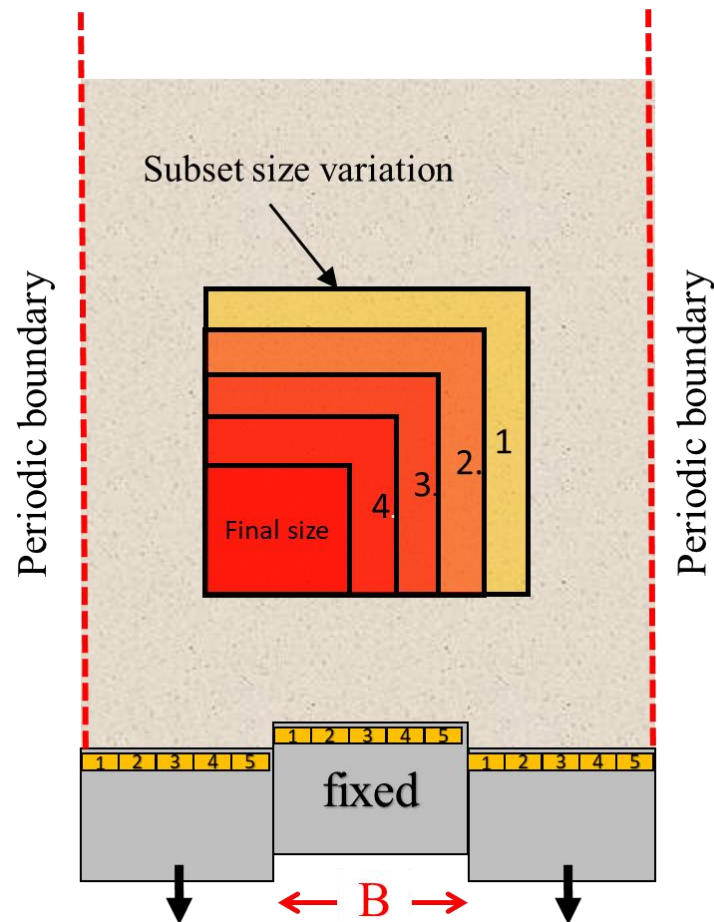


Figure 5.19 Subset size variation to select the minimum size possible

For the given reducing subset sizes, 2nd order contact fabric was evaluated and is represented in Figure 5.20. Furthermore, the number of atoms in each subset are also plotted in the same figure. The sample was selected in a cubical sample wherever possible. However, the sample width by itself consisted of 40mm, resulting in a non-cubical sample when each dimension exceeds 40mm.

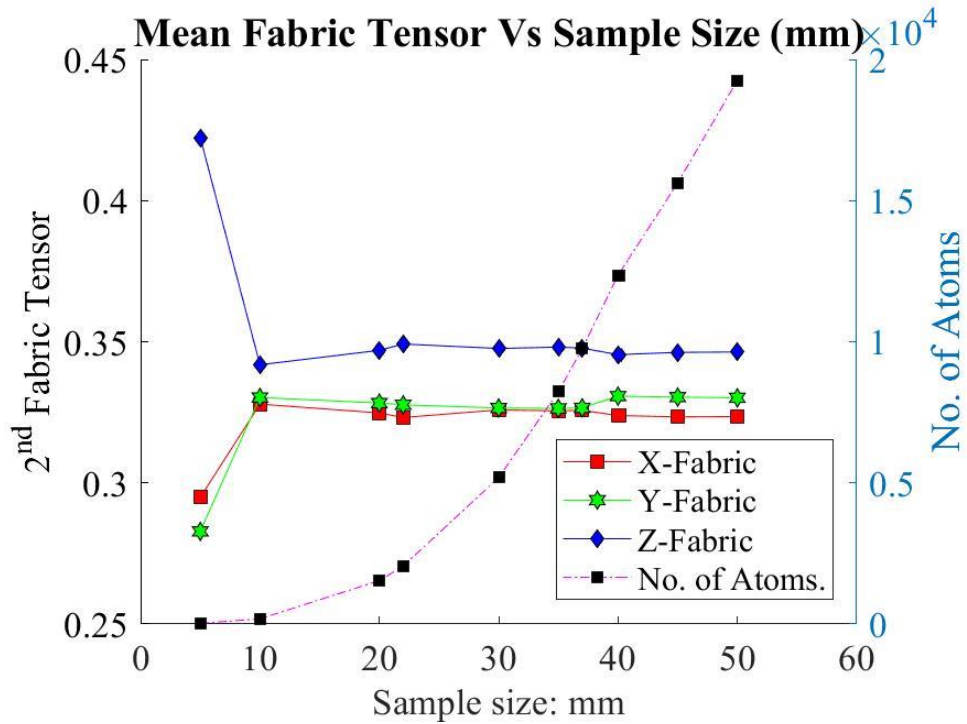


Figure 5.20 2nd order contact fabric and number of atoms in each size, plotted against the sample dimension

Results showed that the number of particles decreased with decreasing the sample dimensional. Similarly, the 2nd order contact fabric values showed a similar trend up to a sample dimension of 30mm. Below that value, the contact fabric increased slightly followed by a slight reduction. However, further reduction of sample size below 10mm produced a drastic change in the contact fabric value.

A slight change at around 20mm sample size could be associated with the general rule of $10 \times D_{\max}$, which is presented by several researchers including Head (1994). Since the sample had a mean diameter close to 2mm, the sample dimensions of 20mm approach the above-cited critical limit to result in a slightly differing contact fabric value. Eventually, a sample dimension of 30x30x30mm was adopted for the evaluation of 2nd order contact fabric.

5.4.2 Contact Fabric for larger H/B

Once the size of the subset is finalized, a DEM numerical simulation with $H/B = 4.35$ was selected as a representative case. Such H/B value is believed to contain a well-

developed soil arching phenomenon, as explained through strong force and vertical displacement plot in the above section of this chapter.

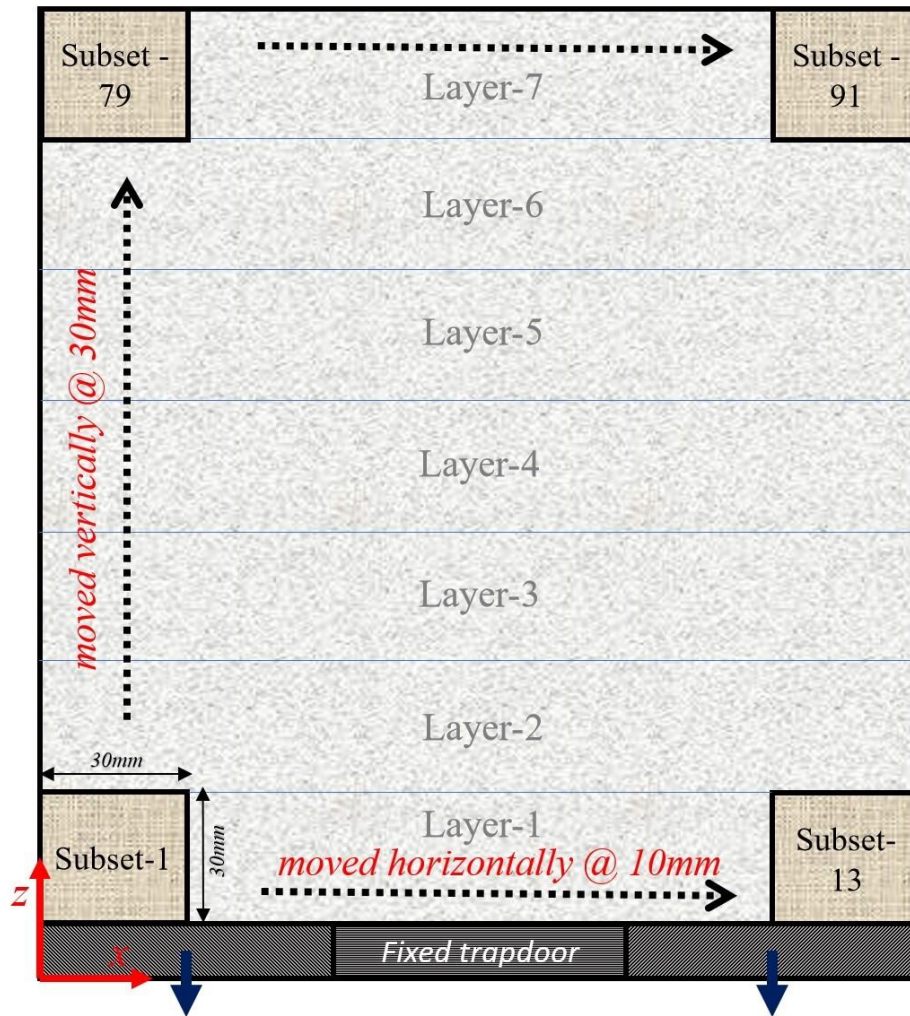
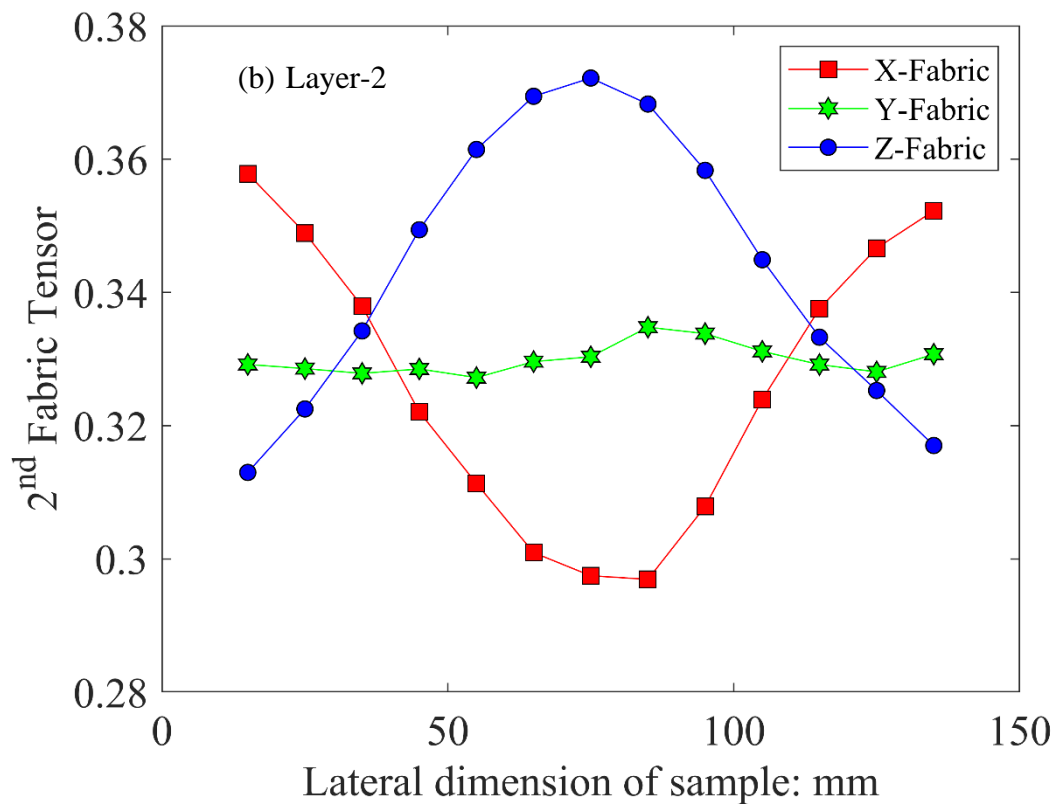
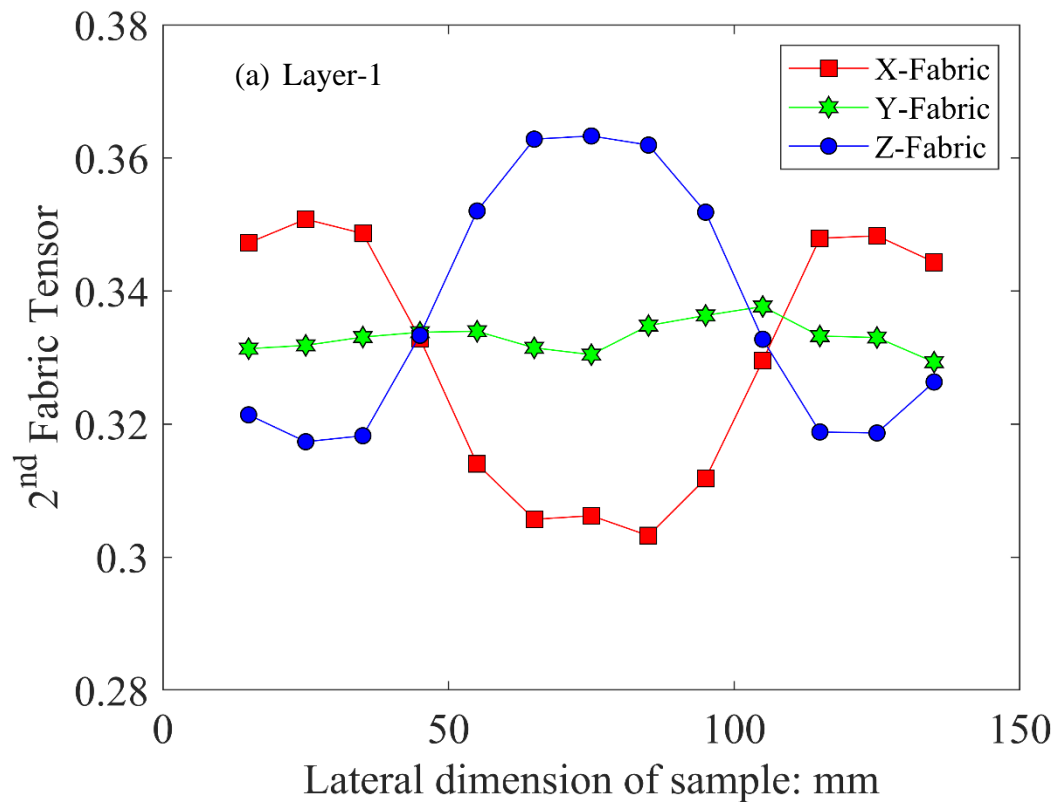
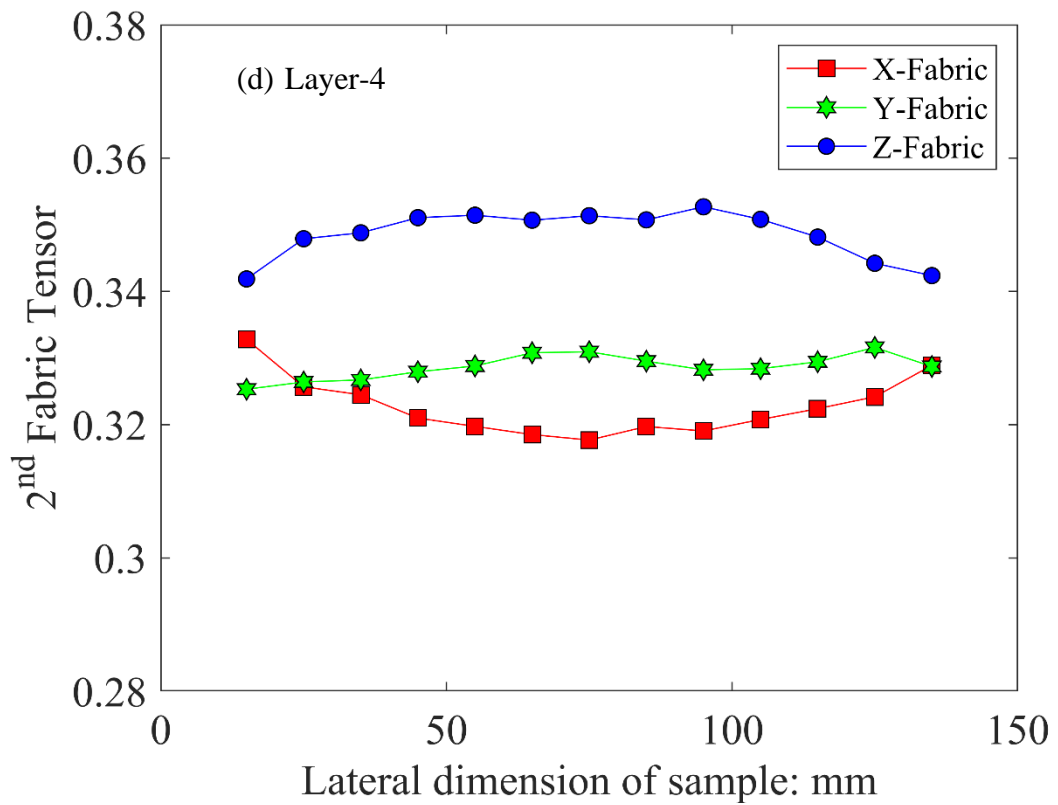
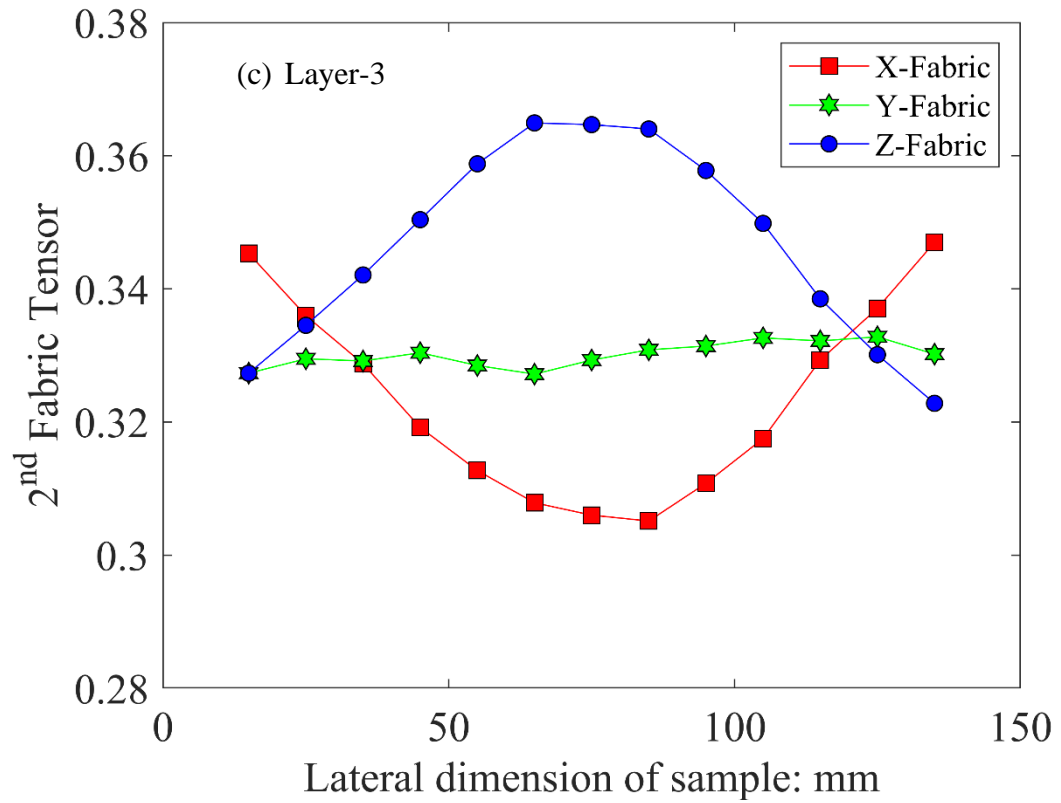
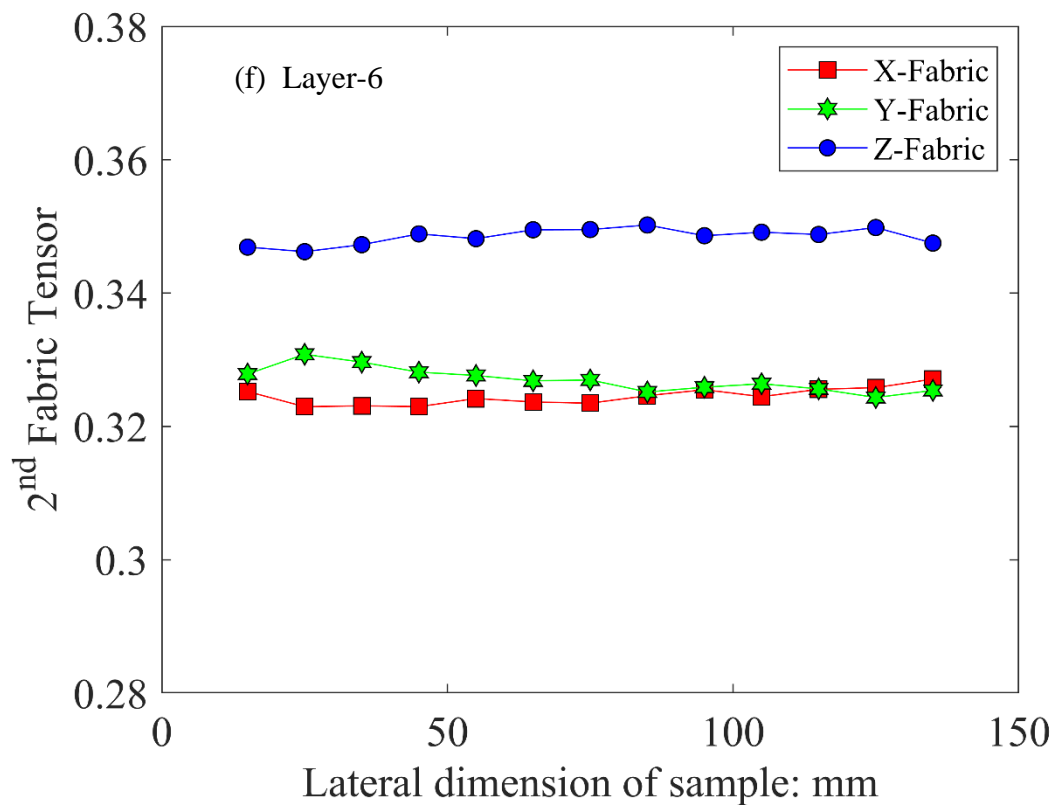
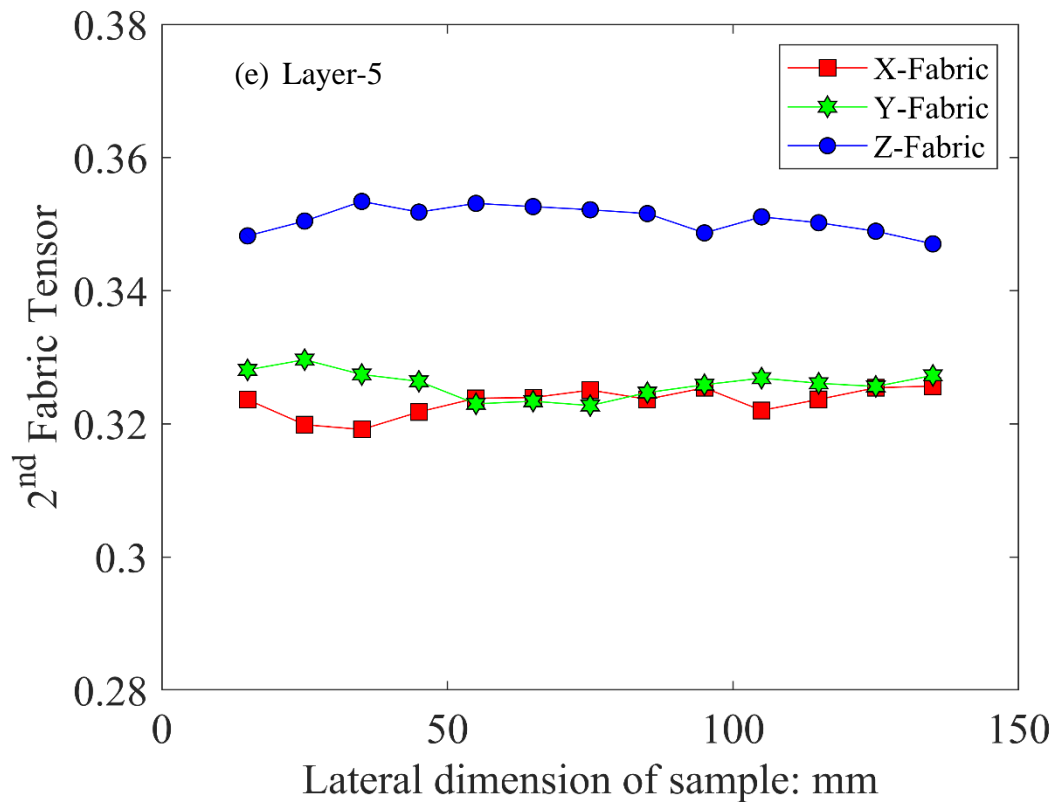


Figure 5.21 Configuration of subsets for the evaluation of 2nd order contact fabric, for an $H/B = 4.35$ using spherical particles

Figure 5.21 above represents the configuration of selected subsets for the analyses of contact fabric using spherical particles in a sample with H/B of 4.35. The subsets were initiated from the extreme left-bottom corner and propagated both horizontally and vertically. However, for horizontal propagation, subsets were moved at a center to center distance of 10mm. Whilst subsets were moved vertically with a distance of 30mm c/c. Such configuration resulted in a total 91 number of subsets, having seven vertical layers and each vertical layer with 13 subsets (Figure 5.21).







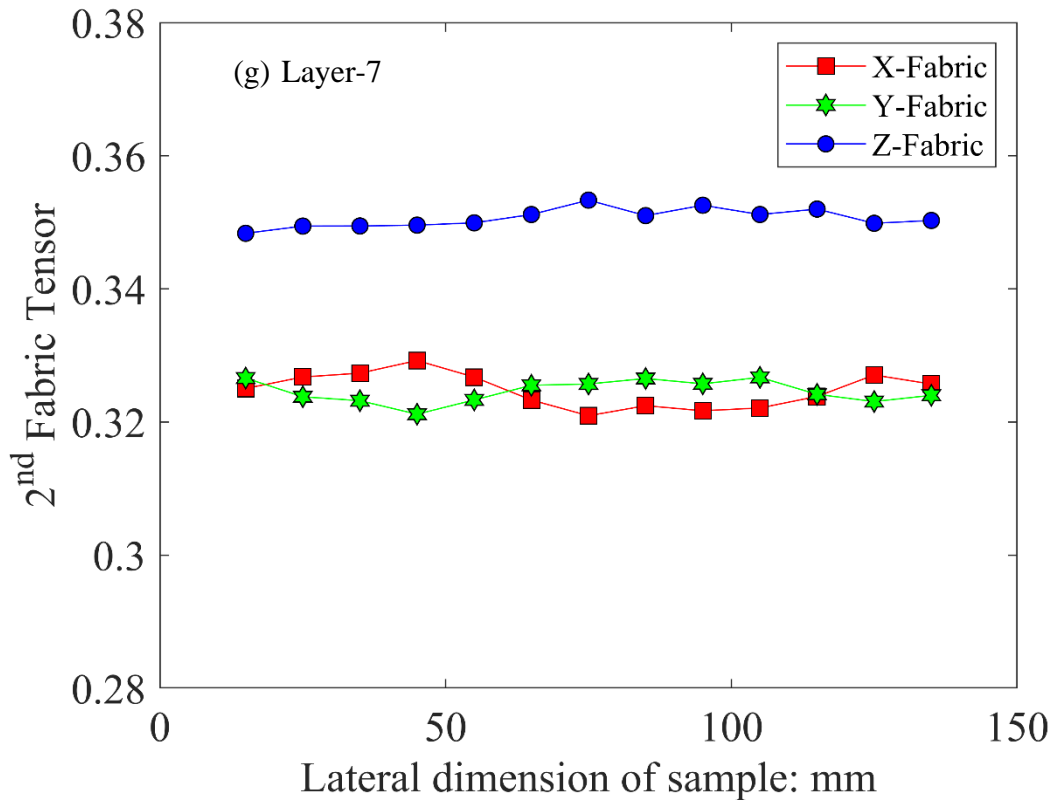


Figure 5.22 2nd order contact fabric distribution in a sample with $H/B = 4.35$ having spherical particles with (a) being the bottom most layer and the (g) being the top most layer

Results of 2nd order contact fabric against sample width for all seven layers of the sample with $H/B = 4.35$, having spherical particles, are provided in Figure 5.22. Layer-1 as shown in Figure 5.22(a) represents the bottom-most sample, just above the base plates, whereas the Layer-7 represents the top-most sample portion. There exists a striking difference between the bottom and top-most layer values. However, before discussing the effect of the arching on the contact fabric results, there is a need to understand the contact fabric distribution at the initial stage prior to the trapdoor lowering.

The sample was prepared and pluviated under gravity, without any external forces. The gravitational pluviation technique imparts an inherent anisotropy in the material. Samples that are pluviated under gravity tends to settle with longer axis parallel to the bedding plane, imparting anisotropy in the contact fabric. However, glass beads or the round-shaped particle, that are considered to be independent of such depositing preferences, still shows a strong anisotropy in contact fabric, as discussed by (R. Wang et al. (2017)).

Presence of anisotropy due to the above phenomenon results in a dominant Z-directional component of contact fabric (ϕ_{zz}). Similar results were obtained in the given DEM simulation condition where the initial condition prior to the lowering of base trapdoor showed a higher value of contact fabric in Z-direction. However, the X(ϕ_{xx}) & Y(ϕ_{yy}) directional components remained close to each other.

The principal components from Eq. 5.2, i.e. ϕ_{xx} , ϕ_{yy} and ϕ_{zz} in each subset are illustrated in Figure 5.23, along with a vertical displacement diagram of particles for the same case. Layer numbers are also superimposed on the particle displacement diagram for clarity.

Figure 5.23 illustrates that ϕ_{yy} is nearly constant since the arching phenomenon occurs in the XZ-plane. Sensitive variations in ϕ_{xx} and ϕ_{zz} are observed in the bottom-most part of the sample (Layer-1). The left and right portions, i.e. above the lowering trapdoors, show higher values of ϕ_{xx} as the arch carrying the load in the lateral direction dominates. However, higher values of ϕ_{zz} ($> \phi_{xx}$) are observed above the central fixed plate as the strong forces dominate vertically in that region (Figure 5.16 c&d). The adjacent layer (Layer-2) exhibits more sensitive variations in both ϕ_{xx} and ϕ_{zz} having a similar trend with Layer-1. However, at further higher elevations, the range of minimum and maximum values of ϕ_{xx} and ϕ_{zz} reduces gradually, and Layer-5 to Layer-7 show almost constant values of ϕ_{xx} and ϕ_{zz} . Note that higher values of ϕ_{zz} compared with ϕ_{xx} in the regions where arching action is absent; as the gravitational forces are dominant, that is also seen throughout the sample space before lowering the trapdoors. The elevation of each layer, superimposed on the vertical movement of particles, is also presented in Figure 5.23. The arching effect is almost diminished in Layer-4, clarifying the flattened curves in Layer-4 and above. Despite a prominent change in contact fabric tensor before and after the trapdoor movement, the mean coordination number, number of contacts per particle, does not show any specific pattern of change, indicating that the arching phenomenon induces a relative redistribution of contact fabric, as was also observed by Lai et al. (2016) in his DEM simulations.

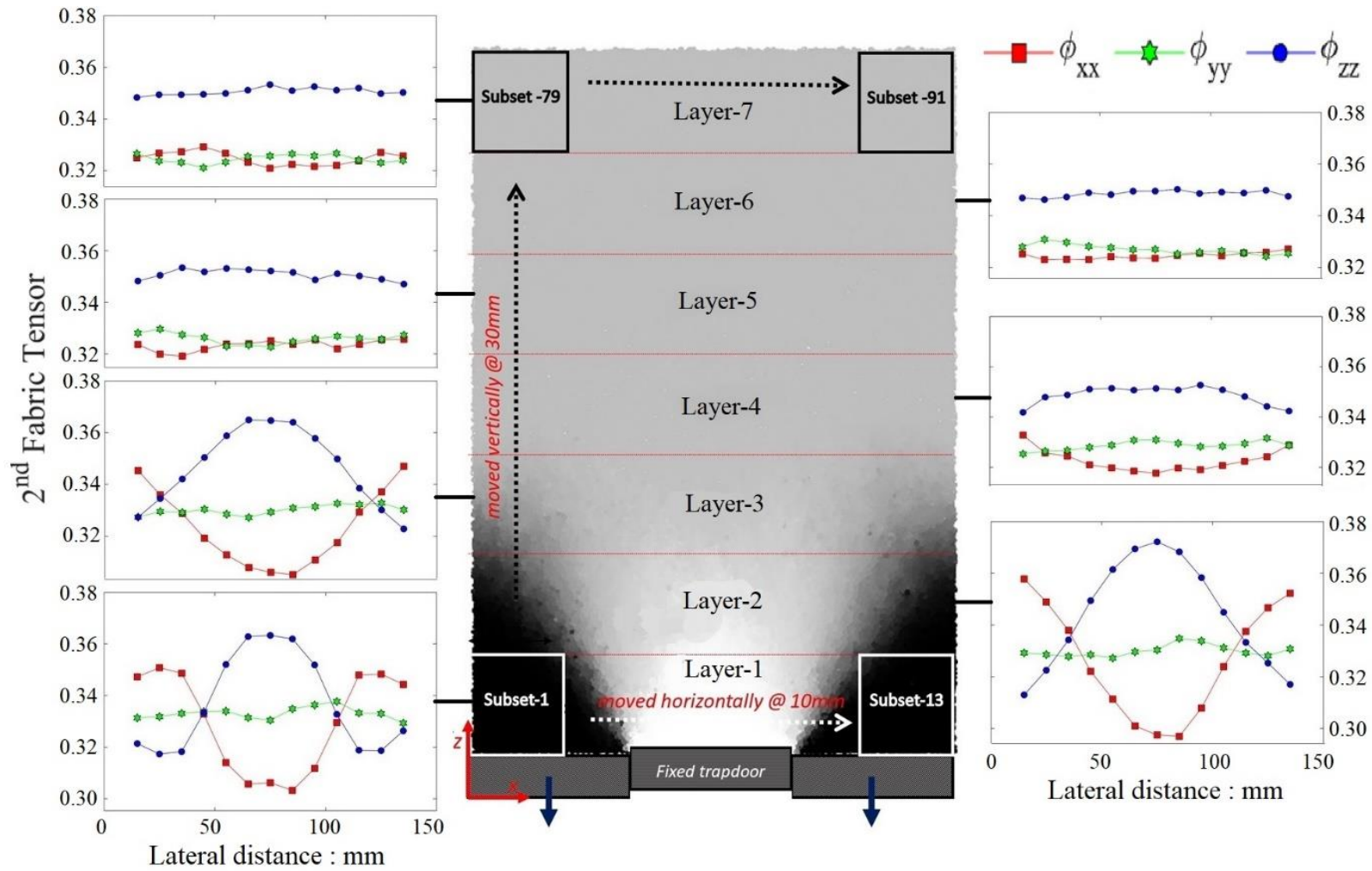
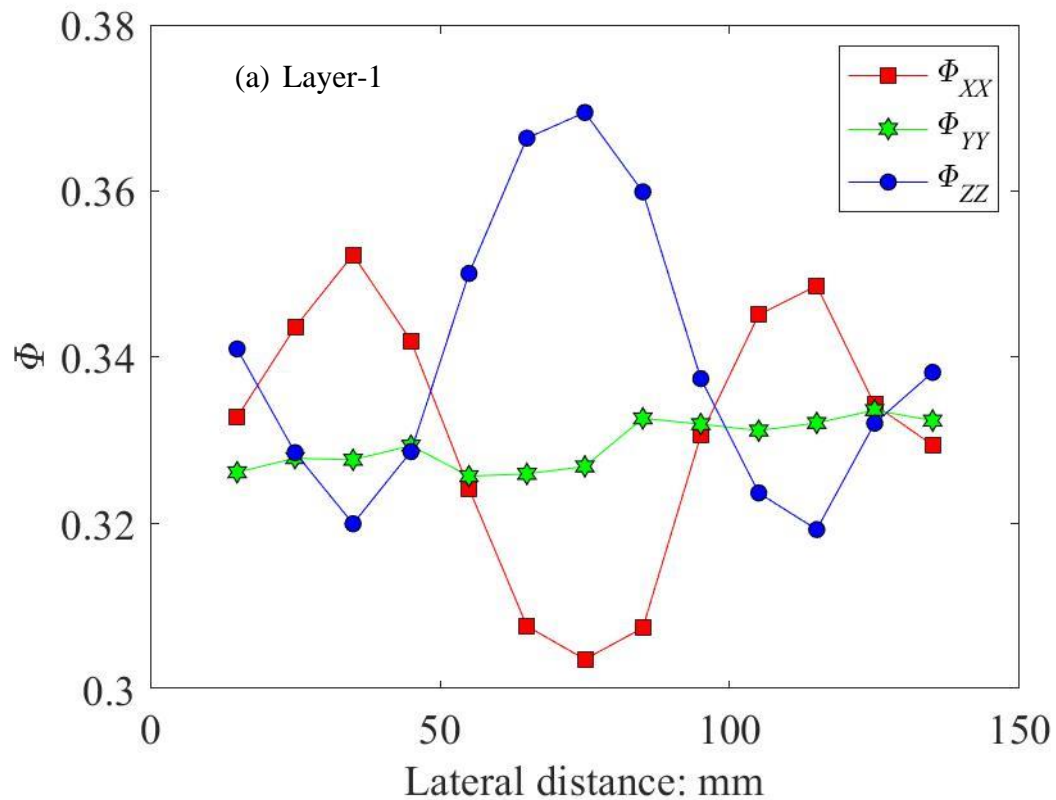


Figure 5.23: 2nd order contact fabric distribution for different layers in a sample, represented along with a vertical displacement diagram of DEM sample with $H/B = 4.35$

5.4.3 Contact fabric for smaller H/B

A similar procedure was also adopted for a simulation with an H/B value of 0.87. Such small H/B is believed to show differential surface settlement due to the absence of stabilized arching action in the soil mass. This was confirmed at multiple times using Figure 5.1, Figure 5.5, Figure 5.9, Figure 5.14, and Figure 5.16, as discussed earlier.

A similar subset distribution technique was followed, which resulted in two (02) number of layers due to a relatively smaller H/B value. The resultant 2nd order contact fabric values for the given sample with smaller H/B are represented in the Figure below. For better clarity, the contact fabric figures are then plotted along with a vertical displacement diagram with the same simulation results. The arching forces clearly touches the ground surface to discontinue to force transmission. Hence, causing a differential surface settlement.



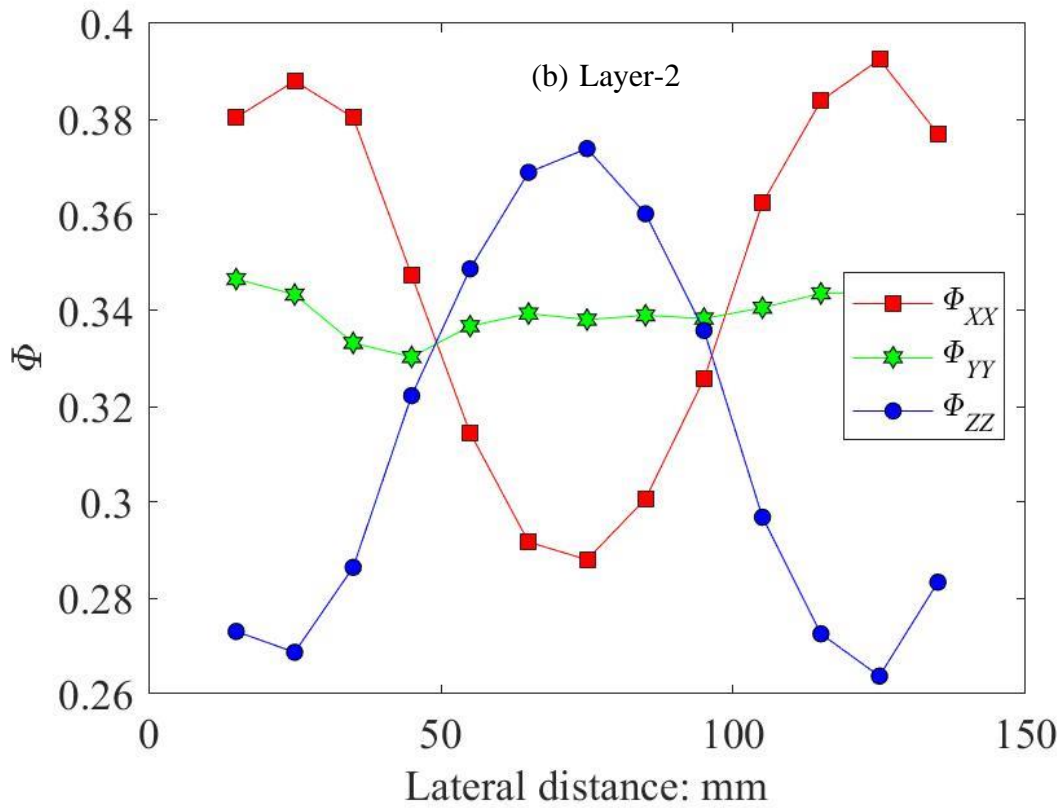


Figure 5.24 2nd order contact fabric values for with $H/B = 0.87$ having spherical particles at (a) bottom layer and (b) at top of the sample

For better understanding the ϕ distribution in each layer, Figure 5.25 included the vertical displacement diagram along with the ϕ_{XX} , ϕ_{YY} and ϕ_{ZZ} distribution. The plot for vertical displacement of particles was obtained using similar simulation conditions and particle type. A strong differential surface settlement was observed in this case, where the portion above the central static base plate did not show significant surface settlement, causing a higher vertical force distribution in that region.

As stated earlier in this chapter, the arching action initiates irrespective of the material surface height. However, small ground heights disrupt the propagating arch and the arching action would become hindered. Resulting in vertical movement of particles above the lowering trapdoors. However, the incomplete arching effect continuously tries to exert forces in a specified catenary shape. That would result in higher values of contact fabric in the region of surface settlement.

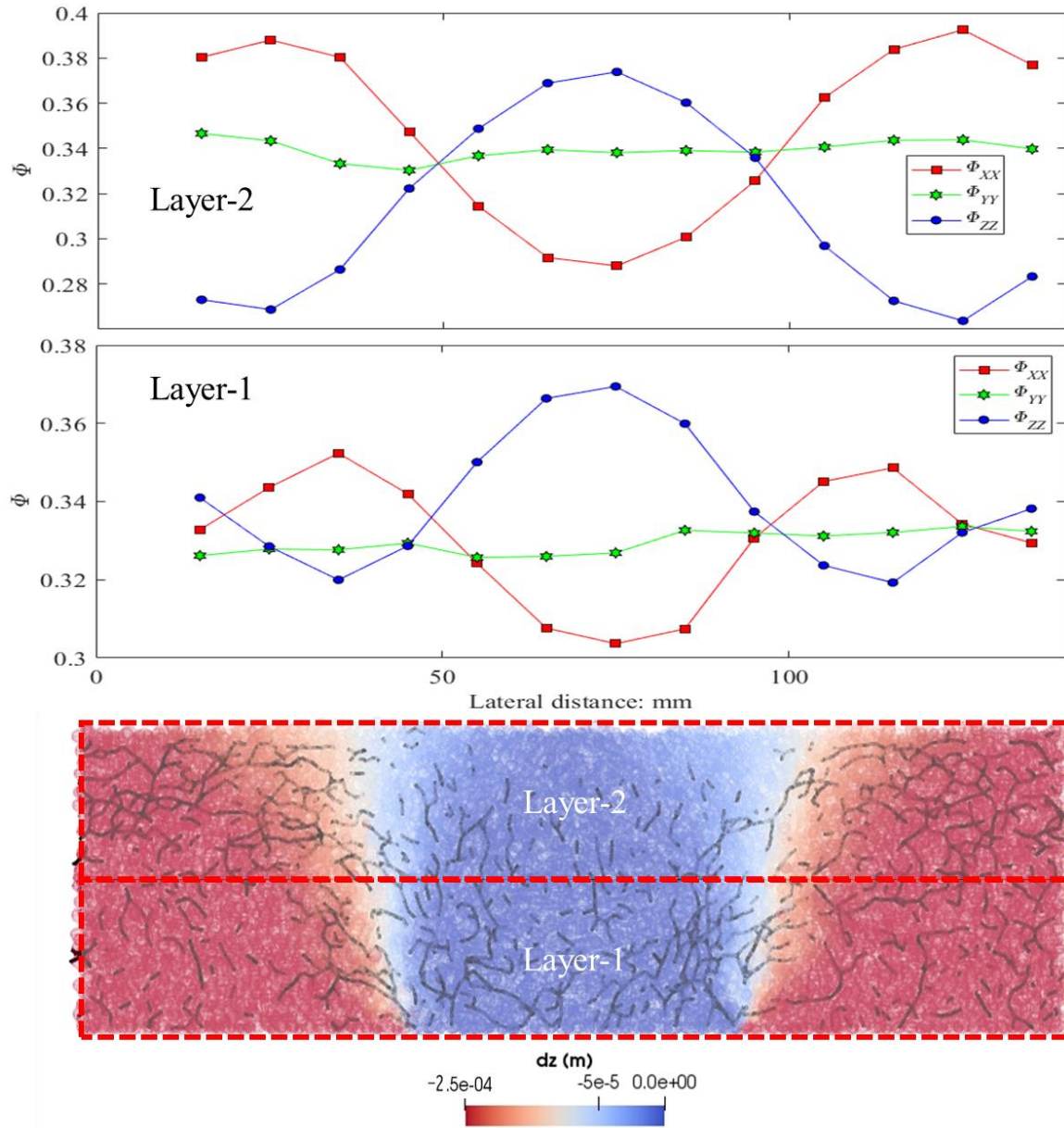


Figure 5.25 2nd order contact fabric distribution for $H/B = 0.87$ along with similar DEM simulation showing vertical displacement and strong contact forces plot

Near the base of the sample in Layer-1, it can be clearly seen in Figure 5.25 that the central portion of the sample has dominant vertical strong forces, which results in a contact fabric distribution with higher ϕ_{ZZ} in the central region. The portion near the sample edges of the sample showed ϕ_{XX} higher than the ϕ_{ZZ} as horizontal strong forces are dominant in that region.

Layer-2 contact fabric distribution (ϕ) follows a similar trend compared to layer-1 with the exception that the effect is more significant in layer-2 fabric distribution. Since layer-2 represents the top portion of the sample, it is pertinent to note that the absolute

magnitude of ϕ_{zz} in the central portion is smaller than ϕ_{xx} magnitude near the edges. This observation is in line with the strong force diagram as shown in Figure 5.25. Strong forces network near the edges of the sample in the top portion is more populous compared to the central portion. Furthermore, the edges show a more horizontal force distribution rather than the central portion with a more vertical strong forces network. Consequently, the ϕ_{xx} values are much higher on the edges compared to the ϕ_{zz} throughout the sample.

Comparing the contact fabric distribution results for the samples with extreme H/B values of 4.35 and 0.87, the main difference can be seen in the top-most layers in both cases. The sample with higher ground heights demonstrated a uniform distribution of ϕ_{xx} , ϕ_{yy} and ϕ_{zz} . However, the smaller height sample showed a markable difference between all contact fabric distribution. The varying contact fabric distribution at any section of the sample can be correlated with the presence of differential surface settlements in that region. Hence, it can again be concluded that the samples with smaller ground height showed significant differential settlement due to the varying contact fabric distribution along the sample width. Such behavior was also observed through several other techniques as well, like surface settlement analyses, vertical displacement plots, and strong force distribution networks, as discussed in the earlier sections of this chapter.

5.5 Particle rotation during the arch formation

Once the trapdoors start lowering, a complete redistribution of stresses is observed in the sample, as discussed in Chapter-4 previously. The stress redistribution in both normal and shear direction occurs due to the formation of the arch action within the soil mass, above the lowering trapdoors. In the literature, the shape of the soil arch is characterized as a catenary, analogous to a freely hanging rope with its two fixed ends (Handy, 1985; Z. Q. Wang et al., 2013). In the vertical movement plot of particles as shown in Figure 5.14 and Figure 5.15, the shape of the arch much resembles the shape as explained in the literature. As the above-referred figures show that a certain mass that circumscribed within the arching zone show much larger displacements compared to remaining mass. To form a specific arching shape, the particles at the boundary of yielding and non-yielding portions face a strong force chain that forces them to rotate and align with the propagation force chain. Particles move and align until the force

transmission along a certain required shape is obtained. Thus, particle rotation is a definite phenomenon that is followed as soon as the arch spreads in the soil mass.

An attempt has been made in this section to investigate the particle rotational behavior under trapdoor tests, that could lead towards the arch development mechanism. Non-spherical particles, that were described in Chapter-2 of this thesis, were utilized for numerical simulations.

5.5.1 Sample preparation and calculation sequence

For the purpose of observing the particle rotation, two representative sample sizes were selected, having H/B values of 4.35 and 0.87 respectively. Both samples are believed to possess different arching conditions, as previously discussed. Each sample was further divided into several subsets, as discussed in the previous section as well. The division of the sample into subsets is shown in Figure 5.26 below.

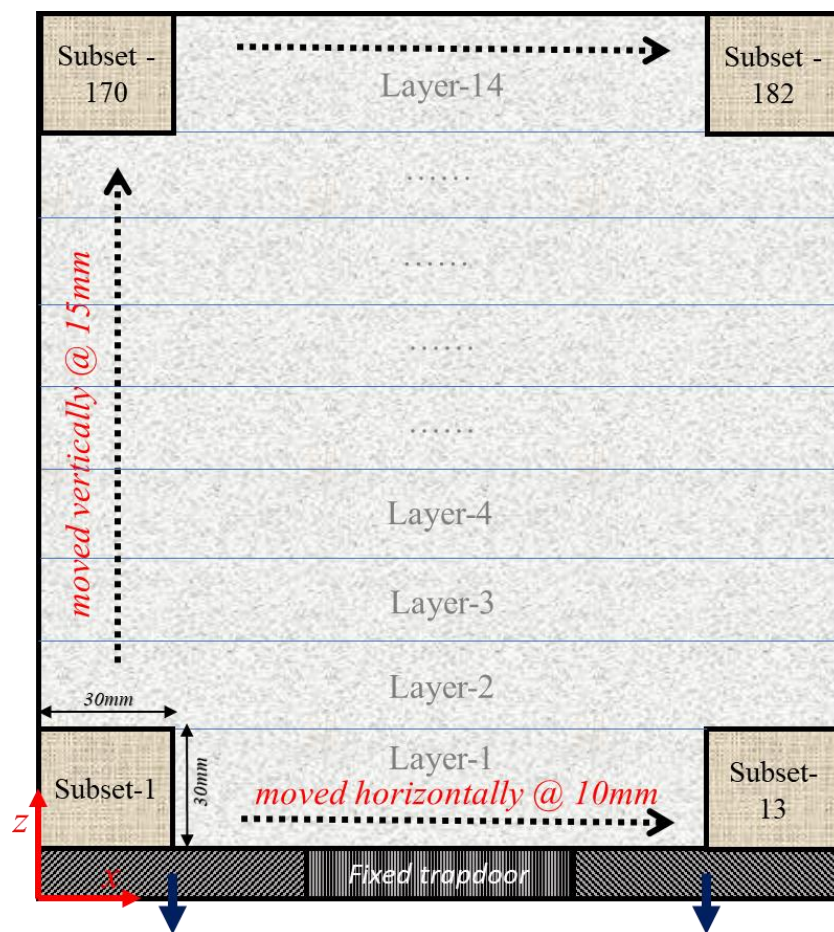


Figure 5.26 Configuration of subset distribution for particle rotation calculation for $H/B = 4.35$ in DEM simulation space

The subset was initiated from the bottom left corner and then moved with a center-center distance of 10mm and 15mm in the horizontal and vertical direction. The resulted configuration produced 14 vertical layers with 13 subsets in each layer, totaling to 182 numbers of subsets. In a similar manner, the sample with $H/B = 0.87$ resulted in total subsets of 39 (three vertical layers).

the orientation of the branch vectors connecting each constituting particle of the rigid non-spherical particle was measured as shown in Figure 5.27.

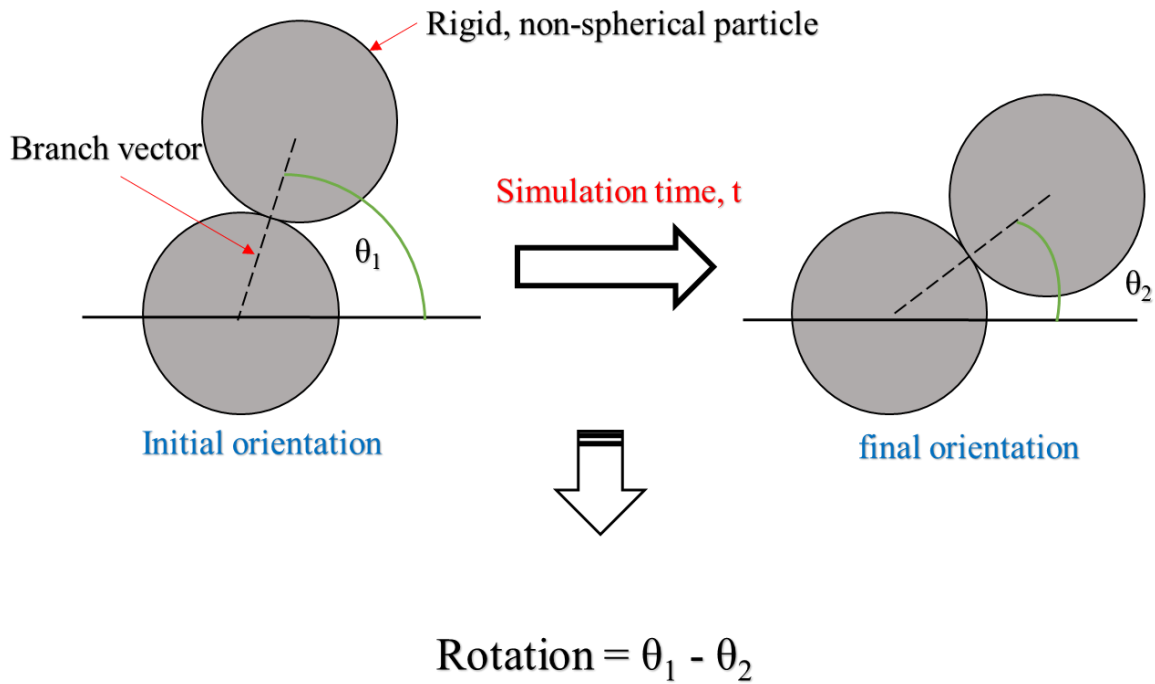


Figure 5.27 Particle rotation calculation sequence in DEM simulations using non-spherical particles

The initial orientation (θ_1) of the rigid particle was calculated using the branch vector connecting the centroid of each constituting particle. The resultant branch vector was divided into X and Z components and the following relation was used to calculate the magnitude of initial orientation (θ_1).

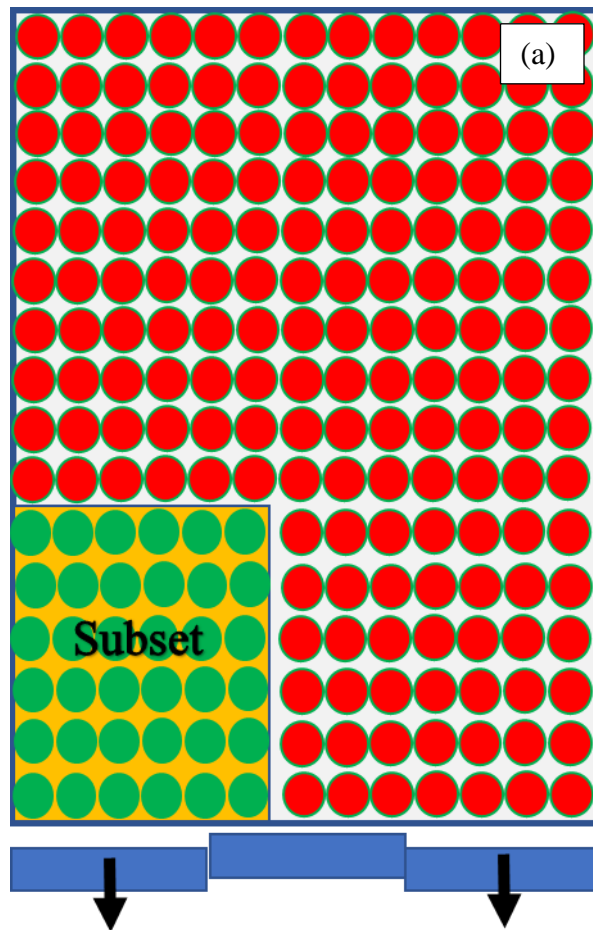
$$\theta = \text{Tan}^{-1}\left(\frac{Z}{X}\right) \quad (5.3)$$

At the end of the simulation, a similar process was repeated to measure the final orientation of the particle (θ_2). Subsequently, the absolute value of rotation Δ was calculated as:

$$\Delta = \theta_1 - \theta_2 \quad (5.4)$$

5.5.2 Particle rotation using subsets

However, there existed a complex situation during the simulation process. For the purpose of calculating the rotation of particles, the initial and the final stages of simulation for any subset space must contain the same particles. Though due to trapdoor movement with the time, the particles shift downwards whilst the boundaries of the subsets remained in the same position. This condition is represented in Figure 5.28 below and required to be corrected before the orientation calculations.



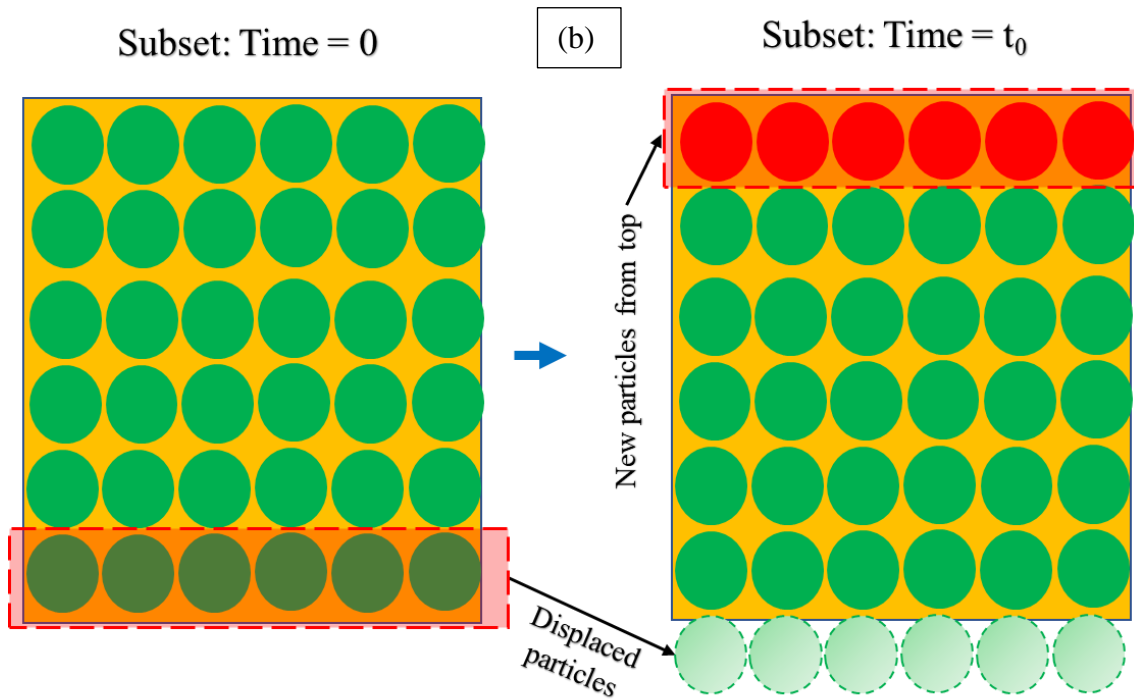


Figure 5.28 (a) Approximate configuration of a subset with a group of particles within, under trapdoor lowering and (b) enlarged subset at the initial and final stage of the simulation

As presented in the above figure, the particles that moved out of the subset domain during the simulation process, as well as the particles that moved into the domain of a given subset during simulation, both groups of these particles were removed from the subset entries. Doing so enabled us to analyze only those particles that remained inside the subset domains throughout the simulation period.

Once, all the subsets were analyzed with the selected groups of particles inside, the magnitude of rotation for each particle in each subset was calculated. Subsequently, the average magnitude of rotation for each subset was calculated based upon the number of particles that it contained. The direction of rotation was also considered in this process so that in each subset, the overall effect of clockwise or counterclockwise rotation could be studied.

The results are presented below in Figure 5.29 for $H/B = 4.35$ and in Figure 5.30 for $H/B = 0.87$ cases.

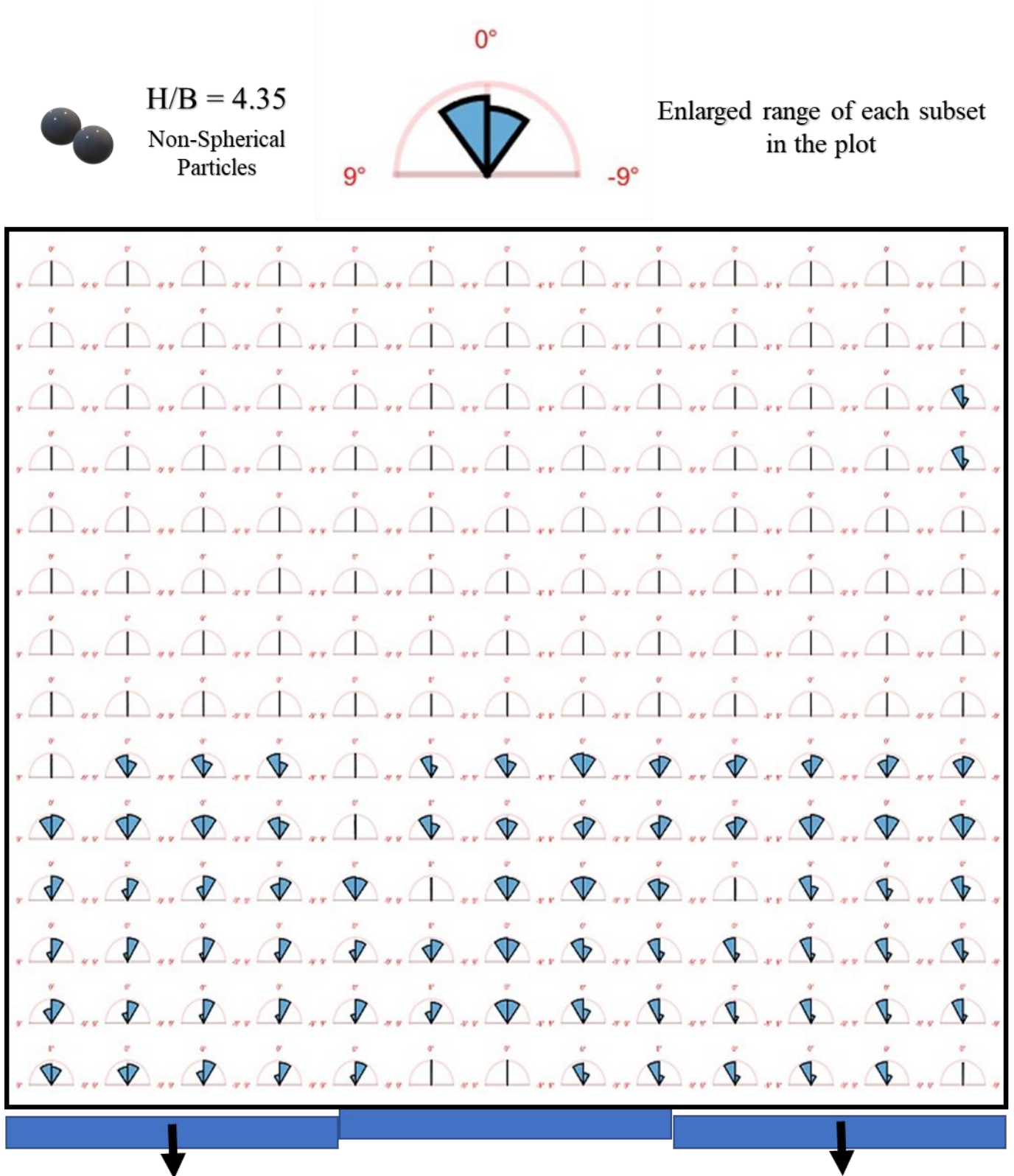


Figure 5.29 Particle rotation magnitude in each subset of DEM simulation with $H/B = 4.35$ having non-spherical particles

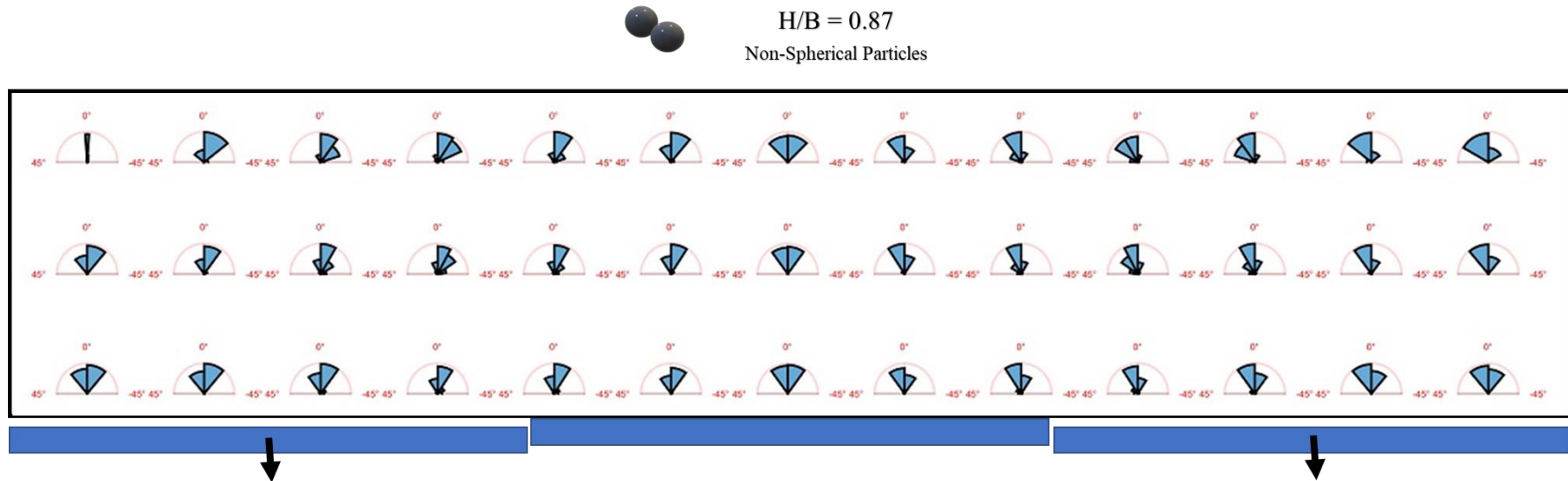


Figure 5.30 Particle rotation magnitude in each subset of DEM simulation with $H/B = 0.87$ having non-spherical particles

For the cases with higher model ground level, as presented in Figure 5.29, the region in the upper half of the sample did not show any significant rotational behavior of particles in either direction. Rather, particles settled in a vertical direction without significant rotation. Such results were counter-verified by the help of earlier presented results of strong force chains and the vertical displacement plots for the sample with similar H/B value. Presence of uniform surface settlement in the upper half portion of the sample as presented in Figure 5.15, or the presence of uniformly distribution strong force chains in the upper half portion of the sample presented in Figure 5.17, both signify that the uniformity of their particular characteristics of strong force and vertical displacement signifies the absence of any significant particle rotation in a particular direction. It is believed that particles do move during the simulation process in each part of the provided model space. However, in the regions without soil arching, the movement of particles is random in either direction, with a mean value approaching zero, which represents the absence of particle rotation in any particle direction.

In Figure 5.30, a case without the presence of a stable soil arching is presented. The central portion of the specimen showed an equal amount of rotation for the particles in either direction, without any particular resultant rotation direction. However, as we move from the central portion to either direction, the rotation plot represents a particular pattern. If we overlay the particle *vertical displacement plot/strong force plot* with the rotation plot, we can relate the trend of rotation with arching and particle movement and forces. Although the arching forces are not stable in this case and touch the surface of the sample, the particle path of the arch propagation as represented in Figure 5.14(a), shows a trend of rotation in a particle direction.

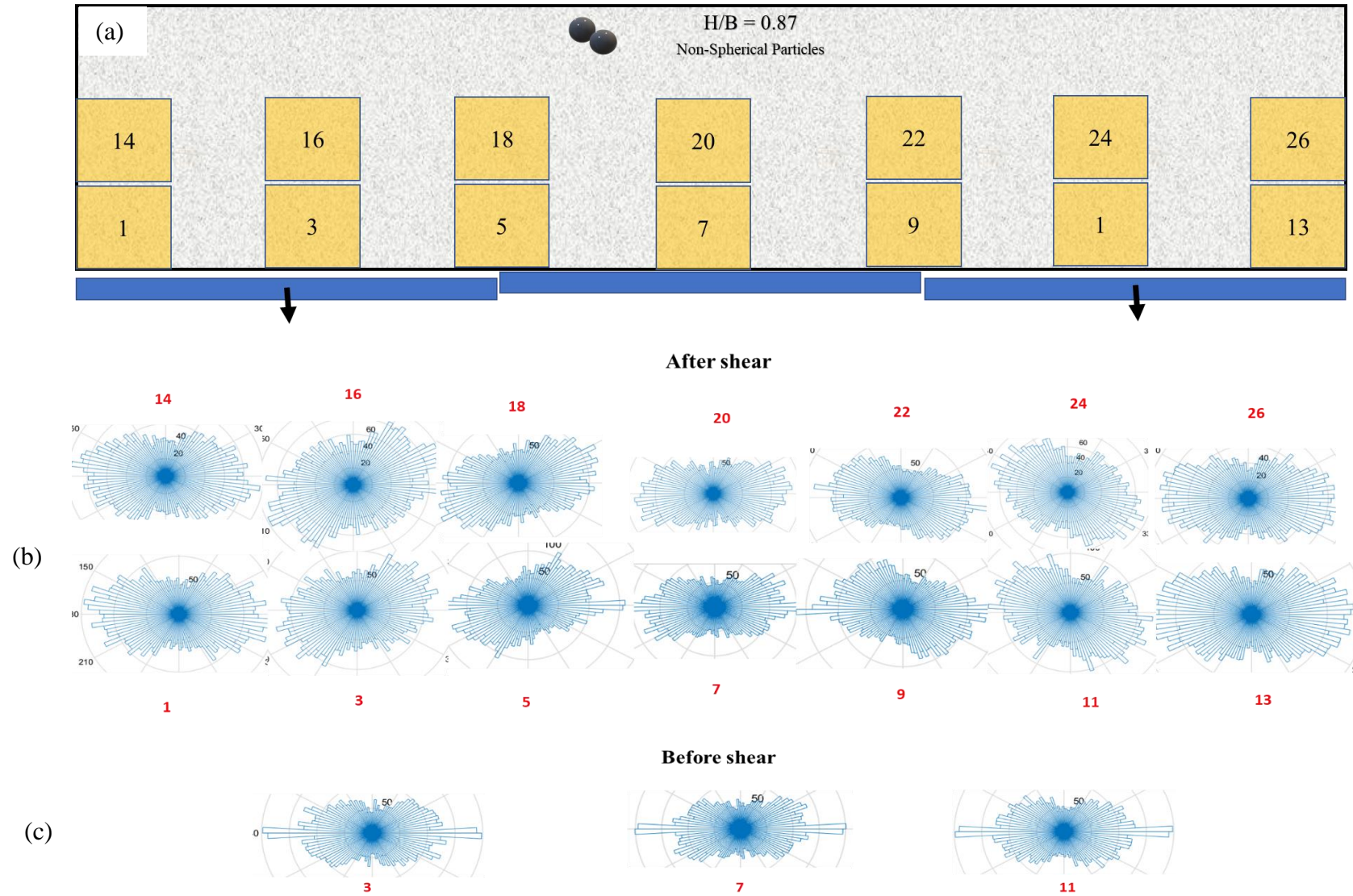


Figure 5.31 Rose plot for particle orientation with (a) location of subset numbers, (b) orientation after simulation and (c) before simulation

5.5.3 The rotation at the particulate level

Till now, the particle rotation is calculated and presented at the subset level. The resultant rotation of each subset is presented in the above plots. However, the particle rotation for each particle individually can also be investigated to represent a rotation trend.

A similar methodology as explained earlier was adopted for the rotation calculation. For the overall sample response against particle rotation, there was no need to filter the particle before and after the simulation, as we did in the case of the subset method. No particle was allowed to leave the sample space and hence the difference in particle orientation before and after the simulation time was possible. A sample with H/B of 4.35 was used having non-spherical particles.

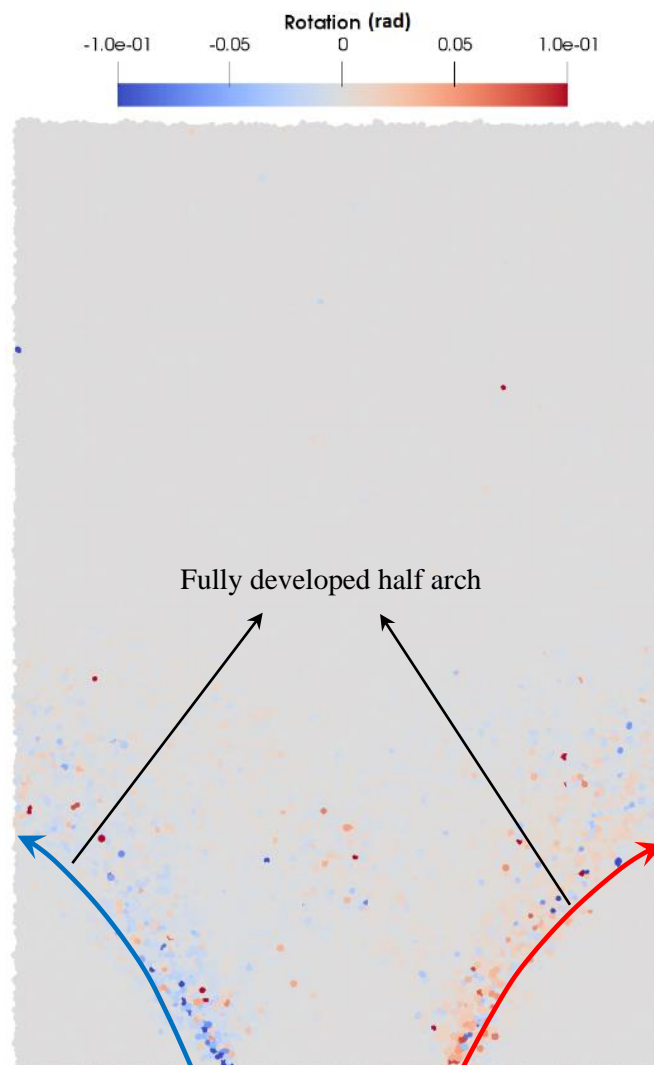


Figure 5.32 Particle rotation diagram for DEM simulation with non-spherical particles having $H/B = 4.35$

Figure 5.32 shows the particle rotation plot in radians for non-spherical particles with $H/B = 4.35$. The clockwise particle rotation is represented in red color whilst the counterclockwise movement is shown in blue color. As clearly seen, the particle rotation phenomenon is significantly dominant in the areas where the arch development is seen (Figure 5.15). The majority of the particles followed a particular rotation direction in either half of the specimen, i.e. the right half showed clockwise rotation whereas the left half of the sample showed counterclockwise rotation trend. However, there existed few particles around other particles having a rotation direction opposite to the majority cases. This can be explained well with the help of Figure 5.33 where the particle movement in the neighboring clump is shown.

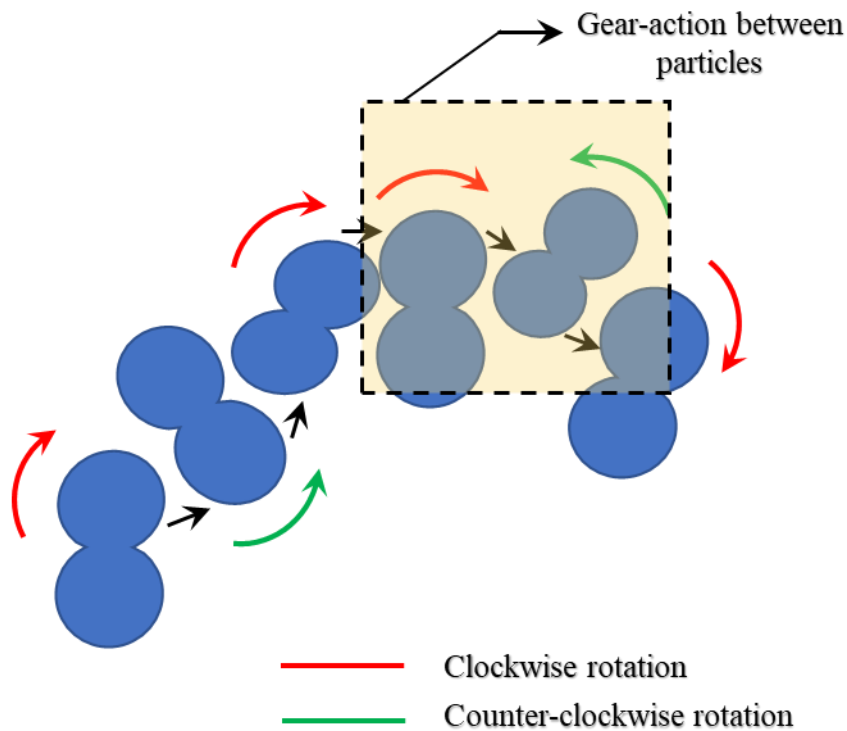


Figure 5.33 Gearing action between neighboring particles to cause opposite rotation

The force redistribution causes the particles to rotate in a particular direction in the arch formation zone. However, some of the particles that intersect the path of the arch but are not directly in the influence zone, rotate in a direction opposite to the neighboring particles due to the formation of gear-action. Gear action forces the neighboring particles

to rotate in the opposite direction that is visible in Figure 5.33 in either half by the presence of reversely rotating particles.

5.5.4 Rotation analysis for spherical particles

Non-spherical particles in the given DEM simulations consisted of two adjoining spherical particles being connected rigidly with each other. Thus, the branch vector connecting the centroid of both adjoining particles can be calculated through the DEM code, resulting in the exact orientation of particle at any instance. However, in the case of spherical particles, the change in the orientation of the branch vector was not possible due to the presence of only one constituting particle. Figure 5.34 below explains the procedure for the calculation of orientation change for both spherical and non-spherical particles.

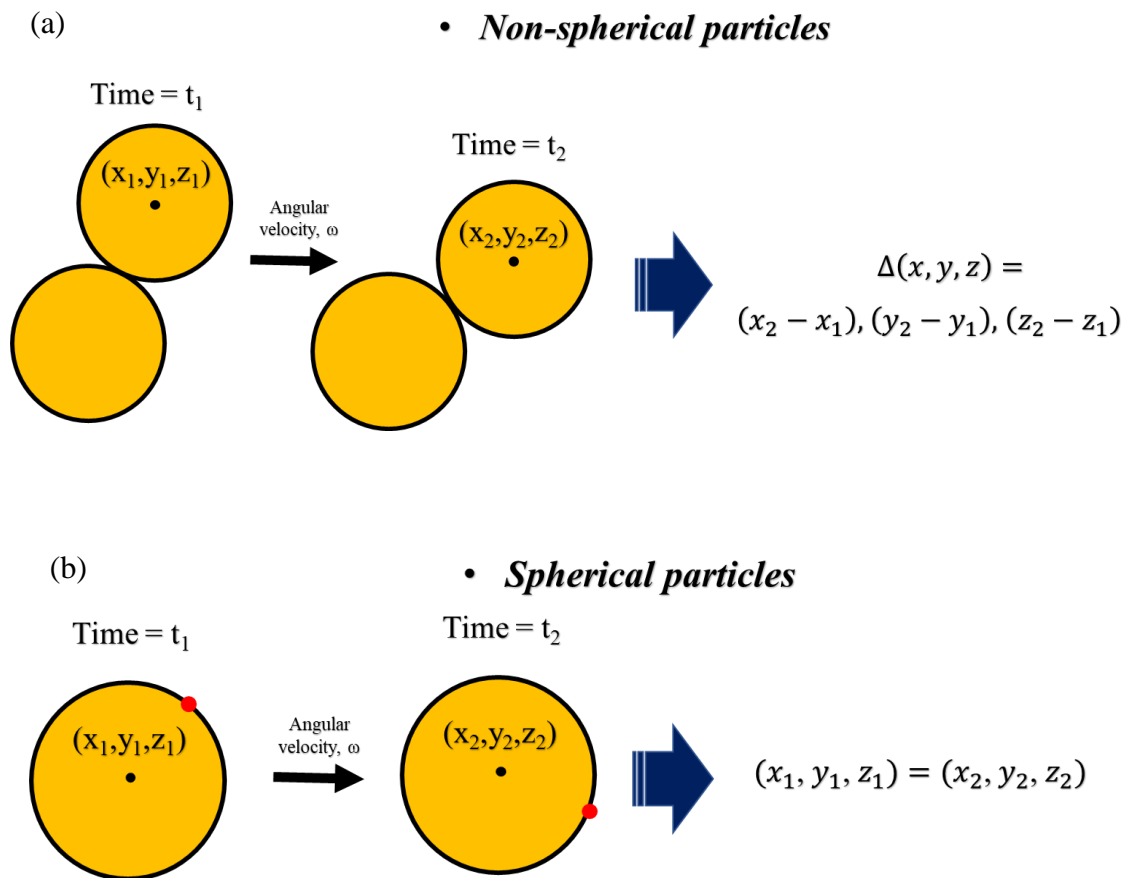


Figure 5.34 change in orientation of (a) non-spherical particle and (b) spherical particles in case of absence of translation motion

In the case of spherical particles when there is no translational movement of particle and there exists only rotational movement, the initial and the final coordinates of the particle does not alter as the position is not changed. Hence, the calculation of rotation based upon the particle coordinates is not possible. Consequently, the given DEM code had a limitation not to be able to calculate the rotation of spherical particles during the simulation process.

Another parameter that was well monitored during the DEM simulations for both spherical and non-spherical particle cases, is the angular velocity, ω . Since the angular velocity ω is the ‘cause’ for obtaining the ‘effect’ of particle rotation, it might be able to demonstrate a similar trend as that of obtained through rotational analyses of particles. However, the limitation of ω is that the value we obtain through the simulation data is the instantaneous angular velocity, not the mean velocity. Hence, the product of simulation time and the accumulative instantaneous angular velocity would not produce the total rotation of any given particle. The only analysis possible is to monitor the effect of instantaneous angular velocity.

To validate the usage of instantaneous angular velocity as a means to judge arching action during simulations, initially, the comparison of ω and rotation plots for non-spherical particles was performed. Figure 5.35 below compares both plots for non-spherical particles.

Non-spherical particles yielded a very similar trend for instantaneous velocity plot (at end of simulation) in Figure 5.35(a), compared to the rotation plot of the same sample as shown in Figure 5.35(b). Both plots demonstrated the arching zones in a clear manner. Thus, it is clear that the trend obtained by the angular velocity plot is similar to the trend of particle rotation. Consequently, the angular velocity plots can be used for the spherical particles to represent the particle rotation behavior under trapdoor conditions.

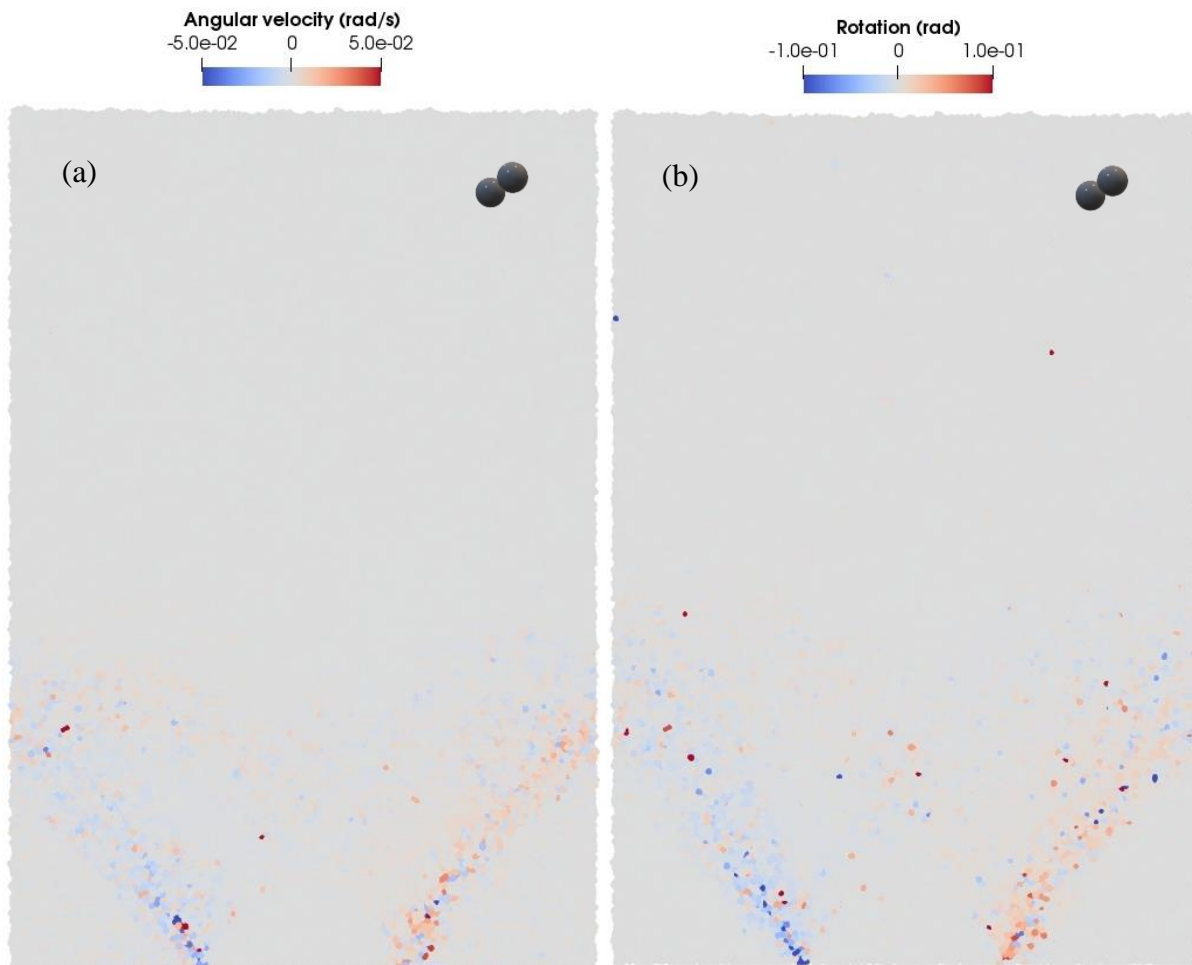


Figure 5.35 Plot for (a) angular velocity and (b) particle rotation with non-spherical particles having $H/B = 4.35$

A similar sample was prepared with similar boundary conditions and input parameters with spherical particles. The instantaneous angular velocity was calculated at the final stage of the simulation and the resultant plot is produced below in Figure 5.36. The bottom portion of the sample above the lowering trapdoors shows particle rotation around the expected arching zone by the colored particles. The disturbed region, having colored particles, mostly exist in a semi-circular region that is anticipated to surround the arching zone in that particular case.

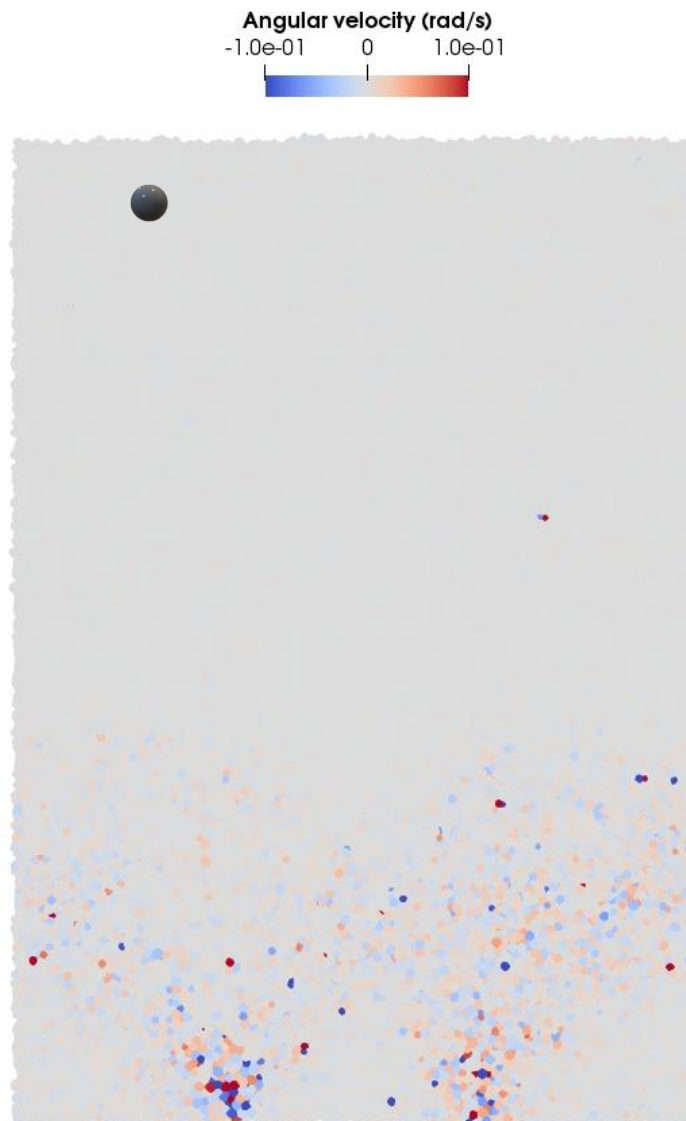


Figure 5.36 Angular velocity plot for DEM simulation with spherical particles under $H/B = 4.35$

To have a better comparison of particle rotation using spherical and non-spherical particles, the combined angular velocity plot for both types is shown in Figure 5.37 by plotting the half portion for each and combining it together. The similarity in the plots is clearly visible. However, the region of particles showing higher angular velocities for non-spherical particles is much thinner and clear, compared to the region of spherical particles.

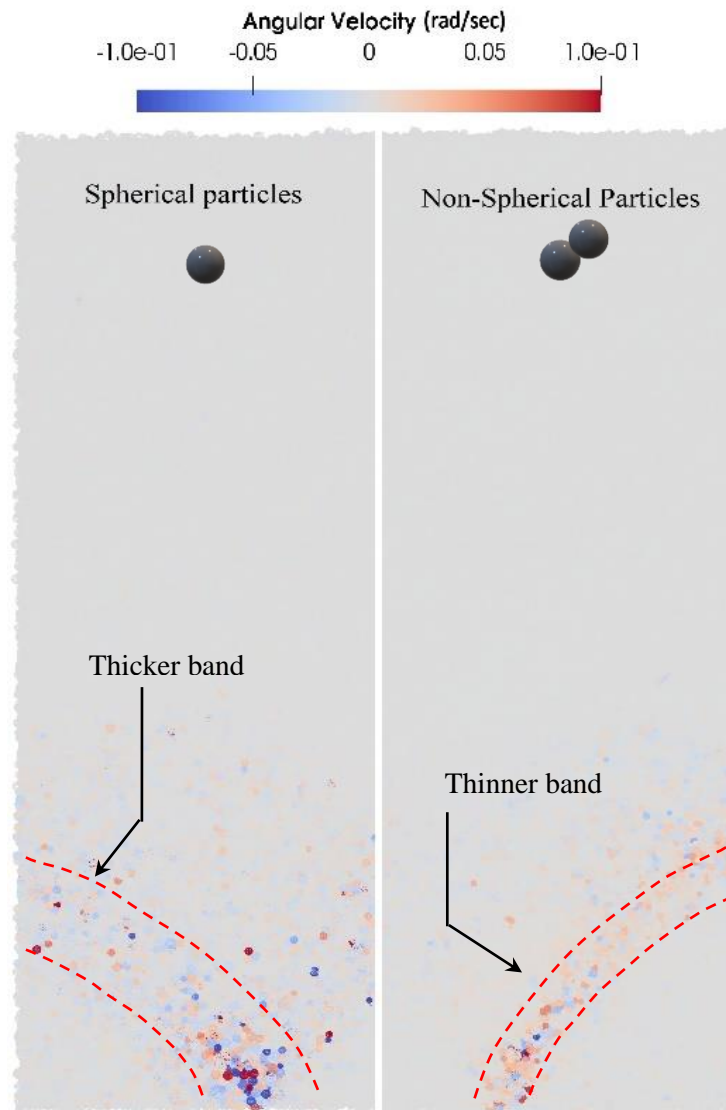


Figure 5.37 Angular velocity plot for spherical (on left) and non-spherical (on right) particles for $H/B = 4.35$

Under the influence of lowering trapdoors, arching forces propagate in a defined geometry, that forces the particles falling within the region of the arch propagation to rearrange and align themselves for transferring the forces through a chain action. Spherical particles being least resistant towards rotation, demonstrate a larger region with angular velocities, as visible with a thicker band of particles with angular movements in the left half of Figure 5.37.

Contrary to the spherical particles, non-spherical particles had a much higher aspect ratio due to the fact that two spherical particles were joined together that increased the length of the particular significantly compared to the width (diameter) of the particle.

Higher aspect ratios along with lower sphericity and convexity (as shown in Chapter-3) and eventually higher angularity of non-spherical particles caused a better chain of force transmission. Non-spherical particles also possessed a higher number of contacts that can better transmit the forces, as visible in Figure 5.17(d). Thus, a better and effect force distribution chain network in non-spherical particles caused a much thinner and precise band of particles showing higher angular velocity (and rotation), as shown in the right half of Figure 5.37.

In conclusion, this chapter included the particle scale analyses of soil arching through different parameters and techniques. The effect of particle shape was also included during the particulate investigation of the arching. The phenomenon of soil arching was well captured by the complementary DEM simulations. DEM based analyses like vertical displacement of particles, strong force chains, surface settlement, particle rotation, and angular velocity plots, all demonstrated that there exists a clear arching within the soil mass above the lowering trapdoors under certain conditions. The effect of soil height on the arch propagation revealed that a stabilized arching action requires a certain ground height, that is dependent upon the trapdoor configuration. The given analyses and results pertain to a certain trapdoor configuration with a central fixed plate and lowering sides. However, with a different arrangement, the absolute results might vary. Though, it is believed that the qualitative results would not be altered much with a change in trapdoor configuration. The effect of trapdoor configuration is discussed in detail in the following chapter.

CHAPTER 6: TRAPDOOR CONFIGURATION EFFECT

This chapter investigates the effect of changing the trapdoor configuration with the corresponding stress redistribution effect. The term *configuration* here corresponds to a varying number as well as the dimensions of the base plates/trapdoors. The results yet obtained demonstrate a particular pattern. However, whether changing the trapdoor configuration alters these results or not, will be discussed in this chapter.

6.1 Trapdoor configuration: Model Tests and DEM Simulations

So far, only a single type of trapdoor configuration has been discussed in the initial chapters. The model trapdoor tests consisted of seven base plate with central and extreme plates as static and other plates were lowered with a constant velocity. However, in DEM simulations, only three base plates were utilized with the central fixed plate and side lowering plates. The periodic boundary was provided on the lateral extents of the sample. The significance of using three plates in DEM simulations is well discussed in the earlier chapters. The basic configuration for both model tests and simulations is briefly explained through Figure 6.1 below:

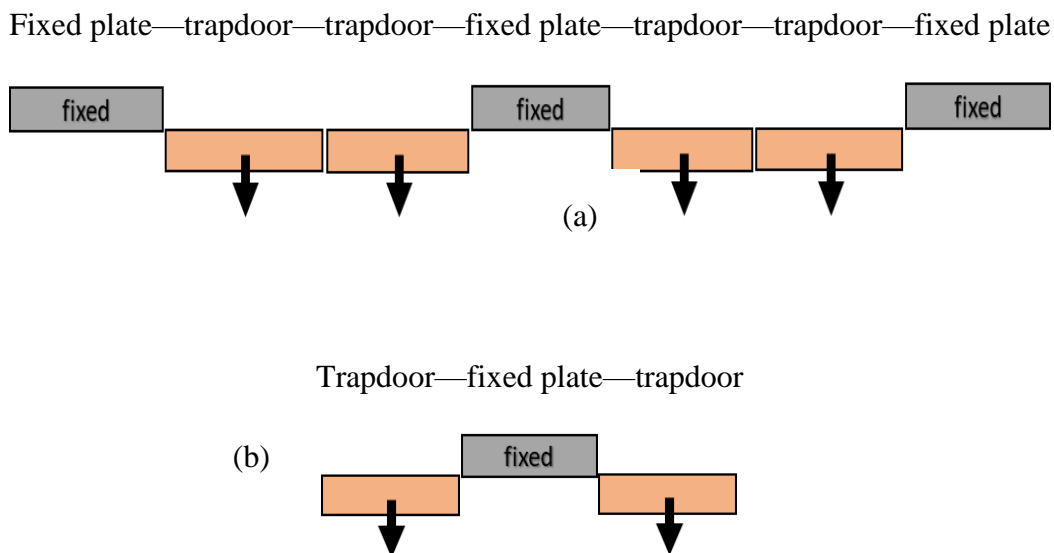


Figure 6.1 Trapdoor configurations used in (a) model trapdoor equipment and (b) DEM simulation

The equivalent configuration used in DEM can effectively reproduce the trapdoor model test behavior and a quick comparison is shown in Figure 6.2 below, where an equivalent DEM simulation model can capture the exact half of symmetrical arch as seen in trapdoor model tests.

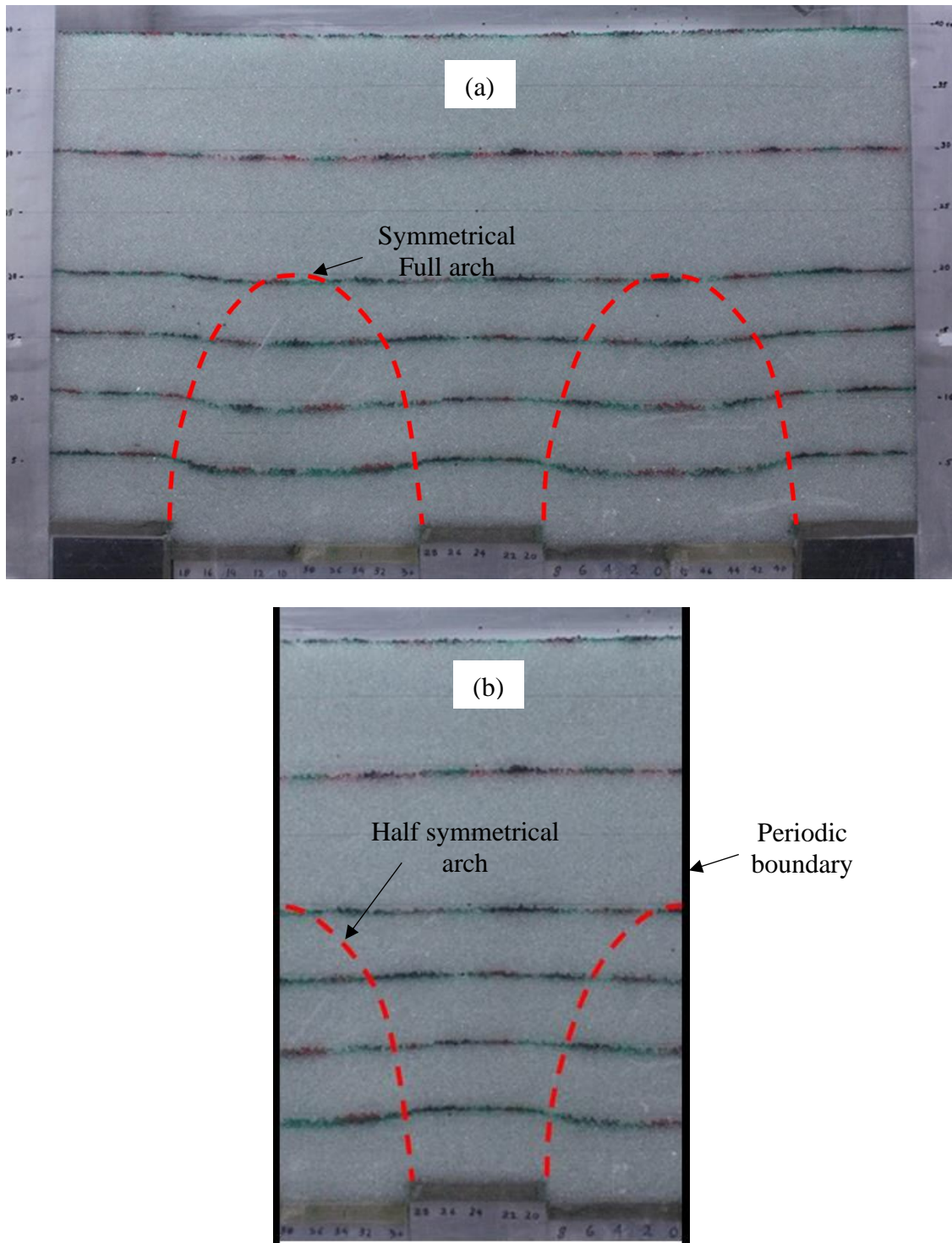


Figure 6.2 (a) Arching as obtained in model trapdoor tests and (b) half arch produced in DEM simulations with lateral periodic boundaries

6.1.1 Model test configuration variation

The model test apparatus consisted of seven base-plates with two extreme side plates immovable, as shown in Figure 6.1 above. However, the remaining five plates can be moved in any direction. To produce a symmetrical arch on either side, the only possible solution was to fix the central base plate and lower the surrounding plates, two on each side.

This resulted in only one possibility for the model test configuration, that was utilized and discussed in earlier parts of this work. Hence, the given model trapdoor test apparatus had a limitation to be used only for a single configuration having symmetrical arching on either side.

6.1.2 Configuration variation in DEM simulations:

The results of DEM simulations as already discussed in the previous chapter, verify the effectiveness and accuracy with model trapdoor tests. Further to that, model test equipment configuration could not be changed due to equipment limitation, the best option was to investigate the configuration effect using DEM simulations.

Hence, a detailed simulation sequence was run using several trapdoor configurations. Each configuration had several model ground heights to explore the impact of effective cover on the stability of the arch. Figure 6.3 below explains the terminologies being used in trapdoor configurations. Four different types of configuration being used resulted in total trapdoor length (L) of 15cm, 25cm, 35cm and 45cms with an L/B values of 3.0, 5.0, 7.0 and 9.0. All configurations were run with a series of ground heights as explained in Table 6.1 to Table 6.4 below.

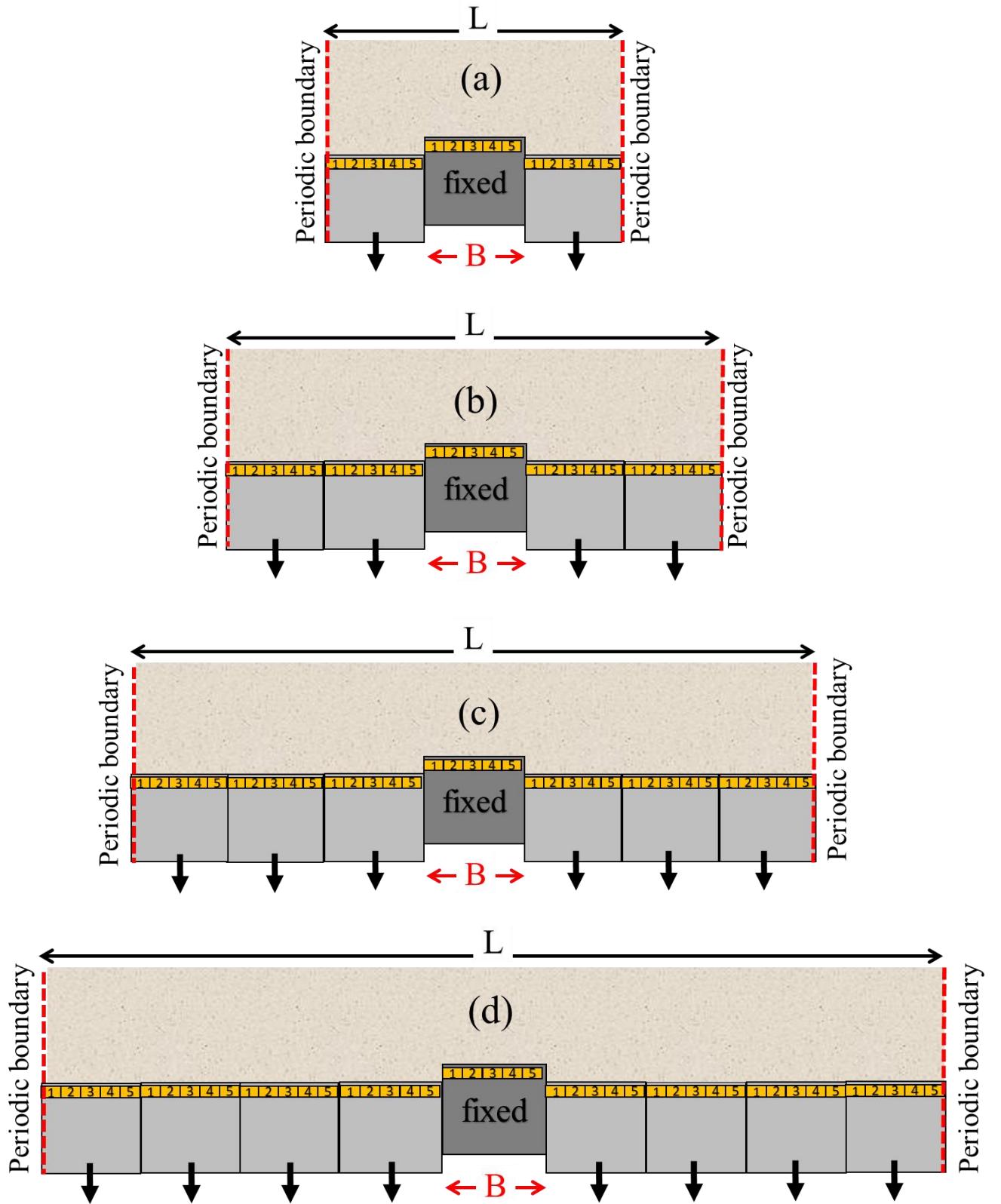


Figure 6.3 Trapdoor configurations in DEM simulations using spherical particles with (a) $L/B = 3.0$, (b) $L/B = 5.0$, (c) $L/B = 7.0$, and (d) $L/B = 9.0$.

Table 6.1 Simulation plan for trapdoor configuration of 15cm length

Configuration No.	L (mm)	L/B	H/B	Void ratio 'e'
1a	150	3.0	0.87	0.624
1b			1.75	0.620
1c			2.61	0.614
1d			3.50	0.613
1e			4.35	0.610
1f			6.95	0.608
1g			10.2	0.606

Table 6.2 Simulation plan for trapdoor configuration of 25cm length

Configuration No.	L (mm)	L/B	H/B	Void ratio 'e'
2a	250	5.0	0.87	0.626
2b			2.61	0.613
2c			4.35	0.611
2d			6.95	0.604
2e			10.2	0.602

Table 6.3 Simulation plan for trapdoor configuration of 35cm length

Configuration No.	L (mm)	L/B	H/B	Void ratio 'e'
3a	350	7.0	0.87	0.626
3b			2.61	0.613
3c			4.35	0.611
3d			6.95	0.605
3e			10.2	0.608

Table 6.4 Simulation plan for trapdoor configuration of 45cm length

Configuration No.	L (mm)	L/B	H/B	Void ratio 'e'
4a	450	9.0	0.87	0.624
4b			2.61	0.614
4c			4.35	0.610
4d			6.95	0.608
4e			10.2	0.607

6.1.3 Sample Pluviation

The samples were prepared in a very similar manner, as explained in Chapter-3 in the methodology of numerical simulations. Only the lateral boundaries were expanded in order to counter for the varying configurations. Similar to earlier cases, all samples were provided with lateral periodic boundaries in order to minimize the boundary effect.

Since the trapdoor configuration variation involves a much larger size of the DEM samples, sample thickness could play an important role in overall simulation time and

computational effort by the HPC machine. The cases described in earlier chapters involved a sample width of 40mm in all cases. During the configuration effect simulations, having $L/B = 5.0$ or larger, the number of particles involved in each case are shown below in Table 6.5 below. The dimension nomenclature is also shown in Figure 6.4.

Table 6.5 Number of particles in each simulation case with full width and half-width, for varying configurations

L/B	No. of base plates	H/B	No. of approx. particles (W = 4cm)	No. of approx. particles (W = 2.2cm)
5.0	5	0.87	$\approx 84,000$	$\approx 45,000$
		2.61	$\approx 250,000$	$\approx 130,000$
		4.35	$\approx 420,000$	$\approx 215,000$
		6.95	$\approx 667,000$	$\approx 340,000$
		10.2	$\approx 1,000,000$	$\approx 520,000$
7.0	7	0.87	$\approx 115,000$	$\approx 59,000$
		2.61	$\approx 345,000$	$\approx 175,000$
		4.35	$\approx 590,000$	$\approx 300,000$
		6.95	$\approx 900,000$	$\approx 470,000$
		10.2	$\approx 1,390,000$	$\approx 700,000$
9.0	9	0.87	$\approx 150,000$	$\approx 80,000$
		2.61	$\approx 450,000$	$\approx 230,000$
		4.35	$\approx 750,000$	$\approx 380,000$
		6.95	$\approx 1,190,000$	$\approx 610,000$
		10.2	$\approx 1,810,000$	$\approx 920,000$

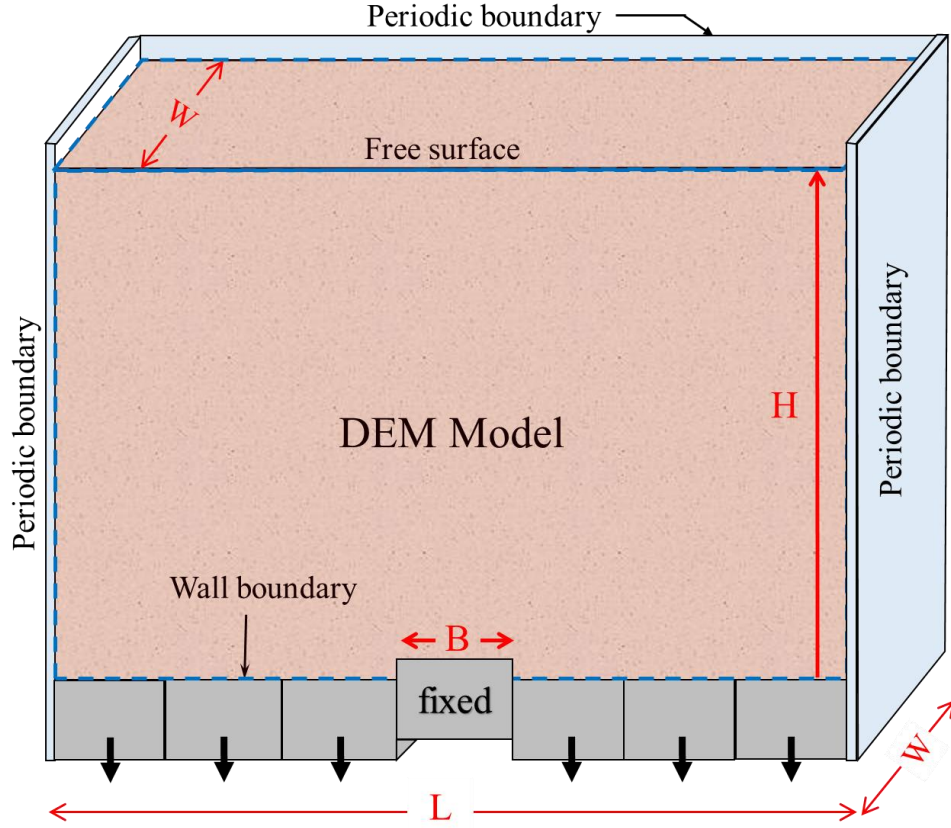


Figure 6.4 Dimension nomenclature in trapdoor configuration effect simulations

As seen above in Table 6.5, the number of particles increases with increasing the length of sample L . The simulation time is directly proportional to the number of particles in a sample size. For the largest case, the particles reached multiple millions, which would require significant time and computational energy to be involved. However, the earlier used sample width W of 40mm seems to be more than sufficient for the accuracy of the results. Head (1994) described that a representative sample should have a minimum dimension of $10 \times D_{\max}$, where D_{\max} is the maximum diameter of the particle inside a sample.

The particle size distribution used in the simulation process possessed a diameter range of 1.2mm-2.2mm. Hence, keeping in view the above-mentioned guidelines and to minimize the computational effort, the Width W of the samples was reduced to 22mm. The approximate number of particles involved in each simulation case after the reduction of sample width are also presented in Table 6.5.

6.2 Theoretical maximum stress concentration factor on the central fixed plate

Since the presence of arching withing the soil mass redistributes the loads on the particles. With proper soil cover, an arch would transfer the majority of the overburden pressure towards the static mass from the yielding mass. Better is the arching, more load would be transferred. In a perfect arching condition, the load taken by the top surface of lowering mass would be very small.

Hence, a condition exists wherein the arching forces represent the most stable condition. Such a condition would try to redistribute the maximum possible load to the central static portion and the corresponding stress concentration factor is called a theoretical maximum value of α . Hence, almost all load of the soil mass is transferred towards the central static portion, provided if the conditions are similar to the trapdoor configurations as presented in this study.

Keeping the same notation, for a trapdoor configuration having three base plates, the central fixed plate would be idealized to take a load of all material above three base plates due to the hypothetical presence of the ideal arching condition. Hence, the increment of load on the central base plate compared to the initial static case would be three times higher. Similarly, the configuration with 5 base plates would result in a theoretical maximum α value of 5 and so on. Hence, the mathematical notation for theoretical maximum α is represented in Eq. 6.3 below:

$$\alpha_{max}^{theoretical} \propto \frac{L}{B} \quad (6.1)$$

In Eq. 6.1 above, since the width of each plate B , is same, hence the $\alpha_{max}^{theoretical}$ can be assumed as proportional to the L/B ratio.

In case a sample produces α value approaching the $\alpha_{max}^{theoretical}$ for the given configuration, it represents that the arch developed withing the mass is in fully stabilized condition with maximum possible load transfer mechanism. However, in case the produced α values are much smaller as compared to the $\alpha_{max}^{theoretical}$, the condition of the sample can correspond to an insignificant sample height that is required for a full arching mechanism. Also,

the density or the particle shape could also be amongst influencing factors causing a smaller stress concentration value (α) compared to the theoretical maximum value.

6.3 Trapdoor simulations

Once the sample pluviation was completed, base trapdoors were lowered with a quasi-static velocity of 1×10^{-4} m/s. The lowering velocity was similar to the earlier discussed cases to have a better comparison. The main aim of lowering trapdoors was to attain the maximum/peak value of stress concentration factor (α_{max}), which is well discussed in detail in chapter 4.

In the Trapdoor condition, the α_{max} is attained with a very small trapdoor displacement, δ . A similar observation was also made by Kolb et al. (1999). Chevalier et al. (2008) noticed similar behavior in his DEM simulations under trapdoor conditions. Even in the model experiments with trapdoor conditions, a similar observation was seen in the current study. Tanaka & Sakai (1993) also showed a rapid increase in earth pressure with a very small trapdoor movement in both model tests and in simulation samples.

To attain the α_{max} in a reasonable simulated time, the trapdoors in the current study were lowered to a maximum of 0.25mm, which was sufficient enough to evaluate the maximum earth pressure increase above the static central base plate.

6.3.1 Trapdoor configuration with three base plates

The configuration for the trapdoor test with three base plates is shown in Figure 6.3(a). This specific configuration is well discussed earlier in the manuscript. However, here it is discussed very briefly to have a better comparison with the other cases.

The plot for vertical displacement of particle for three base plates configuration, having a total sample length of 150mm (15cm), is shown below in Figure 6.5. Whereas the strong force diagram for the same situation is shown in Figure 6.6 with different sample ground heights.

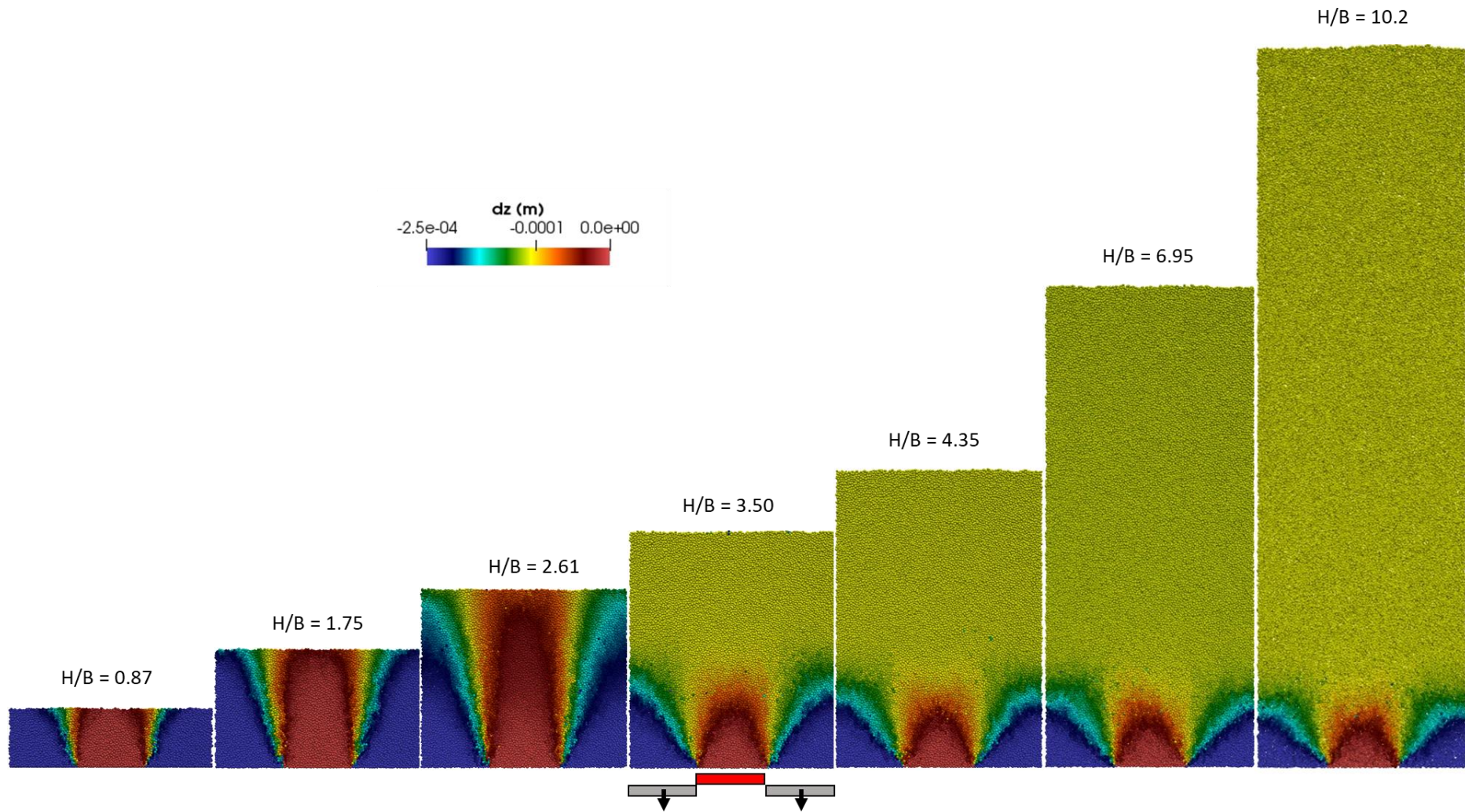


Figure 6.5 Vertical displacement plots for trapdoor configuration with three base plates, for varying sample heights

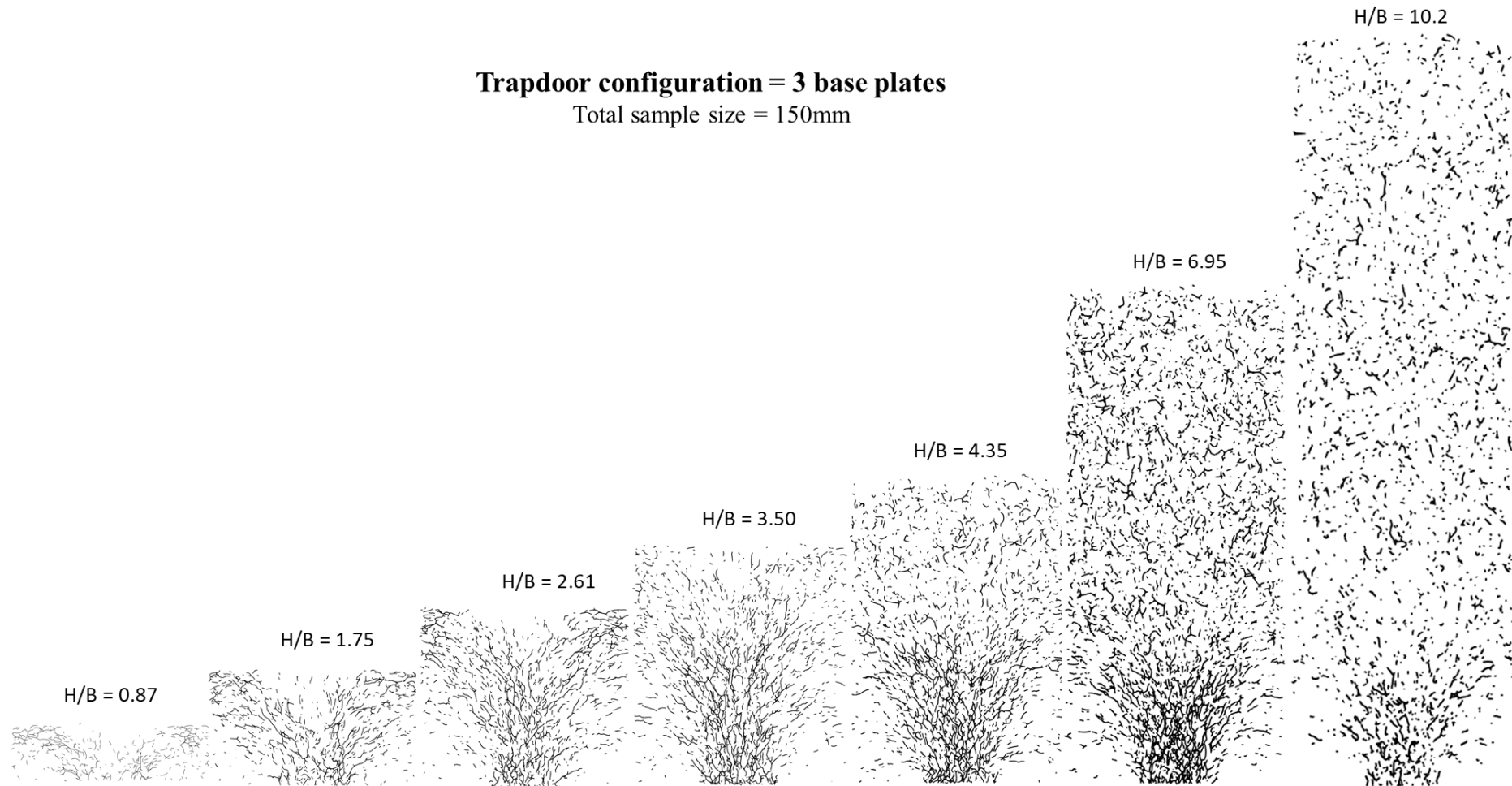


Figure 6.6 Strong force (normalized) plots for trapdoor configuration with three base plates, for varying sample heights

A large differential surface settlement is visible in Figure 6.5 up to a sample ground height corresponding to an H/B value of 2.61. Beyond that, a steady, well-established half arching on either side of the sample is visible. The central portion above the central base plate is showing a static behavior, that is visible by a specific color (red) above that portion.

It is also worth noting that after a certain height of the sample is achieved and arching action is developed, with further increase in the sample height the arching region does not propagate or vary. In Figure 6.5, the arching on either side of samples with higher ground heights, we can observe a similar pattern of arching irrespective of the sample height for a given trapdoor settlement. Hence, it can be concluded that the stress concentration factor (α) would reach a converged value once the arching is fully developed in the sample.

In Figure 6.6 a comparison of strong force distribution within the modeled sample space is made for different sample heights. The figure did not contain any legend as the strong forces presented above are the normalized strong forces (with the height of particles). Each particle in the sample contains a certain coordinate. The particles at the bottom of the sample not only have the forces due to contact with surrounding particles rather they also observe the overburden pressure, which adds to their total stress. As we move upward, this overburden reduces, and the top-most layer of particles would not have any such effect. As the strong forces, we plot in Figure 6.6 above contains only those forces having a magnitude of 90% or above to that of maximum contact force within the particle assembly (Eq. 6.2). Hence, without the consideration of overburden pressure, the top particles would not have sufficiently representative chains of the strong force and causing a misleading interpretation of the force distribution network. Consequently, the forces at each contact were normalized with the height of each corresponding particle, as shown in Eq. 6.3 below.

$$\text{Strong force} \geq 0.9 \times f_{max} \quad (6.1)$$

$$\text{Normalized strong force} = \frac{\text{Strong force}}{h_{particle}} \quad (6.2)$$

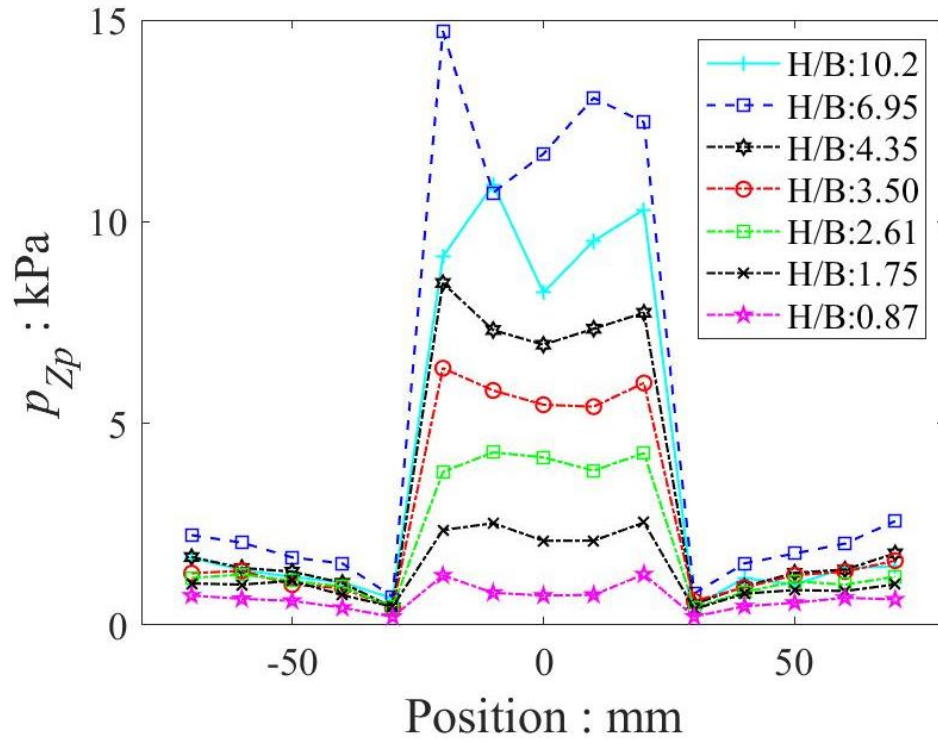


Figure 6.7 Normal stress distribution of trapdoor cases with varying sample height with an $L/B = 3.0$

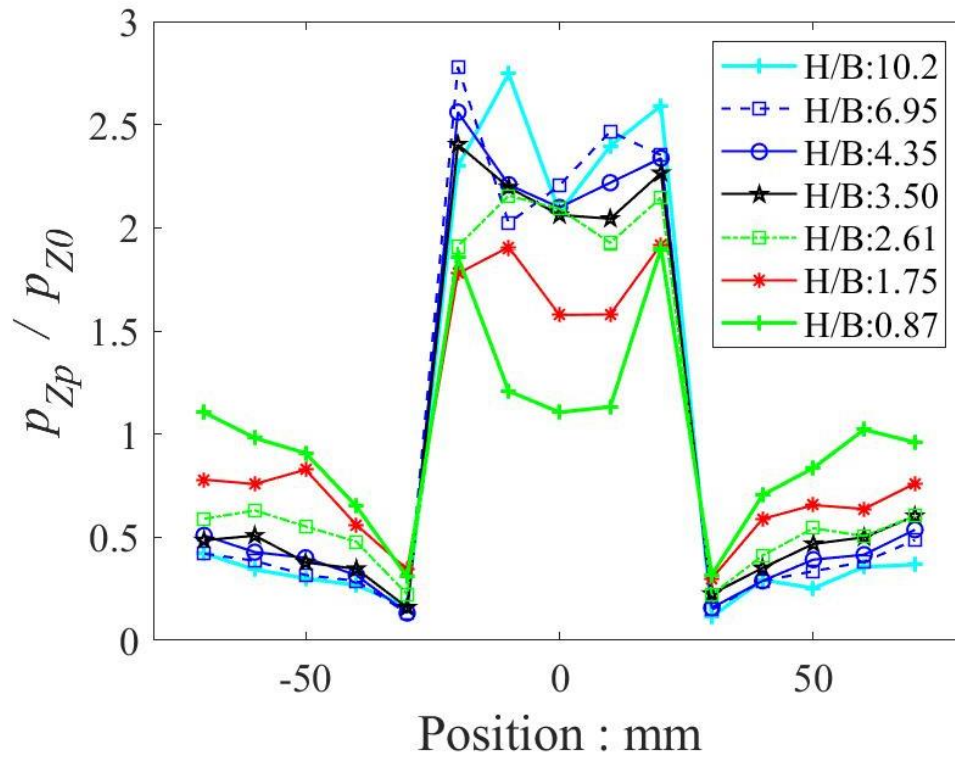


Figure 6.8 Normalized normal stress distribution of trapdoor cases with varying sample height with an $L/B = 3.0$

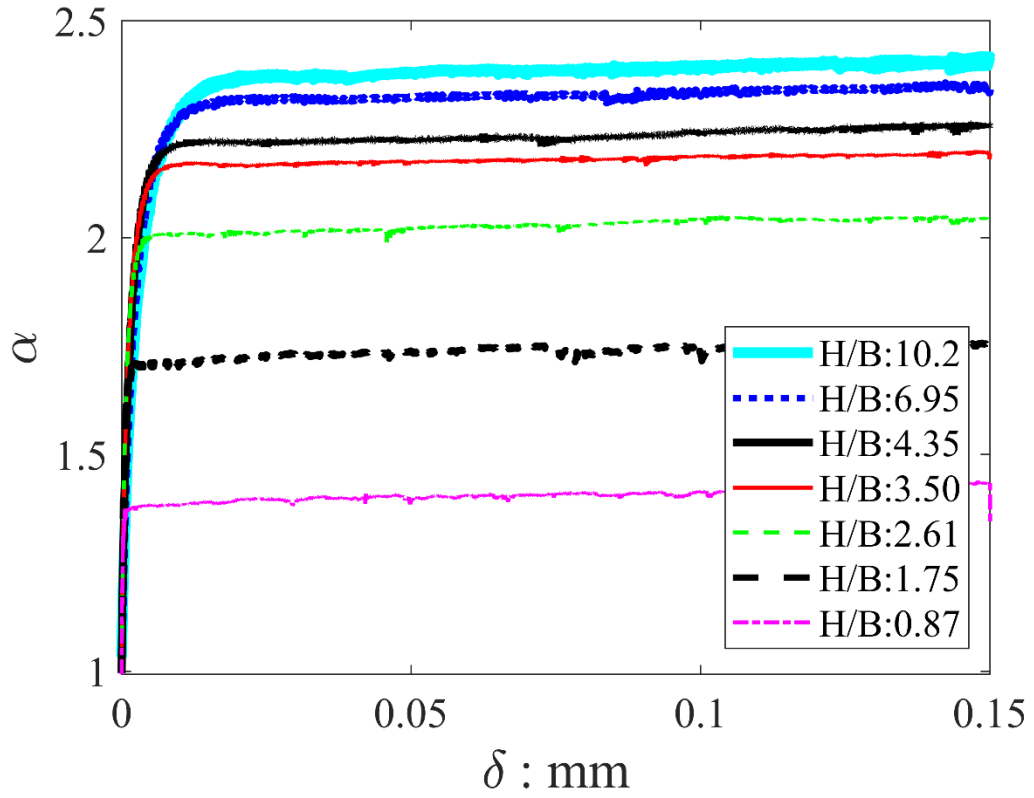


Figure 6.9 α variation under trapdoor cases with varying sample height with an $L/B = 3.0$

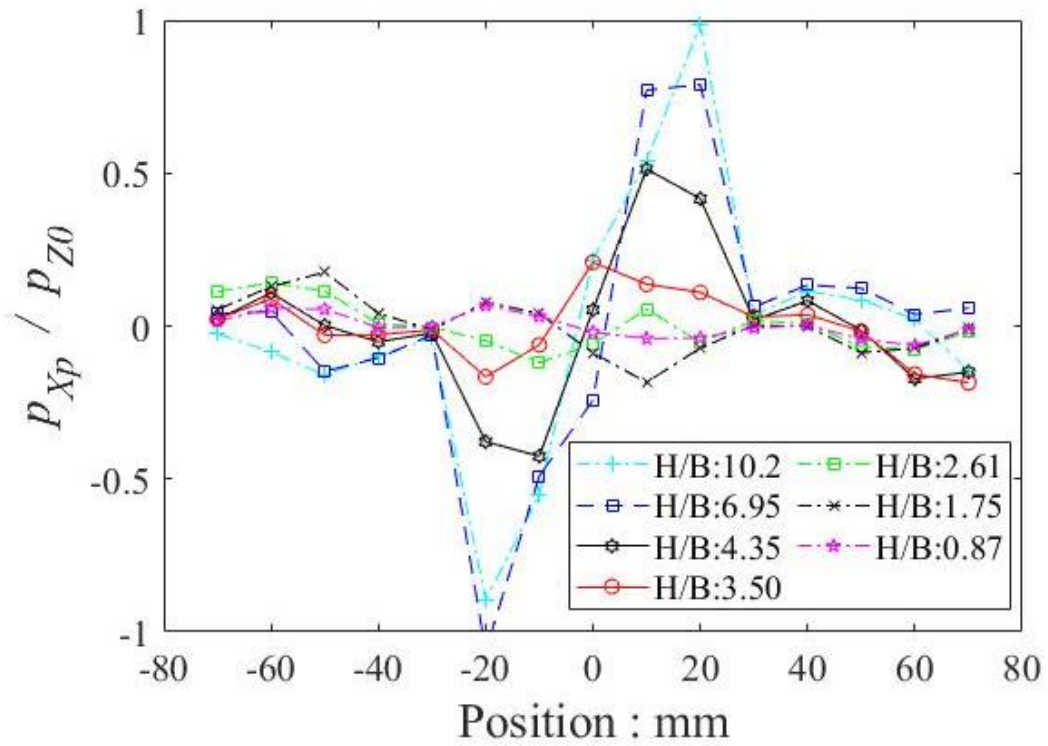


Figure 6.10 Shear stress distribution for $L/B = 3.0$ under varying ground heights

The normal stress distribution is presented in Figure 6.7 for different sample heights. The stress increases with increasing H/B , which is reasonable to understand as the more height of sample particles would generate more overburden pressure, resulting in higher stress values above the base plate. However, normalizing the stress distribution with the initial normal stress distribution results in a converging behavior, as shown in Figure 6.8.

The normalized normal stress distribution has well been explained for this configuration in chapter 4 previously. Though, in this section, more simulations with different sample heights are represented. The general trend is converging with increasing sample heights and the central fixed base plate experiences the highest-pressure distribution. The case with the highest normalized normal stress above the central fixed base plate demonstrated the lowest normalized stress above the side lowering plates. It is believed that the summation of stresses at each instance would remain the same, compared to the initial static condition.

Comparing the alpha (α) values (Figure 6.9), the trend is similar to that of normalized normal stress distribution as discussed in Figure 6.8. With the increasing height of the ground, α showed a converging trend. The α values for the largest presented ground height case approached to a theoretical maximum value of 3.0 for the given configuration. The theoretical maximum values will be discussed later in this chapter. Also, the peak value of α was attained at a very early stage of trapdoor lowering that is also observed by several researchers as discussed at the beginning of this chapter.

The shear stress distribution (Figure 6.10) showed two contrasting trends; each for a specific set of H/B values. Samples with an H/B value of 2.61 or lesser showed very small negative shear stress on the right outer edge of the central fixed plate. Whereas, on the left outer edge showed positive shear stresses. However, the samples with higher H/B showed opposite trends with higher shear stress magnitudes. As seen in Figure 6.5 (H/B : 2.61) the arching region is just touching the surface of the sample and there exists a critical condition of arching. Or in other words, we can say that the arching path is fully developed, but it is not in a stabilized condition. The resultant output is having a shear stress trend similar to the high H/B cases, but with a much smaller magnitude that represents a critical arching condition.

6.3.2 Trapdoor configuration with five base plates

In order to understand the effect of the increase in the length of the lowering-portion during trapdoor tests, the number of trapdoors (base plates being lowered) were increased to five. The configuration is shown in Figure 6.3(b) where the central base plate is fixed and two base plates on each side are lowered with a constant velocity of 1×10^{-4} m/s. Again, to reduce the boundary friction effect, periodic lateral boundaries were provided that produced a stress distribution at the boundary that is quite comparable with the actual conditions. Huang et al. (2014) showed that using periodic boundaries assures not only better homogeneity, but also are more probable to capture the actual stress-strain response of granular materials.

Vertical particle displacement plots (Figure 6.11) shows that the case of $H/B = 4.35$, with a maximum displacement of 0.25mm. The figure showed a clear arching pattern for the $L/B = 3$, did not show a stabilized arching pattern. Rather the developing arch touched the sample surface, causing differential surface settlement. However, the cases having H/B values above 4.35 showed a stable arching region with a specific color, above the lowering trapdoors on either side of the fixed central plate.

An interesting point in Figure 6.11 is the color of material near the sample surface for the cases with stable arch formations. Compared to Figure 6.5, the surface color is in a range that represents a higher settlement value, as shown in the legend of both figures. Both figures still show the presence of uniform surface settlement, rather than a differential surface settlement as seen in the case of smaller H/B values. Hence, with increasing the trapdoor configuration, the amount of uniform surface settlement increased.

Strong force diagrams are again showed for trapdoor configuration having five base plates, in Figure 6 12 for different ground heights. Samples having arching shows a uniformly distributed network of the strong force. This uniform distribution is also mean to justify the presence of uniform surface settlement for such cases. Cases with smaller H/B shows a variation in strong force chain in the central and the side region. The direction of the strong force network also varies compared to the central portion, that is basically the reason we see a differential surface settlement.

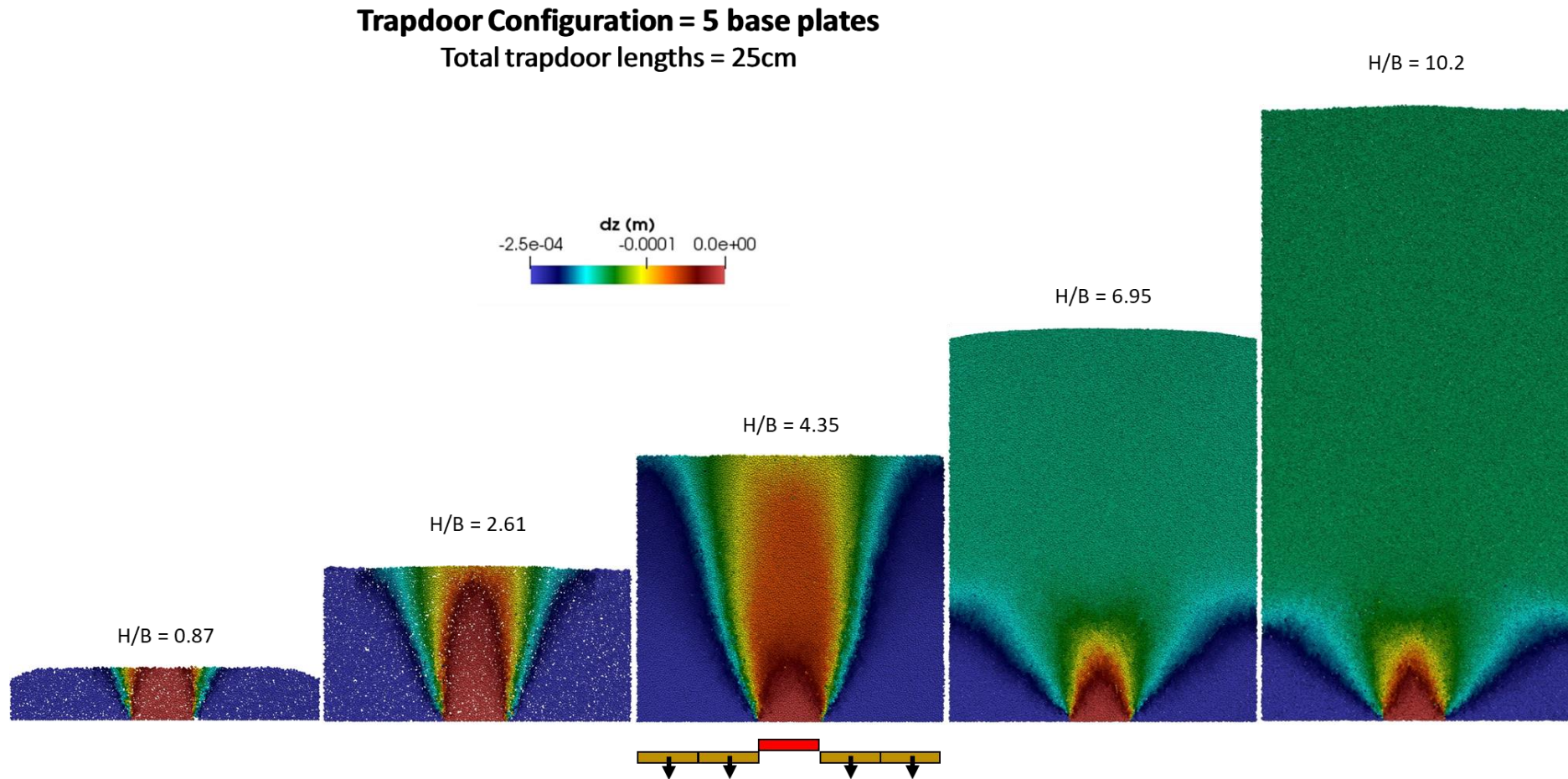


Figure 6.11 Vertical displacement plots for trapdoor configuration with five base plates, for varying sample heights

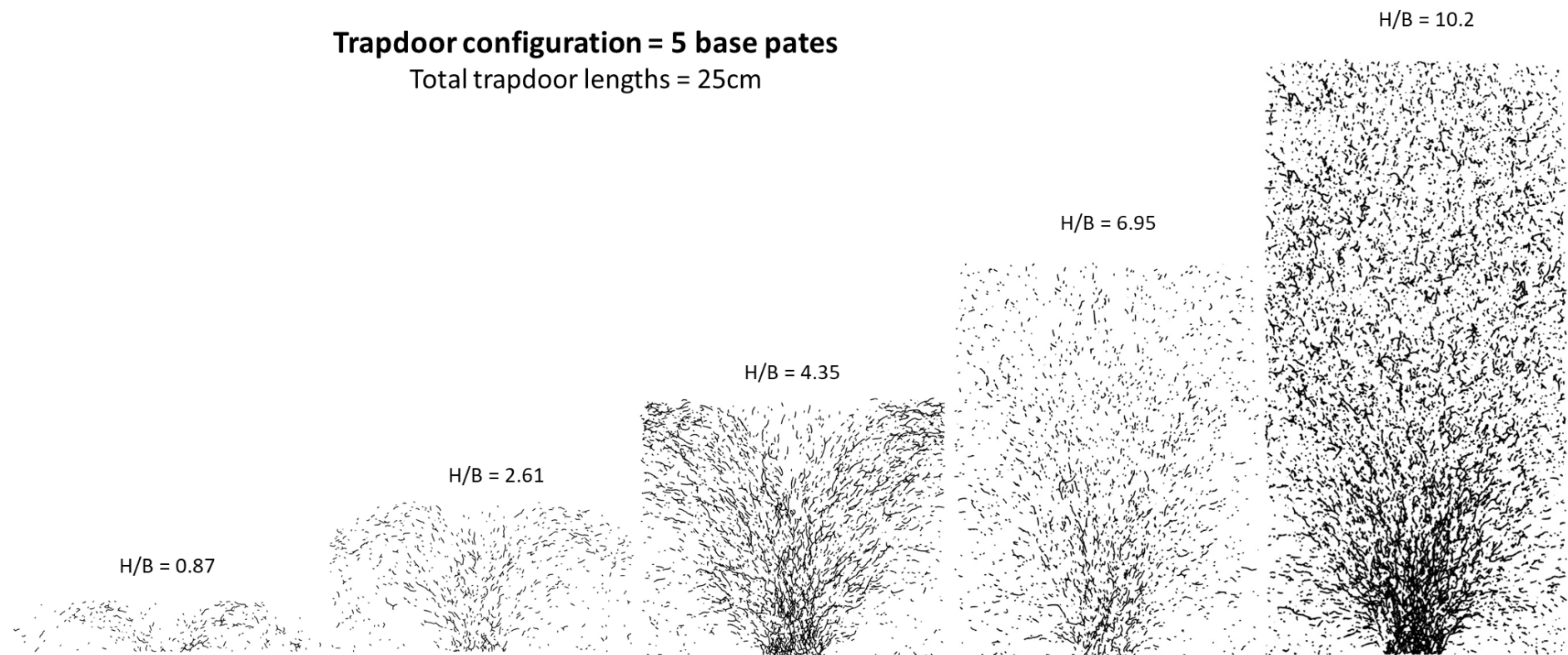


Figure 6 12 Strong force (normalized) plots for trapdoor configuration with five base plates, for varying sample heights

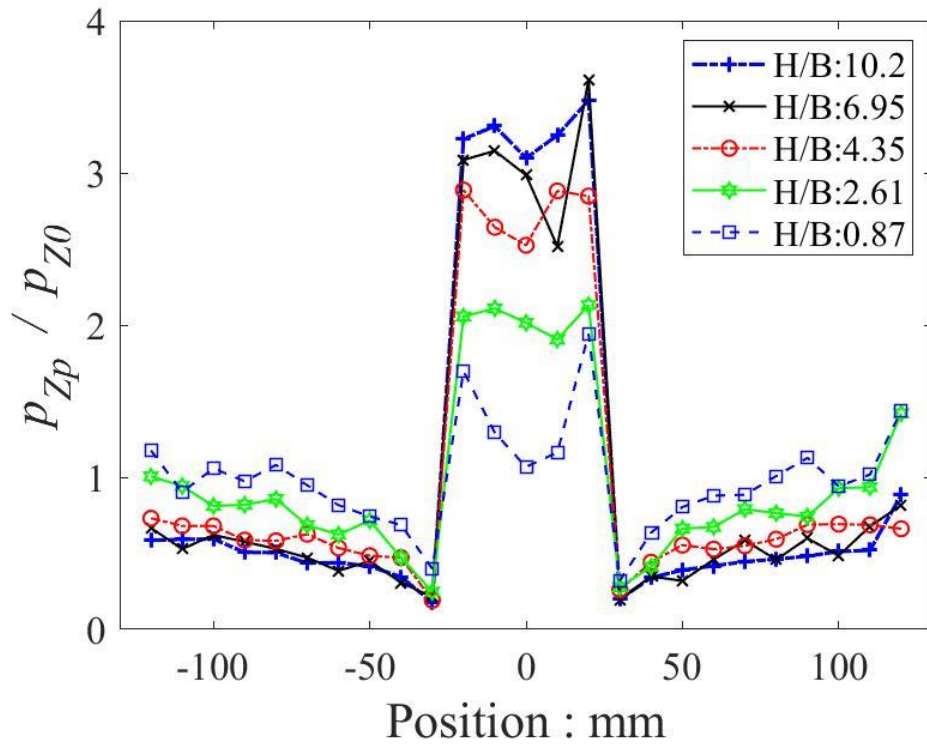


Figure 6.13 Normalized normal stress distribution of trapdoor cases with varying sample height with an $L/B = 5.0$

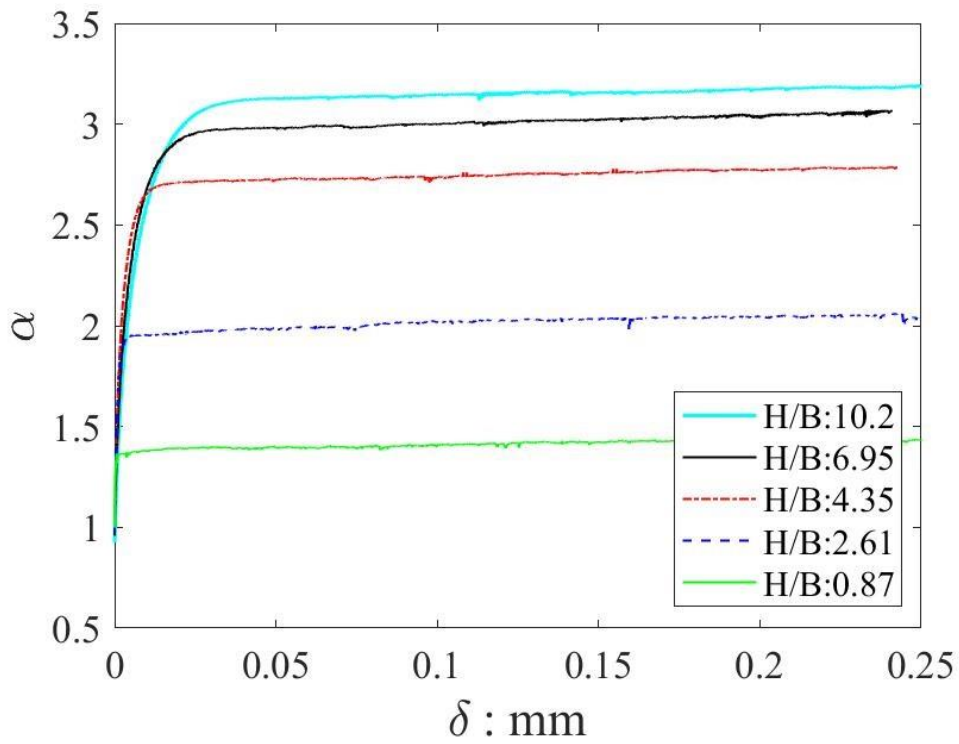


Figure 6.14 α variation under trapdoor cases with varying sample height with an $L/B = 5.0$

Like the other cases, normalized normal stress ratio (Figure 6.13) yielded a converging pattern with increasing sample height. However, looking at the magnitude of normalized stress values, it is clear that the arching is still developing, and further higher heights are required to make the arching process stabilized in the given trapdoor configuration.

The stress concentration factor or the central fixed base plate (α), as shown in Figure 6.14, portrays a converging trend. However, the gap between the subsequent H/B values is quite large and represents that by increasing the further sample height would result in a higher α value. Also, through the examination of the theoretical maximum possible value of α , the values produced by the simulation results are far below the possible maximum values (approaching 5.0) with a fully stabilized arch. Hence, the effect of trapdoor configuration can be examined as we changed the number of base plates.

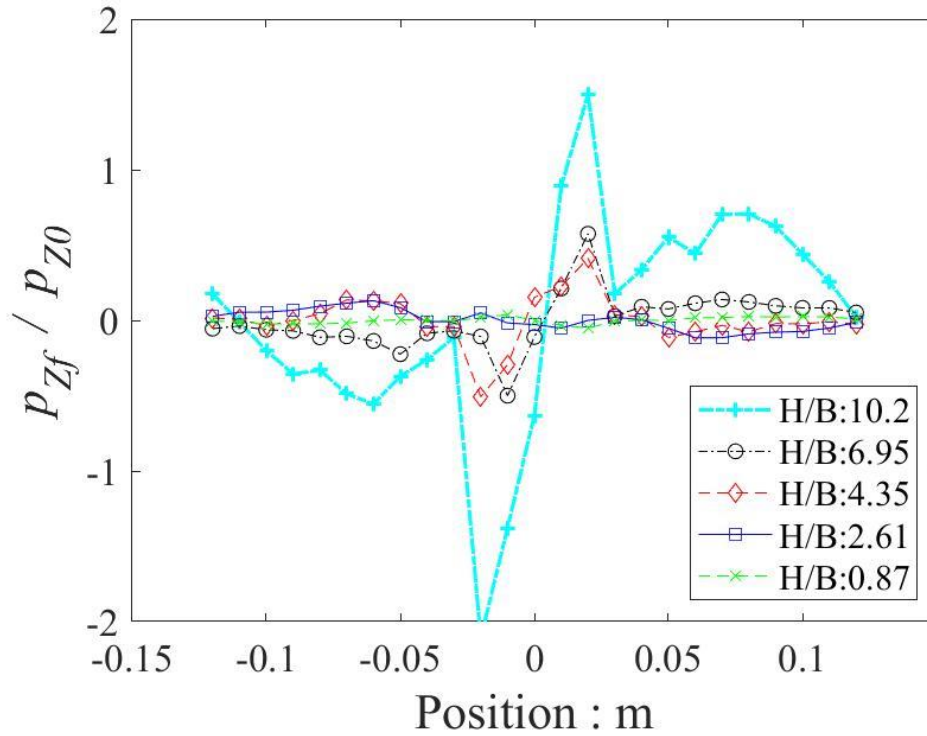


Figure 6.15 Shear stress distribution for $L/B = 5.0$ under varying ground heights

The shear stress distribution as shown in Figure 6.15 represents the similar trends as explained earlier. The opposite trends between the cases with a stable arch and the cases

without the arching action show a totally opposite trend. The absolute values of the shear stresses are a little higher compared to the cases with $L/B = 3.0$.

6.3.3 Trapdoor configuration with seven base plates

The number of base plates were further increased to evaluate the arch formation and properties. Although the basic methodology remained the same, i.e. the central plate was kept static and three trapdoors on each side of the central fixed base plate were moved downwards with a velocity of 1×10^{-4} m/s. Furthermore, the width of each plate/trapdoor was also kept the same, i.e. 50mm.

The lateral boundaries were kept periodic as that of previous configuration cases. The trapdoors were moved downwards up to a maximum displacement $\delta = 0.25$ mm. The reason for selecting this displacement value has already been discussed in earlier sections.

By looking at the vertical displacement plots (Figure 6.16) for the configuration with seven base plates ($L/B = 7.0$), only one sample having $H/B = 10.2$ resulted in an arching condition. Such behavior is Contrary to the earlier case of trapdoor configuration with five base plates, where the case of $H/B = 6.95$ showed an arching behavior. Hence, by increasing the number of base plates resulted in different arching condition, leading to different load distribution.

With increasing the trapdoor simulation length, another varying parameter is the amount of surface settlement. With five base plates, as discussed earlier, the surface settlement amount was smaller compared to the current configuration with seven base plates. The larger surface settlement with seven base plate configurations is visible with the help of legend color that showed a shifting behavior towards higher values with increasing base plates. However, still, the surface settlement values showed by the current configuration plot in Figure 6.16, is much smaller compared to the trapdoor movement, which is represented by the extreme color as shown in the legend. Furthermore, there exists no differential surface settlement for the case of $H/B = 10.2$ as the color distribution is totally uniform at the surface. However, all other cases showed a clear differential surface settlement due to the crossing path of the propagating arch with the ground surface of the sample.

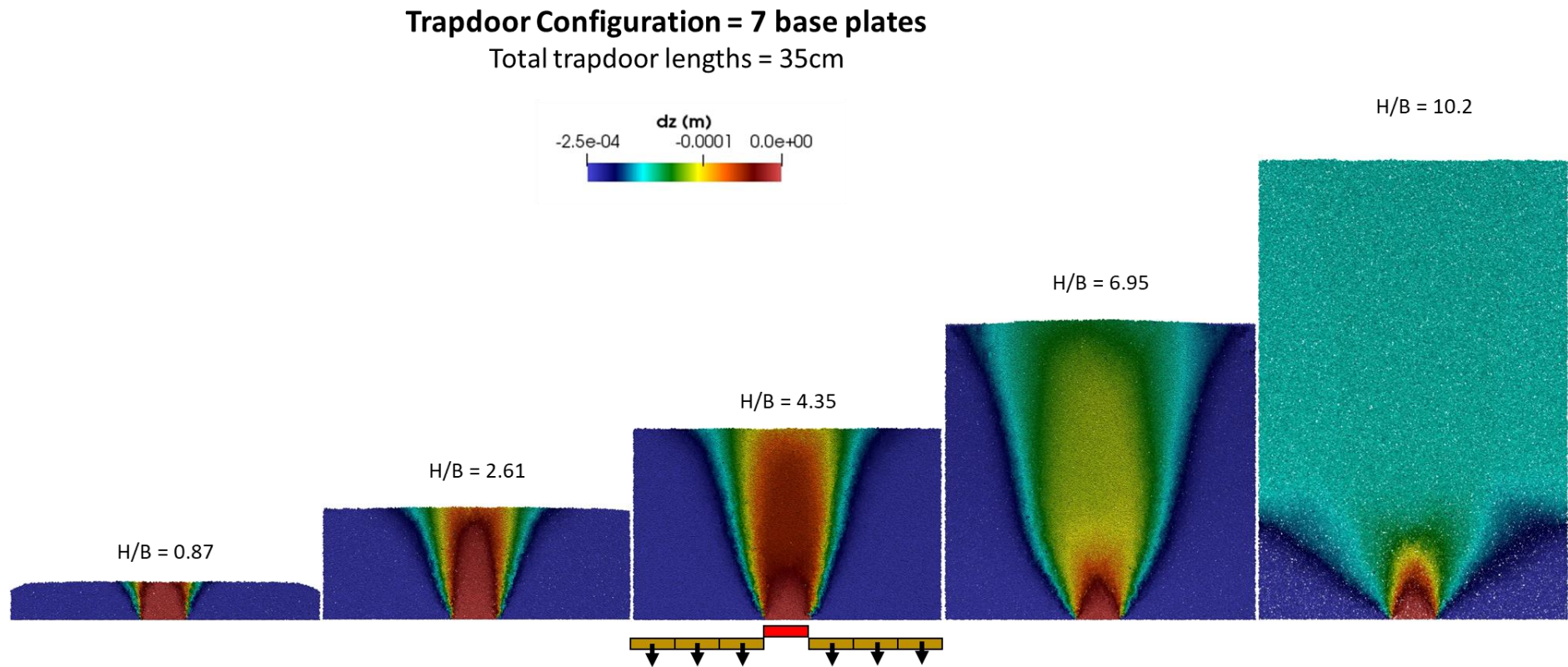


Figure 6.16 Vertical displacement plots for trapdoor configuration with seven base plates, for varying sample heights

Trapdoor configuration = 7 base pates

Total trapdoor lengths = 35cm

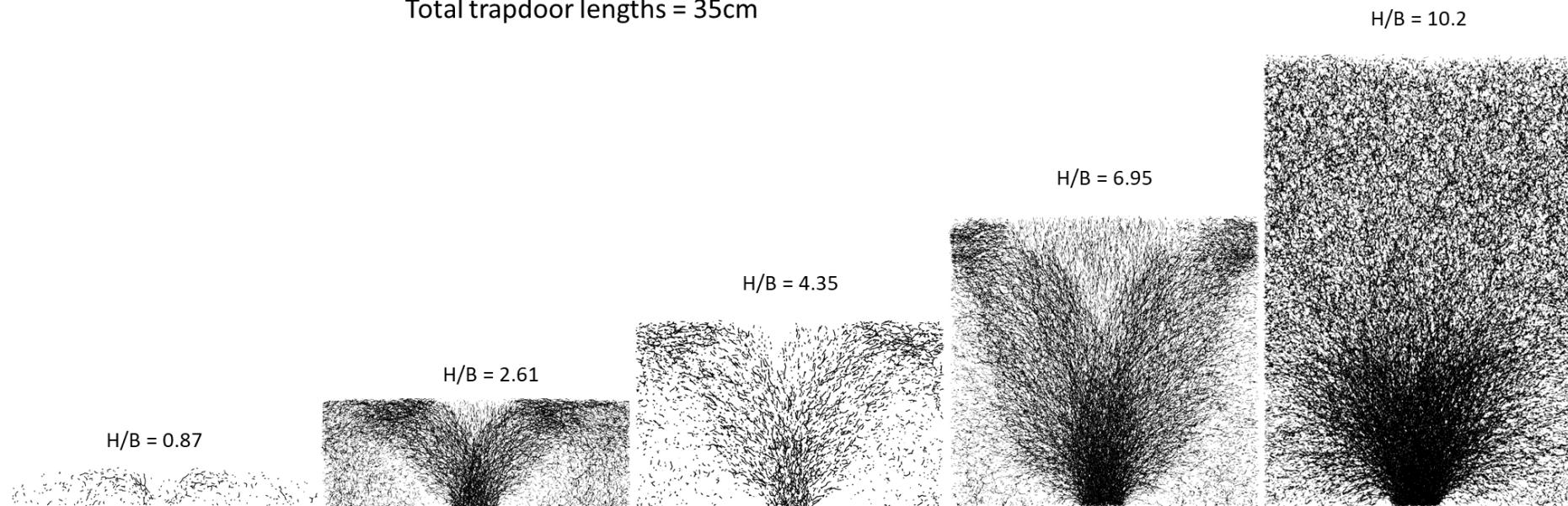


Figure 6.17 Strong force (normalized) plots for trapdoor configuration with seven base plates, for varying sample heights

A strong force plot for the given trapdoor configuration is shown in Figure 6.17. In all cases, except the one with the highest ground height ($H/B = 10.2$), the arching path intercepted the ground surface, causing a disruption in proper propagation of the arch, resulting in the differential surface settlement as shown in Figure 6.16. As seen in the figure above, the arching action initiates for all cases irrespective of their ground heights. For the case with a developed arch, the top portion of the sample showed uniformly distributed strong force chains. However, the force chains are densely populated, representing the resistance of the top sample against the forces developed due to surface settlement. As seen from Figure 6.16 ($H/B = 10.2$), the color of the top surface represents a uniform surface settlement that is larger than the sample with similar ground height for configuration with $L/B = 5.0$ as shown in Figure 6.11. To resist this higher magnitude of surface settlement, the strong forces are seen denser in the top region (Figure 6.17).

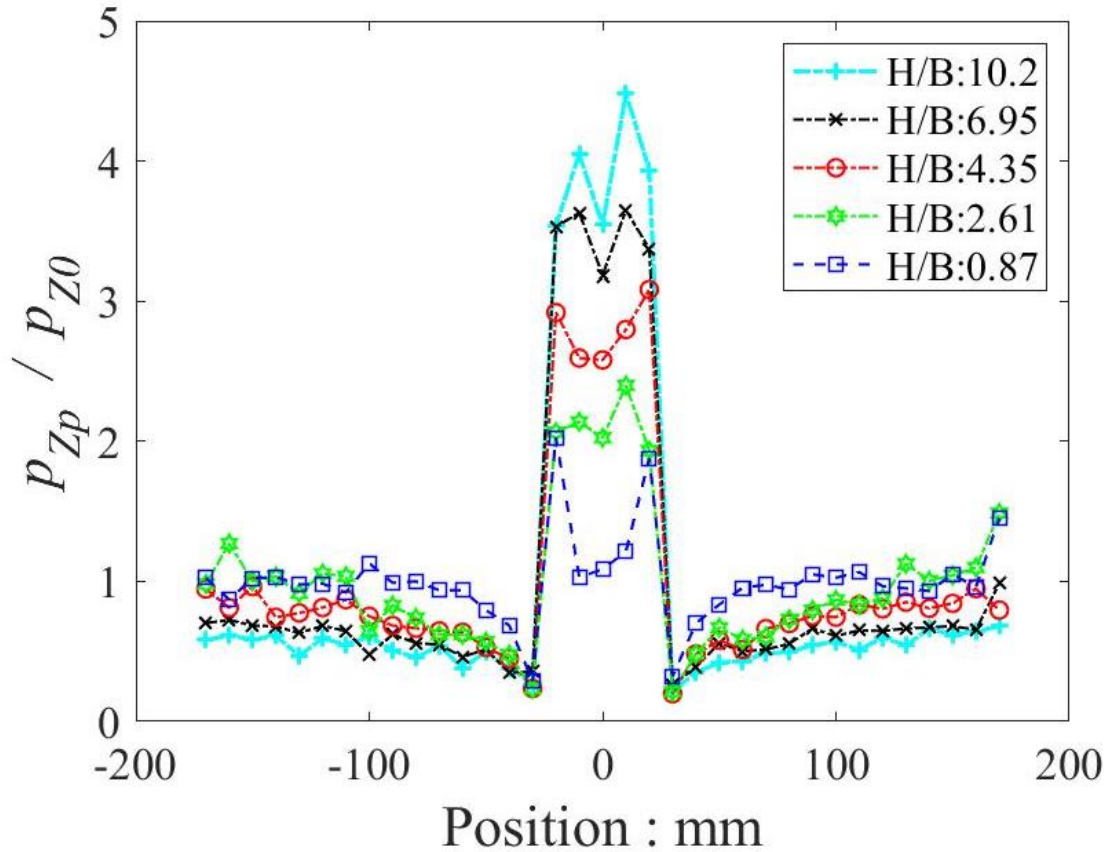


Figure 6.18 Normalized normal stress distribution of trapdoor cases with varying sample height with an $L/B = 7.0$

The normalized normal stress distribution for the given trapdoor configuration is presented in Figure 6.18. The normalized stress values above the central fixed base plate increase with increasing ground heights, as for the previously discussed configurations. The corresponding stresses at the extreme ends, however, showed a reduction. Higher the normalized stress at the central portion, lower the stress at the ends is seen for a similar sample. The cases without any stabilized arching showed normalized stress values approaching unity, representing that there exists a very small difference between the stresses at the central and the side portions.

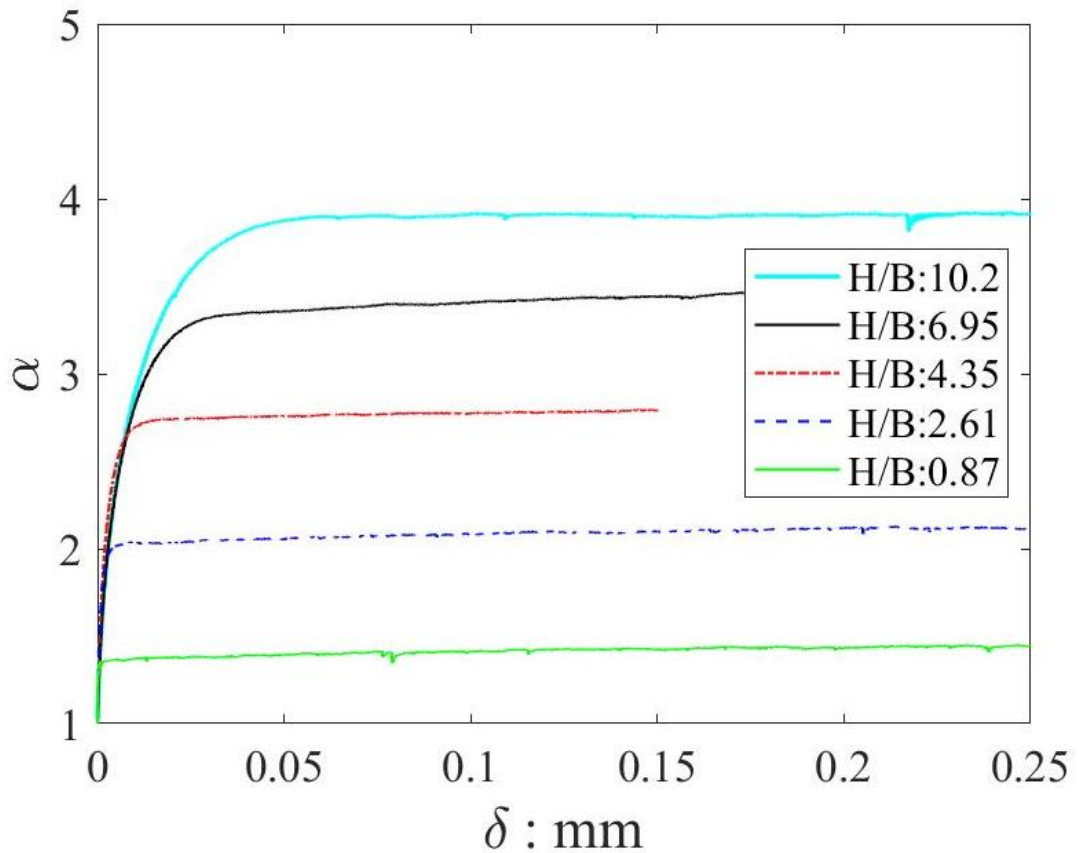


Figure 6.19 ' α ' variation under trapdoor cases with varying sample height with an $L/B = 7.0$

The stress concentration factor at the central fixed base plate represents an increasing behavior with the increasing height of the samples. However, unlike the previously discussed cases, no convergence is seen in this case, showing that the arching action is still evolving, and even higher soil heights are required for the fully established arch. The same can also be represented by the magnitude of α that lies well behind the

theoretical maximum value for the given configuration, approaching 7.0 ($\alpha_{max}^{theoretical} \sim 7.0$).

6.3.4 Trapdoor configuration with nine base plates

Another configuration with a further increased number of base plates is presented in this section, having a total nine (09) number of base plates and having an L/B value of 9.0. Again, all simulation conditions were kept similar to earlier configurations e.g. $\delta = 0.25\text{mm}$, presence of periodic boundaries on the lateral ends and use of spherical particles in all simulations. Similar H/B values were used as discussed in earlier sections.

The current configuration is believed to result in a $\alpha_{max}^{theoretical} \sim 9.0$ as per Eq. 1 presented in the earlier section of this chapter.

The vertical displacement and strong force network for this configuration are presented in Figure 6.20 and Figure 6.21 below, respectively. Similar to Figure 6.16, trapdoor configuration with nine base plates showed a completed arch in only one sample i.e. $H/B = 10.2$. The rest of the samples did not show a completed arch and differential surface settlement was visible at the top portions of the samples.

The strong force chains Figure 6 12 also demonstrated very similar results to that of trapdoor configurations with $L/B = 7.0$. only the sample with the highest ground height showed the existence of uniform surface settlement with the presence of uniformly distributed strong force network in that region.

Trapdoor Configuration = 9 base plates
Total trapdoor lengths = 45cm

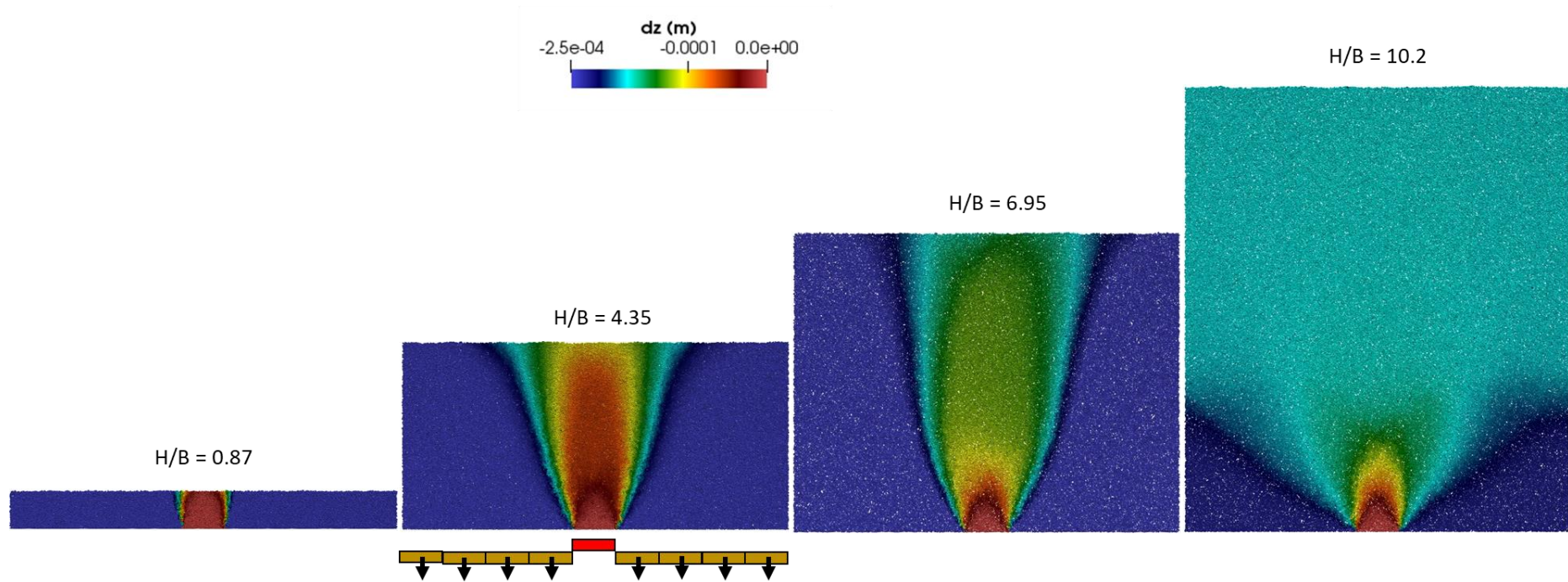


Figure 6.20 Vertical displacement plots for trapdoor configuration with nine (09) base plates, for varying sample heights

Trapdoor Configuration = 9 base plates

Total trapdoor lengths = 45cm

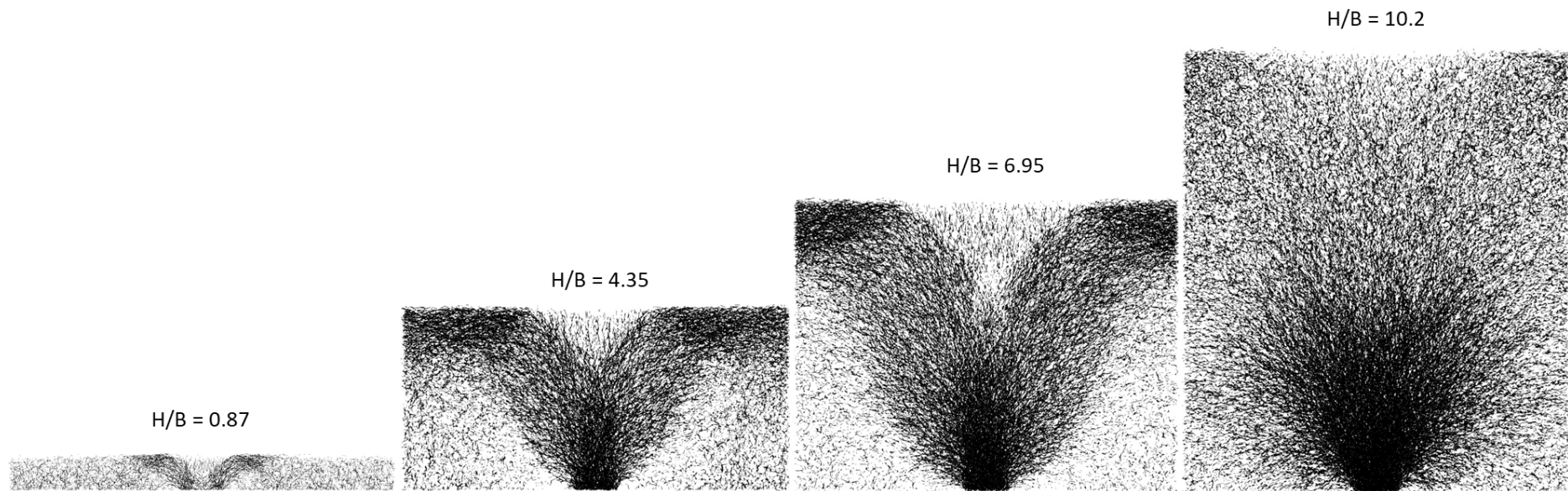


Figure 6.21 Strong force (normalized) plots for trapdoor configuration with nine base plates, for varying sample heights

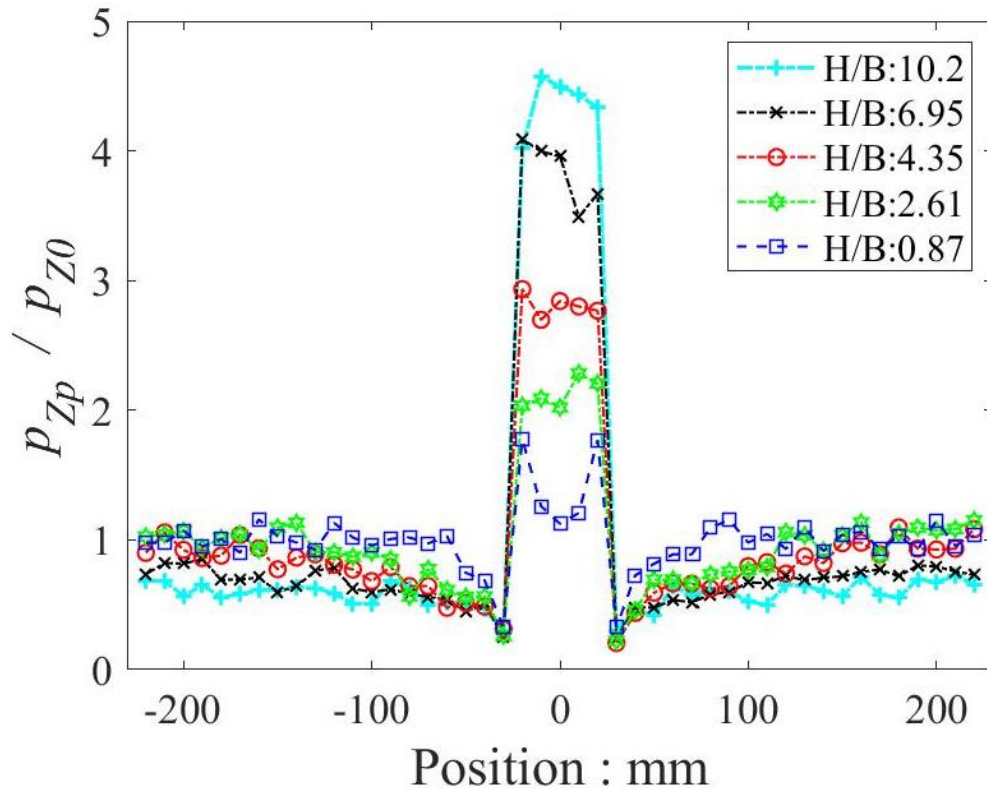


Figure 6.22 Normalized normal stress distribution of trapdoor cases with varying sample height with an $L/B = 9.0$

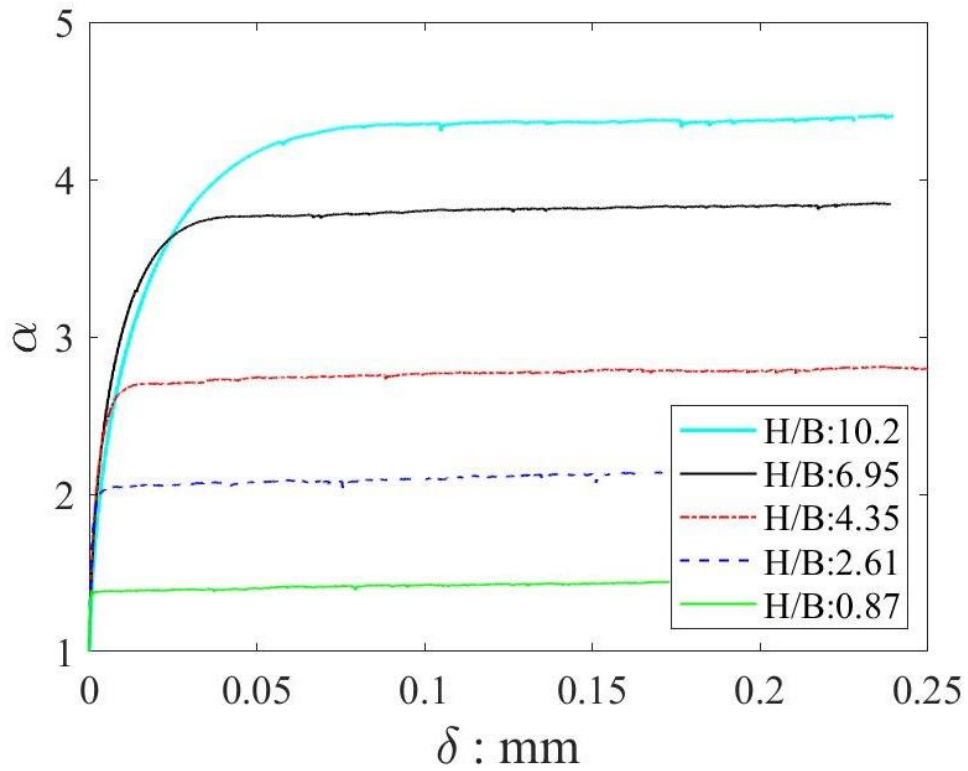


Figure 6.23 ' α ' variation under trapdoor cases with varying sample height with an $L/B = 9.0$

Both normalized normal stress plot (Figure 6.22) and ‘ α ’ plots (Figure 6.23) reiterate the fact that there exists no convergence of normalized normal stress or the stress concentration on the central fixed base plate, with the increasing sample height. This trend is evident that a further higher ground surface level is required for the samples to show a converging trend and to attain the maximum possible normalized stress and the theoretical maximum of stress concentration factor.

6.4 Comparison of different trapdoor configurations

Mutual comparison of varying trapdoor configurations can better focus on the similarities and the differing behaviors. As earlier stated, the highest sample ground surface, having $H/B = 10.2$ showed the presence of the arch through vertical particle displacement plots having uniform surface settlements. However, the amount of this uniform surface settlement increased with an increasing number of base plates. Figure 6.24 shows a similar behavior with $H/B = 10.2$ for all samples, with an L/B value of 3.0, 5.0, 7.0 and 9.0.

The smallest L/B yielded the smallest surface settlement value, represented by the low-value color as associated with the color legend. With increasing L/B , the surface settlement is increasing and the color of the sample near the top boundary changes accordingly as well.

Similarly, in Figure 6.25, a comparison of $H/B = 6.95$ is made for all configuration setups. As seen, an arch exists for the case with $L/B = 3.0$. For the case of $L/B = 5.0$, there is still the presence of the arch. However, the surface settlement values increased, as discussed earlier. Hence, the arching that might be dominant in a particular configuration of trapdoor setup, might not be present in another configuration setup.

The stress concentration factor on the central fixed base plate also varies significantly with the variation in trapdoor configuration. In relation to the theoretical maximum value of stress concentration factor ($\alpha_{max}^{theoretical}$), more and more sample cover above central fixed base plate is required in order to attain a converged value for ‘ α ’. In the case of trapdoor configuration having 15cm total length or $L/B = 3.0$, the ‘ α ’ plot as shown in Figure 6.9, represents a converging behavior with increasing ground surface height. Hence, a further increase in the sample height would not affect arching behavior. Figure 6.5 also shows that there exists no difference between the arching behavior and the amount of surface settlement for H/B values ranging from 3.5 to 10.2, which confirms that a converging state has already been attained for this trapdoor configuration.

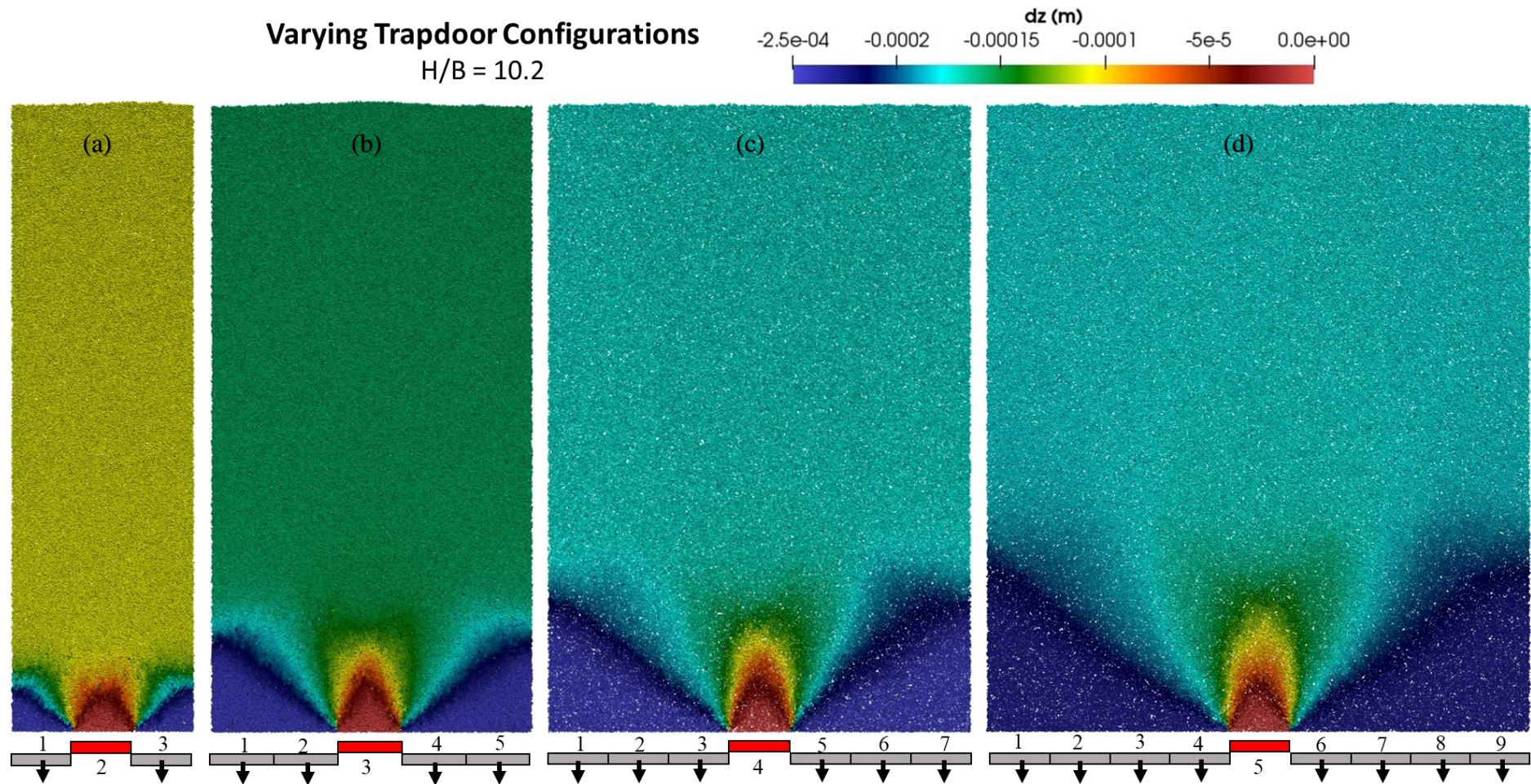


Figure 6.24 Vertical displacement plots for samples with (a) $L/B = 3.0$, (b) $L/B = 5.0$, (c) $L/B = 7.0$ and (d) $L/B = 9.0$, having an $H/B = 10.2$ for all cases

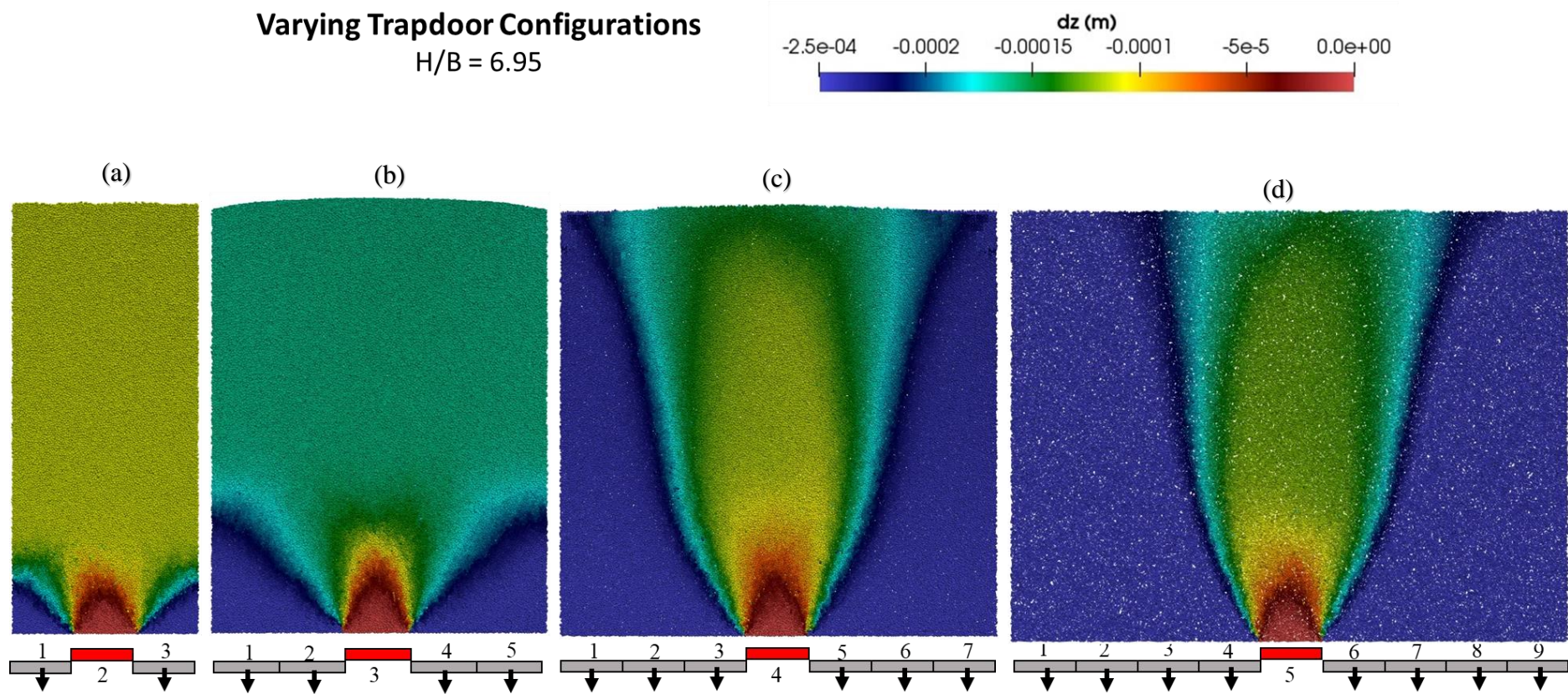


Figure 6.25 Vertical displacement plots for samples with (a) $L/B = 3.0$, (b) $L/B = 5.0$, (c) $L/B = 7.0$ and (d) $L/B = 9.0$, having an $H/B = 6.95$ for all cases

Trapdoor configuration with $L/B = 3.0$ already attained the converging state for the given ranges of sample height. Although, other configurations did not show similar behaviors. The ' α ' values did not reach their maximum possible values for the given cases.

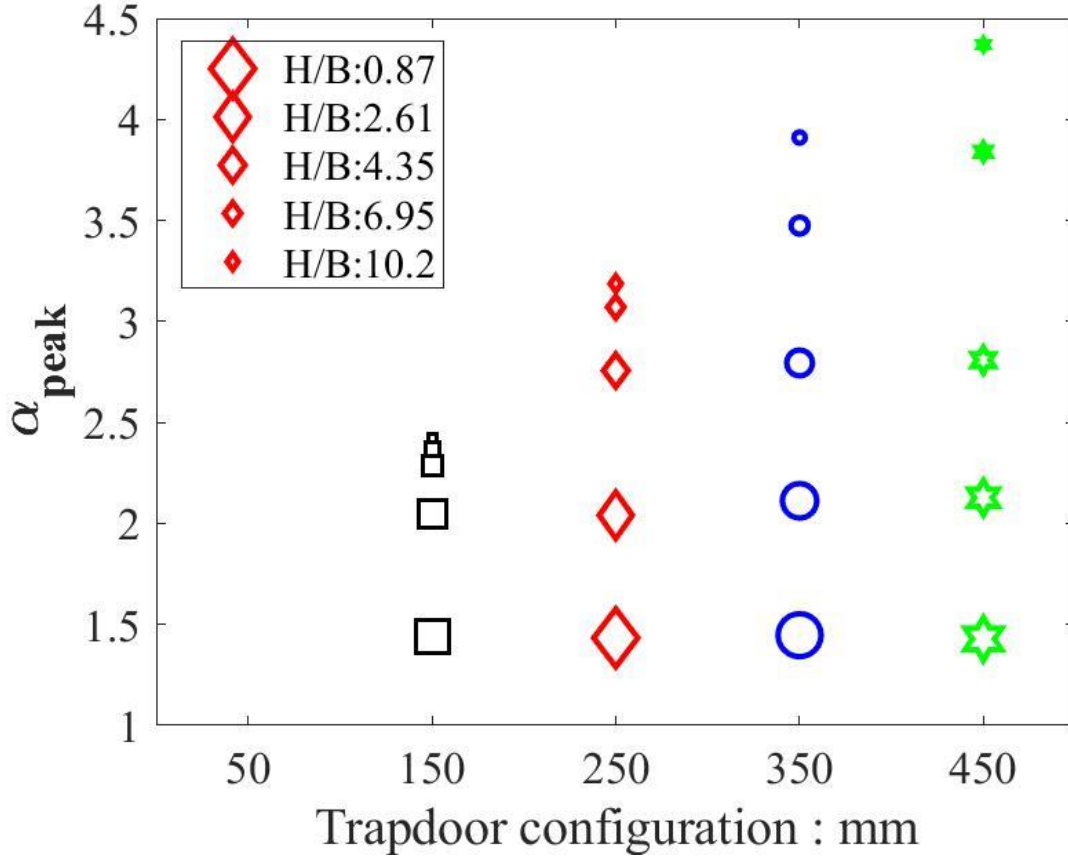


Figure 6.26 Peak values of ' α ' for different sample height with varying configuration values

Figure 6.26 shows the Peak values of ' α ' for all four different configurations of trapdoor simulations. For each type of configuration, different H/B values are plotted. For the 150mm (15cm) configuration case, the α_{peak} values for different sample heights reached a converging value. Similarly, for the 25cm configuration, the α_{peak} values become close to each other. However, the difference is more than the earlier configuration values.

However, for all other configurations, the α_{peak} values are having significant differences amongst themselves, representing a non-convergent behavior. A similar sort of plot with different representation is shown in Figure 6 27. α_{peak} is plotted against the H/B for each trapdoor configuration.

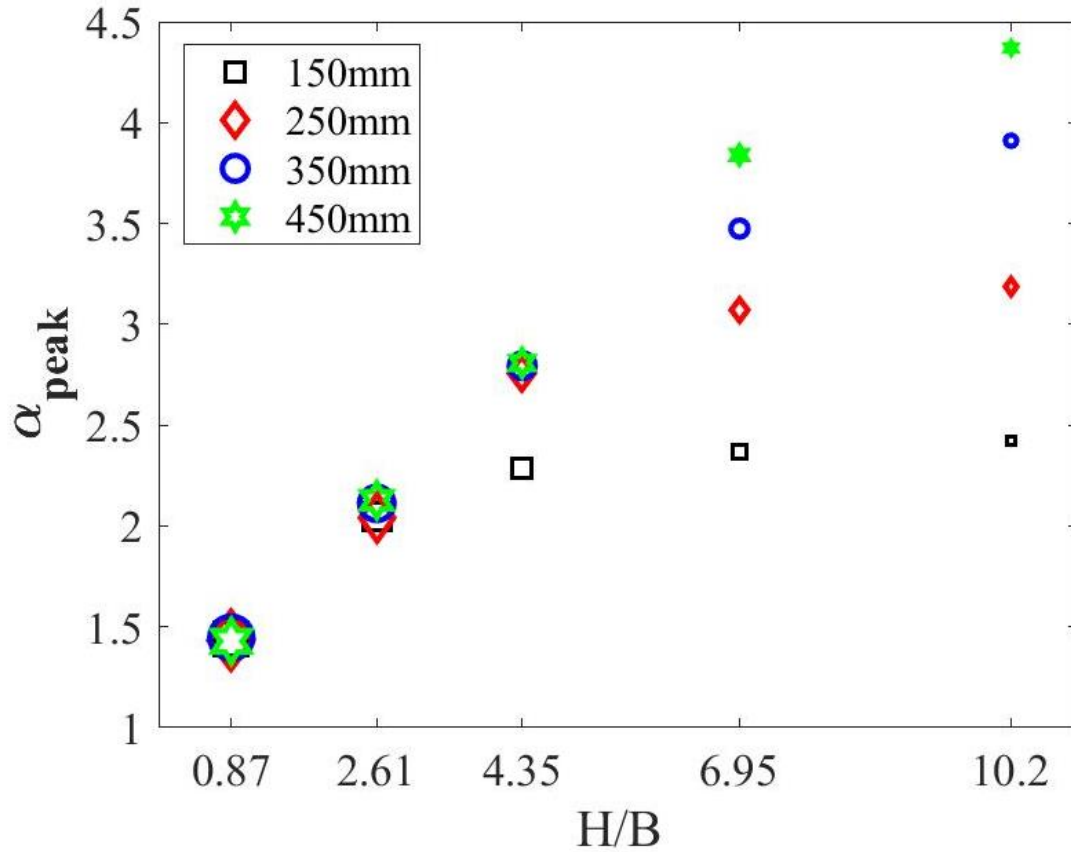


Figure 6 27 ' α_{peak} ' vs H/B for each configuration of trapdoor

A trapdoor configuration with 150mm total length showed an initial rise in α_{peak} with increasing sample ground heights. However, the trend became almost linear, as visible in the above plot. For the 250mm configuration, the trend started reducing for the given range of sample ground heights; however, the trend did not become linear.

For all other trapdoor configurations, the α_{peak} showed a rising trend for the given set of sample heights, and to attain the stable converged value of α_{peak} , much higher ground height sample is required to be analyzed. In short, the cover above static central fixed plate has vital importance in case the configuration of the tests is varied. A specific height of the sample is required under each configuration to attain a stabilized behavior, having a uniform surface settlement with a converged α_{peak} value by having a stabilized arching region inside the sample.

6.5 Converged response of trapdoor condition under any symmetric configuration

As discussed in the earlier section, each trapdoor configuration requires a specific sample ground height above the static central base plate, that keeps increasing with increasing the total length of symmetric trapdoor conditions. However, it is not possible to attain a sample height more than a specific value in model trapdoor tests.

Even in the case of numerical simulations for trapdoor condition, beyond a specific height, it is not feasible to run the simulation, as the number of particles directly increase with increasing trapdoor configuration length (L). A larger number of particles necessitates a significant amount of computational energy. Further to that, increasing particles results in an increasing number of contacts and much larger stiffness matrices in DEM computation, resulting in a much slower response and requiring a significant amount of time for each simulation.

6.5.1 An empirical assessment of stress concentration

Several researchers have performed an empirical assessment of load increment during trapdoor conditions. Mamoru et. al (2004) discussed the estimation of earth pressure around a tunnel face. Similarly, Sloan et al. (1990); Tanaka & Sakai (1993) discussed the stress assessment during trapdoor cases. In connection with the above-stated limitation about using a very large sample size/configuration for obtaining converged values of stress concentration factor, an empirical relation was derived for the trapdoor conditions. The empirical relation was counted for any symmetrical trapdoor configuration to obtain a simple relation between α and H/B .

6.5.1.1 *The shape of the arch*

To evaluate the mechanism about the arch, the shape of the arch is the main factor that influences the load distribution mechanism. It is a prerequisite to have sufficient information about the region occupied by a stable arch.

The arch shape has already been discussed in the literature review (Chapter 2). Different researchers have proposed different arching shapes in soil under varying conditions. Mostly for shallow soil covers, a triangular pattern is suggested

(B. Chevalier et al., 2009). However, for the larger soil sample height, researchers like Handy (1985) and Wang et al. (2013) suggested an inverted catenary shape of the soil arch.

6.5.1.2 The equation for the arch shape

The use of the word ‘catenary’ dates back to the 18th century. It corresponds to a freely hanging chain that is supported by its two ends. The basic shape of the catenary is shown in Figure 6.28 below:

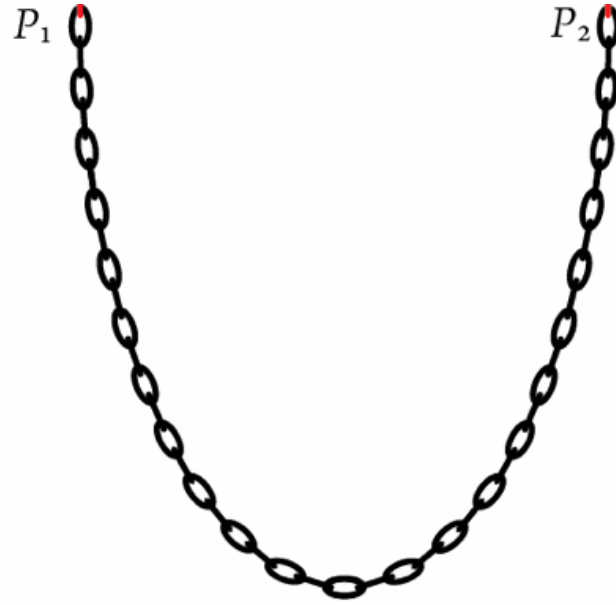


Figure 6.28 Freely hanging chain at two ends, representing a catenary shape

The basic equation for the catenary shape is as below:

$$y = k \cdot \cosh\left(\frac{x}{k}\right) \quad (6.4)$$

where k is a scaling factor for the curve, \cosh is the hyperbolic function of cosine and x is the lowest drop in the curve.

The experimental observations about the shape of the arch during trapdoor conditions also match with the literature as mentioned above. The approximate shapes of the arch while testing Kashima river sand in model trapdoor tests for two

different ground heights are shown in Figure 6.29 below. The arching shapes as observed through model trapdoor tests also matched with the shape of the catenary.

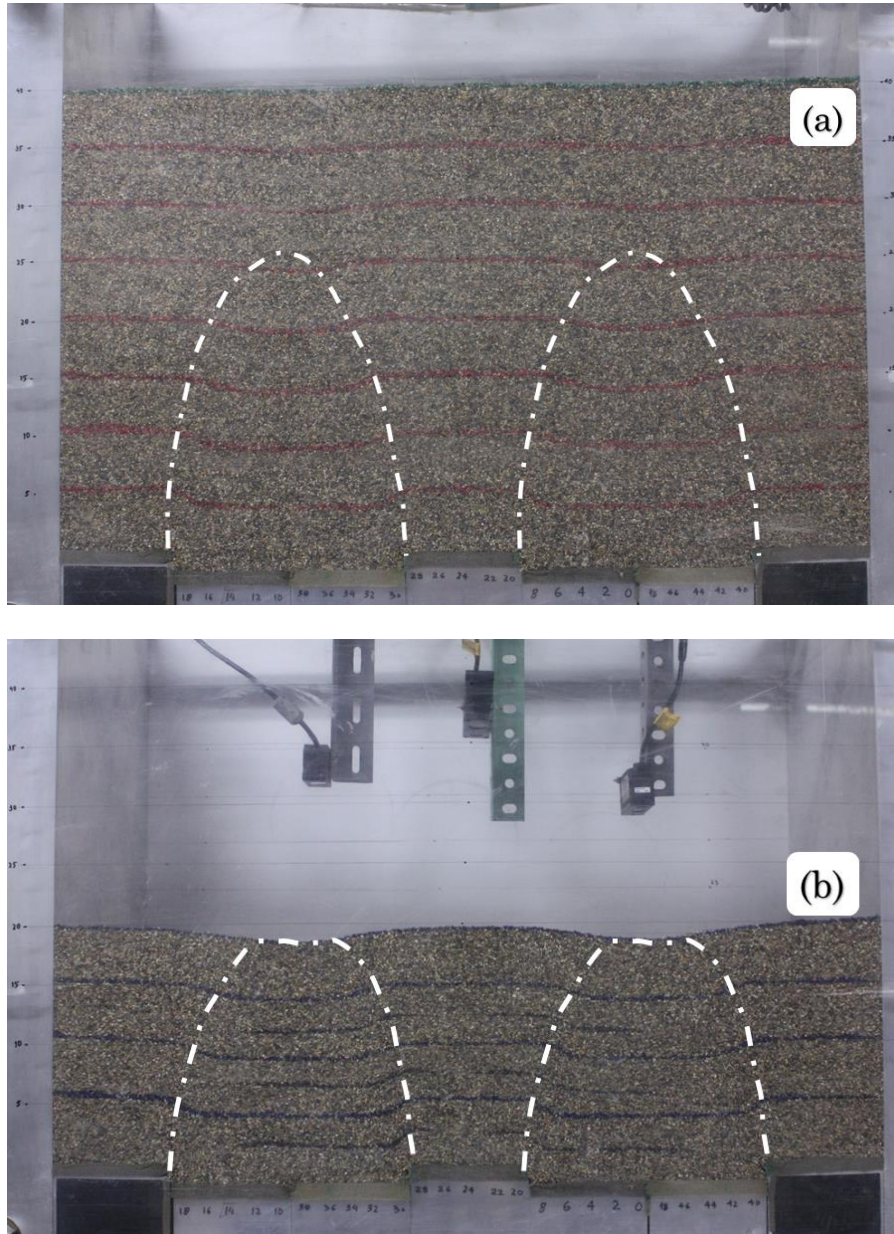


Figure 6.29 Approximate shapes of the arching during model trapdoor tests on Kashima river sand for (a) $H/B = 4.0$ and (b) $H/B = 2.0$

The shape of the arch obtained through DEM simulation results was also believed to follow the equation of catenary by the visual inspection, as shown in the fig below.

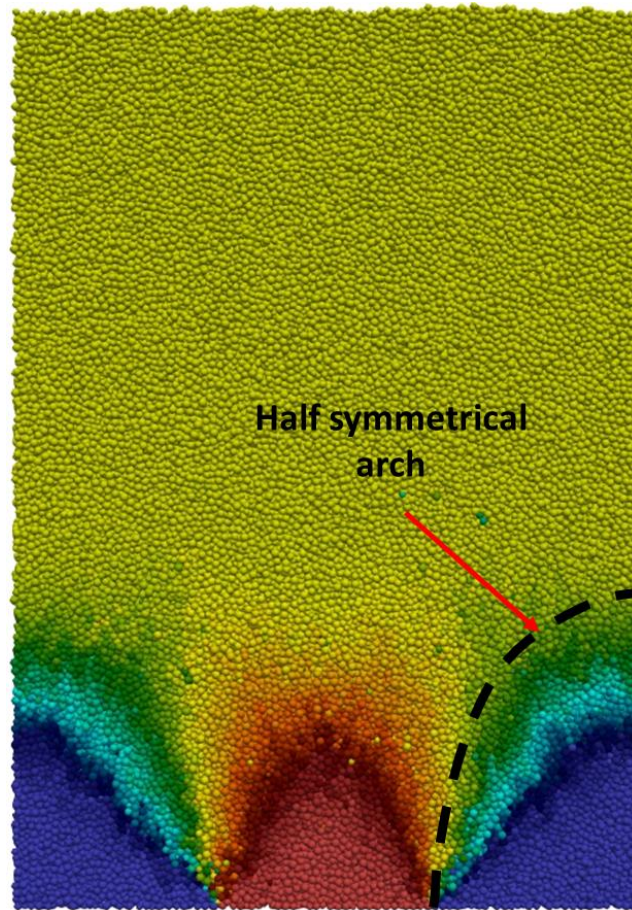


Figure 6.30 Approximate shape of an arch under DEM simulations with a sample having stable arching

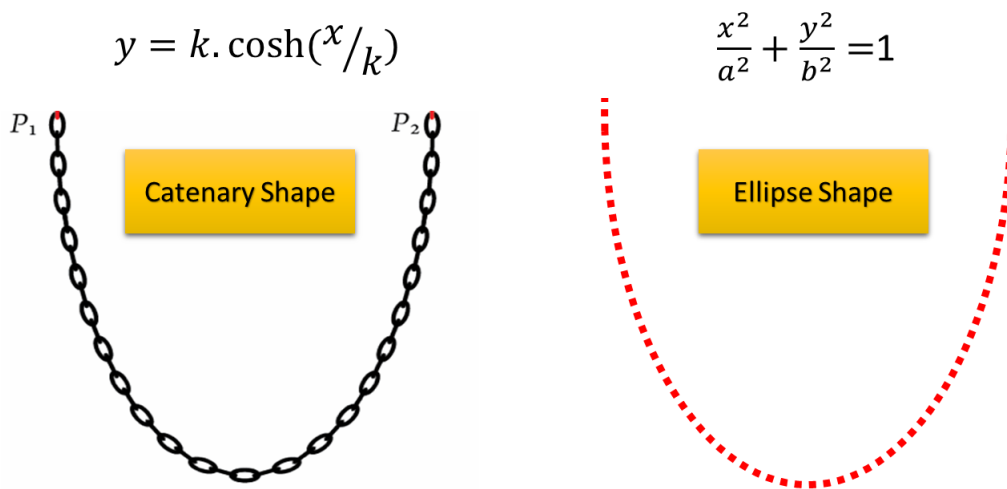


Figure 6.31 Comparison of basic equations for the catenary and the Ellipse shapes

Catenary possesses a shape that is quite similar to the Ellipse shape. However, the equation of Ellipse is much simpler to handle, compared to the catenary shape, as shown in Figure 6.31 above. Hence, for simplicity, the equation of an Ellipse is used to determine the stress distribution in the soil mass under arching action, instead of through catenary shape.

6.5.1.3 Load distribution calculations using Ellipse shape

(a) Fully developed arch

For calculating the load distribution mechanism on the base plates during trapdoor conditions, we need to first understand the basic definition of stress concentration factor, α , as given by Eq. 4.2.

α is the ratio between the final load on the central fixed base plate, representing a buried structure, and the mean of initial load on all base plate including the central static base plate. Foregoing in view, we can re-write the Eq. 4.2 in a simpler manner as under:

$$\alpha = \frac{\text{Final load on fixed plate}}{\text{mean of initial load on all base plates}} \quad (6.5)$$

Where the final load on the central fixed base plate can further be simplified as the difference between the total load (F) and the load taken by the area under arch shape (F'). Also, the mean initial load on all base plates can be represented as the ratio of total initial load (F) to the total number of base plates (N), including the central static base plate; and shown as below:

$$\alpha = \frac{\text{total load} - \text{load taken by arch}}{(\text{total load} / \text{No of plates})} \quad (6.6)$$

$$\rightarrow \alpha = \frac{F - F'}{(F/N)} \quad (6.7)$$

The Eq. 6.7 can further be simplified as follows:

$$\alpha = N \cdot \frac{F-F'}{F} \quad (6.8)$$

$$\rightarrow \alpha = N \cdot \left(1 - \frac{F'}{F}\right) \quad (6.9)$$

Now, in Eq. 6.9, F' is the load excluded by the arching action. As soon as the arch develops, the load of the portion above the arching region is all taken by the arch and transmitted towards each side. Where on each side there exists a fixed central plate (or buried structure). In the presented work, the configuration of DEM simulation is selected in such a way that the half of the symmetrical arch and the whole of the load of the area above the arch is transferred towards the central fixed plate.

Since the arch shape in this section is assumed as Ellipse for simplicity, the basic shape of an ellipse with its dimensions is shown in Figure 6.32 below. The arching pattern developed during the trapdoor simulations is $1/4^{\text{th}}$ of the total area of an ellipse. An ellipse consists of two radii, one with the shorter side is named as ' r_1 ' whilst the one with larger side is named as ' r_2 '.

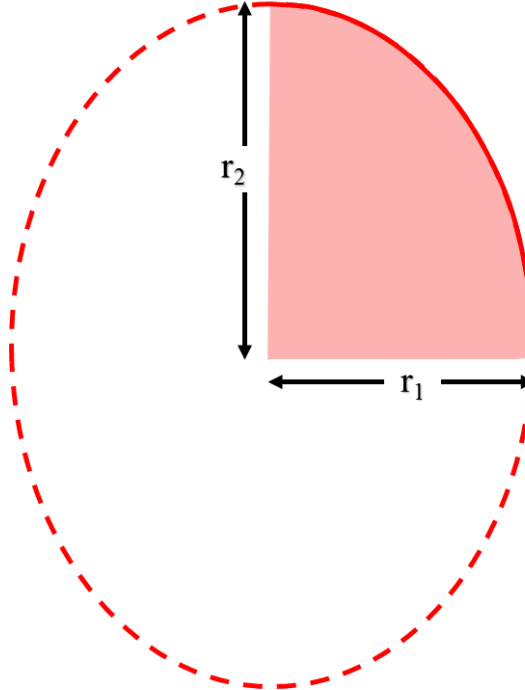


Figure 6.32 Ellipse with its constituting dimensions

An approximate shape of arching in a DEM simulation sample is shown in Figure 6.33 below, where the arching region, which is $1/4^{\text{th}}$ of the shape of an ellipse with radius ' r_1 ' and ' r_2 '. Each simulated sample contains lowering trapdoors on each side of the central fixed base plate, hence there would exist two arching regions on each side.

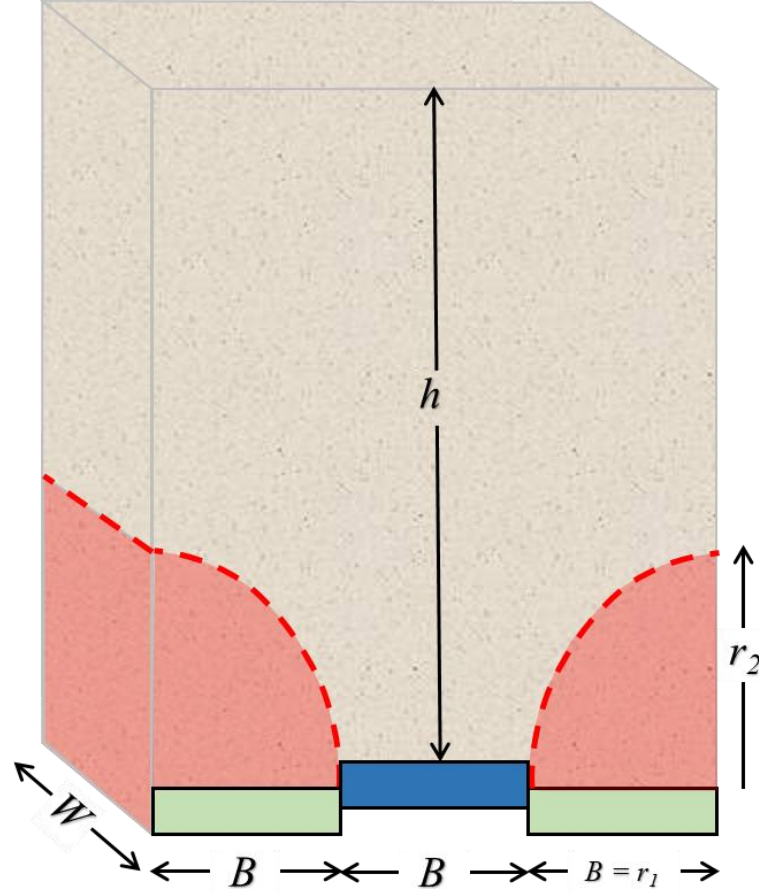


Figure 6.33 Representation of a DEM sample having two ellipsoid portions constituting arch

Subsequently, keeping in view the figures presented above, the load carried by the arch (F') in the soil sample can be simplified by the following equations:

$$\text{are of the ellipse, } A_{\text{ellipse}} = \pi r_1 r_2 \quad (6.10)$$

$$\rightarrow F' = \left[\frac{1}{4} \times A_{\text{ellipse}} \times W \times \gamma \times g \right] \times 2 \quad (6.11)$$

Where the W is the sample width in Y-direction, γ is the unit weight of the sample, g is the gravitational acceleration to convert units into Newton. Since the arching region on either side of the sample constitutes $1/4^{\text{th}}$ of the total ellipsoid shape, the equation is divided by 4; and multiplied by 2 to represent two arching regions. If the width of each base plate is taken as ' B ', and sample ground height as ' h ', the Eq. 6.9 can be re-written as:

$$\alpha = N. \left(1 - \frac{\left[\frac{1}{2} \times A_{\text{ellipse}} \times W \times \gamma \times g \right]}{N.B.W.h \times \gamma.g} \right) \quad (6.12)$$

Here, the product of $N \times B \times W \times h$ defines the overall boundary of the sample and is taken as the volume of the sample, V . Also, the area of the ellipse is dissolved into its constituents. Hence, the modified equation is then represented as:

$$\alpha = N. \left(1 - \frac{[\pi r_1 r_2 \times W]}{2 \times V} \right) \quad (6.13)$$

Now, as seen from Figure 6.33, the shorter radius r_1 can also be represented in terms of the number of base plates. If the total number of plates is N , then the r_1 is given by:

$$r_1 = \frac{N-1}{2} \quad (6.14)$$

Since only one central base plate is kept static, hence the above relation contains $(N-1)$. Furthermore, the longer radius r_2 can also be expressed in terms of r_1 . A factor k , such that $k = r_2/r_1$ is used and the Eq. 14 would result as:

$$\alpha = N. \left(1 - \pi r_1 \times k r_1 \times W / 2V \right) \quad (6.15)$$

$$\alpha = N. \left(1 - \frac{N-1}{2} \times k \frac{N-1}{2} \times \pi W / 2V \right) \quad (6.16)$$

$$\alpha = N. \left(1 - k \left(\frac{N-1}{2} \right)^2 \times \pi W / 2V \right) \quad (6.17)$$

Consequently, the final expression for the stress concentrator factor, α can be represented as below:

$$\alpha = N. \left[1 - \left\{ \pi k (N-1)^2 \cdot W / 8V \right\} \right] \quad (6.18)$$

In Eq. 6.18, k that is the ratio of larger radii to the smaller radii of the elliptical arch, largely depends upon the density of the material and the angularity of the particles. Hence it can be called the ‘dilation factor’. For a circular arch, $r_1 = r_2$, whilst the sample becomes looser or the particle shape becomes less angular, the k becomes larger that results in reduced α value.

(b) Absence of arching

For the cases when sampling ground height is short and the development of the arch is not possible, the load transfer mechanism is different than the earlier discussed cases. From Figure 6.5, Figure 6.11 and similar other plots, it is evident that the soil arching doesn’t exist fully unless the ground sample height is equal or more than twice the length of the lowering portion. Mathematically, the minimum height required for arching h_{arch} can be expressed as:

$$h_{arch} \geq 2 \times (N - 1/2)B \quad (6.19)$$

Through the observation and calculations, it was found that the tangent angle of the arch for the shallow ground sample heights, as specified through Eq. 6.18, measures to be approximately 70 degrees from horizontal. For simplicity, the arching pattern was assumed to be linear with the given angle until it reaches the surface. Hence the area of the portion under the arch for shallower sample heights can be divided into two portions, as shown in Figure 6.34. Portion 1 is rectangular and the portion 2 is the simplified triangular-shaped area. Resultantly, the weight of the sample under the summation of the above-mentioned area is taken for the calculation of stress concentration calculations.

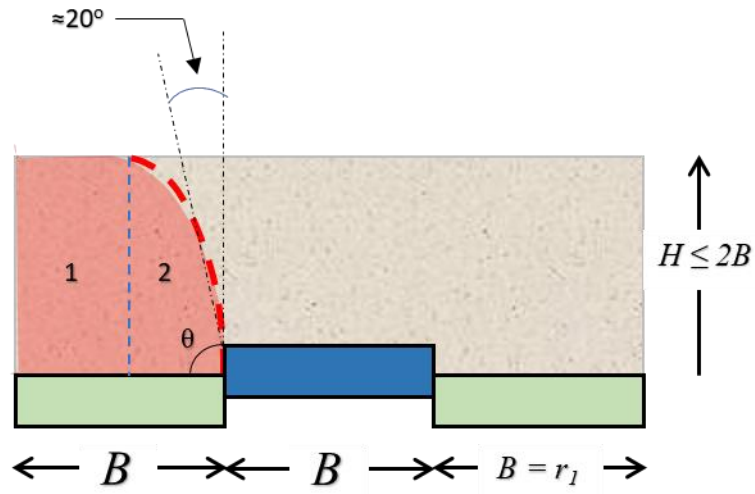


Figure 6.34 Arching surface for shallower ground sample heights

The resultant area for the shallower ground height samples is given by the equation below, having an initial arch angle θ :

$$\text{Area under arch} = A_1 + A_2 \quad (6.20)$$

Where; $A_1 = 1/2[h \times (h/\tan\theta)] \quad (6.21)$

$$= 1/2 \left[\frac{h^2}{\tan\theta} \right] \quad (6.22)$$

$$= \frac{h^2}{2\tan\theta} \quad (6.23)$$

and
$$A_2 = h \times \left[\frac{(N-1)}{2} - \frac{h}{\tan\theta} \right] \quad (6.24)$$

The summation of Eq. 6.23 and Eq. 6.24 gives the total area under the arch and the area is used in a similar manner as described earlier to calculate the load and then stress concentration factor on the central static base plate.

The resultant data, as obtained from the two cases presented above; namely (a) for the stabilized arch case and (b) for the case with the absence of arching action, are plotted with varying trapdoor configurations, having a symmetrical layout around the central fixed base plate. Furthermore, each configuration is further divided into several sample heights, ranging from very shallow to very deep. The dilation factor k was varied, which represented the variation in either sample density or the angularity of the particles.

Approximate arch shape as shown in Figure 6.5 for DEM simulations and Figure 6.29 for model trapdoor tests suggests that an approximate value of $k = 1.5$. Furthermore, from Figure 6.9, the maximum theoretical value of α obtained for the given range of H/B showed a value of approximately 2.5 with trapdoor configuration of $L/B = 3.0$ (total trapdoor length of 150mm). When we plot the similar α_{peak} variation using the above presented empirical relations, the peak value with $k = 1.5$ reached 2.7 (Figure 6.35) approximately, which is not much differing from the experimental and numerical values for a similar setup.

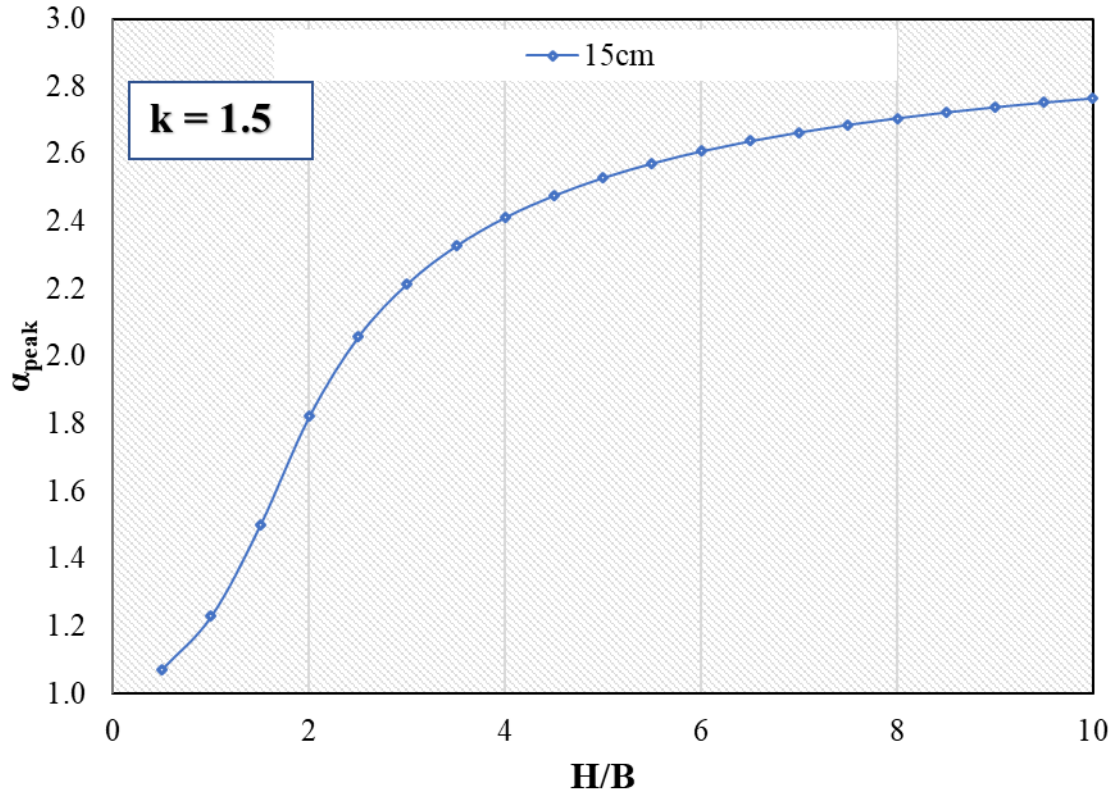


Figure 6.35 α_{peak} values obtained through empirical relation, for varying H/B with $L/B = 3.0$

However, it is believed that a reduction in k values would increase the overall α_{peak} response of the sample. Figure 6.36 represents the stress concentration factors obtained through the above derived empirical equation for the condition having $k = 1.0$, meaning that the arch possessed a circular shape for the presented results. Each line in the plot represents a specific trapdoor configuration, plotted for a large range of H/B .

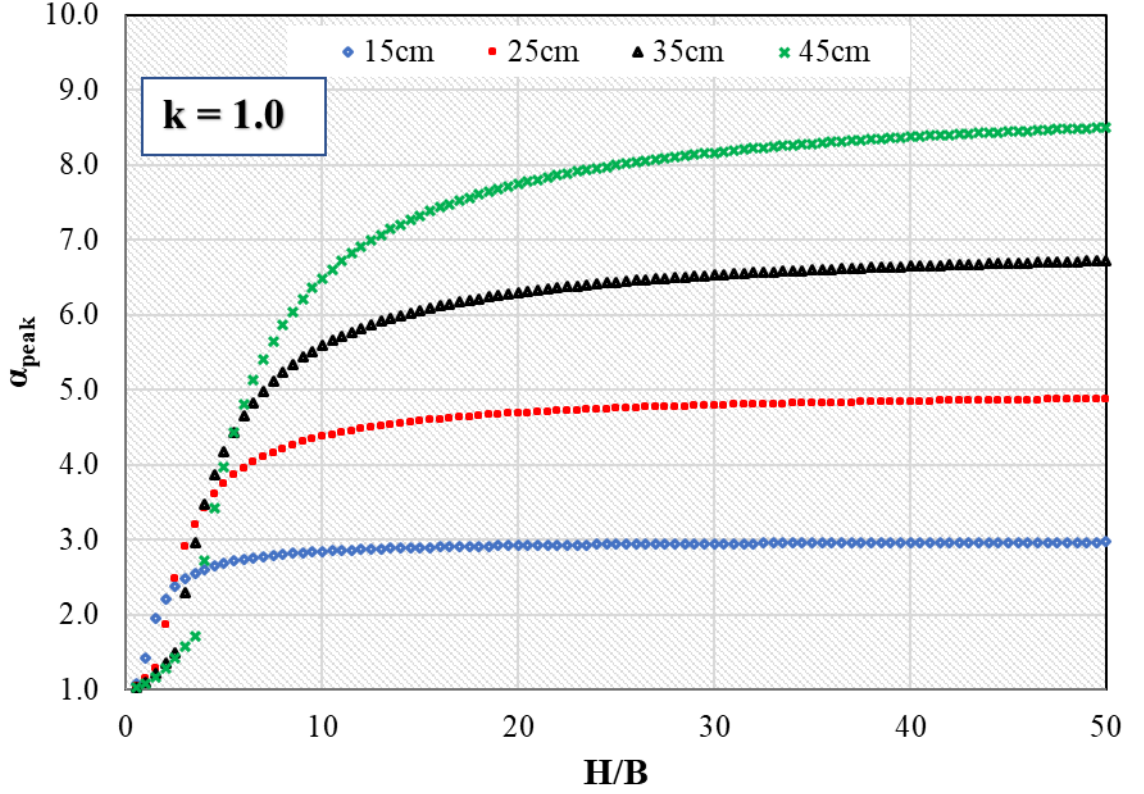


Figure 6.36 α_{peak} values obtained through empirical relation, for different trapdoor configurations with $k = 1.0$

For the initial change in H/B , there is a striding rise in the corresponding α_{peak} , however; the increment slows down with higher H/B values up to a certain limit. Afterward, the slope becomes very gentle and it becomes difficult to obtain the absolute peak value. The maximum value of α_{peak} for the given range of the plot could be referred to as the $\alpha_{max}^{theoretical}$ for the given configuration of the trapdoor test. Though it is impossible to reach the ideal theoretical maximum value for any configuration, a value of α ranging up to $0.9 \times \alpha_{max}^{theoretical}$ value is thought to be the representative maximum value. From the figure above, it clear that the trapdoor configuration with a total length of 15cm (150mm) attained the representative maximum α_{peak} value for a corresponding $H/B \approx 7.0$ m (Figure 6.36).

Similarly, for trapdoor configuration of 25cm ($L/B = 5.0$), the theoretical maximum representative value is approximated at an $H/B = 15$. However, for further increasing trapdoor configuration cases, it becomes difficult to assess the representative theoretical maximum α_{peak} value as the curves still show a significantly increasing trend for the given range of H/B . Though, changing the k

values for the plot could change the overall behavior of the plots. The below figures represent the α_{peak} plots for different k values.

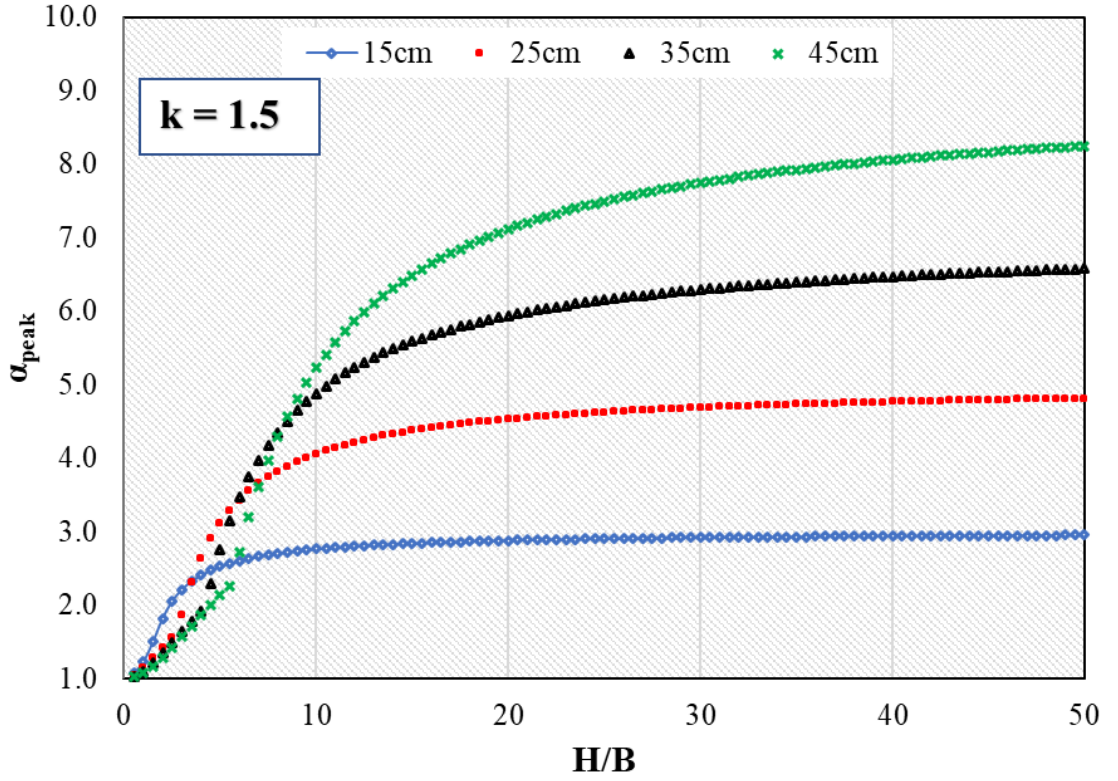


Figure 6.37 α_{peak} values obtained through empirical relation, for different trapdoor configurations with $k = 1.5$

With an increased dilation factor k up to 1.5 (Figure 6.37), the slopes became flatter compared to a smaller value of k with the smaller initial rise in corresponding α_{peak} values. For a trapdoor configuration with a total length of 35cm ($L/B = 7.0$), the representative maximum α_{peak} can be approximated at $H/B \approx 20$. Further increase in k factor significantly reduced the initial α_{peak} values, representing difficulty to obtain a stabilized arch (Figure 6 38).

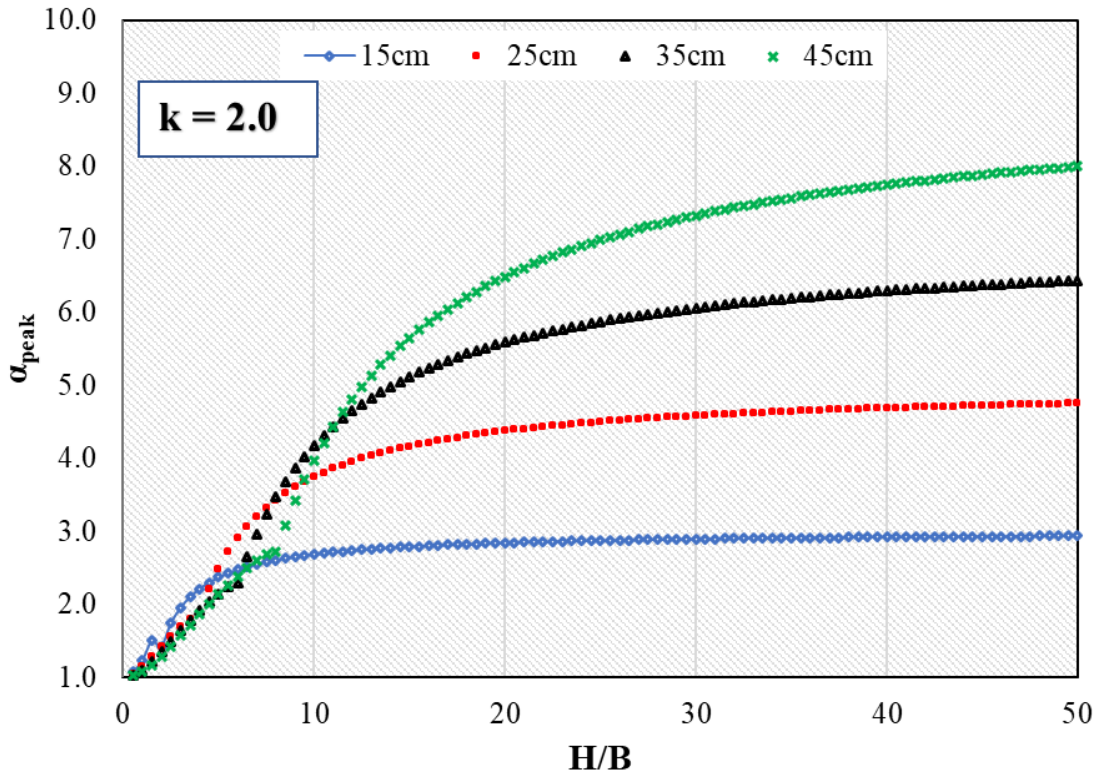


Figure 6.38 α_{peak} values obtained through empirical relation, for different trapdoor configurations with $k = 2.0$

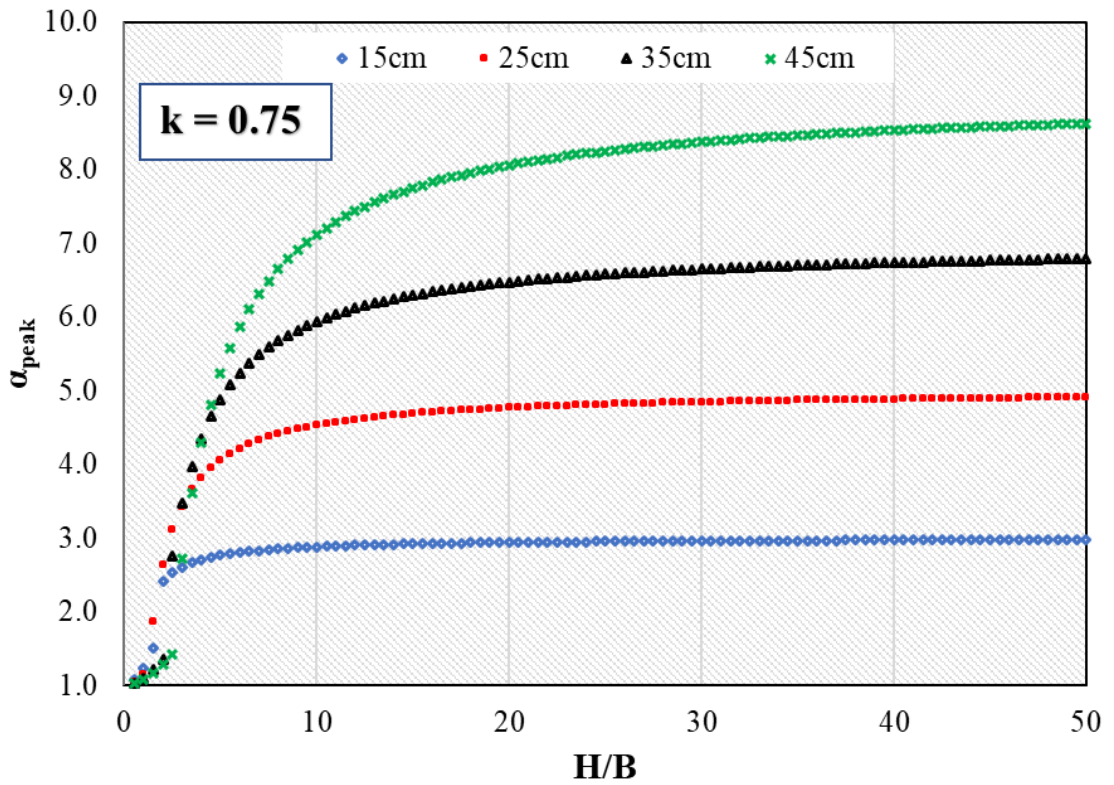


Figure 6.39 α_{peak} values obtained through empirical relation, for different trapdoor configurations with $k = 0.75$

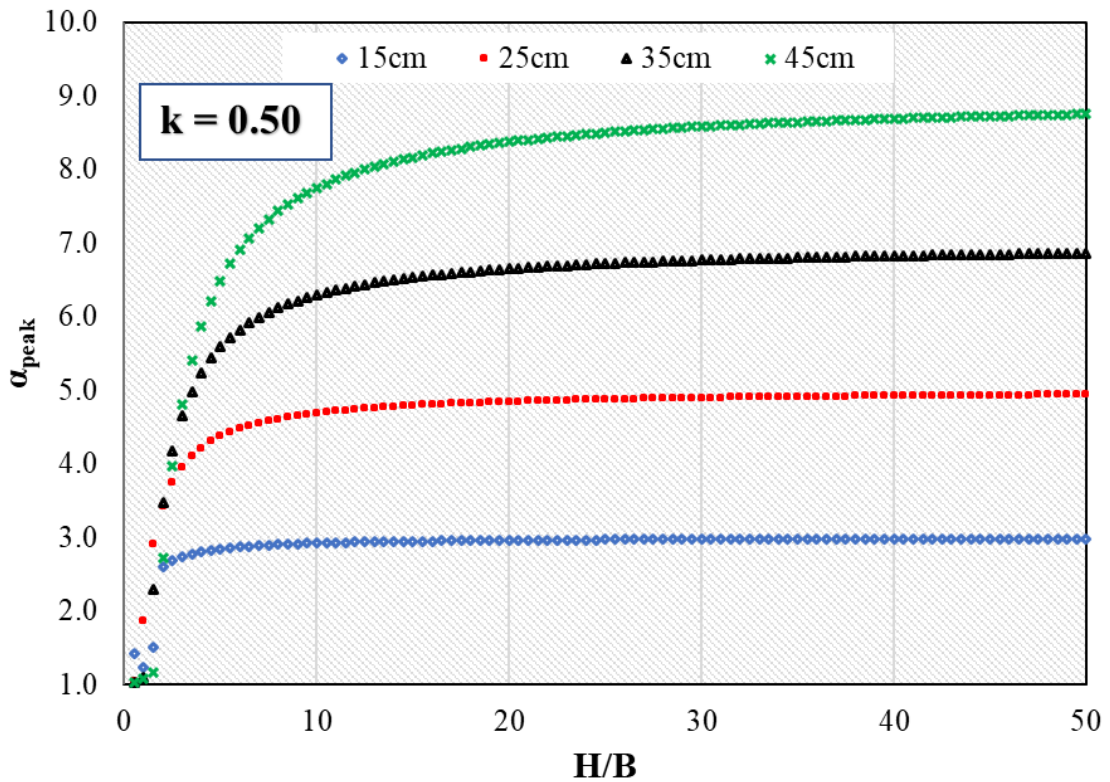


Figure 6.40 α_{peak} values obtained through empirical relation, for different trapdoor configurations with $k = 0.50$

Besides the increase in dilatancy factor k , there could exist a condition that may yield a k value smaller than 1 (i.e. $r_1 > r_2$, or the elliptical shape have the major axis parallel to the horizontal surface). Such a condition can exist for very dense samples with the ones with very high H/B values that could cause a significant accumulated overburden at the base. Figure 6.39 and Figure 6.40 represents such condition with $k = 0.75$ and 0.5 respectively. The maximum theoretical values are obtained much earlier in these conditions and there is a sudden rise in α_{peak} value for the initial rise in H/B .

(c) Limitations:

The empirical method for the stress concentration extrapolation on the buried structures or the central fixed base plate during a trapdoor condition can approximate the trend with different trapdoor configurations. However, there is a

need to do extensive experiments with varying soil types, density and sample heights to define the value ranges for the dilation factor k . The above-presented figures are plotted for hypothetical values of k , that might be used only as an approximation of stress distribution trends during trapdoor conditions with different configurations.

Furthermore, the calculations for stress estimation are divided into two main regions. One with sample height lesser than $2 \times r_I$ and other with the height greater than the given criteria. There exists a critical point when the sample height is exactly as the given condition, causing a sudden change in stress distribution. For a better load distribution network, the stress variation from one condition of sample heights to others should be more gentle for a better comparison.

6.6 Effect of varying static plate width

The trapdoor configuration discussion, including the one in previous chapters, all consisted of a situation where the widths of the central fixed base plate are same as that of the lowering trapdoors, or the widths of lowering trapdoors are larger than the central fixed trapdoor but a multiple of the static plate width. In the current section, the width of the central static base plate is varied and increased than the width of lowering trapdoors on either side.

Table 6.6 Simulation plan with variable central static base plate widths

No.	L (mm)	Central plate width, B (mm)	Side base plate width (mm)	H/B	L/B
1	150	50	50		3.0
2	175	75	50		2.33
3	200	100	50	4.35	2.0
4	250	150	50		1.67
5	250	50	50		5.0

As the model trapdoor test apparatus couldn't be used for this purpose due to the physical limitation of the equipment, DEM based numerical simulations were performed for this specific series. Table 6.6 shows the simulation plan used under this specific work.

The boundary condition for each sample resembled the ones discussed earlier in this chapter. Periodic lateral boundaries were provided with $H/B = 4.35$ for all simulations. Spherical particles having a mean diameter $D_{50} = 1.7\text{mm}$ ($1.2\text{mm} - 2.2\text{mm}$) were used. The void ratio values resulted in approximately 0.610 for all cases. The simulations were performed for a trapdoor settlement $\delta = 0.25\text{mm}$, like that of earlier simulations.

6.6.1 Stress response

The normalized normal stress responses for the samples are presented in Figure 6 41. Four cases with varying central static base plate width are presented in the plot.

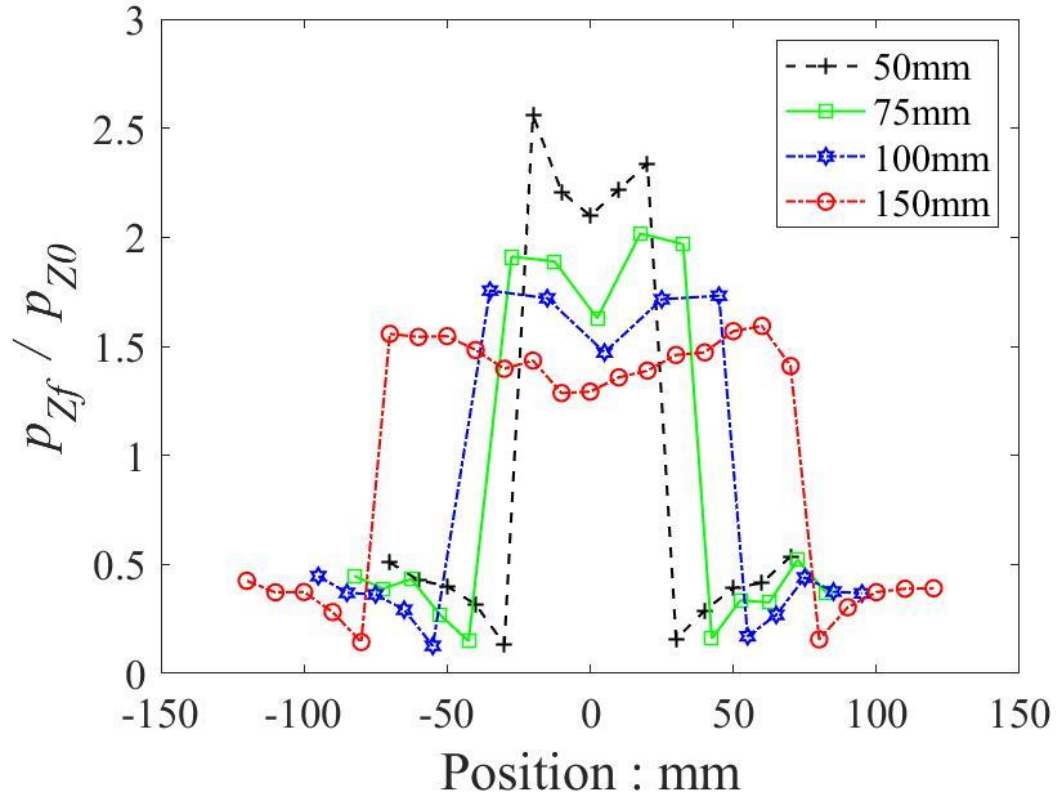


Figure 6 41 Normalized normal stress distribution with different central static plate widths

Surprisingly, the sample with the least central plate width of 50mm, where the maximum normalized stress value reached higher than 2.5, whilst the largest central base

plate width (150mm) resulted in a value of approximately 1.5. This difference is related to the share of the load being distributed on the central base plate.

For the case with a base plate width of 50mm, the central base plate bears not only a load of material right above their location but also a significant portion of the load from the material above side plates, based upon the arch shape being formed. For the cases with smaller side plate widths, the load of the portion added to the load of the central static plate is insignificant when the central base plate itself possesses large width (e.g. 150mm), whilst the load sharing is quite significant when the central base plate had a smaller plate width (e.g. 50mm). Table 6.7 shows a better comparison of the stress increment response under each condition.

Table 6.7 Maximum possible stress increase on the central static plate under different width combinations

Total sample width (mm)	Central plate width (mm)	Max. possible load increase on the central plate (%)
150	50	300
175	75	233
200	100	200
250	150	167

The shear stress distribution under different conditions of central base plate widths is shown in Figure 6.42. The shear stresses did not vary much with varying the width of the central static plate. All samples presented a positive shear stress distribution above the right-half portion of the sample, representing the formation of an arching action within the sample. A similar response mechanism is explained in detail in Chapter 5 under the shear stress distribution section. The relative magnitude of shearing stresses differed slightly to each other for given cases.

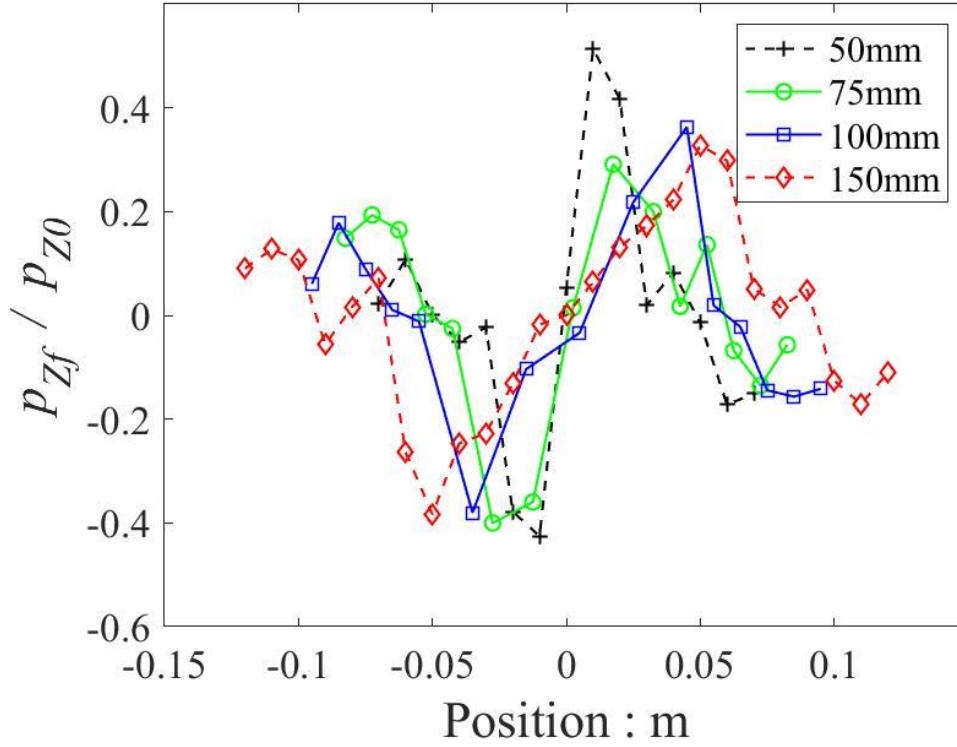


Figure 6.42 Shear stress distribution for varying central static plate widths

6.6.2 Stress concentration factor ' α '

The stress increment on the central static plate showed a similar trend as that of normalized normal stress plots. ' α ' plots for all four samples are presented in Figure 6.43. Similarly, the sample with the least central plate width demonstrated the highest α value and vice versa for the large base plate sample.

' α_{peak} ' values are larger for the smaller values of the central base plate width. However, in terms of maximum theoretical stress concentration factor $\alpha_{max}^{theoretical}$, all four samples tried to attain that maximum value. For example, the sample with a 150mm width of the central plate, each side plate consisted of 50mm, totaling to 100mm of side plates. The dimension of side plates (100mm) corresponds to 0.67 times as that of the dimension of the central fixed plate (150mm). Hence the maximum theoretically possible stress increase that side plates can contribute towards the central plate is 0.67, which makes the total load increment on the central fixed plate to 1.67 times the initial load. In the figure below, however; the largest width sample showed a ' α_{peak} ' value of about 1.4.

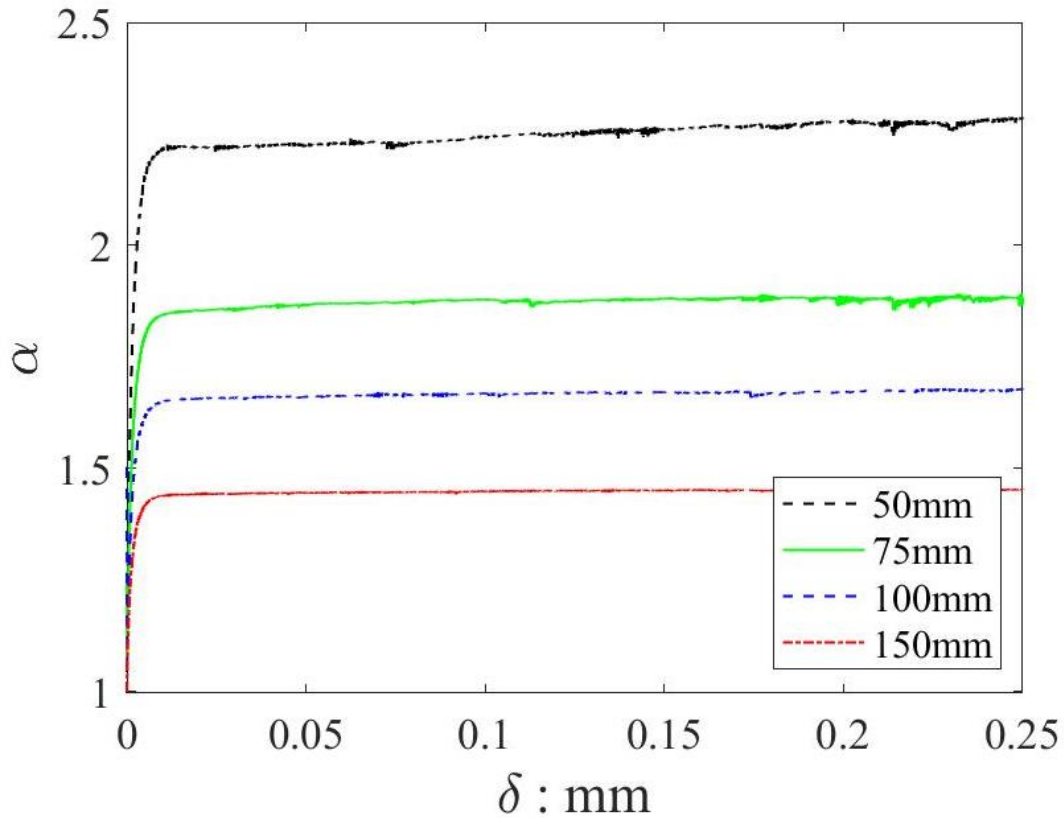


Figure 6.43 ' α ' variation with trapdoor movement for different central base plate widths

In a similar manner, the least width case can have a maximum possible load increment of 3.0 compared to the initial condition, whilst the ' α_{peak} ' value attained in the simulation is around 2.3. Hence, the largest sample yielded around 82% of the maximum possible stress increment, whilst the least width sample showed around 79% of theoretical maximum stress increment.

The variation of ' α ' above the central fixed plate is always increasing compared to the initial condition due to the formation of the arching action in the sample. However, the ' α ' variation above the side lowering trapdoors showed a reverse trend. With the increasing width of the central fixed plate, the ' α ' values reduce more. Though, the reduction is not so significant; however, the reduced value for larger fixed plate width signifies the better efficiency of trapdoor configuration for taking higher stresses due to a better arch formation. It is so, as the more reduction on the sides means higher load transfer in the central portion due to the conservation of total stresses in the soil mass due to overburden at any instance of testing.

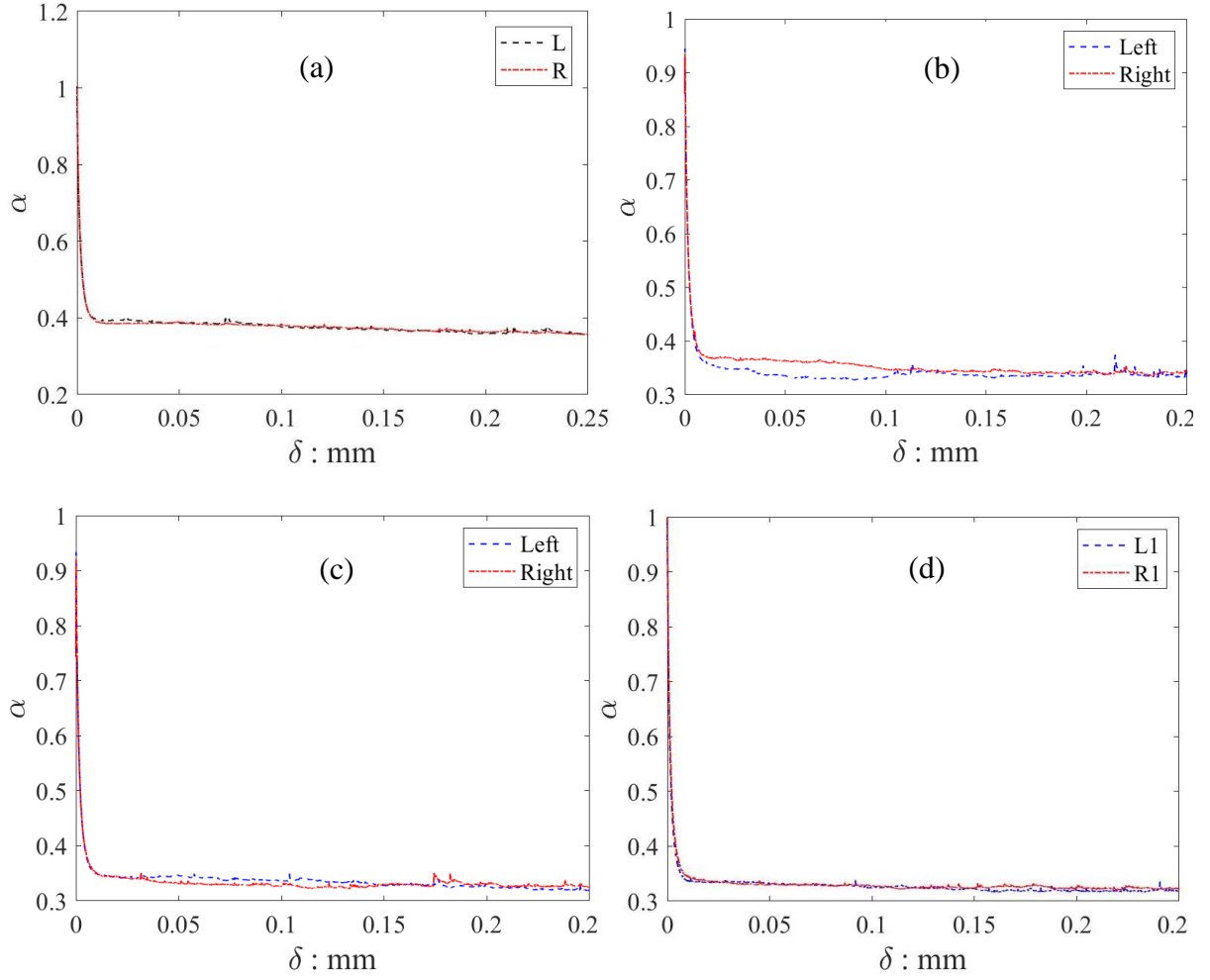


Figure 6.44 ' α ' variation on the side trapdoors for central plate width of (a) 50mm, (b) 75mm, (c) 100mm and (d) 150mm

6.6.3 Particle vertical displacement plots

The best means to visualize the arch formation is the vertical displacement plots at the particulate level. All four conditions of the sample are presented below in Figure 6.45. The blue color in the plots represents the moving particles and the red color corresponds to the static portions. In the plot with 50mm central plate, the arching region showed a little shorter height compared to the rest of the cases that all presented very similar arching conditions. Visually, the arching angle can also be corresponded to have identical values under all different conditions. A similar observation was also made in the earlier sections of this chapter with all samples under certain configurations that demonstrated stable arching.

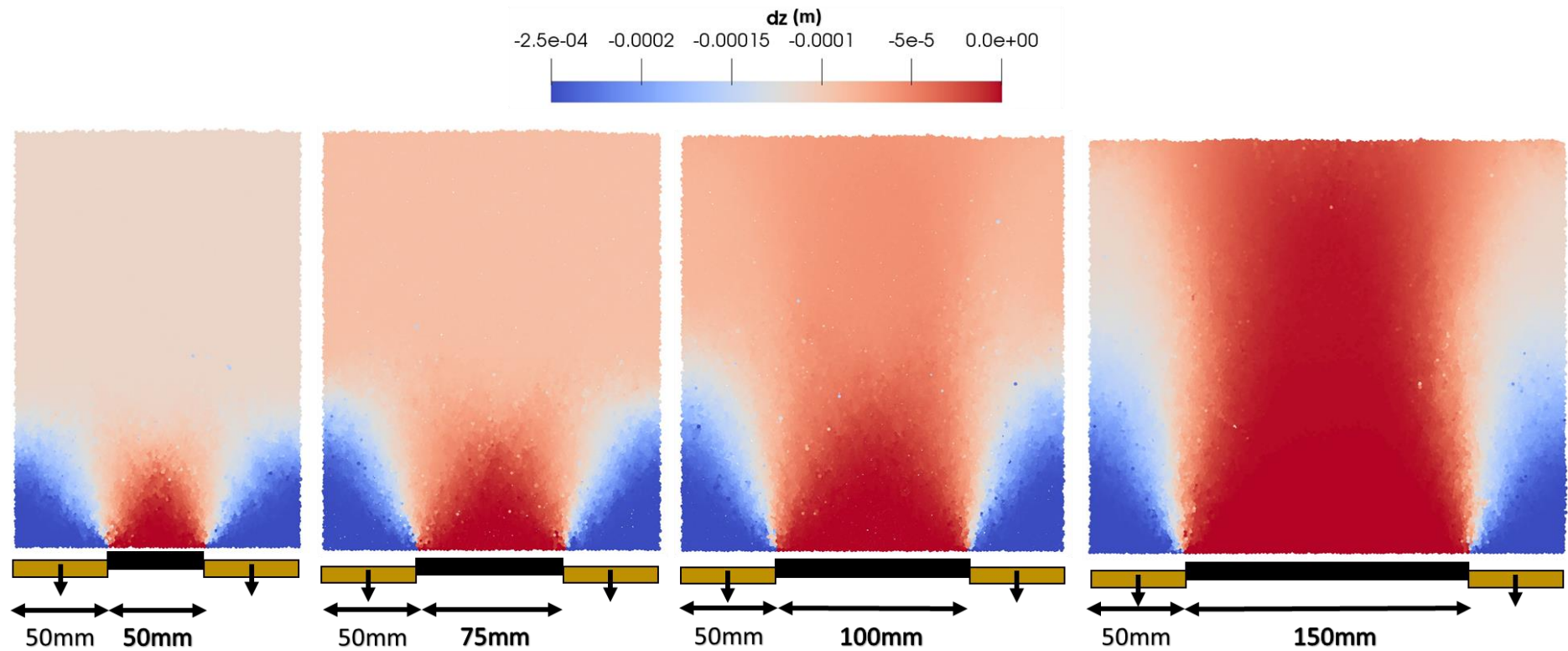


Figure 6.45 Vertical displacement plot at the particulate level for different central static base plate widths

Another observation is the surface settlement. The sample with the least width of the central static plate showed a very minute amount of differential surface settlement. However, no differential surface settlement was seen. As we increased the width of the central static base plate, the amount of uniform surface settlement further reduced and for the sample with the maximum width of the central fixed plate, almost no surface settlement is seen. This observation is due to the fact that the majority of the area under the surface did not move downwards due to the presence of a very large static base plate.

Lastly, the maximum width central base plate case is compared with an equivalent total sample width case. The sample being compared with the current case has an $L/B = 5.0$, with each plate having a width of 50mm and the central plate being held static. The vertical displacement plot for the sample particles is represented in Figure 6.46.

Both samples contained a similar number of particles, similar sample ground height, and similar displacements. However, the resulting trend is totally contrasting. The sample with five base plates having 50mm width for each plate could not form a stable arch in the sample and showed differential surface settlement, visible through the differing colors near the surface. Whilst the sample with 150mm central base plate showed very static behavior at the surface and there was a stable arch formation above the lowering side trapdoors.

The results reiterated the importance of trapdoor configuration and that the change in trapdoor configuration can totally reverse the soil stress conditions. Hence, deep consideration is required while designing and analyzing the buried structures under trapdoor conditions. A small variation in the configuration could result in totally contrasting results from the anticipated outcomes.

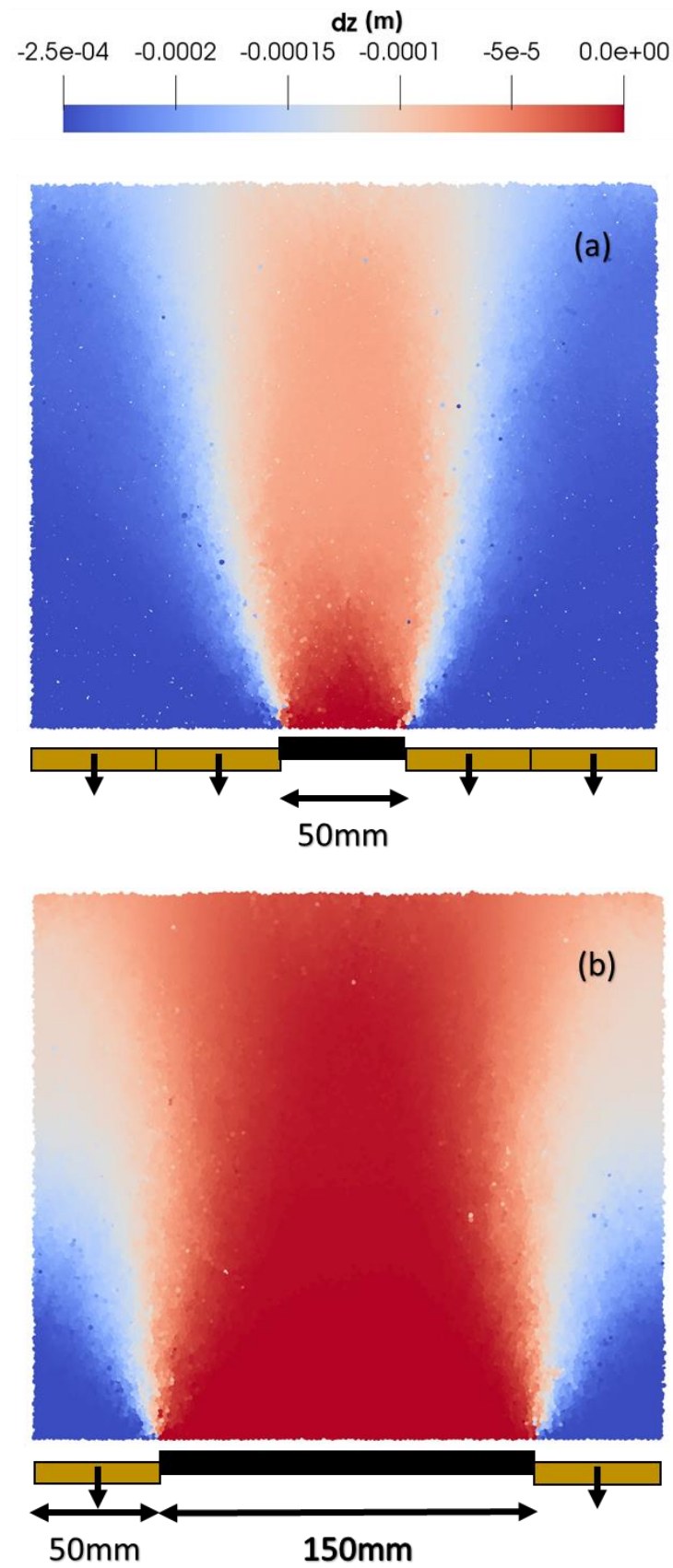


Figure 6.46 Vertical displacement plot for (a) five base-plates with 50mm width and (b) three base plates with central 150mm width plate

6.7 Summary

As a short summary, the trapdoor configuration effect was discussed in this chapter using DEM simulations and it was clarified that varying the trapdoor configurations can significantly affect the stress response. The larger becomes the area being lowered under trapdoor condition, the higher the sample height is required for a stable arch formation. A sample presenting a stable arching phenomenon under a given sample height could result in an absence of the arching with an increased trapdoor configuration.

To assess the theoretical maximum values of stress concentration factor, an empirical extrapolation for the stress distribution was performed that showed that with due care of material parameters, the response under trapdoor conditions can be well captured.

Finally, the effect of changing the width of the static base plate was discussed and it was concluded that the increasing width of the central base plate causes a reduction in the stress concentration factor ' α '. However, the increasing width imparts a more stabilized arching action within the material mass and causes lesser settlement of the ground compared to the cases with a smaller width of the central fixed base plate, under similar conditions.

CHAPTER 7: SOIL ARCHING AROUND CAVITIES & NECESSITY OF CAPILARY FORCES

This chapter extends the discussion on soil arching from trapdoor conditions to the underground cavity conditions, where the soil arching helps in stabilizing the developed cavity and to reduce the cave-in therefrom. The requirements besides the soil arching in order to have better stability of the cavity are also discussed in this chapter with a focus on the DEM model to incorporate the cavity stability prerequisites.

7.1 Underground cavities and soil arching

A trapdoor condition is formed when a certain mass of soil yields with respect to the remaining static soil mass. In response, the soil particles rearrange to reflect the yielding mass movement and eventually forms a soil arch around the yielding mass to distinguish between the static and the moving parts. The movement of soil under trapdoor conditions is normally not so large to form a separation with a lack of physical contact between the yielding and the non-yielding parts. Though, the particles remain still in contact at the interface of both regions with a relatively larger dilation of mass in the yielding portion.

However, in the case when the yielding is large enough to result in a disconnection between the yielding and non-yielding mass, the condition is called as the cavity formation condition. A hollow space with a presence of strong arching forces around the circumfering region keeps the hollow cavity intact.

An underground cavity can exist due to the presence of buried structures/pipelines, having distortion or damages due to aging or improper installments. The details of the cavity formation are given in Chapter 1 of this document. Figure 7.1 shows the case of an underground cavity with the presence of strong arching forces around the cavity. The forces that form arch are stronger near the boundary; however, the arch development requires a region that could easily form a specific arch shape. Hence, the area just beside the boundary of the arch would not contain any forces but still, remain intact. The phenomenon that keeps certain portions of soil mass near cavity boundaries, is known as capillary forces.

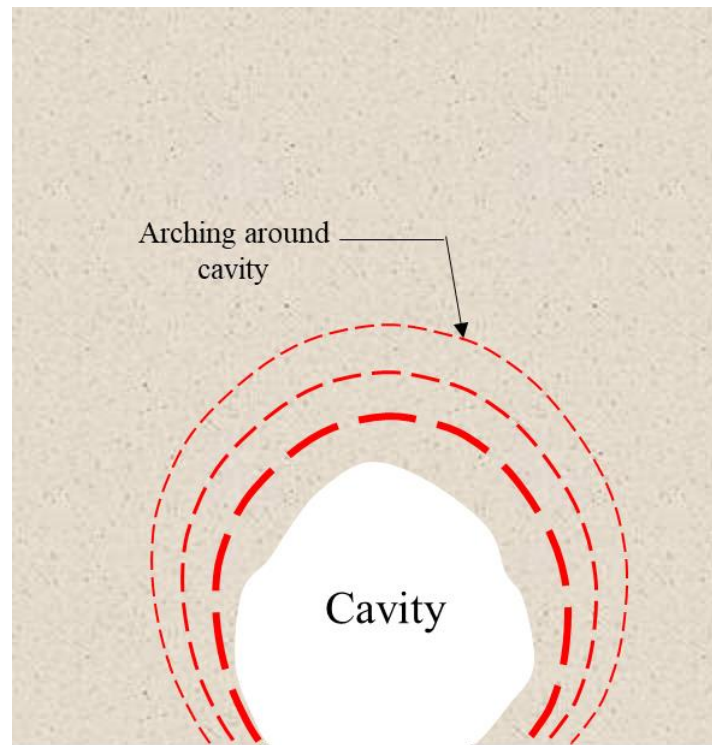


Figure 7.1 Underground cavity and the arch formation around it

7.1.1 Formation of underground cavities in dry conditions

The formation of the arching action in trapdoor tests was analyzed under a dry condition. However, to assess whether the cavity formation process could attain a stable condition under dry conditions, model cavity formation tests were performed in the laboratory with different materials, using test equipment as shown in Figure 7.2 below. The detailed description of model trapdoor test equipment is given later in Chapter-8.

Table 7.1 Model cavity tests with different materials in dry conditions

Material	D ₅₀ (mm)	Relative density, Dr (%)
Spherical glass beads	1.7	≈ 55
Spherical glass beads	0.2	55
Silica sand #5		50
Silica sand #7	≈ 0.2	50

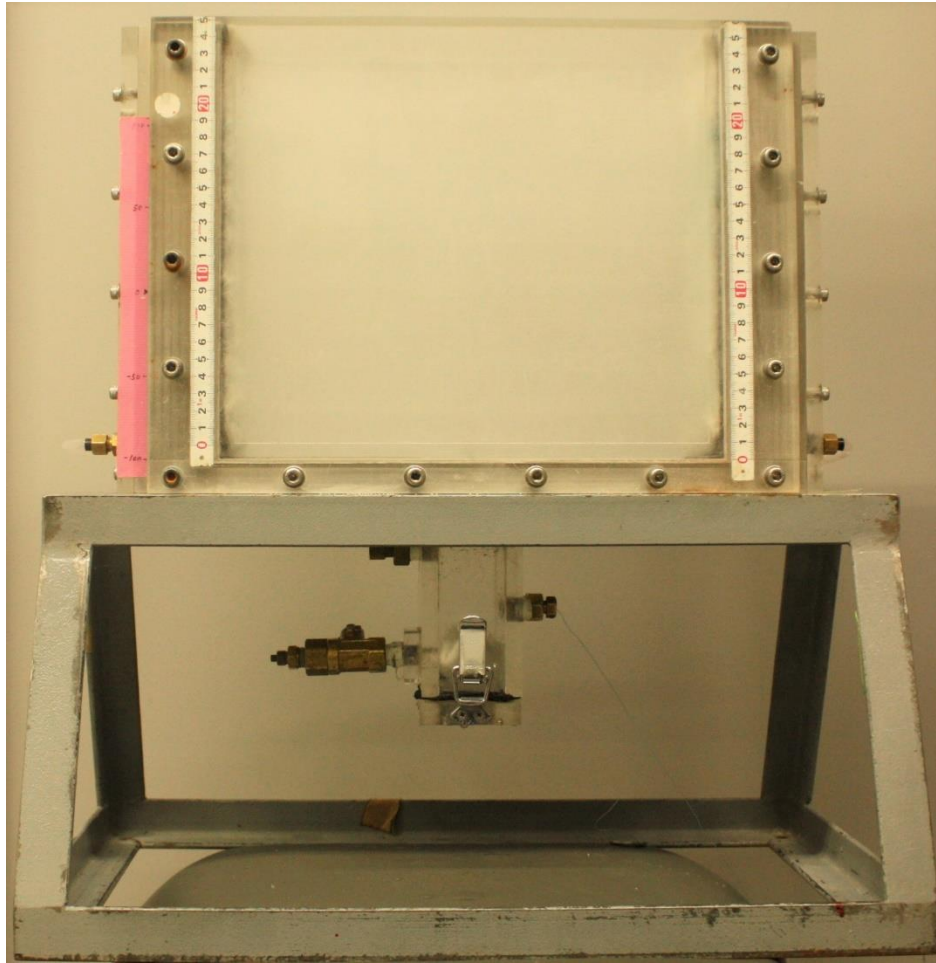


Figure 7.2 Model cavity test apparatus

Table 7.1 shows the details of materials used for the cavity formation model tests using the equipment as shown above in Figure 7.2. the model test equipment had a 5mm bottom opening and the sample was prepared with air pluviation, dropping the sample from a fixed height of 30cm, causing relative density values as shown in Table 7.1.

For the case of spherical glass beads with a mean diameter of 1.7mm, as soon as the bottom slit was opened, the material started flowing out until the natural angle of repose was obtained. Very similar observations were made for the case with spherical particles having a mean diameter of 0.2mm. The initial, intermediate and final stages for both particle types during the tests are shown in Figure 7.3.

Giving a margin of particle shape, silica sand samples with two different sizes were used in similar experiments. Although, the results did not vary much, and no cavity was formed. Figure 7 4 represents the test on silica sand samples.

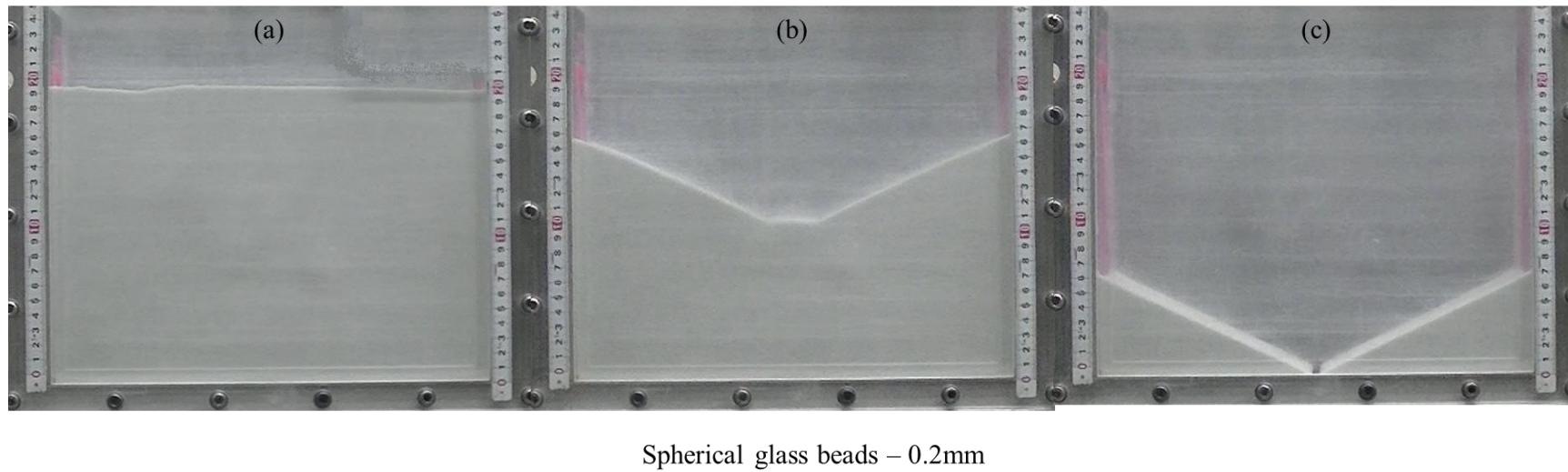
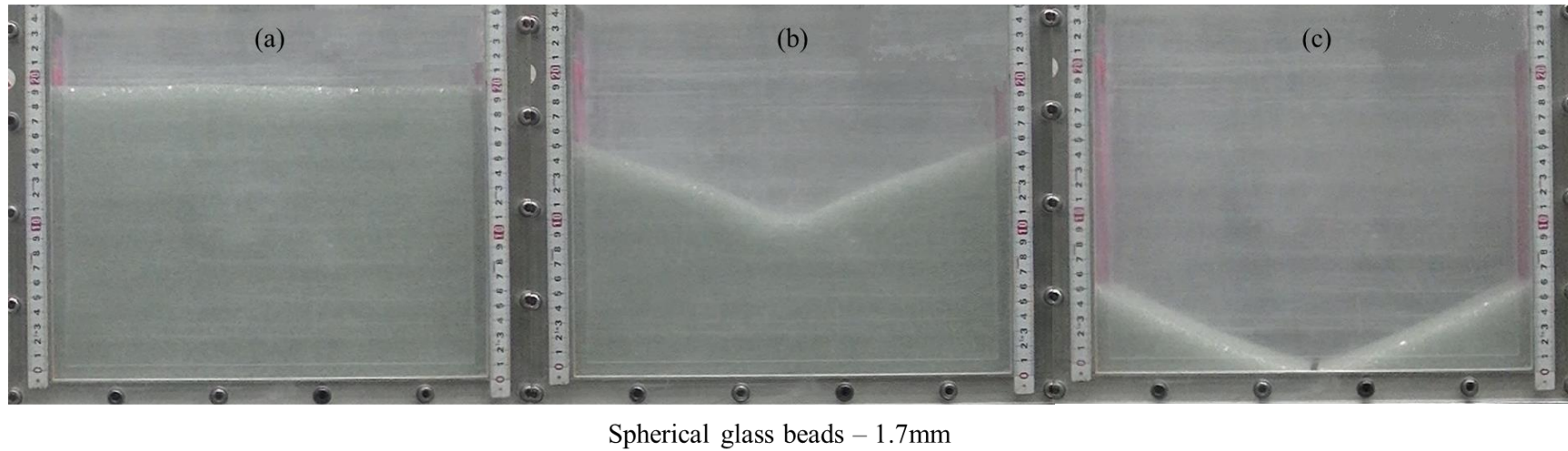
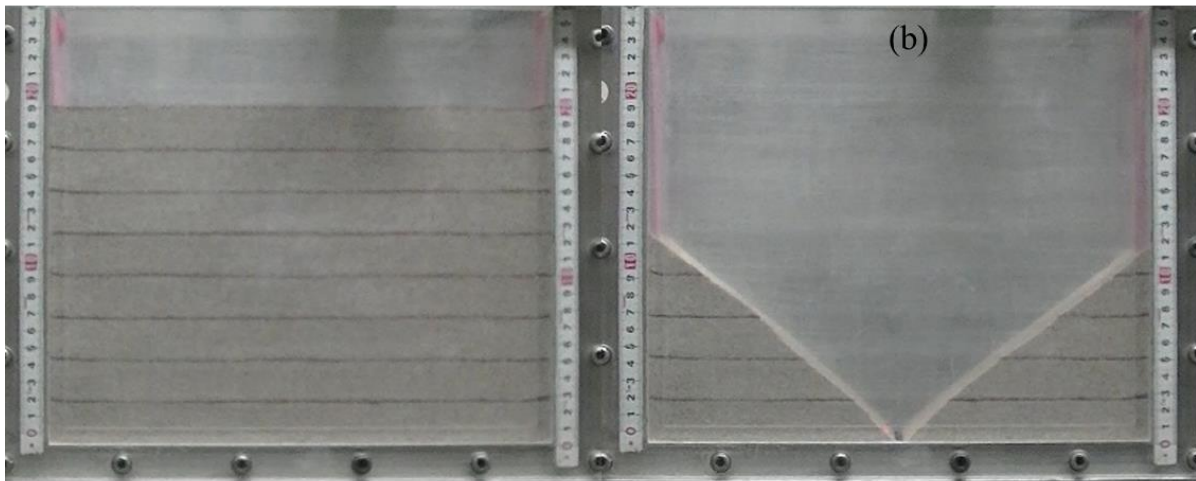
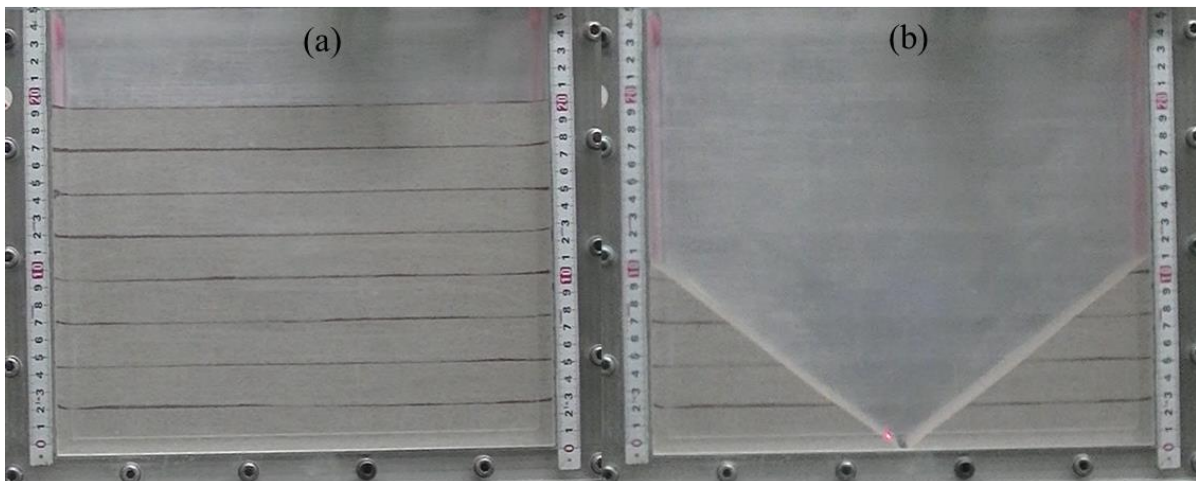


Figure 7.3 Model cavity tests on dry samples with different sizes of glass beads at various stages of test



Silica sand #5



Silica sand #7

Figure 7.4 Model trapdoor tests with different sizes of silica sand at (a) start and (b) end of the test

7.1.2 DEM cavity simulations in dry conditions

As the model cavity tests were unable to demonstrate any underground cavity formation under the action of bottom soil erosion by opening a bottom slit. However, there was a possibility that DEM numerical simulations, that showed very promising results in case of trapdoor conditions, would result in a cavity formation provided if the bottom slit is opened in a similar manner compared to model trapdoor tests.

To do so, two types of particle shapes, as already discussed in the trapdoor related discussion, were used under dry conditions (no effect of water-related forces). The

particles were allowed to escape from the bottom side by removing a portion with 5mm width, as used in the model cavity tests. Figure 7.5 shows the initial and the final stages of simulations under the action of bottom slit removal for both types of particles.

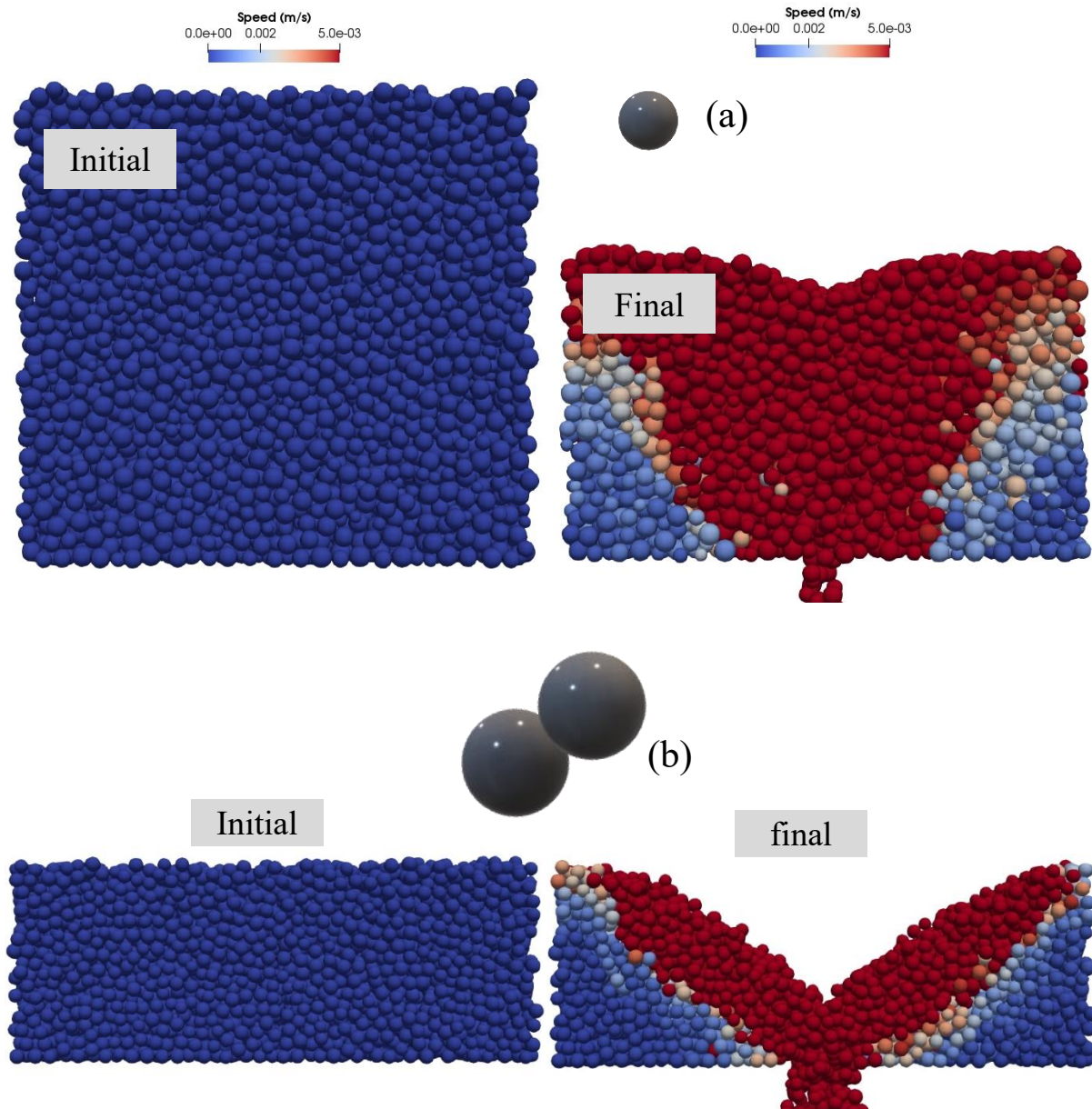


Figure 7.5 DEM based numerical cavity tests using (a) spherical and (b) non-spherical particles at start of simulations and end of the simulation

7.1.3 Necessity of water (capillary) forces

As seen in Figure 7.5, even DEM simulations could not result in any cavity formation and all particles flowed out of the bottom slit, resulting in a sloping ground of

remaining particles with a natural repose angle. The particle tried to form the arch however the arch could not sustain under the continuous movement of the particles.

Comparing both model tests and the numerical simulations for the underground cavity formation under dry conditions, we can observe similar particle movement patterns. However, none of the methods could form a stable underground cavity and it can be said that there exists something additional than just soil arch effect, that keeps the arch stable above the buried structures.

Consequently, it is evident that in order to produce a stable arching condition, there must be an inclusion of water effect, causing the development of capillary forces amongst particles. Capillary forces can impart attractive forces in the soil mass, making them more resistive against the movement and supporting the sustainability of soil arch with its strengthening effects.

7.2 DEM model modification

As discussed above, there is a need to modify the traditional DEM programs in order to perform the underground cavity simulations. The DEM programs that are normally used in geotechnical engineering for the study on granular materials, have only the inter-particle contact force and/or gravitational forces. Such programs are incapable to incorporate the true behavior or soil mass under the combined effect of contact forces and the capillary forces. Hence, to have a better understanding at the particulate level, the modified version of granular LAMMPS was further changed to incorporate the capillary forces.

7.2.1 Constituents of capillary forces

Capillary forces normally consist of two main components:

- i) Surface tension
- ii) Matric suction

The resultant capillary force for any soil mass is the summation of both surface tension and the matric suction.

7.2.1.1 Surface tension:

The surface tension is the force produced at the interface of liquid and the air. The water molecules try to form a shape with a minimum surface area, resulting in an attractive force that is called surface tension. The molecules of any liquid are equally attracted and repelled due to the presence of similar molecules in the vicinity. However, at the interface of air and liquid, the top surface of water molecules does not have equal forces compared to their bottom part. As a result, there exists an inward force on the liquid molecules at the interface, causing a stretched surface, called surface tension. Figure 7.6 explains the process of surface tension at the interface of any liquid and air.

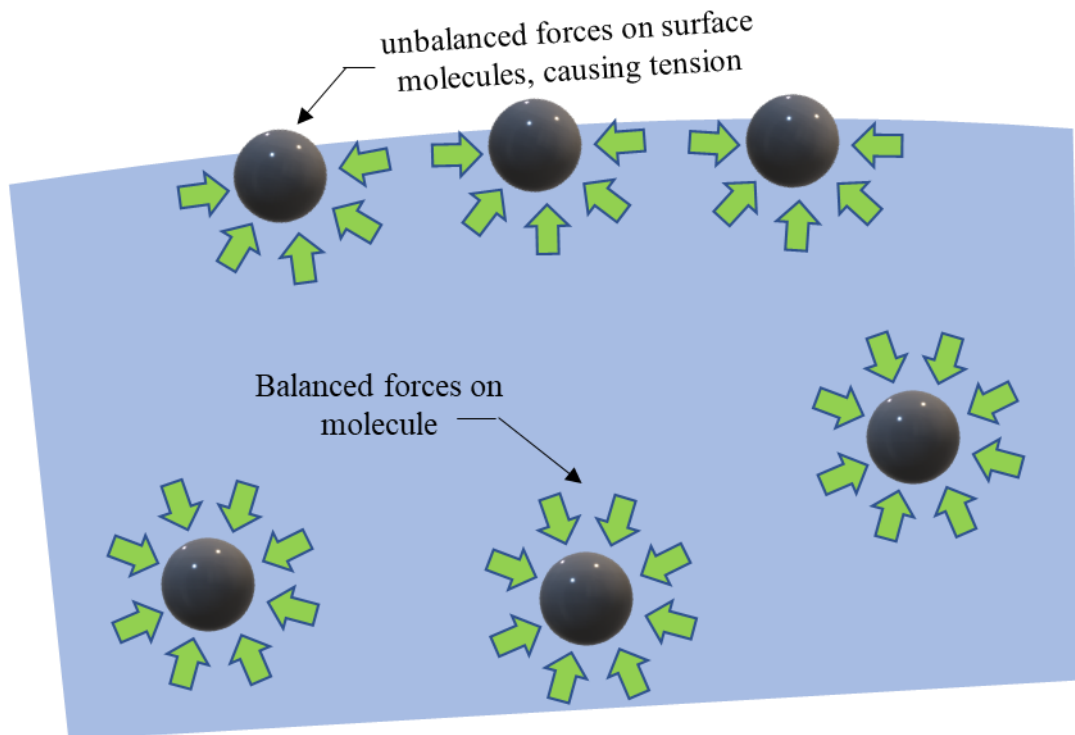


Figure 7.6 Surface tension at interface of liquid and air

Due to the presence of surface tension, the resultant liquid surface depicts a concave or convex shape, depending upon the properties of liquid/air and the atmospheric pressure. The absolute value of surface tension also depends upon the type of liquid. In the case of water, the surface tension value is normally taken as 0.0745 N/m. However, the value depends upon the room temperature. The range

of surface tension values against the room temperature is given in Table 7.2 (Gianino, 2006). The value of surface tension for water decreases with the increasing temperature.

For the current numerical simulations, a surface tension value of 0.074 N/m is adopted for all simulations involving the capillary forces.

Table 7.2 Surface tension of water against temperature

Temperature (°C)	Surface tension, T_c (mN/m)
10	74.01
15	73.26
20	72.53
25	71.78
30	71.03

Ref. Gianino (2006)

7.2.1.2 *Matric suction*

Once the soil sample has the presence of water in the pores, there exists another phenomenon, called matric suction, which can be defined as the difference between the pore air pressure and the pore water pressure. A most recent definition of matric suction is given by Zhang & Lu (2019) by considering the effect of SSP (soil sorptive potential).

In a simpler way, the matric suction exists due to the attractive forces offered by the dry particle towards the pore water. In other ways, it's the pressure of the soil with dry conditions towards the surrounding soils to balance the presence of moisture contents.

Matric suction is the attractive force offered by a lump of soil. However, in the case of the implementation of suction forces at the inter-particle level in the DEM model, it is not feasible to account for the matric suction due to the several

complexities that might arise by this. In the case of matric suction offered by a lump of soil mass (Figure 7.7), there might exist several curvatures of water around a single particle due to the presence of multiple contacts, making it very difficult to inter-relate the suction offered by a single contact. Further to that, a matric suction value may be caused by a condition having both concave/convex curvature of water surface, which is not possible to be isolated individually. Besides these factors, the presence of a wide range of PSD (particle size distribution) in a soil mass can cause a matric suction value that might not be the representative value for a single particle.

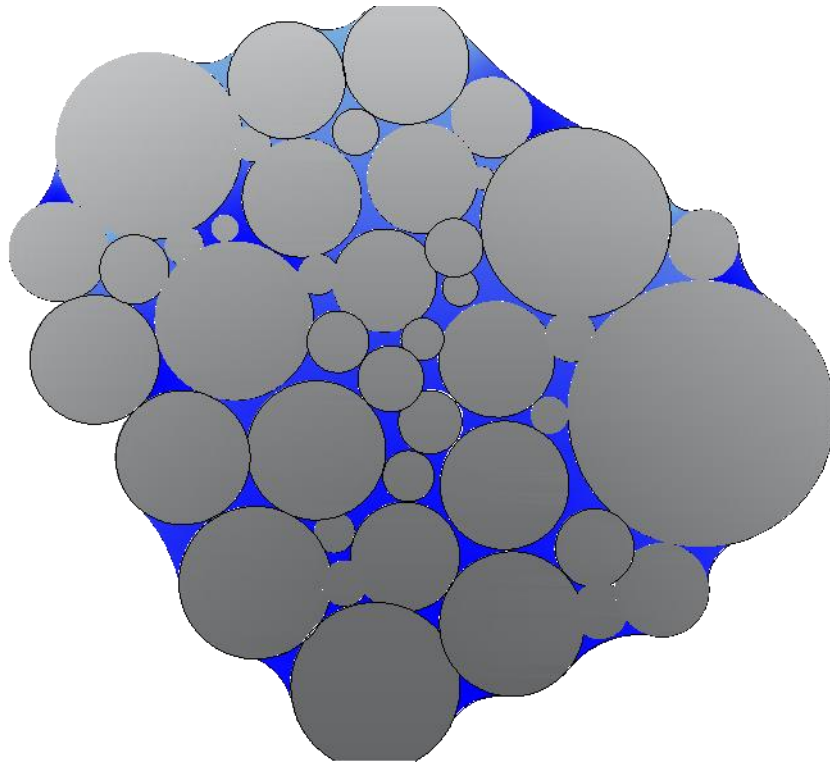


Figure 7.7 A lump of soil with numerous particles in a partially saturated condition, resulting in matric suction

Keeping in view the above limitation, the option to measure the matric suction value physically in the lab and to apply the measured suction in the DEM code was not considered. Rather a new model was derived to calculate the inter-particle suction forces produced between two spherical particles, making it easier to be implemented in the numerical program.

7.2.2 Conditions of inter-particle capillary forces

To start with the inclusion of capillary forces in the DEM code, a basic condition of two spherical particles with radius R_1 and R_2 , connected through a thin water film and having a distance of D between them is shown in Figure 7.8. The particles R_1 and R_2 make an angle of θ_1 and θ_2 respectively, with the edge of the water film. The water film connecting both particles have a concaved surface in the XZ plane, with a radius ' R_{ext} '.

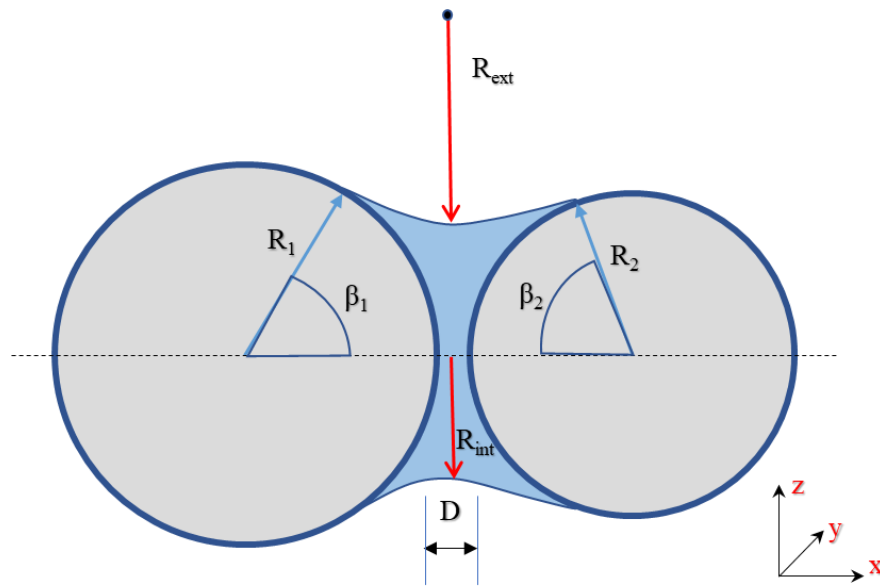


Figure 7.8 Two spherical particles connected through a thin water film

However, besides the external radius, the water film also possesses another radius, i.e. in YZ direction, making a torus shape with a central line passing through the centroids of both spheres. In other words, if we take the cross-section of the water bridge at the central point, as shown in the above figure, the resulting section in the YZ plane would represent a circle, having a radius of R_{int} , or the internal radius of water bridge.

Under the effect of gravitational forces/loading, the particles move and try to come closer or move away from each other. The water film can keep both particles intact up to a certain distance, called rupture distance (D_{rup}), beyond that the particles are no longer connected through water film. Resultantly, the distance between (D) particles changes at each instance. To generalize, the particles can be arranged into three main categories with respect to their mutual distance.

- (i) When particles are very far from each other ($D > D_{rup}$)

- (ii) When particles are at a distance, D ($0 < D < D_{rup}$)
- (iii) Particles are overlapping/touching ($D \leq 0$)

As discussed earlier, the total capillary force (f_c) offered by the water bridge is the summation of both inter-particle suction force (S) and the surface tension (Eq. 7.1).

$$f_c = \text{inter} - \text{particle suction } (S) + \text{Surface tension } (T_c) \quad (7.1)$$

The total contact force is the summation of the Hertzian contact force (f_{HZ}) and the capillary forces, as given in Eq. 7.2.

$$f_{total} = f_{HZ} + f_c \quad (7.2)$$

In terms of force, the above three equations can result in the following three force conditions:

$$D \leq 0 \rightarrow f_{total} = f_{HZ} + f_c \quad (7.3)$$

$$0 < D < D_{rup} \rightarrow f_{total} = f_c \quad (7.4)$$

$$D \geq D_{rup} \rightarrow f_{total} = 0 \quad (7.5)$$

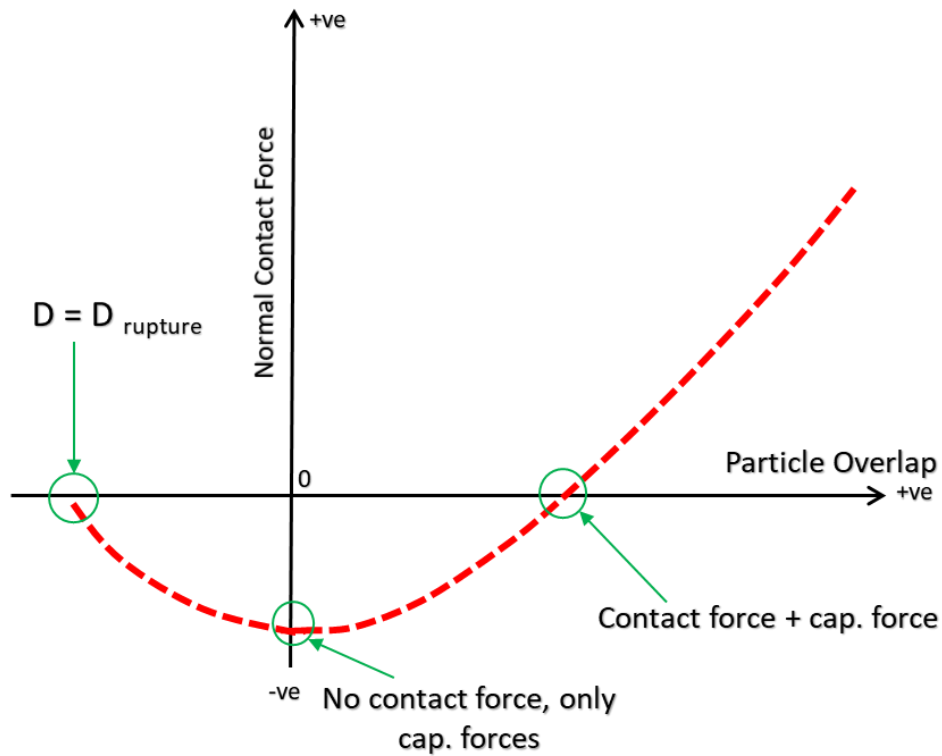


Figure 7.9 Force-overlap plot between two spherical particles having water film between them

The plot between the particle overlap (opposite of interparticle distance) and the total contact force is shown in Figure 7.9. In case the particles are touching each other or have some small overlap due to high applied force, there exists both the Hertzian contact force, as well as the capillary force. As the particles move away from each other, the instance when the distance between the particle exceeds zero, there is no more Hertzian contact force and the only force keeping the particles together is the capillary force. However, it should be kept in mind that both the Hertzian force and the capillary forces are opposite in direction. Capillary force is an attractive force, keeping particles together. In case the particles move away beyond the rupture distance D_r , no force exists between both particles and the force plot touches the zero axes.

7.2.3 DEM model with inter-particle suction as an input parameter

The maximum distance between particles with water film between them, that can withhold both particles, depends largely upon the degree of saturation of the particles (or the volume of water bridge), angle of water contact with particles and the particle size.

Several researchers have studied the effect of rupture distance with different parameters. Lian et al. (1993) obtained a relation for rupture distance involving water contact angle (θ) and the volume of the liquid bridge (V) as:

$$D_{rup} = (1 + 0.5\theta)V^{1/3} \quad (7.6)$$

Similarly, Gras, Delenne, & El Youssoufi (2013) presented their expression for the calculation of rupture distance based upon a dimensionless suction value and contact angle θ .

The capillary forces are maximum when the distance between the particles is zero. With the increase in inter-particle distance, the capillary forces reduce until they vanish. The reduction of capillary forces with distance is an interesting point. Several researchers have studied the variation of capillary forces with particle distance. Gras et al. (2013) showed a relation between the inter-particle distance and the capillary forces (f_c). Similarly, Wang et al. (2017) obtained a similar sort of plot. Both plots are reproduced here for reference, in Figure 7.10 and Figure 7.11 below.

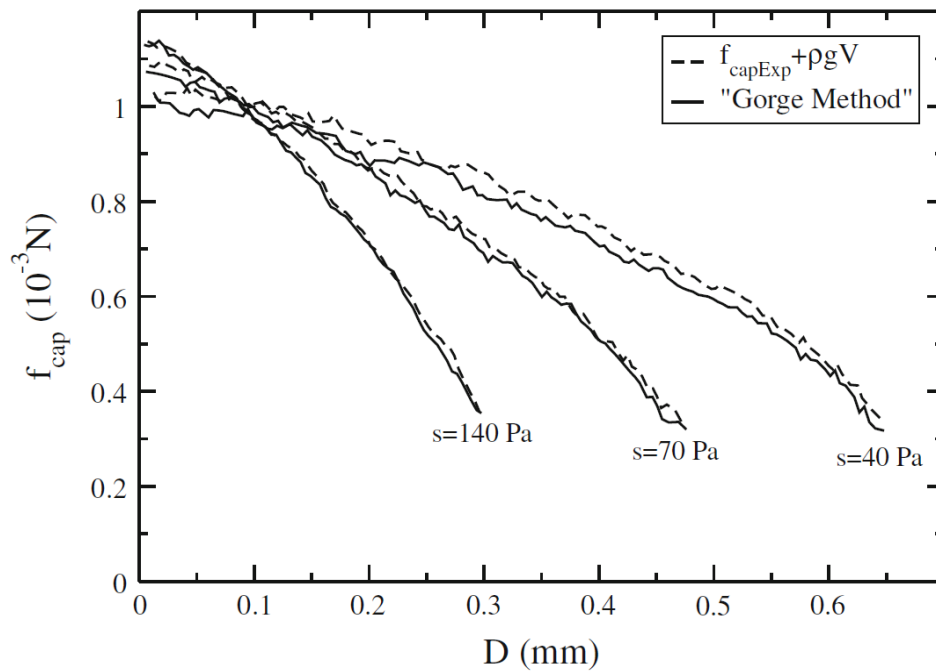


Figure 7.10 Relation between capillary force and inter-particle distance under different suction pressures (Ref. Gras et al., 2013)

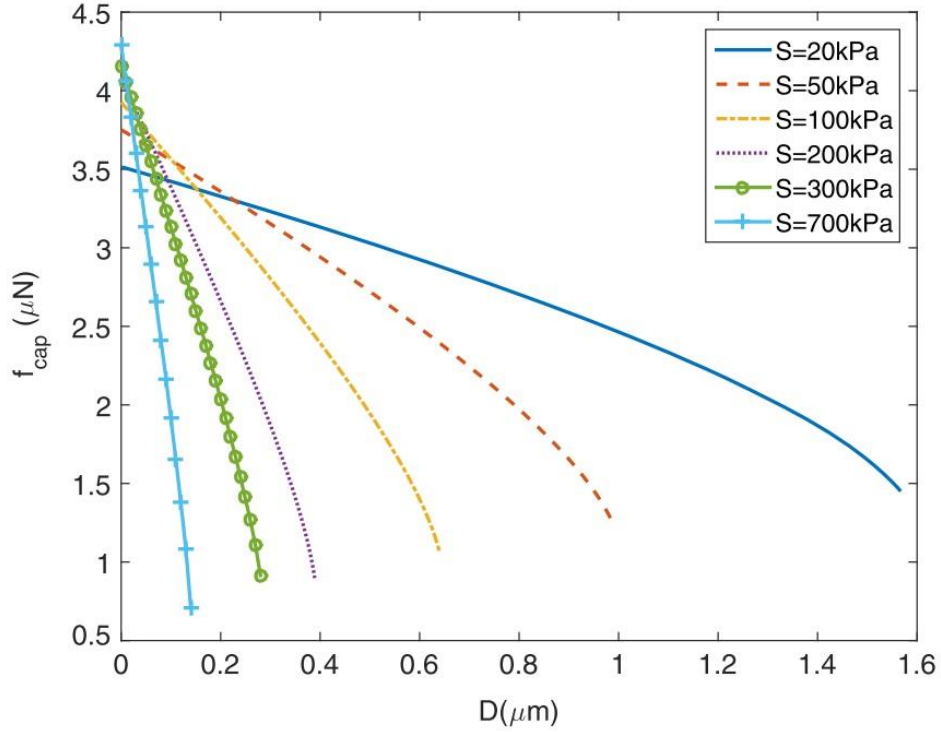


Figure 7.11 Relation between capillary force and inter-particle distance under different suction pressures (Ref. Wang et al., 2017)

For all the above cases with varying suction values, the decrease in capillary force with increasing particle distance follows an approximate path of a second-degree function. It is required to have a function that reduces the capillary force with increasing particle distance. If we select a representative soil suction value of approximately 50kPa, the representative curves show a matching trend as shown in Figure 7.12. The plot shown below followed the following reduction function (f_r) between two particles having a distance D between them:

$$f_r = -\frac{1}{2}(D^2 + D) + 1 \quad (7.7)$$

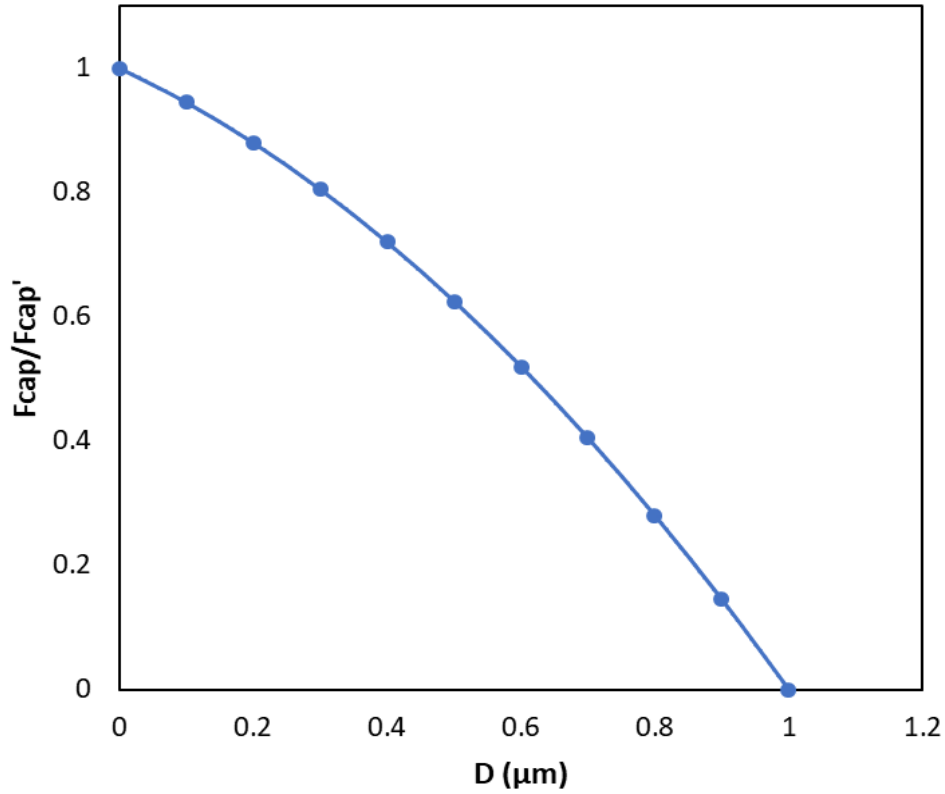


Figure 7.12 Decrease in capillary force with increasing inter-particle distance through a quadratic reduction factor

7.2.3.1 When $D \leq 0$:

Now, to calculate the inter-particle forces for the conditions as given in Eq. 7.3 to Eq. 7.5, there is a need to calculate the maximum capillary force (f_{c_max}). maximum capillary force is calculated as the summation of the surface tension and the inter-particle suction, as described above in Eq. 7.2. The surface tension (T_c) has a fixed value of 0.074 N/m for the water. To calculate the force being applied through the surface tension, we need to multiply the value with the perimeter of the water bridge. Since in this method, the input parameter is the inter-particle suction stress; hence, the suction force can be calculated if we multiply the suction stress with the area of application. Resultantly, the capillary force can be given by the following expression.

$$\text{Capillary force} = \text{suction force} + \text{surface tension force} \quad (7.8)$$

$$f_c = S \times \pi R'^2 + T_c \times 2\pi R' \quad (7.9)$$

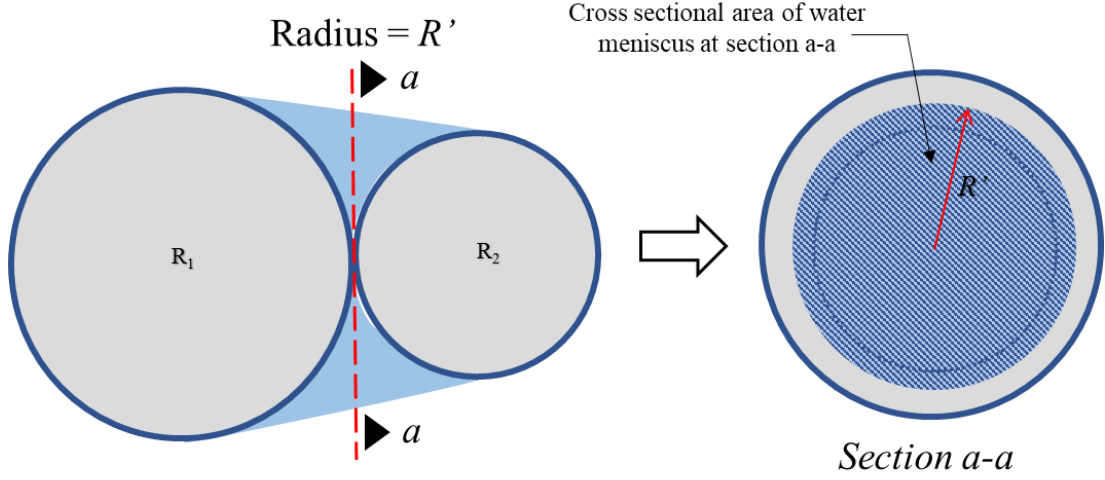


Figure 7.13 Approximate linear variation of water bridge surface between two spherical contacting particles

In the above expression, R' is the radius of water meniscus at the interface of both spherical particles. For simplicity, assuming the water surface distribution between both particles to be linear, as shown in Figure 7.13, R' can be obtained through Derjaguin (1934) approximation as:

$$R' = \frac{2R_1R_2}{(R_1 + R_2)} \quad (7.10)$$

Now, simplifying the Eq. 7.9 by incorporating the R' value from Eq. 7.10, we get the maximum capillary force between two spherical particles touching each other as:

$$f_{c_max} = S\pi \left(\frac{R_1 + R_2}{2} \right)^2 + T \times 2\pi \left(\frac{R_1 + R_2}{2} \right) \quad (7.11)$$

$$f_{c_max} = \frac{\pi}{4} (R_1 + R_2) \times [4T + S(R_1 + R_2)] \quad (7.12)$$

Eq. 7.12 above represents the maximum possible capillary force that is observed under the condition of $D \leq 0$.

7.2.3.2 When $0 \leq D \leq D_r$

The capillary forces reduce in case the distance between particles increases. The reduction factor is given by Eq. 7.7. Hence, to calculate the reduced capillary force for the given condition, the following expressions are used:

$$f_c = f_r \times f_{c_max} \quad (7.13)$$

$$f_c = \left\{ -\frac{1}{2}(D^2 + D) + 1 \right\} \times \left[\frac{\pi}{4}(R_1 + R_2) \times \{4T + S(R_1 + R_2)\} \right] \quad (7.14)$$

For the condition when there is some distance between both particles, the capillary force will be calculated as multiplying the reduction factor with the maximum capillary force.

7.2.3.3 When $D \geq D_{rup}$

This is the simplest condition and no force exists during this condition. The distance between the particles exceeds the limit distance and the water bridge collapses to result in zero capillary and Hertzian contact force.

$$f_c = 0 \quad (7.15)$$

Resultantly, the given three equations (Eq. 7.12, 7.14 and Eq. 7.15) can thus be used in the DEM program code with an input factor of inter-particle suction, that can be varied as per any feasible value or the experimental results.

7.2.4 DEM model with a degree of saturation as an input parameter

In the last section, an attempt was made to modify the existing DEM model to incorporate the capillary forces, that are pre-requisite for the study of the cavity formation and its stability. The capillary forces were controlled by an input parameter of inter-particle suction S , which can be varied to study the effects on soil arching and cavity

stability. However, the selection of an appropriate suction value is of prime importance. Also, as there exists a clear difference between the matric suction and the inter-particle suction, choosing an inter-particle suction to result in a matric suction that is representative of experimental results, is a difficult task.

Hence, in order to improve the accuracy and to simplify the capillary force calculation, the model was further modified. The degree of saturation is a key parameter that controls the volume of water in a soil mass. The amount of water is directly related to the resultant capillary force behavior of the sample. Several researchers like Willett et al. (2000); Farouk, Lamboj, & Kos (2004); Tourani et al. (2016); Monnet et al. (2017); Wang et al. (2017); Sun & Sakai (2018); Gallage & Uchimura (2010) discussed the importance of water volume on the soil-water characteristic curves both in numerical models as well as experimentally.

In order to introduce capillary force equations with an input parameter of the degree of saturation (S_r), the basic equation introduced by the Young-Laplace equation is used. The Young-Laplace equation is based upon the basic theory on surface tension by Thomas Young in 1805 and then later in 1806 the mathematical expressions for the same were provided by Pierre-Simon Laplace. The equation is given below:

$$S = T_c \cdot \left(\frac{1}{r} - \frac{1}{b} \right) \quad (7.16)$$

Where T_c is the surface tension in N/m, S is the suction (stress units). r and b are the internal and external radii of water meniscus formed between two particles (referred to as R_{int} and R_{ext} previously). r is called ‘radius of water meniscus’ and b is called the ‘radius of the torus of the meniscus’. The figure explains the basic parameters of the Young-Laplace equation.

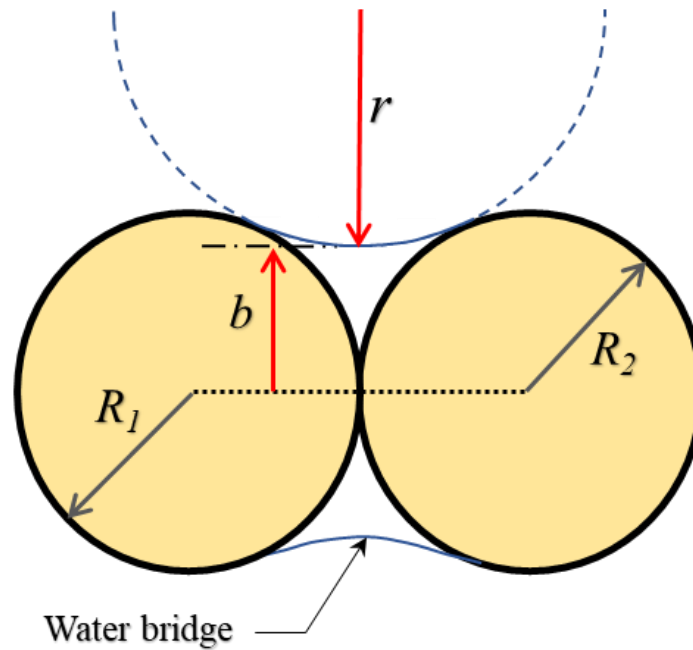


Figure 7.14 Representation of Young-Laplace equation parameters in water bridge between two spherical particles

Here, in Figure 7.14, the radius of the torus of meniscus b can be physically related to the height of water film around the particles, or the degree of saturation between two particles. In order to relate the radius of the torus of meniscus b to the saturation of the particles, we need to look into the particle volume to water volume relations.

Assuming a case, as shown in Figure 7.15 where the assembly of two connecting spherical particles is enclosed into a rectangular box, the fully saturated condition would exist in case the whole box is filled with water. In that particular case, the b value would approach to R .

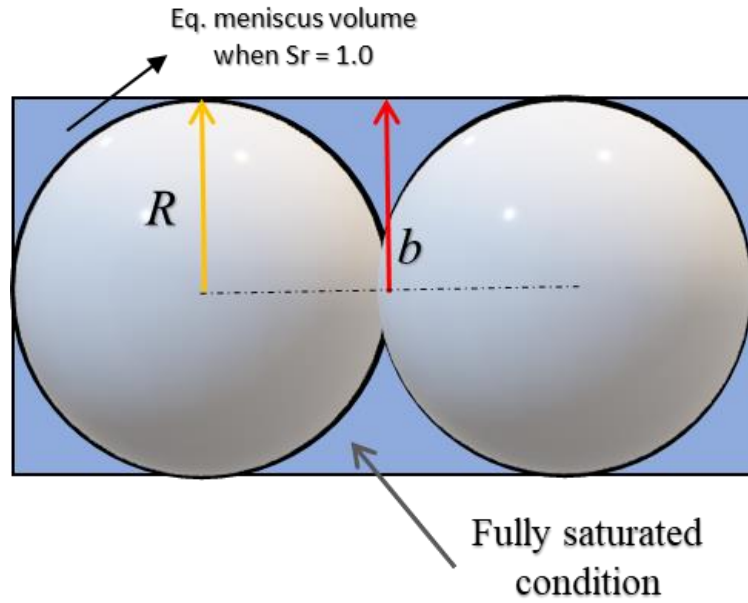


Figure 7.15 Fully saturated condition for spherical particles in rectangular assembly

The relation between the volume of the box and the volume of the water inside the box for a fully saturated condition can be drawn.

$$\text{volume of box, } V_{box} = 4R \times 2R \times 2R \quad (7.17)$$

$$V_{box} = 16R^3 \quad (7.18)$$

$$\text{volume of spheres, } V_{sph} = 2 \times \frac{4}{3} \pi R^3 \quad (7.19)$$

$$V_{sph} = \frac{8}{3} R^3 \quad (7.20)$$

$$\text{volume of meniscus, } V_{men} = V_{box} - V_{sph} \quad (7.21)$$

$$V_{men} = 16R^3 - \frac{8}{3} R^3 \quad (7.22)$$

$$V_{men} \propto R^3 \quad (7.23)$$

Since the change in meniscus water volume is proportional to the cubic power of radius ' R ', we can represent the change in ' b ' value with the change in saturation using ' R '.

$$b = R \times \left(\frac{S_r}{100} \right)^3 \quad (7.24)$$

Where S_r is in percentage.

Now in order to calculate the variation of r with saturation level, we need the angle of water meniscus surface with the center of the particles. To do so, basic trigonometric functions were utilized as per Figure 7.16 below. The central angle θ can be calculated by following Eq.

$$\theta = \sin^{-1}(b/R) \quad (7.25)$$

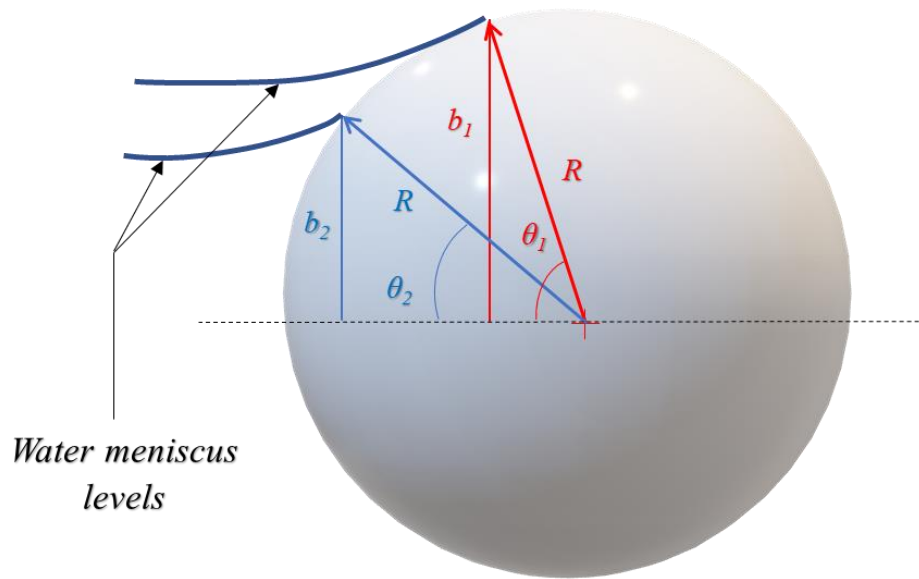


Figure 7.16 Water meniscus angles with the centroid of particle

However, the above trigonometric function for calculation of meniscus angle uses the upper level of the meniscus. Whereas, the real b value is measured from the center of the sagging curvature, resulting in value slightly smaller than the currently calculated one. From Figure 7.17, the difference between the actual b value and the calculated b value is clear. Hence, for clarification, the real value is termed as b' and the apparent one as b .

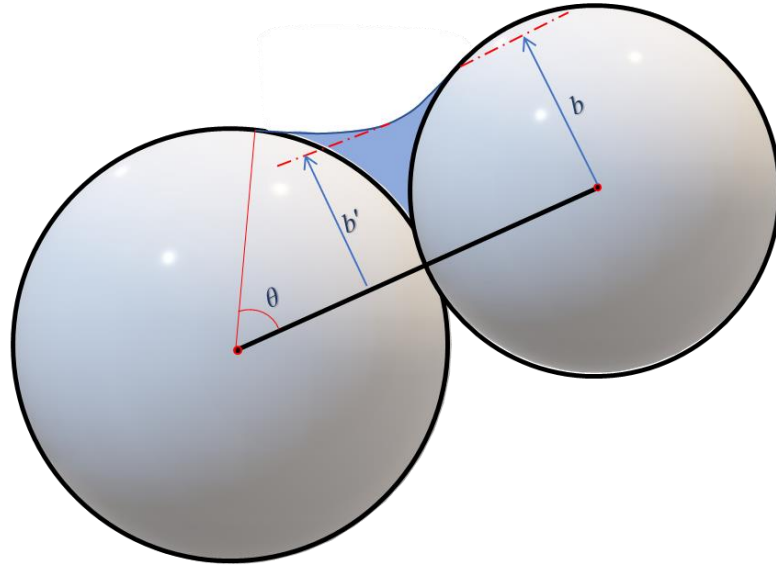


Figure 7.17 Difference between apparent and real 'b' value

For the calculation of b' , the trigonometric functions as proposed by Liu & Sun (2002) are used, which are presented below.

$$b' = R(\tan\theta + 1 - \sec\theta) \quad (7.26)$$

Again, using Liu & Sun (2002) trigonometric formula to re-calculate the precise value of the radius of the meniscus, termed as r' here.

$$r' = R(\sec\theta - 1) \quad (7.27)$$

Now, the values of the radius of meniscus r' and radius of the torus of meniscus b' from above Eq. 7.26 and Eq. 7.27 are used in Eq. 7.16 to result in final expression as:

$$S = T_c \cdot \left(\frac{1}{r'} - \frac{1}{b'} \right) \quad (7.28)$$

$$S = T_c \cdot \left(\frac{1}{R(\sec\theta - 1)} - \frac{1}{R(\tan\theta + 1 - \sec\theta)} \right) \quad (7.29)$$

Eq. 7.29 is the final equation to find the inter-particle suction in terms of pressure units. In the above equation, radii of the meniscus are replaced with trigonometric functions and the equivalent particle radii R , which is directly connected to the saturation of the sample through Eq. 7.24. Now, in order to change the above equation to the force units, we again need to add both components of suction and surface tension and multiply with the corresponding area, as follows:

$$f_c(force) = \left[T_c \cdot \left(\frac{1}{R(\sec\theta - 1)} - \frac{1}{R(\tan\theta + 1 - \sec\theta)} \right) \times \pi b'^2 + (T_c \times 2\pi b') \right] \quad 7.30$$

Eq. 7.30 is the finally obtained equation that is used in the DEM program to modify it throughout sample saturation and radii.

7.2.4.1 Initial debugging:

For initial verification of the model, the plot between the total force, that is the sum of Hertzian force and the capillary force, and the particle overlap was plotted for the model response and through the empirical relation.

For the Empirical relation, the Hertzian contact force model was used, which is well documented by Johnson (1985) and is applicable to smooth surfaces.

$$N = \frac{4}{3} E'_p \sqrt{R'} \delta^{1.5} \quad (7.29)$$

Where N is the Hertzian contact force, E'_p is the equivalent young's modulus, R' is the equivalent radius of particles and δ is the overlap between particles. All these factors are described in detail in Chapter 2.

The response is shown in Figure 7.18. The model response for the calculation of total contact forces for a sample against the inter-particle distance shows a very high repulsive force for the portion where the particles are overlapping. The force reduced as the overlap reduced and at a very small overlap, the small repulsive Hertzian contact force was equalized by the maximum capillary force and the overall force response showed zero at that overlap value.

For the condition when there was no overlap, but particles were overlapping, the response showed the presence of negative capillary forces, that showed their maximum value and the force reduced in a quadratic manner with further increase in particle distance.

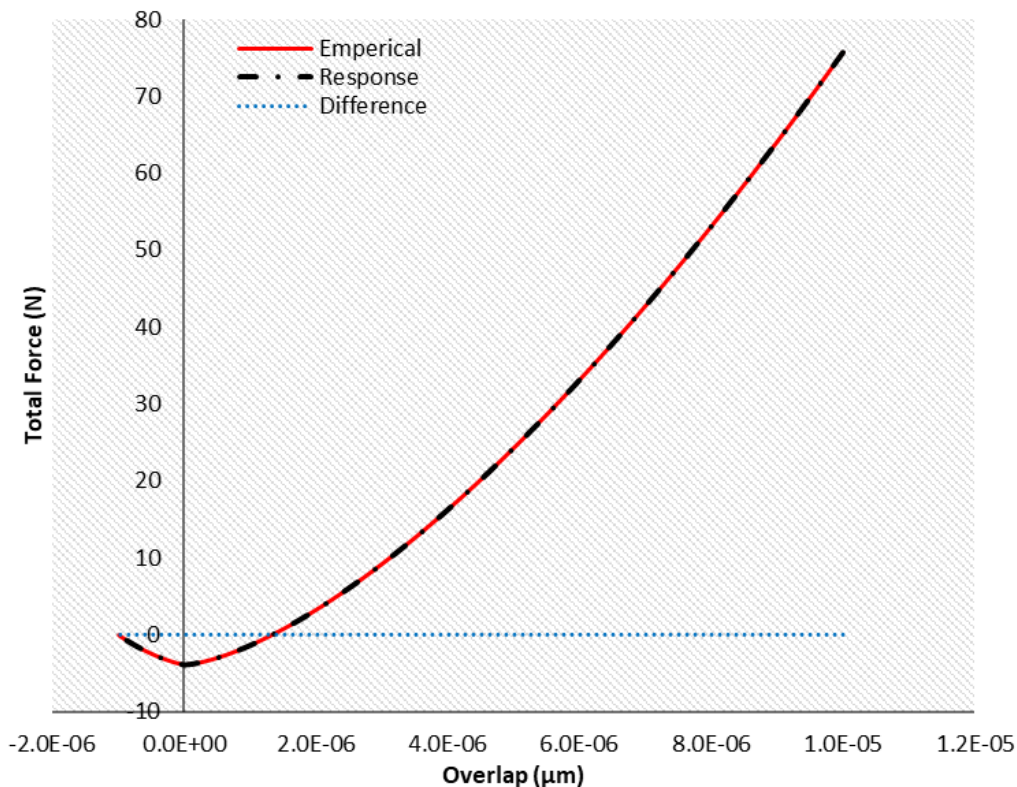


Figure 7.18 Comparison of contact force calculation through model response and an empirical relation

The model response was then compared with the Hertzian contact force through empirical relation. Both approaches resulted in very similar values and no difference was observed at any overlap value, as represented in Figure 7.18 above.

7.3 Capillary force model validation

The capillary force model including the interparticle suction-tension forces was utilized in DEM based program and validated against other models and experimental data. At first, the model was used to plot the saturation vs suction plot, which is equivalent to the soil-water characteristic curve for the experimental results.

The saturation-suction relation was plotted for varying sizes of particles with a degree of saturation ranging from 1.0 to approaching zero. The response is shown in Figure 7.19. the suction pressure reduced with increasing particle size, which is very similar to the experimental results. Also, the shape of the response matches well with the prevailing experimental finding, e.g. Gallage & Uchimura (2010).

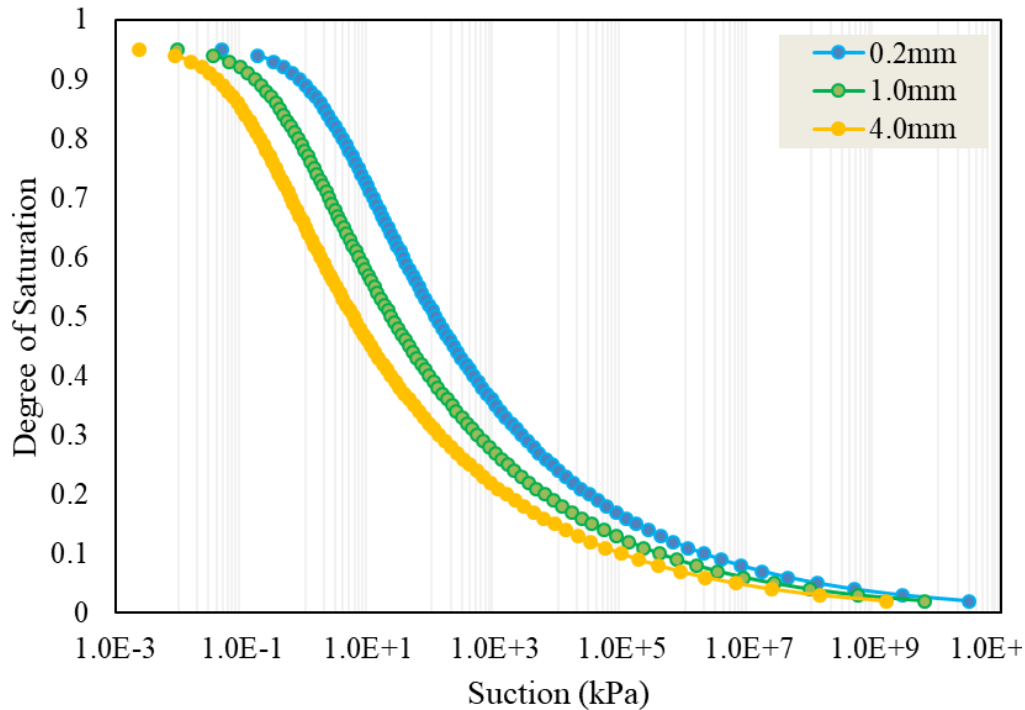


Figure 7.19 Capillary force model response against the degree of saturation

It is worth noting that the sample having a degree of saturation as 1.0 (fully saturated) does not offer any capillary attraction amongst particles and the suction force approaches zero. Similarly, when the degree of saturation approaches zero, the suction pressure approaches to infinity, which is not realistic. The current model in consideration thus does not incorporate the extreme limits of saturation, i.e. $S_r \approx 95-100\%$ and $S_r \rightarrow 5-0\%$. This can be considered as the limitation of the model.

The plot for the suction forces against the degree of saturation is shown in Figure 7.20 below. Similar to Figure 7.19 above, three different types of particle sizes are showed. Along with the suction forces, the unit weight of each particle size is plotted, showed by a dotted line in the plot. The color of each force plot and corresponding particle weight plot are kept similar for better clarity.

Contrary to the suction pressure case, the suction force showed increased values with increasing particle size. Further to that, the trend became more non-linear with the increasing sizes of the particles, showing that the water meniscus variation is more prominent in larger particles.

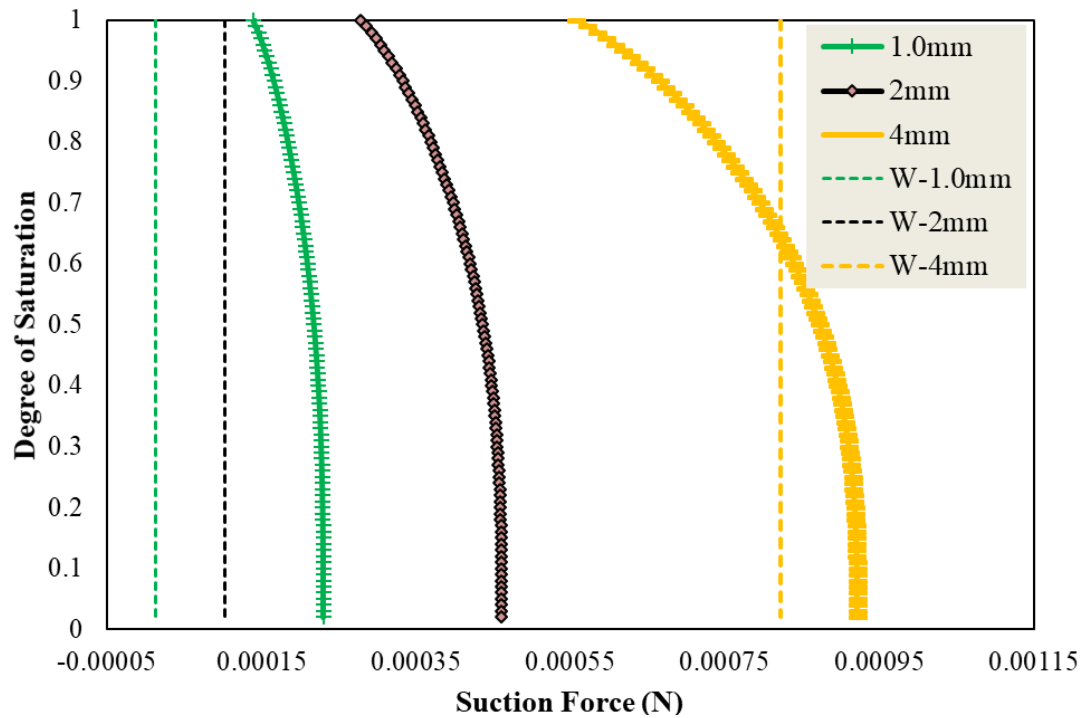


Figure 7.20 Model response for the degree of saturation vs suction force

Comparing the unit weights of particles, the cases with particle diameters of 1.0mm and 2.0mm demonstrated the unit weights far lesser than the developed suction force due to the presence of water in the voids. The higher values of suction forces are observed at all degrees of saturation. However, for the case with a particle diameter of 4.0mm, a higher degree of saturation resulted in smaller suction force; whilst by reducing the degree of saturation the suction force kept increasing until a specific level where both weights of particle and suction forces equivalized each other. Further reduction in the degree of saturation; however, resulted in much higher suction force, far enough to hold another particle due to capillary effects.

The same condition is more clearly shown in Figure 7.21 below. Two particles of the same size for each particle type initially attached to each other using the capillary force model in DEM simulations. Particles having a diameter smaller than 4mm did not separate due to the

presence of strong inter-particle suction compared to the self-weight of the particle. However, the particle with a 4mm diameter could not sustain the load of another particle and got detached.

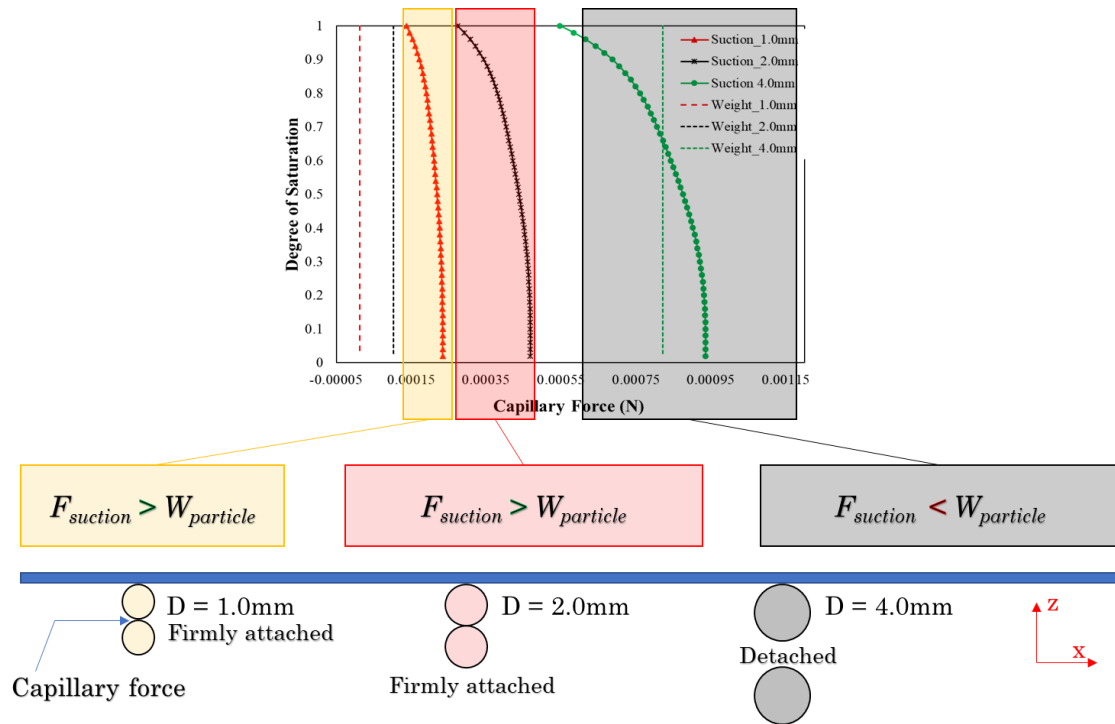


Figure 7.21 Capillary force through modified model against particle size

Further to that, several DEM-based numerical simulations were performed on cavity stability and loading cases, and the model was found to have satisfactory results when compared to equivalent experimental data. The results will be discussed later in the discussion of other chapters.

Lastly, the model was then compared with another existing model of Sun & Sakai (2018), that is being used in the field of powder technology and pharmaceuticals. Although the fields of application for both are quite far from each other, the basic response for both is compared here. The Sun & Sakai (2018) model is developed for fully saturated conditions, which makes it hard to compare with the currently modified model. To have a better comparison, Sun & Sakai (2018) model was then incorporated with the saturation variation conditions and then compared with the current model with similar conditions.

Both, suction pressure and the suction force plots for varying sizes of particles are presented in Figure 7.22 and Figure 7.23 and then compared with the current capillary force model.

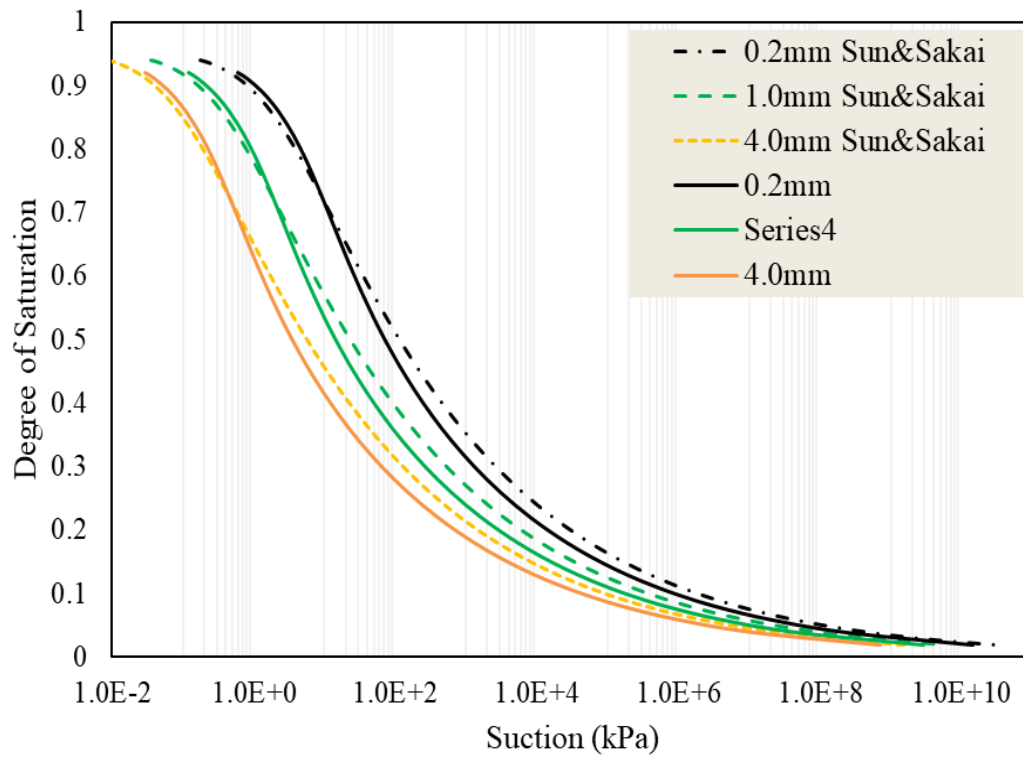


Figure 7.22 Comparison of Sun (2018) model to the current model for inter-particle suction pressure with varying diameters of particles

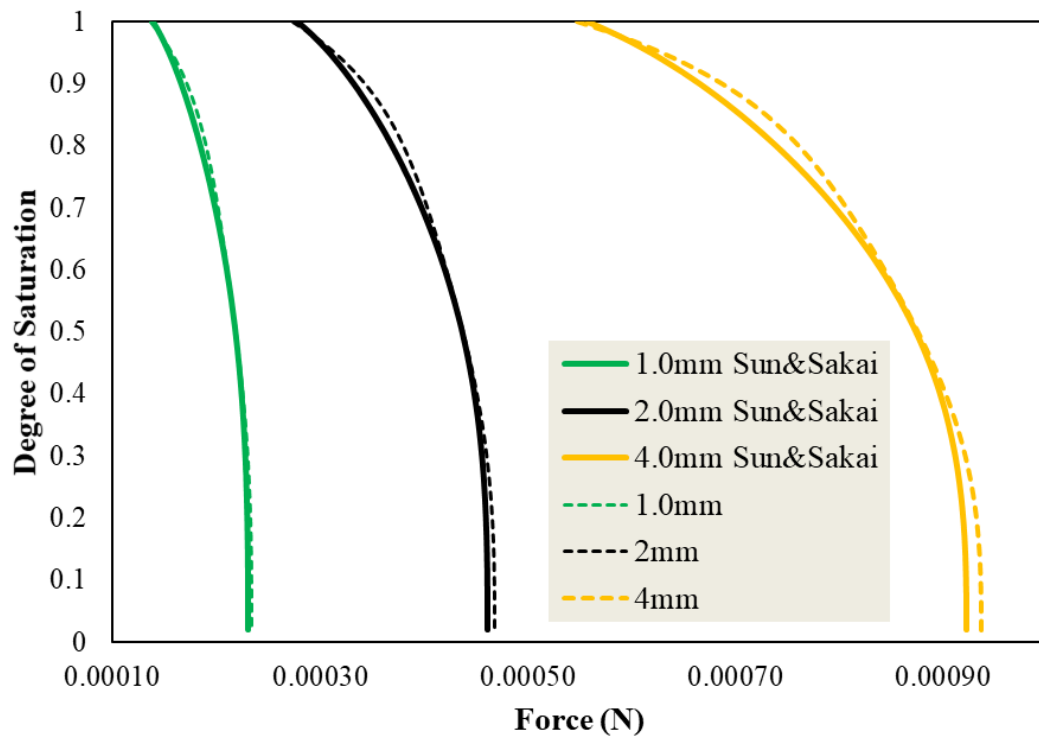


Figure 7.23 Comparison of Sun (2018) model to the current model for inter-particle suction forces with varying particle diameters

In both of the plots, as shown in Figure 7.22 and Figure 7.23, the current capillary model produced results slightly varying quantitatively from the Sun & Sakai (2018) model. However, the qualitative response of the current model is well in line with other available models and the experimental results.

7.4 Summary

In this chapter, the necessity of water-induced capillary forces was discussed, which is a pre-requisite for simulating the behavior of soil for an underground cavity formation and its stability. To incorporate the capillary forces in the traditional DEM models, a new inter-particle based suction-tension model is introduced in this chapter that can operate with inputting the degree of saturation of the sample and subsequently the model can output the capillary forces in the material. The model was then validated against the empirical results of the contact force and the other prevailing capillary force models being used in other fields of engineering. The model was found to have a significant match with the experimental results as well.

CHAPTER 8: EXPERIMENTAL AND NUMERICAL SETUP FOR CAVITY TEST CONDITIONS

Another important natural phenomenon for soil arching is the formation of underground cavities. The cavity is formed due to the internal erosion of soil. A strong arching encompasses the formed cavity and the stability of the cavity is ensured due to the combined action of soil arching and the attractive forces amongst particles by the development of capillary forces.

The current chapter discusses the experimental setup for the Model cavity tests been performed for the study of the cavity stability and arching around it. Further to that, the numerical setup for the cavity stability will also be discussed in this chapter.

8.1 Experimental setup for model cavity tests

8.1.1 Basic construction

To investigate the soil arching under cavity formation condition, a model cavity test apparatus, as shown in Figure 8.1, is used. The model test apparatus comprises of two main parts: the upper soil chamber and the lower water supply mechanism.

The soil chamber has a dimension of 300mm × 250mm in horizontal and vertical direction respectively. The width of the sample that can be accommodated inside is 80mm. The front and back walls are constructed with smooth acrylic plates with enough thickness and transparent in nature to have a better visualization of the sample during testing. On each side, there are vertical chambers to measure the water level in the sample. The walls along the sample width (YZ plane) have small holes along the height to help soil water seep through them and collect in the side chambers. The water collector chambers are also made up of acrylic smooth plates to visualize the movement of the water level.

The lower part consists of a small rectangular box, with a bottom door that can be opened and closed as and when required. The bottom door is sealed against water leakage. The base box connects the upper box through a small slit, 5mm in width. The lower small box is connected through a thin pipe to the water source, which is a small water bucket attached with a pulley system and can be brought up or down at any required level. The

base slit is inserted with fiber cloth to block the passage of soil material but to allow the passage of water.

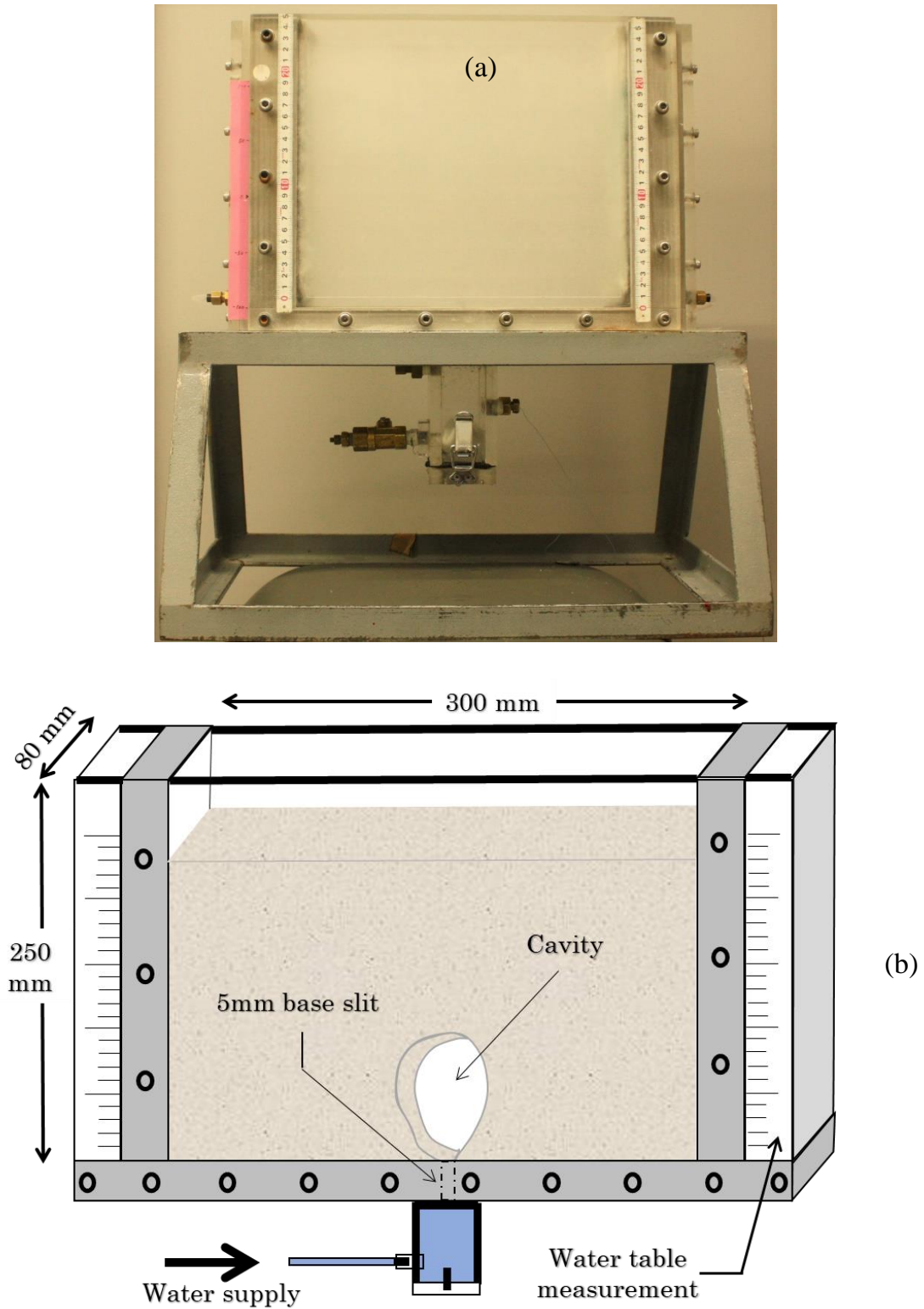


Figure 8.1 (a) Cavity model test apparatus and (b) schematic diagram

8.1.2 Working mechanism

The working principle for the cavity model test apparatus is the internal erosion of soil through the base slit to form a cavity. A total sample height of 200mm is selected for all the tests. Each test is then further divided into ten layers, each with a height of 20mm to result in a specific sample density, as per requirement. However, for some of the cases, the sample was prepared by air pluviation method where the sample was dropped from a fixed height of 250mm (top edge of the apparatus).

Before the commencement of sample preparation, the base slit is inserted with the fiber cloth to clog it, causing a blockage of the sample to pass through. Subsequently, the sample is prepared as described above. Once the sample is prepared, the base box is connected with the water supply and the water seeps through the base fiber cloth to the sample.

The height of the water bucket is adjusted with the top height of the sample. The sample is given ample time to let water seep through and reach the top level of the sample. This bottom-feed process ensures the slow removal of air pockets from bottom to the top, as the water propagates into the sample. The water flow is temporarily stopped once the sample attains a fully saturated condition.

As explained in the earlier chapter, the fully saturated condition does not impart any capillary effect on the grains and the particles are in free-flow condition if the sample density is low enough. Hence, in order to produce a cavity, the water table is reduced by removing the water from the side water chambers up to a level where the new water table is desired. Once, the water table is reduced, enough time is given to the sample to become stabilized again.

The next step is to remove the fiber cloth slowly into the small base box with the help of strings attached to it. The soil portion near the bottom of the soil chamber is still in a fully saturated condition with no capillary forces. Hence, once the fiber cloth is removed, the water within the soil mass forces the soil particles to erode and flow in the base chamber. Hence, a chain of particle flow is initiated that develops slowly. The particles as a combined effect form a largely yielding portion of soil mass and initiate the cavity development. However, as the cavity moves upwards, the sample does not remain fully saturated in the upper levels and hence there is the presence of strong capillary forces in the soil mass, causing splitting of soil mass into yielding and non-yielding

portions. That phenomenon constitutes the cavity boundary and the soil below that partition flows out of the base slit. The top-most portion of the sample being the one with the least amount of saturation and hence the strong capillary action, remain intact with a firm surface.

Once the fiber cloth is taken off and the particles start moving downwards through the slit, the bottom door of the base box is opened to let the water flow out. In this way, the eroded sample is pushed out to form a clear cavity. The cavity remains stable in the capillary forces combined with the soil arching around the cavity is strong enough to keep the suspended particles intact and transfer the normal stresses to the side portions of the sample. However, the soil cover above the soil and the initial water level also plays a role in the stability of the sample

In order to investigate the critical size of the cavity that can be sustained under the given conditions, the water is re-filled in the sample and then drained again to result in cavity expansion, which eventually results in cave-in occurrence. The size of the cavity just before the cave-in is the maximum possible stable size of the cavity under the given conditions of the sample.

8.2 Materials

8.2.1 Spherical glass beads

As explained in chapter 7, a new model capable of implementing the capillary forces in the DEM simulations is utilized, based upon the basic interaction between two spherical particles. Hence, to have a better comparison, different kinds of glass beads were used in the model cavity tests. Glass beads, being the simple shape of the material, can offer the best possible comparison between the numerical and the experimental work during cavity formation condition and its stability analyses.

As the particle size strongly affects the capillary behavior of the sample, a wide range of particle sizes was selected to be tested in the cavity model test apparatus. The particle sizes with other properties are shown in Table 8.1 below. Some of the particle sizes were then further classified into smooth and rough categories to study the particle roughness effect.

Besides the spherical glass beads, a few tests were also conducted with the silica sand with different sizes under the dry condition to relate the effect of particle shape.

Table 8.1 Material properties for spherical glass beads

Sr. No.	Particle type	Mean size, D_{50} (mm)	e_{max}	e_{min}
1	Smooth spherical glass beads	1.70	0.694	0.581
2		0.75	0.726	0.583
3		0.50	0.694	0.589
4		0.35	0.708	0.582
5		0.20	0.734	0.563
6	Mixed grading			

Table 8.2 Material properties for spherical glass beads

Sr. No.	Particle type	Mean size, D_{50} (mm)	e_{max}	e_{min}
1	Rough spherical glass beads	1.70	0.717	0.602
2		0.50	0.720	0.611

For the cases with spherical glass beads, not only the particle size was varied, but also density was varied and checked with the output results. Furthermore, the variation of the initial water level was also performed for certain particle sizes and the effect of sample saturation on the stability of the cavity was observed. Lastly, the particle surface texture was varied in order to have a better comparison between the rough and the smooth cases of spherical glass beads in cavity model tests.

8.2.2 Rough and smooth surface particles

The glass beads in their manufactured form, offer a very small amount of surface resistance due to the extremely smooth surface. Lack of interlocking and negligible resistance to sliding can result in a non-stable cavity formation cases, or complete non-existence of the cavity formation.

To have a better comparison of surface smoothness and the roughness on the stability of the cavity for similar conditions, some of the particle sizes were made rough through a special process of milling and mixing. A milling apparatus as shown in Figure 8.2 was used, which comprises two cylindrical shaped ceramic vessels.



Figure 8.2 Milling machine for the particle roughness

There is a need for a fine material with angular particle shape to scratch the top surface of glass beads during the rotation of cylindrical vessels in the rotating machine. For the case of glass beads with a mean diameter of 1.7mm, silica sand ($D_{50} = 0.19\text{mm}$) was used in such a way that one part of glass beads was mixed with two parts of Toyoura sand to allow for a maximum possibility for each glass beads to have enough contact with Toyoura sand. Furthermore, there should be sufficient size difference between both

materials in order to have the maximum contacts of grinding material with the glass beads, and also to facilitate sieving off the fine material after the roughness test.

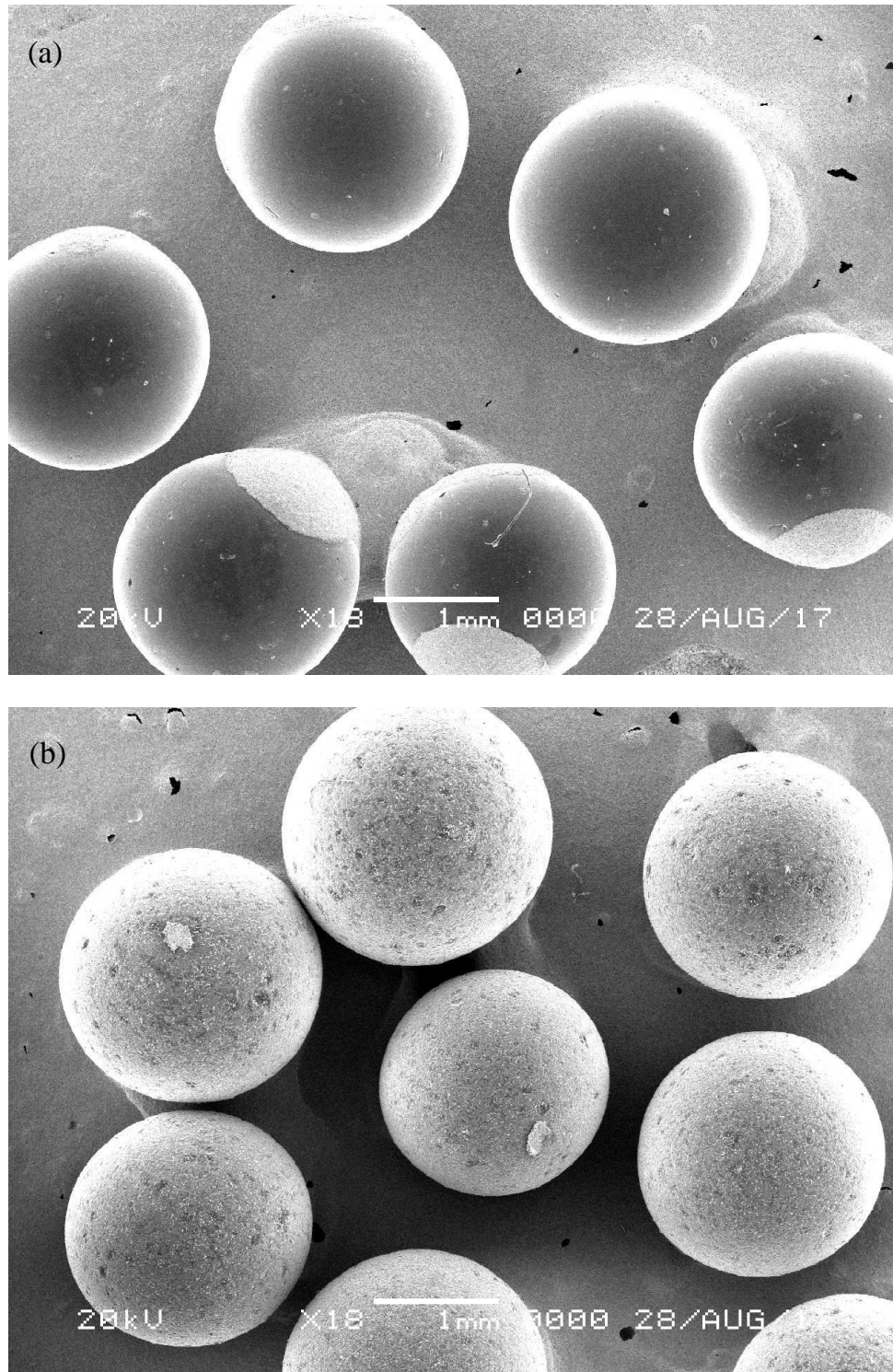


Figure 8.3 Comparison of surface texture for the (a) smooth and (b) rough glass beads using SEM analyses, having a mean diameter of 1.7mm

In the case of particles with a D_{50} of 0.5mm, silica number 8 sand was mixed, having a mean diameter of around 0.1mm. the mixing ratio was similar to that of the earlier cases. At each time, two cylindrical vessels can be used simultaneously to mill the glass beads. Each type of glass bead was rolled/milled for two whole days (48-hours) to allow sufficient surface scratching of material.

Once the rotation is stopped after due time, the sample is sieved with an appropriate size, washed with distilled water and then dried for 24 hours in the oven at a controlled temperature. Subsequent to all these procedures, the sample was thought to be sufficiently prepared for the testing.

A comparison of both smooth and rough shaped glass beads with a mean diameter of 1.7mm is shown in Figure 8.3 below. A clear difference between the surface texture of both can be seen, which is believed to impart some effect in the stability of samples under cavity formation cases.

8.2.3 Deformed and clumped glass beads

A further investigation of the particle shape effect was made by using deformed and clumped glass beads. The details of the particles along with the conditions of testing are given in Table 8.3. The deformed glass beads are the glass beads with a non-spherical deformed shape as shown in Figure 8.5(a).

The clumped glass beads were constituted by the combination of several spherical/non-spherical glass beads, varying sizes. However, the mean diameter was measured to be around 0.6mm for the rigid clumped particles. Figure 8.5 explains the shape of the clumped particle.

Both clumped and deformed glass beads were also tested with a rough surface and the comparison of rough surface for both materials is presented in Figure 8.5, Figure 8.6 and Figure 8.6 (b & c).

Table 8.3 Test cases and properties for non-spherical glass beads

Sr. No.	Particle type	Mean size, D_{50} (mm)	Surface condition	e_{max}	e_{min}	Relative density, D_r (%)
1	Deformed glass beads	1.0	Smooth	0.494	0.666	≈ 55
			Rough	0.509	0.683	
2	Clumped glass beads	0.60	Smooth	0.862	0.629	55, 90
			Rough	0.902	0.654	

8.3 Experimental testing plan

The model cavity tests were divided into two main categories:

- (i) Cavity stability tests
- (ii) Cavity surface loading tests

Details for both types are given below:

8.3.1 Cavity stability tests

The materials presented in the previous section were tested in the model test apparatus as shown in Figure 8.1. Several factors were varied during the tests e.g. the particle size, initial water level, density of the sample, and surface texture. The tests were performed as stated in the working mechanism in section 8.1.2 above.

Table 8.4 below illustrated the basic testing plan with various variable factors. In the case of a mixed gradation sample, all available particle sizes were utilized. Spherical glass bead samples with smooth surfaces, having a mean diameter (D_{50}) of 1.7mm, 0.725mm, 0.50mm, 0.375mm and 0.2mm were all mixed in equal weight proportions in a big container. A gentle mixing was assured to avoid damage to the particle surface and

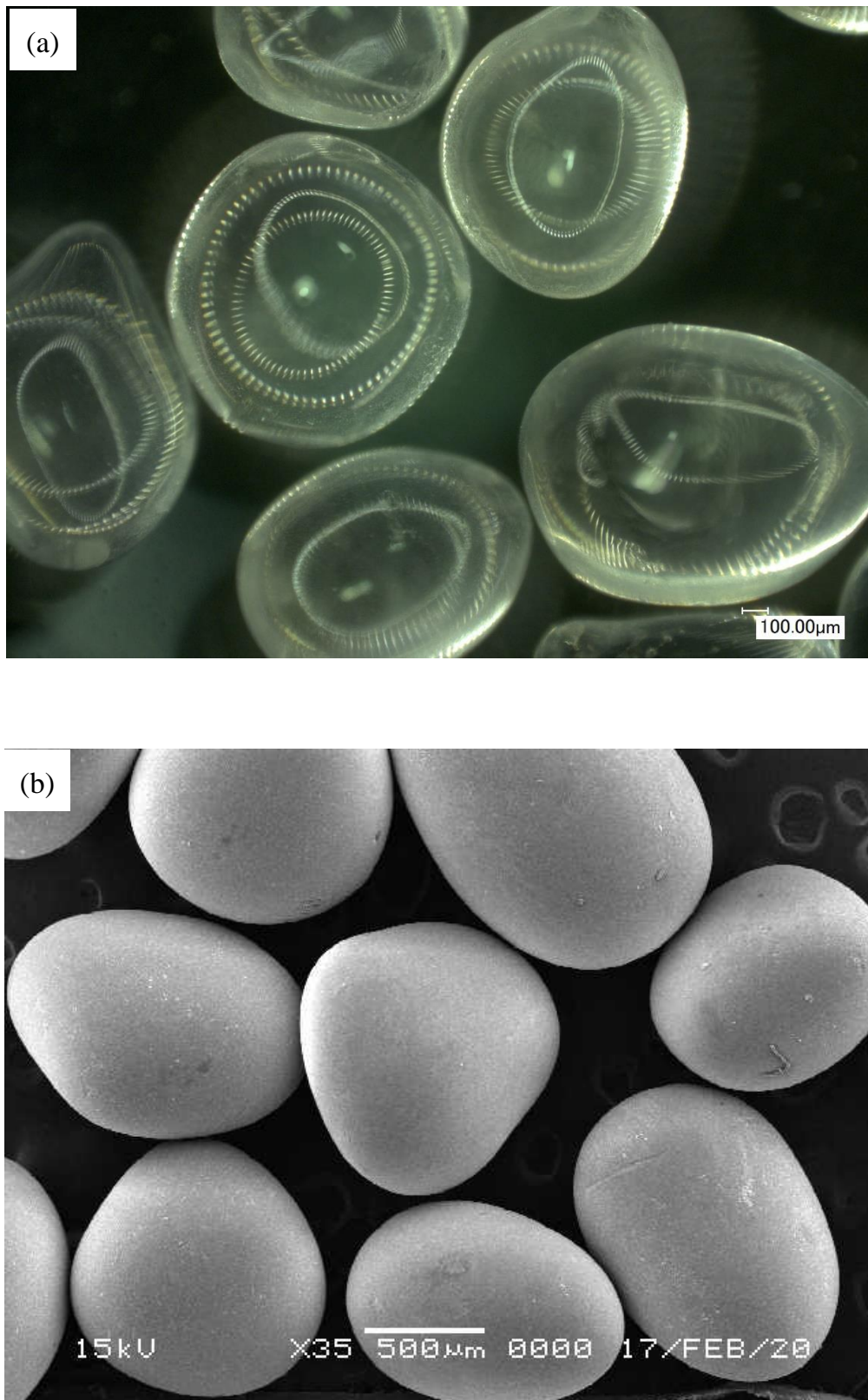


Figure 8.4 Deformed glass beads in (a) Digital image and (b) SEM image having a smooth surface

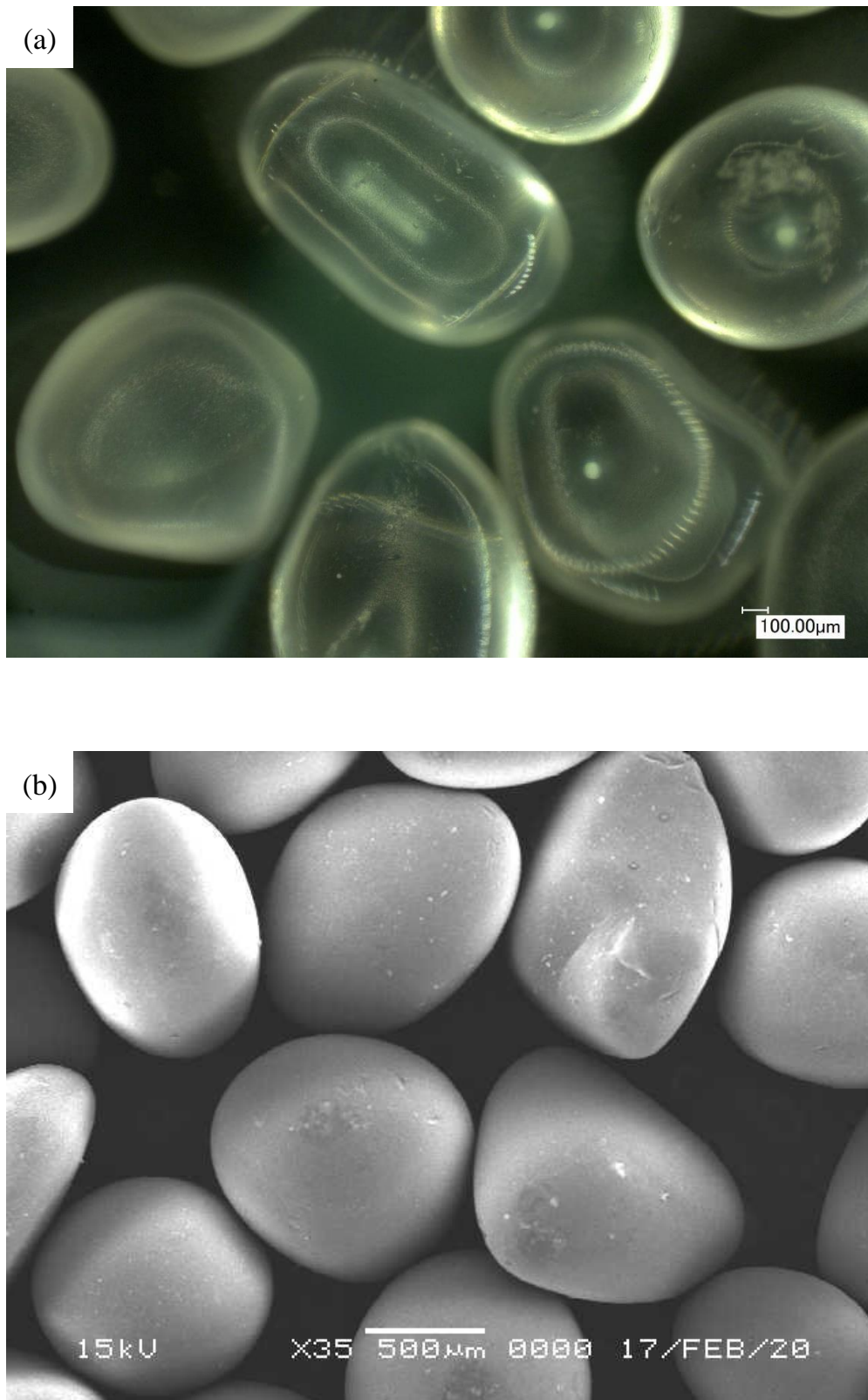


Figure 8.5 Deformed glass beads in (a) Digital image and (b) SEM image having a rough surface

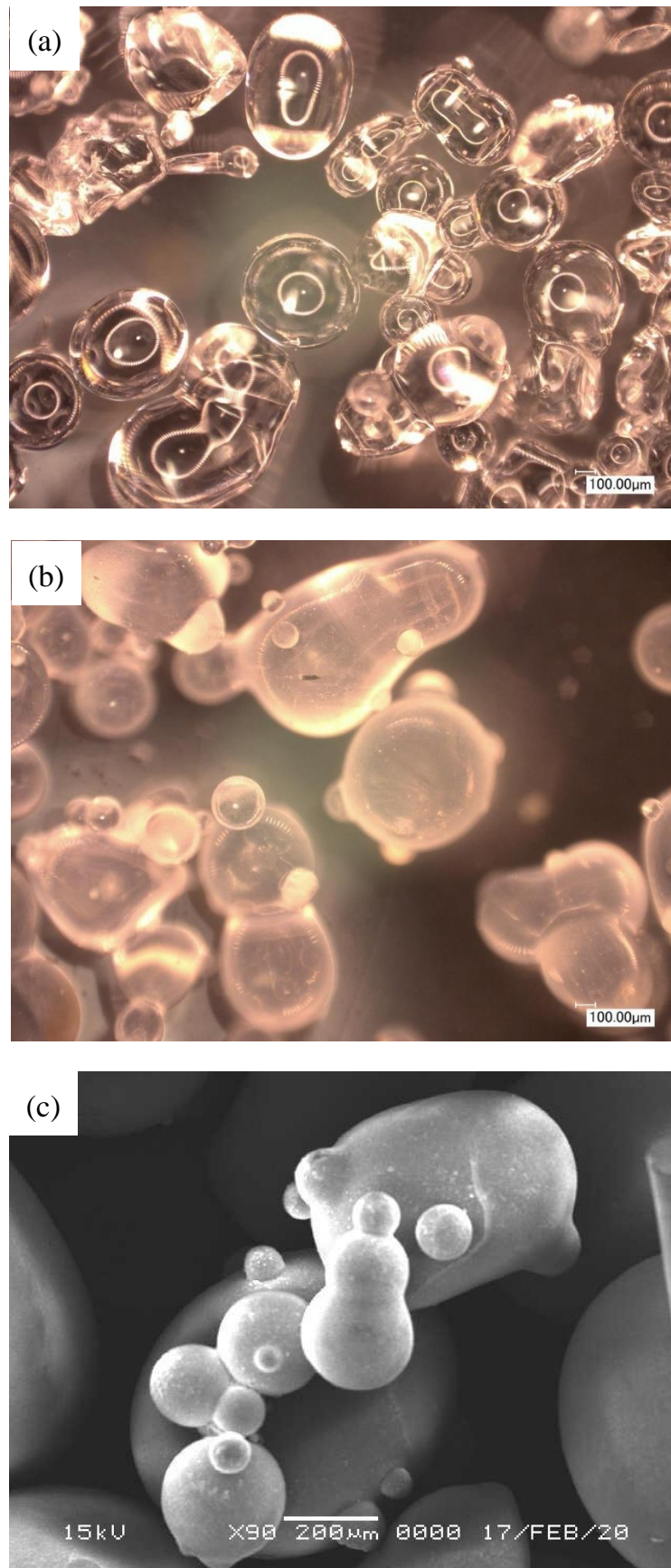


Figure 8.6 Comparison of clumped glass beads images at (a) smooth and (b) rough condition using digital imaging and (c) rough condition using SEM

the sample was prepared with the air pluviation method. The sample was dropped from a fixed height of 250mm, which is the maximum height of the model test apparatus. The sample was dropped slow enough and was spread all over the sample space to avoid significant variation of sample density due to the deposition process.

Since the mixed grading sample was composed of all available particle sizes with a large variation in size, the minimum and maximum void ratios of the sample was not determined. However, due to the presence of very fine grains (0.2mm), that could easily occupy the voids between the largest particles (1.7mm), the density of the sample is assumed to be around 80% of maximum dry density.

8.3.2 Cavity surface loading tests

The cavity development process in the cavity stability tests showed the presence of stable arching around the cavity surface for the cases where no collapse was observed. The presence of a stable cavity does not impart any surface effects. However, in case the cavity is developed under the road surface with surface loading due to traffic, the loading might result in the collapse of the cavity and cause a cave-in incident.

In order to determine the response of a stable cavity under the surface loading, the model cavity test apparatus was used in a triaxial loading system to apply the top load on the sample. Figure 8.7 shows the schematic diagram of surface loading tests.

Table 8.4 Cavity model test plan for stability analyses

Sr. No.	Particle mean dia (D_{50}), mm	Surface texture	Initial water level, (h_w), cm	Relative density, (D_r), %
1a	1.7	Smooth	20	≈ 55
1b		Rough	2	≈ 55
1c		Smooth	0 (drained to zero)	≈ 55
1d		Smooth	0 (dry)	≈ 55
2a	0.725	Smooth	15	90
2b		Smooth	13	90
2c		Smooth	9	90
2d		Smooth	9	≈ 50
2e		Smooth	7.5	≈ 50
2f		Smooth	5	≈ 50
3a	0.50	Smooth	10	≈ 50
3b		Smooth	5	
3c		Smooth	0	
3d		Rough	9	
4a	0.375	Smooth	9	≈ 50
5a	0.20	Smooth	20	≈ 50
6a	Mixed grading	Smooth	9	≈ 80

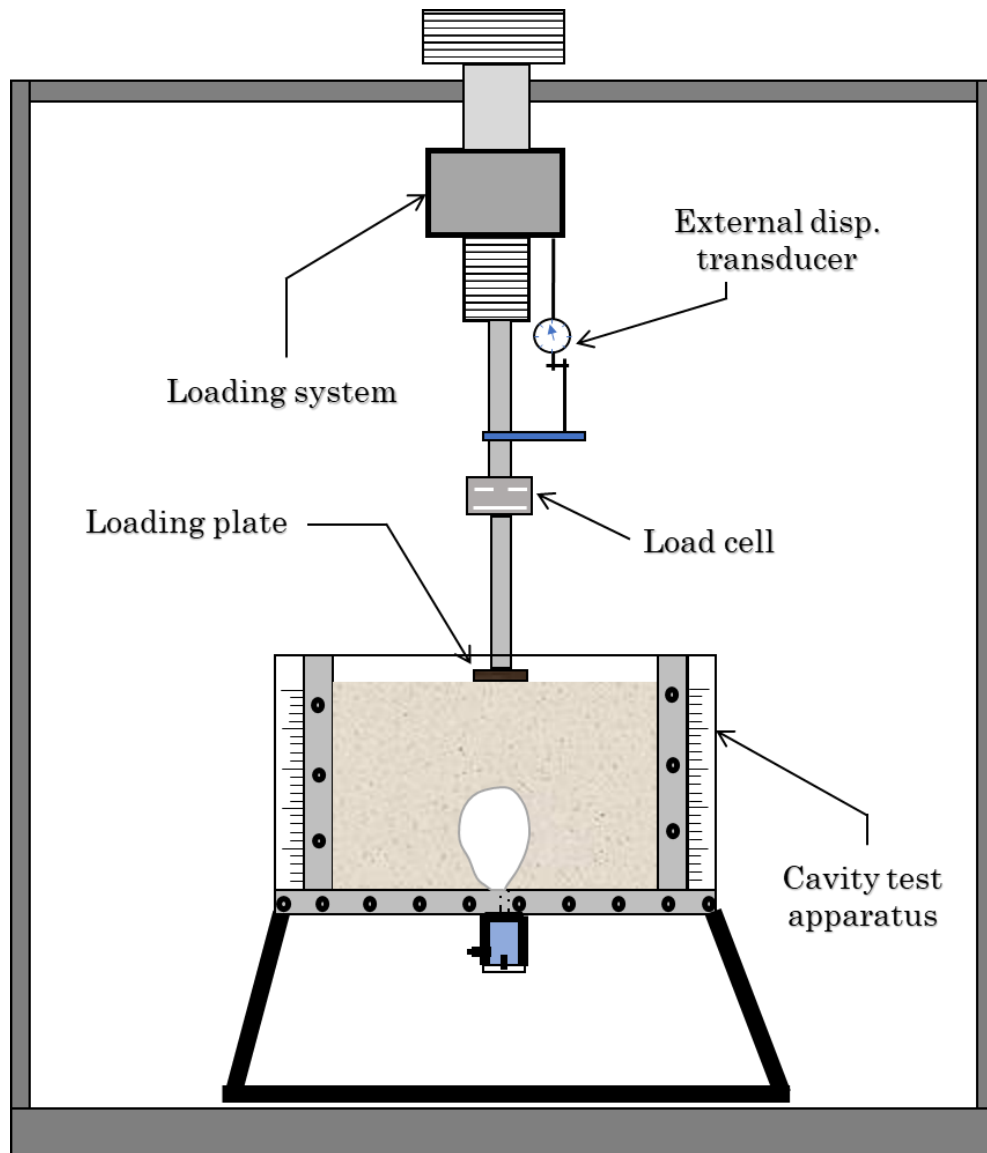


Figure 8.7 Cavity surface loading test under triaxial machine loading system

The loading system was equipped with a load cell and external displacement transducer, connected to a data logger and to a computer for automated data recording. Several load cells and external displacement meters were used in the surface loading tests. All used load cells and displacement meters were calibrated up to a range that was anticipated to be encountered during the test conditions. Further to that, the loading system was also calibrated against the motor RPM and the settlement rate. The calibration curves for the load cells, external displacement transducers, and the displacement rates are shown in Figure 8.8 to Figure 8.14 below.

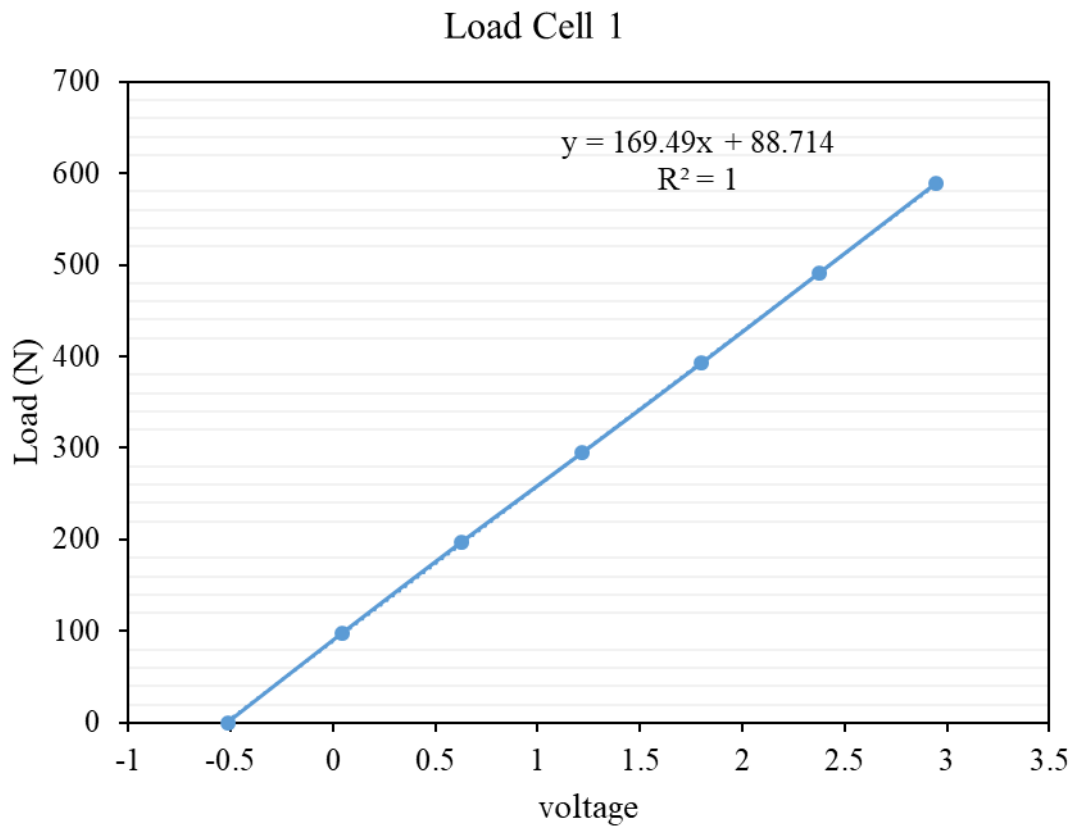


Figure 8.8 Calibration curve for load cell 1

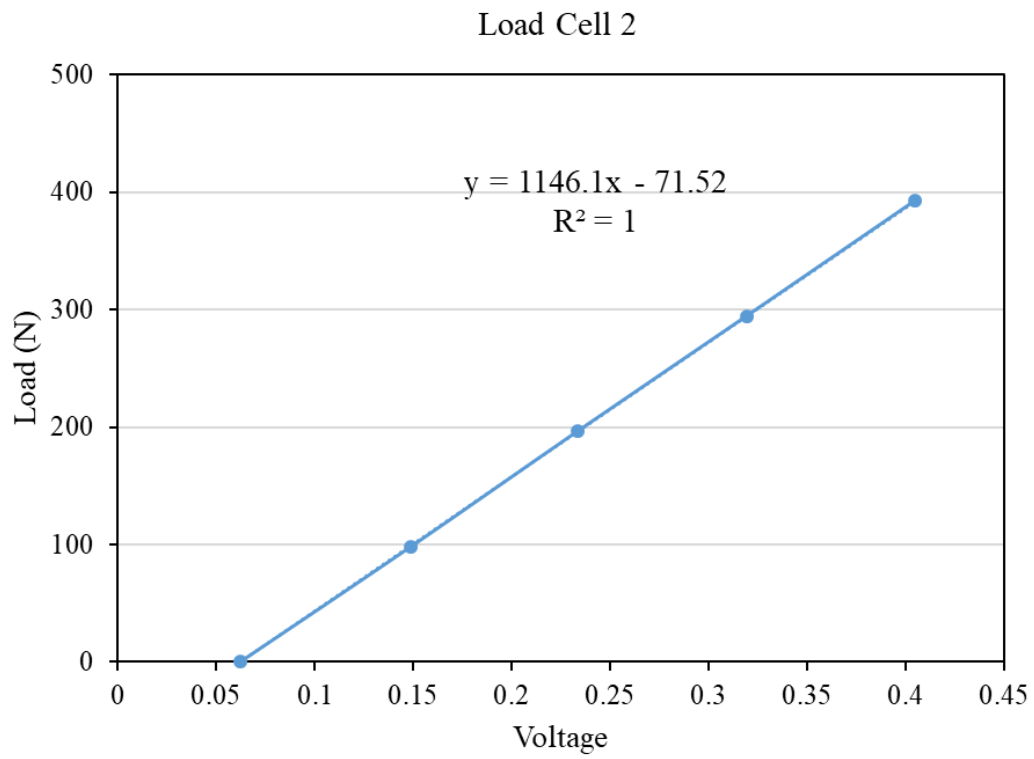


Figure 8.9 Calibration curve for load cell 2

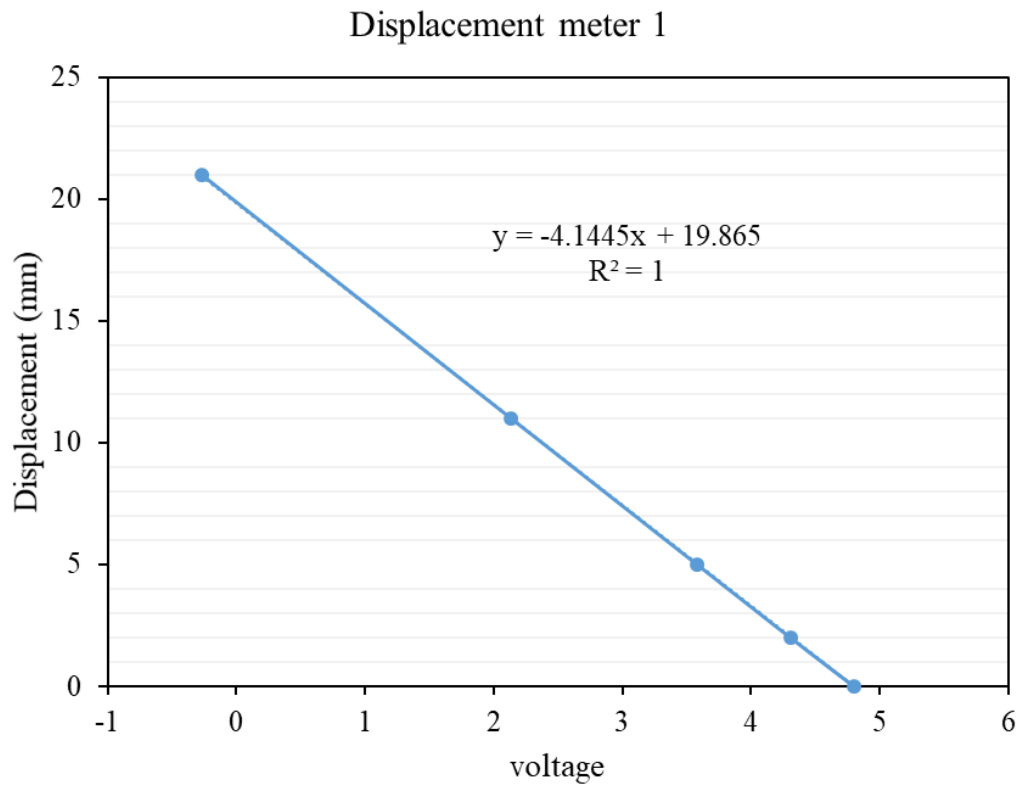


Figure 8.10 Calibration curve for external displacement meter 1

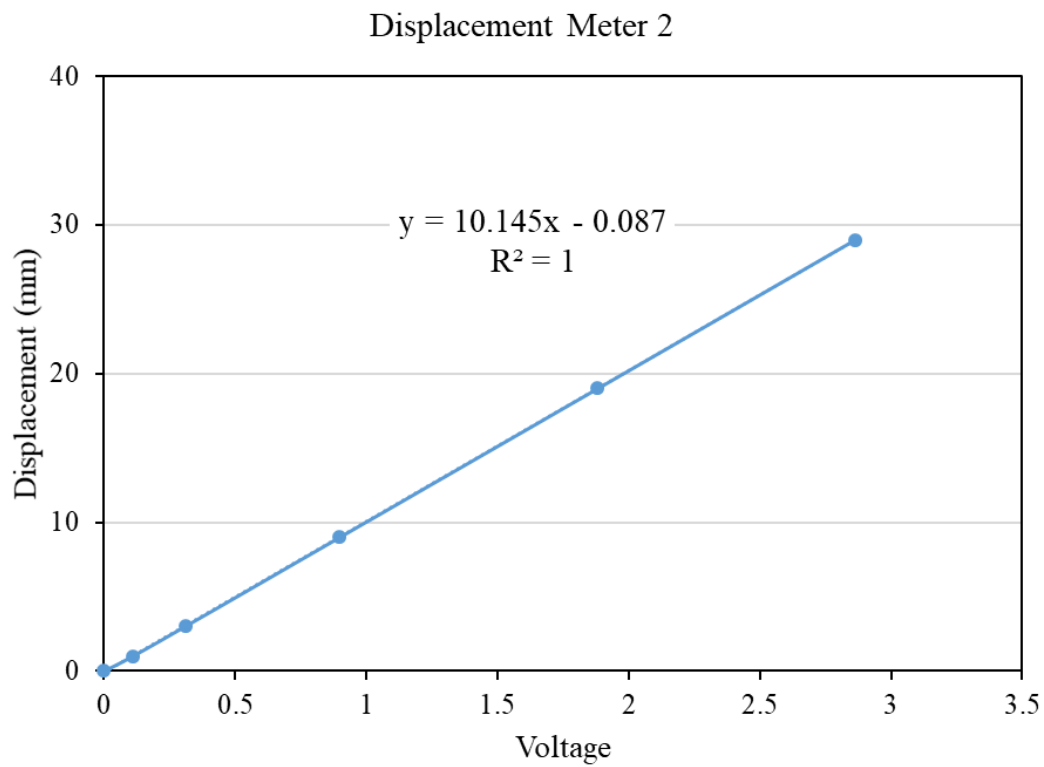


Figure 8.11 Calibration curve for external displacement meter 2

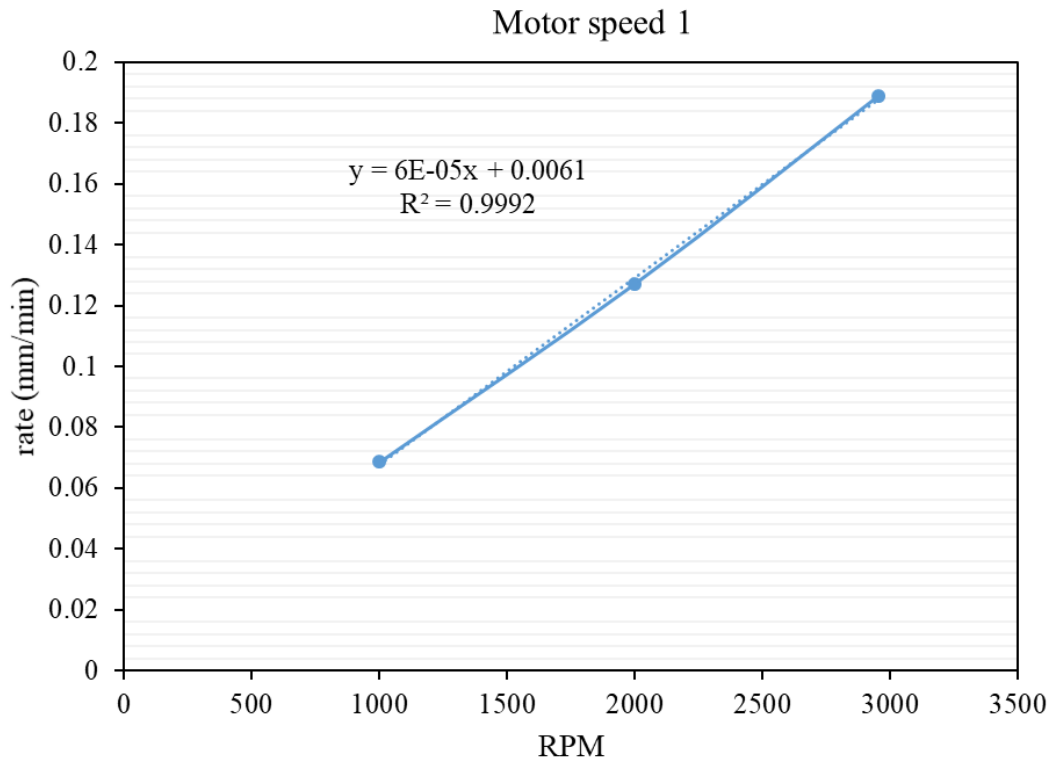


Figure 8.12 Calibration curve for motor speed 1

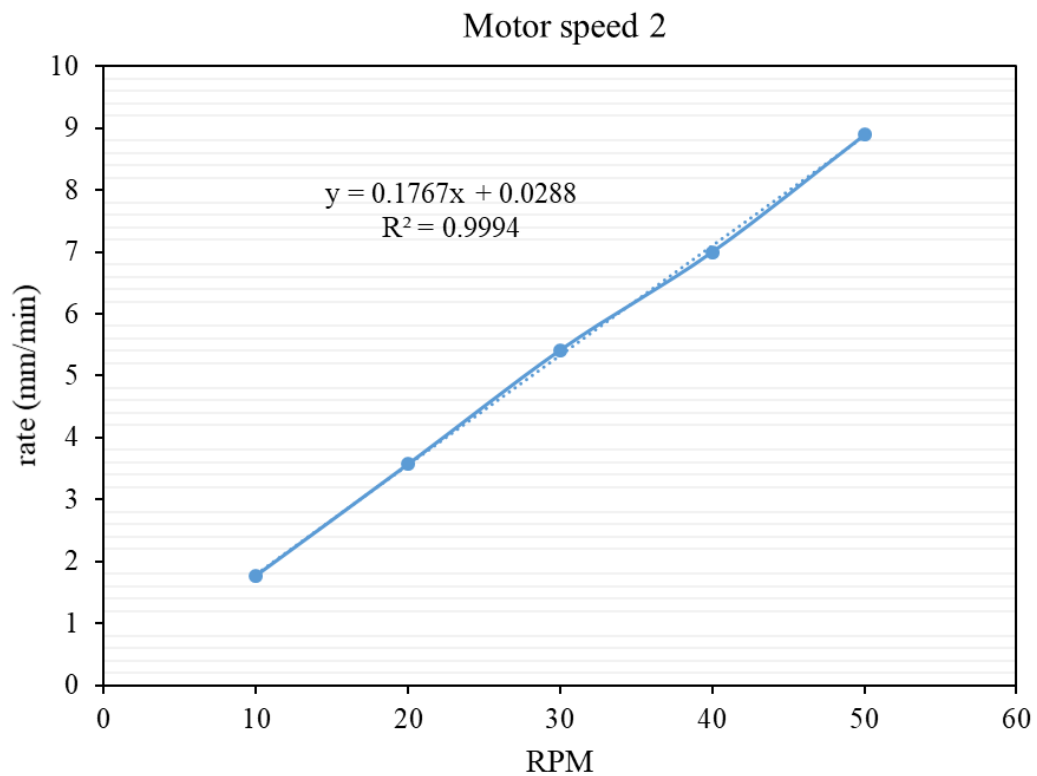


Figure 8.13 Calibration curve for motor speed 2

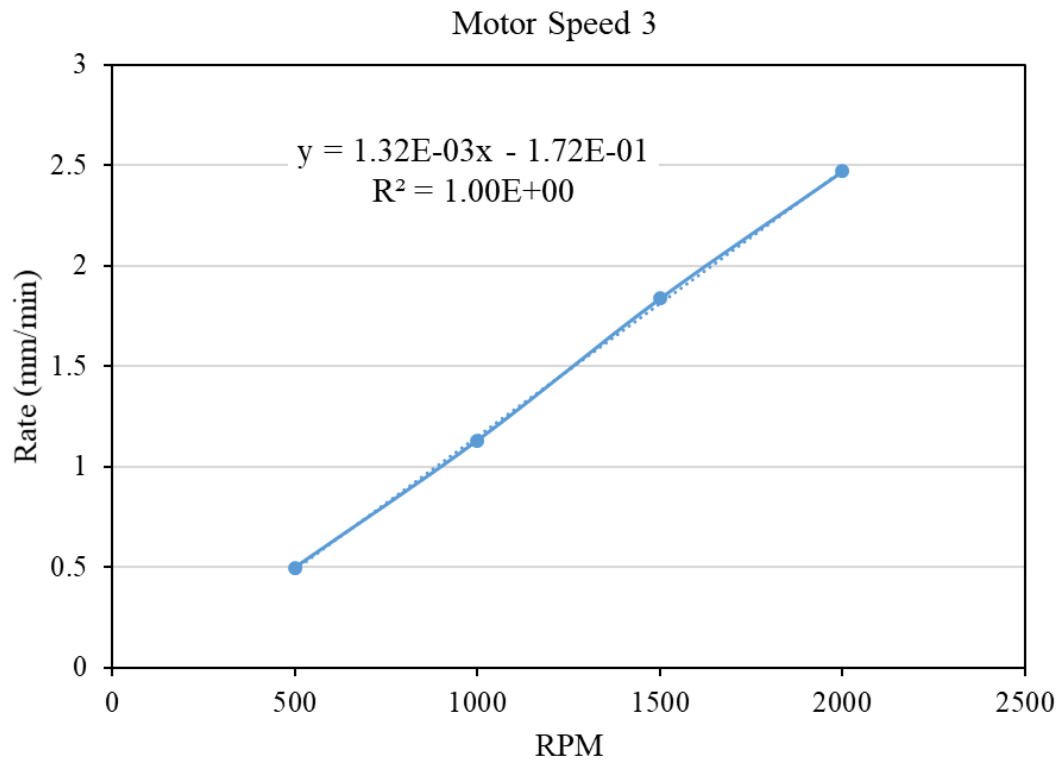


Figure 8.14 Calibration curve for motor speed 3

8.3.2.1 *Types of the loading plate*

The cavity size developed above the bottom slit for all cases measured to be in the range of 50mm width and the height varied as per the other prevailing sample conditions like particle size, surface roughness, initial water level, and density. In real conditions, the cavity produced beneath the road surface can have multiple types of surface loading due to passing vehicles. These loading types might produce a pattern that could either be smaller than the size of the cavity by itself or sometimes much larger as well. Hence, in order to study the effect of the area of loading above the cavity, three different sizes of top-loading plates were used in the surface loading tests.

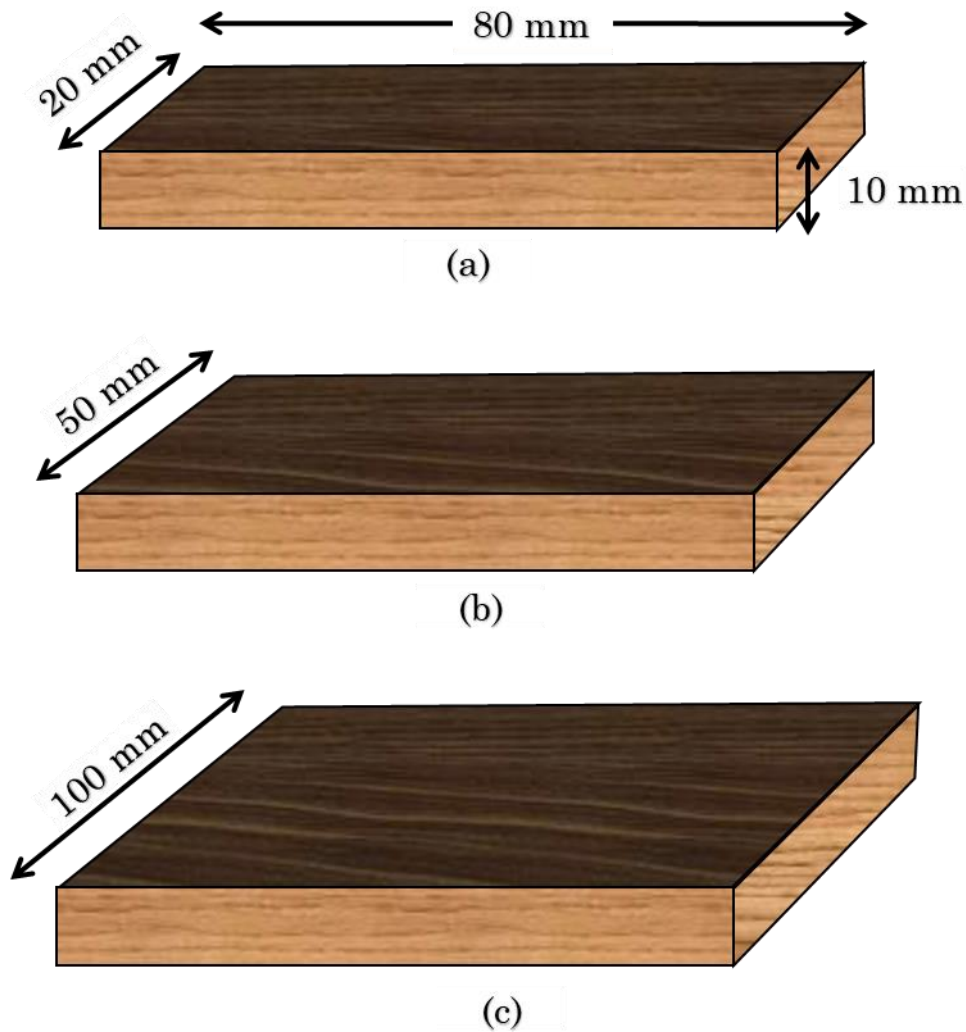


Figure 8.15 Different sizes of the plates used in cavity surface loading tests

The sizes of different plates used in the cavity surface loading tests are shown in Figure 8.15 above. A total of three different sizes were used, having a width of 20mm, 50mm and 100 mm. All plates occupied full sample width and the thickness of each plate was approximately 10mm. The plates were composed of rigid laminated wood with enough stiffness to transmit the machine load to the material surface without being bent. The plates were centered above the stabilized cavity in the sample and the load was then applied at different speeds, from slow to the fast.

Table 8.5 shows the plan of tests performed on surface loading of cavities having a mean particle diameter of 0.5mm (spherical), for the cases with the presence of a stable cavity.

Table 8.5 Cavity surface load test on spherical particles with 0.5mm mean diameter

D_{50} , mm	Surface texture	Initial water level, (h_w), mm	Relative density, (D_r), %	Plate size, mm	Loading speed, mm/min
0.50	Rough	100	90	50	0.069
		100	90	50	0.189
		80	90	50	0.88
		80	90	50	1.767
	Smooth	80	90	20	0.069

Table 8.6 shows the plan of tests performed on surface loading of cavities having a mean particle diameter of 0.5mm (spherical) for both rough and smooth conditions, for the cases without the presence of any initial cavity in the prepared sample.

Table 8.6 surface load test on spherical particles with 0.5mm mean diameter without the presence of the cavity

D_{50} , mm	Surface texture	Initial water level, (h_w), mm	Relative density, (D_r), %	Plate size, mm	Loading speed, mm/min
0.50	Rough	100	90	50	0.88
		100	90	50	1.77
		100	90	50	3.57
	Smooth	100	90	50	0.88

Besides the spherical particles, the tests were performed on the clumped and deformed particles as well. The deformed particles possess a particle shape that is considered to be more angular and having a higher asperity ratio compared to the spherical particles. However, the clumped particles show much more angularity and behave more or less like real sand particles due to the attachment of several small glass beads of varying sizes at varying angles to form a clumped particle. The shapes of both clumped and deformed beads are shown in Figure 8.5 and Figure 8.6 above.

The testing plan for the deformed and clumped glass beads consisted of having three different plate sizes, as described in Figure 8.15 above. For each type of plate width, the initial conditions were kept similar to each other. Three different loading rates were applied for each plate width to investigate if there exists any dependency of shearing rate on the sample.

Although, immense care was taken while sample preparation and formation of the cavity to result in a cavity shape that has significant resemblance with all cases. However, the micro-interaction between particles and interparticle orientation varied at each test case. Furthermore, the presence of small human error in the sample preparation was out of control that all resulted to form cavities that differed slightly to each other in most of the cases. In a few cases, there was a significant difference between the formed cavity compared to the earlier cases.

Table 8.7 below summarizes the tests conducted using clumped particles.

The testing plan for the deformed particles is illustrated in Table 8.8 below. Only rough particle type was used to perform the cavity surface loading tests for the deformed particles.

Table 8.7 Cavity surface loading test plan for clumped particles

Particle type	D_{50} , <i>mm</i>	Surface texture	Initial water level, (h_w), <i>mm</i>	Relative density, (D_r), %	Plate size, <i>mm</i>	Loading speed, <i>mm/min</i>
clumped	0.60	Rough	100	90	20	0.66
					20	1.32
					20	2.65
					50	0.66
				90	50	1.32
					50	2.65
					100	0.66
					100	1.32
clumped	0.60	Smooth	100	≈ 70	100	2.65
					50	3.57

Table 8.8 Cavity surface loading test plan for deformed particles

Particle type	D_{50} , <i>mm</i>	Surface texture	Initial water level, (h_w), <i>mm</i>	Relative density, (D_r), %	Plate size, <i>mm</i>	Loading speed, <i>mm/min</i>
deformed	1.0	Rough	100	90	20	0.66
					20	2.65
				90	50	0.66
					50	2.65
				90	100	0.66
					100	2.65

8.4 Numerical simulation plan for Cavity stability analyses

As discussed in earlier chapters, the presence of water (capillary forces of water) is a pre-requisite for the formation and stability of the cavity due to the internal erosion of the soil. Consequently, a new suction-tension model was developed for this purpose and was then used to perform the numerical simulations using both spherical and non-spherical particles.

The capillary force model for DEM consisted of three main stages, as illustrated below:

- (i) Inter-particle suction as input parameter, that is the simplest case and the effect of suction amount on the stability of the existing cavity is discussed with it.
- (ii) Degree of saturation as input parameter, that is the extended form of earlier stage and the suction between the particles is automatically calculated as per the degree of saturation and the particle size. However, the degree of saturation used in a simulation represented the saturation level in all of the samples.
- (iii) Variable degree of saturation as input, that is a further extension of the earlier case. Here, as per experimental results of degree of saturation for each particle size, the top and the bottom degree of saturation is given as an input to the sample and the saturation is varied linearly between these two extremes.

For most of the simulations, spherical and non-spherical particles constituted by rigidly attaching two spherical particles were used in numerical simulations. However, for a few cases, a rigid particle formed by attaching three spherical particles in different directions was also used to have a better understanding of particle shape effect. The particle shapes for the spherical and the non-spherical with two constituent particles have already been explained in Chapter-3 of this manuscript. A non-spherical particle with two constituent spherical particles is termed as *R2* here in this manuscript. However, the particle shape for the 3-constituent spherical particles, attached rigidly with each other without overlapping, is explained in Figure 8.16.

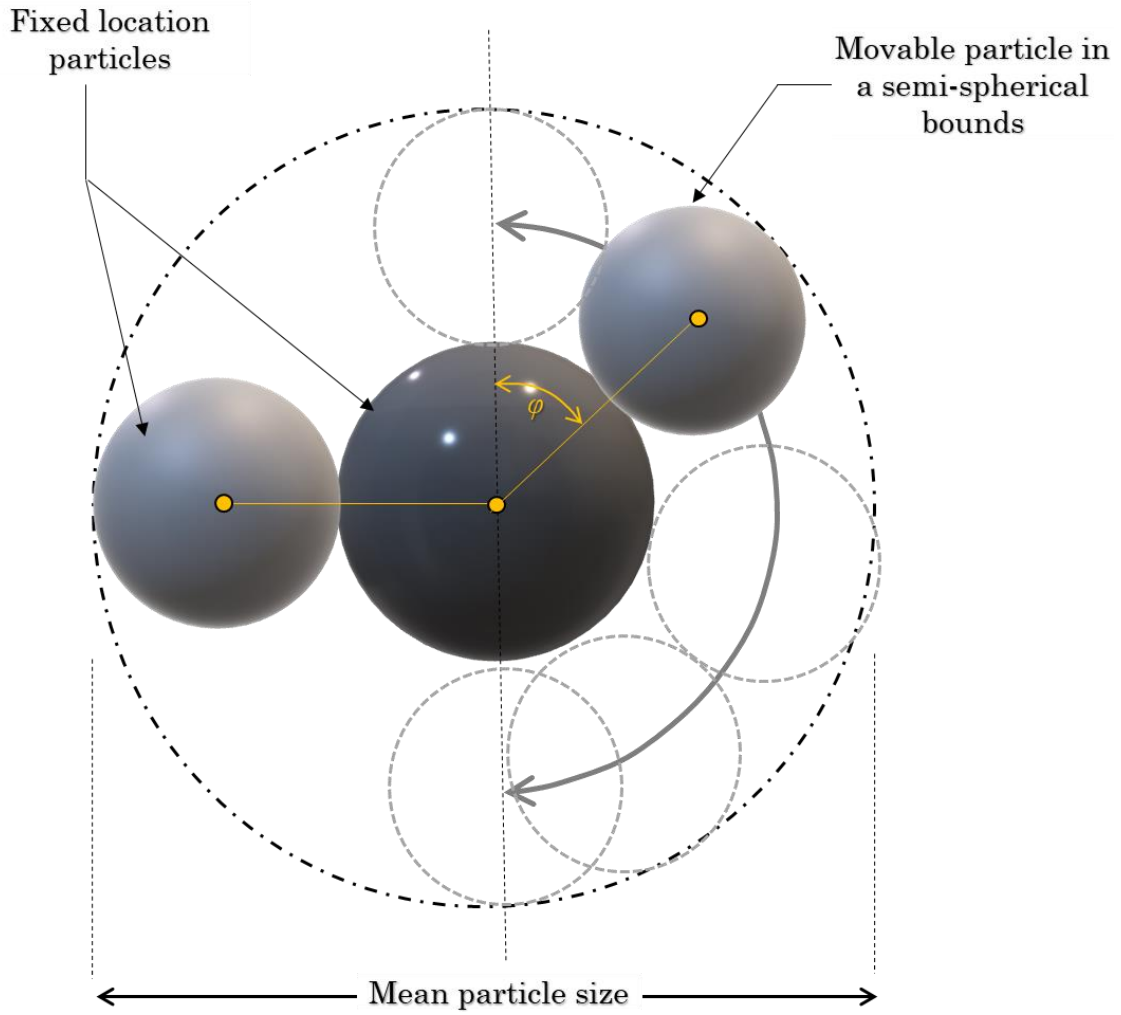


Figure 8.16 Rigid particle $R3$, with three constituent spherical particles

The rigid particle with three constituent spherical particles is referred to as $R3$ particle, possesses a central spherical particle with a central fixed particle and another spherical particle is attached with it in the negative z -axis. However, the third spherical particle is randomly located in only positive z -axis while touching with the central particle. Thus, the resultant particle can have extreme shapes of all in a single line to 'elbow' shape with the third particle at 90° . Hence, a maximum variation of ϕ that can be achieved in this particle shape is 180° . the third spherical particle cannot exceed the angle beyond 180° .

This shape of the particle was selected based upon the digital images of clumped glass beads, as shown in Figure 8.6, where the clumped particle is constituted with the attachment of several other spherical particles of varying sizes at varying angles resulting in a random

particle size. However, the total length of branch vectors connecting the centroid of all three constituent spherical particles would always be 1mm.

8.4.1 Simulation plan using Suction as input

For the initial testing of the DEM code, the first type of simulations involved changing input suction values, as explained earlier. Two types of particles were selected in this group of simulations, spherical and non-spherical particles.

The sample consisted of *fpf* boundary (fixed, periodic, fixed), i.e. periodic boundary was applied in the y-axis, that is the inward to the paper plane, whilst in other directions, fixed wall boundary wall provided.

The sample was pluviated in a similar manner, as described for the trapdoor test case, and a small sample was prepared with a dimension of 45mm × 25mm × 45mm. at the center of the sample, a small box was selected with a size of 9mm × 9mm (*XZ* plane) that extended to the full breadth of the sample. This box was then deleted from the sample and consequently, all particles pertaining to that box were also deleted.

As a result, a hollow space with a rectangular section was created. Inter-particle suction was then instantly introduced in the sample, that tried to keep the particles intact due to the capillary forces. For different values of input suction, the behavior of the sample was examined. Table 8.9 below shows the details of the simulation for both spherical and non-spherical particles during the *Suction-input* condition.

8.4.2 Simulation plan using the degree of saturation as input

Another set of simulations was run using saturation as input in the DEM code, which helped in the calculation of automated inter-particle suction values for all particles, based upon their diameters and the distance between them. The value of saturation level, as described earlier, is applied throughout the sample as a uniform parameter.

The small sample described in the previous section was then tested for the degree of saturation variation. The simulation plan is shown below in Table 8.10.

Table 8.9 Simulation plan with Input Suction using small samples

Type of particle	D_{50} (mm)	Void ratio, e	Cavity size (mm × mm)	Input suction (kPa)
Spherical particles	1.7mm	0.65	9 × 9	0
				0.050
				0.30
				0.50
				1.0
				2.0
				3.0
				4.0
				5.0
				0
				0.30
				0.50
				0
				0.30
				0.50
Non-Spherical, $R2$	1.7mm	0.71	9 × 9	0
				0.30
				0.50
				0.80
				1.0
				2.0
				0

Table 8.10 Simulation plan on a small sample with saturation as an input parameter

Type of particle	D_{50} (mm)	Void ratio, e	Cavity size (mm x mm)	Degree of saturation, S_r (%)
Spherical particles	1.7	≈ 0.65	9 x 9	20
				50
				90
	0.6	≈ 0.65	9 x 9	20
				50
				90
Non-Spherical, $R2$	1.0	≈ 0.71	9 x 9	20
				50
				90
	1.7			50

For saturation as input parameter, larger samples were also prepared to have a better understanding of the higher number of particles to form arching action around the cavity. However, the larger the size of the sample, the shape of the cavity was also modified to be more representative of the actual cavity shape, having a semi-circular top surface.

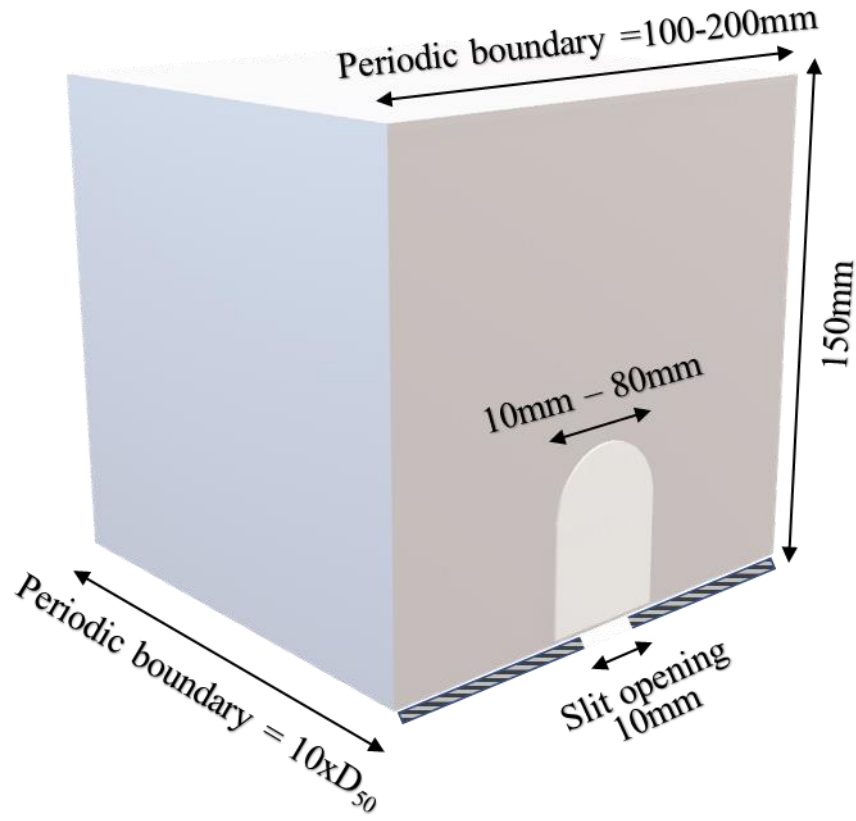


Figure 8.17 Shape of the sample used in cavity stability simulations with saturation as an input parameter

Only non-spherical particles *R2* were tested in this stated condition and the testing plan is given below (Table 8.11). Different cavity sizes were selected with varying both the width and the height of the cavity. Two sizes of non-spherical particles were selected as 1.0mm and 0.6mm. 1.7mm particles having higher self-weight were neglected in this simulation plan. The saturation levels were also varied for the case of 1.0mm size particles.

Table 8.11 Simulation plan with the larger sample having saturation as input with 1.0mm particle dia

Type of particle	D_{50} (mm)	Cavity width, mm	Cavity height, mm	Degree of saturation, S_r (%)
Non-spherical particles, $R2$	1.0	10	10	10
				90
		20	20	10
				90
		30	30	10
				90
			45	10
				10
			60	10
				10
			75	10
				10
		40	40	10
			60	10
			70	10
		50	50	10
				90
			60	10
				10
			70	10

In the case of non-spherical particles with a diameter of 0.5mm, only the saturation level of 10% was selected as the effect of sample saturation is already clarified through the above simulation plan. Also, since the number of particles increases to several times when decreasing the mean particle size from 1.0mm to 0.5mm, that requires more higher computational energy and smaller critical time step due to the presence of small particles. Hence, the total sample length was reduced to 100mm for testing with this particle size. The simulation plan with $D_{50} = 0.5\text{mm}$ is given below in Table 8.12.

Table 8.12 Simulation plan with the larger sample having saturation as input with 0.5mm particle dia

Type of particle	D_{50} (mm)	Cavity width, mm	Cavity height, mm	Degree of saturation, S_r (%)
Non-spherical particles, $R2$	0.5	10	10	10
			20	
			30	
			40	
			60	
			80	
		20	10	10
			20	
			30	
			40	
			50	
		30	10	10
			20	
			30	
			40	
			60	
			80	
		40	20	10
			40	
			60	
		50	20	10
		60	20	10
		80	10	10
			20	

8.4.3 Simulation plan using a variable degree of saturation

This series contained an input value for two regions of the sample, namely the top and the bottom region. As seen in the model cavity tests, as soon as the bottom slit is opened and the water is allowed to be drained through it, the water in a sample quickly drains out until stable residual water is maintained in the sample with the presence of a cavity.

Since the current cavity stability scenario involves the presence of a pre-defined cavity in the sample and its stability is analyzed against various varying factors, hence the saturation of the sample should be the residual saturation for the corresponding particle size in the model tests.

The sample should possess the least saturation value at the top, and the maximum at the bottom region near the opening. The variation in the top and the bottom saturation is assumed/approximated to be linear, as observed from the moisture content determination at regular intervals for a representative sample.

The simulations were performed only for a limited number of cases using *R2* particles, a sample with a cavity of 20mm and 30mm, with a cavity height of 20mm and 30mm respectively, for a saturation level varying from 10% at the top to 90% at the base of the sample. Using a similar saturation variation in *R3* particle samples, simulations were run with cavity sizes of 30mm and 40mm. The details of the simulation plan are given below in Table 8. 13 for the variable saturation cases using *R3* particle type. The sample size after pluviation consisted of about 200mm x 90mm (XZ).

Table 8. 13 Simulation plan having variable saturation with three constituent rigid particles (*R3*)

Type of particle	Particle mean size (mm)	Cavity width, mm	Cavity height, mm	Degree of saturation, S_r (%) [top/bottom]
<i>R3</i>	1.0mm	30	30	10/90
		40	40	10/90

8.4.4 Increase in the self-weight of particles due to saturation:

As only a hypothetical presence of water in the sample is assumed in the DEM code, without any physical presence of water, there is no self-weight of water assumed in the model. However, in reality, the water film surrounds the particles of the sample and imparts a specific force due to its weight, resulting in increased weight of the sample.

The particle closer to the base of the sample face higher water weight effect due to the higher degree of saturation at that region. Increased weight can have effects on the overall stability of the sample. Therefore, the measurements were also performed to include the weight of the hypothetical water effect by considering the degree of saturation of the sample at different levels.

The sample was divided into several layers, assuming that each layer would contain a similar saturation level, hence a uniform distribution of water weight in the particle, according to their particle size distribution. The saturation level was converted into a volume of water by using the sample void ratio. This volume was then divided into each particle of that particular layer, based upon the particle size. As the larger particles would have a higher amount of sticking water due to its higher surface area, more water weight is assigned to that specific particle.

Eventually, the weight of the water to each particle is assumed to be the constituent weight of that particle. Subsequently, the unit weight of the particle was increased in a proportionate manner, which was later used as an input parameter in the input file of the given DEM program.

8.5 Simulation plan for cavity surface loading

Similar to the model tests of the cavity surface loading using various types of glass beads, DEM based numerical simulations were also performed for the surface loading tests. For this purpose, initially, a cavity was produced in a sample and the stability was observed. Once the sample showed a stable cavity, surface loading was applied to that sample using a rigid wall movement right above the stable cavity.

8.5.1 Loading rate comparison

A fixed wall region on the surface of the sample, above the cavity, was moved downward for the cavity surface loading tests. However, the choice of the velocity of wall movement is also critical. Very high speeds can produce a dynamic sample response, resulting in an unstable simulation. However, a very slow speed although ensures the quasi-static behavior with stable simulation, but the time and the computational energy required for it is not feasible. Hence, such a plate loading speed is required that can produce a stable simulation within a limited timeframe.

Two types of samples were selected for the loading rate comparison:

- (i) Sample with a base cavity
- (ii) Sample without a base cavity

For case 1, a sample with a 30mm wide and 30mm high cavity was selected. Such a sample resulted in a stable behavior with a particle mean size of 0.5mm in the cavity stability analyses. Right above the cavity, on the surface of the sample, a rigid wall region with a width of 30mm and spreading all across the breadth of the sample was lowered with varying velocities. The details of the lowering velocities are given in Table 8 14.

Based upon the results of plate loading rates, a feasible plate loading rate was selected that was then applied for the plate loading tests on numerical samples with a stable base cavity.

As Ohara et al. (2019) discussed the effect of surface loading on cavity stability using various sizes of silica sand, the width of plate comparable to the size of the cavity might also influence the load-settlement characteristics. Hence, various plate sizes were selected that included sizes both smaller and equal to the width of the base cavity. The simulation plan for surface loading is given below in Table 8.15.

Table 8 14 Numerical simulation plan for plate loading rate using non-spherical particles of 0.5mm mean diameter

Sr. No.	Case	Cavity size, <i>mm</i>	Plate width, <i>mm</i>	Loading speed, <i>m/sec</i>
1a	Base cavity With capillary forces & plate friction	30 x 30	30	0.2
1b				0.1
1c				0.05
1d				0.01
1e				0.005
2a	Without cavity With capillary forces – frictionless plate	30 x 30	30	0.2
2b				0.1
2c				0.05
2d				0.025
3a	Without cavity With capillary forces – Plate friction	30 x 30	30	0.2
3b				0.1
3c				0.05
3d				0.025
4a	Without cavity Without capillary forces – frictionless plate	30 x 30	30	0.2
4b				0.1
4c				0.05
4d				0.025

Table 8.15 Surface loading simulation plan with different plate sizes with a mean particle diameter (non-spherical, $R2$) of 0.5mm

Sr. No.	Case	Cavity size, <i>mm</i>	Plate width, <i>mm</i>	Loading speed, <i>m/sec</i>
1	Base cavity With capillary forces & plate friction	30 x 30	2	0.01
2			5	0.01
3			10	0.01
4			30	0.01

8.6 Summary

This chapter contained the methodology and the testing plan for both experimental and numerical tests. The basics of the model cavity test apparatus are explained with the limitations of the apparatus. Several types of glass beads were utilized in the tests including rough and smooth surface textures. Particle shape effect was studied by using non-spherical particles, including deformed and clumped glass beads.

Cavity surface loading tests were also discussed in this chapter, for both model tests and the numerical simulations. Models tests for cavity surface loading were performed for both spherical and non-spherical clumped particles. Numerical simulations were performed on non-spherical particles with different sizes of plates for the surface loading.

CHAPTER 9: CAVITY STABILITY ANALYSES

Once a cavity is developed inside a soil mass, the capillary forces amongst the soil particles act in parallel with the soil arching to stabilize the yielding portions and result in a stagnant behavior. This chapter includes the experimental results performed on the model cavity test apparatus and the equivalent DEM based numerical simulations while utilizing the capillary force model as described in the last chapter.

9.1 Model tests on cavity stability

Model cavity formation and stability tests were performed using the test apparatus as described earlier in methodology. The equipment consisted of a rectangular box with acrylic front and back walls, with dimensions of 25cm height, 30cm length and 8cm width. The base consisted of a slit of 5mm, that is clogged with a fiber cloth and could be open as and when required with the help of the attached strings. The water supply was also connected through the base slit.

The internal stability of soils is directly related to the geometric conditions as well as the hydraulic conditions and material properties (Chang & Zhang, 2013; Fannin & Moffat, 2006; Indraratna, Nguyen, & Rujikiatkamjorn, 2011; Wan & Fell, 2008). The geometric conditions correlate with the dimensions of the test apparatus, boundary conditions, bottom slit size and shape etc. Material properties include, but not limited to particle size, particle shape, particle surface conditions, the relative density of the sample etc. The hydraulic conditions can correspond to the type of flowing liquid inside soil mass and the saturation level of the sample. The hydraulic head could also be considered as an influential parameter.

9.1.1 Material description

As discussed in chapter 8, different varieties of glass beads were utilized for the model cavity testing. The glass beads consisted of both spherical and non-spherical particle shapes. Spherical particles ranged from 0.2mm mean diameter to 1.7mm mean diameter. Furthermore, few of the sizes were also compared with the increasing surface roughness of particles.

Non-spherical particles included deformed glass beads and the clumped glass beads. Clumped glass beads were constituted by an assembly of several spherical/deformed glass beads with varying sizes. Figure 8.4 and Figure 8.5 shows the enlarged images of both deformed and clumped particles.

9.1.2 Effect of particle size

The capillary forces inside an unsaturated soil mass depend largely upon the mean particle size and the particle size distribution of the sample. For a sample with a given saturation level, smaller particles portray much higher inter-particle suction compared to the sample with larger size particles. Gallage & Uchimura (2010) discussed the particle size effect on the soil-water characteristic curves of the sandy samples. Similarly, the particle size effect for predicting the soil water characteristic behavior is discussed by Mohammadi & Vanclooster (2011).

The glass beads samples for the cavity stability analyses consisted of particle mean sizes (D_{50}) ranging from 0.2mm to 1.7mm. Glass beads with various sizes were deposited in the model test apparatus as described in Chapter 8. The samples were initially saturated fully and then the water level was lowered up to a specific limit to create a boundary of the fully saturated and partially saturated specimen. In the fully saturated state, the particles are supposed to be free of capillary forces and can float/slip freely. To avoid that and to produce additional balancing forces for the stability of the cavity, some of the portions in the sample are kept at a partially saturated state.

As soon as the bottom slit is opened for the apparatus, under the action of gravity along with the water flow, the particles near the bottom try to slide out. In case there exists a sufficient amount of stabilizing capillary forces and the soil arching, a stabilized cavity is developed above the bottom slit. Initially, a glass bead sample with a mean diameter of 1.7mm was tested at fully saturated conditions to verify the absence/presence of capillary forces amongst the particles. Figure 9.3 and Figure 9.2 show the tests for 1.7mm size particles for fully saturated conditions and partially saturated conditions for the initial and the final stages of the test.

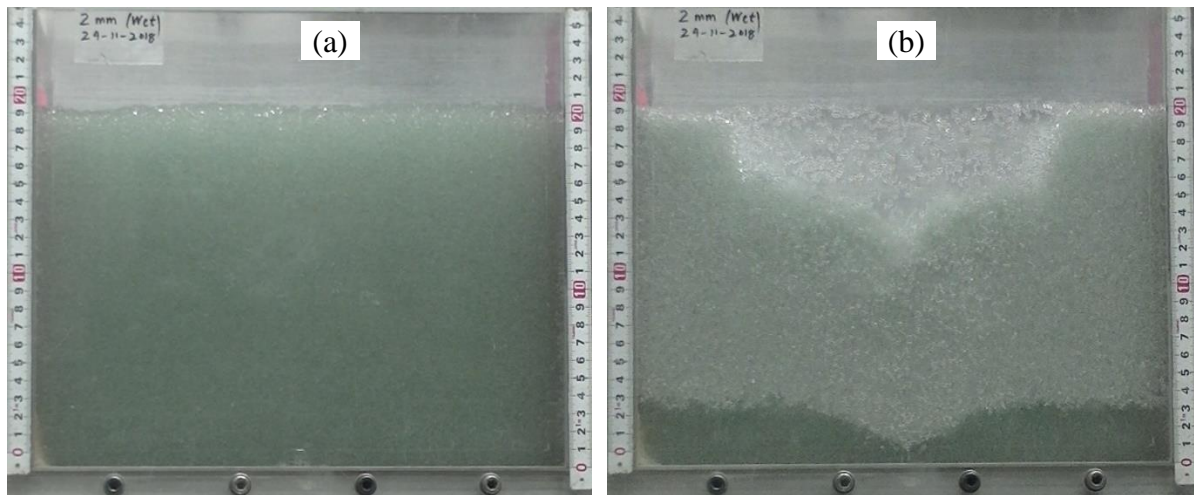


Figure 9.1 Model cavity tests for glass beads with $D_{50} = 1.7\text{mm}$ for a fully saturated condition at (a) initial stage, and (b) after bottom slit opening

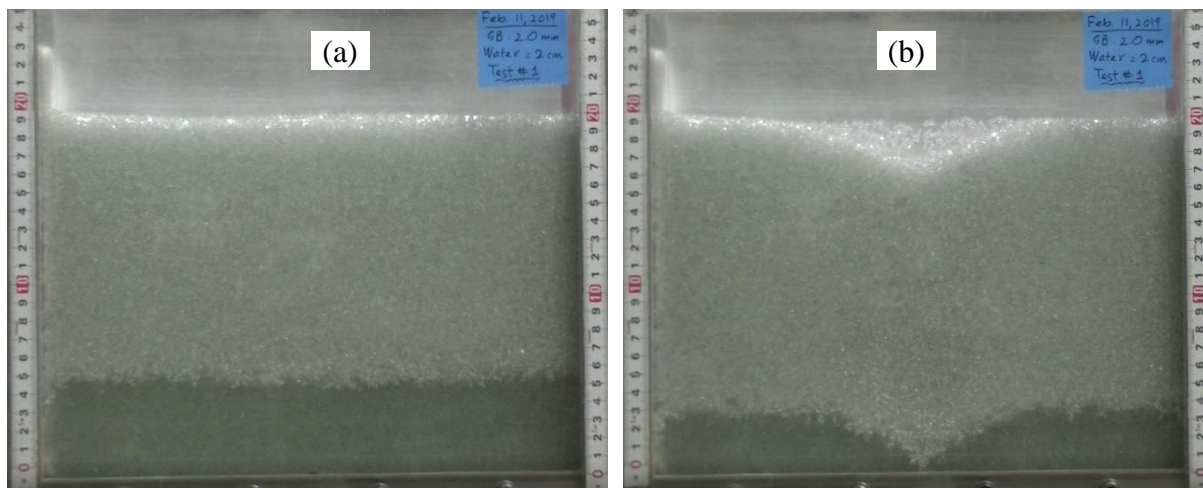


Figure 9.2 Model cavity tests for spherical glass beads with $D_{50} = 1.7\text{mm}$ for a partially saturated condition at (a) initial stage, and (b) after bottom slit opening

The figures above showed that glass beads with $D_{50} = 1.7\text{mm}$ could not sustain the cavity in either condition of being fully saturated or partially saturated. In fully saturated conditions, it was presumed that the capillary forces are absent and consequently, the sample could not produce a stable cavity with the slit opening. However, even for the case when the majority of the sample was in a partially saturated state, the capillary forces amongst particles were not sufficient enough to sustain a stable cavity condition and the result was visible in form of a surface cave-in. As the size of the particle was large enough to have a higher value of particle self-weight, the inter-particle capillary forces were not

enough to balance the particle weight and resultantly the higher particle weight caused the sample collapse.

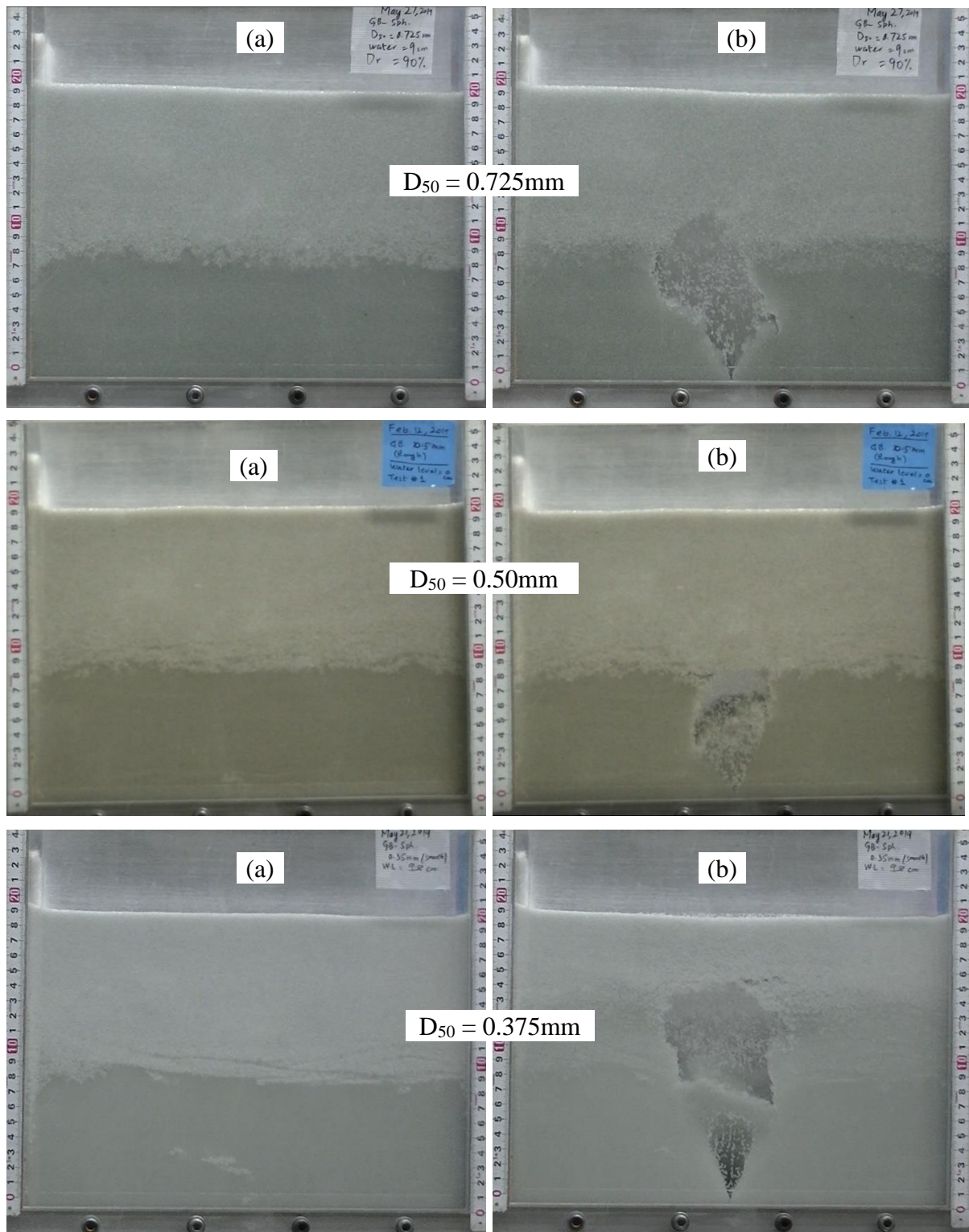


Figure 9.3 Model cavity stability tests for various sizes of spherical glass beads at (a) initial condition and (b) at end of the test

To verify the dominant effect of particle self-weight, the tests were performed with reducing mean diameter (spherical particles). Similar to the earlier figures, both initial and the final stages of the tests are shown in Figure 9.3. All samples are in a partially saturated state above the 9cm level. Below 9cm, the sample is in a fully saturated state. The effect of particle size is clearly seen as there existed a stable cavity for all ranges of particle diameter shown in the above figure. The smaller is the particle diameter, the stronger is the capillary force, which implies that larger cavity sizes can be stabilized with smaller particles. Therefore, the cavity developed by 0.375mm particles is much larger compared to the larger sized particles.

The smallest particle had a mean diameter of 0.2mm, which is quite interesting as well. Once the sample attained full saturation, the water level was tried to get lowered. However, the strong capillary forces did not allow the water level to be lowered significantly and the sample did not portray any visible signs of water reduction under the gravitational effect.

$D_{50} = 0.20\text{mm}$

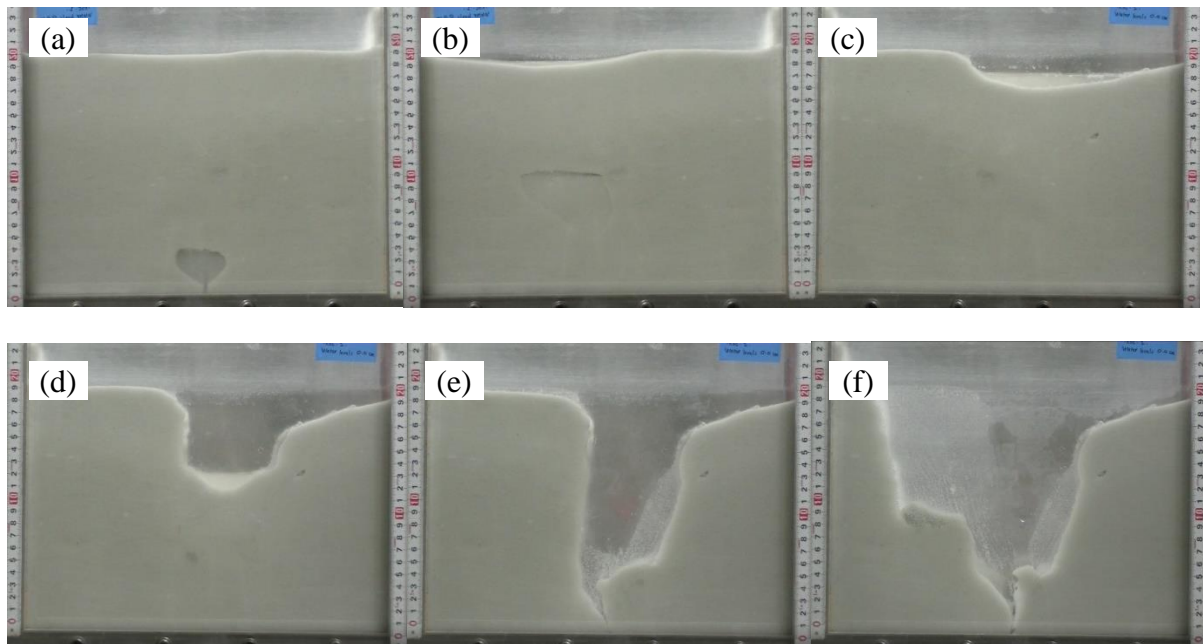


Figure 9.4 Model cavity stability test for spherical glass beads with a mean diameter of 0.2mm at various stages of the test

Figure 9.4 shows the various stages of the test for 0.2mm diameter spherical glass beads. Once the bottom slit is opened, an instant cavity is formed above the slit, however, the high saturation level does not allow the cavity to get stabilized and the particles at the

ceiling of the cavity get separated from the top static mass. Meanwhile, the cavity starts expanding and eventually touched the surface to cause a cave-in scenario. With further time, the particles keep getting washed through the bottom slit and eventually a deep trench is formed as a consequence.

Earlier it was discussed that smaller the particle size, stronger will be the capillary action and stronger will be the stabilizing force amongst particles. However, the above-presented case did not show any presence of strong capillary forces. The reason being that the residual degree of saturation for smaller particles is much larger than that of larger diameter particles. This effect does not allow the water level to get drained even under gravitational effect. External pressure is required to reduce the water level in the sample. Consequently, almost all of the samples portrayed fully saturated conditions that lead to insignificant development of capillary forces and higher value of lubrication between particles due to larger water contents.

The residual moisture contents for various sizes of the spherical glass beads are presented in Table 9.1 under the gravitational forces, measured in the same model test apparatus. The saturation values vary with the depth of the sample. However, in the given table, a mean value of three samples is presented, which was measured at the top, center, and bottom of the sample.

Table 9.1 Degree of residual saturation for different materials

Sr. No.	Material type	Mean diameter, D_{50} (mm)	Degree of saturation, $S_{r_residual}$ (%)
1	Spherical glass beads	1.7	7.35
2		0.725	8.99
3		0.5	18.41
4		0.375	28.47
5		0.2	95.8
6	Silica sand #7	≈ 0.2	93.25

As seen in the table above, the residual degree of saturation for the 0.2mm diameter spherical glass beads is approaching a fully saturated condition. Even the similar-sized silica sand showed a similar value of the residual degree of saturation.

As the particle size does matter in the formation of a stable cavity using spherical glass beads, a sample was prepared by mixing equal-weight proportions of all above mentioned spherical glass beads sizes to result in a mixed proportion sample. That sample was then tested for the cavity formation under similar conditions as used earlier. Figure 9.5 shows that the sample with mixed grading of spherical glass beads ranging from 1.7mm to 0.2mm showed a stable cavity with a size larger than corresponding samples with other particle sizes. The reason being the presence of almost all sizes in the sample, causing a strong capillary force and resulting in a much denser sample with lesser voids to form a stable cavity formation.

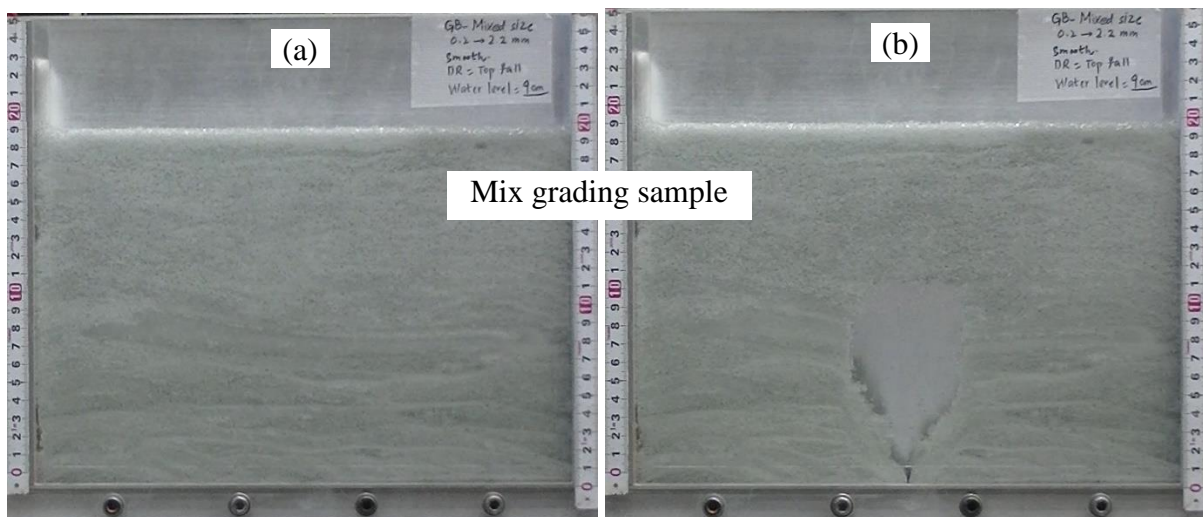


Figure 9.5 Model cavity stability tests for mixed grading of spherical glass beads at (a) initial condition and (b) at the end of the test

9.1.3 Effect of surface roughness

The spherical glass beads in their initial condition contain a very smooth surface that contains a friction coefficient approaching 0.1. Such a smooth surface sometimes causes easy slippage of contacts to result in distortion of the arching mechanism. This condition can sometimes lead to a collapse of an initially formed cavity. To verify the

effect of surface roughness, a glass bead size of 0.5mm was selected and was milled for 48 hours in the milling equipment, as shown in the earlier chapter.

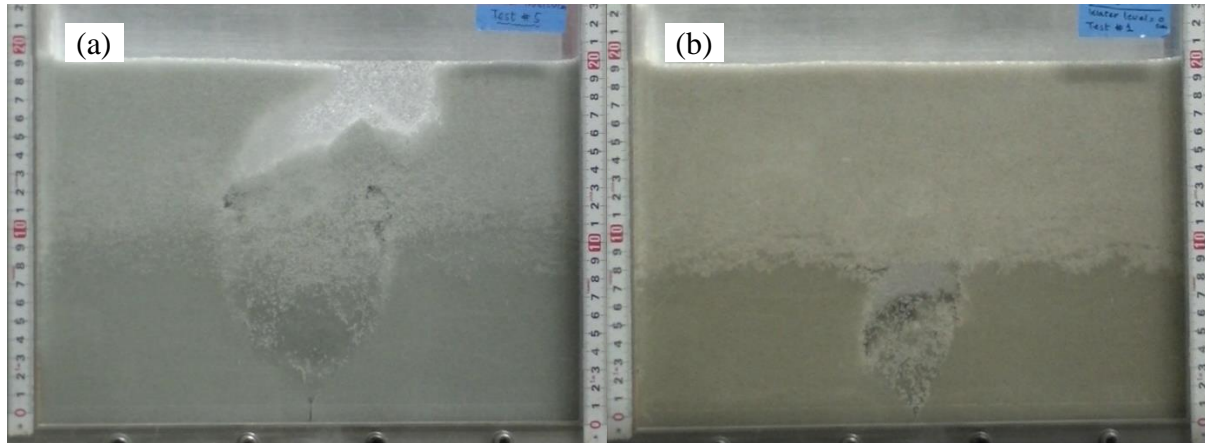


Figure 9.6 Comparison of the cavity stability using spherical glass beads having a mean diameter of 0.5mm with (a) smooth and (b) rough surface

The surface roughness effect is clearly seen in Figure 9.6 above, where the sample with spherical glass beads having a mean diameter of 0.5mm with the smooth surface could not form a stable cavity and the sample collapsed. However, under similar conditions, the rough particle could develop a stable cavity. Hence, it can be said that using rough particles induced larger shear resistance of particle, inducing larger contact force and helping in stronger arching around the cavity. Consequently, the sample can show a well-stabilized condition of the underground cavity.

9.1.4 Effect of initial water level

As described earlier, the water level in the sample divides it into two regions; partially saturated and the fully saturated regions. The height of water just before the bottom slit opening can play an important role in deciding the overall behavior of the sample under the cavity formation process. Higher water heights result in larger regions with the absence of capillary forces due to fully saturated conditions.

The effect of the initial water level in the sample on the stability of the cavity for the spherical glass beads with $D_{50} = 0.725\text{mm}$ is shown in Figure 9.7.

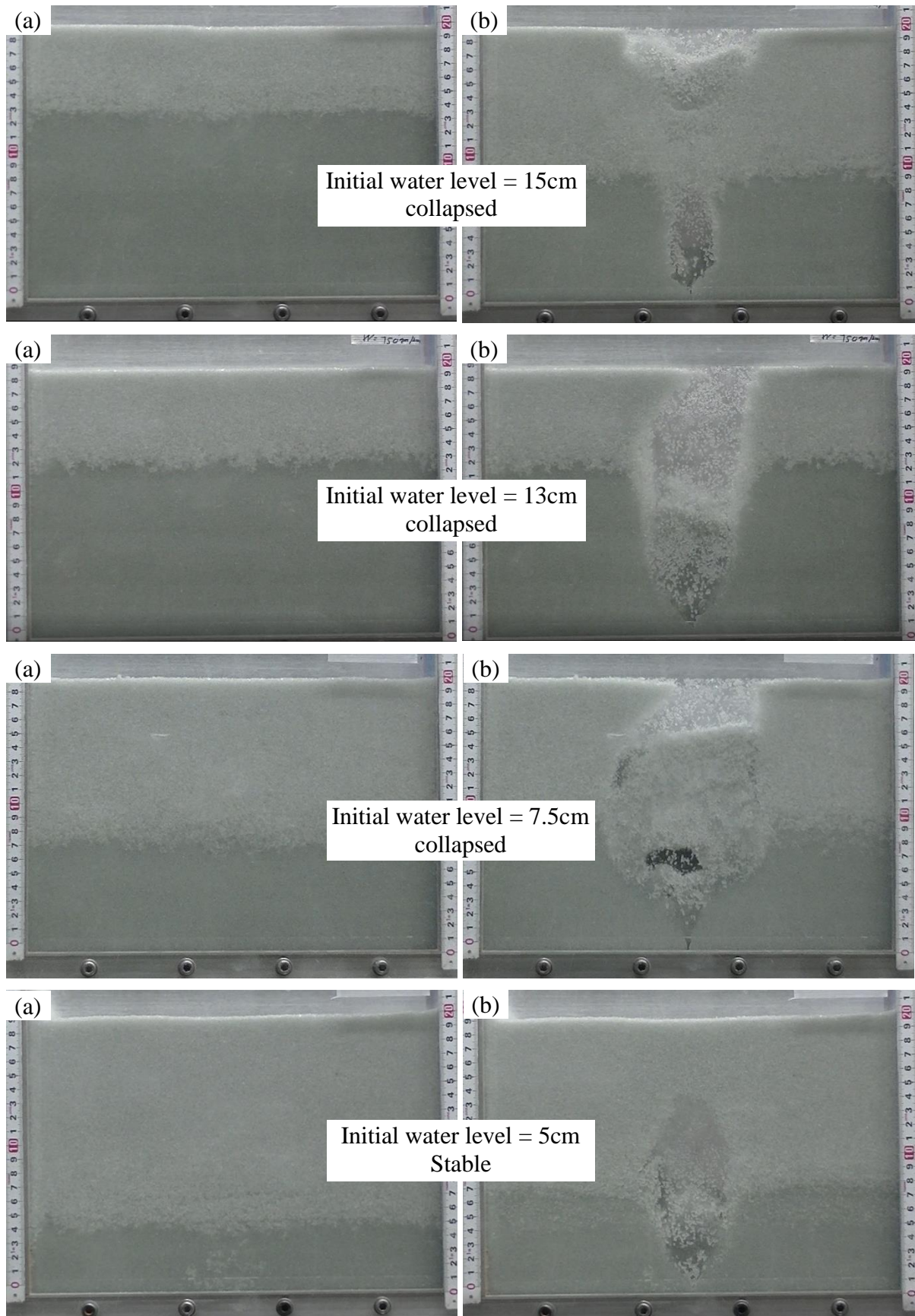


Figure 9.7 Effect of initial water level on cavity stability for spherical glass beads with $D_{50} = 0.725\text{mm}$ at (a) initial state and (b) final state of the test

As seen in Figure 9.7, a clear difference in the stability was observed with changing the initial water level for similar particle size and density levels. With decreasing water surface level, the cavity could not get stabilized until the 5cm level, where a stable cavity condition was observed inside the sample. However, a little further increase in the water level after the formation of a stable cavity for the 5cm case, the particles could not maintain a stable arching and the sample collapsed.

9.1.5 Effect of sample density

The effect of sample density on the stability of the cavity is discussed by Kuwano et al. (2006) and Ohara et al. (2019) for various sand types. The spherical glass beads were used to perform similar experiments to verify whether a similar phenomenon is followed by glass beads or not.

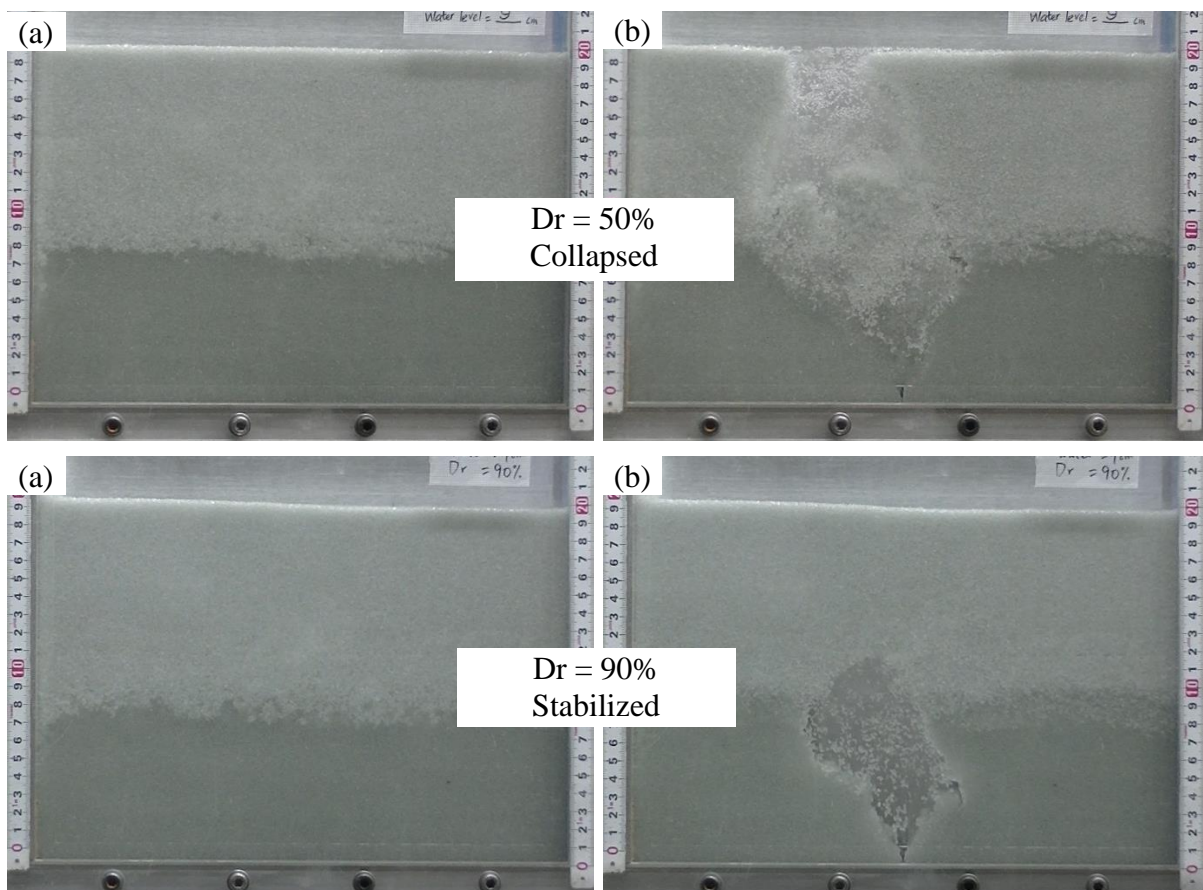


Figure 9.8 Effect of sample density on the stability of the cavity for spherical glass beads having $D_{50} = 0.725\text{mm}$ at (a) initial state and the (b) final state of the test

A sample with spherical glass beads (smooth) having a mean diameter of 0.725mm, at 50% relative density (D_r) was selected and it was found that the cavity couldn't develop in the sample for a given initial water height (Figure 9.8). However, under similar conditions, when the density of the sample was increased to 90%, the sample exhibited the formation of a stable cavity, representing a strong effect of density on the stability characteristics. Hence, the density effect was also valid for the spherical glass beads as well.

9.1.6 Effect of particle shape

The effect of particle shape on the stability of the cavity is not well discussed in the literature. Although, a general understanding is that more angular particles can better transfer the inter-particle loads and demonstrate higher friction angles, leading to higher peak strengths in the element tests.

The stability of the cavity was hence verified by changing the shape of the basic material. The usual spherical glass beads were then compared with two different shapes, namely deformed glass beads and clumped glass beads, as described in Chapter 8 in detail along with the basic properties. However, the density and the initial water level were kept the same in order to have a better comparison with the spherical particles.

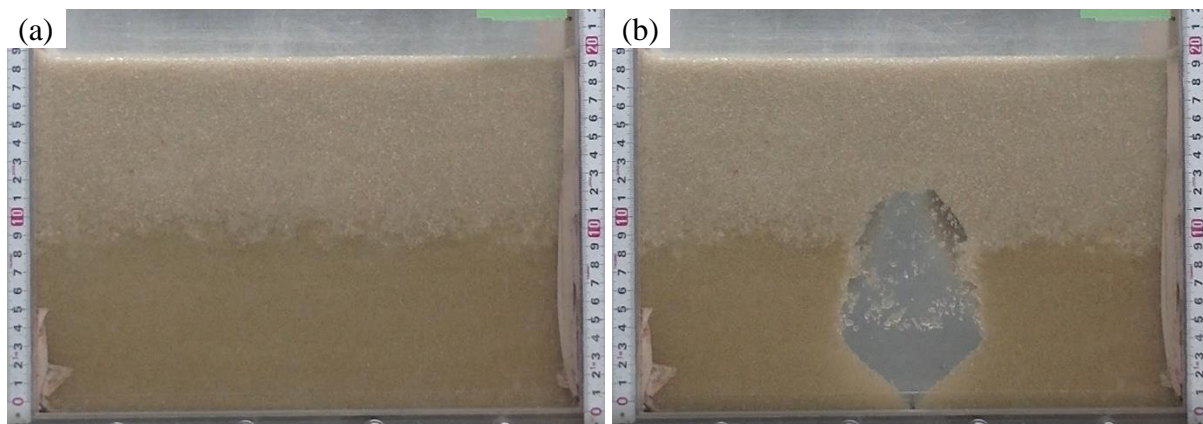


Figure 9.9 Cavity stability test using rough deformed glass beads with a mean particle size of 1.0mm at (a) initial and (b) final state

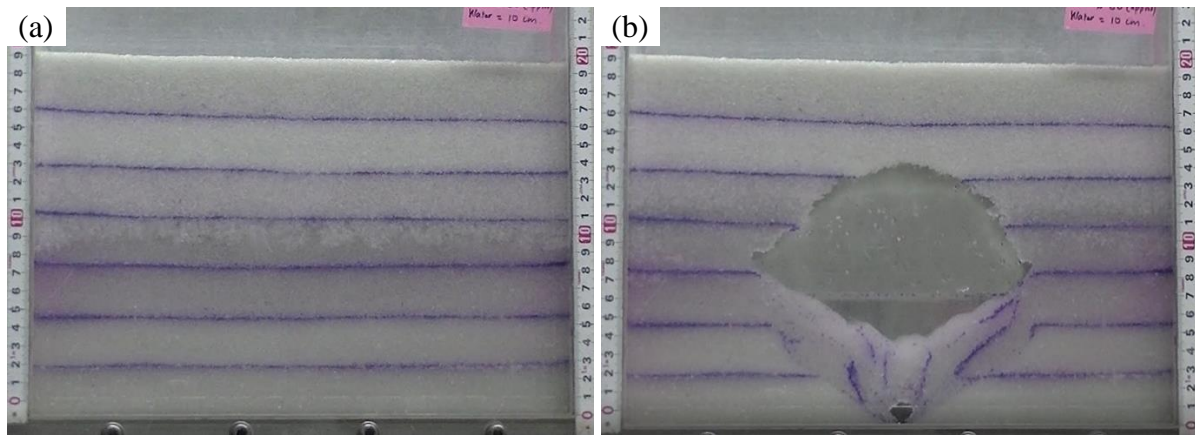


Figure 9.10 Cavity stability test using smooth clumped glass beads with a mean particle size of 0.6mm at (a) initial and (b) final state

Figure 9.9 and Figure 9.10 show the initial and the final stage of the test under a similar water level of approximately 10cm from the bottom. The cavity size visible in Figure 9.9(b) and Figure 9.10(b) are the sizes of the cavity just before the collapse condition and the presented shape is the maximum possible stable shape and repeated water drainage cycles. Deformed particles were made rough in order to increase their particle interlocking as the mean size of deformed particles is 1.0mm that might cause stability issues under high particle self-weight under smooth conditions.

Clumped particles are constituted using several spherical particles that are attached/fused together with varying sizes to result in a non-spherical shape with a mean particle size of 0.6mm. The shapes and basic properties of both clumped and deformed glass beads are given in Chapter 8. The void ratio for clumped particles possesses a wide range, implying the higher angularity of clumped particles compared with spherical or deformed glass beads.

Although both particle types showed the formation of a stable cavity as the base slit is opened, the maximum stable cavity size shown by the clumped particle is much larger than the deformed particles. Even the smooth particle condition of clumped particles resulted in higher stability forces compared to the rough deformed particles. The difference could be the combined effect of particle angularity, as well as the smaller size of clumped particle that causes the development of much stronger capillary forces within the soil mass. The void ratio range of deformed particles shows that due to their particular shape, the particles can come much closer to each other to result in a much denser state compared to the other spherical glass beads or the clumped particles, giving them the

advantage to transmit the interparticle forces in a much more efficient way. However, the effect of angularity and particle size is more dominant compared to the density effect.

9.2 Experimental comparison with cavity stability chart

Normally, the shallow cavities are formed under the roads due to the presence of buried infrastructures that causes internal erosion of soil when accompanied by moist conditions. For certain road construction/improvement projects, the presence of shallow buried cavities is estimated through cavity surveys with the measurement of the cavity sizes. The cavity sizes are then compared with an in-practice chart that is divided into stable and unstable regions depending upon the dimensioning of cavities. A typical cavity stability chart is presented below in Figure 9.11 below.

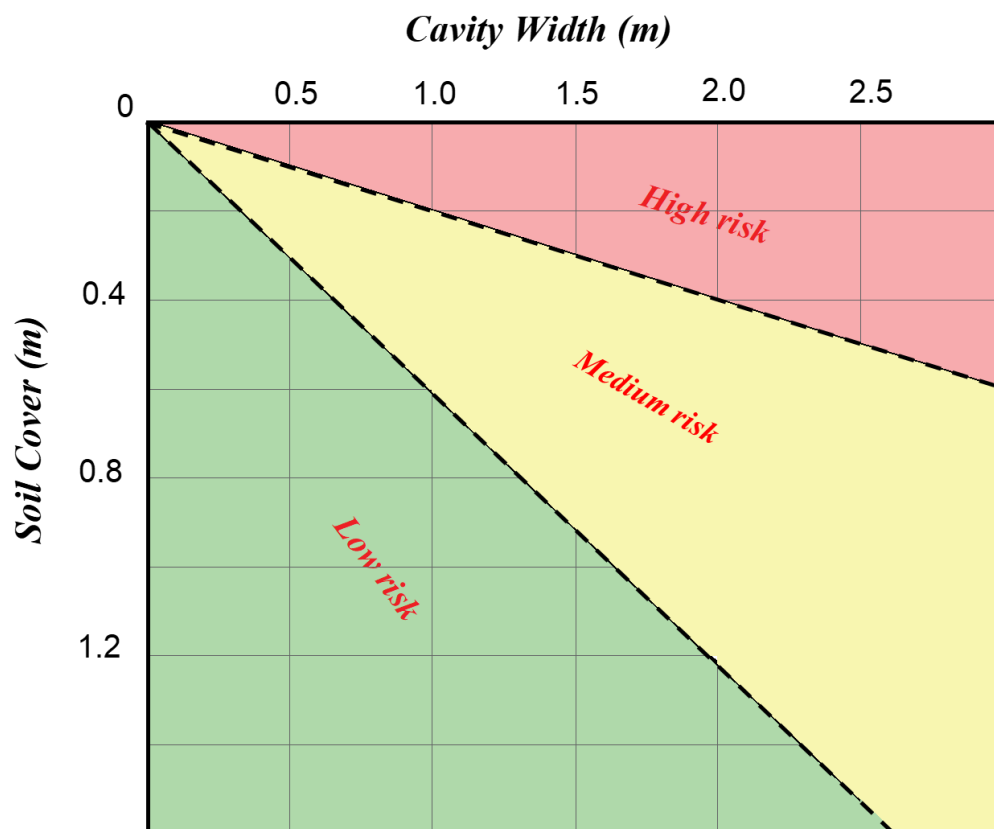


Figure 9.11 Cavity stability chart being followed generally in the construction industry of Japan

According to the above cavity stability curve, the cavities with larger width are more prone to the failure and they support a larger mass of soil above it against the gravitational

forces. Soil cover above the cavity is also very important in deciding the stability of the cavity. A case with a smaller value of soil cover and larger width is the most critical case, as seen in the above plot. The experimental importance of *medium risk* range is not well established, as it is difficult to decide what size would be prone to a near-future failure. However, the limit of *high risk* can be well established, being the cavity dimensions just before the failure of the cavity.

The results of the cavity stability for all types of glass beads were also plotted in a similar manner. However, for each type, the maximum possible cavity size was monitored just before the collapse. The dimensions of the cavity below the critical value were thought to be in partially stable or fully stable conditions.

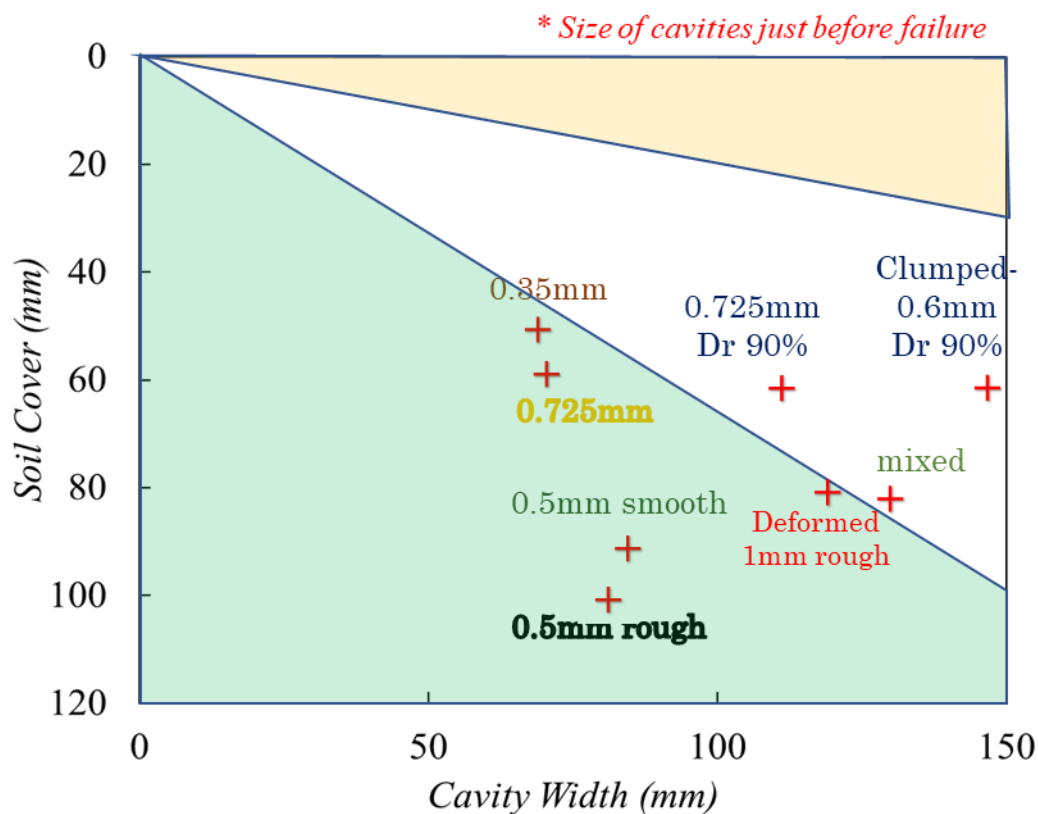


Figure 9.12 Experimental results of critical cavity size just before collapse, plotted on cavity stability chart

As Figure 9.12 represents the experimental results for all types of glass beads used in the study, each type of material possesses a different range of high risk or low risk. Major factors in deciding the range are particle mean size, surface texture, and most importantly, the shape

of the material particles. As seen above, the clumped particles showed the maximum range of stable regions, being quite close to the range given in the cavity stability chart for practical implications of under-road cavities. The reason for the clumped particles showing behavior similar to the cavity stability chart can be associated with the high angularity of clumped particles along with the void ratio ranges, that can correspond with the actual behavior of real sands being used in the field projects. The mixed graded sample and the sample with higher densities can also provide a better stability of the cavity under similar conditions. However, the spherical glass beads with low relative densities and having a smooth texture and the least stable cases within the given range. Only a small cavity width with a much larger material cover above cavity can result in a stabilized behavior. Hence, such cases where the material densities are lower and the backfill/native material does not possess high angularity, retain high chances to collapse in the near future.

9.3 Numerical analyses of the cavity stability using suction-tension model

The experimental results strengthened that glass beads can sustain a stable cavity under specific environment and conditions due to the combined action of the arching and the capillary forces amongst particles. Glass beads have the simplest shape that can be easily modeled in DEM simulations as well. An effort is made in this section to validate the experimental results that glass beads can result in a stable cavity. Furthermore, the force distribution and arch development for various cases are also discussed.

9.3.1 Numerical simulations with inter-particle suction as an input parameter

The importance of suction amongst particles in the unsaturated state is well established experimentally and numerically. Researchers like Marinho & Chandler (1994); Skempton & Brogan (1994); Indraratna et al. (2011) and Mukunoki et al. (2012) and others have discussed the effect of soil suction on the soil-water characteristic curves in details.

The development of a suction-tension based model is discussed in detail in Chapter 7, where the initial part was to introduce relations of capillary forces between particles with a value of inter-particle suction as an input parameter. Initially, spherical particles were tested with the given model under various values of inter-particle suction, starting from zero. The simulations were performed using a relatively smaller sample size, having

dimensions of 45mm x 45mm, whereas the sample dimension perpendicular to the plane (Y-axis) was kept as $10 \times D_{max}$. The mean particle diameter for these simulations was 1.7mm and 0.5mm. Larger particle diameter was selected so as to reduce the simulation time and as the purpose was to investigate the effect of suction value on the stability characteristics. Hence, even the bigger particle diameters did not affect the objectives.

A rectangular cavity, extending throughout the breadth of the sample, was introduced in the sample, having a dimension of 9mm x 9mm. All particles inside the region of the cavity were deleted from the system just before the introduction of inter-particle suction. Under increasing values of inter-particle suction, the stability of the samples was monitored, and the value of stabilizing inter-particle suction was monitored. Figure 9.13 below shows the images for cavity stability simulations at the initial and the terminating state of the simulation with various inter-particle suction values.

Particle speed in Figure 9.13 is represented by the color legend. The red color in the plots represents the movement of the particles, whereas the blue color shows the static particles. Initially, the plot shows that all particles are in total static conditions. For the first case, when inter-particle suction had the least value of zero, the particles could not develop any capillary force and a large movement was detected as shown in Figure 9.13(b). The cavity was collapsed soon after the start of the simulation. With increasing inter-particle suction values, the particle movement reduced and at the value of $S = 3\text{kPa}$, no movement of particles was observed even after a long time of the simulation.

9.3.1.1 *Particle size effect*

As discussed earlier as well, the mean size of the particle also plays a significant effect on the stability of the cavity and overall magnitude of capillary forces. For the similar sample size, particle mean size was reduced to approach 0.6mm and the plots for the particle velocity are then shown in Figure 9.14.

The effect of particle size is clearly visible as the particles with a mean diameter of 0.6mm were able to demonstrate a stable cavity under 500 Pascal inter-particle suction value. Whereas, under the same value of suction, 1.7mm diameter particle showed a total collapse of the cavity.

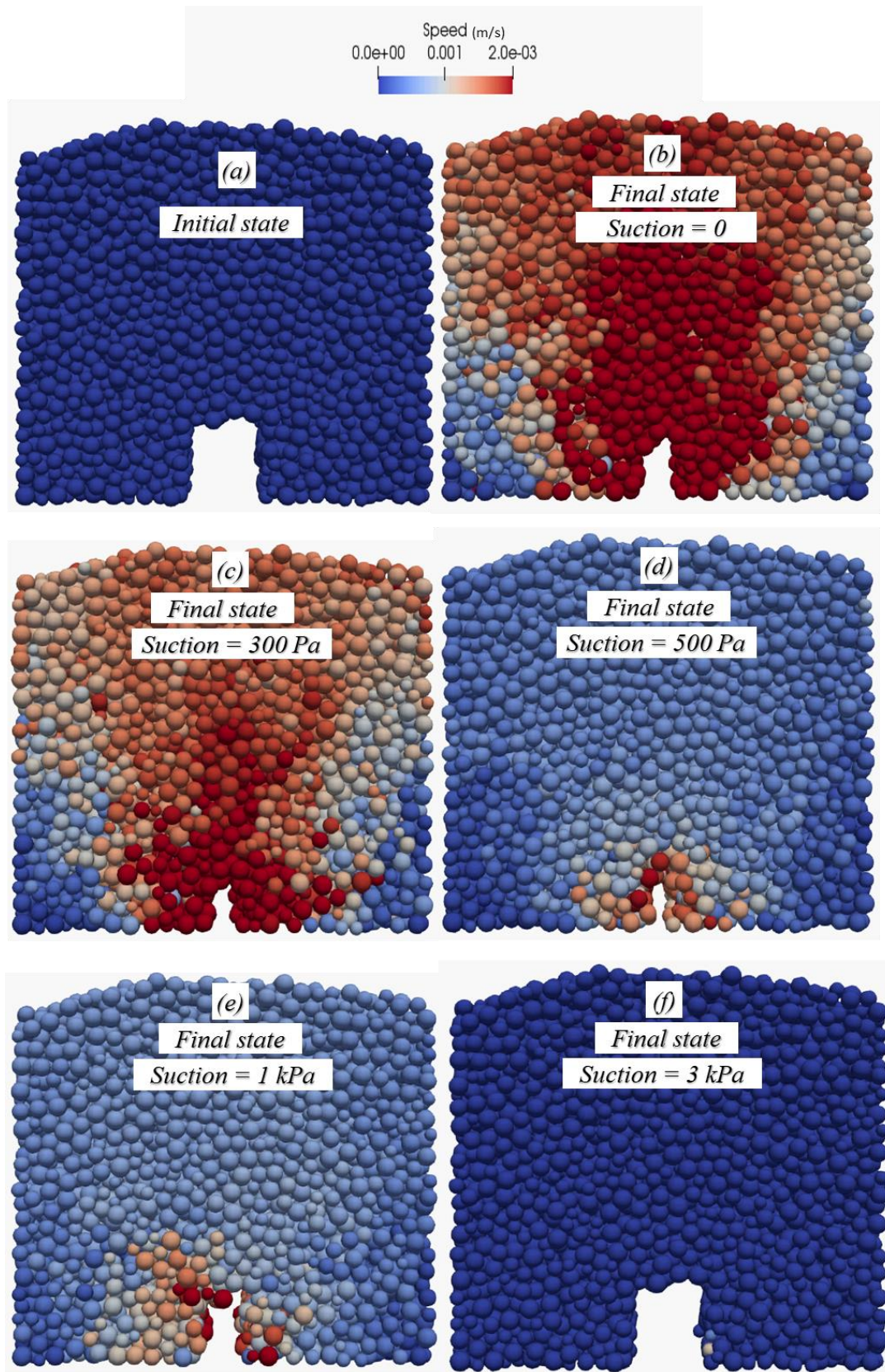


Figure 9.13 Particle speed plot using spherical particles with a mean diameter of 1.7mm, at various inter-particle suction values

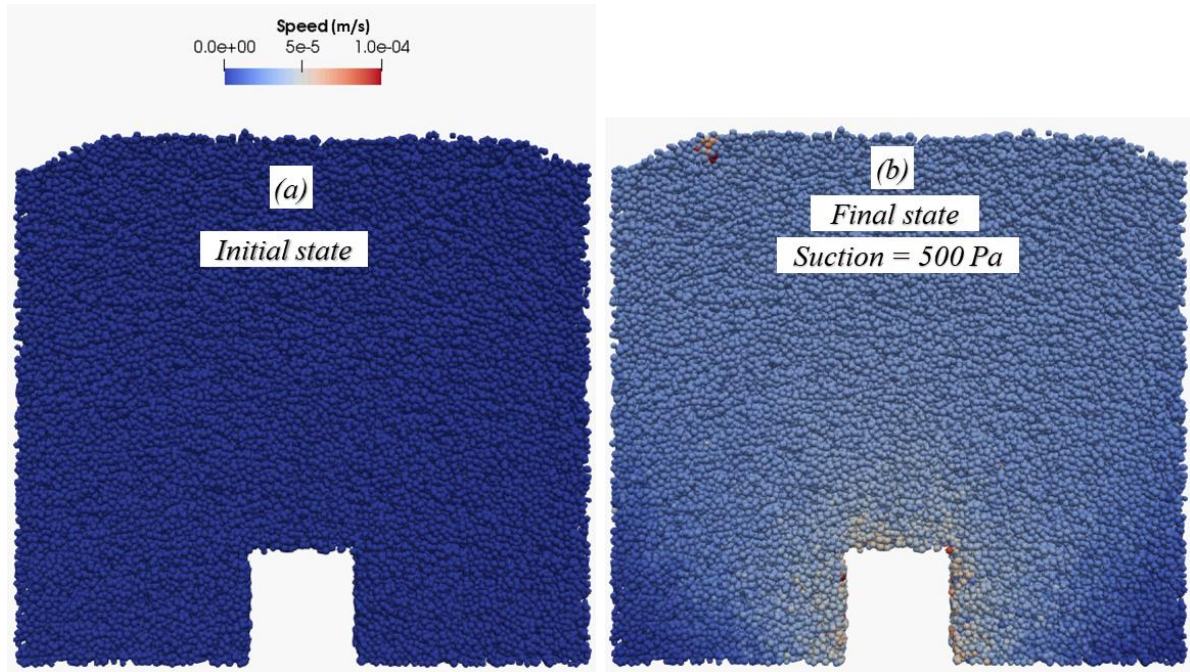


Figure 9.14 Particle speed plot using spherical particles with a mean diameter of 0.6mm, with 500 Pa inter-particle suction value

The stability of the cavity is believed to exist due to combined action of capillary forces and the arching developed around the cavity. There is a certainty that capillary forces exist within the sample as the contact model is modified for this purpose. However, in order to verify the presence of the arching forces around the cavity, the strong force diagram is shown in Figure 9.15. A strong force is defined as the force whose magnitude is equal to or more than 95% of the maximum contact force within the sample.

As seen in Figure 9.15(a), before the creation of cavity shape by deleting the atoms, the strong force distribution exists very uniformly. However, once the cavity was created and simulation was run for a certain time, the strong force network rearranged and formed an arch-like shape around the cavity in a particular manner. In the vicinity of the cavity, strong forces are absent, and dilation of material occurs in this region. However, the material in the cavity vicinity remains intact due to the presence of capillary forces and inter-particle suction, that is introduced in the sample with a magnitude of 500 Pascals. Hence, the presence of the arching around the cavity is verified by a strong force diagram.

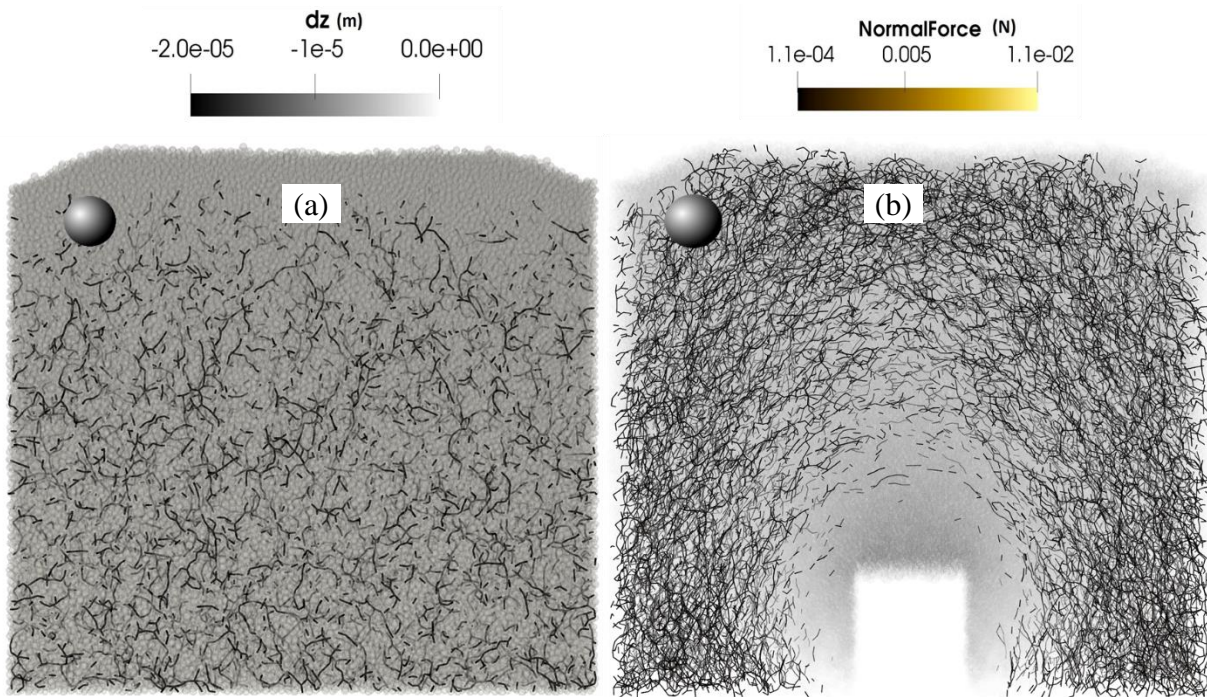


Figure 9.15 Strong force distribution for 0.6mm spherical particles at (a) initial stage before making cavity and (b) end of simulation with 500 Pa suction

9.3.2 Numerical simulations with a degree of saturation as an input parameter

The improved version of the suction-tension model was to introduce the degree of saturation as the controlling factor. Once the sample is supplied with any given saturation level, based upon the particle size distribution each contact calculates the inter-particle suction automatically. Hence, no suction value was input to the sample in this case.

For the purpose of numerical simulations, two kinds of samples were prepared:

- i- Small-sized sample
- ii- Large-sized sample

The small-sized sample consisted of the same dimensions as used in the last section. However, for the large-sized sample, the dimensions of the simulation box were kept either 200mm in length or 100mm, based upon the size of the particle. Furthermore, in the small-sized sample, the cavity shape was kept as rectangular. However, for the large sample, the cavity shape was designed to match in a better way with the experimental conditions and a combination of rectangular and cylindrical shape was used to create the initial cavity.

For the larger sample, analyses were performed using several factors, including the following factors

9.3.2.1 *Small-sized sample*

Sample saturation effect

The suction pressure increases significantly with a decrease in the saturation level of the sample. This phenomenon has been discussed by several researchers in their experimental observations, e.g. Gallage & Uchimura (2010) and several others. The variation of saturation force has not been discussed experimentally, as the measurement of related parameters like contact area of particles is not possible for the natural soils. However, numerically the suction force can easily be determined by considering the simple interaction between two particles.

The variation of suction force; however, does not vary as significantly as that of suction pressure. For certain sizes of the particles, the higher self-weight of particles does not allow the suction force to overcome the gravitational weight at any saturation level. However, for certain particle sizes, there could exist a transition phase with decreasing saturation level, enabling the capillary force to become dominant and making the sample stabilized. The effect of sample saturation was checked for spherical particles with $D_{50} = 1.7\text{mm}$. The particle speed plots for varying saturation levels is shown below in Figure 9.16.

The effect of saturation level for the given size of the particle and the given dimensions of the simulation box was found to be insignificant. The initial cavity of the sample collapsed under all saturation levels cases without a significant difference. The reason can be associated with the large size of the particles in the simulations that could not sustain the larger self-weight forces against the capillary forces at a given degree of saturation (S_r).

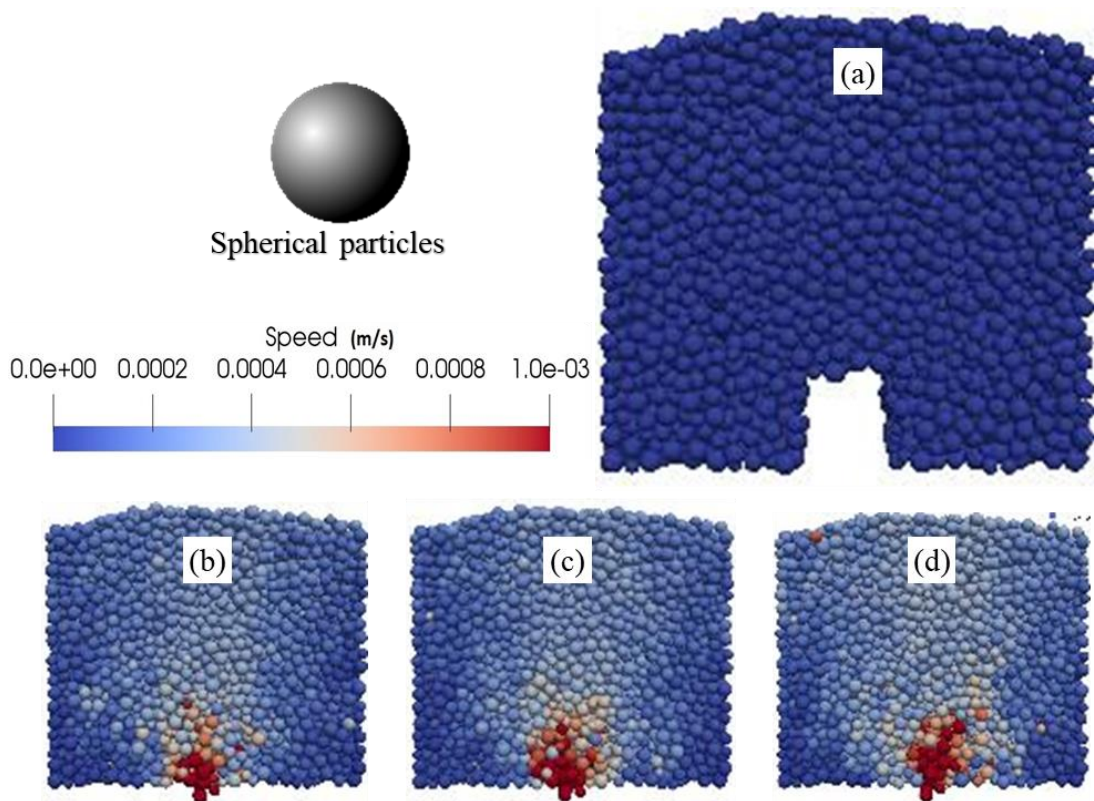


Figure 9.16 Particle velocity for spherical 1.7mm diameter case (a) initial state, (b) final state for 5% S_r , (c) 50% S_r and (d) 90% S_r

Particle size effect with non-spherical particles

The shape of the particle showed a dominant effect in the laboratory cavity stability tests, as discussed earlier in this chapter. To verify it numerically, non-spherical particles that are constituted by clumping two spherical particles together were used in two different sizes to study the effect on cavity stability.

Two sizes of the non-spherical particles were used: 1.7mm and 1.0mm. The particle velocity plot is shown below in Figure 9.17, where the larger particles can be seen to have more dynamic behavior with the propagation of simulation. However, having similar conditions, particles with a mean size of 1.0mm showed a stabilized behavior as seen in Figure 9.17(d).

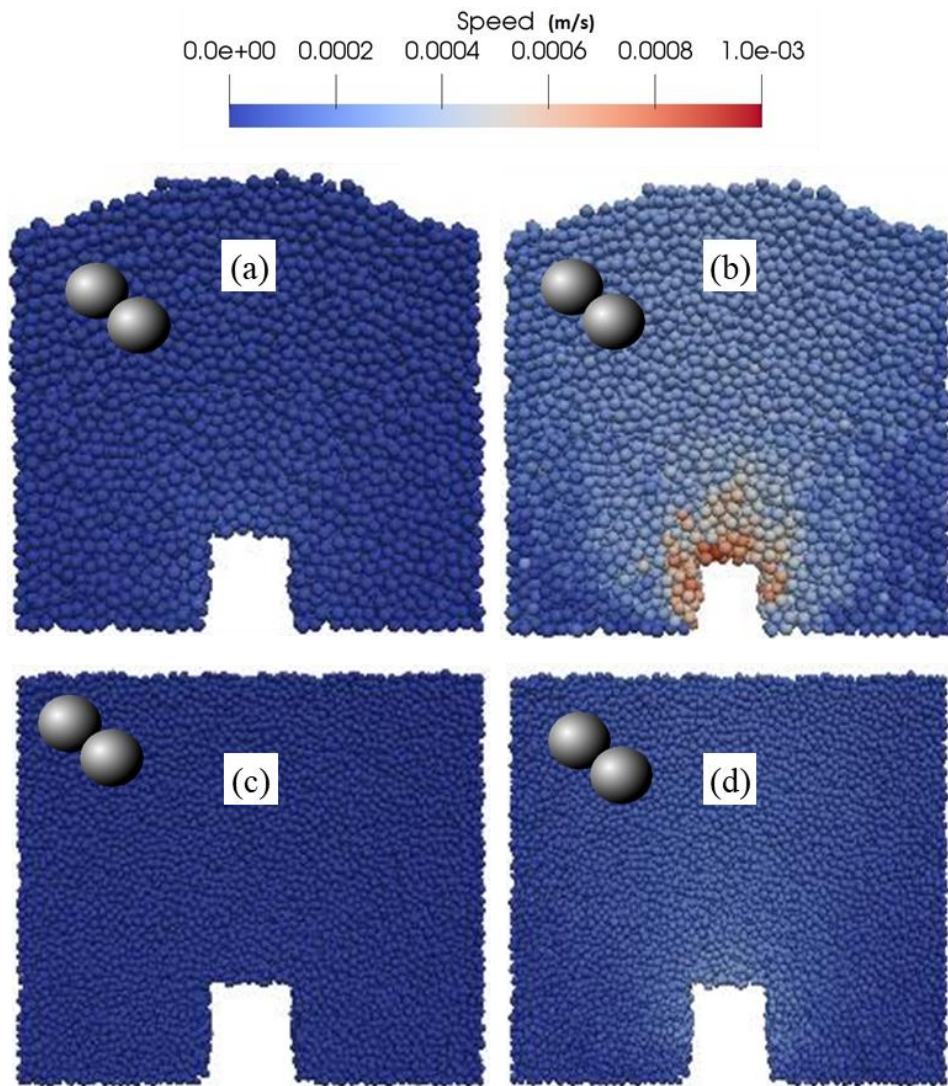


Figure 9.17 Particle velocity plot for non-spherical particles (a) initial state 1.7mm (b) final state 1.7mm and (c) initial state 1.0mm (d) final state 1.0mm

Contact fabric distribution around arching

The 2nd order contact fabric is described in detail in the chapter of Literature Review. The normalized 2nd order contact fabric is calculated as the number of contacts in a particular direction divided by the total number of contacts. If we divide the 2nd order contact fabric into three basic constituent directions of X, Y, and Z, then the sum of contact fabric in all these directions would always sum up to unity. However, under the isotropic conditions, the contact fabric value for each constituent direction would not be similar due to the gravitational effects. The Z-directional fabric would always result in slightly higher values under isotropic conditions.

During the arch development process, the particles in the arching region try to rotate in order to come in line with the force transmission line. That force transmission line is normally described to hold an inverted catenary shape. The catenary shape is not much different from the ellipsoid shape.

In order to calculate the 2nd order contact fabric values for the sample with non-spherical particles having 1.0mm mean diameter, the sample was divided into several sub-sets with a square shape. Contact fabric was then calculated for each subset, which would result in a data point of X, Y and Z directions. The process of calculating contact fabric is explained in detail in the chapters of the Trapdoor series.

The process of creating subsets during the simulation for calculating 2nd order contact fabric is shown in

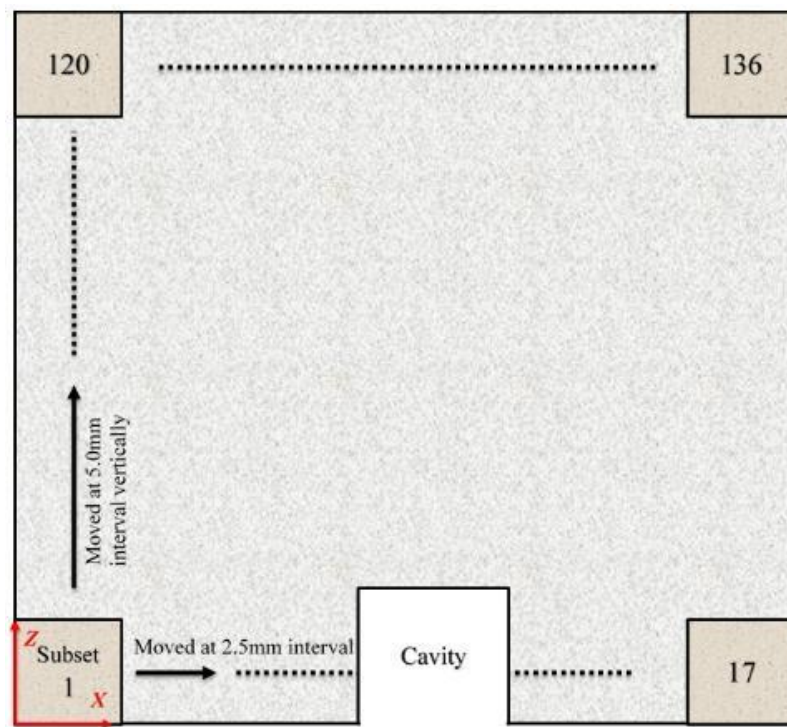
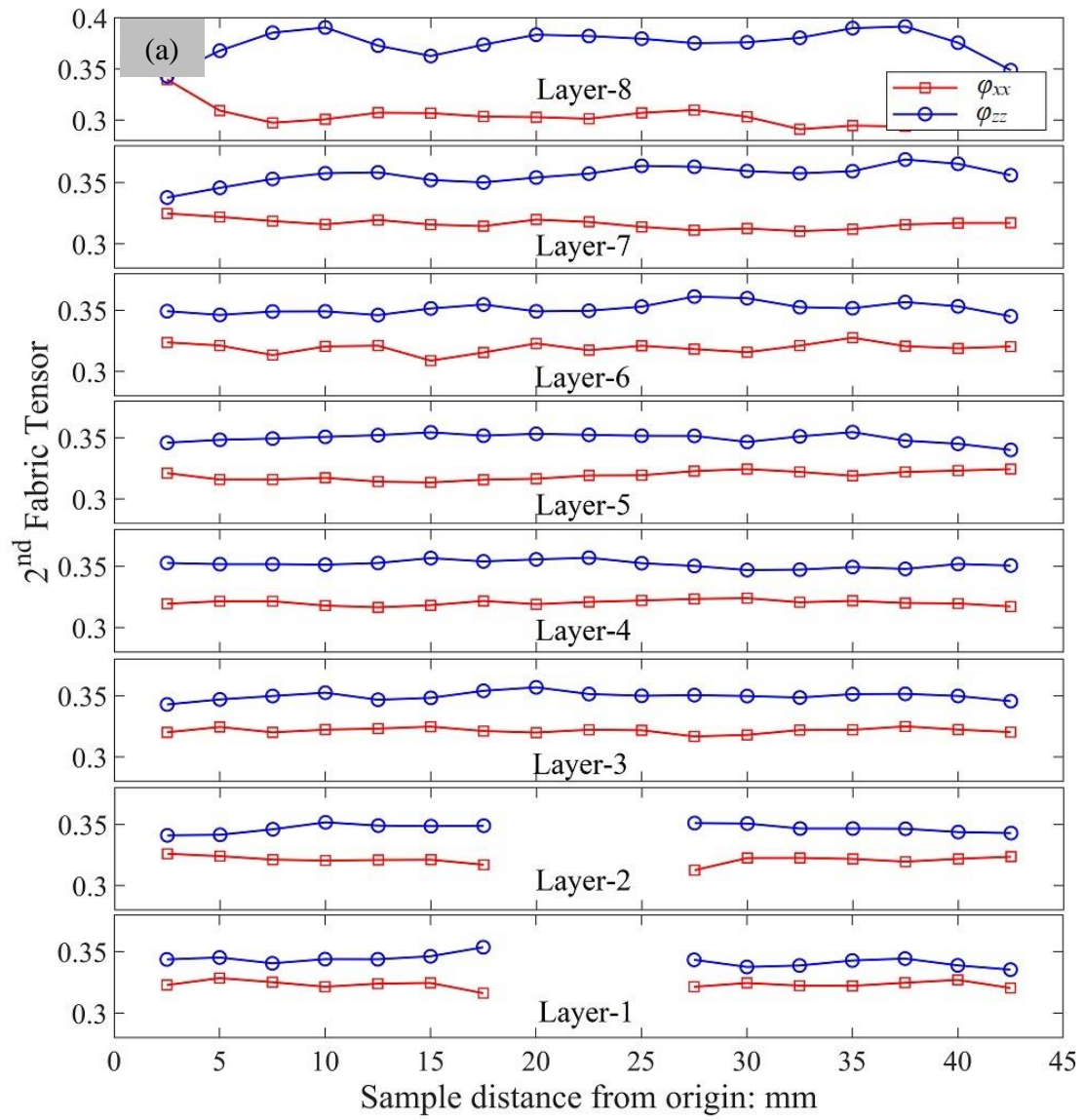


Figure 9.18 Division of model space into 136 number of overlapping subsets



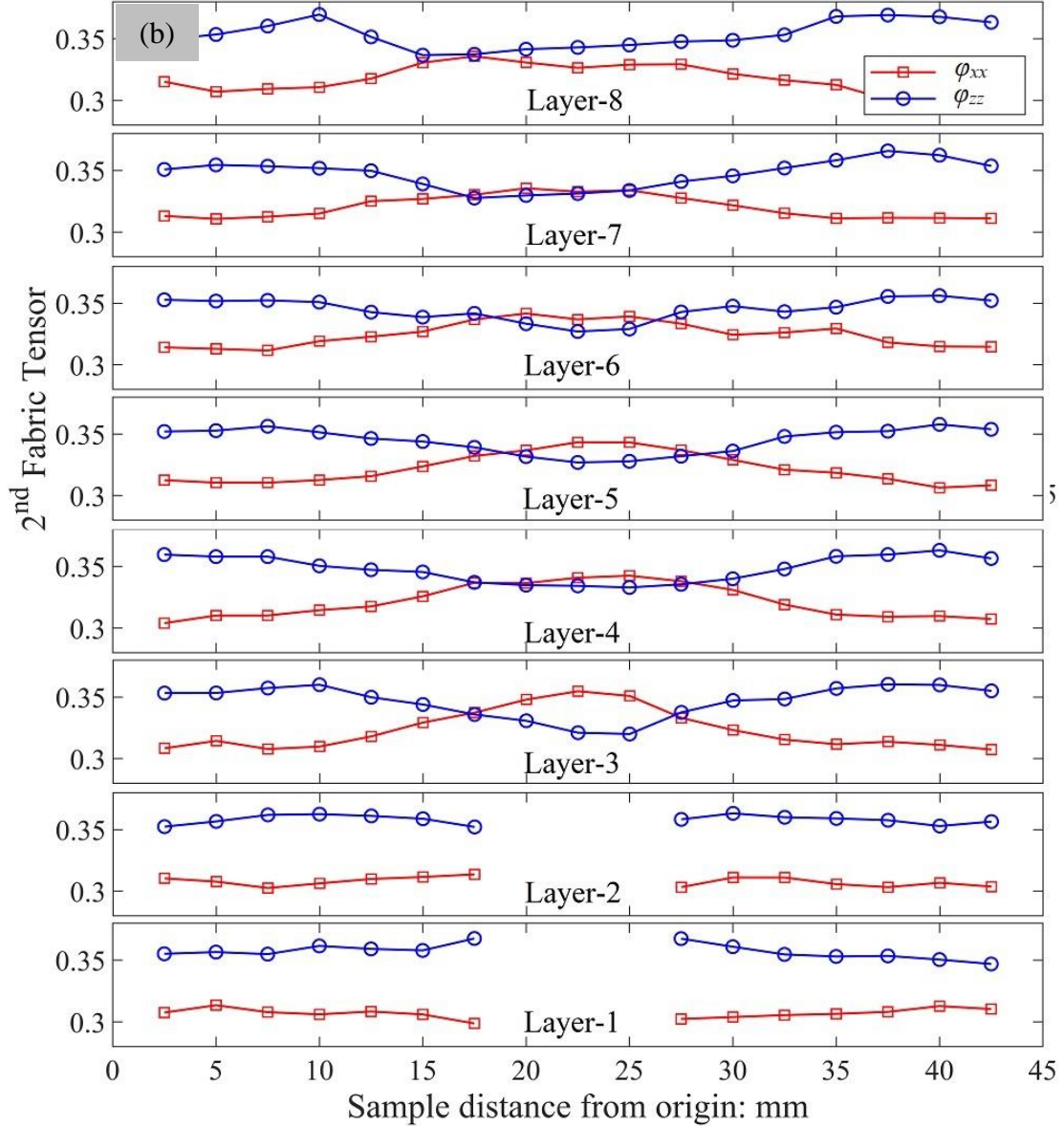


Figure 9.19 2nd order contact fabric for simulation with non-spherical particles having a mean size of 1.0mm at (a) initial state and (b) final state of the simulation

For the 2nd order fabric analyses, only X and Z axes values (ϕ_{xx} , ϕ_{zz}) are plotted, as seen in Figure 9.19, the reason being that the arching phenomenon in the given configuration exists only in the XZ plane and the Y-axis represents uniform behavior. The initial condition of the sample as shown in Figure 9.19(a) shows a constant distribution of contact fabric in both Z and X values through the sample width. However, the ϕ_{zz} values are slightly higher compared to the ϕ_{xx} , due to the gravitational effects that cause an increase in Z contacts and consequently increase in ϕ_{zz} .

Once the cavity simulation is run and particles are allowed to relocate as per the prevailing conditions, the fabric redistribution occurs along with the change in force network. Figure 9.19(b) shows that right above the cavity, the arching forces are almost horizontal in direction, resulting in higher ϕ_{zz} values. However, on extreme left and right sides, the arch direction is vertically downwards resulting in a higher number of contacts in Z-direction. Consequently, the ϕ_{zz} values are larger than ϕ_{xx} values. With increasing vertical distance from the cavity, the arching effect diminishes slowly and hence the contact fabric value trend also tries to become flat. Overall, the change in contact fabric clearly represents the arch development around the cavity space.

9.3.3 Cavity stability simulations using a large sample size – 1.0mm particle size

For accurate analyses in DEM simulations, different authors have presented guidelines and conducted a parametric study to result in a minimum sample dimension/number of particles for any simulation (Head, 1994; Kuhn & Bagi, 2009). Hence, in order to increase the reliability of results, the larger sample size was prepared for DEM simulations and the cavity stability analyses were performed. Mainly two types of non-spherical particles were used with a mean particle size of 1.0mm and 0.5mm. The detailed simulation plan for both is presented in the earlier chapter. Furthermore, the degree of saturation was used as an input in all of the simulation series here.

The simulation plan for the non-spherical particle having a mean particle size of 1.0mm is shown in Figure 9.20 below. The sample consisted of a 200mm sample length and approximately 150mm height. The base of the base contained a 10mm wide slit that would facilitate the falling particle to drop out of the sample box, similar to that of model cavity tests. The saturation levels were selected to be 5 percent and 90 percent, which would represent the value close to extreme limits of saturation, resulting in the maximum and the minimum possible suction force respectively, in the sample. The void ratio for the samples is given in Chapter 8. However, the overall void ratio for all samples was representing a dense sample.

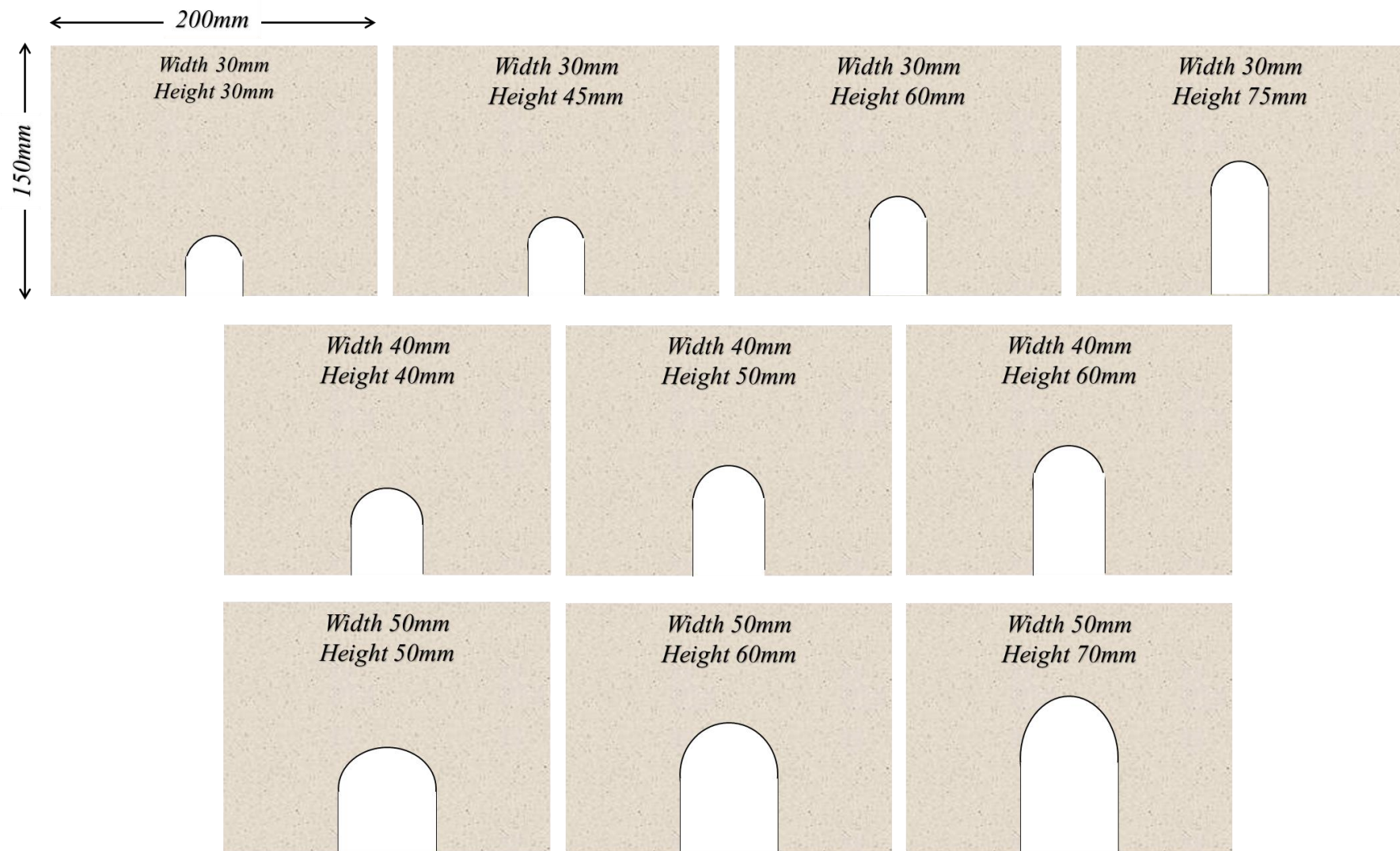


Figure 9.20 Simulation plan for non-spherical particles with a mean particle size of 1.0mm

9.3.3.1 Effect of cavity size on stability

The cavity size is directly proportional to its stability. As shown by several researchers through experimental work on cavity stability issue (Kuwano et al., 2006; Sato & Kuwano, 2015; Ohara et al., 2019 and others), both soil cover above the cavity surface and the width of the cavity are important in determining the overall behavior of the material. Larger cavity widths represent a larger unsupported region directly under the gravitational effects, whose self-weight is being either transferred to the stable sides of the cavity or due to the presence of attractive capillary forces that do not let the soil mass to fall below.

The cover above the soil mass is necessary to provide adequate space for the arching forces to develop its propagating path adequately, without intersecting the sample surface. In case the soil cover is not sufficient, and the arching forces touch the sample surface, there exists an imbalance in the particle forces near the surface of the sample, causing a differential settlement of the surface that eventually leads towards cave-in of the sample. Hence, for better stability, an adequate material cover should be provided to keep an existing underground cavity in stable conditions.

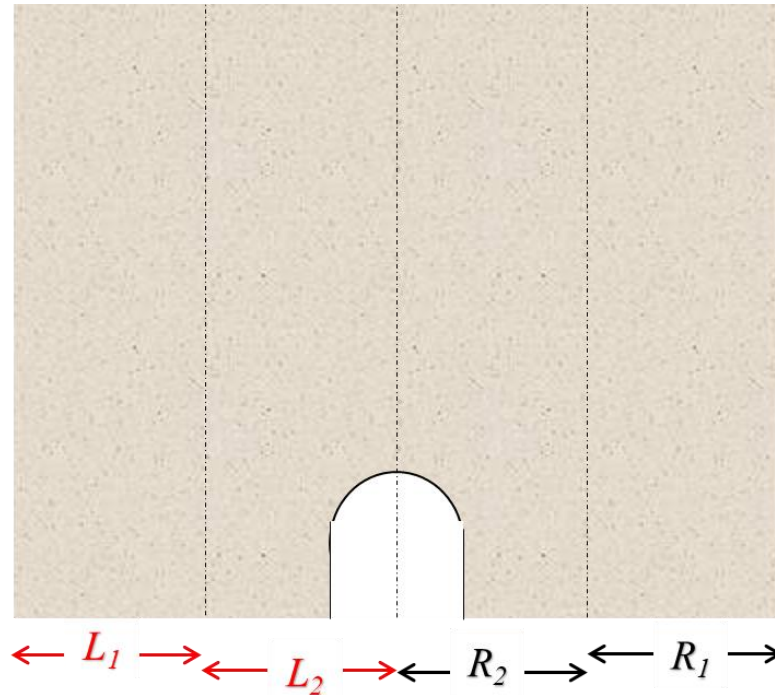


Figure 9.21 Division of numerical sample into four regions for analyses

The DEM sample is divided into four equal distance portions; two on the left side and two on the right side, as shown in Figure 9.21. This is done so as to differentiate the stress distribution at different locations of the sample, as due to the formation of soil arching, the region near the cavity would be having a reduction in stresses and the surrounding static portions would feel increased stress on it.

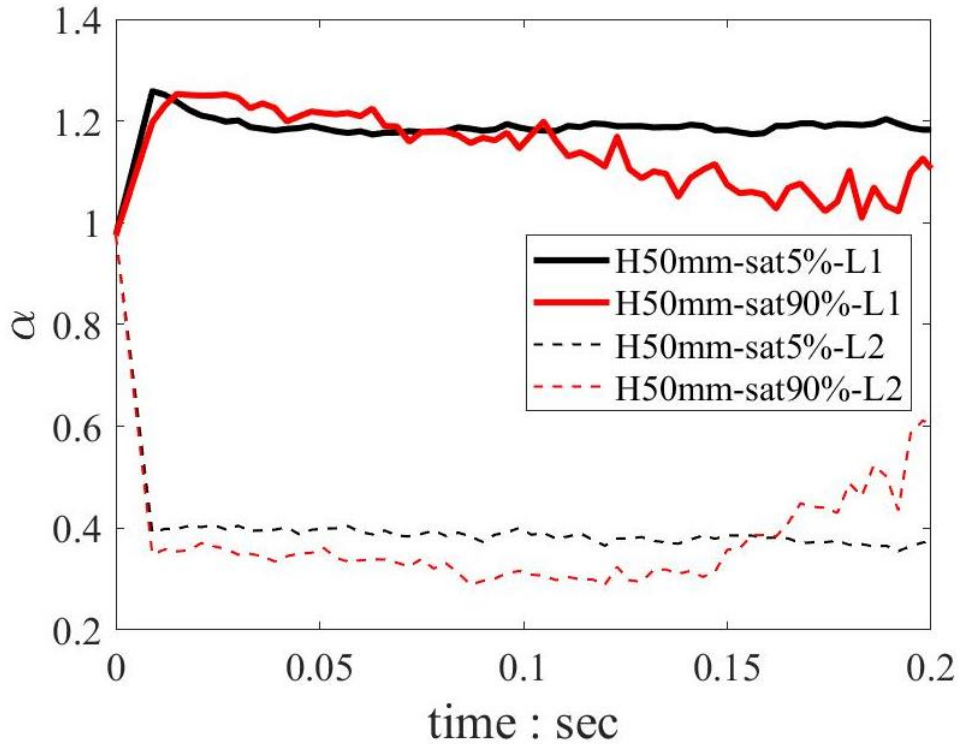


Figure 9.22 ' α ' variation for varying degree of saturation of the sample

The variation of ' α ' value, that is the stress concentration on the bottom static plates, for two extreme degrees of saturation with a cavity width of 50mm and height of 50mm is shown in Figure 9.22. The initial behavior of ' α ' is not much different for both samples. However, with the passage of time, the sample with a higher degree of saturation showed more dynamic responses and resultantly the stress concentration factor started to decrease. This decrease in ' α ' value corresponds to a failing arching mechanism. The change in the distribution of force chain with simulation time is visible in Figure 9.23, verifying the failure of the arching forces to result in sample collapse. Furthermore, the difference in strong forces with increasing cavity heights is shown in Figure 9.25.

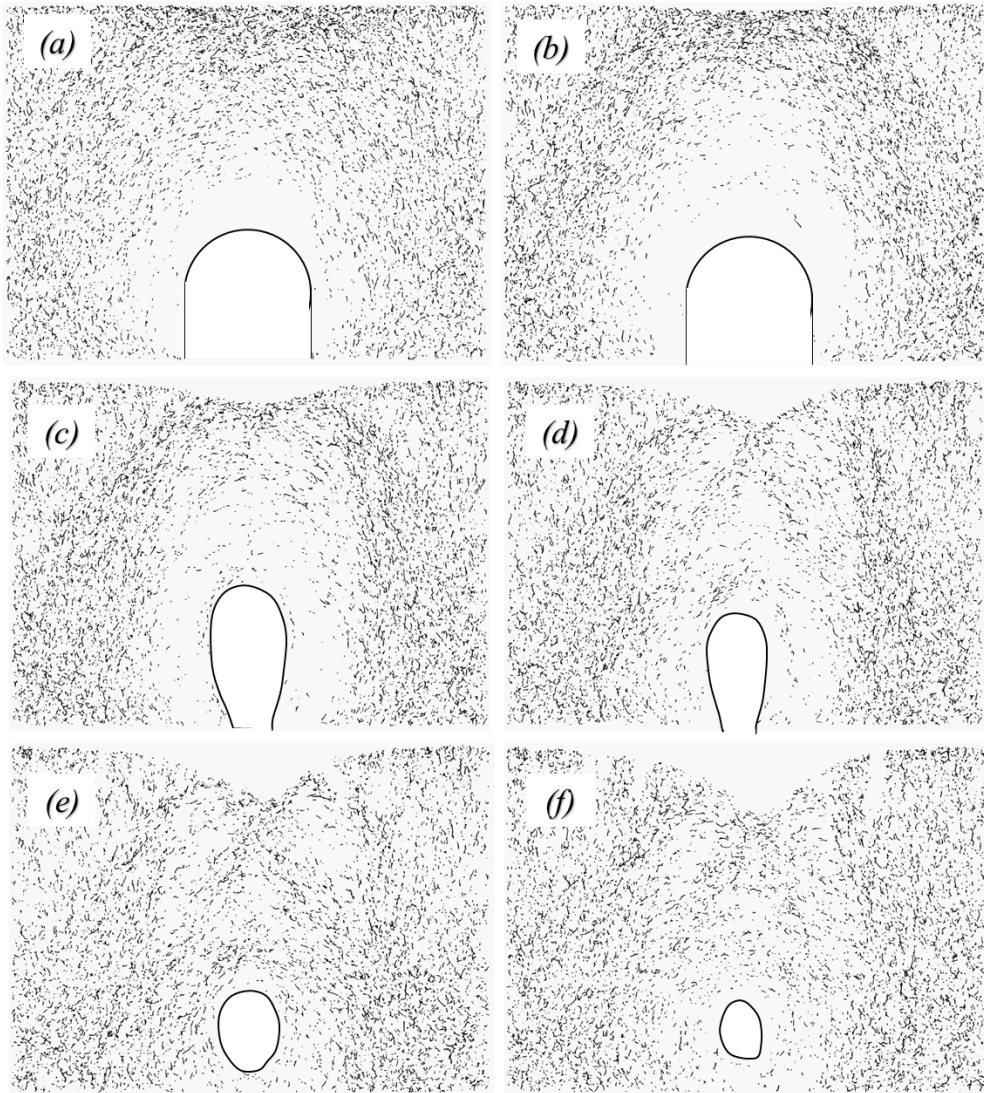


Figure 9.23 Strong force variation with time in the sample with a 50mm wide cavity with 50mm height

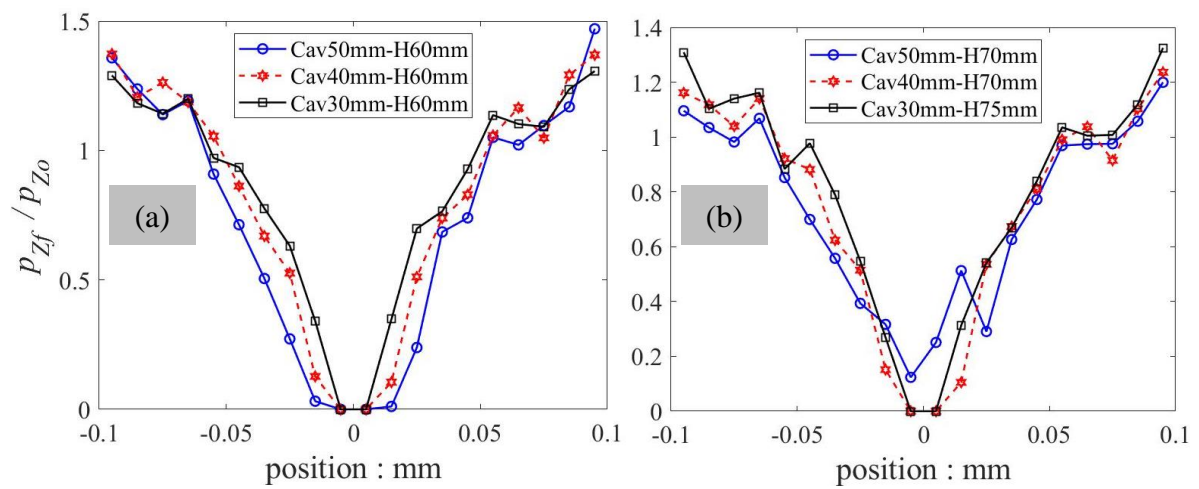


Figure 9.24 Normalized normal stress distribution for different cavity widths having (a) height of 60mm and (b) 70mm

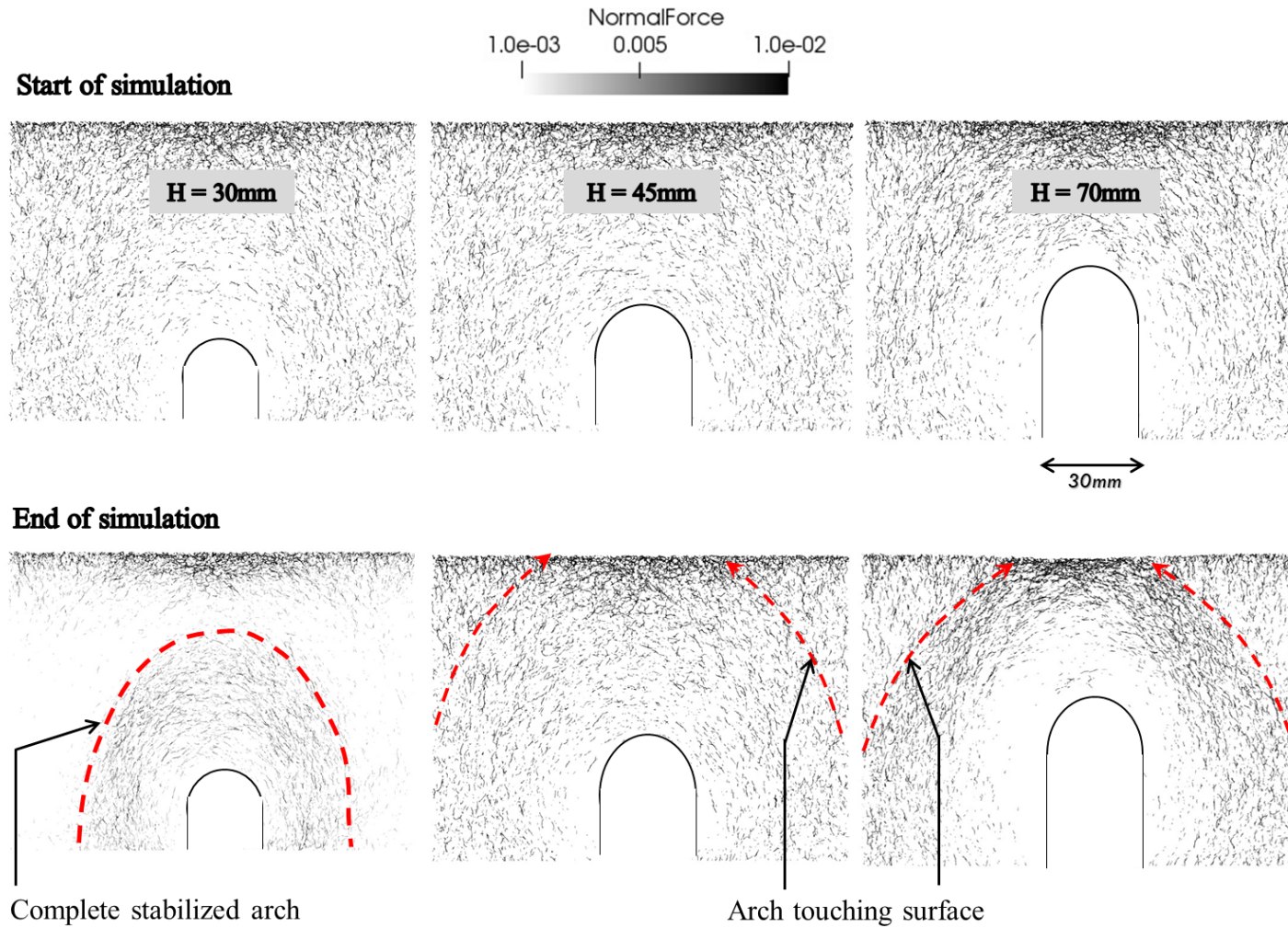


Figure 9.25 Strong force distribution for 30mm cavity width with different heights at initial and final states of the simulation

Normalized normal stress distribution, that was explained in Chapter 4 of this manuscript, was calculated for all simulations and the results of cases with cavity heights of 60 and 70mm with varying widths, are provided in Figure 9.24. The central portion showed zero stress due to the presence of a cavity at that location. However, the load of the mass above that portion was transferred to the sides of the cavity with the help of soil arching, resulting in increased normalized normal load on those side portions. The overall difference in load distribution is not much different from each other. However, as an overall behavior, cavities with larger width showed a lesser increase in stress due to the fact that larger mass of soil was missing once the simulation started, compared to the initial stress distribution when there was no cavity.

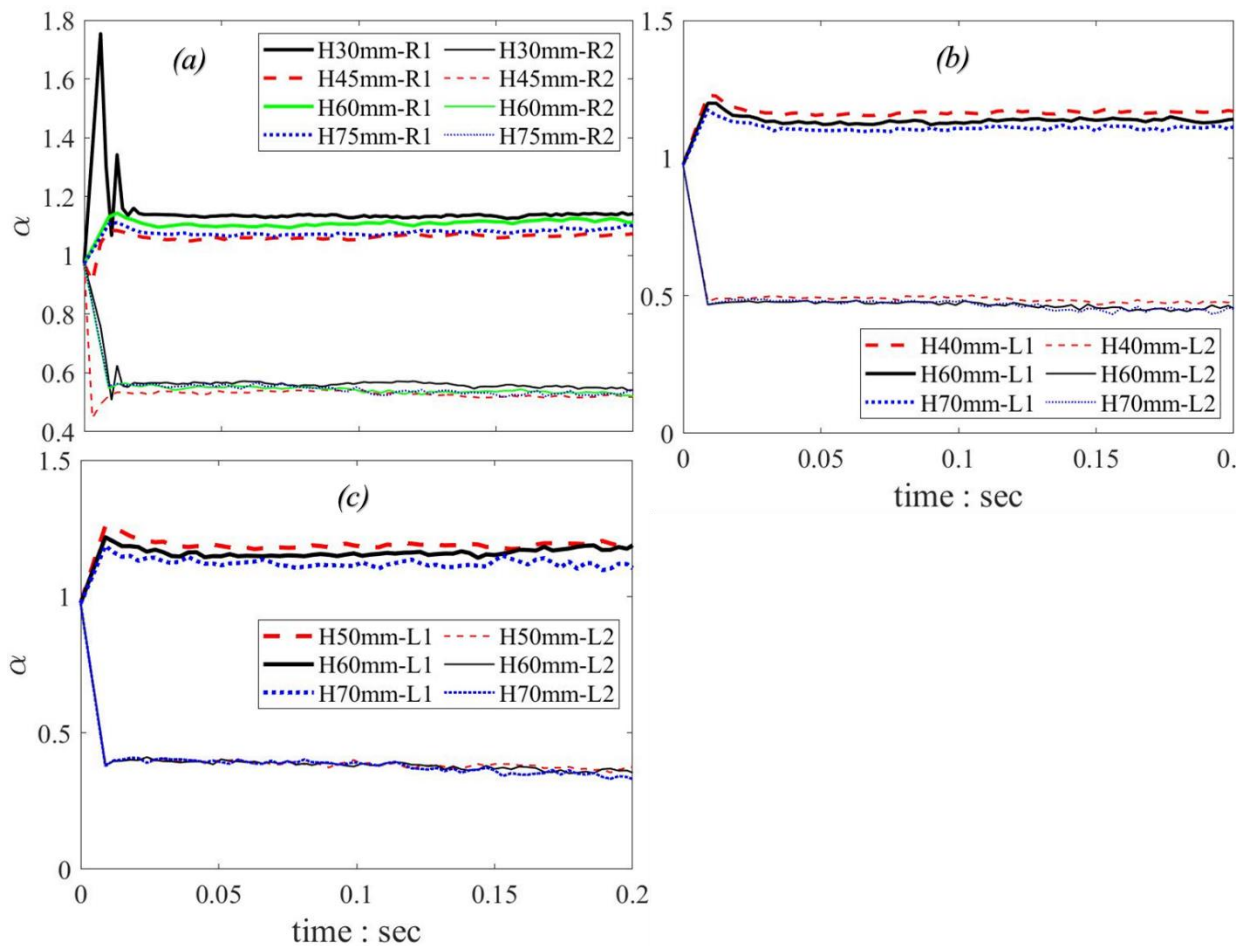


Figure 9.26 ' α ' variation for varying cavity height under a cavity width of (a) 30mm, (b) 40mm, and (c) 50mm

The variation of ' α ' for different width and height of cavities show that a minor increase in α_{peak} occurs with decreasing height of the cavity under a specific

cavity width. Similarly, the stress on the central portion near the cavity observed a decrease in ' α ' value with time, contrary to its neighboring portion that faced increasing ' α '.

The ' α ' plot gives information about the stress redistribution once the arching action is initiated in a mass under cavity conditions. However, the outcome of any case whether it was collapsed or stabilized, is difficult to abstract from the stress concentration plots. In this case, the plots of Kinetic energy could be of great help. The samples that are stabilized experience a strong reduction in particle movement, leading to a minimizing Kinetic Energy ($K.E$) of the sample. However, the samples that result in collapse, never experience a reducing trend in $K.E$, rather the energy of the system increases slowly or rapidly as soon as the frictional resistance between the particles is overcome in collapsing sample.

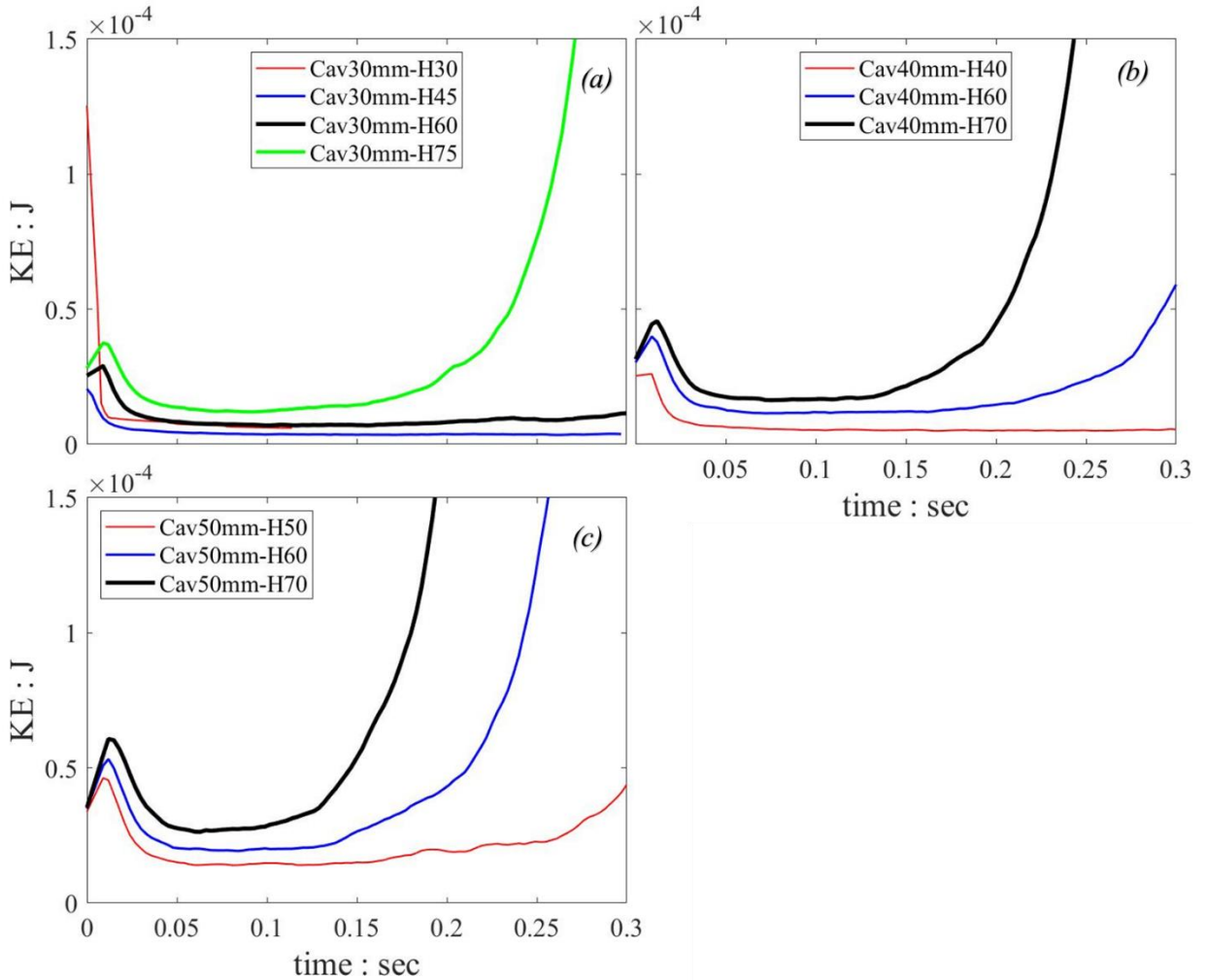


Figure 9.27 Kinetic energy plot for all cavity stability simulations grouped into (a) 30mm width (b) 40mm width and (c) 50mm width of the cavity

The K.E plots as shown above in Figure 9.27 for various widths of the cavity with different cavity heights show that only the cavities with a smaller width and higher soil cover (shorter height of cavity) are stabilized with passing time. The increasing behavior of the energy plots shows a collapsing trend of the sample. Within the group of simulations with 30mm width of the cavity, only the cases having shorter heights of 30mm and 45mm showed a converging trend of K.E.

Similarly, for the group having a cavity width of 40mm (Figure 9.27b), all samples showed collapsing behavior except the one with a 40mm cavity height. However, in the case of a cavity width of 50mm, all samples showed an increasing trend of Kinetic energy (K.E), showing that none of the samples could form a stable cavity under the given conditions.

Figure 9.28 compares the similar plots with matching heights of the cavity for the cases with different cavity widths. From Figure 9.28(a), it can be seen that under similar heights, the sample with larger width showed a collapsing behavior, showing the importance of cavity width on its stability. Similarly, in Figure 9.28(b), under a cavity height of 60mm, both samples with the cavity width of 40mm and 50mm showed a failing sample. Whereas the least width sample (30mm) did not show any increasing trend of energy and moved towards the stability of the sample.

Kinetic energy variation with the change in saturation degree of the sample also imparts a significant difference. Higher saturation causes more particle slippage due to the development of lesser capillary forces. Such behavior results in higher particle velocities resulting in higher kinetic energy of the system. Figure 9.29 shows the difference between the 5% saturation and the 90% saturation for similar cavity dimensions.

The Kinetic energy difference for higher saturation is clearly visible. For the cases with the cavity of 40mm and 50mm, the difference of Kinetic energy for $S_r = 5\%$ and $S_r = 90\%$ is more than ten times. With a smaller saturation value, the sample with a cavity width of 40mm showed a stable behavior. However, a similar case with higher saturation resulted in the failure of the sample. The case of 30mm cavity width showed stable behavior for both saturation values. The reason being that the cavity size is small enough to enable strong arching action around the cavity. The combined action of the arching and smaller magnitude of capillary

force would result in a resultant force larger than the self-weight effect of the soil mass. Although, both cases of 30mm cavity width showed stable behavior. Although, the relative magnitude of K.E is slightly smaller for the lesser degree of saturation. Similarly, the case of cavity width 50mm showed a failure/collapsing trend for both samples having $S_r = 5\%$ and $S_r = 90\%$. Still, the higher saturation sample showed a significant difference in the magnitude of energy, showing that the higher saturation sample would fail much quicker than the smaller saturation sample.

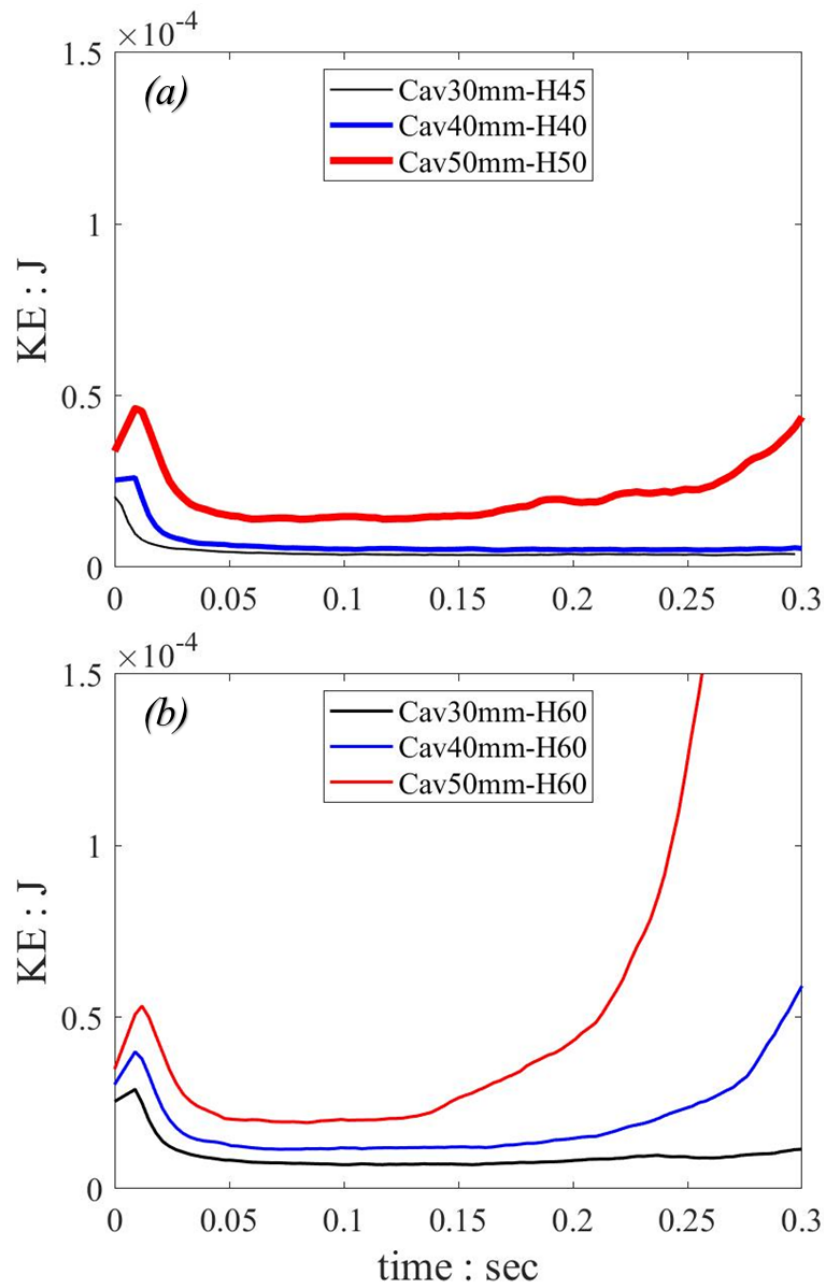


Figure 9.28 Kinetic energy plot for matching cavity heights with varying widths

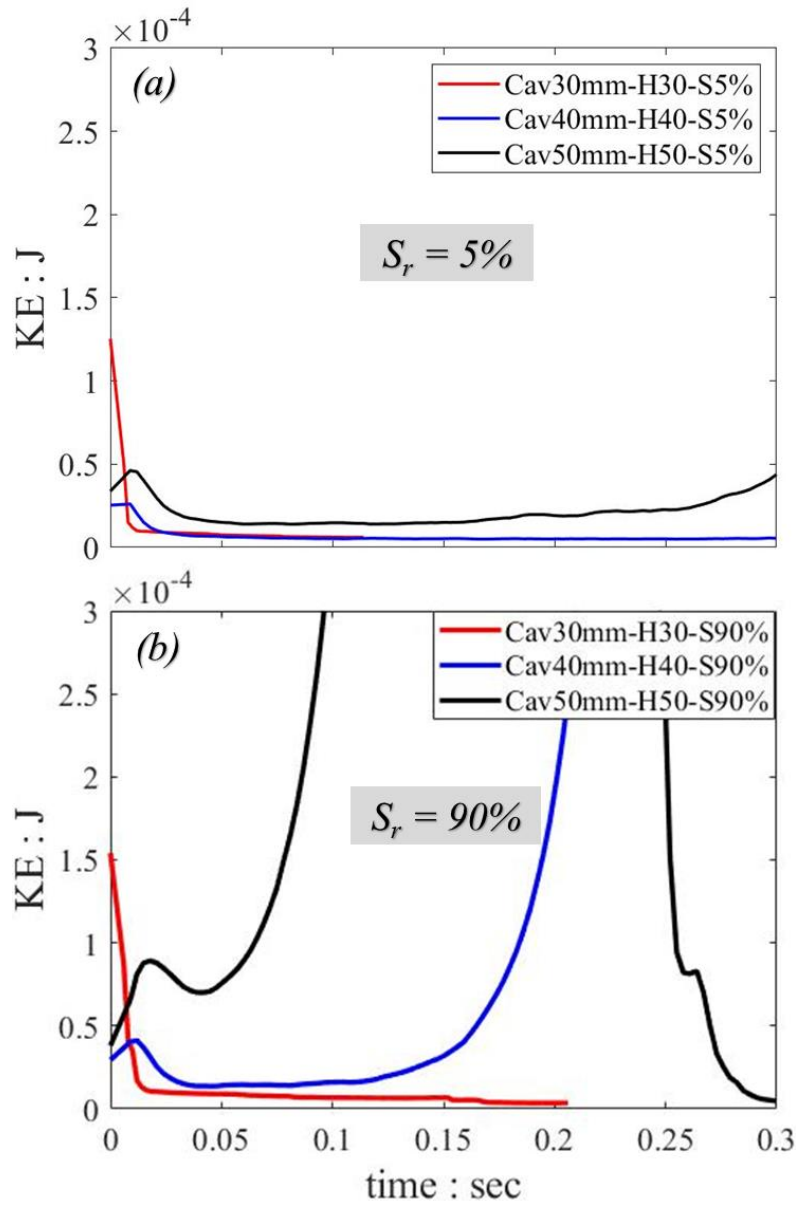


Figure 9.29 Comparison of Kinetic Energy variation with similar cavity dimensions for (a) $S_r = 5\%$ and (b) $S_r = 90\%$

In general, using a non-spherical particle of 1.0mm diameter, it was verified using numerical simulations that the current suction-tension model can capture the cavity stability trend as seen in laboratory tests using various glass beads. Furthermore, the arch development around the stable cavities was verified by both strong force and 2nd order fabric contact distribution plots.

9.3.4 Cavity stability simulations with 0.5mm mean particle size

Since the particle size has a significant effect on the capillary force behavior, as explained in the model test results, the particle size was further decreased from a clumped particle of 1.0mm to 0.5mm. By decreasing the mean particle size resulted in a significant increase in the total number of particles for a similar model dimension. Furthermore, reducing the particle size results in a further reduction in the critical time step in the DEM code. Both an increase in the number of particles and a reduction in critical time step resulted in a significant increase in computational energy and calculation time.

Foregoing in view, the sample dimension for the smaller particle size of 0.5mm was further reduced to result in a total length of 100mm and a height of approximately 130mm. The sample breadth was kept $10 \times D_{max}$. Overall, the number of particles and the dimensions were enough to satisfy the criteria of a representative sample as described by both Head (1994) Kuhn & Bagi (2009).

The simulations were performed for a number of cases, consisting of variation in cavity width and then further variation with cavity height for each width of the cavity. The simulation plan is explained in Chapter. However, a graphical representation of each simulation case is shown in Figure 9.30 below.

9.3.4.1 Cavity dimension effect on stress variation

The effect of cavity width on the normalized normal stress is shown in Figure 9.31. With increasing cavity width for a small cavity height, the maximum normalized stress increases. For a wider and short heightened cavity, the stresses of the hanging portion above the cavity are balanced/transferred to the smaller side areas due to arching action, resulting in a higher stress ratio.

For a higher cavity height, as shown in Figure 9.32, again the wider cavity showed larger normalized stress. However, due to the presence of taller cavities, the net transfer of load from the hanging portion to the sides of the sample was not so significant, resulting in a minor difference of stresses. Similar to the effect of cavity width, increasing the cavity heights for a certain width (Figure 9.33) increases the normalized normal stress, due to the fact that lesser soil mass is there to transfer a load of the hanging portion and the lack of the arching action in the soil mass.



Figure 9.30 Simulation plan for cavity stability with a mean particle size of 0.5mm (non-spherical)

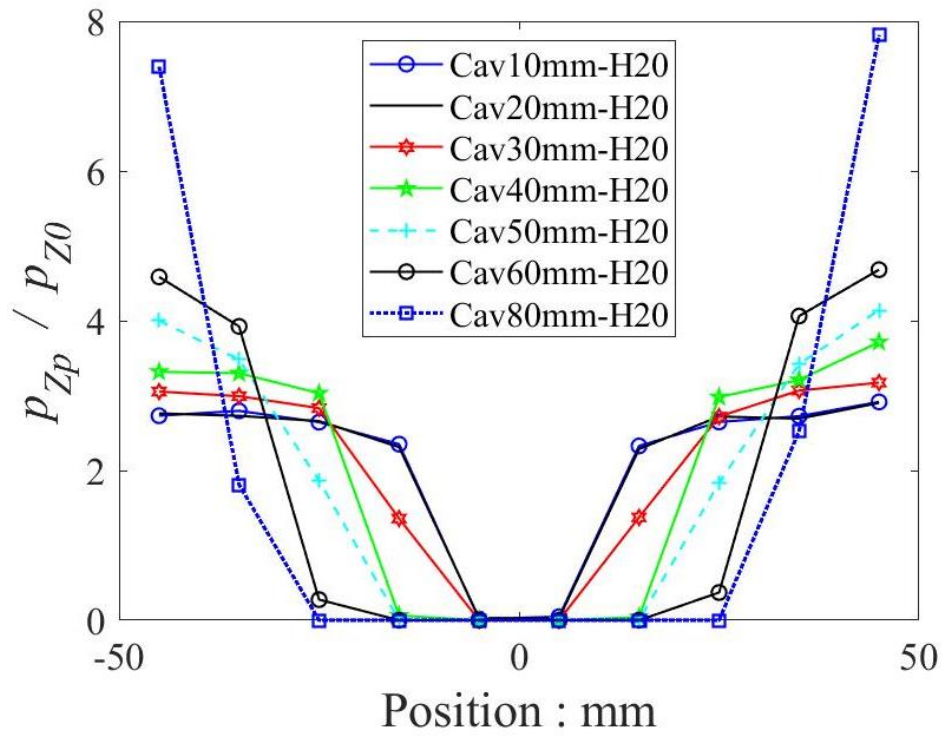


Figure 9.31 Normalized normal stress distribution under varying cavity widths for a cavity height of 20mm

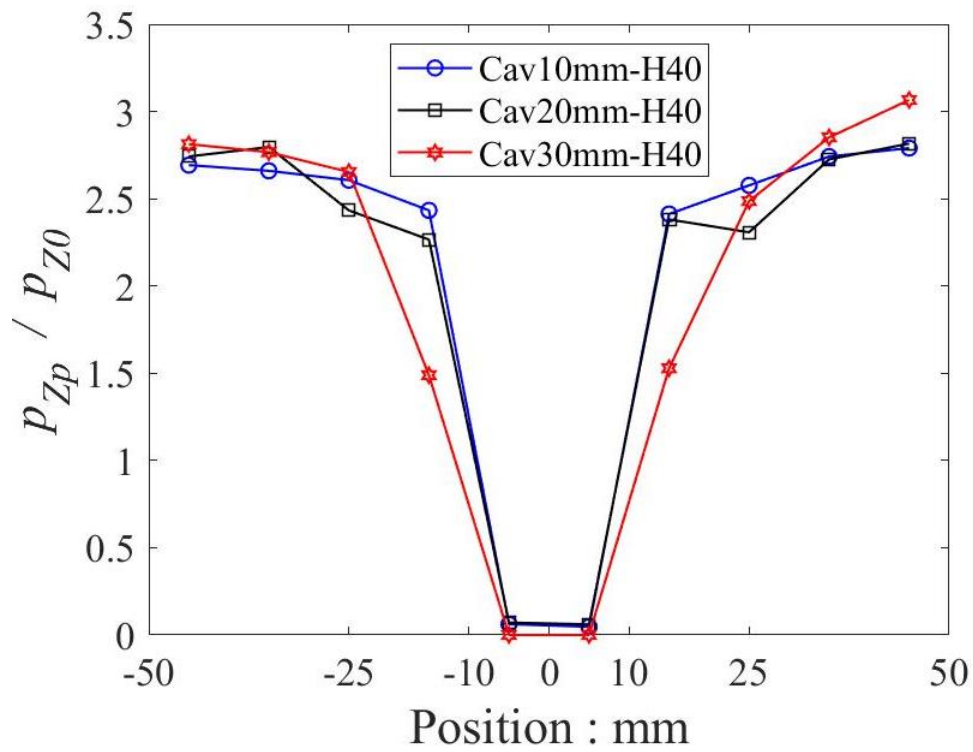


Figure 9.32 Normalized normal stress distribution under varying cavity widths for a cavity height of 40mm

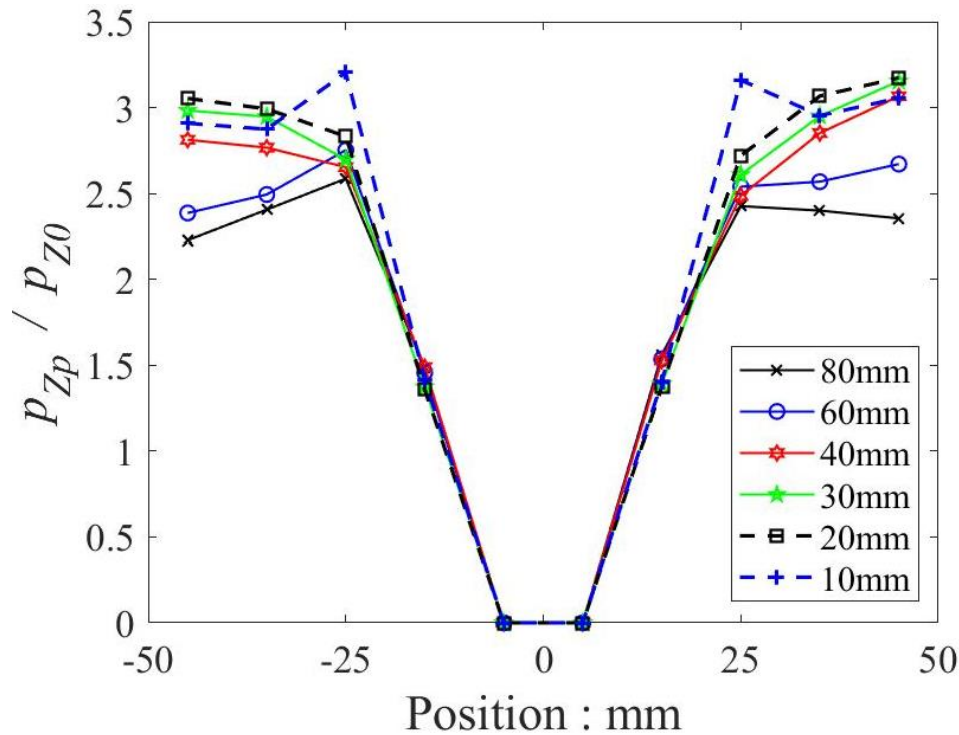


Figure 9.33 Normalized normal stress distribution under varying cavity heights for a cavity width of 30mm

Similarly, the α decreases with increasing height of the cavity, for a certain cavity width, as shown in Figure 9.34. The peak value is shown when the cavity height is small enough to allow proper arch development around the cavity. In the given case, the cavity heights of 10mm to 40mm yielded the maximum α value, which is quite close to each other as well. All these cases also showed a stable behavior and did not have any surface collapse.

For the case of changing cavity widths for given cavity heights, the α value on the extreme end portions increased with increasing the width of the cavity (Figure 9.35). The reason being the presence of a higher area of unsupported soil mass whose weight is to be transferred to the portions near ends of the sample. Furthermore, the cases with a cavity width of 30mm and 40mm, the overall sample trend was found to be stable. However, the α value was smaller compared to the unstable cases with higher cavity widths. This pattern suggests that α value can be used to analyze the stress redistribution at the bottom of the cavity. However, for stability analyses, α should be combined with other parameters to assess the sample behavior.

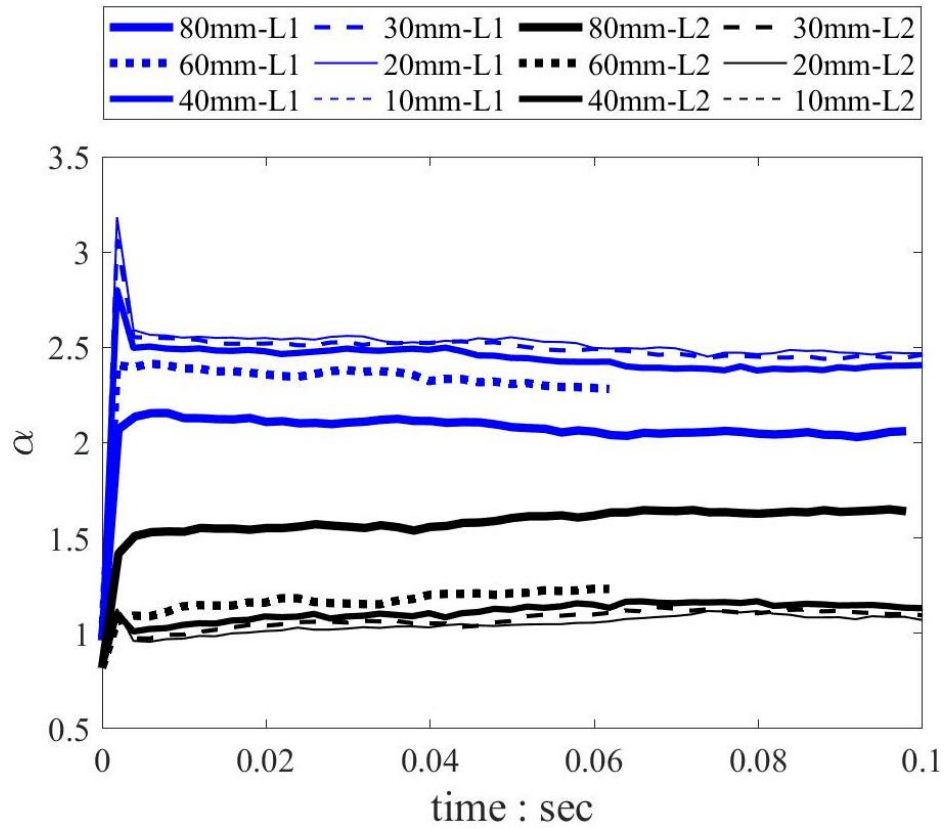


Figure 9.34 ' α ' variation with increasing cavity height for a cavity width of 10mm

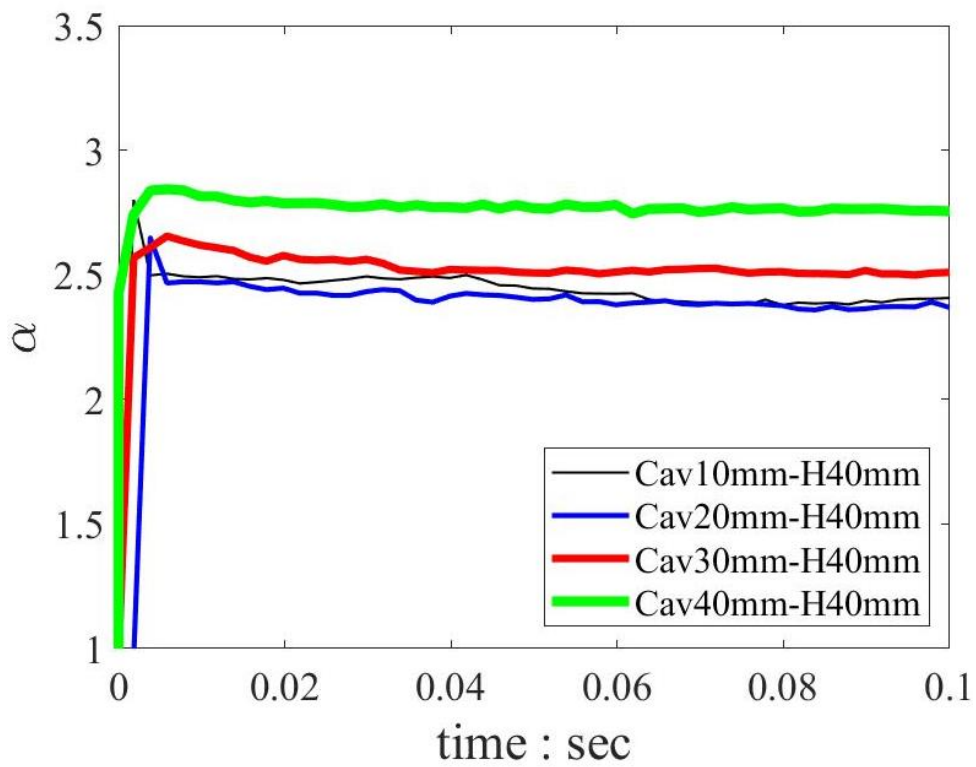


Figure 9.35 ' α ' variation with increasing cavity width for a cavity height of 40mm

9.3.4.2 *Cavity stability and kinetic energy variation*

As explained earlier, in case of a stable behavior of a sample with the presence of a cavity, the soil mass ceases to move and the particles would show a negligible movement. Such a small movement would result in a Kinetic energy response approaching zero. By analyzing the energy response, the true nature of particle motion can be detected, and it can be concluded whether or not the sample is portraying a static behavior or not.

Figure 9.36 and Figure 9.37 shows the kinetic energy distribution under various cavity width and height. From both plots, it is clear that either by increasing the cavity width, or the cavity height, both result in an increasing trend of kinetic energy as lesser soil mass is there to balance the vertical forces (for wider cavities) or the strong horizontal forces (for taller cavities). This results in more movement of particles to result in either a stabilized case or the collapse case. The effect of cavity height for a given cavity width is shown in Figure 9.36. Increasing the cavity height for a particular width does not affect the normal stresses to a great extent. However, the taller cavities possess a higher degree of instability for horizontal forces. The role of vertical forces is more compared to the horizontal forces due to the gravitational effects. Hence, for a smaller cavity width, even taller cavities could result in a stabilized behavior, unless the cavity height reaches a critical limit.

For increasing the cavity width, the critical cavity height reduces, and the larger top cover of material is required to balance the system. As the arch propagation is normally in an inverted catenary shape, the most feasible shape for a cavity would be a balance in the width and height of the cavity. However, in case the material does not offer good interlocking amongst particles, or the density is not enough to effectively transfer the stresses within particles, the catenary shape would result in a more elongated region, with a vertical range larger than the horizontal range. (as also seen in trapdoor experimental cases, for loose or medium dense materials, in Figure 5.9). In such a case, a stable sample can accommodate much taller cavities compared to a dense sample with higher particle interlocking. Due to a similar reason, in experimental cavity tests, using clumped glass beads with higher interlocking, showed a wider stable cavity, compared to the spherical glass beads that showed more taller cavities compared to their widths.

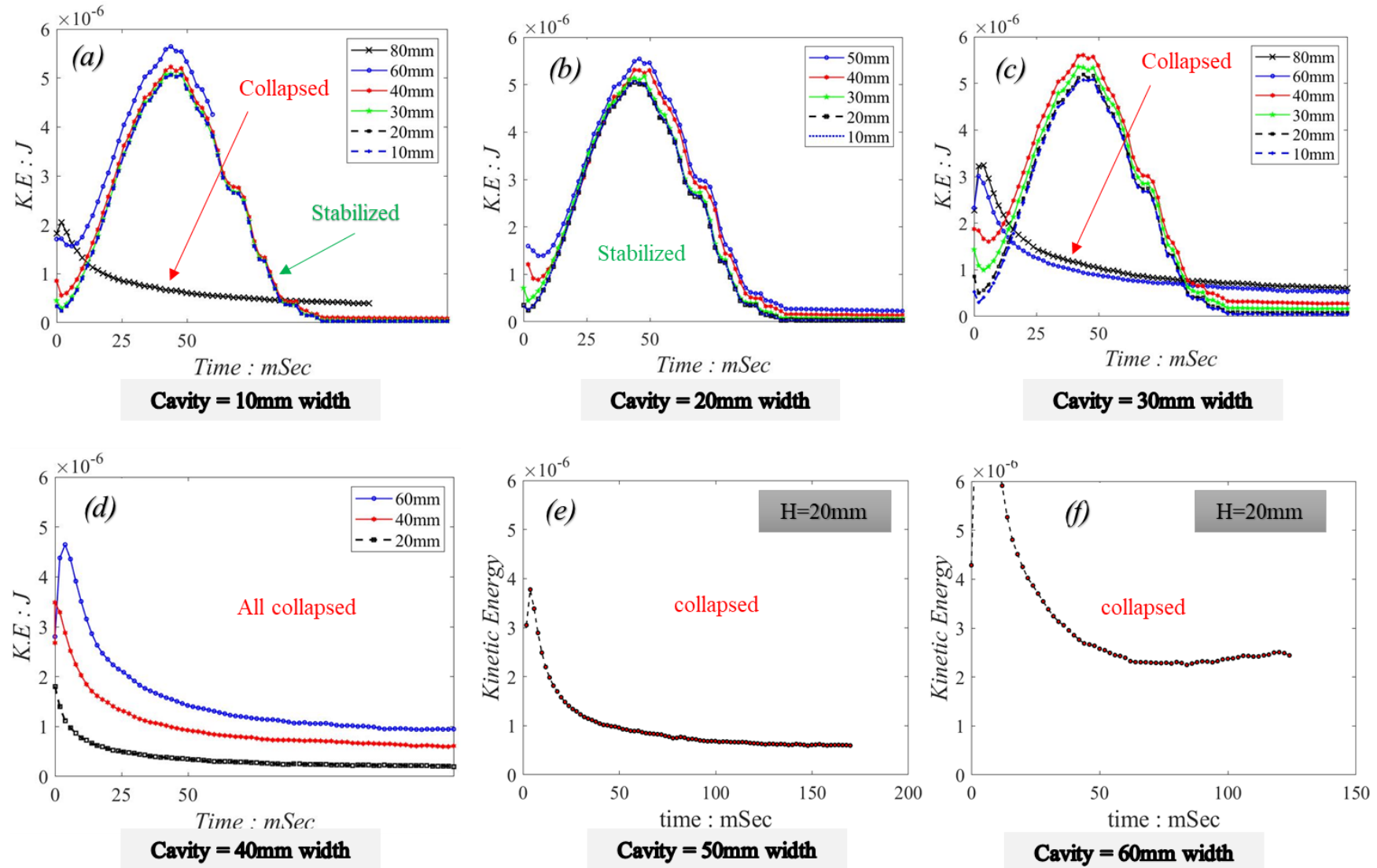


Figure 9.36 Kinetic energy variation with changing cavity height for a given cavity width, using non-spherical particle mean size of 0.5mm

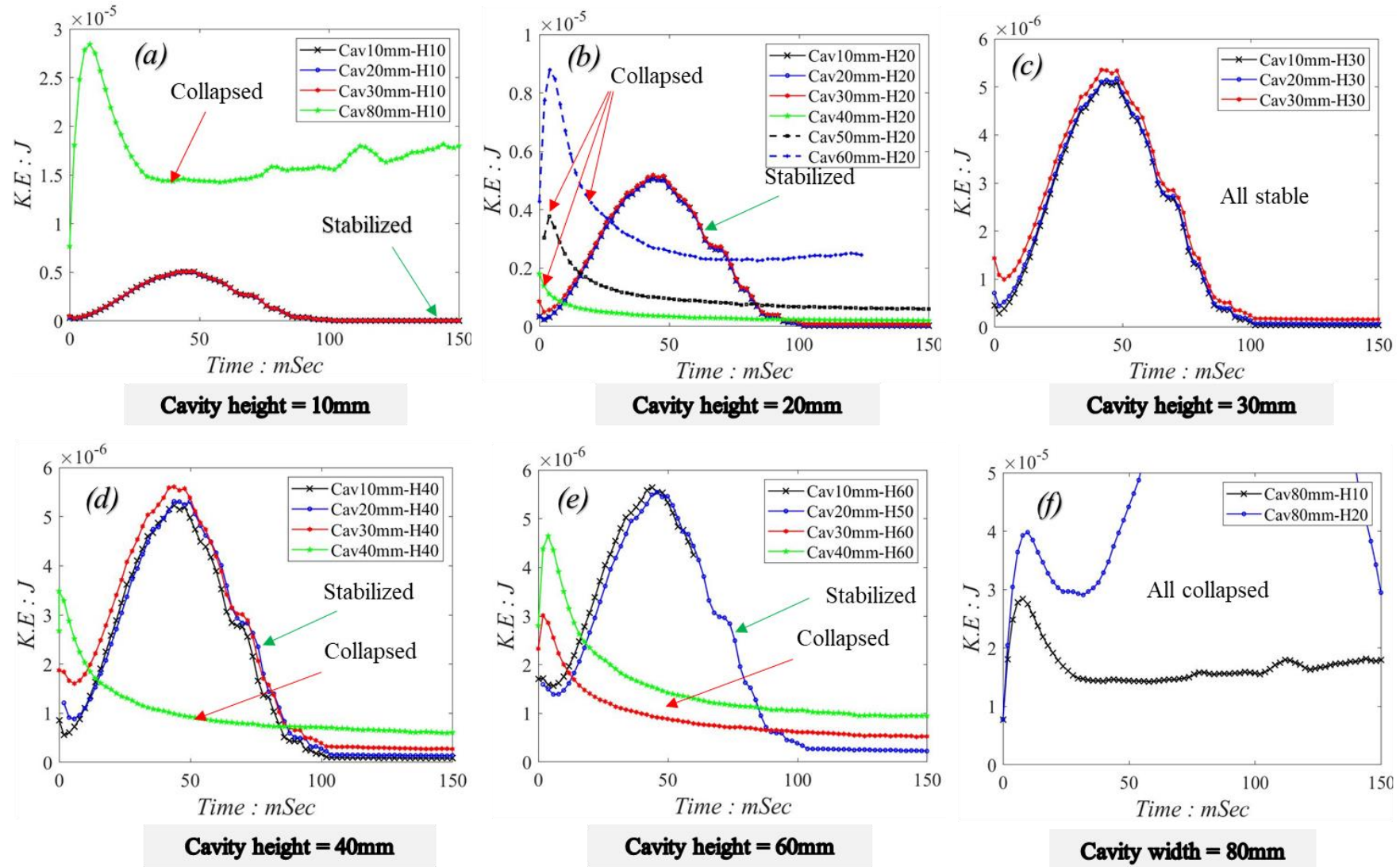


Figure 9.37 Kinetic energy variation with changing cavity width for a given cavity height, using non-spherical particle mean size of 0.5mm

Based upon the simulation results using non-spherical particles of 0.5mm mean size, the K.E plots were used as a source to decide the stable or unstable behavior of the sample and the results were plotted on the cavity stability chart, as discussed in section 9.2 above. Figure 9.38 summarizes the results of the cavity simulation plotted on the cavity stability chart.

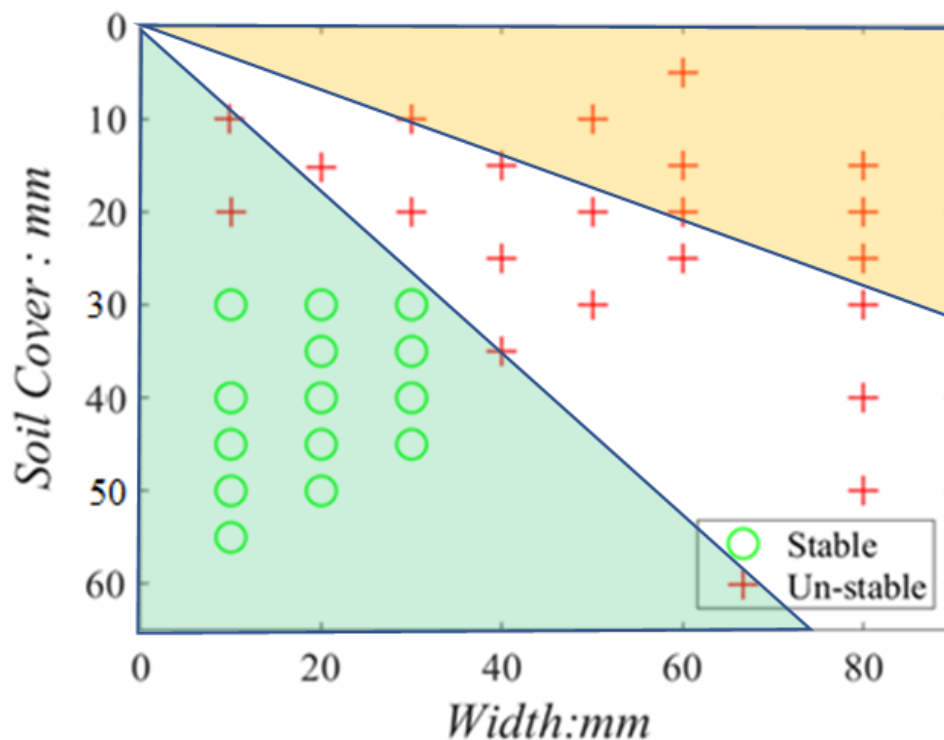


Figure 9.38 Cavity stability chart plotted for the numerical simulation results of cavity tests using non-spherical particles with a mean size of 0.5mm

When the lines were drawn in a similar manner as used in the cavity stability chart for field projects, a clear distinction was found between the stable and the unstable cases. However, the cavity stability chart being practiced in the field based upon some experimental/empirical observations portrays a cavity having a small width and small soil cover as a stable case. Whereas, a numerical simulation in that region showed unstable behavior, contrary to the field practice chart. The numerical result for that particular simulation showed a side wall collapsing behavior as the cavity height was large enough to make it difficult being stabilized sideways.

In the field, however, it is not necessary that a low-width cavity with small soil cover may also be tall as well. A floating cavity with small depth and width might be able to withstand in the field. In our simulation plan, such occurrence would not be considered as a *low soil cover* case as all cavities are initiated from the base of the sample.

To verify the stability in that particular critical region, a few more simulations were performed, and the result was found to be similar to earlier cases, i.e. unstable. Hence, the cavity stability chart was slightly modified, and the new plot is shown in Figure 9.39.

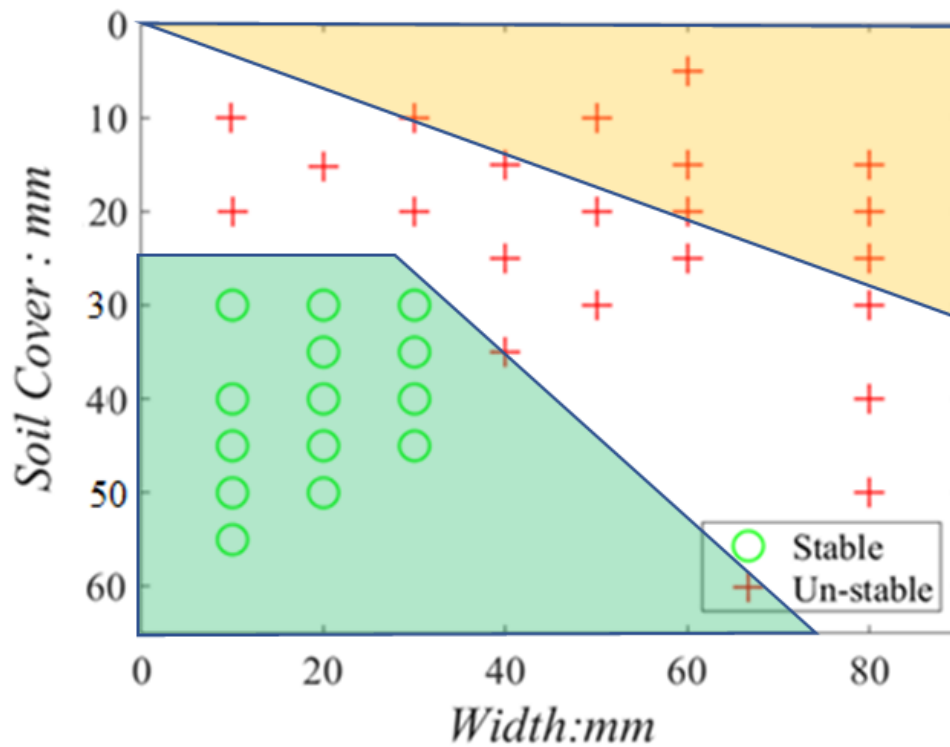


Figure 9.39 Modified cavity stability chart plotted for the numerical simulation results of cavity tests using non-spherical particles with a mean size of 0.5mm

9.3.4.3 Force distribution under extreme shapes of cavities

The extreme cavity shapes could exist in either very deep and narrow or very wide and thin. These extreme shapes were analyzed for the strong force distribution and the results are shown in Figure 9.40. As seen, for the tall and narrow cavity cases, the strong force network has much lesser density along the vertical walls of the cavity. Similarly, a wide cavity showed a similar observation above the top surface of the cavity. However, a case with a balanced width and height of the cavity showed uniformly distributed arching through strong force network around the cavity. Hence, due to a lack of strong forces, it is presumed that the tall cavities are more prone to sidewall collapse and wider cavity are more prone to top-wall collapse.

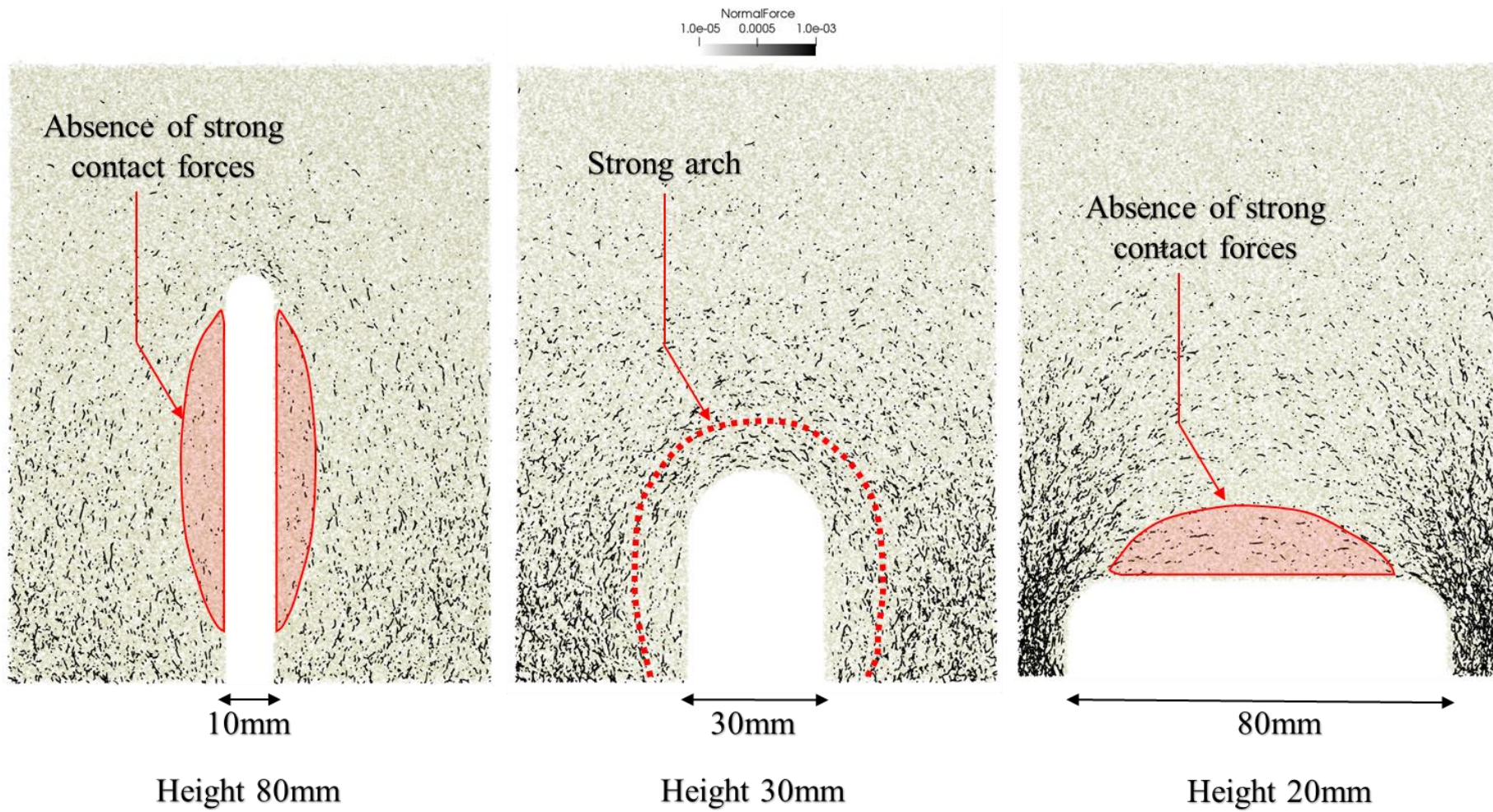


Figure 9.40 Strong force distribution for the extreme cases of cavity formations using non-spherical particles having a mean size of 0.5mm

There are chances that the above observation made for wide cavities might be influenced or affected by the overall dimensions of the sample space. A similar cavity within a larger soil mass might show a stabilizing behavior due to the presence of abundant force interactive contacts. To verify this, a similar simulation was run on a wider sample having a length of 200mm and the effect of top wall collapse was verified.

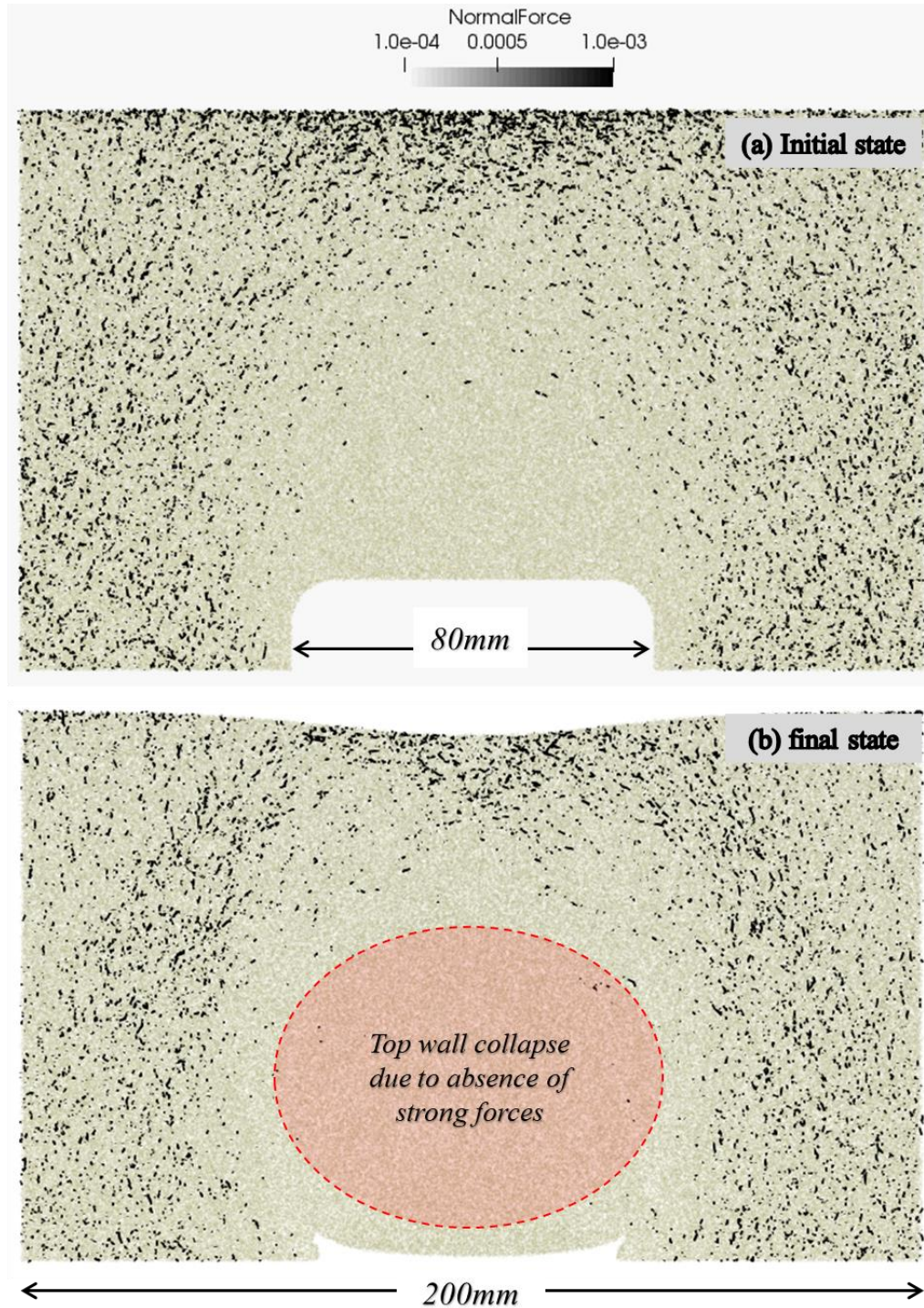


Figure 9.41 Strong force comparison before and after the simulation with larger sample dimensions having cavity width of 80mm

The strong force distribution as shown in Figure 9.41 verified the above assumption of top wall collapse for the wider cavities. Figure 9.42 strengthened the point of view by showing the vector diagram of particle movement direction, overlaid on a color plot showing vertical displacement of particles. Both the color bar and the arrow directions showed that particles above the cavity top were moving maximum and vertically downwards. The concern of the overall sample dimension was also eradicated by using the larger sized sample with similar width in Figure 9.41.

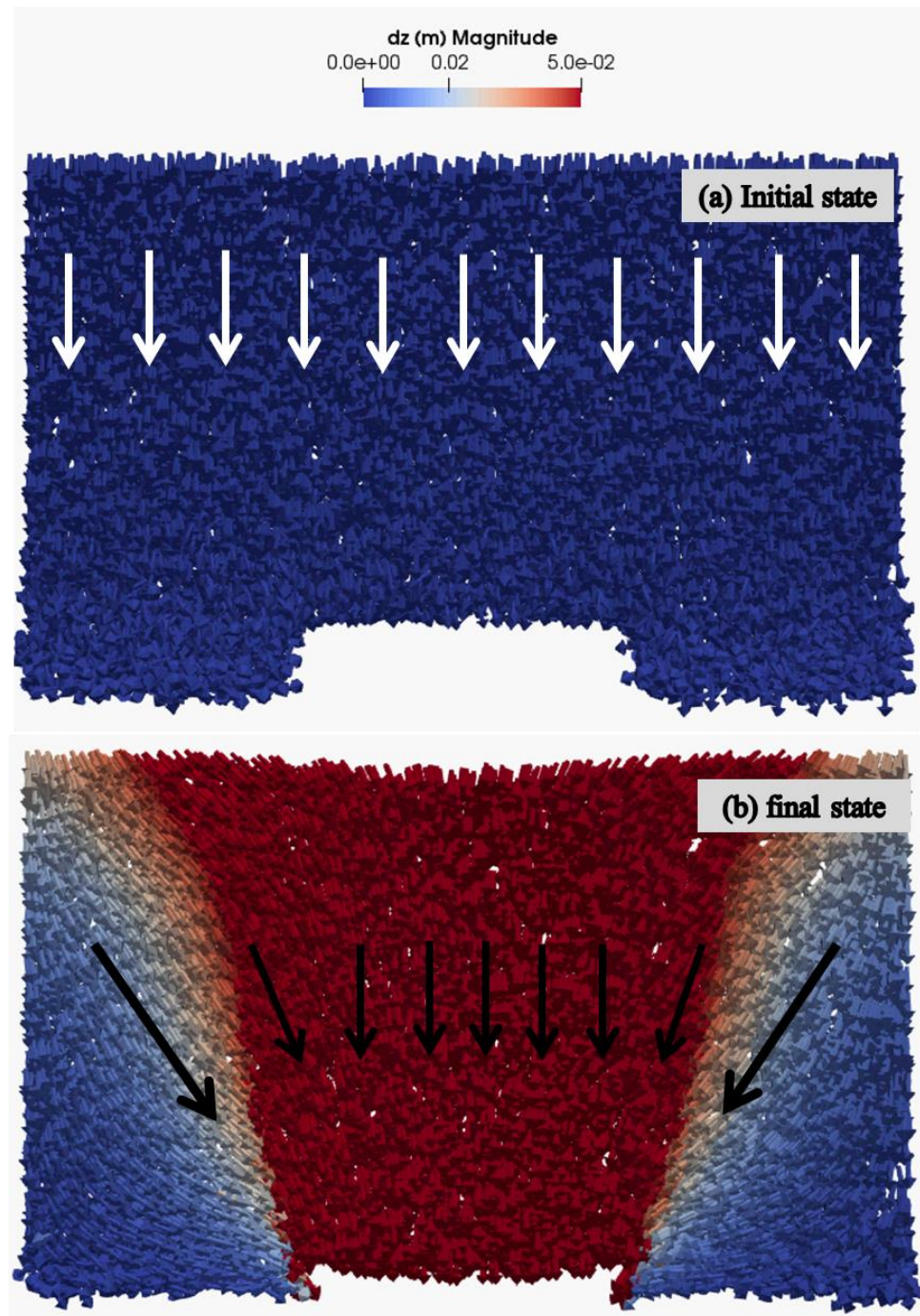


Figure 9.42 Vector diagram of particle movement overlaid on dz color plot

9.3.5 Cavity stability simulations using variable saturation and weight of the water

9.3.5.1 *Using R2 particles with 0.5mm mean size*

To investigate the effect of varying saturation with the sample height, a test case was run having a cavity size of 30mm using *R2* rigid particle type having a mean diameter of 0.5mm. The simulation results on a similar sample and cavity size using a constant degree of saturation showed a stable behavior. However, to study whether the variable saturation imparts a weakening or a strengthening effect, sample saturation was varied linearly from 10% at the top to 90% at the bottom of the sample.

Furthermore, the high saturation means a larger amount of water volume attached to the particles, resulting in a higher weight of the sample. Hence, to incorporate the increased sample weight, the sample was divided into 100 layers in Z-direction. For each layer, the saturation level was assumed to be constant and the corresponding volume of water attached to each particle was calculated. Later, the weight of water attached to each particle was then added to re-calculate the unit weight of the material for that specific layer. Each particle within a layer possessed a unique volume of water due to the varying particle sizes.

Consequently, to have a better comparison, three types of samples were compared.

- i- Sample with uniform saturation & without water weight effect
- ii- Sample with variable saturation & without water weight effect
- iii- Sample with variable saturation & with water weight effect

The particle movement diagram for all three conditions of samples is presented below in Figure 9.43. The color variation depicts the particle dynamics and the red color corresponds to the movement of particles. Similarly, the blue color represents the particles with static conditions.

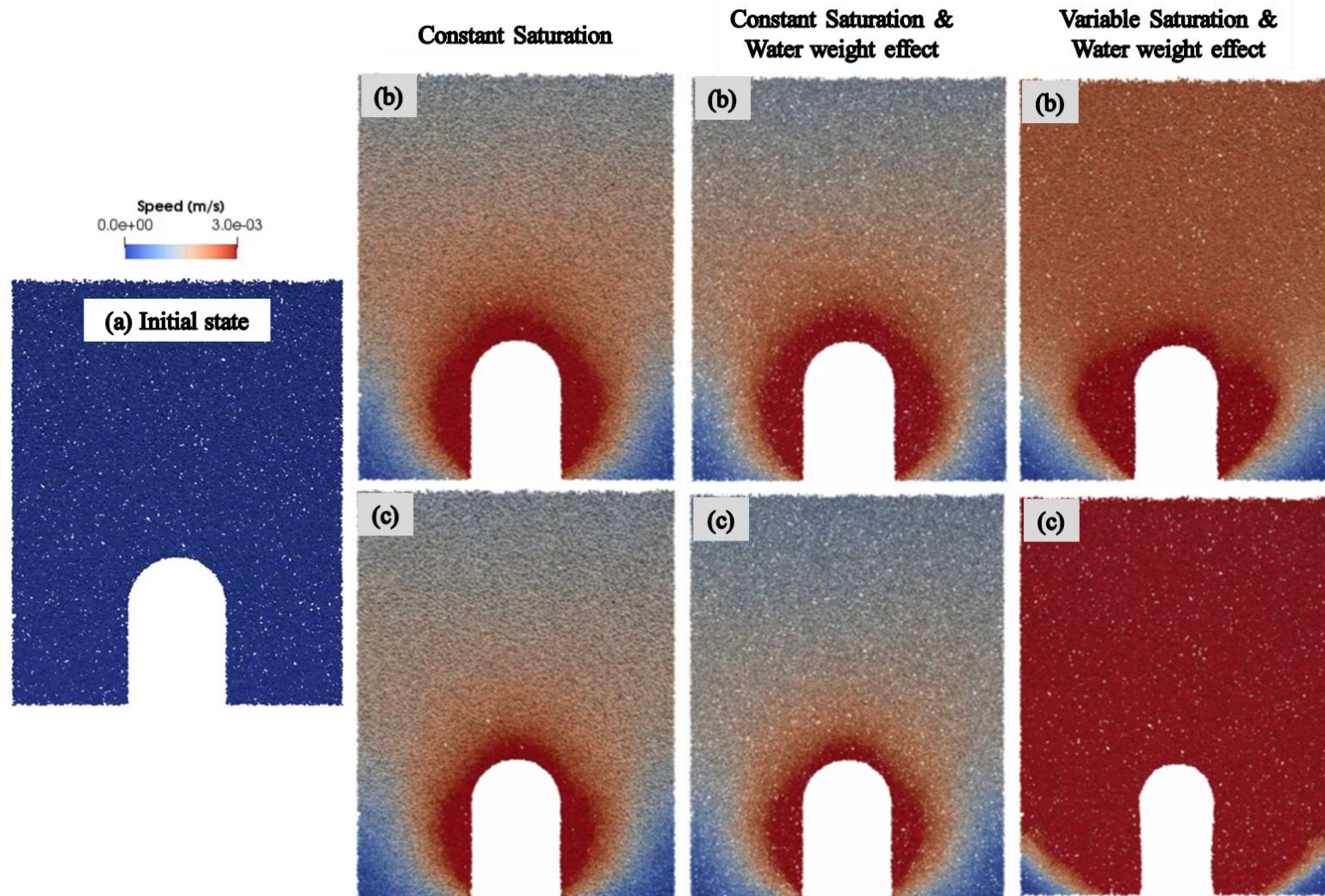


Figure 9.43 Particle movement plots with a cavity size of 30mm x 30mm on R2 particles under three different conditions at (a) start of the simulation, (b) mid of simulations and (c) at the end of the simulation

The cases with a constant degree of saturation throughout the sample and throughout the simulation time showed a matching trend to the case with constant saturation but having increased particle weights due to the incorporation of water weight effect. Both conditions approached a stable sample where the particle movement started to reduce once after it increased initially. However, the case with a variable degree of saturation and taking the weight of water showed a more dynamic response and the sample approached the collapsing condition. The comparison shows that variable saturation along with the water weight effect imparted a more dynamic response compared with the other conditions. Hence, the variable saturation conditions are more critical and need to be selected carefully based upon the particle size and the properties of the material being modeled.

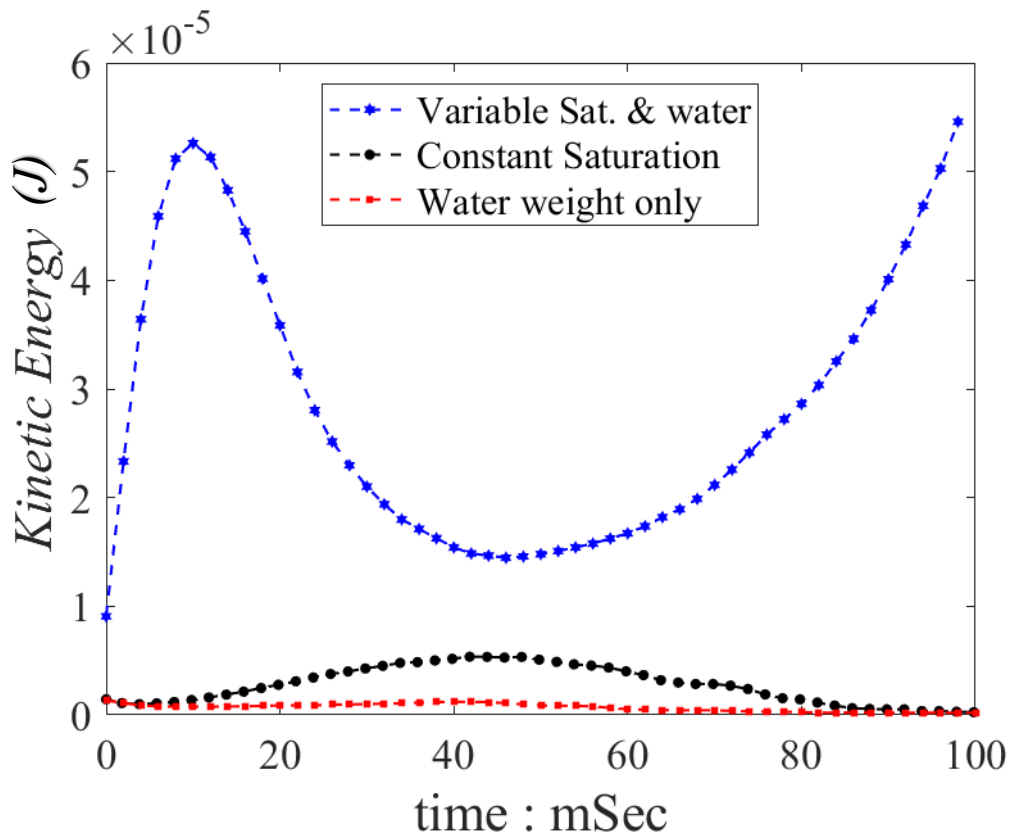


Figure 9.44 Kinetic energy variation for the R2 particle sample with a cavity size of 30mm x 30mm, under different conditions

Collapsing behavior can be more clearly seen in Figure 9.44, wherein the kinetic energy plot is shown. Out of all three samples, the sample with variable

saturation showed the most dynamic behavior. However, the sample with increased particle weight under the constant saturation level showed the least particle movement due to the increased stability caused by the heavier particles.

9.3.5.2 *Using R3 particles with 1.0mm diameter*

The shape effect was further explored with the help of R3 particle, which consisted of a rigid clumped assembly of three spherical particles. Out of the three, two of the particles lied in the same axis, whereas the third particle was situated at a variable angle from -90° to $+90^\circ$ around the central particle. The size of both side particles was kept the same and the diameter for the central and size particles was changed constantly. However, the diameters of the constituent particles were changed in such a way that the edge particles always touched the 1mm diameter circle in all cases, originating from the center of the central particle. The shape of the R3 particle is more clearly shown in chapter-8 previously.

Simulations were performed under the variable saturation conditions, having a cavity size of 30mm and 40mm. The particle movement plot for the R3 particles having a mean particle size of 1.0mm and a cavity of 40mm is shown in Figure 9.45. Under the variable degree of saturation, the sample with a 40mm cavity could not withstand and showed a collapsing behavior.

In the case of the simulation with a 30mm cavity size, the sample started to collapse initially, as shown in Figure 9.46. However, after a certain dilation, the particles rearranged and were manage to form a strong arching around the cavity (Figure 9.46). Eventually, the cavity was stabilized and even after a long simulation time, the sample did not show any collapsing behavior and the movement of the particles was ceased.

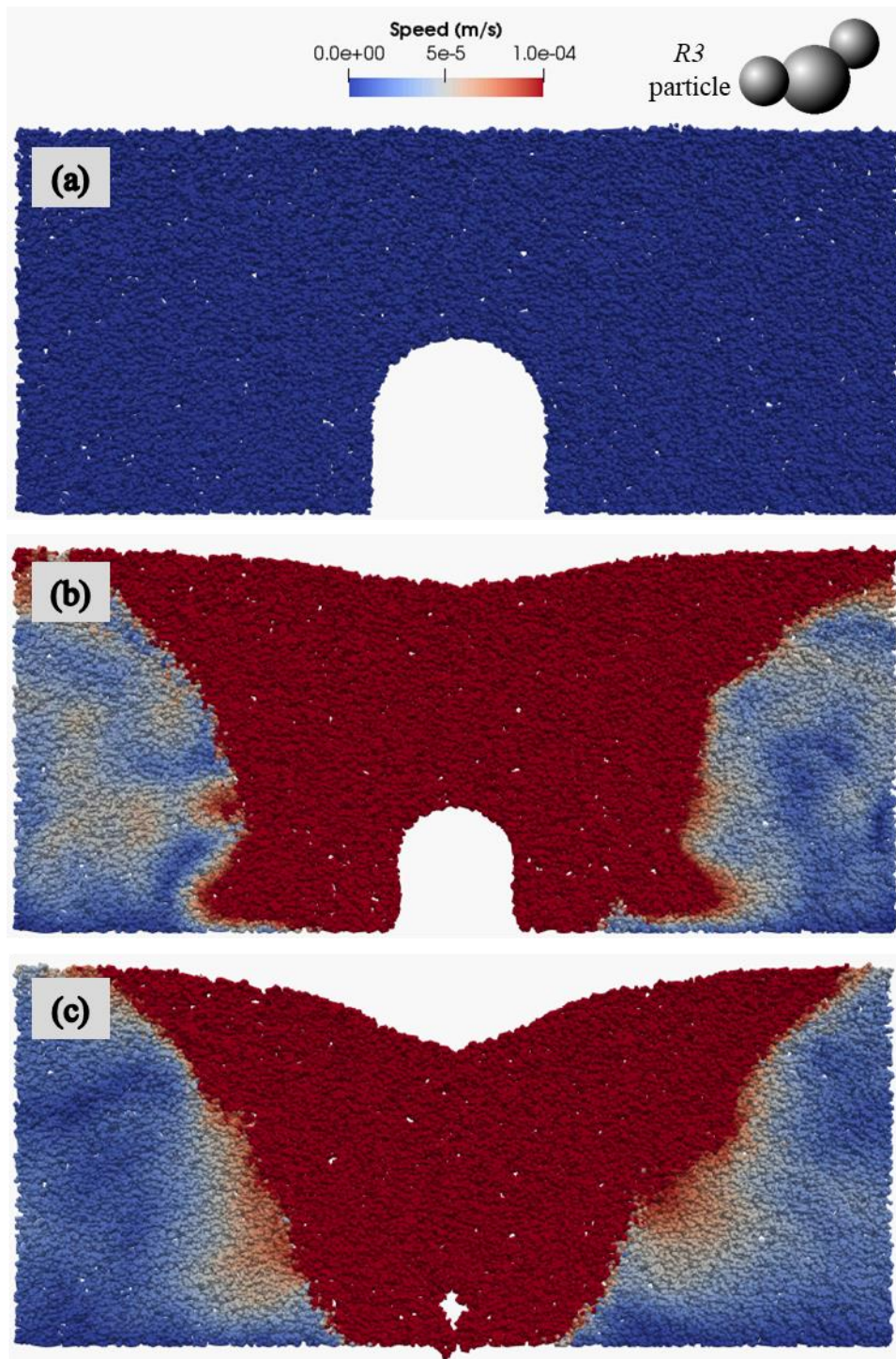


Figure 9.45 Particle movement plot for R3 particle sample having a cavity of 40mm x 40mm at the (a) start, (b) mid and the (c) end of the simulation

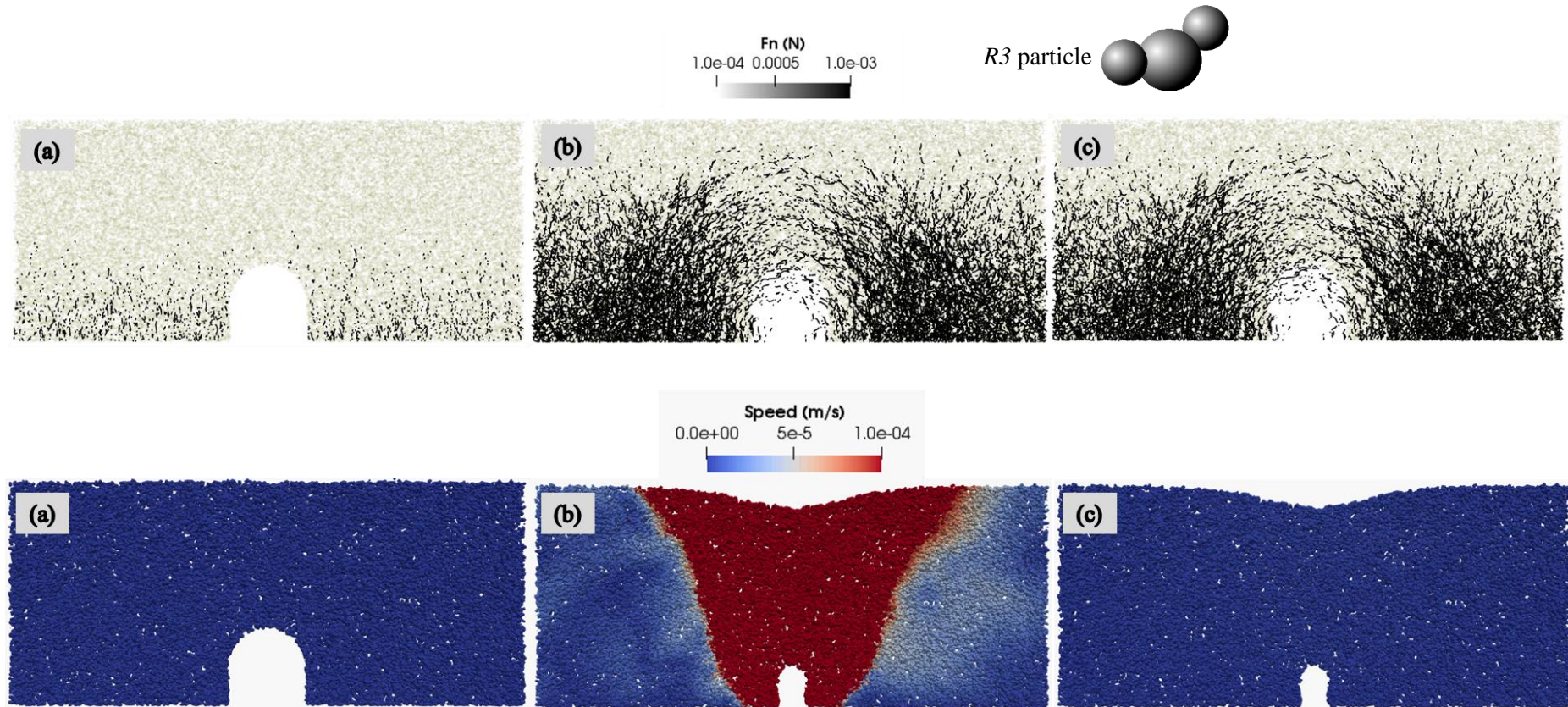


Figure 9.46 Strong force and particle movement plot for R3 particle sample with a cavity size of 30mm x 30mm under variable saturation condition at (a) the start, (b) mid and (c) end of the simulation

It is worth noting that the R2 case with a mean particle size of 0.5mm, did not show a stabilizing behavior under the influence of variable saturation. However, with changing the particle shape and forming a more angular particle shape with R3 type, even the mean particle size of 1.0mm showed a stabilized condition under the variable saturation scenario.

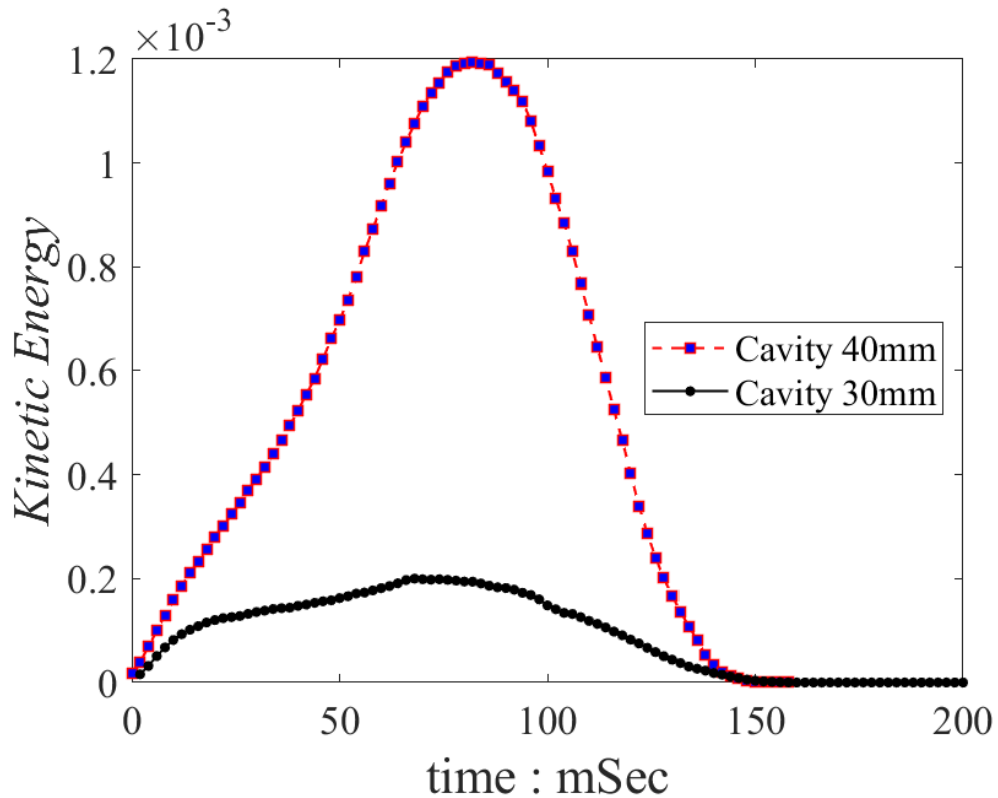


Figure 9.47 Kinetic energy plot for the R3 particles having different cavity sizes, under varying degree of saturation

Figure 9.47 shows the kinetic energy plot for the R3 particle samples having two different cavity sizes. The larger cavity (40mm) showed a total collapsing behavior under the variable degree of saturation condition. However, the smaller cavity (30mm) showed an initial particle movement, which later stabilized to result in a static behavior. As seen from the figure above, the kinetic energy for the larger cavity case is much larger compared to the other case. However, both cases eventually resulted in a static behavior with a very minimal kinetic energy in the system. This might create confusion that both samples were eventually stabilized, which is not true. The sample with a 40mm cavity size showed an instant collapsing

behavior which led to the sample to fall down and touch the base of the boundary. The particle movement was halted as soon as they touched the base surface and eventually resulted in a decreased energy of the system. However, the sample had already failed/collapsed before the system came to a static nature.

9.4 Summary

In short, the current chapter described the testing and simulations for the cavity stability analyses. The similarities and differences between both approaches were discussed. The model tests were performed using several types of glass beads, including spherical and non-spherical. Similarly, the DEM based numerical simulations were performed using spherical and non-spherical particles with different sizes. The Capillary force model developed in this study and explained in the earlier chapter was utilized to perform all numerical simulations. The results of both experimental and numerical approaches for glass beads showed the overall cavity behavior using prescribed materials is matching the general trend of soils and the stability criteria of the cavities being utilized currently in the field matched with the numerical results of the cavity stability. Furthermore, the effects of the degree of saturation, density, particle size, specimen size, and surface roughness were discussed combinedly in experimental and numerical analyses. Arching around cavity through strong force distribution and contact fabric distribution was discussed numerically and, in the end, the authenticity of using a new capillary force model was established.

CHAPTER 10: EXPERIMENTAL AND NUMERICAL ANALYSES OF CAVITY SURFACE LOADING

This chapter includes the results of surface loading performed above a stabilized cavity in the cavity model test apparatus using several types of glass beads. Equivalent DEM based numerical simulations were performed using the suction-tension model and the inter-particle response was investigated and the macroscopic response was compared with model test results. For the surface loading tests, several variables like loading speed, particle shape, surface loading area, etc. were investigated as well.

10.1 Experimental analyses of cavity surface loading

The initial step for the cavity surface loading test included the formation of a cavity, as discussed in the earlier chapter. Once a stable cavity is formed, the sample was then used to perform surface loading tests, with the help of a triaxial loading apparatus as shown in Figure 8.6 of the previous chapter. The loading setup and other control parameters are discussed in detail in the earlier chapters.

Several types of glass beads were utilized in the cavity surface loading tests, including smooth spherical glass beads, rough spherical glass beads, clumped particles, etc. The test cases with spherical glass beads are discussed first in this section.

10.1.1 Effect of surface roughness

To measure the effect of surface smoothness on the surface loading, initially, a sample without any cavity, having initial water level at 10cm to produce both partially saturated and fully saturated regions with spherical glass beads having a mean diameter of 0.5mm, was tested for both smooth and rough particle types. Figure 10.1 shows the difference between the load-settlement graph for both.

The peak strength for both samples without the presence of any cavity showed almost similar peak strain value (ϵ_{v_peak}). However, the peak strength differed slightly with rough particles being on the higher side. Overall, due to very high sphericity and

less particle interlocking, the effect of only surface roughness does not impart any significant effect on the strength characteristics. Similar behavior was noticed for the case with the presence of a base cavity for both rough and smooth glass beads having a mean diameter of 0.5mm, as shown in Figure 10.3.

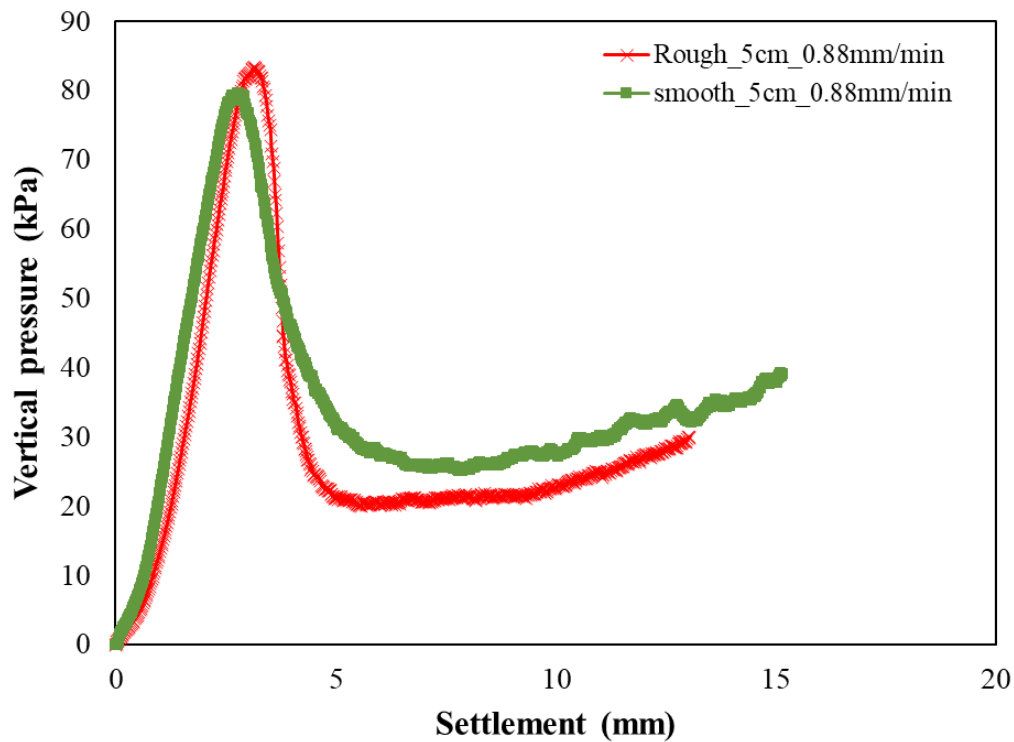


Figure 10.1 Load-settlement plot for smooth and rough surface texture with spherical glass beads having a mean diameter of 0.5mm, without any cavity

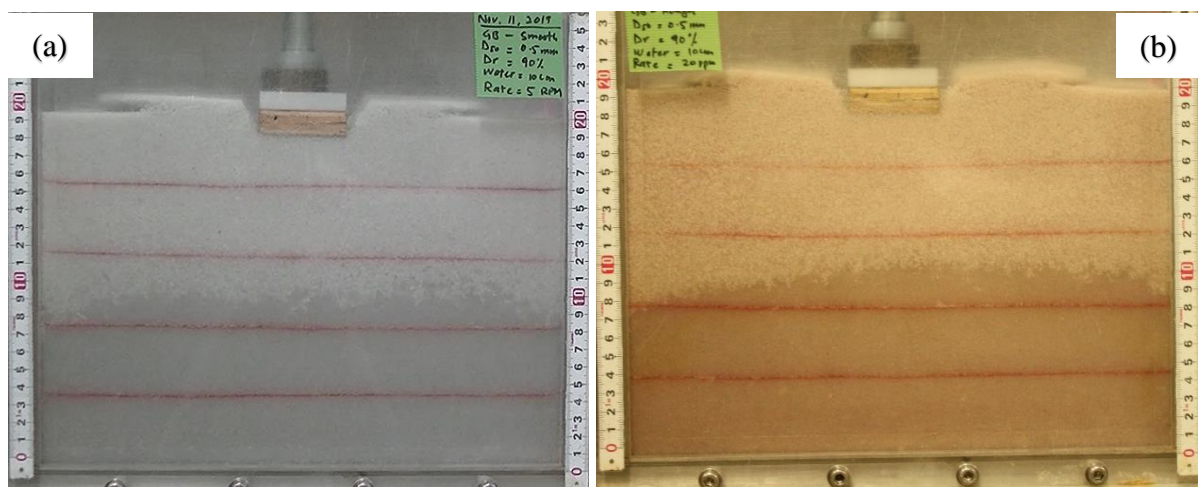


Figure 10.2 Final state of samples after surface loading using 5cm wide plate for (a) smooth and (b) rough glass beads having a mean diameter of 0.5mm

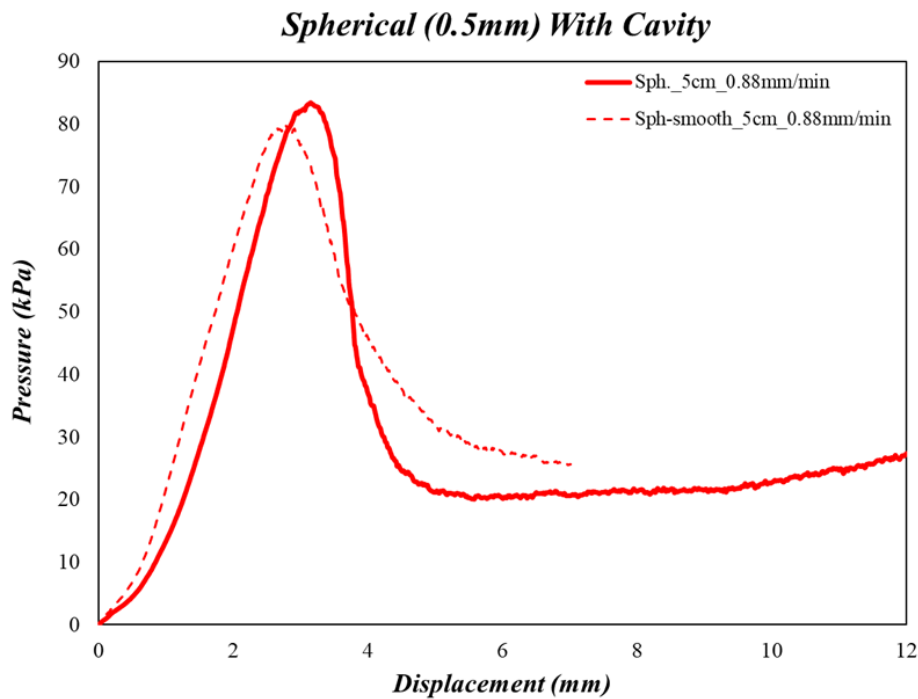


Figure 10.3 Load-settlement plot for smooth and rough surface texture with spherical glass beads having a mean diameter of 0.5mm, with a base cavity

From Figure 10.2 and Figure 10.3, the difference between the smooth and the rough particles can be seen visually. It can be seen that after the surface loading using a plate of 5cm width, the material just around the plate has bulged up in both cases. The color sand line placed at regular intervals did not show any variation in their elevation, concluding that the applied load did not reach even up to the level of first colored layer and all load was transferred in the very top portion of the sample. Another reason could be associated with the development of pore pressure in the sample, that did not allow any quick drainage of water under the given loading rates and the majority of the particles remained intact in their original position except the top portion where the pore pressure was dissipated from the top free surface.

10.1.2 Effect of surface loading rate on cavity stability using spherical particles

The rate of loading is of concern for several researcher during the element testing on various granular and cohesive materials e.g. Enomoto et al, (2016); Hayano et al. (2001); Kongsukprasrt & Tatsuoka (2005); Tatsuoka et al. (2008); Tatsuoka et al. (2002)

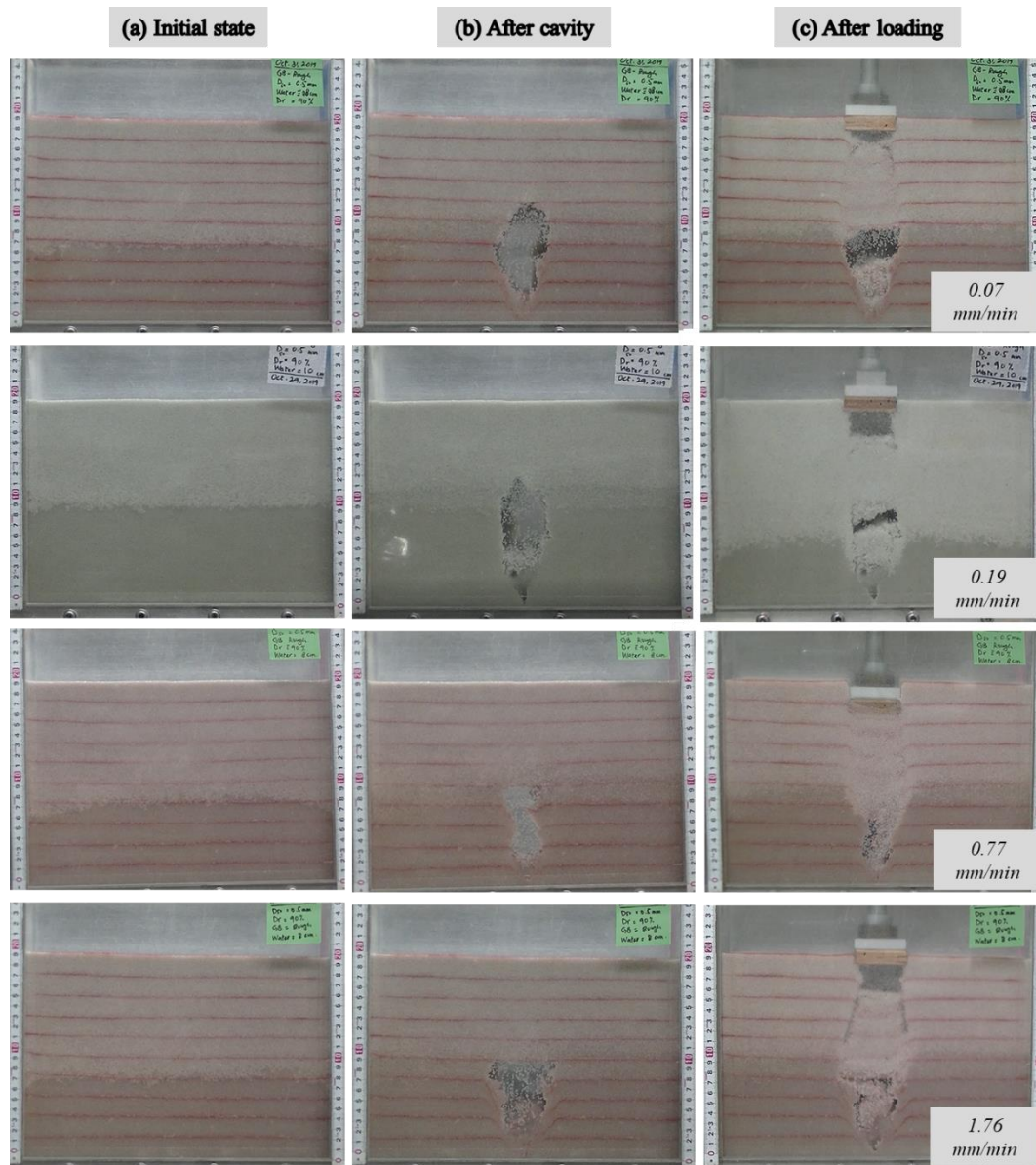
and many other. Similarly, Ohara, Kuwano, & Sera (2019) performed cavity loading tests using different loading rates for silica sand samples.

To evaluate the loading rate effect on the glass beads, several loading rates were applied using a surface plate of a certain width using spherical and non-spherical types of glass beads. For each case, similar sample density and the position of initial water level was adopted. The presence of water level divided the sample into two regions of unsaturated and fully saturated. However, once the cavity was formed, the water was freely drained through the bottom slit, making the sample to drain under gravity and hence resulting in a very thin region of full saturation near the bottom of the sample.

The experimental pictures for the cavity formation and surface loading tests are shown in Figure 10.4, for four different surface loading rates at three different conditions for the spherical glass beads ($D_{50} = 0.5\text{mm}$) under the rough texture. These conditions consisted of the initial condition after achieving a certain water level, after the formation of a stable cavity and lastly after the surface loading tests, showing the collapsed cavity. The loading rate against the settlement of the cavity surface for the spherical glass beads with a mean diameter of 0.5mm is shown below in Figure 10.5

The glass beads with a mean diameter of 0.5mm showed a rate-dependent behavior. The least loading rate resulted in the maximum normal stress. Whereas the fastest loading rate yielded the least strength, for a given plate width for surface loading. This trend was opposite to the normally observed trend of the geomaterials where the higher loading rates result in higher peak strengths and vice versa. Although the residual strengths for all loading rates are similar, showing a similar force required to develop a shear band due to the similar material and density.

The probable reason for such abnormal behavior is still to be discovered. However, one of the factors for such behavior could be the differing shapes of the cavities for each test. Different shapes can impart a strong effect on the stability characteristics of the cavity, as explained in the earlier chapter, using both experimental and numerical results. A taller cavity would have a lesser soil cover, resulting in the intersection of inter-particle strong forces with the sample surface, resulting in a lesser strength against surface loading. Similarly, a wider cavity would experience high vertical stresses on the ceiling region and might result in a similar way. However, a cavity with a balance between height and width could demonstrate a very strong behavior against the surface loading.



noticed in DEM simulations as well, the particle at the shear band for spherical particles just slide with each other and could not transfer significant forces across the shearing band.

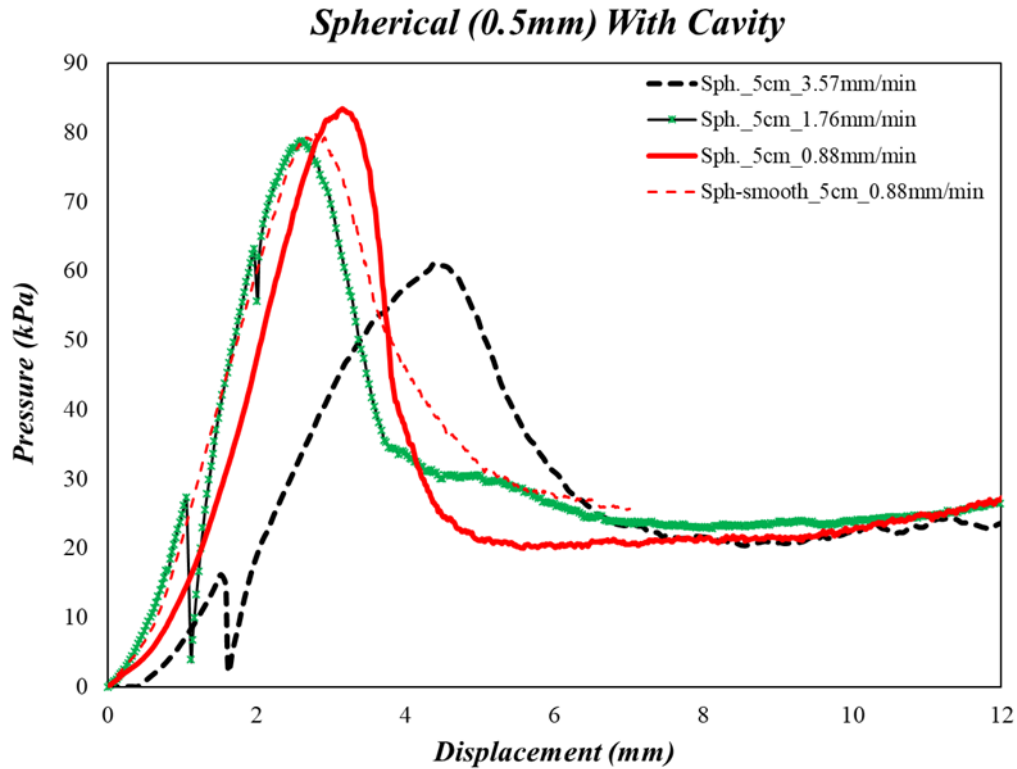


Figure 10.5 Load-settlement curves for spherical glass beads with a mean diameter of 0.5mm, for various surface plate loading rates

10.1.3 Effect of surface loading rate on cavity stability using deformed particles

Sample constituting the deformed glass beads with a mean particle size of 1.0mm was used to compare the effect of particle shape. The shape of the deformed particles as shown in Figure 8.5, represents a higher angularity of the particles compared with the spherical particles with equivalent size. Furthermore, the minimum void ratio for the deformed sample was found to be much smaller compared with the spherical particles of equivalent size (Table 8.3). The deformed particles yielded much denser sample due to the fact that they can adjust in a much better packing compared to the spherical particles due to more elongated shape and lesser presence of angular corners.

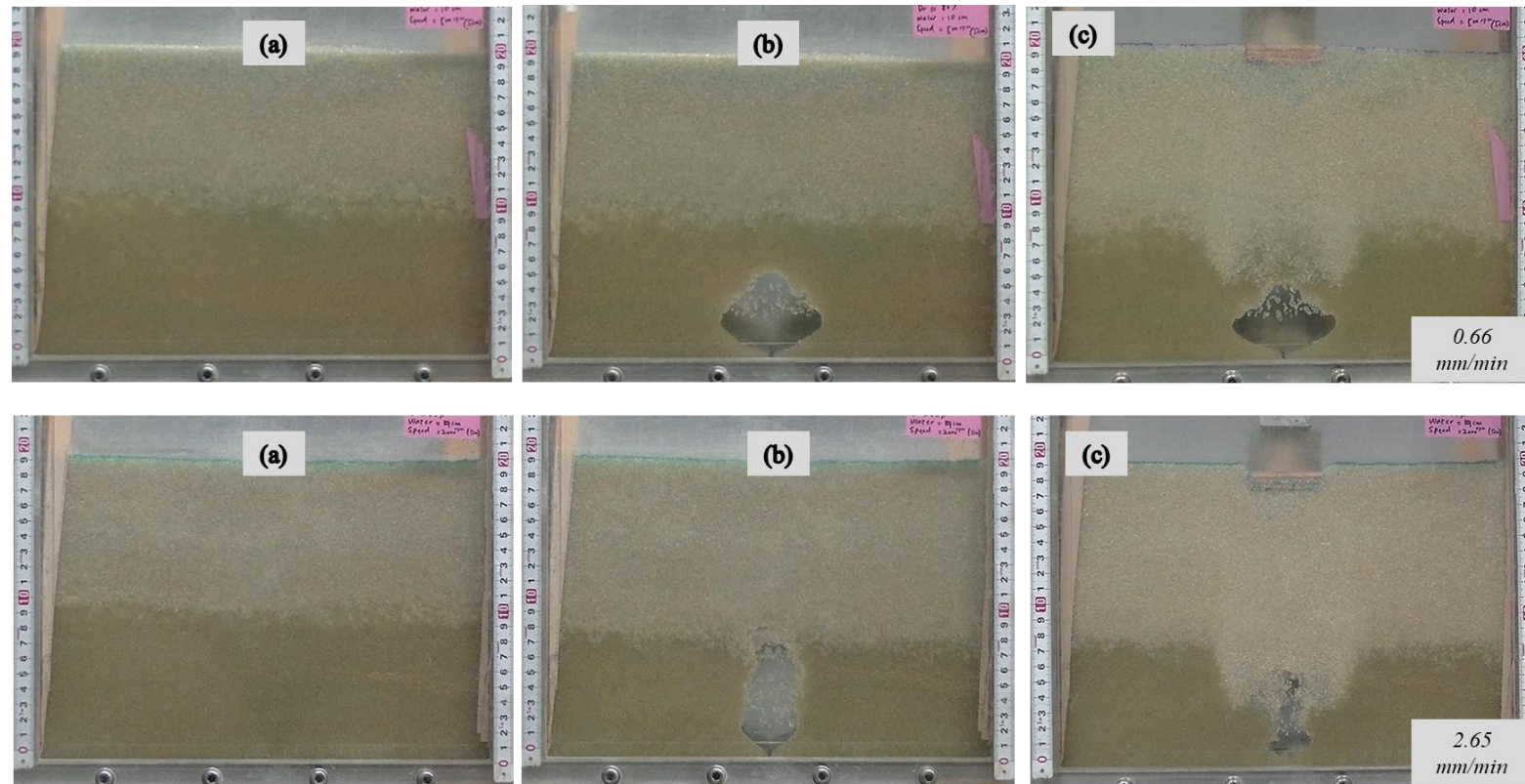


Figure 10.6 Cavity surface loading tests for different loading rates, shown at (a) initial condition, (b) after cavity formation and (c) after surface loading, for rough deformed glass beads with mean size of 1.0mm and 85% relative density

The cavity surface loading test was then performed on the sample with deformed particles under the similar saturation conditions to that of other glass beads samples. Figure 10.6 shows the cavity surface loading tests for the deformed particles having a mean size of 1.0mm under rough conditions. The tests are performed for two types of loading rates using a 5cm wide wooden surface plate.

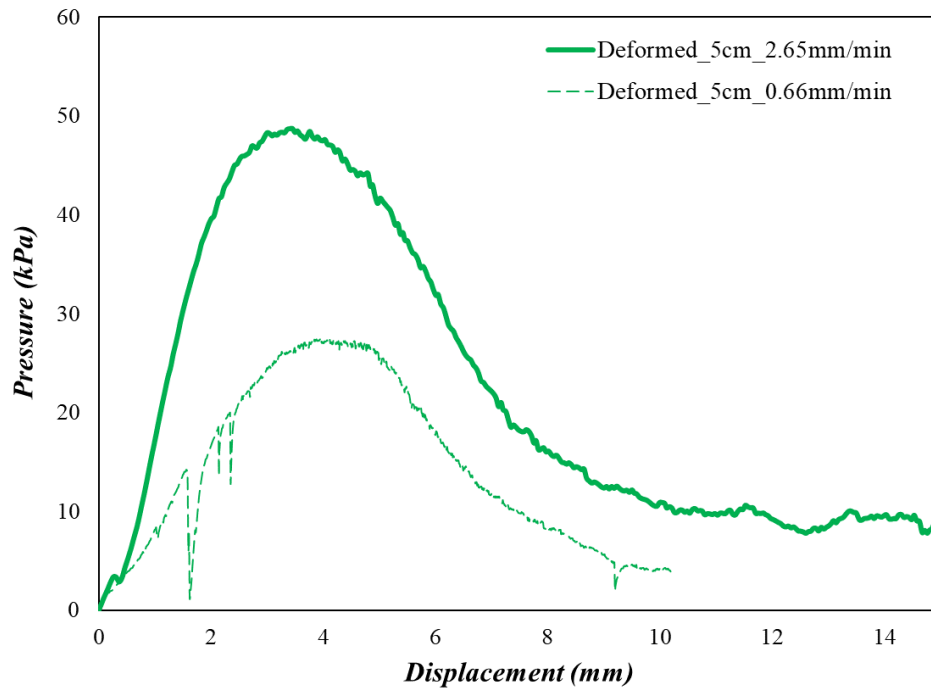


Figure 10.7 Cavity surface loading test results on rough deformed particle samples with different surface loading rate

Figure 10.7 compares the loading rate difference with the sample strength against surface loading under a fixed width of the loading plate. Similar to the earlier cases, the deformed particles also demonstrated the loading rate effect and the faster loading rate produced higher peaks of vertical stress. However, the magnitude of the peak stress was not much contrasting compared to the spherical particles. The reason being that both particles possessed very smooth. Although the aspect ratio for the deformed particles was relatively higher compared to the spherical, the size of the particles was also a variable in comparing the strengths. For the case of spherical particles with similar particle size, the condition of a stable cavity was not fulfilled, and the sample collapsed.

10.1.4 Effect of surface loading rate on cavity stability using clumped particles

As the spherical particles showed rate dependency on the peak strength under cavity surface loading tests, clumped glass beads particles were introduced that resemble more with the actual sands. The mean diameter of the clumped particles was also similar to the spherical glass beads and measured to be approximately 0.6mm. Each clumped particle consisted of adjoining and fused spherical particles, varying in numbers and sizes to form a single clumped particle. The shape of the clumped particle is already described in Chapter 8.

Similar to the spherical glass beads, the clumped particles were also tested with a similar relative density of 90%, water level at 10cm and different surface loading rates. The experimental stages for the surface loading tests at different stages of the test are shown in Figure 10.8below.

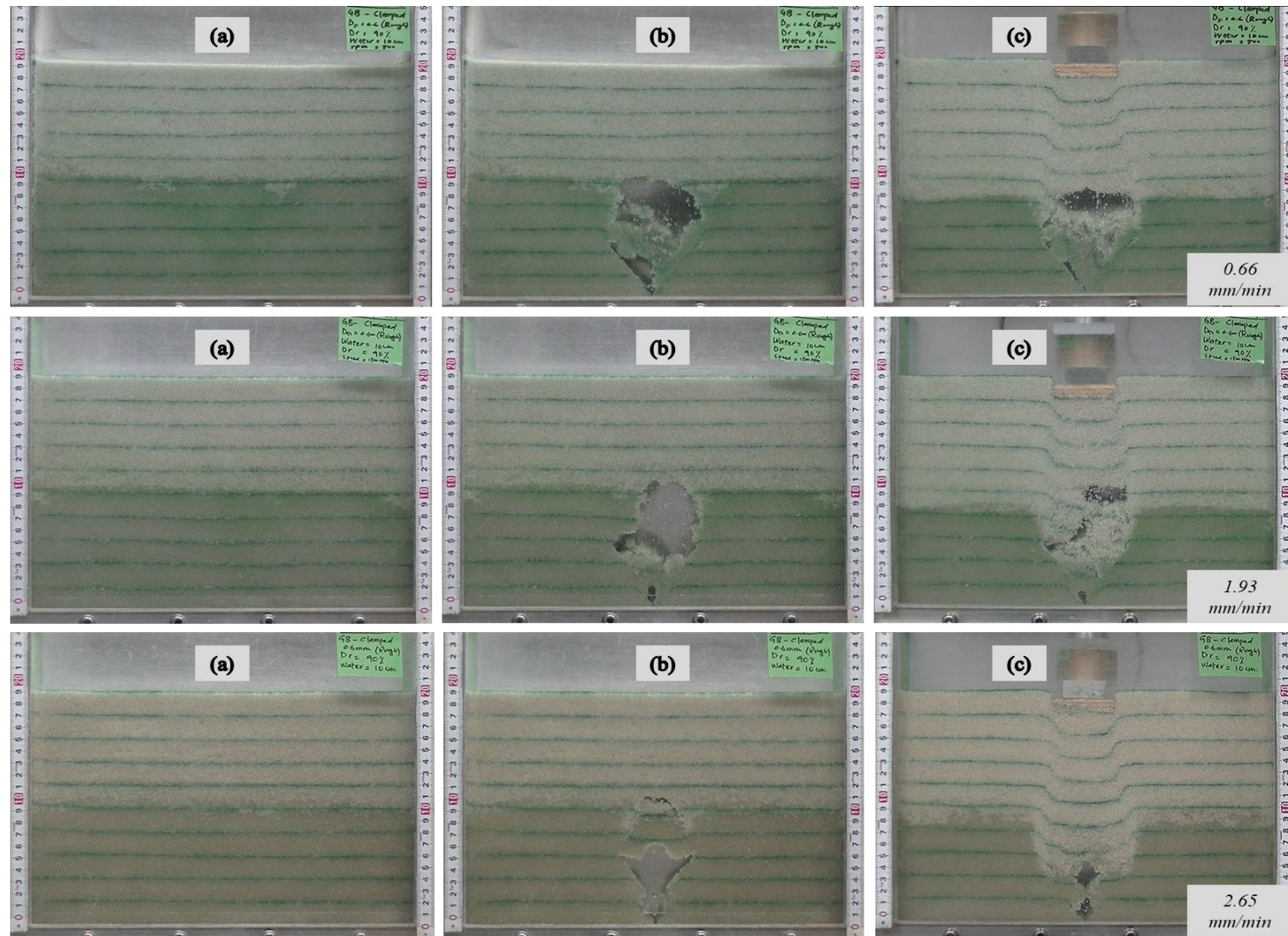


Figure 10.8 Cavity surface loading tests for different loading rates, shown at (a) initial condition, (b) after cavity formation and (c) after surface loading, for clumped glass beads with mean size of 0.6mm and 90% relative density

For clumped glass beads sample, when different loading rates were applied under a mixed sample condition of unsaturated and fully saturated, the sample resulted in rate-dependent behavior, as shown in Figure 10.9.

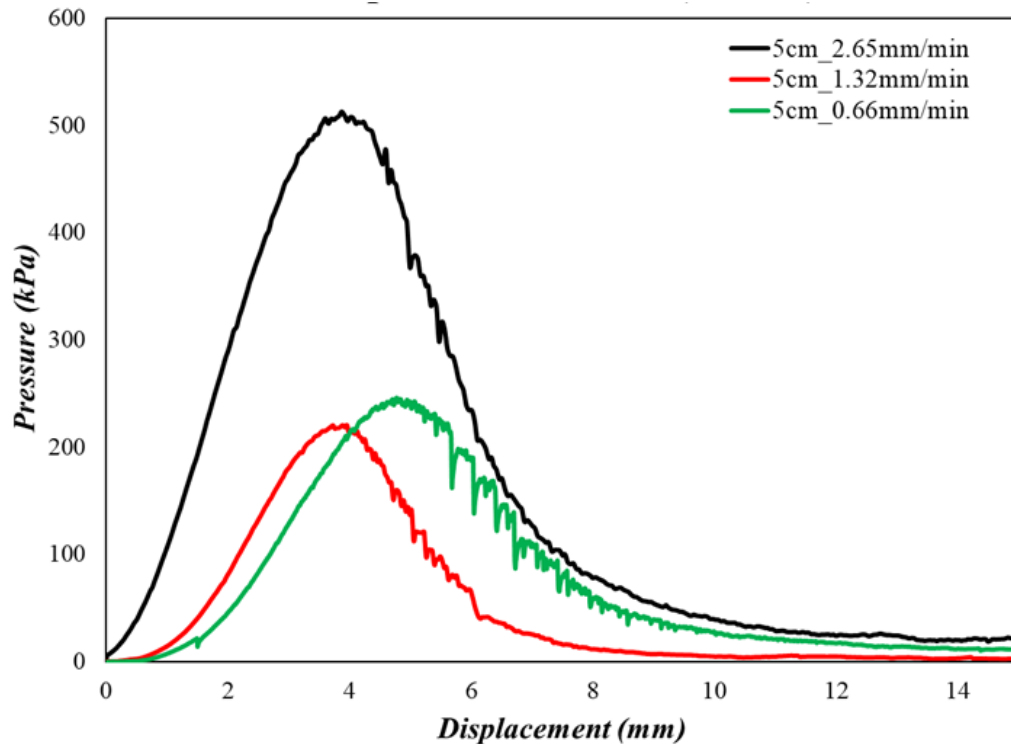


Figure 10.9 Cavity surface loading test results on clumped particle samples with varying surface loading rate

The time dependency of the sample is similar to the spherical glass beads. However, the trend is opposite as seen in the earlier cases. In the case of clumped particles, a higher surface loading rate resulted in higher peak strengths and vice versa. The trend shown by clumped particles resembled the general trend of loading rate dependency using natural soils. The samples showed a post-peak/residual strength approaching zero, as the cavity surface almost collapsed, thus taking virtually no load.

Due to the limitation of equipment, the loading rates for spherical and clumped particle samples could not be maintained alike. However, the general trend can still yield an interesting comparison. The relative magnitudes of the load-settlement curves for all three materials, i.e. spherical, deformed and clumped particles are shown in Figure 10.10.

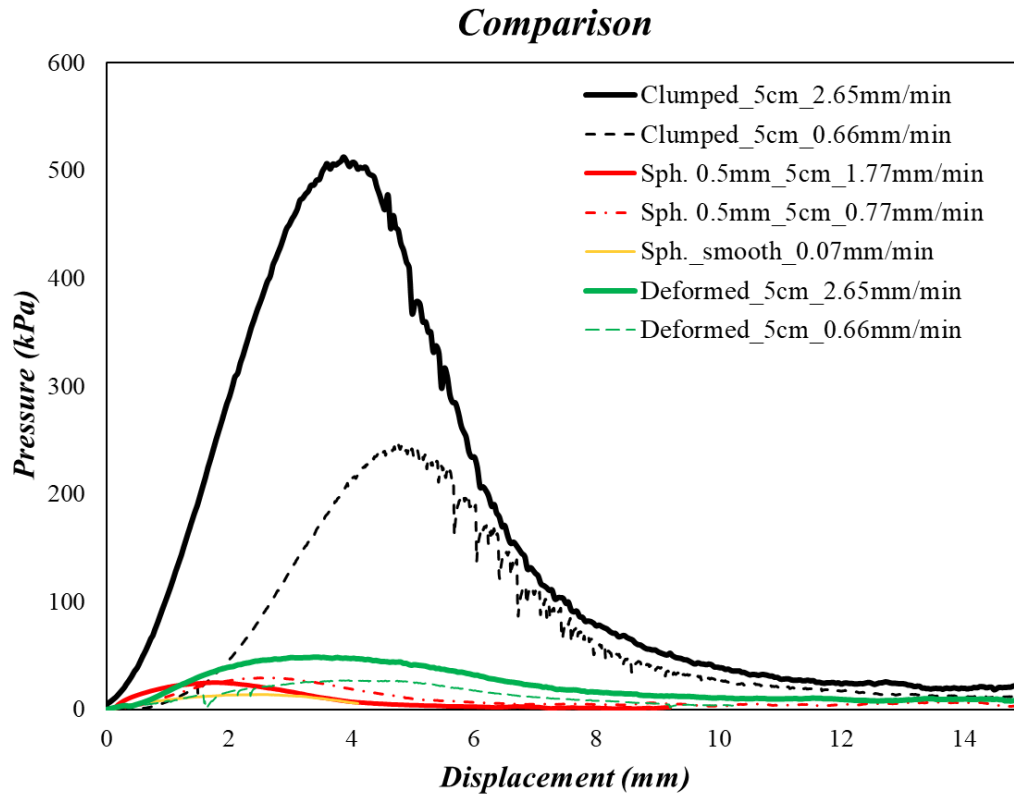


Figure 10.10 comparison of resistance to surface loading above cavity using spherical and clumped type particles

The comparison between clumped, deformed and spherical glass beads samples showed a distinctive behavior for each material in terms of the magnitude of peak strength. The clumped particles showed much higher peaks compared to equivalent shearing rates of spherical glass beads. Even the faster loading rates of spherical particle samples could not match with the high strength of the clumped particle samples having the least loading rate and the peak strength was measured to be around $1/10^{\text{th}}$ of the clumped particle sample with highest surface loading rate. Such behavior is evidence that the particle shape can play a vital role in establishing the stability of any ground under cavity conditions.

Further to that, the comparison of the deformed and the spherical particles does not show a drastic difference between the peak strengths, though the deformed particles showed relatively stronger behavior compared to the spherical samples due to their higher aspect ratio and better interlocking. However, the small difference can be attributed to the ability of the deformed particles to slide easily against each other without forming a

strong connection with the neighbors due to a lack of sharp edges. Furthermore, the size of the deformed glass bead particles was larger than the spherical glass beads. As discussed earlier, the size affects significantly the stability of a cavity. Hence, the ability of a deformed shaped glass bead particle sample to form a stable cavity is sufficient to justify the differing behavior with the spherical particles. Spherical particles having a mean diameter of approaching 1.0mm could not form a stable cavity under similar saturation conditions.

Overall, a clear difference of sample strength against the cavity surface loading with the particle shape is seen through the above-presented results. Higher the angularity of the particles, the higher would be the stability of the cavity and the higher the resistance against surface loading.

10.1.5 Effect of plate width for the surface loading

The nominal size of the cavity formed in the model tests ranged from 3cm to 7cm for the spherical and the clumped particles. However, initially, the plate size for the surface loading was selected as 5cm only. The size of the cavity was approximately equal to the loading width, though there are chances in the practical applications that a much thinner or thicker loading area can exist compared to the width of the cavity, in case the cavity existed below a highway/road. Hence, in order to check whether or not the surface loading area compared to the width of the cavity imparts any significant effect, three different widths of the surface loading plate were used, which are shown in Chapter 8 in detail. The plates were made up of plywood sheets, hard enough to transfer the applied load to the sample in a rigid manner, without being bent/cracked.

A comparison of the 10cm plate width with different loading rates for the case of clumped particles having a mean size of 0.6mm, in Figure 10.11 below. For the varying plate loading rates, the sample did not show any significant difference in the peak and residual strengths. The reason can be associated with the size of the plate compared with the cavity width. The plate size of 10cm was observed to be larger than all cavity sizes formed in the cavity tests. The failure pattern was observed to be almost vertical, with a very small inclination. Also, the failure plane developed right under the edges of the plates in all cases. Consequently, the majority of the load taken was under the edges of

the plates that did not encounter any cavity underneath. Consequently, the loading rate did not affect significantly in that case.

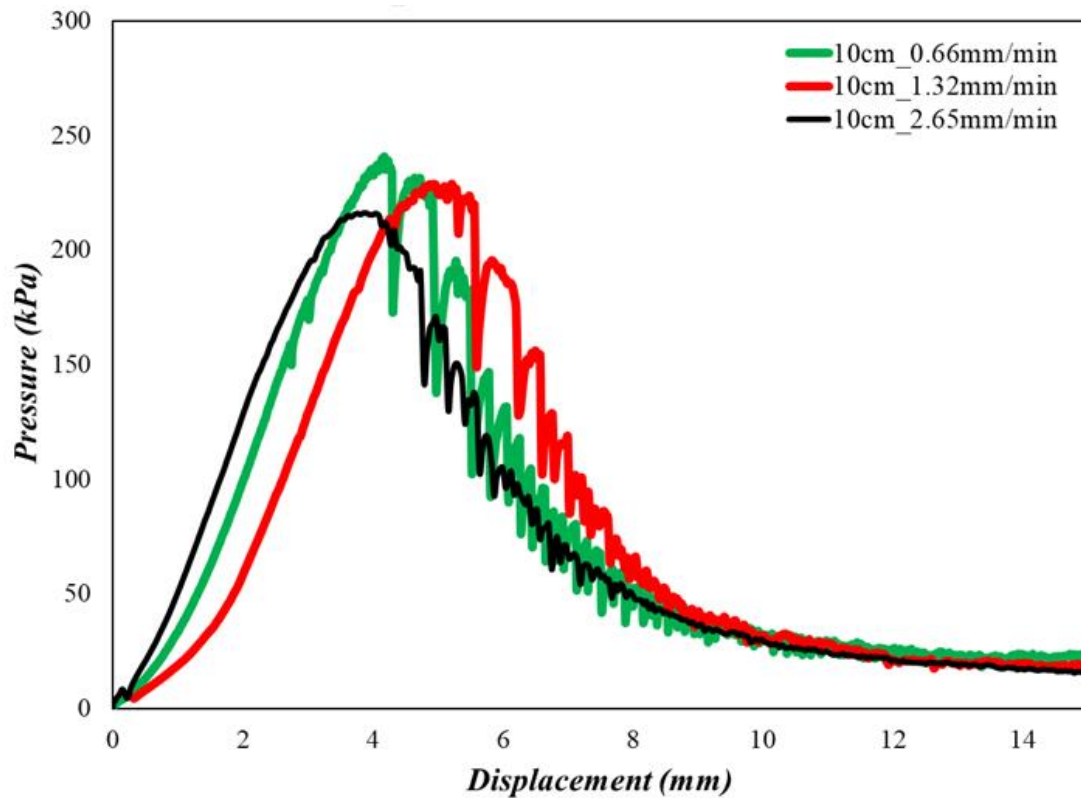


Figure 10.11 Cavity loading rate comparison with a plate with of 10cm on clumped particle sample

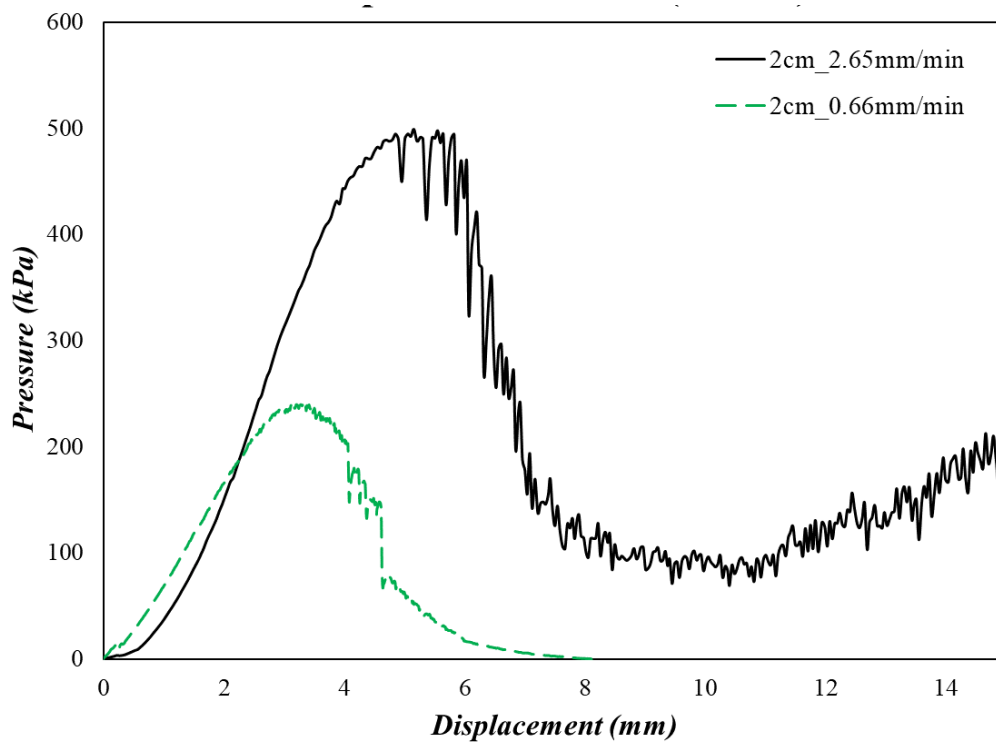


Figure 10.12 Cavity loading rate comparison with a plate with of 2cm on clumped particle sample

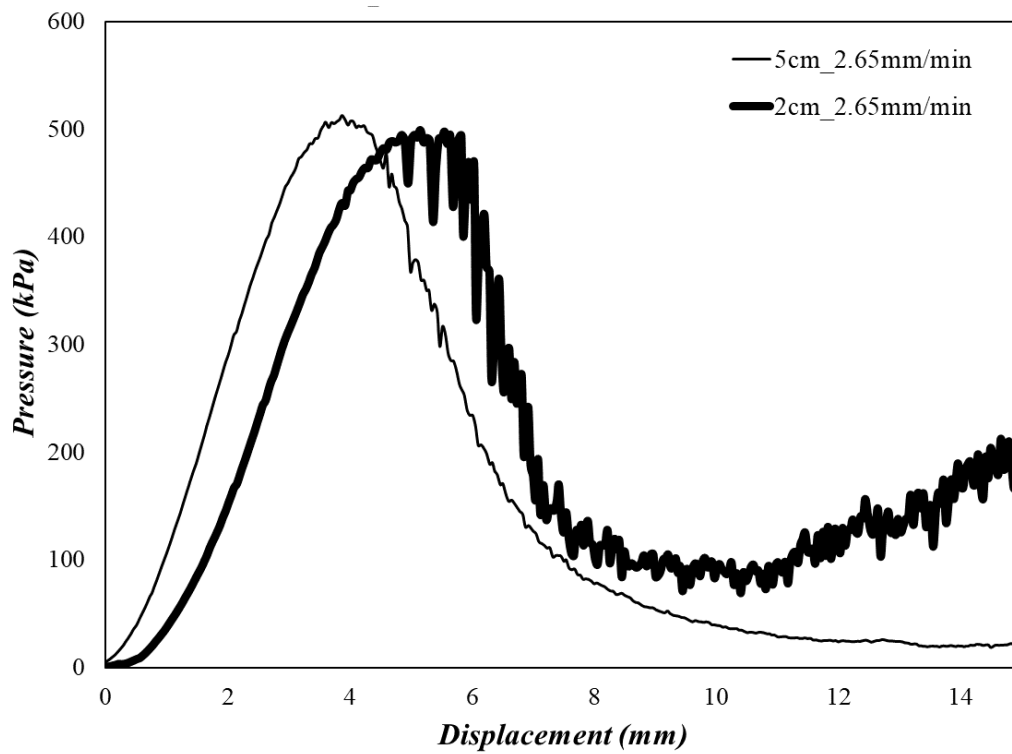


Figure 10.13 Comparison of plate width effect on cavity strength on clumped particle sample using 5cm and 2cm wide plates at the highest loading rate

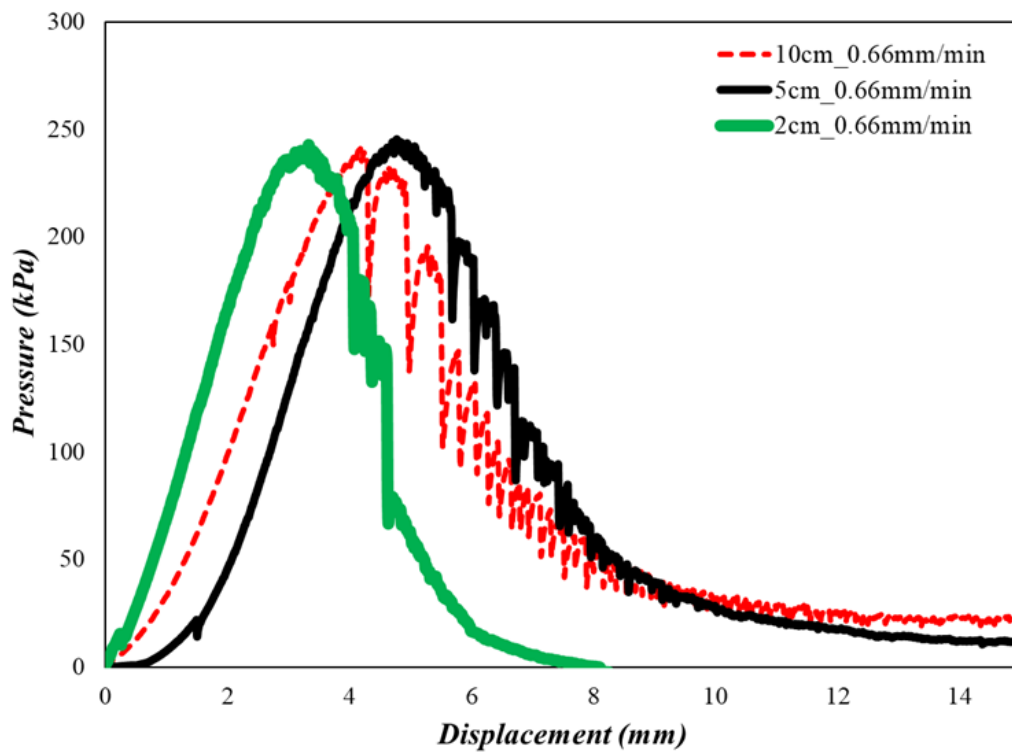


Figure 10. 14 Comparison of plate width effect on cavity strength on clumped particle sample at the lowest loading rate

Using a plate width of 2cm (Figure 10.12) for the clumped particle samples, there was a clear difference of loading rates on the peak strength, as noticed in the case of 5cm width samples, shown in Figure 10.9. However, while comparing the different plate widths for similar loading rates, the peak strength did not show any prominent difference, as seen in Figure 10.13 and Figure 10. 14. Hence, it was concluded that the surface loading area does not have any significant effect on the cavity stability, provided if the stresses are kept the same for different surface areas. In terms of the total load scenario, it is definite that a larger loading area can take much larger loads.

10.2 Model surface loading tests without cavity

In all cases presented above, the control on the shape of the cavity was very difficult and each time a different cavity shape was formed. An effort was made to maintain a similar cavity height for all cases. However, the width of the cavity and the overall cavity area differed slightly in each case. In order to eliminate the effect of cavity shape and size on the peak strength characteristics, and to evaluate the loading rate dependency, tests were performed on the clumped particles without any presence of a cavity.

However, even in the absence of the cavity, the peak strength and its dependency on loading rates is connected to several factors like full saturation or partially saturation or the dry case. Hence, the following types of conditions were utilized for the tests without the presence of a cavity.

- i- Presence of both fully and partially saturated portions
- ii- Dry sample
- iii- Fully saturated samples
- iv- Partially saturated sample

Details of each are given below:

10.2.1 Combination of fully saturated and partially saturated sample

In this case, the samples were initially saturated to full and then the water table was lowered to a certain level (10cm in this case). Resultantly, the sample consisted of both fully saturated conditions below 10cm height and partially saturated condition above 10cm height.

As the absence of any significant effect for the width of the loading plate was concluded in the last section, only 5cm plate width was used to evaluate the present condition. Two types of loading rates, i.e. highest and the lowest, were used for a sample consisting of clumped glass beads with a relative density of 90%.

Figure 10.15 shows the loading rate comparison for the samples having both saturated and unsaturated regions with a top-loading plate width of 5cm. The faster loading rate yielding a much higher peak strength compared to the slower rate. The main reason for this behavior can be attributed to the development of pore pressure under the loading. Since there was no drainage condition at the base of the sample, for high loading rates the pore pressure could not dissipate quick enough to let particles settle and resulted in higher peak strengths. However, for a slower rate, the dissipation of pore pressure was much higher compared to the earlier cases, resulting in lesser peak strength.

The stick and slip (Nasuno et al., 1998) was observed once the sample attained the peak conditions. After the peak strength, the shear band initiates, and the particles experience a strong effect of stick-slip. The magnitude of this stick-slip largely depends upon the surface characteristics and is more for the cases of glass beads.

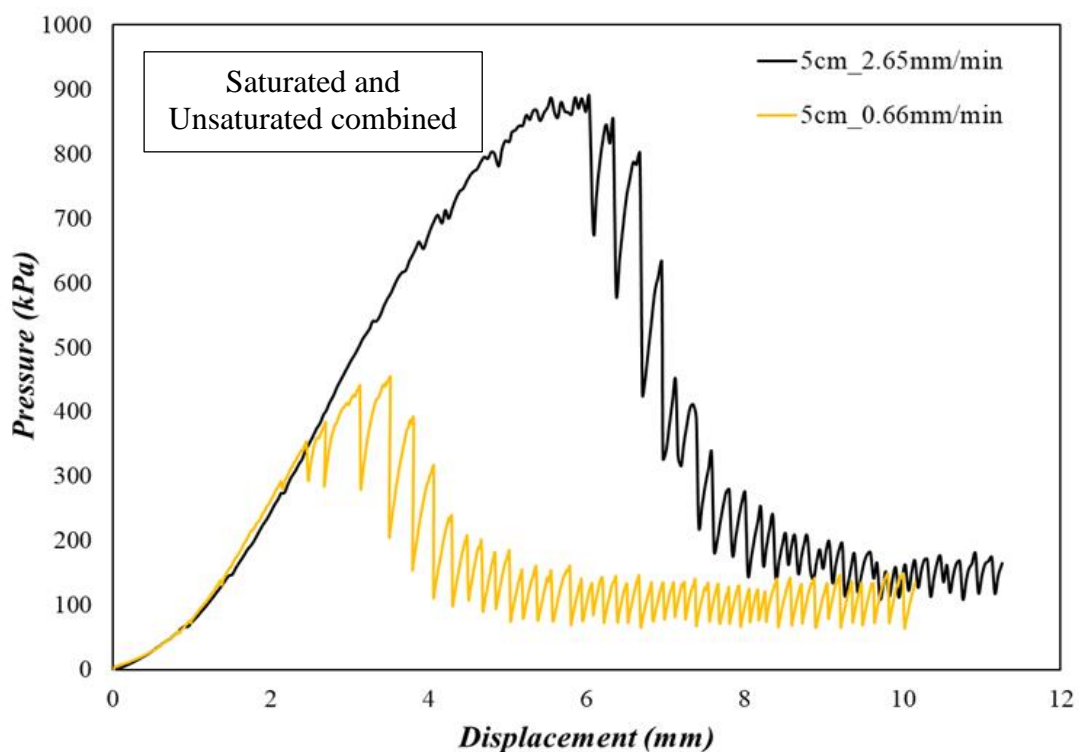


Figure 10.15 Loading rate effect for clumped particle sample under saturated and unsaturated combined condition, without the presence of the cavity

10.2.2 Surface loading on dry conditions

As the pore pressure and the capillary forces present in fully saturated and unsaturated conditions respectively, can impart the loading rate dependency. However, in dry conditions, none of these forces are present amongst the particles. In order to verify the effect of capillary and pore pressure on loading rate dependency, the dry sample was used to perform similar tests under similar conditions of density and loading plate width.

Figure 10.16 shows the loading results for the dry samples consisting of clumped particles. As anticipated, the dry samples for different loading rates did not show any noticeable difference in the peak strength. Also, the residual strengths were also measured to be quite similar. The lowest loading rate, although, showed the least strain value for developing peak stress response.

Hence, it was thus proved that using dry samples did not demonstrate any significant difference in peak strengths and the change in strength with loading rate is associated with the sample having water interaction and due to the development of capillary forces or the pore pressure.

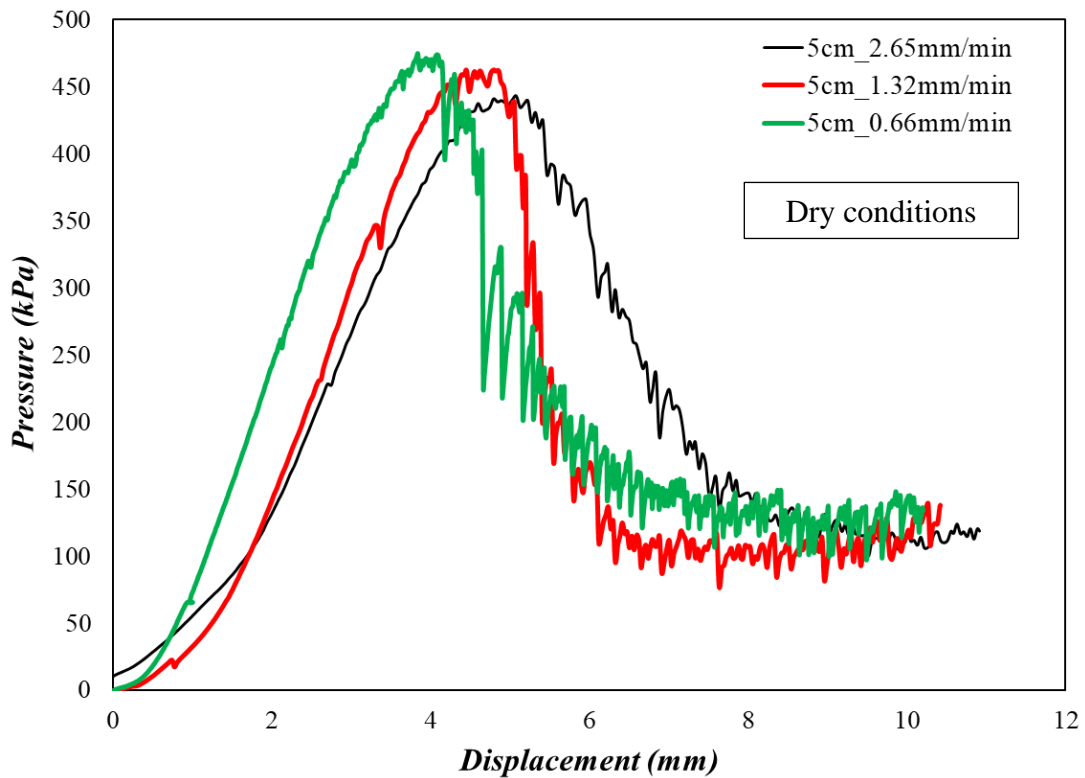


Figure 10.16 Loading rate effect for clumped particle sample under dry condition, without the presence of a cavity

10.2.3 Surface loading tests for fully saturated samples

In section 10.2.1, tests were performed for a condition that contained regions of both saturated and unsaturated particles. The dependence of pore pressure on the loading rate is an established fact. However, the dependence of capillary forces on the loading rate is yet to be determined. Hence, in order to quantify the effect of capillary forces on the loading rate effect, tests were also conducted on fully saturated samples.

Such tests would quantify the difference between the pore pressure and capillary forces, as the fully saturated condition does not allow the development of any capillary forces. Figure 10.17 shown the loading test results for the fully saturated condition using clumped particles having a relative density of 90%. The loading rate dependency is clearly visible in both cases. A higher loading rate resulted in a significantly higher peak strength compared to the other slower rate. However, the residual strength did not show any difference and converged.

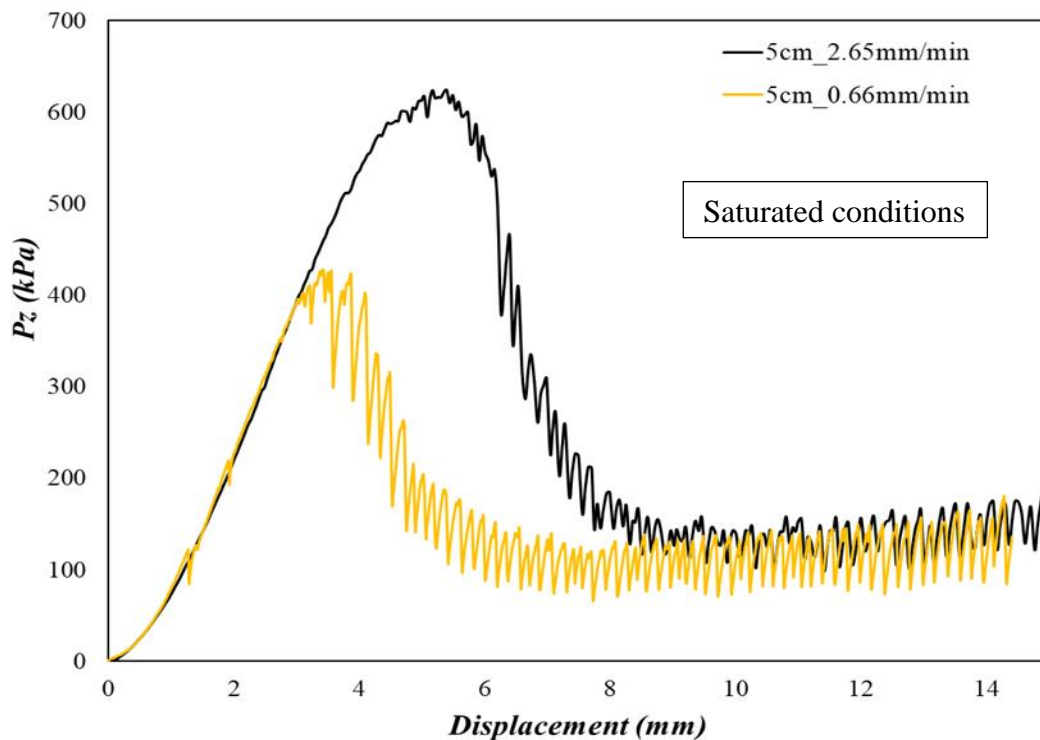


Figure 10.17 Loading rate effect for clumped particle sample under fully saturated condition, without the presence of a cavity

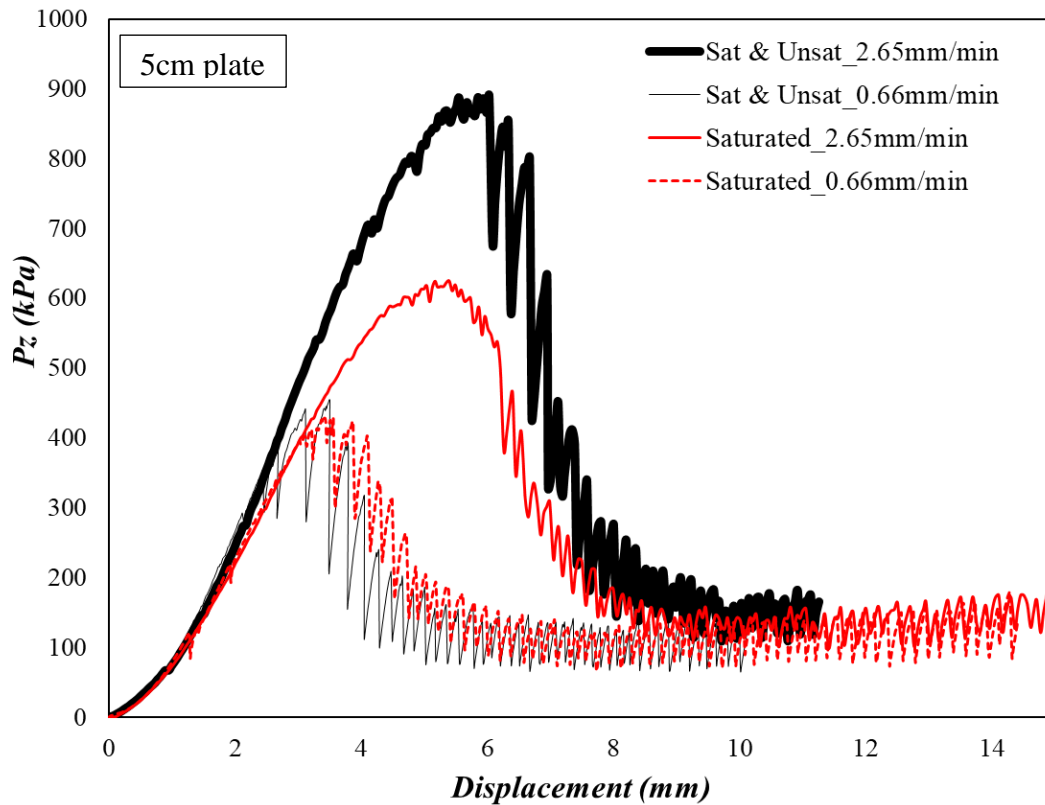


Figure 10.18 Comparison of surface loading tests with the fully saturated condition and the combination of saturated and unsaturated condition, using clumped particles

A combined plot showing the cases of fully saturated sample results and the samples with a combination of fully saturated and unsaturated conditions is presented in Figure 10.18. As seen, for the slower loading rate, the peak strength shown by the combined saturated and unsaturated sample is slightly more than the fully saturated sample results. As the loading rate is slow enough, both kinds of samples with different conditions could dissipate the excess pore pressure and resulted in a peak strength not much different from another.

In the case of higher loading rates, the strength of a fully saturated sample was significantly smaller than the other sample, showing that the combined effect of capillary forces and the pore pressure is much larger than the only effect of pore pressure. The difference between the peak strengths of both curves can result in the strength offered by the capillary forces.

10.2.4 Surface loading tests with unsaturated condition

Lastly, to assess how much is the contribution of the capillary forces in the loading rate dependency, similar tests were performed on the samples with a uniform degree of saturation. The material was mixed with a 3% water by weight of the dry sample, at a relative density of 90%.

The results are presented in Figure 10.19 with all other results. However, it is seen that the partially saturated samples showed rate dependency as well, though the pore water pressure development was not anticipated in this condition due to the presence of a very small volume of water. The peak strength offered by the partially saturated sample showed a value much lesser than the value offered by a sample with combined saturated and unsaturated regions, implying that the effect of both capillary forces and pore water pressure was observed in the latter case.

By comparing the partially saturated sample results with the fully saturated samples, it is clear that the peak strength offered by the partially saturated samples is slightly higher than the other case, showing that the effect of capillary forces is more than the effect of pore pressure development for a specific loading rate. Furthermore, for all three conditions of the saturated, unsaturated, mixed condition and dry conditions; the displacement corresponding to the peak strength is almost similar for the highest loading rate. However, for the smaller rate, a small discrepancy was observed in the dry condition.

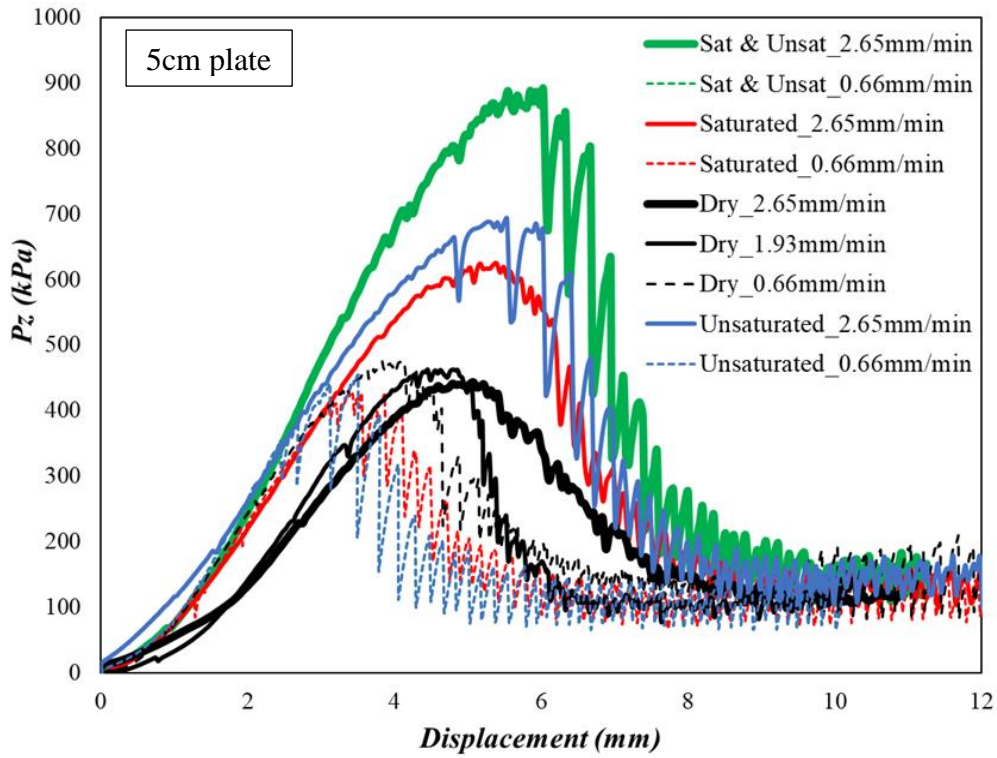


Figure 10.19 Combined plot of all cases for surface loading tests using clumped glass beads without any presence of the cavity

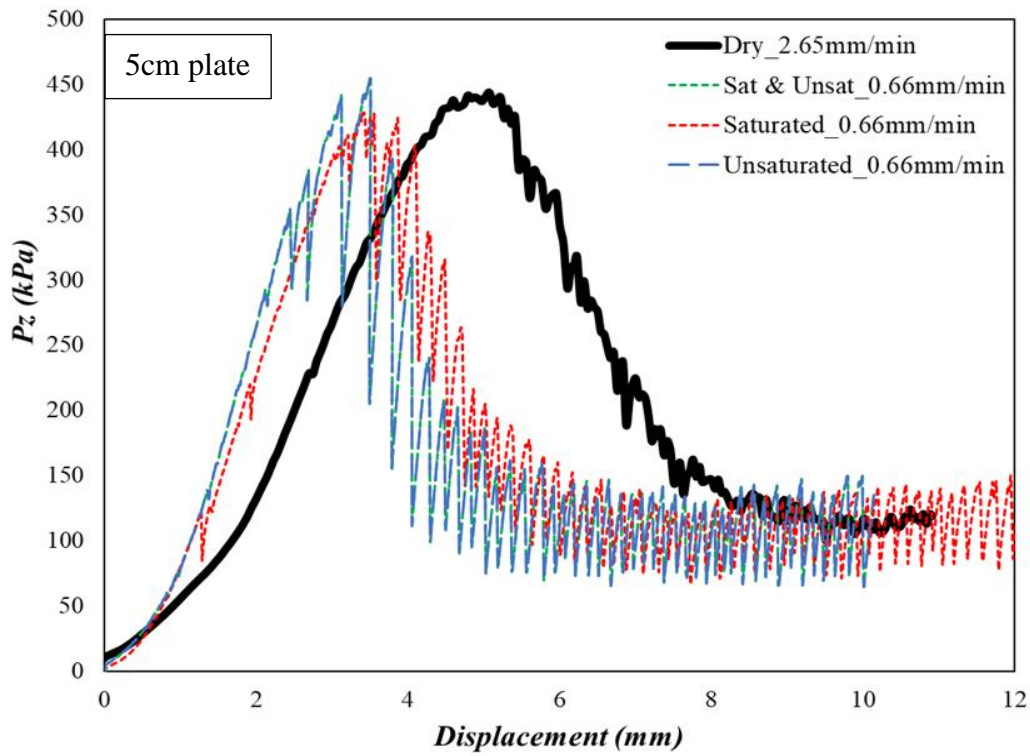


Figure 10.20 Cavity loading test results on clumped glass beads without a cavity for a dry case with maximum loading rate and all other cases with least loading rate

Lastly, by comparing the highest loading rate of 2.65mm/min for the dry case with the lowest loading rates of 0.66mm/min for all other cases, as shown in Figure 10.20, the peak strength is observed to be the same. As the dry sample showed a similar strength for different loading rates (Figure 10.16), due to the absence of any inter-particle attractive forces or the pore water pressure development. It can be implied that at smaller loading rates, the effects of both capillary forces and the pore water pressure approaches to be nullified. The effect of reducing pore water pressure development with a slower loading rate is a well-known fact. However, the effect of loading rate on the capillary force reduction is yet to be explored in detail.

10.3 Numerical analyses of cavity surface loading

The experimental results showed the dependence of the loading rate on the strength of the glass beads. For dry cases, no dependence was observed. The phenomenon can be related to capillary forces and pore water pressure. However, whether the DEM can observe similar trends and investigate the forces distribution, the suction-tension model was further utilized in DEM simulations to apply the matching conditions as that of experimental work and the surface loading tests were performed.

10.3.1 Effect of loading plate width

In experimental cases, the width of the loading plate did not show any prominent difference in the strength characteristics. To verify the DEM simulation response, initially, a sample with non-spherical particles having a mean size of 1.0mm, with a cavity size of 30mm width and 30mm height was selected. The given cavity showed a stable behavior as discussed in Chapter 9 earlier.

For the loading plates, four types of plate widths were selected as given under:

- i- 2mm
- ii- 5mm
- iii- 10mm
- iv- 30mm

The loading plates were placed right above the cavity on the surface of the sample and were lowered with a constant velocity of 0.05m/sec. The loading plate spread all

across the sample breadth (Y-direction). A total of 6mm indentation into the sample was performed, as the higher penetration would cost a long time and computational energy. However, as seen in the experimental cases, the peak strength of the sample was attained much earlier than 6mm. Hence, the given case would be able to capture the peak strength characteristics of the sample.

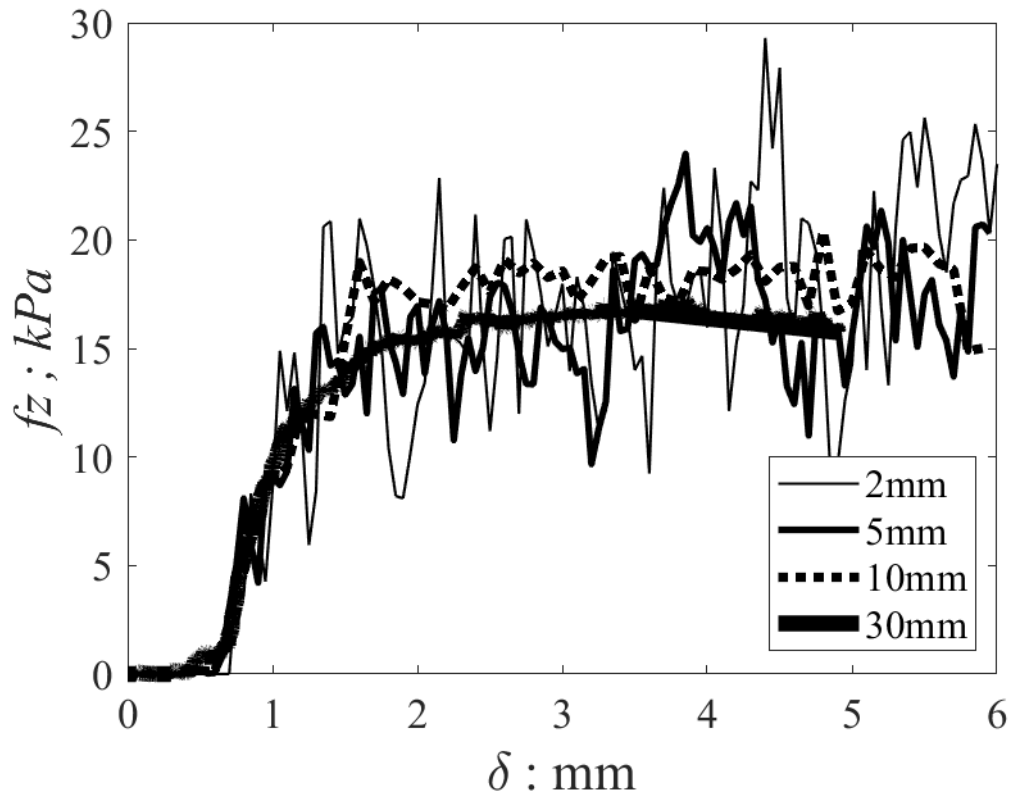


Figure 10.21 Load-settlement plots for DEM simulations using non-spherical clumped particles for different widths of loading plate on a sample with a 30mm wide cavity

The load-settlement plots as shown in Figure 10.21 represent similar behavior as seen in the case of model cavity tests. An insignificant difference was observed when the sample was loaded with different plate widths. However, for very small plate widths, e.g. 2mm, the response showed high fluctuation or stick-slip behavior. The reason for such behavior is the relative size of the loading plate width with the mean size of the particles. The mean size of clumped spherical particles was 1.0mm in the given cases, which represents 50% of the total plate width. In case some particle slips just under the edge of the plate, a large instant reduction in the stress would be observed by the plate, which would balance after small-time as new particles would interact with the plate. However,

for the cases having plate width much larger compared to the mean particle size, no such fluctuation was measured.

The absolute magnitude of the peak stress for DEM cases was observed smaller than the experimental results on the spherical glass beads with a mean diameter of 0.5mm. The difference can be correlated with a particle size as well, smaller particles being much stronger due to the presence of strong capillary forces for a similar saturation. Another factor is the presence of a uniform saturation level in the sample for the DEM cases. Whereas the experimental tests would never contain a uniform distribution of saturation.

10.3.2 Effect of loading rate in numerical simulations

A strong effect of loading rate was observed in the experimental cases. However, the response varied based upon the presence/absence of water in the sample. To validate the DEM suction-tension model, and to observe the inter-particle distribution of forces, DEM simulations were performed similar to experimental cases, using five different surface loading rates, as given below:

- i- 0.2m/s
- ii- 0.1m/s
- iii- 0.05m/s
- iv- 0.01m/s
- v- 0.001m/s

For all cases, a loading plate width of 30mm was selected, which was equal to the width of the base cavity.

10.3.2.1 Simulations with a base cavity & uniform saturation level

The response of the sample with a 30mm cavity width and 30mm height, being loaded on the surface with a rigid plate of 30mm width, is shown in Figure 10.22 below. A clear difference in the peak strengths was observed and the higher loading rates yielded higher peak strengths. For the least loading rates, the amount of plate settlement was not performed equivalent to higher rates as the time required for the similar displacement would be many folds compared to the higher loading

rates. Hence, it was not possible to have a larger plate settlement for small loading rates.

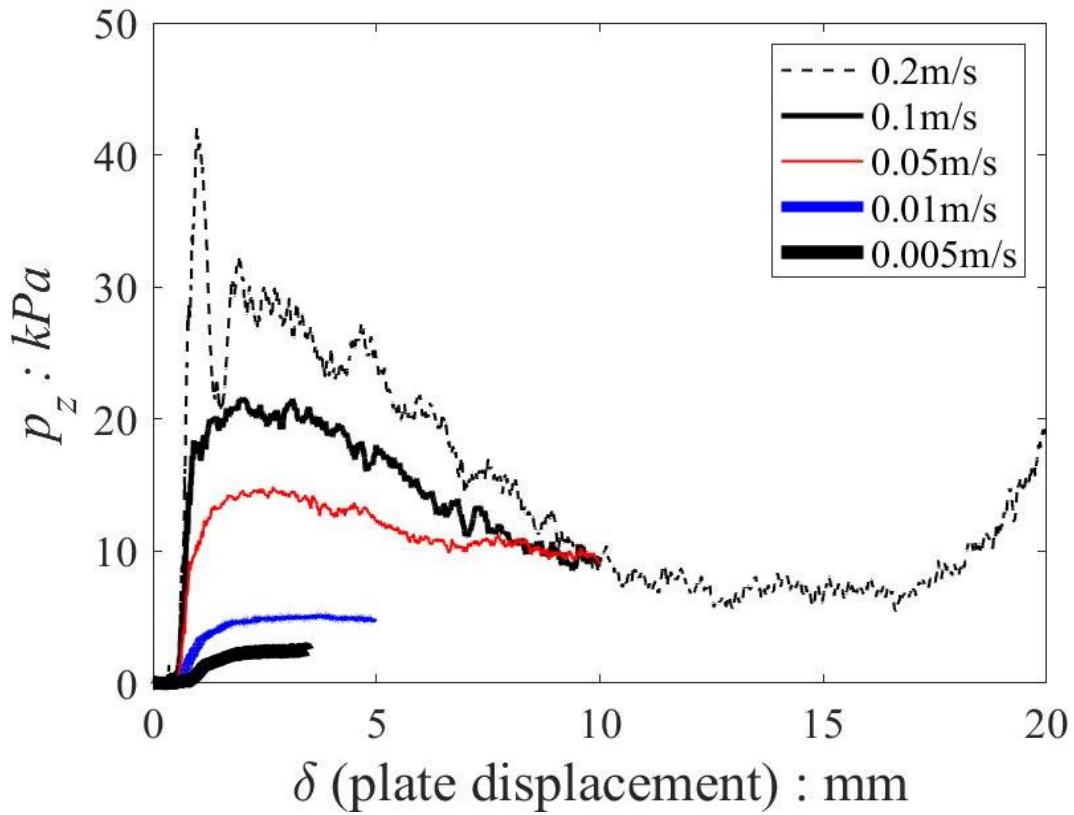


Figure 10.22 Load-settlement response of numerical simulations for varying loading rates with the presence of a base cavity

The trend of the smaller loading rates is slightly increasing. However, for all other loading rates, the residual strength converged to a single value, as observed in experimental cases. Also, in the lab experiments, samples with a uniform degree of saturation and the ones with both saturated and unsaturated regions showed strong loading rates dependency, which is similar to that observed in numerical simulations.

The particle velocity plots showed an almost vertical region of particles that observed high movement (Figure 10.23). The cavity that was present at the base of the sample at initial condition, showed a collapse under the plate loading for all shearing rates. The area just above the cavity surface is joined together due to the presence of inter-particle suction. However, such regions do not participate in load transfer and the arching forces cannot be transferred through it.

The absence of strong arching forces can be seen through Figure 10.24, where the strong inter-particle forces are plotted for all loading rates for the initial static and the final stages. The initial state represents a uniformly distributed strong force network throughout the sample. However, the application of surface loading at the central part of the sample induces the redistribution of strong forces. A strong arching action is a development with the plate movement. However, as the cavity starts collapsing with increasing plate settlement, the area around the cavity can be seen to have no strong force network.

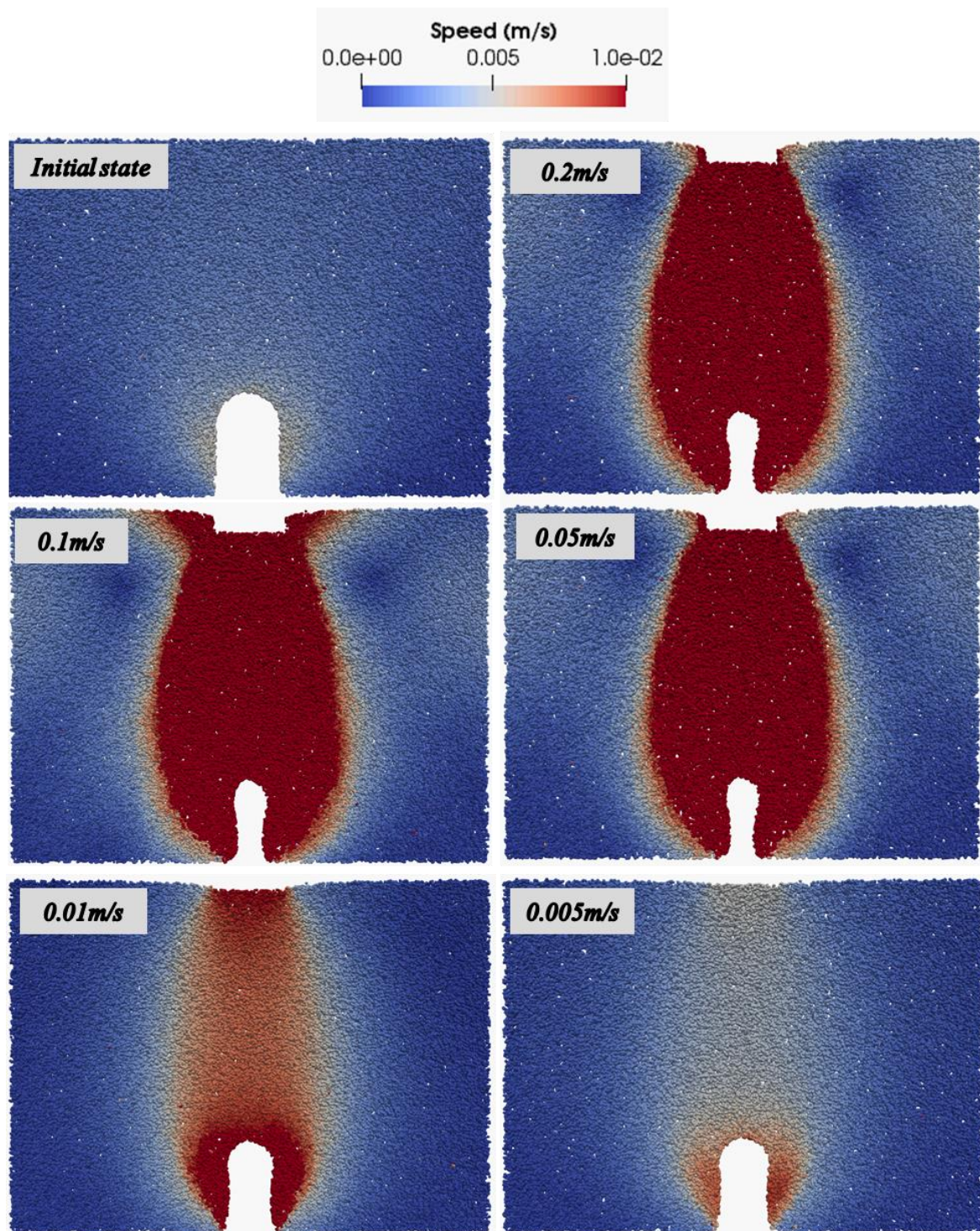


Figure 10.23 Particle velocity plot for various loading rates

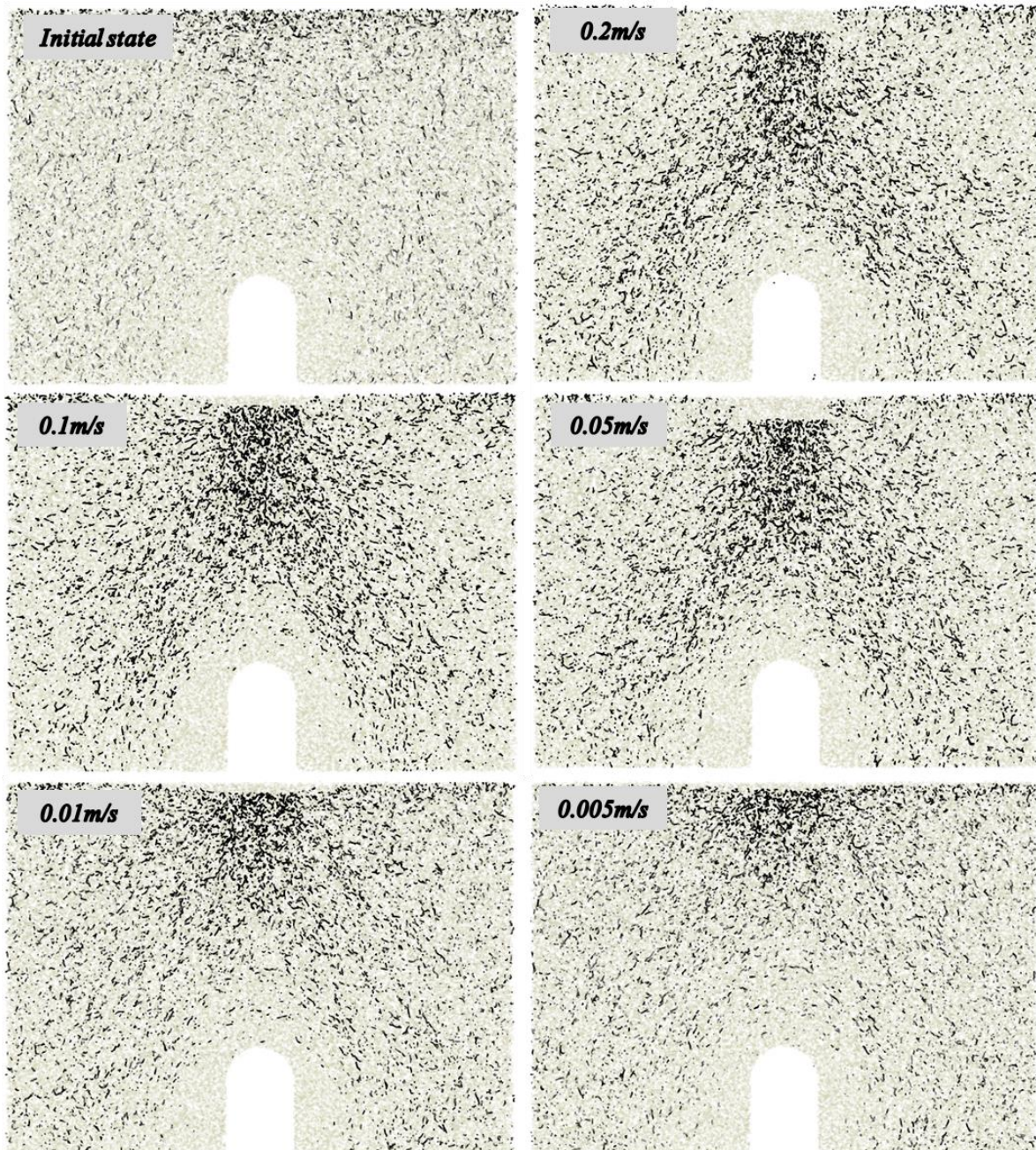


Figure 10.24 Strong force chains for various loading rates

The inter-particle forces induced by the plate loading have the maximum intensity right under the plate and vertically down in direction. These forces then propagate both laterally and vertically. With the vertical movement, these forces are then transformed into an arch shape, transferring the vertical load on the sides of the specimen through arching action. Whilst the laterally spreading forces at the base of the surface plate cause the side bulging of the sample

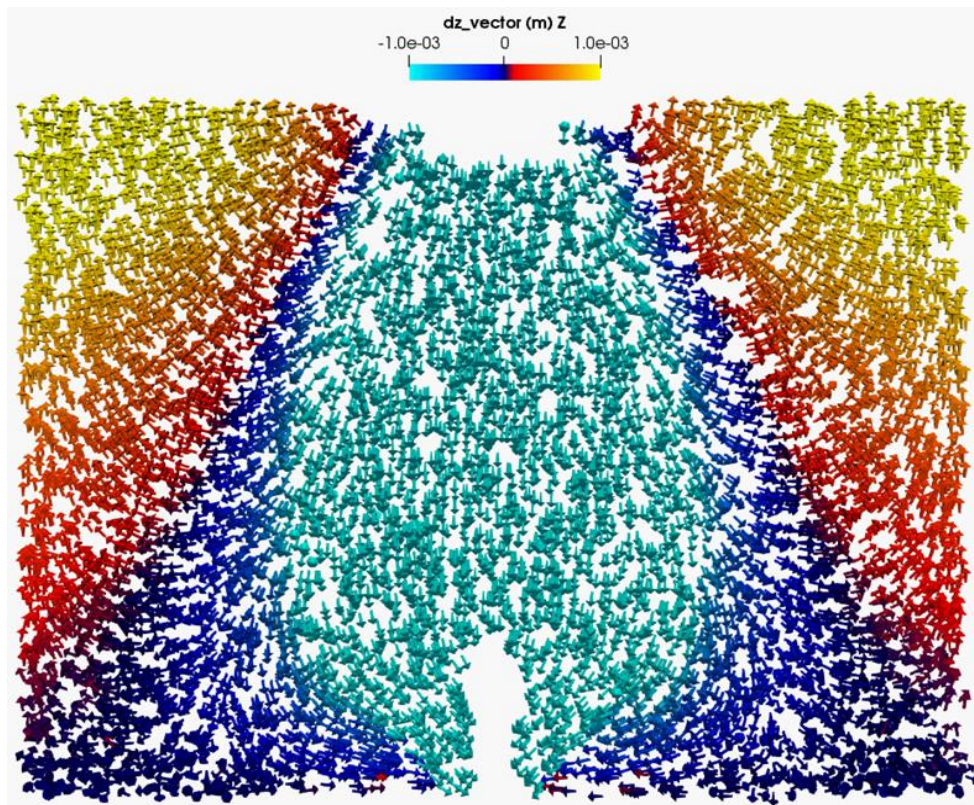


Figure 10.25 Particle vector movement plot overlaid on a color plot of dz for 0.1m/s loading rate

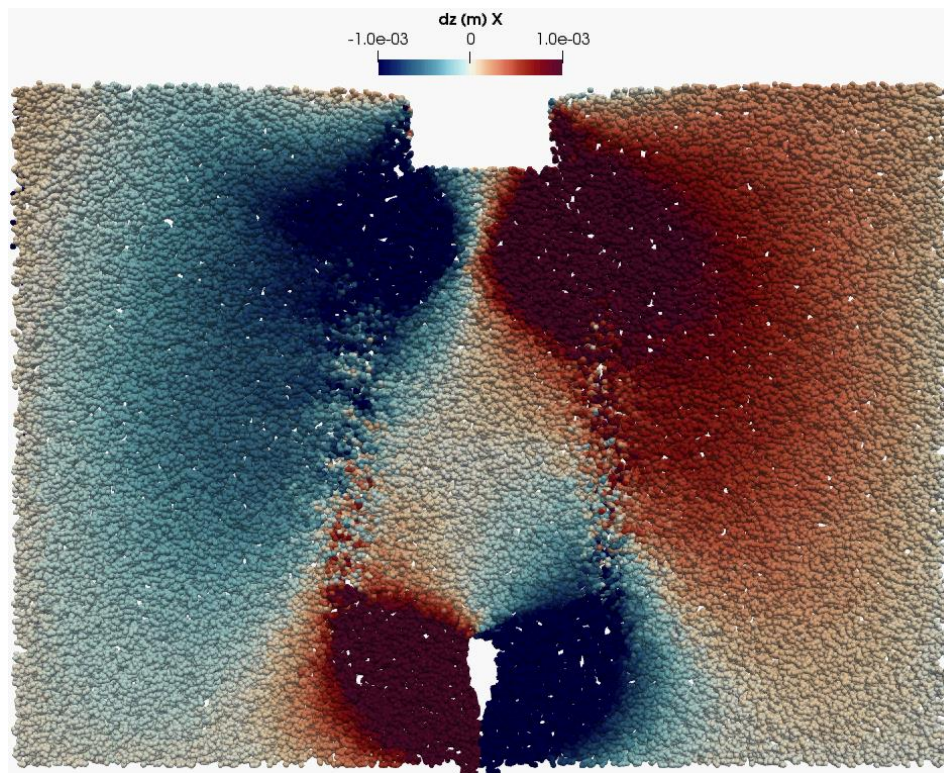


Figure 10.26 Failure plane as observed in DEM simulation for a larger settlement of surface plate loading

The vertical movement of the particles originating at the sides of the loading plate can be seen in Figure 10.25, where the vector diagram of particle movement is overlaid on a color scale of vertical particle movement (dz). A clear upward movement can be observed, that causes the side bulging of the sample. A similar sort of side bulging for the samples in experimental results was observed in unsaturated conditions, as seen in Figure 10.2 as well.

The failure plane for almost all samples in experimental testing was observed to be approaching verticality (Figure 10.4 and Figure 10.8). The DEM samples showed a very similar failure plane as observed in Figure 10.26. The particle slippage was observed starting just under the surface plane and propagating in a vertical line up to the base of the sample.

10.3.2.2 Surface loading without base cavity for uniformly saturated conditions

As the simulations showed a rate dependency for the surface loading above the base cavity, the simulations were performed on a sample without the presence of any base cavity to eliminate any potential effect of the presence of a cavity.

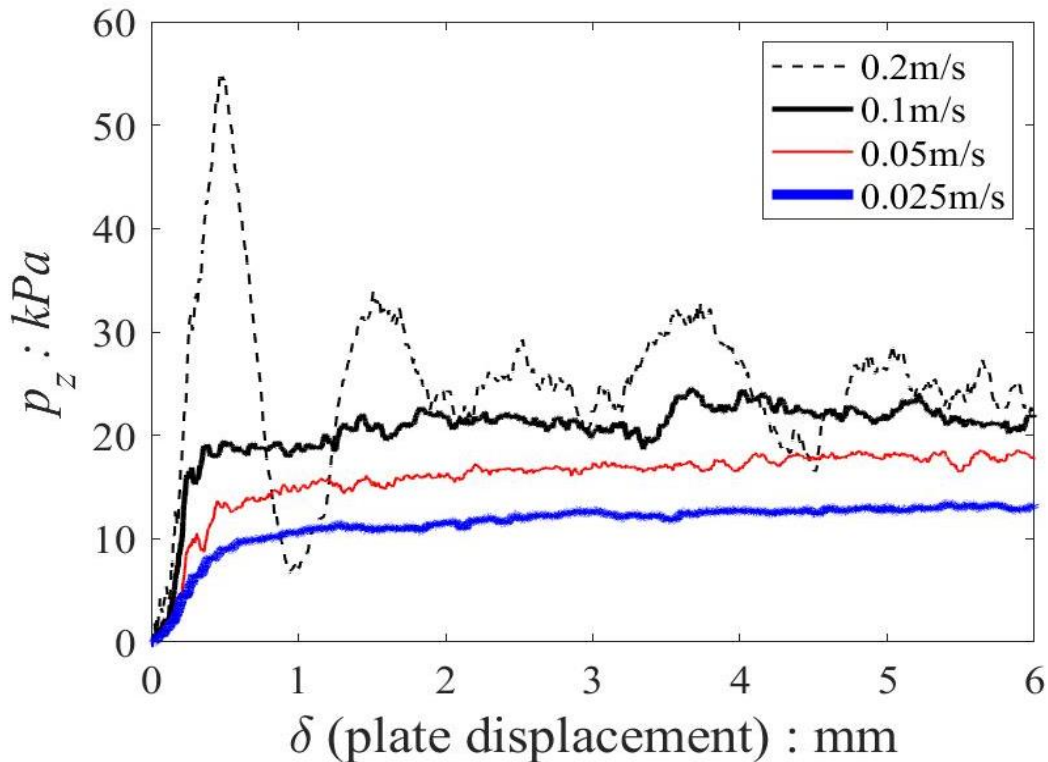


Figure 10.27 Load-settlement response of numerical simulations for varying loading rates without a base cavity under unsaturated conditions

Four different loading rates were selected, and the simulations were performed on a sample similar in conditions as explained in the earlier section. Figure 10.27 shows the load-settlement response of numerical simulations using a 30mm wide surface loading plate under unsaturated conditions on samples without the base cavity. As the experimental results, the DEM simulations showed a rate dependency. The highest rate of 0.2m/s showed a varying response of forces due to the dynamic response caused by a higher loading speed. However, for other loading rates, the simulations showed stable behavior and showed rate dependency on the stress response.

10.3.2.3 Surface loading without the capillary forces

As a last measure, like experimental cases, simulations were performed on the samples with similar conditions to the earlier explained case, under the dry conditions (without capillary force model). Similarly, four loading rates were selected for the samples without any base cavity.

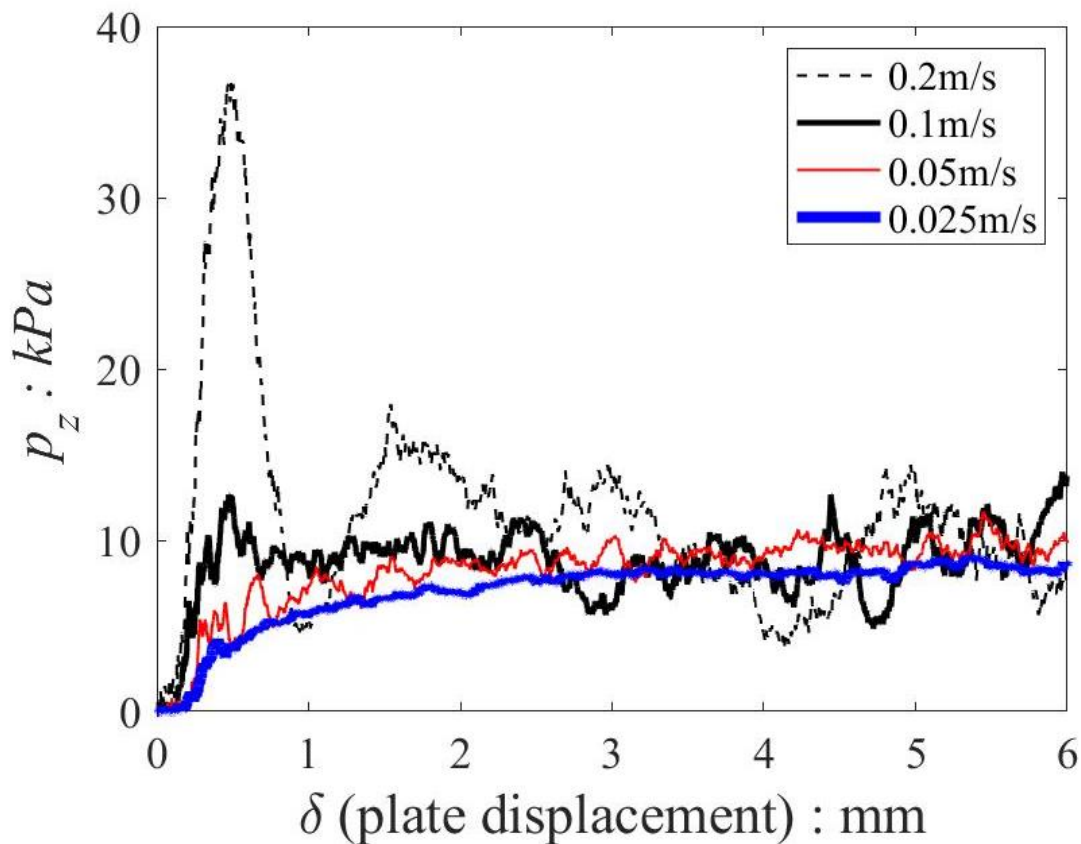


Figure 10.28 Load-settlement response of numerical simulations for varying loading rates without a base cavity without capillary forces

Unlike the other cases of numerical simulations, the absence of capillary forces resulted in a converged behavior under different loading rates, as shown in Figure 10.28. A similar observation was made in the model cavity tests as well, where the dry samples resulted in a converged behavior and all other conditions could not exclude rate dependency characteristics. Hence, in terms of qualitative analyses, DEM simulations could reproduce the trend of experimental results. Similarly, the capillary force model (suction-tension model) was able to capture the essence of the model cavity tests.

10.3.3 Effect of rupture distance between particles

Rupture distance (D_{rup}) is the maximum inter-particle distance where the capillary forces can be experienced. Beyond the rupture distance, particles can no longer sustain attractive contact and the net forces between two particles become approaches zero. The rupture distance plays a vital role in the overall behavior of the material. Wang et al. (2017) measured the suction force and the rupture distances for spherical particles. Mason & Clark (1965) was one of the earlier researchers to correlate rupture distance with the volume of liquid bridge. Similarly, Willett et al. (2000) did an experiment to measure the suction force based upon the rupture distance for sphere-sphere and sphere-flat surfaces.

The capillary force model developed in the current study considered the rupture distance as a constant value and correlating the D_{rup} with specimen parameter was out of the current scope. However, for most of the simulations, the D_{rup} was taken as 10% of the particle mean size.

Similar surface loading tests were performed with varying D_{rup} values to investigate its effect on strength characteristics. Three values of rupture distances were selected for a particle mean size of 1mm, as under:

- i- 0.0001m
- ii- 0.00001m
- iii- 0.000001m

Three different loading rates were selected, and simulations were performed in a similar way as explained in the earlier sections, without the presence of a base cavity.

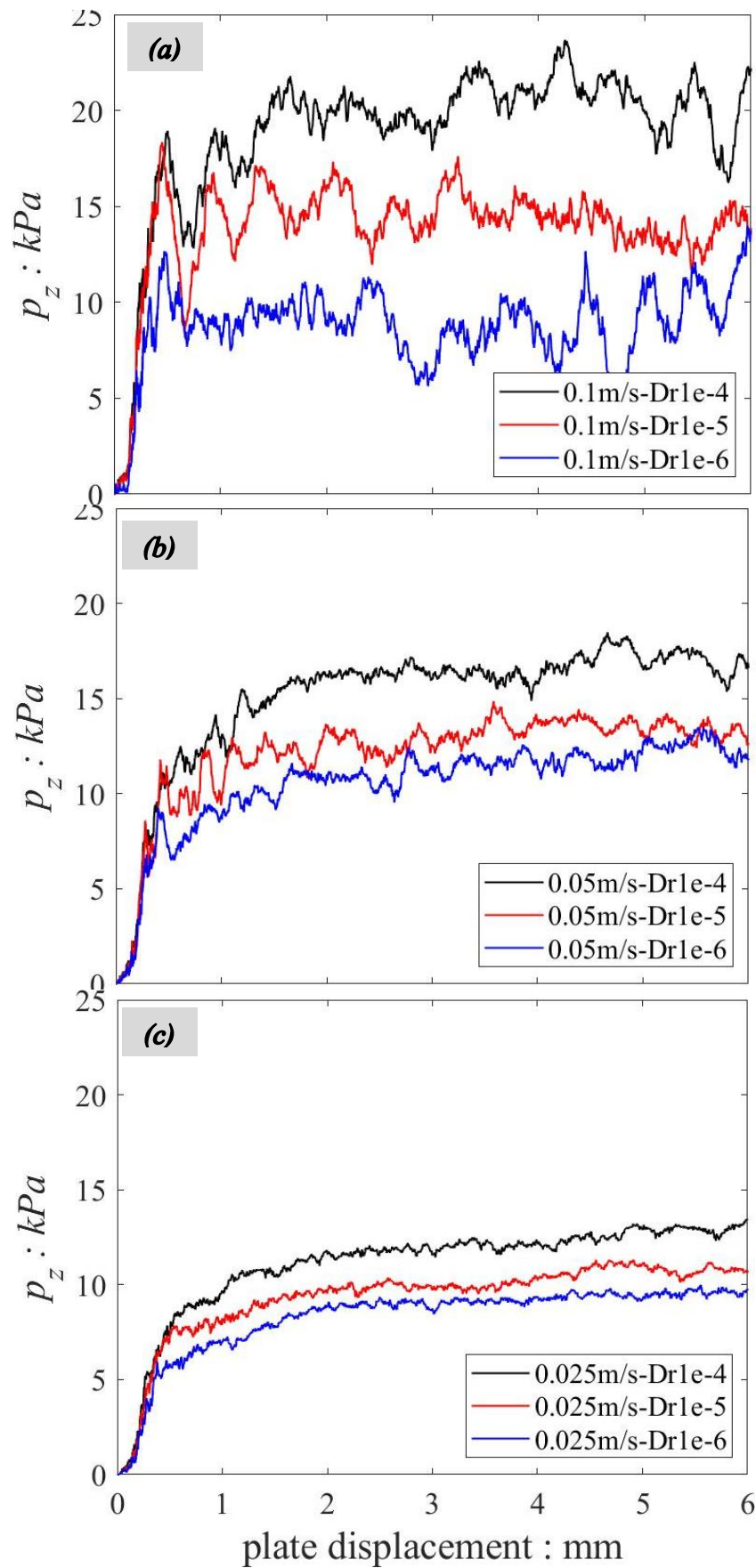


Figure 10.29 Effect of rupture distance on sample shear strength for (a) 0.1m/s, (b) 0.05m/s and (c) 0.025m/s loading rate

Figure 10.29 gives an interesting comparison of both rupture distance and the loading rates. For each loading rate, reducing the rupture distance reduced the shear strength of the sample, showing a more brittle response as the particles get to a no-force condition at a very small distance. However, for a similar rupture distance, while reducing the loading rate, the absolute magnitude of the shear strength reduced, as was observed in the earlier simulation cases and the experimental results as well.

For higher loading rates, the difference between the different rupture distance strengths was observed to be significant. As the loading rate was reduced, the differences between the strengths for different rupture distances reduced. For the least rate of 0.025m/s plate loading, the samples with different rupture distance showed comparable shear strengths. However, the overall trend of higher strength for larger rupture distance and lower strength for lower rupture distance was maintained for all loading rates.

As seen, the capillary forces do imply a loss in strength due to the loading rate. However, the rate of dependency can be reduced by reducing inter-particle rupture distance. A more detailed investigation is required to study the rupture distance effects on the strength of the material. For better accuracy of the DEM results, a model should be used that can accurately relate the rupture distance between particles based upon surface characteristics, shape, and mineralogy of material.

10.4 Summary

This chapter included both experimental tests and numerical simulations for the cavity surface loading tests. Besides the cavity surface loading tests, the rate of loading and the effect of the width of the loading area were also explored both numerically and experimentally. Material strength dependency with the particle shape was observed. Similarly, the rate dependency was seen for the cases with the presence of water, either saturated or unsaturated. Numerical simulations validated the trend observed in the experimental results. In the end, the effect of particle rupture distance was explored, and it was found that with a combination of smaller rupture distance and smaller loading rate, the loading rate dependency can be minimized for unsaturated samples in numerical simulations.

CHAPTER 11: CONCLUSIONS AND RECOMMENDATIONS

11.1 Overall Summary

Soil arching is one of the most abundantly occurring natural phenomena. It exists whenever there is a soil mass yielding compared to other static mass. Yielding can be related to small strain like a settlement or even the large strain like soil washout or the underground cavity formation. Two of the main conditions where small and the large yielding is experienced are the trapdoor and the underground cavity conditions respectively. As soon as the soil arching initiates, earth pressure re-distribution is observed in the soil mass.

For the trapdoor conditions, the majority of the researchers explored the stress reduction under the settling soil. The stress redistribution for the static soil mass and its relationship with the yielding mass has not been discussed extensively. Numerically, a limited number of DEM studies have been performed on trapdoor conditions, that focused on the validation of experimental results and discuss the shape of shear bands. No criteria for evaluating the presence/absence of the arching in a soil mass was found in the literature. In the case of underground cavity conditions, the studies are still in progress for the mechanism of cavity formation, propagation and repair as the urgency of repairing a collapsed site inhibits the detailed investigation. Researchers in the past have performed the cavity stability tests using various sands with different densities. Furthermore, almost negligible work has been done numerically for the analyses of cavity phenomenon, due to the absence of a proper numerical model for assessing the capillary forces.

The current work includes the deficiencies as observed above to perform both model trapdoor and cavity tests, along with the numerical assessment through full-scale DEM simulations. A new model that incorporates capillary forces was developed and used to perform the cavity stability and surface loading simulations.

Chapter 2 discusses the literature review for the work that has already been done in the past. There is a lack of numerical simulation work for the trapdoor conditions for a buried structure. Emphases exist on the trapdoor condition for the group of piles and their configuration effect. Quantitative analyses of stress increment/reduction due to trapdoor condition is missing. The numerical work mostly focused on the strong force chain during the trapdoor along with the surface settlement analyses and failure patterns. However, the shear force distribution during the trapdoor conditions has not been discussed in the past. There is a

need to further clarify the inter-particle response during trapdoor conditions like particle rotation, contact fabric variation, etc. to better understand the phenomenon. For the case of cavity formation, mostly the experimental work-related cavity stability with the material density, saturation level. Furthermore, in this chapter, the basics of DEM simulations with the different input parameters are discussed.

Chapter 3 includes the description of trapdoor model test equipment along with the loading system and the sensors attached to it. The method to prepare the samples and the basic properties of the samples used in the test are also explained. The testing plan for different materials is described in this chapter. The numerical setup is also briefly discussed along with the basic sample construction along with the sample preparation. The input parameters and the simulation plan are discussed here as well.

Chapter 4 relates the stress redistribution during the trapdoor tests. As the trapdoors are lowered, the central static portion of the sample experienced an increase in the load. The effects of normal stress distribution on the ground sample height and on the type of materials are discussed in this chapter, along with a stress increment factor for the central fixed plate that is then related to the arching conditions. The influence of shear stress variation on the arching mechanism is also discussed. The effect of sample density, particle size, and shape on the stress concentration factor is included in this portion.

Chapter 5 explores the relation between the sample height and the surface settlement through experimental and numerical results for the trapdoor condition. Furthermore, the presence of the arching inside a sample was then correlated with the strong force chains, vertical movement of particles, 2nd order contact fabric, particle rotation and the angular velocity plot for the particles.

Chapter 6 discusses the effect of trapdoor configuration. The stress distribution changes as soon as the trapdoor configuration is changed. The arching condition can vary significantly with the increase in the length of settling regions. The relation of central plate width and the width of the lowering portions is included in this chapter along with the development of an empirical relation for prediction of stress concentration factor for any given configuration of trapdoor condition.

Chapter 7 explores the underground cavity condition and the results for the cavity model tests and the simulations for the dry conditions. The importance of capillary forces for the formation and stability of cavity is discussed and an ‘interparticle suction and surface tension’

based model is derived to be implemented in DEM simulations for the analysis of cavity formation and stability analysis. The model is also validated with an existing model of powder technology and with the results of basic model tests.

Chapter 8 consists of a description for the mechanism, materials, apparatus and the numerical simulation plan for the cavity conditions. The model cavity apparatus is discussed in detail with the material description. A detailed model testing plan is explained in this chapter. For the numerical simulations, a detailed simulation plan, boundary conditions, pluviation method, and the input parameters are described.

Chapter 9 includes cavity stability analyses for both model tests and numerical simulations. For the model tests, both spherical and non-spherical clumped glass beads were utilized. The effect of sample density, saturation level, particle size, and surface roughness are explored in this chapter. For the numerical simulations, several cavity widths are selected, and each width further consisted of several cavity heights. In short, the effect of cavity size, particle size, saturation level, and particle shape are investigated. A cavity stability chart is then formed for both experimental and numerical results and compared with the in-practice cavity stability chart. Furthermore, the particulate level force distribution and the contact fabric distribution are also discussed here.

Chapter 10 relates to the experimental and numerical assessment of cavity surface loading. It was found experimentally that there is not much difference in the width of the loading plate on the peak stress during cavity surface loading. However, a strong loading rate dependency was observed for the given plate width in saturated or unsaturated samples. Similar observations were made through numerical simulations and the effect of loading rate, rupture distance, and the loading plate width is discussed in relation to the load-settlement plots.

The current chapter concludes the given work and the main findings are explained here. In the end, some recommendations are given for the future incorporation of this study. The major findings are stated as below:

11.2 Main findings

11.2.1 Normal stress distribution under trapdoor conditions

- The stresses on the lowering part always reduce than the initial condition, whereas the static part/rising part faces an increase in the stresses

- The peak rise in normal stress is observed at a very small displacement of the trapdoors.
- The maximum normal stress is observed just at the edges of the central fixed plate.
- For the sample with lesser relative density to form loose material, the maximum normal stresses are observed at the center of the central fixed plate.
- Soil cover above trapdoors affects the normal stress distribution. Higher soil cover produces higher normal stress.
- The normalized normal stress (normalized by the initial stress) also depends upon the soil cover. However, after a critical value, it becomes independent of the soil cover.
- Particle shape affects the relative magnitude of normalized normal stress. More angular particles showed higher stresses.
- The distribution of normal stress at the central fixed plate and above the lowering parts is inter-dependent. Higher is the normal stress above the central fixed plate, lower will be the stress on the lowering trapdoors.
- The stress concentration factor ' α ' approaches to a converging value under the arching action.
- The peak values of ' α ' were found to be dependent upon particle shape and density.
- The residual value of ' α ' is independent of the particle shape, size, and density, for the given range of materials.
- Particle size has an insignificant effect on the peak ' α ' value, for the given range.
- The stress concentration factor ' α ' determined experimentally and numerically, was found to be higher than the values prescribed by Japan Road Association 1999.
- Both numerical and experimental results showed a close relation qualitatively and quantitatively.
- Conservation of normal stresses between the initial uniform state and after the trapdoor condition was observed in numerical simulations, confirming the balanced simulation.
- For the experimental cases, the summation of initial uniform normal stresses and the normal stresses after the trapdoor movement had a small difference. That difference is related to the frictional effect of the side boundaries and the accuracy

of the measurement devices. However, the difference was found to be insignificant.

11.2.2 Shear stress distribution under trapdoor conditions

- For the given conditions, the central portion of the sample always experienced a shear stress value approaching zero.
- The shear stress distribution about the center of the sample was found to be always in opposite directions and approaching to a mirror image.
- Once the stable arching is present inside a sample, the direction of the shear stresses around the central fixed plate is to move particles outward from the central point.
- In case the arching action is absent, the shear stress trend would be the opposite, and the particles will try to move inward to the central plate.
- Shear stress distribution can be utilized to determine the absence or presence of the arching in a soil mass under trapdoor conditions.

11.2.3 Trapdoor configuration effect

- The arching pattern can change significantly with change in trapdoor configuration
- The stress concentration factor ' α ' increases with increasing the widths of lowering plates, for a given soil cover.
- Larger soil cover is required to produce a stable arch with an increase in lowering portion widths.
- Once the arch is developed, the sample does not show differential surface settlement, rather a uniform surface settlement is observed.
- For different trapdoor configurations with a stable arching, uniform surface settlement increases with an increase in lowering widths.
- Increasing the width of the central fixed plate does not affect the arching pattern.
- Stress concentration factor ' α ' reduces with an increase in the width of the central fixed plate.
- The maximum possible value of ' α ' (α_{max}) is approached once the fully stabilized arching is developed in the system.

- With larger central fixed plate widths, α_{max} can be approached more easily.
- The empirical relation developed for the prediction of α can be used to roughly evaluate the soil height required for any configuration for a stabilized behavior of the sample. However, more experimental data is required to improve the relation.

11.2.4 Particulate level analyses of soil arching

- In the absence of soil arching, the strong force chain intersects the sample surface, resulting in differential surface settlement.
- For the cases with a stable arch, strong contact forces are concentrated in the arching regions. Near the sample surface, a strong force network is uniformly distributed, causing a small uniform surface settlement instead of differential surface settlement.
- Due to better particle interlocking, non-spherical particles showed more dense regions of strong contact forces, compared to the spherical particles.
- 2nd order contact fabric can be used to correlate with the soil arching. The increase and decrease in the vertical and horizontal contacts are largely influenced by the strong force network of the sample.
- The 2nd order contact fabric for the Y -axis showed a constant distribution throughout the sample, as the arching phenomenon was observed in the XZ plane only.
- The Z -directional contact fabric showed a higher value compared to the X -directional contacts under uniform conditions due to the gravitational effects.
- Particle rotation analyses can be used to assess the arching in the sample for non-spherical particles.
- Particles rotate only in a specified region above the lowering trapdoors only, representing the presence of the arching action in that region.
- Angular velocity plot for any type of particles can well represent the presence of the arching in the samples.

11.2.5 Use of periodic boundaries

- The use of periodic boundary along the lateral dimensions was found to be consistent with the experimental results.

11.2.6 **Model cavity stability tests**

- For a given saturation level, reducing particle size in the sample resulted in a more stabilized behavior.
- Spherical particles with rough texture showed more stabilized behavior under similar conditions.
- For a certain size of the particle, higher regions of full saturation resulted in a larger size of the cavity, and eventually collapse if the saturation level was high enough.
- Glass beads with a mean diameter of 1.7mm could not sustain a stable cavity under any saturation level.
- The height of the cavity can be controlled by the initial water level of the specimen; however, the width of the cavity is dependent upon the density and shape characteristics of the material.
- Samples with higher densities showed better stability under cavity formation for similar conditions.
- The stability of the non-spherical glass beads (clumped) was much higher compared to the spherical glass beads.
- Glass beads with a mean particle diameter of 0.2mm could not demonstrate any stable cavity formation due to the higher residual moisture contents. The permeability of the smaller sized particles is much lower compared to the larger particles, resulting in higher retention of moisture. Thus, a higher saturation level resulted in weak capillary forces and eventually in a collapsed sample.

11.2.7 **Numerical simulations on cavity stability**

- Both width and the height of the cavity are important for the stability of a sample.
- It is difficult for the spherical glass beads to maintain a stable cavity due to the very high slippage due to a small friction coefficient. Furthermore, interaction with water can act as a lubricant to trigger the slippage of contacts.
- Non-spherical particles showed better stability compared to the spherical particles under similar boundary conditions and input parameters.

- The regions around the cavity surface were observed to have no strong force chains and the particles showed connectivity through capillary forces only.
- The cavity stability chart for numerical simulations matched with the chart being used in practice.
- Higher saturation of samples showed more dynamic behavior compared to the lower saturation samples.
- For the cases with a stable cavity, a clear strong force chain was observed around the cavity perimeter.
- Wide cavities are more prone to the collapse of the top wall as they support a wider area against the gravitational effects.
- Tall cavities are more prone to side-wall collapse due to the absence of strong forces around the sides of the cavity.
- Kinetic energy plots can be used to determine the stability of the cavity under specified conditions.
- The suction tension model well captured the trend of experimental results for the numerical simulations.

11.2.8 Cavity surface loading

- The strength against cavity surface loading for spherical particles was observed to be significantly smaller compared to the clumped glass beads in the experimental tests due to the lack of particle interlocking.
- Cavity shape can affect the strength of the sample significantly, for the similar conditions of the samples.
- Clumped glass beads possess very high particle interlocking compared to the spherical glass beads.
- Peak stress in cavity surface loading tests was observed to be independent of the loading plate width, for both experimental and numerical cases.
- Loading rate dependency was seen during experimental cavity surface loading tests for the peak stress of the sample. However, the residual strength was independent of the loading rate.
- The loading rate dependency was observed for all samples with saturated or unsaturated conditions, either with a base cavity or without a cavity, except for the dry condition that did not show any such behavior.

- For the samples with uniformly unsaturated conditions, rate dependency was also observed, resulting in that capillary forces can also show a rate-dependent behavior. However, the detailed mechanism requires further investigation.
- Similar to experimental results, DEM simulations showed a loading rate dependency on peak stress.
- DEM simulations also showed the loading rate dependency for the samples with partially saturated conditions, with or without the cavity.
- DEM simulations with dry conditions did not show any change in stress with changing loading rates.
- Rupture distance in the capillary force model can affect the overall behavior of the sample. A smaller rupture distance makes the behavior of the sample more brittle.
- Reducing rupture distance reduces the peak stress under surface loading tests.
- For higher loading rates, different rupture distance results in more diverged load-settlement plots.
- The effect of rupture distance becomes reduced by reducing the loading rate. In any condition, the larger rupture distance yields higher peak stress for the surface loading simulations.

11.2.9 Capillary force model

- Under dry conditions, neither the experimental cases nor the numerical simulations could produce a stable cavity formation using both spherical and non-spherical particles
- To incorporate the capillary forces, a suction-tension model was introduced and utilized in the DEM simulations.
- The new suction-tension model could capture the cavity stability trend, as observed in the experimental results on glass beads.
- The new model also captured the essence of cavity surface loading and the failure planes were identical as observed in the experimental results.
- The model was validated with other famous models being used in powder technology, that differed minutely with the current model.
- The bulging behavior around the loading plate as seen in experimental results was also captured by the DEM simulations.

- The particle vector plot showed that the particles at the sides of the loading plate move laterally and force the neighboring particles to bulge up.

11.2.10 Soil arching under cavity conditions

- For the stable cavity conditions, strong arching forces are observed around the cavity surface.
- Capillary forces are dominant in the area near the perimeter of the cavity. No arching was seen in that area.
- Arching was verified in stable cavity cases with the help of both strong contact force distribution and the 2nd order fabric distribution.
- For the cases with collapsing behavior of the cavity, the strong forces reached the surface of the sample, creating a difference in the force distribution at the surface of the sample and resulting in sample collapse.

11.3 Recommendations

Although an effort was made to thoroughly investigate the arching phenomenon under trapdoor and cavity formation conditions, both experimentally and numerically, there are always some aspects requiring further examination. Below are some of the work that needs to be improved for a better understanding of soil arching.

- The Model tests need to be performed for a wide range of materials, differing both in size, shape and at different relative densities
- The model trapdoor test apparatus could not perform the tests at different trapdoor configurations due to the limitation in construction and other reasons. If possible, the number of base plates, with the sensor, should be increased to explore further configuration possibilities.
- Another limitation of the apparatus was that only dry materials could be tested. The arching can be affected by the presence of capillary force due to water. A sealed soil chamber could be of great importance for understanding the arching mechanism in unsaturated conditions.
- The model cavity test apparatus can be installed with load cells at the base to determine the stress redistribution once the cavity is formed.

- The capillary force model used in this study although captured the general behavior of the model tests. However, further improvements can be done in order to have a better quantitative analysis.
 - Rupture distance can be correlated with the particle size and shape, along with the particle material properties.
 - The model can be improved to incorporate initial saturated condition and then the saturation drop can be taken as a factor of time, that is based upon the void ratio and particle size.
 - The model can also be improved to incorporate the weight of water with the saturation level of the sample.
 - As the presence of water can act as a lubricant as well, the drop in inter-particle friction with the saturation level can also be incorporated.
- The current study involved using spherical and non-spherical particles. Non-spherical particles consisted of clumped spherical particles touching each other to result in a rigid body. However, accurate particle shape is of prime importance to the correctness of analyses. Many researchers are working on simulating the exact particle shape though it is numerically very expensive. In the future, an effort can be made to model a more representative shape of the particle to further reduce the quantitative gap between experimental and numerical results.

REFERENCES

- Abedi, S., & Mirghasemi, A. A. (2011). Particle shape consideration in numerical simulation of assemblies of irregularly shaped particles. *Particuology*, 9(4), 387–397. <https://doi.org/10.1016/j.partic.2010.11.005>
- Abraham, D. M., & Wirahadikusumah, R. (1999). Development of prediction models for sewer deterioration. In *Proceedings of the Eighth International Conference on Durability of building materials and components* (pp. 1257–1268). Vancouver.
- Adachi, T., Kimura, M., Nishimura, T., & Koya, N. (1997). Trap door experiment under centrifugal conditions. In *Deformation and progressive failure in geomechanics* (pp. 725–730). Nagoya, Japan.
- Altuhafi, F., Matthew, C., & Vasiliki, G. (2016). Effect of Particle Shape on the Mechanical Behavior of Natural Sands. *Journal of Geotechnical and Geoenvironmental Engineering*, 142(12), 4016071. [https://doi.org/10.1061/\(ASCE\)GT.1943-5606.0001569](https://doi.org/10.1061/(ASCE)GT.1943-5606.0001569)
- Altuhafi, F., O’Sullivan, C., & Cavarretta, I. (2013). Analysis of an image-based method to quantify the size and shape of sand particles. *Journal of Geotechnical and Geoenvironmental Engineering*, 139(8), 1290–1307. [https://doi.org/10.1061/\(ASCE\)GT.1943-5606.0000855](https://doi.org/10.1061/(ASCE)GT.1943-5606.0000855)
- Bagherzadeh-Khalkhali, A., & Mirghasemi, A. A. (2009). Numerical and experimental direct shear tests for coarse-grained soils. *Particuology*, 7(1), 82–91. <https://doi.org/10.1016/j.partic.2008.11.006>
- Bagherzadeh-Khalkhali, A., Mirghasemi, A. A., & Mohammadi, S. (2008). Micromechanics of breakage in sharp-edge particles using combined DEM and FEM. *Particuology*, 6(5), 347–361. <https://doi.org/10.1016/j.partic.2008.07.002>
- Balkaya, M., Moore, I. D., & Sağlam, A. (2012). Study of non-uniform bedding due to voids under jointed PVC water distribution pipes. *Geotextiles and Geomembranes*, 34, 39–50. <https://doi.org/10.1016/j.geotexmem.2012.01.003>
- Barbosa, R., & Ghaboussi, J. (1992). Discrete finite element method. *Engineering Computations*, 9, 253–266. <https://doi.org/10.1108/eb023864>

- Baudouin, G., Thorel, L., & Rault, G. (2010). 3D load transfer in pile-supported earth platforms over soft soils: Centrifuge modeling. In *Physical Modelling in Geotechnics - Proceedings of the 7th International Conference on Physical Modelling in Geotechnics 2010, ICPMG 2010* (pp. 1303–1308). <https://doi.org/10.1201/b10554-217>
- Behringer, R. P., Daniels, K. E., Majmudar, T. S., & Sperl, M. (2008). Fluctuations, correlations and transitions in granular materials: Statistical mechanics for a non-conventional system. In *Philosophical Transactions of the Royal Society A: Mathematical, Physical and Engineering Sciences*. <https://doi.org/10.1098/rsta.2007.2106>
- Belytschko, T., Liu, W. K., & Moran, B. (2000). *Nonlinear finite elements for continua and structures*. *Choice Reviews Online*. Wiley, New York. <https://doi.org/10.5860/choice.38-3926>
- Benahmed, N., & Bonelli, S. (2012). Internal erosion of cohesive soils: laboratory parametric study. In *ICSE6 Paris*. Paris, France.
- Bowden, F. P., Tabor, D., & Palmer, F. (1951). The Friction and Lubrication of Solids. *American Journal of Physics*, 19(7), 428. <https://doi.org/10.1119/1.1933017>
- Burenkova, V. V. (1993). Assessment of suffusion in non-cohesive and graded soils. In *First International Conference “Geo-Filters”* (pp. 357–360). Karlsruhe, Germany.
- Burn, S., Desilva, D., Eiswirth, M., Hunaidi, O., Speers, A., & Thornton, J. (1999). Pipe Leakage – Future Challenges and Solutions. In *Pipes Wagga Wagga*. Wagga, Australia.
- Chang, D. S., & Zhang, L. M. (2013). Extended internal stability criteria for soils under seepage. *Soils and Foundations*, 53(4). <https://doi.org/10.1016/j.sandf.2013.06.008>
- Chevalier, B., Combe, G., & Villard, P. (2009). Experimental and numerical study of the response of granular layer in the trap-door problem. In *AIP Conference Proceedings*. <https://doi.org/10.1063/1.3180010>
- Chevalier, B., Combe, G., & Villard, P. (2008). Experimental and numerical studies of load transfers and arching effect. In *International Association for Computer Methods and Advances in Geomechanics (IACMAG)*.
- Chevalier, Bastien, & Otani, J. (2011). Arching observation in three-dimensional trapdoor problem with x-ray ct and discrete element method. *Soils and Foundations*. <https://doi.org/10.3208/sandf.51.459>

- Costa, Y. D., Zornberg, J. G., Bueno, B. S., & Costa, C. L. (2009). Failure Mechanisms in Sand over a Deep Active Trapdoor. *Journal of Geotechnical and Geoenvironmental Engineering*. [https://doi.org/10.1061/\(ASCE\)GT.1943-5606.0000134](https://doi.org/10.1061/(ASCE)GT.1943-5606.0000134)
- Cui, L., & O'Sullivan, C. (2006). Exploring the macro- and micro-scale response of an idealised granular material in the direct shear apparatus. *Geotechnique*, 56(7), 455–468. <https://doi.org/10.1680/geot.2006.56.7.455>
- Cundall, P. A. (1987). Distinct element models of rock and soil structure. *Analytical and Computational Methods in Engineering Rock Mechanics*, 129–163.
- Cundall, P. A., & Strack, O. D. L. (1979). A discrete numerical model for granular assemblies. *Geotechnique*, 29(1), 47–65. <https://doi.org/10.1680/geot.1979.29.1.47>
- Derjaguin, B. (1934). Friction and adhesion IV. The theory of adhesion of small particles. *Kolloid-Zeitschrift*. <https://doi.org/10.1007/BF01433225>
- Dewoolkar, M. M., Santichaianant, K., & Ko, H.-Y. (2007). Centrifuge modeling of granular soil response over active circular trapdoors. *Soils and Foundations*. <https://doi.org/10.3208/sandf.47.931>
- Dong, Y., Fatahi, B., Khabbaz, H., & Kamruzzaman, A. H. M. (2018). Investigating Effects of Particle Scaling for Cavity Expansion Simulation Using Discrete Element Method. In *Proceedings of GeoShanghai 2018 International Conference: Fundamentals of Soil Behaviours*. https://doi.org/10.1007/978-981-13-0125-4_104
- Dutta T., T. (2019). Effects of grain characteristics on the anisotropic mechanical properties evaluated by elastic waves. Ph.D. Thesis in Civil Engineering, the University of Tokyo, Japan.
- Ebizuka, H. (2010). Trapdoor tests for the evaluation of earth pressure on a buried structure in embankment and the visualization of stress distribution in a model ground. Masters thesis, the University of Tokyo.
- Elhoud, A. M. (2012). Internal degradation of buried sewage pipe causes sinkhole in a main road. *Indian Concrete Journal*, 86(5), 52–56.
- Ellis, E., & Aslam, R. (2009a). Arching in piled embankments: comparison of centrifuge tests and predictive methods - part 1 of 2. *Ground Engineering*, 42(7), 28–31.
- Ellis, E., & Aslam, R. (2009b). Arching in Piled Embankments: comparison of centrifuge tests

- and predictive methods part 2 of 2. *Ground Engineering*, 42(6), 34–38.
[https://doi.org/10.1061/\(ASCE\)0733-9410\(1996\)122:4\(318\)](https://doi.org/10.1061/(ASCE)0733-9410(1996)122:4(318))
- Enomoto, T., Koseki, J., Tatsuoka, F., & Sato, T. (2016). Rate-dependent behaviour of undisturbed gravelly soil. *Soils and Foundations*, 56(3), 547–558.
<https://doi.org/10.1016/j.sandf.2016.04.018>
- Eskişar, T., Otani, J., & Hironaka, J. (2012). Visualization of soil arching on reinforced embankment with rigid pile foundation using X-ray CT. *Geotextiles and Geomembranes*, 32, 44–54. <https://doi.org/10.1016/j.geotexmem.2011.12.002>
- Evans, C. H. (1984). *An examination of arching in granular soils*. Retrieved from <http://hdl.handle.net/1721.1/45181>
- Fannin, R. J., & Moffat, R. (2006). Observations on internal stability of cohesionless soils. *Geotechnique*, 56(6), 497–500. <https://doi.org/10.1680/geot.2006.56.7.497>
- Farouk, A., Lamboj, L., & Kos, J. (2004). A numerical model to predict matric suction inside unsaturated soils. *Acta Polytechnica*, 44(4), 3–10.
- Feld, J. (1948). Early history and bibliography of soil mechanics. *Proceedings, Second International Conference on Soil Mechanics and Foundation Engineering, Rotterdam, 1*, 1–7.
- Fisher, R. A. (1928). Further note on the capillary forces in an ideal soil. *The Journal of Agricultural Science*, 18(3), 406–410. <https://doi.org/DOI: 10.1017/S0021859600019432>
- Fredlund, D. G., Sheng, D., & Zhao, J. (2011). Estimation of soil suction from the soil-water characteristic curve. *Canadian Geotechnical Journal*. <https://doi.org/10.1139/T10-060>
- Gallage, C. P. K., & Uchimura, T. (2010). Effects of dry density and grain size distribution on soil-water characteristic curves of sandy soils. *SOILS AND FOUNDATIONS*, 50(1), 161–172. <https://doi.org/10.3208/sandf.50.161>
- Galve, J. P., Gutiérrez, F., Guerrero, J., Alonso, J., & Diego, I. (2012). Optimizing the application of geosynthetics to roads in sinkhole-prone areas on the basis of hazard models and cost-benefit analyses. *Geotextiles and Geomembranes*, 34, 80–92.
<https://doi.org/10.1016/j.geotexmem.2012.02.010>
- Garnier, J., Gaudin, C., Springman, S. M., Culligan, P. J., Goodings, D., König, D., ... Thorel, L. (2007). Catalogue of scaling laws and similitude questions in geotechnical centrifuge

- modelling. *International Journal of Physical Modelling in Geotechnics*, 7(3), 1–24. <https://doi.org/10.1680/ijpmg.2007.070301>
- Gianino, C. (2006). Measurement of surface tension by the dripping from a needle. *Physics Education*, 41(5), 440–444. <https://doi.org/10.1088/0031-9120/41/5/010>
- Gras, J. P., Delenne, J. Y., & El Youssoufi, M. S. (2013). Study of capillary interaction between two grains: A new experimental device with suction control. *Granular Matter*. <https://doi.org/10.1007/s10035-012-0388-2>
- Graton, L. C., & Fraser, H. J. (1935). Systematic Packing of Spheres: With Particular Relation to Porosity and Permeability. *The Journal of Geology*, 43(8), 785–909. <https://doi.org/10.1086/624386>
- Guo, S., Shao, Y., Zhang, T., Zhu, D. Z., & Zhang, Y. (2013). Physical modeling on sand erosion around defective sewer pipes under the influence of groundwater. *Journal of Hydraulic Engineering*, 139(12), 1247–1257. [https://doi.org/10.1061/\(ASCE\)HY.1943-7900.0000785](https://doi.org/10.1061/(ASCE)HY.1943-7900.0000785)
- Haines, W. B. (1927). Studies in the physical properties of soils: IV. A further contribution to the theory of capillary phenomena in soil. *The Journal of Agricultural Science*, 17(2), 264–290. <https://doi.org/DOI:10.1017/S0021859600018499>
- Hakon, W. (1935). Volume, Shape, and Roundness of Quartz Particles. *The Journal of Geology*. <https://doi.org/10.2307/30056250>
- Handy, R. L. (1985). The Arch in Soil Arching. *Journal of Geotechnical Engineering*. [https://doi.org/10.1061/\(ASCE\)0733-9410\(1985\)111:3\(302\)](https://doi.org/10.1061/(ASCE)0733-9410(1985)111:3(302))
- Hart, R., Cundall, P. A., & Lemos, J. (1988). Formulation of a three-dimensional distinct element model-Part II. Mechanical calculations for motion and interaction of a system composed of many polyhedral blocks. *International Journal of Rock Mechanics and Mining Sciences And*, 25, 117–125. [https://doi.org/10.1016/0148-9062\(88\)92294-2](https://doi.org/10.1016/0148-9062(88)92294-2)
- Härtl, J., & Ooi, J. Y. (2011). Numerical investigation of particle shape and particle friction on limiting bulk friction in direct shear tests and comparison with experiments. *Powder Technology*, 212(1), 231–239. <https://doi.org/10.1016/j.powtec.2011.05.022>
- Hayano, K., Matsumoto, M., Tatsuoka, F., & Koseki, J. (2001). Evaluation of time-dependent deformation properties of sedimentary soft rock and their constitutive modeling. *Soils and Foundations*, 41(2), 21–38. https://doi.org/10.3208/sandf.41.2_21

- Head, K. H. (1994). *Manual of soil laboratory testing. Vol. 2. Permeability, shear strength and compressibility tests. Geoderma*. [https://doi.org/10.1016/0016-7061\(95\)90001-2](https://doi.org/10.1016/0016-7061(95)90001-2)
- Hertz, H. (1882). Ueber die Berührung fester elastischer Körper. *Journal Fur Die Reine Und Angewandte Mathematik*, 92, 156–171. <https://doi.org/10.1515/crll.1882.92.156>
- Holtzman, R., Silin, D. B., & Patzek, T. W. (2008). Mechanical properties of granular materials: A variational approach to grain-scale simulations. *International Journal for Numerical and Analytical Methods in Geomechanics*, 33(3), 391–404. <https://doi.org/10.1002/nag.725>
- Hornbaker, D. J., Albert, R., Albert, I., Barabasi, A. L., & Schiffer, P. (1997). What keeps sandcastles standing? [4]. *Nature*, 387, 765–767. <https://doi.org/10.1038/42831>
- Huang, X., Hanley, K. J., O’Sullivan, C., & Kwok, C. Y. (2014a). Exploring the influence of interparticle friction on critical state behaviour using DEM. *International Journal for Numerical and Analytical Methods in Geomechanics*, 38, 1276–1296. <https://doi.org/10.1002/nag.2259>
- Huang, X., Hanley, K. J., O’Sullivan, C., & Kwok, F. C. Y. (2014b). Effect of sample size on the response of DEM samples with a realistic grading. *Particuology*, 15, 107–115. <https://doi.org/10.1016/j.partic.2013.07.006>
- Iglesia, G. R., Einstein, H. H., & Whitman, R. V. (2013). Investigation of Soil Arching with Centrifuge Tests. *Journal of Geotechnical and Geoenvironmental Engineering*, 140(2), 04013005. [https://doi.org/10.1061/\(asce\)gt.1943-5606.0000998](https://doi.org/10.1061/(asce)gt.1943-5606.0000998)
- Iglesia, G. R., Einstein, H. H., & Whitman, R. V. (2014). Investigation of soil arching with centrifuge tests. *Journal of Geotechnical and Geoenvironmental Engineering*, 140(2), 04013005. [https://doi.org/10.1061/\(ASCE\)GT.1943-5606.0000998](https://doi.org/10.1061/(ASCE)GT.1943-5606.0000998)
- Indiketiya, S., Jegatheesan, P., & Rajeev, P. (2017). Evaluation of defective sewer pipe-induced internal erosion and associated ground deformation using laboratory model test. *Canadian Geotechnical Journal*, 54, 1184–1195. <https://doi.org/10.1139/cgj-2016-0558>
- Indraratna, B., Nguyen, V. T., & Rujikiatkamjorn, C. (2011). Assessing the potential of internal erosion and suffusion of granular soils. *Journal of Geotechnical and Geoenvironmental Engineering*, 137(5), 550–554. [https://doi.org/10.1061/\(ASCE\)GT.1943-5606.0000447](https://doi.org/10.1061/(ASCE)GT.1943-5606.0000447)
- Itasca. (2007). PFC3D version 4.0 user manual. Itasca Consulting Group.

- Jensen Adrin, Fraser, K., Laird, G., Karajan, N., Han, Z., Teng, H., ... Trierweiler, J. O. (2014). Improving the Precision of Discrete Element Simulations through Calibration Models. *13 Th International LS-DYNA Users Conference*, 1–12. <https://doi.org/10.1002/aic>
- Jensen, R. P., Bosscher, P. J., Plesha, M. E., & Edil, T. B. (1999). DEM simulation of granular media-structure interface: Effects of surface roughness and particle shape. *International Journal for Numerical and Analytical Methods in Geomechanics*, 23, 532–547. [https://doi.org/10.1002/\(SICI\)1096-9853\(199905\)23:6<531::AID-NAG980>3.0.CO;2-V](https://doi.org/10.1002/(SICI)1096-9853(199905)23:6<531::AID-NAG980>3.0.CO;2-V)
- Johnson, K. L. (1985). *Contact Mechanics*. Cambridge University Press. <https://doi.org/https://doi.org/10.1017/CBO9781139171731>
- Kenney, T. C., & Lau, D. (1985). Internal stability of granular filters. *Canadian Geotechnical Journal*, 22(2), 215–225. <https://doi.org/10.1139/t85-029>
- Khatami, H., Deng, A., & Jaksa, M. (2019). An experimental study of the active arching effect in soil using the digital image correlation technique. *Computers and Geotechnics*. <https://doi.org/10.1016/j.compgeo.2018.12.023>
- Khosravi, M. H., Pipatpongsa, T., Takahashi, A., & Takemura, J. (2011). Arch action over an excavated pit on a stable scarp investigated by physical model tests. *Soils and Foundations*, 51(4), 723–735. <https://doi.org/10.3208/sandf.51.723>
- Kikumoto, M., Kimura, M., Kishida, K., & Adachi, T. (2011). Three dimensional trapdoor experiments and its numerical analyses on the mechanical behavior during tunnel excavation. *Doboku Gakkai Ronbunshu*. https://doi.org/10.2208/jscej.2003.750_145
- Kishino, Y. (1989). Investigation of quasi-static behavior of granular materials with a new simulation method. In *Proceedings of Japanese Society of Civil Engineers (in Japanese)* (pp. 97–106).
- Kolb, E., Mazozi, T., Clément, E., & Duran, J. (1999). Force fluctuations in a vertically pushed granular column. *European Physical Journal B*, 8, 483–491. <https://doi.org/10.1007/s100510050715>
- Kongsukprasrt, L., & Tatsuoka, F. (2005). Ageing and viscous effects on the deformation and strength characteristics of cement-mixed gravelly soil in triaxial compression. *Soils and Foundations*, 45(6), 55–74. <https://doi.org/10.3208/sandf.45.55>
- Konishi, J., Oda, M., & Nemat-Nasser, S. (1983). Induced anisotropy in assemblies of oval cross-sectional rods in biaxial compression. In *Studies in Applied Mechanics* (pp. 31–39).

<https://doi.org/10.1016/B978-0-444-42192-0.50010-4>

- Kuhn, M. R. (1999). Structured deformation in granular materials. *Mechanics of Materials*, 31(6), 407–429. [https://doi.org/10.1016/S0167-6636\(99\)00010-1](https://doi.org/10.1016/S0167-6636(99)00010-1)
- Kuhn, M. R., & Bagi, K. (2009). Specimen Size Effect in Discrete Element Simulations of Granular Assemblies. *Journal of Engineering Mechanics*, 135(6), 485–492. [https://doi.org/10.1061/\(asce\)0733-9399\(2009\)135:6\(485\)](https://doi.org/10.1061/(asce)0733-9399(2009)135:6(485))
- Kuwano, R., Hori, T., & Kohashi, H. (2006). Evaluation of loose ground surrounding a cavity due to outflow of soil. In *41st Japan Geotechnical Society Conference* (pp. 1785–1786). (in Japanese).
- Kuwano, Reiko, & Ebizuka, H. (2010). Trapdoor tests for the evaluation of earth pressure on a buried structure in an embankment. *SEISAN KENKYU*, 62(4), 339–342. <https://doi.org/10.11188/seisankenkyu.62.339>
- Ladanyi, B., & Hoyaoux, B. (1969). A study of the trap-door problem in a granular mass. *Canadian Geotechnical Journal*, 6(1), 1–15. <https://doi.org/10.1139/t69-001>
- Lai, H., Zheng, J., Zhang, R., & Cui, M. (2016). Visualization of the formation and features of soil arching within a piled embankment by discrete element method simulation 桩承式路堤中土拱结构的形成与形态特征离散元数值分析. *Journal of Zhejiang University-SCIENCE A*, 17(10), 803–817. <https://doi.org/10.1631/jzus.a1500302>
- Li, J., Cui, X. L., Chan, A. H. C., Kong, L. W., & Zhang, X. W. (2015). Numerical simulation of localised fluidisation due to a leaking pipe. In *Geomechanics from Micro to Macro - Proceedings of the TC105 ISSMGE International Symposium on Geomechanics from Micro to Macro, IS-Cambridge 2014*. <https://doi.org/10.1201/b17395-95>
- Lian, G., Thornton, C., & Adams, M. J. (1993). A theoretical study of the liquid bridge forces between two rigid spherical bodies. *Journal of Colloid And Interface Science*, 161, 138–147. <https://doi.org/10.1006/jcis.1993.1452>
- Lin, X., & Ng, T. T. (1997). A three-dimensional discrete element model using arrays of ellipsoids. *Geotechnique*, 47(2), 319–329. <https://doi.org/10.1680/geot.1997.47.2.319>
- Liu, S. H., & Sun, D. A. (2002). Simulating the collapse of unsaturated soil by DEM. *International Journal for Numerical and Analytical Methods in Geomechanics*. <https://doi.org/10.1002/nag.215>

- Lu, N., Godt, J. W., & Wu, D. T. (2010). A closed-form equation for effective stress in unsaturated soil. *Water Resources Research*, 46(5). <https://doi.org/10.1029/2009WR008646>
- Lu, N., Kaya, M., & Godt, J. W. (2014). Interrelations among the soil-water retention, hydraulic conductivity, and suction-stress characteristic curves. *Journal of Geotechnical and Geoenvironmental Engineering*. [https://doi.org/10.1061/\(ASCE\)GT.1943-5606.0001085](https://doi.org/10.1061/(ASCE)GT.1943-5606.0001085)
- Magnanimo, V., Ragione, L. La, Jenkins, J. T., Wang, P., & Makse, H. A. (2008). Characterizing the shear and bulk moduli of an idealized granular material. *EPL*, 81(3), 34006. <https://doi.org/10.1209/0295-5075/81/34006>
- Mamoru KIKUMOTO, Makoto KIMURA, Kiyoshi KISHIDA, & Takeshi TAMURA. (2004). Estimation of the Distributions of Earth Pressure around a Tunnel. *Journal of Tunnel Engineering, JSCE*, 14, 27–34. <https://doi.org/https://doi.org/10.11532/journalte2004.14.27>
- Marinho, F. A. M., & Chandler, R. J. (1994). On the Relationship Between Suction and Degree of Saturation of Soils. In *2 Simpósio sobre solos não saturados* (pp. 37–44). REcife, Brazil.
- Mason, G., & Clark, W. C. (1965). Liquid bridges between spheres. *Chemical Engineering Science*, 20(10), 859–866. [https://doi.org/10.1016/0009-2509\(65\)80082-3](https://doi.org/10.1016/0009-2509(65)80082-3)
- Matsushima, T., Saomoto, H., Matsumoto, M., Toda, K., & Yamada, Y. (2003). Discrete Element Simulation of an Assembly of Irregularly-Shaped Grains: Quantitative Comparison with Experiments. In *16th ASCE Engineering Mechanics Conference*.
- Matuttis, H. G., Luding, S., & Herrmann, H. J. (2000). Discrete element simulations of dense packings and heaps made of spherical and non-spherical particles. *Powder Technology*, 109(1), 278–292. [https://doi.org/10.1016/S0032-5910\(99\)00243-0](https://doi.org/10.1016/S0032-5910(99)00243-0)
- McNulty, J. W. (1965). *An Experimental Study of Arching in Sand*. Ph.D. Thesis in Civil Engineering, University of Illinois.
- Mindlin, R. D. (1949). Compliance of Elastic Bodies in Contact. *Journal of Applied Mechanics*, 16, 259–268.
- Mindlin, R. D., & Deresiewicz, H. (1953). Elastic Spheres in Contact Under Varying Oblique Forces. *American Society of Mechanical Engineers - Transactions - Journal of Applied Mechanics*, 20(3), 327–344.

- Mirghasemi, A. A., Rothenburg, L., & Matyas, E. L. (1997). Numerical simulations of assemblies of two-dimensional polygon-shaped particles and effects of confining pressure on shear strength. *Soils and Foundations*, 37(3), 43–52. https://doi.org/10.3208/sandf.37.3_43
- Mirghasemi, A. A., Rothenburg, L., & Matyas, E. L. (2002). Influence of particle shape on engineering properties of assemblies of two-dimensional polygon-shaped particles. *Geotechnique*, 52(3), 209–217. <https://doi.org/10.1680/geot.2002.52.3.209>
- Mitchell, J. K., & Soga, K. (1976). *Fundamentals of soil behavior. Fundamentals of Soil Behavior*. John Wiley and Sons, Inc. New York.
- Mohammadi, M. H., & Vanclooster, M. (2011). Predicting the Soil Moisture characteristic curve from particle size distribution with a simple conceptual model. *Vadose Zone Journal*, 10(2), 594–602. <https://doi.org/10.2136/vzj2010.0080>
- Monnet, J., Mahmutovic, D., Boutonnier, L., & Taïbi, S. (2017). A theoretical retention model for unsaturated uniform soils. *European Journal of Environmental and Civil Engineering*, 23(3), 345–360. <https://doi.org/10.1080/19648189.2016.1277376>
- Moore, I. . D. (2008). Assessment of Damage To Rigid Sewer Pipes and Erosion Voids in the Soil, and Implications for Design of Liners. In *North American Society for Trenchless Technology 2008 No-Dig Conference & Exhibition*. Dallas, Texas: North American Society for Trenchless Technology.
- Mukunok, T., Kumano, N., Otan, J., & Kuwano, R. (2009). Visualization of three dimensional failure in sand due to water inflow and soil drainage from defective underground pipe using x-ray CT. *Soils and Foundations*, 49(6), 959–968. <https://doi.org/10.3208/sandf.49.959>
- Mukunoki, T., Kumano, N., & Otani, J. (2012). Image analysis of soil failure on defective underground pipe due to cyclic water supply and drainage using X-ray CT. *Frontiers of Structural and Civil Engineering*, 6(2), 85–100. <https://doi.org/10.1007/s11709-012-0159-5>
- Munjiza, A. (2004). *The combined finite-discrete element method. The Combined Finite-Discrete Element Method*. John Wiley. <https://doi.org/10.1002/0470020180>
- Nasuno, S., Kudrolli, A., Bak, A., & Gollub, J. P. (1998). Time-resolved studies of stick-slip friction in sheared granular layers. *Physical Review E - Statistical Physics, Plasmas*,

- Fluids, and Related Interdisciplinary Topics*, 58(2), 2161–2171.
<https://doi.org/10.1103/PhysRevE.58.2161>
- Ng, T. T. (1994). Numerical simulations of granular soil using elliptical particles. *Computers and Geotechnics*, 16(2), 153–169. [https://doi.org/10.1016/0266-352X\(94\)90019-1](https://doi.org/10.1016/0266-352X(94)90019-1)
- Ng, T. T. (2006). Input parameters of discrete element methods. *Journal of Engineering Mechanics*, 132(7), 723–729. [https://doi.org/10.1061/\(ASCE\)0733-9399\(2006\)132:7\(723\)](https://doi.org/10.1061/(ASCE)0733-9399(2006)132:7(723))
- Ng, T. T., Zhou, W., Ma, G., & Chang, X. L. (2015). Damping and particle mass in DEM simulations under gravity. *Journal of Engineering Mechanics*, 141(6), 04014167. [https://doi.org/10.1061/\(ASCE\)EM.1943-7889.0000889](https://doi.org/10.1061/(ASCE)EM.1943-7889.0000889)
- NILIM, N. I. for L. and I. M. (2006). Annual report of waste water management and water quality control. Ministry of Land, Infrastructure and Transport, Japan.
- O’Sullivan, C. (2011). Particulate discrete element modelling: a geomechanics perspective. *International Journal of Geomechanics ASCE*. [https://doi.org/10.1061/\(ASCE\)GM.1943-5622.0000024](https://doi.org/10.1061/(ASCE)GM.1943-5622.0000024).
- O’Sullivan, C., & Bray, J. D. (2001). A comparative evaluation of two approaches to discrete element modeling of particulate media. In *Proceedings of the Fourth International Conference on Discontinuous Deformation* (pp. 97–110). University of Glasgow, Scotland, UK.
- Ohara, Y., Kuwano, R., & Sera, R. (2019). A study on expansion and collapse of subsurface cavities for risk evaluation of road cave-ins. *Engineering for Resilient Society, Institute of Industrial Science, the University of Tokyo*, 52.
- Otsubo, M., Ali, U., & Kuwano, R. (2018). Discrete element method analysis on loosening of surrounding subsoil associated with cavity creation. In *Japan Society of Civil Engineers 2018 Annual Meeting* (pp. 283–284). Sapporo, Japan.
- Otsubo, M., Kuwano, R., Ali, U., & Ebizuka, H. (2018). Trapdoor model test and DEM simulation associated with arching. In *Physical Modelling in Geotechnics*. <https://doi.org/10.1201/9780429438660-29>
- Otsubo, Masahide, O’Sullivan, C., & Shire, T. (2017). Empirical assessment of the critical time increment in explicit particulate discrete element method simulations. *Computers and Geotechnics*, 86, 67–79. <https://doi.org/10.1016/j.compgeo.2016.12.022>

- Paikowsky, S. G., & Tien, H. S. (2002). Experimental examination of the arching mechanism on the micro level. *Geotechnical Special Publication*, 22–228. [https://doi.org/10.1061/40647\(259\)40](https://doi.org/10.1061/40647(259)40)
- Pardo, G. S., & Sáez, E. (2014). Experimental and numerical study of arching soil effect in coarse sand. *Computers and Geotechnics*. <https://doi.org/10.1016/j.compgeo.2014.01.005>
- Peck, R. B. (1969). Deep excavation and tunneling in soft ground. In *Seventh International Conference on Soil Mechanics and Foundation Engineering* (Vol. 1, pp. 225–258). Mexico City.
- Phillips, E. (n.d.). De l'équilibre des solides elastiques semblables. *C. R. Acad. Sci., Paris*, 68, 75–79.
- Plimpton, S. (1995). Fast parallel algorithms for short-range molecular dynamics. *Journal of Computational Physics*, 117(1), 1–19. <https://doi.org/10.1006/jcph.1995.1039>
- Proctor, R. V., & White, T. L. (1977). *Earth tunnelling with steel supports*. Commercial Shearing, Inc.
- PWRI, P. W. R. I. (2006). Investigation of cavity generation in ground around an underground model. Annual report of PWRI (in Japanese).
- Ramkumar, M., Kumaraswamy, K., Balasubramani, K., Abdul Rahaman, S., Jegankumar, R., Kumara Ganesh, U., ... Sivakumar, P. (2018). Discovery of buried historical structures in the Kaveri–Kollidam interfluve, southern India. *Archaeological Prospection*, 26(1), 73–88. <https://doi.org/10.1002/arp.1724>
- Renuka, I. H. S. (2012). *Evaluation of ground loosening behavior and mechanical properties of loosened sand associated with underground cavities*. Ph.D. Thesis in Civil Engineering, University of Tokyo.
- Rogers, C. J., & Britain, W. R. C. (Great. (1986). *Sewer Deterioration Studies: The Background to the Structural Assessment Procedure in the Sewerage Rehabilitation Manual*. Water Research Centre. Retrieved from <https://books.google.co.jp/books?id=pVNKNwAACAAJ>
- Rothenburg, L., & Bathurst, R. J. (1992). Micromechanical features of granular assemblies with planar elliptical particles. *Geotechnique*, 42(1), 79–95. <https://doi.org/10.1680/geot.1992.42.1.79>

- Rothenburg, L., & Kruyt, N. P. (2004). Critical state and evolution of coordination number in simulated granular materials. *International Journal of Solids and Structures*, 41(21), 5763–5774. <https://doi.org/10.1016/j.ijsolstr.2004.06.001>
- Rowe, P. W. (1962). The stress-dilatancy relation for static equilibrium of an assembly of particles in contact. In *Proceedings of the Royal Society of London. Series A. Mathematical and Physical Sciences* (Vol. 269, pp. 500–527). <https://doi.org/10.1098/rspa.1962.0193>
- Rui, R., van Tol, F., Xia, X. L., van Eekelen, S., Hu, G., & Xia, Y. you. (2016). Evolution of soil arching; 2D DEM simulations. *Computers and Geotechnics*, 73(March 2016), 199–209. <https://doi.org/10.1016/j.compgeo.2015.12.006>
- Sato, M., & Kuwano, R. (2010). Model tests for the evaluation of formation and expansion of a cavity in the ground. In *Physical Modelling in Geotechnics - Proceedings of the 7th International Conference on Physical Modelling in Geotechnics 2010, ICPMG 2010* (pp. 751–758). Beijing, China. <https://doi.org/10.1201/b10554-94>
- Sato, M., & Kuwano, R. (2013). Effects of buried structures on the formation of underground cavity. In *18th International Conference on Soil Mechanics and Geotechnical Engineering: Challenges and Innovations in Geotechnics, ICSMGE 2013* (pp. 1769–1772). Paris.
- Sato, Mari, & Kuwano, R. (2015). Influence of location of subsurface structures on development of underground cavities induced by internal erosion. *Soils and Foundations*. <https://doi.org/10.1016/j.sandf.2015.06.014>
- Scheel, M., Seemann, R., Brinkmann, M., Di Michiel, M., Sheppard, A., Breidenbach, B., & Herminghaus, S. (2008). Morphological clues to wet granular pilestability. *Nature Materials*, 7(3), 189–193. <https://doi.org/10.1038/nmat2117>
- Schofield, A. N. (1980). Cambridge Geotechnical Centrifuge Operations. *Geotechnique*, 30, 227–268. <https://doi.org/10.1680/geot.1980.30.3.227>
- Sekiguchi, H., Li, F. Y., Miyamoto, J., & Minakuchi, M. (2003). Experimental study on washout and cavity formation in granular backfill behind a seawall. In *38th Annual Japan Geotechnical Society Conference* (pp. 1191–1192). (in Japanese).
- Shahin, H. M., Nakai, T., Hinokio, M., & Yamaguchi, D. (2004). 3D effects on pressure and displacements during tunnel excavations. *Soils and Foundations*, 44(5), 37–49.

https://doi.org/10.3208/sandf.44.5_37

- Skempton, A. W., & Brogan, J. M. (1994). Experiments on piping in sandy gravels. *Geotechnique*, 44, 449–460. <https://doi.org/10.1680/geot.1994.44.3.449>
- Sloan, S. W., Assadi, A., & Purushothaman, N. (1990). Undrained stability of a trapdoor. *Géotechnique*, 40(1), 45–62. <https://doi.org/10.1680/geot.1990.40.1.45>
- Smith, W. O., Foote, P. D., & Busang, P. F. (1929). Packing of homogeneous spheres. *Physical Review*, 34(9), 1271–1274. <https://doi.org/10.1103/PhysRev.34.1271>
- Soltanbeigi, B., Podlozhnyuk, A., Papanicolopoulos, S. A., Kloss, C., Pirker, S., & Ooi, J. Y. (2018). DEM study of mechanical characteristics of multi-spherical and superquadric particles at micro and macro scales. *Powder Technology*, 329, 288–303. <https://doi.org/10.1016/j.powtec.2018.01.082>
- Spangler, M.G., & Handy, R. L. (1982). Soil Engineering. *Harper & Co. Publishing*.
- Stone, K. J. L., & Muir-Wood, D. (1992). Effects of dilatancy and particle size observed in model tests on sand. *Soils and Foundations*. <https://doi.org/10.1248/cpb.37.3229>
- Sun, X., & Sakai, M. (2018). A liquid bridge model for spherical particles applicable to asymmetric configurations. *Chemical Engineering Science*, 182, 28–43. <https://doi.org/10.1016/j.ces.2018.02.034>
- Tanaka, T., & Sakai, T. (1993). Progressive failure and scale effect of trap-door problems with granular materials. *Soils and Foundations*, 33(1), 11–22. <https://doi.org/10.3208/sandf1972.33.11>
- Tatsuoka, F., Dibenedetto, H., Enomoto, T., Kawabe, S., & Kongkitkul, W. (2008). Various viscosity types of geomaterials in shear and their mathematical expression. *Soils and Foundations*, 48(1), 41–60. <https://doi.org/10.3208/sandf.48.41>
- Tatsuoka, F., Ishihara, M., Di Benedetto, H., & Kuwano, R. (2002). Time-dependent shear deformation characteristics of geomaterials and their simulation. *Soils and Foundations*, 42(2), 103–129. https://doi.org/10.3208/sandf.42.2_103
- Terzaghi, K. (1936). Stress distribution in dry and in saturated sand above a yielding trap-door. *Proceedings, First International Conference on Soil Mechanics and Foundation Engineering, Cambridge, Massachusetts*, 307–311.
- Terzaghi, K. (1943). Arching in Ideal Soils. In *Theoretical Soil Mechanics* (pp. 66–76). John

- Wiley & Sons, Ltd. <https://doi.org/10.1002/9780470172766.ch5>
- Thongrapha, T., Fuenkajorn, K., & Daemen, J. J. K. (2015). Study of surface subsidence above an underground opening using a trap door apparatus. *Tunnelling and Underground Space Technology*, 46(February), 94–103. <https://doi.org/10.1016/j.tust.2014.11.007>
- Thornton, C. (2000). Numerical simulations of deviatoric shear deformation of granular media. *Geotechnique*, 50(1), 43–53. <https://doi.org/10.1680/geot.2000.50.1.43>
- Ting, J. M., Khwaja, M., Meachum, L. R., & Rowell, J. D. (1993). An ellipse-based discrete element model for granular materials. *International Journal for Numerical and Analytical Methods in Geomechanics*, 17, 603–623. <https://doi.org/10.1002/nag.1610170902>
- Tohda, J., & Hachiya, M. (2005). Response and design of buried pipeline subjected to differential ground settlement. In *16th ICSMGE* (pp. 1659–1662).
- Tohda, J., & Yoshimura, H. (2004). A new design method for buried pipes. In *15th ICSMGE* (pp. 1319–1322). Istanbul.
- Toll, D. G. (1988). *The behaviour of unsaturated compacted naturally occurring gravel*. Ph.D. Thesis, Imperial College London.
- Tourani, K., Mahboubi, R., & Seyedi Hosseininia, E. (2016). Discrete Element Method for Modeling the Mechanical Behavior of Unsaturated Granular Material. *Journal of Computational Methods In Engineering*, 35(1). <https://doi.org/10.18869/acadpub.jcme.35.1.157>
- Vanapalli, S., Sillers, W., & Fredlund, M. (1998). The meaning and relevance of residual state to unsaturated soils. In *51st Canadian Geotechnical Conference*. Alberta, Canada. <https://doi.org/10.1145/2010425.2010448>
- Vardoulakis, I., Graf, B., & Gudehus, G. (1981). Trap-door problem with dry sand: A statical approach based upon model test kinematics. *International Journal for Numerical and Analytical Methods in Geomechanics*. <https://doi.org/10.1002/nag.1610050106>
- Wan, C. F., & Fell, R. (2008). Assessing the potential of internal instability and suffusion in embankment dams and their foundations. *Journal of Geotechnical and Geoenvironmental Engineering*, 134(3), 401–407. [https://doi.org/10.1061/\(ASCE\)1090-0241\(2008\)134:3\(401\)](https://doi.org/10.1061/(ASCE)1090-0241(2008)134:3(401))
- Wang, J.-P., Li, X., & Yu, H.-S. (2017). Stress–Force–Fabric Relationship for Unsaturated

- Granular Materials in Pendular States. *Journal of Engineering Mechanics*.
[https://doi.org/10.1061/\(asce\)em.1943-7889.0001283](https://doi.org/10.1061/(asce)em.1943-7889.0001283)
- Wang, J. P., Gallo, E., François, B., Gabrieli, F., & Lambert, P. (2017). Capillary force and rupture of funicular liquid bridges between three spherical bodies. *Powder Technology*, 305, 89–98. <https://doi.org/10.1016/j.powtec.2016.09.060>
- Wang, L., Leshchinsky, B., Evans, T. M., & Xie, Y. (2017). Active and passive arching stresses in $c'-\phi'$ soils: A sensitivity study using computational limit analysis. *Computers and Geotechnics*, 84(February), 47–57. <https://doi.org/10.1016/j.compgeo.2016.11.016>
- Wang, M. C., & Hsieh, C. W. (1987). Collapse load of strip footing above circular void. *Journal of Geotechnical Engineering*, 113(5), 511–515. [https://doi.org/10.1061/\(ASCE\)0733-9410\(1987\)113:5\(511\)](https://doi.org/10.1061/(ASCE)0733-9410(1987)113:5(511))
- Wang, R., Fu, P., Tong, Z., Zhang, J.-M., & Dafalias, Y. F. (2017). Strength anisotropy of granular material consisting of perfectly round particles. *International Journal for Numerical and Analytical Methods in Geomechanics*, 41(17), 1758–1778. <https://doi.org/10.1002/nag.2699>
- Wang, Z. Q., Zhang, Y. X., Wang, C. J., & Chen, Z. M. (2013). Mechanical analysis of soil arch and suitable spacing between cantilever piles. *Electronic Journal of Geotechnical Engineering*.
- Willett, C. D., Adams, M. J., Johnson, S. A., & Seville, J. P. K. (2000). Capillary bridges between two spherical bodies. *Langmuir*, 16(24), 9396–9405. <https://doi.org/10.1021/la000657y>
- Witt, W., Köhler, U., & List, J. (2004). Direct Imaging of Very Fast Particles Opens the Application of the Powerful (Dry) Dispersion for Size and Shape Characterization. In *PARTEC 2004*. Nürnberg, Germany.
- Yan, W. M. (2009). Fabric evolution in a numerical direct shear test. *Computers and Geotechnics*, 36(4), 597–630. <https://doi.org/10.1016/j.compgeo.2008.09.007>
- Yun-min, C., Wei-ping, C., & Ren-peng, C. (2008). An experimental investigation of soil arching within basal reinforced and unreinforced piled embankments. *Geotextiles and Geomembranes*. <https://doi.org/10.1016/j.geotexmem.2007.05.004>
- Zhang, C., & Lu, N. (2019). Unitary definition of matric suction. *Journal of Geotechnical and Geoenvironmental Engineering*, 145(2), 02818004–1.

[https://doi.org/10.1061/\(ASCE\)GT.1943-5606.0002004](https://doi.org/10.1061/(ASCE)GT.1943-5606.0002004)

Zhou, A., Wu, S., Li, J., & Sheng, D. (2018). Including degree of capillary saturation into constitutive modelling of unsaturated soils. *Computers and Geotechnics*, 95, 82–98. <https://doi.org/10.1016/j.compgeo.2017.09.017>

Zhu, H. P., Zhou, Z. Y., Yang, R. Y., & Yu, A. B. (2007). Discrete particle simulation of particulate systems: Theoretical developments. *Chemical Engineering Science*, 62(13), 3378–3396. <https://doi.org/10.1016/j.ces.2006.12.089>